Observation-Domain Sidereal Filtering for High-Rate GPS Precise Point Positioning

Christopher Leslie Edwin Atkins

Department of Civil, Environmental and Geomatic Engineering
University College London

August 2016

Supervisors:

Prof. Marek Ziebart
Dr. Paul Groves

Thesis submitted for the degree of Doctor of Philosophy

Declaration

I, *Christopher Atkins*, confirm that the work presented in this thesis is my own. Where information has been derived from other sources, I confirm that this has been indicated in the thesis.

.....

Abstract

Accurate and timely determination of coseismic displacement (the quasi-permanent displacement of the ground caused by an earthquake) is crucial for tsunami warning and situational awareness systems. Seismometers measure acceleration or velocity very precisely. However, the process of integrating such data to yield displacement data is difficult and error-prone. In contrast, The Global Positioning System (GPS) can measure displacement directly, but is also subject to errors, one of which is multipath. Multipath errors can lead to errors in the measurement of small displacements or obscure the displacement entirely.

Errors due to multipath are highly dependent on the geometry of GPS satellite orbits and surrounding reflectors relative to the receiving antenna itself. Each satellite has a ground track repeat period of approximately one sidereal day. Hence, this relative satellite-reflector geometry will repeat with the same period. Using this fact, it is possible to identify and remove the error signature induced by multipath by analysing data from adjacent days, yielding an improved time series of displacements and hence a more discernible coseismic offset. This process is commonly known as 'sidereal filtering'.

This thesis describes a sidereal filter algorithm that attempts to remove the multipath error signature from the GPS measurements themselves before processing them rather than from the resulting position time-series. It is shown to generally produce a more stable position time series over periods from a few tens to a few hundred seconds, remove high-frequency multipath error more effectively, yield better stability during satellite outages and measure small centimetre-level displacements more accurately than a position-domain sidereal filter. However, results are inconclusive when applying the algorithm to the measurement of the coseismic displacements of a real earthquake, but it is demonstrated that an observation-domain sidereal filter is better at enabling one to distinguish certain types of seismic wave from a position time series.

Acknowledgements

I would like to thank my supervisors, Prof. Marek Ziebart and Dr. Paul Groves for their support, advice and guidance throughout the course of this research.

I am very grateful to Dr. John Davis and Peter Whibberley of the National Physical Laboratory, Teddington, for providing a suitable rooftop venue for an experiment and Les Irwin for constructing the moving platform necessary for it. I would like to thank Dr. Alex Parkins for his generous assistance during the early stages of this project and other colleagues in the Space Geodesy and Navigation Laboratory for their help and advice. Finally, I would like to thank my family and friends for their unrelenting encouragement and support throughout this period of study.

GPS measurement data was kindly provided by Leica Geosystems UK. Further GPS data was provided by the University Navstar Consortium (UNAVCO) Facility with support from the National Science Foundation (NSF) and National Aeronautics and Space Administration (NASA) under NSF Cooperative Agreement No. EAR-0735156. Seismometer data was provided by the Incorporated Research Institutions for Seismology (IRIS). IRIS Data Services are funded through the Seismological Facilities for the Advancement of Geoscience and EarthScope (SAGE) Proposal of the National Science Foundation under Cooperative Agreement EAR-1261681.

This research was funded by a scholarship from University College London. This research is a result of collaboration between University College London and the Centre for the Observation and Modelling of Earthquakes, Volcanoes and Tectonics (COMET).

Contents

List of Figures

List of Tables

Chapter 1

Background

1.1 Chapter Overview

This chapter begins by describing the principal motivation behind this research: to improve earthquake measurement using the Global Positioning System (GPS). In section 1.3, the relevant aspects of the GPS are described in sufficient detail necessary for this thesis including a summary of the errors affecting GPS carrier phase measurements and two methods of processing them: positioning using double-differenced measurements and precise point positioning (PPP). Again, these are both described in sufficient terms to initially allow adequate comparison between the two with particular focus on their application to seismology. One particular source of error affecting GPS measurements, phase multipath interference, is described in detail in section 1.4 followed by a detailed description of one method used to reduce its effect, *sidereal filtering*, in section 1.5. A number of research questions are stated in section 1.7 and an overview of the remainder of the thesis is given in section 1.8.

1.2 Motivation

1.2.1 Accurate (and rapid) calculation of earthquake magnitude for tsunami early warning

At 00:58:53 Coordinated Universal Time (UTC) on 26$^{\text{th}}$ December 2004, a large earthquake of moment magnitude (M_{W}) 9.1 occurred roughly 80 km off the west coast of Sumatra, Indonesia.[1] The resulting tsunami caused the deaths of over 250,000 people (Sobolev et al. 2007). An initial magnitude estimate of M_{W} 8.0 was made by the Pacific Tsunami Warning Center (PTWC) eleven minutes after the earthquake origin time (Blewitt et al. 2006). After one hour, this estimate was revised upwards to M_{W} 8.5—an earthquake considered strong enough to trigger an ocean-wide

[1] Magnitude estimated by the United States Geological Survey (USGS)

tsunami but not thought to cause widespread destruction. Note that due to the logarithmic scale of moment magnitude, a M_W 9.0 earthquake releases much more energy—about 32 times more energy—than a M_W 8.0 earthquake. Even an increase of only one tenth in moment magnitude corresponds to an increase in energy of over 40%. So these initial estimates of earthquake magnitude were below the true magnitude by a considerable margin. Around 20–30 minutes after origin time, the tsunami had reached the coast of Indonesia (Sobolev et al. 2007), and after two hours, the tsunami had already reached the coastlines of Thailand and Sri Lanka.

Consider also the Tohoku-Oki earthquake of 11th March 2011. An initial magnitude estimate of M_W 8.1 was made by the Japan Meteorological Agency (JMA) 120 seconds after the start of the earthquake. The initial alert issued by the USGS put the magnitude at M_W 7.9 30 minutes after the earthquake began by which time the most destructive waves of the tsunami had already reached the coast of Japan. This magnitude estimate was revised upwards to M_W 8.8, then M_W 8.9 and eventually M_W 9.0 three days later. So despite the very prompt initial tsunami warning issued by the JMA, which estimated waves up to 6 m high, and undoubtedly saved many lives, the tsunami was actually much larger than expected with sea walls 10 m high being breached (Fraser et al. 2012).

The accurate, reliable and prompt estimation of the M_W and slip distribution of a large undersea earthquake is very important for reliable tsunami forecasting because any displacement of the sea floor is directly related to the size the tsunami (Sobolev et al. 2007). Damaging ocean-wide tsunamis are considered highly unlikely if $M_W < 8.5$ (Blewitt et al. 2009). However, the examples above illustrate that it can be very difficult to estimate the magnitude of very large earthquakes with sufficient accuracy and timeliness to be able to issue an appropriate alert. The reason for this lies with the limitations of the methods used to determine magnitude.

The local magnitude (M_L) scale, commonly known as the Richter scale, is used to estimate the 'size' of an earthquake using the maximum amplitude of seismic waves as measured by seismometers and their respective distances from an earthquake epicentre. However, this scale is not suited to the measurement of large earthquakes because seismometers tend to saturate above about M_L 7 (Crowell et al. 2013): Broadband seismometers are very sensitive and can detect seismic activity from distant earthquakes thousands of kilometres away, but they tend to 'clip' (i.e. go off the scale) if located close to the source of such large earthquakes where they can be subjected to extreme accelerations. The size of larger earthquakes are hence underestimated, which is obviously not ideal for a reliable early warning system. The magnitude of an earthquake can also be estimated by measuring the amplitude of surface waves (i.e. seismic waves that propagate through the earth's crust and upper mantle) that have a period of around 20 s. This is known as surface wave magnitude (M_S). However, this method under-estimates the magnitude of earthquakes above about M_S 8 (Doyle 1995) and is therefore also unsuitable for use in a reliable early warning system. Surface wave magnitude is discussed further in chapter 9.

Although often referred to as the 'Richter scale' by the media, the magnitude of earthquakes, particularly large earthquakes, is usually given in reference to the moment magnitude (M_W)

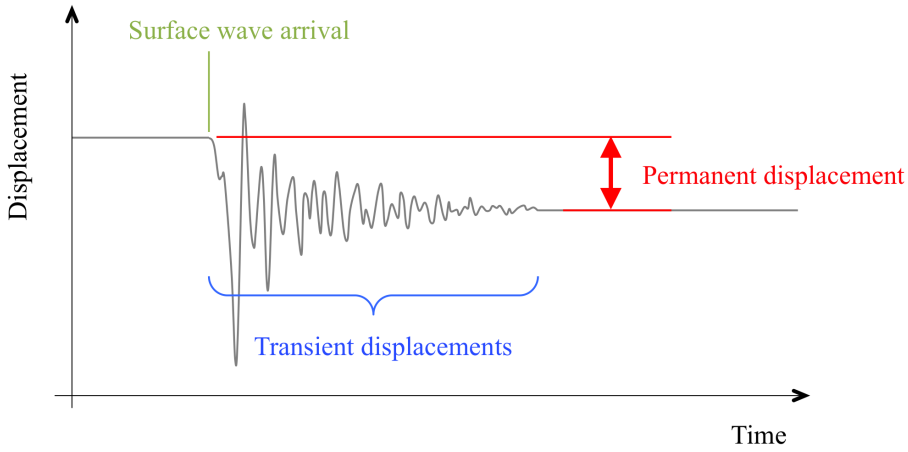

Figure 1.1 – Schematic diagram showing permanent and transient coseismic displacements in any dimension (east, north or vertical) of a monitoring station close to an earthquake epicentre. Unless otherwise stated, 'coseismic displacement' and 'coseismic offset' refer to the permanent displacement.

scale. This scale does not saturate at large magnitudes, but the calculation of that magnitude is more complicated. Equation (1.1), derived by Hanks & Kanamori (1979), describes how moment magnitude—a dimensionless number—is defined:

$$M_{\mathrm{W}} = \frac{2}{3} \log_{10} M_0 - 6.07 \tag{1.1}$$

where seismic moment (M_0), in units of Newton-metres, is calculated as follows:

$$M_0 = \mu A D \tag{1.2}$$

where: μ is the shear modulus of the rocks ($\mathrm{N/m^2}$)
A is the area of the rupture along the fault plane ($\mathrm{m^2}$)
D is the average displacement of area A (m)

Hence, to determine moment magnitude, it is necessary to determine the rupture area, have knowledge of the associated rock type(s), their rigidity and, crucially, accurate knowledge of the average amount of slip along the earthquake fault itself. One way to estimate this displacement is to measure the displacement of the ground at various locations around the rupture and use mathematical modelling to estimate the amount of slip along the fault plane. The *permanent* displacement of the ground caused by an earthquake is hereafter referred to as *coseismic offset* or *coseismic displacement*. Figure 1.1 illustrates the difference between a permanent displacement and the transient displacements associated with passing seismic waves.

However, seismic activity is generally monitored by seismometers. These measure the acceler-

ations or velocities experienced by the seismometer itself. As mentioned above, these instruments can be used to estimate earthquake magnitude by measuring the amplitude of the various types of seismic wave and estimating the distance to the earthquake epicentre. However, if the desire is to obtain *displacements* from velocity or acceleration data, then the integration of the data once or twice respectively becomes necessary. Unfortunately, the process of integration can magnify errors and distort the true seismic signal (Boore 2002, Emore et al. 2007). Strong-motion seismometers are less prone to saturation or 'clipping' when subjected to strong shaking, but they are still prone to a number of adverse effects including any tilting and rotation of the instrument causing biases and distortions in the acceleration measurements (Boore 2002, Graizer 2006, Allen & Ziv 2011). According to Graizer (2006), biases such as those attributed to the tilting of a seismometer will be magnified by integration potentially leading to large errors in the estimated coseismic displacements. Allen & Ziv (2011) state that much of the effect of these errors can be removed by applying high-pass filters, but points out that this would also remove any permanent offset in a displacement time series. Correcting for these errors is not trivial and the calculated coseismic displacements may still be inaccurate, which in turn can lead to an incorrect calculation of earthquake magnitude.

1.2.2 GNSS for earthquake magnitude estimation

One way to address the above shortcomings associated with seismometers is to use an alternative technology entirely: Global Navigation Satellite System (GNSS). The Global Positioning System (GPS) is one of a number of GNSS. Other examples include the Russian Globalnaya Navigatsionnaya Sputnikovaya Sistema (GLONASS), Galileo built by the European Union and the Chinese BeiDou satellite navigation system. The use of GNSS is beneficial to seismology because of its ability make up for the disadvantages of using seismometers mentioned above: GNSS is immune to the effects of tilt, can measure displacement directly and does not saturate when subject to strong seismic signals. The Global Positioning System (GPS) in particular has been used in seismological studies for a number of years, but only relatively recently as part of an earthquake and tsunami early warning system. One such example is the Real-time Earthquake Analysis for Disaster Mitigation Network (READI) research project, a prototype warning system, on the west coast of the United States (Sopac.ucsd.edu 2015).

Blewitt et al. (2006) demonstrated that a magnitude estimate of M_{W} 9.0 for the 2004 Sumatra-Andaman earthquake could have been obtained using only GPS data "up to 15 minutes after earthquake initiation" in a simulated real-time scenario. This was achieved by using GPS measurements from a relatively sparse network of 38 receivers at distances of up to 7,500 km from the epicentre. According to Vigny et al. (2005), this earthquake caused permanent displacements of 5–10 mm at locations over 3,000 km from the epicentre. In contrast, Japan possesses a much denser nationwide array of over 1,000 GPS monitoring stations with an average spacing of about 25 km, forming the country's GPS Earth Observation Network (GEONET), but it did not contribute to the country's tsunami early warning system at the time of the 2011 Tohoku-Oki earthquake (Hoechner et al. 2013). However, Wright et al. (2012) demonstrated that real-time GPS data

could have been used to calculate the moment magnitude as M_W 8.8 within only two minutes of the onset of the earthquake. In another example, Allen & Ziv (2011) demonstrated the ability of GPS to estimate the moment magnitude of the 2010 El Mayor–Cucapah earthquake as M_W 7.0 in less than a minute, which compares with the true magnitude of M_W 7.2.[2] This event was of course much smaller than the Tohoku-Oki earthquake and occurred far inland, hence there was no potential for tsunami generation. However it does demonstrate the ability of GNSS to determine the magnitude of a seismic event promptly and accurately: the largest measured coseismic offsets were on the order of a few centimetres rather than a few metres. Chapter 8 of this thesis describes the use of GPS measurements taken during this event to determine coseismic offsets at a number of different monitoring stations.

However, there are disadvantages to using GNSS as well: GNSS is much less sensitive to small movements of the ground than seismometers. Survey-grade GNSS technology can detect displacements of the order of a few centimetres. For example, the method used to determine earthquake magnitude described in Wright et al. (2012) involves waiting for a GPS receiver to move at least 8 cm before the initiating the process to avoid any false alarms. This is because a time series of displacements output by the method of precise point positioning, or PPP (which will be discussed in section 1.3.3), particularly in real-time, is accurate only to within a few centimetres: For example, (Li et al. 2013) calculated a root-mean-square error (RMSE) of within 5 cm horizontally and 7.6 cm vertically for a 5 Hz PPP position time series spanning two hours (without fixing phase ambiguities to integers—see sections 1.3.1 and 1.3.3). This is due to the fact that GNSS measurements are contaminated by a large number of time-varying error sources and each of them need careful consideration to minimise their effect. These errors include satellite orbit and clock errors, errors associated with signal propagation through the earth's atmosphere, receiver clock error, multipath interference, measurement noise, non-line-of-sight signal reception and cycle slips. These errors will be described in more detail in section 1.3.1.

Wright et al. (2012) demonstrated that the size of the 2011 Tohoku earthquake could be estimated as M_W 8.8 within 100 s of the onset using a subset of just ten monitoring stations with a spacing of around 100 km, despite the dense network of GPS monitoring stations in Japan. Blewitt et al. (2006) demonstrated that using data from a sparse network of 38 monitoring stations located between 300 km and 7,500 km from the epicentre, after only 15 minutes, could have produced a more accurate estimate of the magnitude of the 2004 M_W 9.1 Sumatra-Andaman earthquake as M_W 9.0. This would have been more accurate than that calculated by Pacific Tsunami Warning Center at the time of M_W 8.0. This could have been the case even if the closest station was 900 km distant. Placing more monitoring stations close to oceanic subduction zones, such as the 'GPS-shield' arrays proposed in Sobolev et al. (2007), would speed up the reliable determination of earthquake parameters. Wright et al. (2012) suggests that around 400 stations would be sufficient for a tsunami warning system for the whole of the Pacific rim. Such a system would be of great benefit for many of the countries in that area since they would likely not be able to afford the

[2]Magnitude estimated by the USGS

expense of installing a dense array of monitoring stations such as that of GEONET in Japan. It is however acknowledged that "additional stations would leave the inversion less susceptible to outliers" (with *inversion* meaning the determination of earthquake source parameters such as the location, depth and rupture direction from seismometer data (Nabelek 1984) and other data, such as GPS position time series, for example). Removing outliers and increasing the precision of the position time series is therefore important if a relatively sparse distribution of stations is to be used. This is because the true coseismic displacements at these stations may be very small, maybe only a few centimetres, and large errors in their measurement could lead to an incorrect calculation of earthquake magnitude. Indeed, Crowell et al. (2012) states that "a small spurious motion at a station far from the fault will lead to a large estimate of slip during the inversion." Therefore, many of the errors associated with GNSS have to be overcome, or their impact reduced, in order to facilitate a reliable calculation of earthquake magnitude. All of the error sources mentioned in the previous paragraph are active areas of research in the GNSS community. However, this thesis focuses on one particularly troublesome source of error: multipath interference.

Multipath, where a signal from a GNSS satellite reaches a receiving antenna via more than one path, is a significant error source in GNSS. In high-precision applications, multipath typically induces oscillating positioning errors with periods as small as a few tens of seconds and amplitudes of a few centimetres. Such errors will be described in more detail section 1.4. In the case of using GNSS for seismology, these small errors could inhibit the prompt and accurate measurement of small coseismic displacements. Of course, very large coseismic displacements of over 2 m were measured by the International GNSS Service (IGS) site at Mizusawa, Japan during the 2011 Tohoku-Oki earthquake despite being 140 km from the epicentre (Branzanti et al. 2013). However, as noted above, coseismic displacements may only amount to a few centimetres for smaller earthquakes or for receivers further from the epicentre.

As well as the measurement of permanent coseismic displacements, GNSS receivers stationed well away from the fault rupture, perhaps even by hundreds or thousands of kilometres, can be subjected to motion caused by transient surface waves with amplitudes of just a few centimetres and periods of tens of seconds. By coincidence, these are very much like errors associated with multipath interference. Therefore, there is a risk that multipath errors may be misinterpreted as seismic waves (Ogaja & Satirapod 2007). For stations that are thousands of kilometres from the epicentre of large earthquakes, such as the 2002 M_{W} 7.9 Denali Fault earthquake (Bilich, Cassidy & Larson 2008), or indeed for very large earthquakes, such as the 2010 Tohoku-Oki earthquake, there may be no measurable permanent coseismic displacement at all, but the small-amplitude transient displacements of surface waves can still be detectable, especially if steps have been taken to reduce multipath error.

This thesis focuses on one method of multipath mitigation in particular: *sidereal filtering*. This technique exploits the fact that GPS satellites in particular have a ground-track repeat time of approximately one sidereal period (around 23 hours 56 minutes) which means that, for a static receiver, error due to multipath interference will repeat at the same frequency. The error signature

can then be identified and removed from the resulting time series of positions. The technique will be described in more detail in section 1.5. However, it is necessary to cover the relevant aspects of the theory behind GPS beforehand in the following section.

As a consequence, this thesis focusses almost entirely on the Global Positioning System (GPS). Other GNSSs such as GLONASS, Galileo and BeiDou possess different ground-track repeat times and hence *sidereal* filtering cannot be applied. However, the possibility of applying similar techniques to these navigation systems is discussed in section 1.6.

1.3 GPS: a brief overview

This section describes the relevant aspects of the Global Positioning System (GPS) necessary for the understanding of the remainder of this thesis, i.e. to understand how GPS measurements are processed, how they are affected by phase multipath interference and to understand the methods used for the mitigation of this error. The reader is recommended to refer to textbooks such as Leick (2004) and Misra & Enge (2006) for a much more comprehensive description of GPS.

GPS is a satellite-based navigation system developed by the United States Department of Defense to provide positioning and timing, 24 hours a day in all weather conditions anywhere on earth with a direct line-of-sight view of four or more GPS satellites. The underlying principle of the system is that a user's receiver can calculate it's position by determining the ranges between it and a number of satellites in well-determined orbits around the earth. The first experimental satellites of the system were launched in 1978 and full operational capacity was declared in 1995. It was developed primarily for military applications but has spawned the development of a vast array of civilian applications that were not envisaged at inception.

GPS as a whole consists of three 'segments': the control segment, the space segment and the user segment. The control segment consists of two control stations, 16 monitoring stations and 12 uplink stations and is responsible for predicting the orbits of each of the satellites and characterising the behaviour of their on-board atomic clocks (Groves 2013*b*). This information in the form of a navigation message is made available to users via the GPS satellites themselves so that users can calculate the positions of the satellites and their respective clock offsets from GPS Time, which are necessary to calculate the user's position.

The space segment is made up of between 24 and 32 active satellites orbiting in six orbital planes each inclined at 55° with respect to the equator and spaced apart from each other by 60° of right ascension (Leick 2004). These orbits are elliptical (but near-circular) and have a semi-major axis of around 26,600 km. The control segment may also initiate manoeuvres to keep satellites in their correct orbits. During such manoeuvres, satellites are temporarily rendered unusable. This situation and other situations that cause satellite 'outages' have important consequences for the method described in this thesis to reduce the effect of multipath interference and is therefore addressed in chapter 6.

Being so high above the surface of the earth, multiple GPS satellites are visible to a user's

receiver at any one time. If at least four satellites are visible, the signals broadcast from these satellites can be used by a single receiver to calculate a geocentric three-dimensional position. Also, each satellite has an orbital period of nearly half a sidereal day. From the point of view of a user, this means that a satellite will rise above and fall below the horizon around four minutes earlier each day. Importantly, it is this repeatability that is exploited in this thesis to reduce positioning errors caused by multipath interference—see section 1.5 below.

Each GPS satellite carries three or four atomic clocks which provide a fundamental frequency of $f_0 = 10.23\,\text{MHz}$. All broadcast signals are derived from this frequency: the two carrier frequencies, L1 and L2, have frequencies of $f_0 \times 154 = 1575.42\,\text{MHz}$ and $f_0 \times 120 = 1227.60\,\text{MHz}$ respectively. As of October 2015, ten GPS satellites are broadcasting at a third navigation frequency, L5, which has a frequency of $f_0 \times 115 = 1176.45\,\text{MHz}$. More will do so as new satellites are launched as part of the modernisation of GPS. Modulated onto these carrier frequencies are pseudorandom noise codes (PRNs) and navigation messages using binary phase shift keying (BPSK). Until 2004, only the course/acquisition (C/A) code on the L1 frequency, frequently notated as C_1, was available for civilian users while an encrypted code, P(Y), was (and is) available to military users on both the L1 and L2 frequencies. These are frequently notated as P_1 and P_2, respectively. Since then, with the launch of newer satellites, other civil signals have become available on other frequencies including a second civil code, L2C, broadcast on the L2 frequency, and a third on the L5 frequency, which are both part of the modernisation of the GPS constellation. For 'stand-alone' positioning, having access to two codes enables a compatible receiver to largely eliminate the effect of signal delay caused by the ionosphere and hence increase accuracy (see section 1.3.1 below).

However, many survey-grade receivers are able to make P-code pseudorange measurements using sophisticated algorithms despite the encryption (Weinbach 2013). For a receiver that tracks C_1 and P_2 measurements, the C_1 measurements can be converted to P_1 measurements using the P1-C1 'differential code bias' provided by an analysis centre such as the Centre for Orbit Determination in Europe (CODE).

Continuing with the C/A code as an example: each C/A ranging code, unique to each satellite, is used by a receiver to calculate the time taken for the signal to travel to the receiver by correlating the received code with an identical PRN generated by the receiver itself. This 'time of flight' is multiplied by the speed of light to obtain a *pseudorange*. This is not equal to the true range for a number of reasons, not least because of the offset of the clock in the receiver from GPS system time. The navigation message contains sufficient information to enable the receiver to determine the position of a satellite at the time of transmission and correct the satellite clock offset from GPS system time. Assuming at least four satellites are visible, this data can be used to calculate the position, in three dimensions, of a receiver antenna to an accuracy of a few metres and the receiver's clock offset from GPS system time using the method of least squares. This technique is the most basic form of GNSS stand-alone positioning. A detailed description of how this is achieved is available in Leick (2004).

This technique is not sufficiently accurate to be of much use in a reliable earthquake or tsunami

early warning system. Fortunately, other techniques exist that are able to calculate a position to a much higher accuracy, but they require additional information in order to do so, as will be described shortly. Some of those techniques can determine a position to a precision at the centimetre level. To do this, a receiver must be able to observe the phase of the carrier wave which can be measured to a precision of 0.01–0.05 cycles (2 mm–1 cm) (Misra & Enge 2006). Each cycle is equivalent to the wavelength of the carrier frequency, which for the GPS L1 and L2 frequencies is approximately 19 cm and 24 cm respectively. Receivers able to measure the carrier phase are also designed to count the number of complete cycles accumulated since the start of a measurement period.

One method that can be used achieve centimetre-level accuracy is to calculate a position relative to one other static receiver with accurately known geocentric coordinates that is relatively close-by—generally within a few tens of kilometres. This three-dimensional vector between the two receivers is known as a 'baseline'. Such a strategy enables many of the errors affecting carrier phase measurements to be eliminated or to be dramatically reduced. This is achieved by forming 'double-differenced' phase measurements from raw phase measurements logged simultaneously at both the receiver(s)—a technique described briefly below. Double-differencing is not applied in this thesis, and reasons for this will be stated shortly in sections 1.3.2 and 1.3.3, but a general understanding of double-differencing is necessary in order to appreciate the history of sidereal filtering.

The 'single-baseline' technique mentioned above relies upon the assumption that many of the errors affecting carrier phase measurements at two closely-spaced receivers are highly correlated. This assumption becomes less valid as the length of the baseline increases. A solution to this problem would be to create a network of reference stations where the position of each receiver antenna is accurately known. By collating the simultaneous measurements from these receivers, the distance-dependent ionosphere and troposphere errors can be interpolated accurately for any location within the network. Appropriate corrections can then be broadcast to a suitably equipped user to determine the position of a receiver (often referred to as a 'rover' receiver) to within a few centimetres in near-real-time. This requirement constrains the receivers that make up the network to be placed with a spacing of up to about 50 km (Urquhart et al. 2012). However, the problem remains that the rover receiver must be located within the area covered by that network to avoid the decorrelation of errors. If larger station spacings are used, then models for ionosphere and troposphere errors have to be considered as well as natural phenomena not yet discussed such as ocean tide loading, solid earth tides and polar motion (Kouba 2009).

Another method used to achieve high accuracies is known as precise point positioning (PPP). This technique, introduced by Zumberge et al. (1997), can be used to calculate the position of a receiver antenna to an accuracy of within a few centimetres. PPP requires the precise modelling of satellite orbits and clocks. Such models are typically determined by a network of reference stations distributed globally and are then provided to the user using geostationary communications satellites or via the Internet. A PPP user does not need to be close to this network or any reference receiver. However, other errors, which would otherwise cancel when using double-differenced measurements

such as tropospheric delays and receiver clock offset, require careful modelling or are actually calculated along with position.

Brief outlines of the techniques of positioning using double-differenced measurements and PPP follow in sections 1.3.2 and 1.3.3 respectively, with a particular focus on the application of these to tsunami early warning. This is preceded by an overview of the errors affecting carrier phase measurements and a brief description of each the positioning techniques.

1.3.1 Pseudorange and carrier phase measurements

A pseudorange measurement P' and a phase measurement Φ', in units of metres, can be modelled as shown by the following observation equations:

$$P' = \rho - \mathbf{l}_r \cdot \hat{\mathbf{r}} + \mathbf{l}^s \cdot \hat{\mathbf{r}} + c(\delta t_r - \delta t^s) + O + I + T + M_P + B_{r,P} + B^s_P + \varepsilon_P \tag{1.3}$$

$$\Phi' = \rho - \mathbf{l}_r \cdot \hat{\mathbf{r}} + \mathbf{l}^s \cdot \hat{\mathbf{r}} + c(\delta t_r - \delta t^s) + O - I + T + M_\Phi + \lambda N + B_{r,\Phi} + B^s_\Phi + W + \varepsilon_\Phi \tag{1.4}$$

where:

ρ	is the *geometric range* between the receiver antenna reference point and the satellite centre of mass in metres.
$\mathbf{l}_r$	is a vector representing the receiver antenna phase centre offset from the receiver antenna reference point in metres.
$\mathbf{l}^s$	is a vector representing the satellite antenna phase centre offset from the satellite centre of mass in metres.
$\hat{\mathbf{r}}$	is a unit vector ($\|\hat{\mathbf{r}}\| = 1\,\text{m}$) from the receiver antenna to the satellite.
c	is the *speed of light*, 299,792,458 m/s.
δt_r	is the *receiver clock offset* from GPS system time in seconds.
δt^s	is the *satellite clock offset* from GPS system time in seconds.
O	is the line-of-sight *error in the satellite coordinates* or *ephemeris error*.
I	is the line-of-sight *ionospheric delay* in metres.
T	is the line-of-sight *tropospheric delay* in metres.
M_P, M_Φ	is the *multipath error* affecting the pseudorange and phase measurements respectively in metres.
λ	is the carrier wavelength in metres.
N	is the *integer phase ambiguity* in cycles.
$B_{r,P}$, B^s_P	are the *pseudorange biases* of the receiver and satellite respectively in metres.
$B_{r,\Phi}$, B^s_Φ	are the *phase biases* of the receiver and satellite respectively in metres.
W	is the *phase wind-up* error in metres.
ε_P, ε_Φ	is the *measurement noise* affecting the pseudorange and phase measurements respectively in metres.

Similar equations to (1.3) and (1.4) and their derivations can be found in textbooks such as Leick (2004) and Misra & Enge (2006). The terms that appear in these equations require some

clarification and an overview of the relative size of each in units of length, bearing in mind that centimetre-level precision is desirable for a tsunami monitoring system:

1. In this thesis, the ρ term in equations (1.3) and (1.4) above denote the true **geometric range** between the antenna reference point of a receiver r with instantaneous coordinates (x_r, y_r, z_r) at the time of signal reception and the centre of mass of a satellite s with coordinates (x^s, y^s, z^s) at the time of signal transmission in an earth-centred inertial (ECI) reference frame coincident with an earth-centred earth-fixed (ECEF) frame at the time of signal reception; i.e.

$$\rho = \sqrt{(x^s - x_r)^2 + (y^s - y_r)^2 + (z^s - z_r)^2} \tag{1.5}$$

   The coordinates of the satellite in the precise orbit products provided by the IGS or analysis centres such as the Centre for Orbit Determination in Europe (CODE) refer to the centre of mass of the satellite, not the antenna phase centre implied by the broadcast navigation message.

   However, the coordinates of a satellite in precise orbit products refer to a rotating ECEF coordinate system. Therefore, after using a precise orbit file to interpolate a satellite position at the time of signal transmission, that position must be rotated about the z-axis by an angle equal to the rotation of the earth during the time taken between the epoch of transmission and the epoch of reception t (Weinbach 2013), i.e.

$$\begin{pmatrix} x^s \\ y^s \\ z^s \end{pmatrix}_{\mathrm{ECI}(t)} = \begin{pmatrix} \cos(\omega\tau) & \sin(\omega\tau) & 0 \\ -\sin(\omega\tau) & \cos(\omega\tau) & 0 \\ 0 & 0 & 1 \end{pmatrix} \begin{pmatrix} x^s \\ y^s \\ z^s \end{pmatrix}_{\mathrm{ECI}(t-\tau)} \tag{1.6}$$

   where: ω is the earth's rate of rotation, $7.2921151467 \times 10^{-5}$ rad/s.
   τ is the time taken between signal transmission and reception (in seconds).
   $(x^s\ y^s\ z^s)^{\mathrm{T}}_{\mathrm{ECI}(t)}$ are the coordinates of the satellite at the time of signal transmission with respect to an ECI coordinate system coincident with an ECEF at the time of signal *reception*.
   $(x^s\ y^s\ z^s)^{\mathrm{T}}_{\mathrm{ECI}(t-\tau)}$ are the coordinates of the satellite at the time of signal transmission with respect to an ECI coordinate system coincident with an ECEF at the time of signal *transmission*.

   An initial estimate of τ is made by calculating the range between the satellite and an initial estimate of the receiver position and dividing by the speed of light. After applying equation (1.6), a refined estimate of τ can be made using the updated satellite position. Equation (1.6) is applied once more to yield final values for x^s, y^s and z^s.

2. The terms $\mathbf{l}_r \cdot \hat{\mathbf{r}}$ and $\mathbf{l}^s \cdot \hat{\mathbf{r}}$ represent the components of the receiver and satellite **antenna phase centre offsets** in the receiver-satellite direction. These are necessary because the

pseudorange and phase measurements P' and Φ' actually refer to the range between the satellite and receiver antenna phase centres rather than between an antenna reference point and a satellite's centre of mass. The size of these offsets can be as much as a few metres for GPS satellites and several centimetres for receiver antennas. For stand-alone positioning using only pseudorange measurements, the satellite antenna phase centre offset term is not required because the orbit implied by the broadcast navigation message refers to the 'ionosphere free' phase centre of the satellite anyway. (The ionosphere-free phase centre is a linear combination of the L1 and L2 phase centre offsets—see item 5 below). The receiver phase centre offsets are also ignored. However, antenna phase centre corrections are essential if high-accuracy positioning at the centimetre level using phase measurements is desired.

The location of a phase centre of a measurement relative to any fixed point on an antenna is not stationary: it can vary by a few millimetres depending on the signal frequency and the direction of the signal path relative to the orientation of the antenna. The location of the receiver antenna phase centre, for example, varies over time as the direction of the incoming signal changes as the satellite moves across the sky. Absolute antenna phase centre offsets with respect to a specified antenna reference point for various receiver antenna types can be interpolated for a specific elevation angle (and usually an azimuth angle) from Antenna Exchange Format (ANTEX) files available from the IGS. Phase center offsets for satellites with respect to its centre of mass can also be interpolated from ANTEX files.

For the remainder of this thesis, P and Φ will, respectively, denote pseudorange and phase measurements that have been corrected for phase centre offsets, i.e.:

$$P \;=\; P' \;+\; \mathbf{l}_r \cdot \hat{\mathbf{r}} \;-\; \mathbf{l}^s \cdot \hat{\mathbf{r}} \tag{1.7}$$

$$\Phi \;=\; \Phi' \;+\; \mathbf{l}_r \cdot \hat{\mathbf{r}} \;-\; \mathbf{l}^s \cdot \hat{\mathbf{r}} \tag{1.8}$$

Equations (1.7) and (1.8) can be used to simplify equations (1.3) and (1.4), respectively:

$$P = \rho + c(\delta t_r - \delta t^s) + O + I + T + M_P + B_{r,P} + B^s_P + \varepsilon_P \tag{1.9}$$

$$\Phi = \rho + c(\delta t_r - \delta t^s) + O - I + T + M_\Phi + \lambda N + B_{r,\Phi} + B^s_\Phi + W + \varepsilon_\Phi \tag{1.10}$$

3. According to the IGS (igscb.jpl.nasa.gov 2015), the predicted **satellite clock offsets** implied by the broadcast GPS navigation messages have a root-mean-square (RMS) of around 5 ns which is equivalent to about 1.5 m in range. For higher accuracies, the IGS provides 'final' satellite clock offset information with RMS of around 75 ps (2 cm) but with a latency of 12–18 days. For real-time applications, the IGS also provides 'ultra-rapid' (predicted) orbits that have a RMS of around 3 ns (0.9 m). A satellite's clock offset from GPS system time can vary by around 0.1 m over 100 s (Groves 2013*b*).

4. The accuracy of a **satellite's coordinates** implied by the GPS navigation message is only at the metre level. However, the IGS produces 'final' orbit files by post-processing and also produces real-time predicted 'ultra-rapid' orbit files with a quoted accuracy of 2.5 cm and 5 cm respectively. For positioning, the satellite's coordinates are assumed to be true and the ephemeris error term O in equations (1.3), (1.4), (1.9) and (1.10) ommitted.

5. Between about 50 km and 1,000 km above the surface of the earth lies a region of gases that become ionised (i.e. they form free electrons and ions) when subjected to solar radiation. This ionisation has the effect of delaying the modulated navigation signal but advancing the phase velocity of the carrier frequency itself. **Ionospheric delay** I is highly variable but can reach as high as several tens of metres (Leick 2004). About 99% of the ionospheric delay is inversely proportional to the square of the carrier frequency (Petrie et al. 2010) and so the effect can be largely eliminated by making pseudorange or phase measurements using the two frequencies (L1 and L2 in the case of GPS) and combining them to form 'ionosphere-free' pseudorange or phase measurements, P_{IF} and Φ_{IF} respectively:

$$\begin{aligned} P_{\mathrm{IF}} &= \frac{{f_1}^2}{{f_1}^2 - {f_2}^2} P_1 - \frac{{f_2}^2}{{f_1}^2 - {f_2}^2} P_2 \\ &\approx 2.546\ P_1 - 1.546\ P_2 \end{aligned} \tag{1.11}$$

$$\begin{aligned} \Phi_{\mathrm{IF}} &= \frac{{f_1}^2}{{f_1}^2 - {f_2}^2} \Phi_1 - \frac{{f_2}^2}{{f_1}^2 - {f_2}^2} \Phi_2 \\ &\approx 2.546\ \Phi_1 - 1.546\ \Phi_2 \end{aligned} \tag{1.12}$$

where: f_1, f_2 are the frequencies of the GPS L1 and L2 carriers, 1575.42×10^6 Hz and 1227.60×10^6 Hz, respectively.

P_1, P_2 are pseudorange measurements using code modulated onto the GPS L1 and L2 carriers, respectively, in metres.

Φ_1, Φ_2 are phase measurements of the GPS L1 and L2 carriers, respectively, in metres.

However, in the case of GPS, the formation of an ionosphere-free measurement using the L1 and L2 frequencies increases measurement noise by a factor of about three (Misra & Enge 2006). For example, if L1 and L2 measurements are made to the same level of precision with a standard deviation of $\sigma = \sigma_1 = \sigma_2$, then the standard deviation of an ionosphere-free measurement can be estimated:

$$\sigma_{\mathrm{IF}} = \sqrt{2.546^2\ {\sigma_1}^2 + 1.546^2\ {\sigma_2}^2} \ \approx\ 3\sigma \tag{1.13}$$

Forming an ionosphere-free measurement can also amplify multipath error (see section 1.4.3).

6. The **tropospheric delay** term T, which represents the signal delay caused by the atmosphere from ground level up to an altitude of around 60 km, can be divided into two components:

   - The hydrostatic (or 'dry') delay, T_{hd} is caused by the 'dry' gases—mostly nitrogen and oxygen—and accounts for around 90% of the total tropospheric delay. It can cause delays of around 2.4 m in the zenith direction at sea level (Leick 2004). Thankfully, the *zenith* hydrostatic delay, T_{zhd}, can be modelled to a reasonable level of accuracy by the user, either calculated using air pressure readings at the antenna, or by using a troposphere model from a third party, such as the *UNB3* model from the University of New Brunswick, Canada. Obviously, if the satellite is not at the zenith, the delay caused by the troposphere will increase because the signal has to pass through more of the atmosphere. A simple mapping function could be applied that multiplies the zenith hydrostatic delay by the co-secant of the elevation angle to the satellite. More sophisticated mapping functions have been developed such as the hydrostatic Global Mapping Function (GMF) (Boehm et al. 2006).
   - The 'wet' delay, T_{wd} is less amenable to a priori modelling. Although this component is much smaller than the hydrostatic component, it can cause signal delays of up to 40 cm in the zenith direction (Leick 2004) and can vary by in the region of 0.1–1.5 m over the course of 100 s (Groves 2013*b*). Again, a mapping function is used to translate a zenith wet tropospheric delay to one at a lower elevation angle. The wet GMF (Boehm et al. 2006) is one example.

7. **Multipath**, as mentioned above, is the phenomenon whereby a signal from a GNSS satellite reaches a receiving antenna via more than one path. The reflected signals interfere with direct signals causing errors in pseudorange and phase measurements. For pseudorange measurements, this is typically a few metres. For carrier phase measurements, the measurement error due to multipath interference, M_Φ, can reach theoretical maximums of ± 4.8 cm and ± 6.1 cm for the GPS L1 and L2 frequencies respectively (see section 1.4.2). However, if L1 and L2 phase observations are combined to form 'ionosphere-free' measurements, then phase multipath error can in theory be over 20 cm. The reason for this is explained in a more detailed discussion about the nature of carrier phase multipath interference in section 1.4.

   It is possible that a direct signal is blocked and only a reflected signal is received. This is called **non-line-of-sight (NLOS) reception**. Strictly speaking, NLOS error should not be classed as multipath error because it can be much larger and because some of the techniques used to mitigate multipath error cannot be used to mitigate NLOS error (see section 1.4.4). For pseudorange measurements, such errors are typically tens of metres, but their size is potentially unlimited (Groves 2013*a*). Phase measurement error due to NLOS reception is within half a wavelength of the pseudorange error, modulo one wavelength (Groves 2013*a*). NLOS reception is not so much of a problem for antennas placed in open environments with few obstructions than it is for urban positioning, particularly at street level.

8. As mentioned above, some receivers are able to measure the phase of the carrier signal, relative to a reference signal generated in the receiver, to a precision of just a few millimetres in length. Receivers are then able keep track of the number of complete cycles accumulated since the start of a measurement period. The distance between the satellite and the receiver therefore consists of this measured integer number of complete cycles, plus the measured fractional part plus an unknown integer number of whole cycles, termed here as the **integer phase ambiguity** N, plus the non-integer receiver and satellite **phase biases**, $B_{r,\Phi}$ and B^s_Φ, respectively. Assuming that there are no interruptions in the tracking of the carrier phase, then the integer phase ambiguity N remains constant from one measurement epoch to the next.

   The fact that the phase ambiguity is an integer can be exploited to yield a more accurate position solution. This involves the user either eliminating the phase bias terms by using double-differenced measurements (see section 1.3.2 below) or, for PPP processing, using specialised orbit and clock products, provided by third parties, that allow corrections to be made to the measurements for the satellite phase biases. A user is then able to fix phase ambiguities to integers and solve for the receiver phase bias (igs.org 2013). The process of integer ambiguity resolution in PPP is not implemented in this thesis for the reasons stated below in section 1.3.5. Instead, the slowly-varying phase bias terms and the constant phase ambiguity term are combined into a single term (see section 1.3.3). Phase biases can be considered to be stable over the course of a few minutes. For example, Ge et al. (2008) treats these biases as constant values over 15-minute intervals.

   However, it is possible for discontinuities to occur in the tracking of the carrier phase, either because the signal is obstructed for some reason or because of high ionospheric activity. This is often referred to as a **cycle slip**. When this occurs, the value of the integer phase ambiguity N, which would otherwise be assumed to be constant between measurement epochs, changes. For precise positioning techniques, either the value of the cycle slip is calculated in order to 'repair' the discontinuity (e.g., Liu (2010) proposes a method to determine the value of cycle slips in high-rate GPS measurement data in real-time) or a value for the new integer phase ambiguity is calculated.

9. A GPS satellite moving along it's orbital path must perform a slow rotation so that the solar panels continue to face the Sun while the transmitting antenna points towards the centre of the earth. Since the transmitted signals are right-hand circularly polarized (RHCP), such a rotation will affect phase measurements Φ made at the receiver. Without correction, **phase wind-up** can cause errors to accumulate to the level of decimetres (Kouba 2009). Corrections can be found using open-source software from GPS Toolkit (Tolman et al. 2004).

10. The **measurement noise** term ε_P represents the measurement noise associated with pseudorange measurement, which is around 30 cm for P(Y)-code measurements and worse for C/A-code measurements (Leick 2004). In contrast, the value of the phase **measurement**

noise term ε_Φ is relatively small: the phase of the carrier signal which can be measured to a precision of 0.01–0.05 cycles (2 mm–1 cm) (Misra & Enge 2006).

1.3.2 Double Differencing: a brief overview

One method of dealing with most of the errors described above is to largely eliminate them from the positioning calculation. This can be achieved by forming *double-differenced* measurements using pairs of un-differenced simultaneous measurements from a 'rover' receiver and another fixed 'reference' receiver within a few tens of kilometres distance, with the assumption that the position of the reference point of the reference receiver's antenna is known and that many of the errors affecting the measurements made at both receivers, including ionosphere and troposphere errors, are the same or very similar to each other. The position of the rover receiver relative to the reference receiver can then be calculated with an accuracy of a few millimetres, depending on the distance between the two receivers (i.e. the length of the *baseline*) and the length of the observation period.

For a comprehensive description of the process of double differencing, the reader is recommended to refer to Leick (2004). A brief description follows here: consider one pair of receivers, placed no more than 20 km apart and denoted by subscripts p and q, and one pair of visible satellites, denoted by superscripts a and b. Assuming measurements are made at each receiver simultaneously and that antenna phase centre corrections are applied directly to those measurements, there are four phase measurements available at any one epoch, denoted here as Φ_p^a, Φ_q^a, Φ_p^b and Φ_q^b. Considering equation (1.10), two receiver-to-receiver single-difference measurements can be formed:

$$\begin{aligned}\Phi_{pq}^a &= \Phi_q^a - \Phi_p^a \\ \Phi_{pq}^b &= \Phi_q^b - \Phi_p^b\end{aligned}$$

A double-differenced measurement can then be formed as follows:

$$\begin{aligned}\Phi_{pq}^{ab} &= \Phi_{pq}^b - \Phi_{pq}^a \\ &\approx \rho_{pq}^{ab} + M_{pq,\Phi}^{ab} + \lambda N_{pq}^{ab} + \varepsilon_{pq,\Phi}^{ab}\end{aligned} \tag{1.14}$$

where:
$$\begin{aligned}\rho_{pq}^{ab} &= (\rho_q^b - \rho_q^a) - (\rho_p^b - \rho_p^a) \\ M_{pq,\Phi}^{ab} &= (M_{q,\Phi}^b - M_{q,\Phi}^a) - (M_{p,\Phi}^b - M_{p,\Phi}^a) \\ N_{pq}^{ab} &= (N_q^b - N_q^a) - (N_p^b - N_p^a) \\ \varepsilon_{pq,\Phi}^{ab} &= (\varepsilon_{q,\Phi}^b - \varepsilon_{q,\Phi}^a) - (\varepsilon_{p,\Phi}^b - \varepsilon_{p,\Phi}^a)\end{aligned}$$

Notice that troposphere delay, ionospheric advance, satellite and receiver clock offsets, satellite ephemeris errors, phase biases and phase wind-up terms are not present in equation (1.14). They have each been largely eliminated through the process of double-differencing. Notice in particular, that the double-differenced phase ambiguity N_{pq}^{ab} is an integer and, assuming there are no cycle

slips, will be the same for all following epochs until both satellites are no longer visible at both receivers. By collecting more double-difference phase measurements across multiple epochs and from other pairs of visible satellites, the position of the 'rover' receiver and the double-differenced phase ambiguities can be estimated. Once these double-differenced ambiguities have been *fixed* to their integer values, the position of the rover can be calculated with much higher accuracy since the only remaining unknown parameters are the double-differenced phase multipath errors and measurement noises, which in practice amount to only a few millimetres.

However, for longer baselines, the assumption that ionosphere and troposphere errors being highly correlated between the reference and rover receivers becomes less valid. This is a very pertinent issue if GPS data is to be used in seismology. For example: in the case of a large seismic event, a rover receiver close to the epicentre of an earthquake will measure movement relative to a reference receiver a few kilometres away, which is likely to have also moved. In order to estimate the true movement of the rover receiver relative to an ECEF reference frame, any movement of the reference station must also be accounted for. One could extend the baseline so that the reference receiver is further away from the rupture and less susceptible to movement, but the accuracy of the double-differencing technique will decrease, largely due to the spatial decorrelation of atmospheric errors which in turn makes the process of fixing integer wavelength ambiguities more difficult.

Special consideration has to be given to the use of differencing techniques if applied in the context of a tsunami warning system. Ordinarily, differencing techniques assume that a 'reference' station (or multiple reference stations) is stationary and has accurately known coordinates. The coordinates of a 'rover' receiver can then be found by collecting a sufficient number of double-differenced measurements. However, an earthquake large enough to generate a dangerous tsunami is likely to cause a significant movement of the earth's crust over a large area, both from transient surface waves and a possible permanent coseismic offset. For example, as mentioned in section 1.2.2, the 2004 M_W 9.1 Sumatra-Andaman earthquake caused measurable displacements of up to 10 mm at distances of 3,000 km from the epicentre. Therefore, it is likely that *both* the 'rover' and 'reference' station(s) will be subjected to movement. So, in order to obtain the true displacement of the rover receiver, any movement of the reference receiver(s) must also be accounted for, otherwise true displacement may be estimated incorrectly and hence leading to an incorrect calculation of earthquake magnitude. One way to resolve this is to use measurements from an additional receiver(s) placed even further from the epicentre. However, if that receiver is also subjected to significant movement, then yet more measurements are required from stations even further from the epicentre. This increases the complexity of data processing and necessitates the existence of a sufficiently large and dense network of reference stations in the first place. Nevertheless, Bock et al. (2011) describes such a strategy and states that it has been "effective in real-time analysis of medium to large earthquakes within dense geodetic networks of large extent with station spacing of ∼20–40 km".

1.3.3 Precise Point Positioning

Precise point positioning (PPP), introduced by Zumberge et al. (1997), is a GNSS positioning technique that can achieve centimetre to decimetre level accuracy globally for a single static or kinematic receiver (Gao & Chen 2004). For a user, double-differencing requires measurements from a receiver to be processed together with simultaneous measurements from a nearby reference receiver or network of receivers. In contrast, PPP does not require such measurements from nearby receivers but instead needs high-accuracy orbits and clock offsets of the visible satellites which are themselves determined by a network of reference stations distributed globally. Zumberge et al. (1997) suggested that 35–40 stations was adequate for such a purpose.

Instead of eliminating most measurement errors via differencing, PPP uses *un*-differenced measurements and so each of these errors have to be either carefully modelled, solved for as an unknown parameter or eliminated by other means. Much of the effect of the ionosphere is eliminated by forming 'ionosphere-free' measurements by combining measurements of two signals with different frequencies via equations 1.11 and 1.12. The receiver clock offset and tropospheric delay parameters have to be solved for alongside the position of the antenna and the phase ambiguities for each visible satellite. To achieve centimetre-level accuracy, other errors such as phase wind-up, ocean tide loading, solid earth tides and polar motion have to be accurately modelled (Kouba 2009) in addition to those listed in section 1.3.1.

In 'classical' PPP processing, it is not possible to determine and fix a phase ambiguity to an integer value due to the use of ionosphere-free measurements without further knowledge of the satellite phase biases. Instead, the phase biases and the integer ambiguity on one frequency are combined into a single non-integer phase ambiguity term A_Φ. When forming an 'ionosphere-free' measurement, the respective phase ambiguity terms are combined to form an 'ionosphere-free' phase ambiguity $A_{\Phi_{\text{IF}}}$: For example, if applying GPS L1 and L2 phase measurements in equation (1.12), the ionosphere-free phase ambiguity term is $A_{\Phi_{\text{IF}}} \approx 2.546 A_{\Phi_1} - 1.546 A_{\Phi_2}$ where A_{Φ_1} and A_{Φ_2} are the L1 and L2 non-integer phase ambiguity terms, respectively. Satellite phase biases can be considered to be stable at least over the course of a few minutes (Ge et al. 2008). Hence, the classical approach to PPP is to solve for this slowly-varying *non-integer* ionosphere-free phase ambiguity $A_{\Phi_{\text{IF}}}$ for each visible satellite. This is often termed as 'float' PPP and can yield decimetre-level accuracy in kinematic mode (Chen 2004).

However, in recent years, various methods have been devised to fix phase ambiguities, thereby increasing accuracy (Collins et al. 2008, Ge et al. 2008, Laurichesse et al. 2009, Bertiger et al. 2010, Geng, Teferle, Meng & Dodson 2010). The details of these methods are not covered here, but they all allow the fixing of 'wide-lane' and 'narrow-lane' phase ambiguities to integers using further knowledge of the satellite phase biases. The reader is recommended to refer to Bisnath & Collins (2012) for a summary of the different techniques used to fix phase ambiguities in PPP processing. Ge et al. (2008), for example, reported an average improvement in RMSE (compared with IGS weekly solutions) from 4.1 mm, 3.1 mm and 8.3 mm to 2.8 mm, 3.0 mm and 7.8 mm for easting, northing and height respectively. These techniques are often referred to as 'fix' PPP or

precise point positioning with ambiguity resolution (PPP-AR).

The positioning accuracies acheivable when using double-differenced measurements will exceed those of PPP as long as the coordinates of nearby reference stations are accurately and precisely known. In contrast, while positioning by PPP is less precise, the accuracies achievable are relative to a *global* coordinate system which, from the point of view of the user, is realised through the precisely known locations of GNSS satellites rather than a nearby reference station.

This thesis implements 'float' PPP using a Kalman filter, where the position of the receiver, the receiver clock offset, the troposphere delay and the non-integer phase ambiguities are all estimated simultaneously. The details of this process will be described in chapter 2.

1.3.4 Advantages of PPP for tsunami warning

- PPP positions each receiver with respect to a globally consistent coordinate system without the need for a nearby reference station or network. If using double-differencing, each receiver is positioned with respect to nearby receivers. Therefore, if multiple receivers have moved as the result of a large earthquake, it is simpler to determine how much each receiver has moved using PPP.

- As mentioned above, in PPP there is no need for a nearby reference station or network and yet decimetre accuracy is still achievable globally, at least for 'float' PPP. This has implications in terms of cost: Bock et al. (2011) states that the real-time analysis of medium to large earthquakes using double-differenced measurements has been effective for large networks of receivers with station spacing of 20–40 km. Such networks exist in Japan (GEONET) and the west coast of the United States (Plate Boundary Observatory), but could be prohibitively expensive for other tsunami-prone countries to set up. PPP allows for a lower station density, thereby reducing cost. Wright et al. (2012) demonstrated that just 10 stations spaced 100 km apart roughly parallel to the fault line were needed to estimate the magnitude of the 2011 M_{W} 9.0 Tohoku-Oki earthquake with sufficient accuracy for a reliable tsunami warning.

1.3.5 Disadvantages of PPP for tsunami warning

- As described in section 1.3, GNSS processing techniques such as double-differencing largely eliminate many of the errors associated with GNSS positioning such as satellite and receiver clock offsets and atmospheric delays, especially on short baselines. In contrast, PPP processing uses undifferenced observables and therefore these errors have to be minimised by other means. Errors have to be carefully modelled or solved for in order to calculate an accurate position. Of course, no model is perfect. As a consequence, the position solutions yielded by PPP are not as precise as those found by the processing of double-differenced measurements over a short baseline. Accuracies achieved through PPP have however improved with the advent of advanced techniques that fix phase ambiguities to integers (PPP-AR).

However, for a tsunami warning system, it is not necessarily the absolute accuracy of the position solution that is important. The aim is in fact to accurately measure the permanent coseismic offset, i.e. a *change* in position over the course of a few seconds to a few minutes. Fortunately, many of the errors associated with PPP are slowly-varying: hardware delays can be considered to remain constant over the course of a few minutes (Ge et al. 2008) and satellite ephemeris errors can vary by around a centimetre over 100 seconds (Groves 2013*b*). With this in mind, PPP still has the potential to accurately measure small displacements over a few minutes if the position solution is otherwise stable over such a period.

- In 'float' PPP processing, the receiver position, receiver clock offset, the troposphere delay parameters and the non-integer phase ambiguities are all estimated simultaneously. The estimation of these 'states' is usually achieved using an algorithm known as an extended Kalman filter (EKF). Put simply, this is an algorithm that estimates the optimal values of a 'state vector' by combining noisy measurements observed at the 'current epoch' with a predicted state vector propagated forward in time from the previous epoch. This algorithm is described in detail in section 2.1 from page 68 onwards.

  However, the state vector needs plenty of time to 'converge', i.e. as much as 30 minutes of measurements are required for the position solution to reach an accuracy of within a decimetre (Bisnath & Gao 2007) for conventional 'float' PPP processing. This contrasts with the ability of differential positioning to achieve centimetre accuracy within just a few tens of seconds (Collins et al. 2009), assuming ideal conditions such as plenty of visible satellites (at least five) well-distributed across the sky and a short baseline.

  Although not within the scope of this thesis, the reduction of convergence time is important. As Collins et al. (2009) points out, any temporary power cut to the receiver during the earthquake itself would hinder any effort to determine coseismic displacement rapidly because the position solution has to take a relatively long time to re-converge. A lot of research has focused on reducing this convergence time by applying or improving error models. For example, the fixing of phase ambiguities to integers in PPP-AR can reduce convergence time significantly, sometimes to within 10 minutes (Collins et al. 2009, Bisnath & Collins 2012, Geng, Meng, Dodson, Ge & Teferle 2010). Convergence time can also be reduced by using more GNSS constellations and through the use of additional GNSS frequencies (Jokinen et al. 2011, Juan et al. 2012, Geng & Bock 2013, Li et al. 2014).

- PPP is often used as a post-processing technique using the most precise satellite clock and orbit products available. If PPP is required in (near) real-time, an internet connection, satellite data links or some other form of communication is required to allow the reception of real-time precise satellite clock and orbit products from organisations such as the International GNSS Service (IGS). The highest accuracies are only available when using post-processed precise clocks and orbits, for which one has to wait 12–18 days for them to become available.

  However, satellite orbit and clock modelling has steadily improved over the years. The IGS

now provides predicted 'ultra-rapid' satellite orbit and clock files with quoted accuracies (RMSE) of 5 cm and 3 ns (0.9 m) respectively. The IGS Real-time Service enables PPP to achieve decimetre-level accuracy in real-time with quoted orbit and clock accuracies of 5 cm and 300 ps (8 cm) respectively (igs.org 2013). It is even possible to achieve integer ambiguity resolution in real-time (Laurichesse et al. 2008, Geng 2011).

One can expect PPP to improve further with the addition of more satellites and signal frequencies via new GNSS constellations such as BeiDou and Galileo. Using three frequencies rather than just two should enable PPP convergence times to reduce to just a few minutes rather than a few tens of minutes (Laurichesse 2015). These improvements in performance, coupled with the advantages of lower cost and the lack of need for a nearby reference station, provides a strong case for the use of PPP in tsunami monitoring systems. However, it is phase multipath interference—a problem not unique to PPP—that can cause instability over these sorts of time intervals. The reason for this will be discussed in section 1.4 below.

The fixing of phase ambiguities in PPP is not implemented in this thesis because the software that is used for PPP processing does not yet have this capability, although its implementation is identified as future work. However, as was mentioned above, many of the error sources present in PPP are slowly-varying, such as satellite ephemeris errors and phase biases, or constant, such as the phase ambiguity assuming that no cycle slips occur. If the aim is to measure coseismic offset accurately over the course of just a few minutes, then these errors should have little impact on such a measurement. In chapter 2, which describes the implementation of the PPP EKF used in this thesis, each non-integer phase ambiguity term A_{IF} (which combines ionosphere-free phase ambiguities and phase biases, as described above) is assumed to be almost constant, but is assigned a small power spectral density (PSD) to counter numerical errors and keep the EKF stable.

1.4 Phase multipath error

In this study, multipath refers to the phenomenon whereby a signal transmitted from a GNSS satellite reaches a receiving antenna via more than one path, principally due to objects in the vicinity of the receiver acting as reflectors. The indirect signals are delayed with respect to the direct line-of-sight signals. The reflected signals interfere with the processing of the direct signals within the receiver, producing errors in both code and carrier-phase measurements, hence causing errors in position determination. It is also possible for the direct line-of-sight signal to be blocked and only a reflected signal(s) to be received. This phenomenon, called non-line-of-sight (NLOS), was discussed on page 40, but is not considered as 'multipath' in this thesis.

Both positioning using double-differencing and PPP are adversely affected by multipath and both code and carrier-phase measurements are affected. For precision applications, it is carrier-phase multipath that is of most concern because code measurements are given very little weight: In this thesis, ionosphere-free phase and code measurements (if used) are assigned standard deviations of $1/\sin\theta \times 0.015$ m and $1/\sin\theta \times 2$ m, respectively, where θ is the satellite elevation angle. As shall be

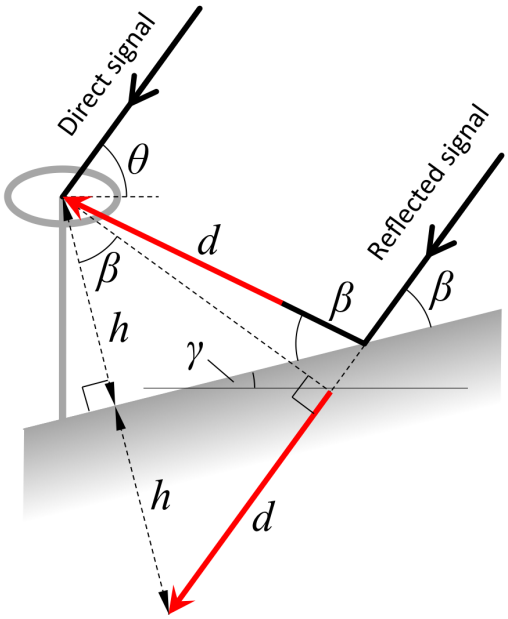

Figure 1.2 – Diagram showing the geometry of a single direct signal from a satellite at elevation angle θ to a receiver antenna and a single indirect signal reflected by a specular reflector, with gradient angle γ, at a perpendicular distance h below the antenna. d is the extra path length travelled by the reflected signal.

described below, phase multipath interference causes errors in GNSS carrier phase measurements at a stationary antenna that are sinusoidal in character with periods potentially as small as a few seconds and amplitudes of a few centimetres. These characteristics are very similar to those of surface waves that emanate from an earthquake epicentre. In order to gain a better understanding of the nature of phase multipath errors in terms of frequency and magnitude, a simple example is used.

Consider figure 1.2. This shows the geometry of an intentionally simple two-dimensional example of the paths taken by a single direct and a single indirect signal reflected off a smooth surface of constant slope below the receiver antenna. From the diagram, the extra path length d travelled by the reflected signal relative to the direct signal can be expressed as a function of angle β and the perpendicular distance h between the reflector surface and the antenna phase centre, i.e. $d = 2h \sin \beta$. The symbol ψ is used to denote the difference in phase between the indirect and direct signals, i.e. $\psi = \phi_{\mathrm{M}} - \phi_{\mathrm{D}}$ where ϕ_{M} denotes the phase of the reflected signal and ϕ_{D} the phase of the direct signal. This value ψ, hereafter referred to as *multipath relative phase*, is related to the extra path length by equation (1.15), where ψ_0 is a possible phase shift—which is 180° for a reflection off a smooth surface at an angle of incidence less than Brewster's angle (Groves

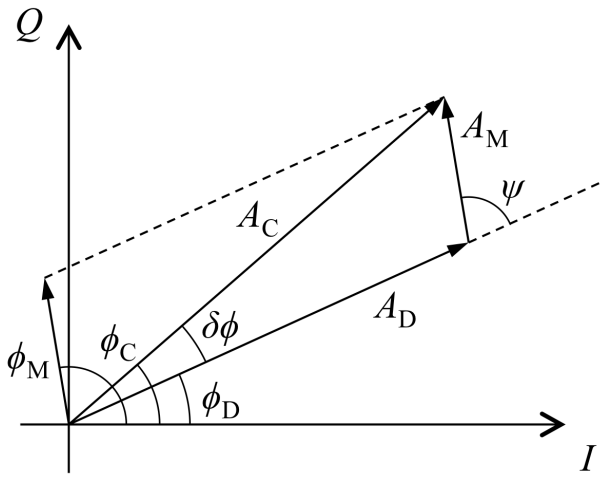

Figure 1.3 – Phasor diagram showing the effect of multipath interference on carrier phase measurement. Note that ψ denotes the difference in phase between the direct signal and the reflected signal, i.e. $\psi = \phi_{\mathrm{M}} - \phi_{\mathrm{D}}$. I and Q denote the in-phase and quadrature signal components, respectively.

2013*b*)—and λ is the signal wavelength:

$$\begin{aligned} \psi =& \frac{2\pi}{\lambda} d + \psi_0 \\ =& \frac{4\pi}{\lambda} h \sin\beta + \psi_0 \end{aligned} \tag{1.15}$$

The angle β is related to the reflector tilt angle γ and the satellite elevation angle θ by $\theta = \gamma + \beta$. Hence, equation (1.15) becomes:

$$\psi = \frac{4\pi}{\lambda} h \sin(\theta - \gamma) + \psi_0 \tag{1.16}$$

In this simple example, h and γ are assumed to be constant over time. Therefore the only quantity in equation (1.16) that does vary with time is the satellite elevation angle θ. The angular frequency ω of the relative phase ψ is given by the derivative of ψ with respect to time t which is shown by equation (1.17) (Bilich, Larson & Axelrad 2008):

$$\omega = \frac{\mathrm{d}\psi}{\mathrm{d}t} = \frac{4\pi}{\lambda} h \cos(\theta - \gamma) \frac{\mathrm{d}\theta}{\mathrm{d}t} \tag{1.17}$$

Figure 1.3 is a phasor diagram showing the effect of multipath interference on carrier phase measurements. Assuming that there is no multipath signal, a receiver tracks the phase ϕ_{D} and amplitude A_{D} of a direct signal. However, in the presence of a reflected signal with phase ϕ_{M} and amplitude A_{M}, the phase and amplitude of a composite signal, rather than the direct signal, is

tracked with phase ϕ_C and amplitude A_C. Using figure 1.3, the error in the phase measurement, $\delta\phi = \phi_C - \phi_D$, can be described geometrically:

$$\delta\phi = \arctan\left(\frac{A_M \sin\psi}{A_D + A_M \cos\psi}\right) \tag{1.18}$$

The amplitudes of the reflected and direct signals, A_M and A_D respectively, can be related as follows:

$$A_M = \alpha R(\tau) A_D \tag{1.19}$$

where the damping factor α is the ratio of the antenna gain of the reflected signal to the antenna gain of the direct signal ($0 \leq \alpha \leq 1$, assuming the direct signal is not attenuated), and the PRN code correlation function R is a function of the time delay τ of the reflected signal relative to the direct signal and is defined by Lau & Cross (2007) as:

$$\begin{aligned} R(\tau) &\approx 1 - \frac{|\tau|}{T} \qquad |\tau| \leq T \\ &= 0 \qquad\qquad\quad |\tau| > T \end{aligned} \tag{1.20}$$

where T is the PRN code chip period (which is approximately $1\,\mu$s for GPS C/A code). Equation (1.18) can therefore be re-written as follows:

$$\delta\phi = \arctan\left(\frac{\alpha R(\tau)\sin\psi}{1 + \alpha R(\tau)\cos\psi}\right) \tag{1.21}$$

The phase error expressed in metres, $\delta\Phi$, can be obtained by multiplying $\delta\phi$ by $\lambda/2\pi$.

1.4.1 Multipath error frequency

If one further simplifies the above example by assuming that the value of $\alpha R(\tau)$ is fixed over the course of a few minutes, then the value of the carrier phase error $\delta\phi$ depends on the value of the multipath relative phase ψ. In the simple example shown in figure 1.2, it can be seen from equation (1.16) that, regardless of whether the satellite in question is ascending or descending (i.e. whether satellite elevation angle θ increases or decreases), the value for the relative phase ψ will cycle through values between 0 and 2π. How quickly it does so is determined by the value of the angular frequency ω in equation (1.17). The value of ω therefore determines how quickly the carrier phase error $\delta\phi$ oscillates.

For example, consider figure 1.4 which shows an example of the elevation angle of a single GPS satellite pass plotted over time. In this case, the satellite rises quite rapidly from 10° to 80° within three hours, which is equivalent to about 0.0074°/s or 0.13 mrad/s. Consider then a satellite at a low elevation angle of $\theta = 10°$ rising at this rate of $\frac{d\theta}{dt} = 0.0074°/s$ and a horizontal reflector ($\gamma = 0°$) at a perpendicular distance of $h = 1.5\,m$ below the receiving antenna. For the GPS L1 carrier signal, which has a wavelength of about $\lambda = 0.19\,m$, the rate of change of relative phase, $\frac{d\psi}{dt}$, is

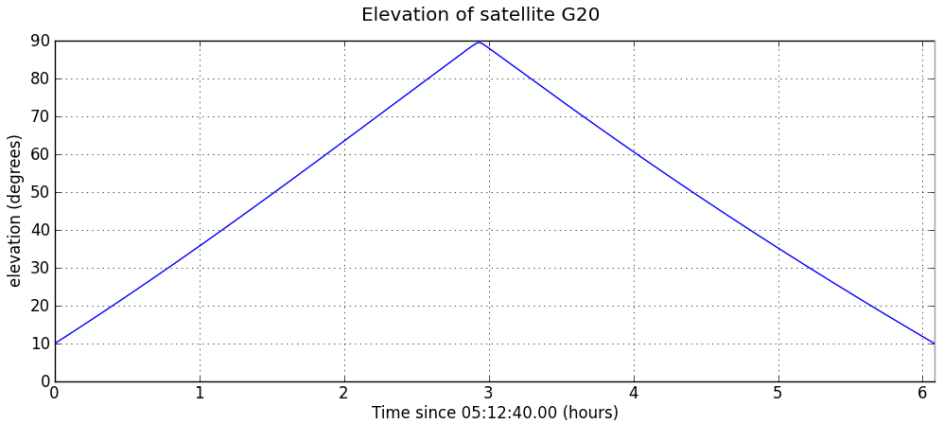

Figure 1.4 – Elevation of GPS satellite PRN 20 from Leica SmartNet receiver UCL, at University College London on 26$^{\text{th}}$ March 2012.

about 0.72°/s, which translates to a period of almost 500 s (8 minutes 20 seconds).

As a second example, consider the same satellite at the same elevation angle and rising at the same rate, but with a 'far-field' vertical reflector ($\gamma = 90°$) at a horizontal distance of $h = 100\,\text{m}$ away from the receiving antenna. Again, for the GPS L1 carrier signal, the rate of change of relative phase is about 8.5°/s, which translates to a period of only about 42 s. Hence, to realise the potential of PPP for use in applications such as seismology, it is necessary to reduce the effect of multipath interference, particularly that caused by distant vertical reflectors, since the frequency of these errors are similar to those of seismic waves (Larson et al. 2007).

1.4.2 Multipath error amplitude

When examining equation (1.21), and assuming $0 \leq \alpha \leq 1$, the maximum possible value for the phase multipath error, $\delta\phi$, is $\pm\pi/2$ or a quarter of one wavelength. This occurs when $\psi = \pm\pi$ and $\alpha = 1$, although the likelihood of a multipath signal with such a large amplitude is low. For the GPS navigation frequencies L1 and L2, which have wavelengths of $\lambda_1 \approx 19\,\text{cm}$ and $\lambda_2 \approx 24\,\text{cm}$ respectively, the corresponding maximum phase multipath errors are approximately ±4.8 cm and ±6.1 cm.

1.4.3 Ionosphere-free Multipath

In PPP, the phase measurements of the GPS L1 and L2 signals are combined to form *ionosphere-free* measurements, denoted Φ_{IF}, as per equation (1.12). So the phase multipath error for ionosphere-free measurements, in metres, is

$$\delta\Phi_{\text{IF}} \approx 2.546\ \delta\Phi_1 - 1.546\ \delta\Phi_2 \tag{1.22}$$

Therefore, the maximum possible phase multipath error for an ionosphere-free measurement is approximately ±21.6 cm. Although ionosphere-free phase errors of this magnitude are unlikely, they are generally too large to be ignored if centrimetric accuracy is desired.

Regarding the periodicity of the ionosphere-free phase observable: this is complicated by the fact that at any one time there will be two different values for the angular frequency ω of the two different GPS signals, L1 and L2. Nevertheless, it is easy to see from equation (1.22) that if $\delta\Phi_1$ and $\delta\Phi_2$ exhibit oscillatory behaviour, then $\delta\Phi_{\mathrm{IF}}$ will also oscillate.

1.4.4 Methods of phase multipath mitigation

Simply by placing an antenna in a low-multipath environment will obviously reduce the effect of multipath, but the effect cannot be eliminated. From the point of view of a country or organisation that is developing a tsunami warning system, there may be a motivation to use any existing GNSS networks to save the expense of building entirely new monitoring stations. In such a scenario, the antennas—which may not be sited in the most suitable locations from the point of view of minimising multipath—cannot be moved. For example, antennas placed in urban environments will be more vulnerable to distant reflectors. The issue of multipath mitigation would then be more pertinent.

There are numerous techniques to mitigate the effect of multipath: High performance 'choke ring' antennas have concentric rings surrounding the antenna which attenuate signals from low elevation angles and signals that arrive from below the level of the antenna. Also, signals received directly from GPS satellites are right-hand circular polarised (RHCP); signals reflected once by a highly specular reflector have their polarisation changed to left-hand circular (LHCP), assuming that their angle of incidence with the reflecting surface is less than Brewster's angle, and antennas can be designed to attenuate such signals that arrive from medium to high elevation angles (Groves et al. 2013). Although not applied in this thesis, this property can also aid the identification of NLOS signals which can have lower signal-to-noise ratio (SNR) values than direct signals. Such measurements can be either excluded or down-weighted (Groves 2013*a*). Dual-polarisation antennas can also aid the identification of NLOS signals (Groves et al. 2013).[3]

Other mitigation techniques can be applied. For example, more weight can be given to measurements from satellites with higher elevation angles which are less likely to be contaminated by multipath. One can also weight the measurements based on SNR measurements, but this is complicated by the fact that there is a 90° phase difference between SNR measurements and phase multipath error (Lau & Cross 2006). Innovation filtering, where new measurements are compared with measurements predicted from previous epochs, can help to identify NLOS measurements (Groves et al. 2013).

Instead of down-weighting or excluding contaminated measurements, another approach would be to predict the measurement errors due to multipath interference by some method and apply

[3]These techniques used to detect NLOS signals are not applied in this thesis. GPS measurements are sourced from antennas sited in areas with few obstructions. An outlier detection algorithm is applied (see section 2.1.8).

them directly to those measurements as corrections. Some studies such as Granström (2006) and Fuhrmann et al. (2014) map GPS phase multipath residual values onto a hemispherical 'skyplot' by the azimuth and elevation of the associated satellite. Granström (2006) in particular maps residuals from the PPP processing of six years of data from a number of receivers. However, for each skyplot, the residuals are grouped into 'cells' of 2° and 5° in elevation and azimuth respectively and a mean value is calculated for each. As will be demonstrated in chapter 5, this resolution does not capture the relatively high-frequency nature of phase multipath, which can oscillate by several millimetres even over just one degree of satellite elevation angle (Park 2004). These studies usually aim to capture the slowly oscillating multipath effect that often affects measurements from satellites at low elevation angles and are not actually used as corrections for multipath. However, if these values were to be used to correct measurements directly, high-frequency multipath error would remain. In this thesis, 'high-frequency multipath' refers to oscillatory multipath errors with periods under about 100 s. Other studies have also mapped measurement residuals onto skyplots, but these are applicable to other types of measurements, such as pseudorange (Harris 2002, Kerkhoff et al. 2010) or double-differenced phase measurements (Wanninger & May 2000). One major disadvantage is that a complete 'multipath map' can take many months or even years to form and relies upon the surrounding multipath environment to remain static for that period of time.

There is another method to mitigate the effect of multipath, commonly known as *sidereal filtering*, that in principle can be considered equivalent to using skyplots to determine corrections. This is described in the following section.

1.5 Sidereal Filtering

Sidereal filtering, first proposed in Genrich & Bock (1992), is another method for mitigating the effect of multipath. It takes advantage of the fact that GPS satellites have an orbital period of about 11 hours 58 minutes. For a static receiver, this means that the geometry relating the satellites, reflectors and receiver antenna will repeat approximately every sidereal day. Since positioning errors caused by multipath are highly dependent on this geometry, then the multipath error should also repeat every sidereal day. Assuming the receiver and its surrounding environment remains static and the reflective properties of surrounding surfaces remains the same (i.e. they remain wet or dry, for example), the repeating multipath pattern can be empirically derived and removed.

Before the method of sidereal filtering is described, there are some further aspects of the technique to consider:

- Sidereal filtering can create a multipath model even for complex reflector environments, as long as the environment (reflector geometry and reflective properties) does not change significantly from one day to the next.

- Although it is assumed that the receiver antenna is located in an environment where the reflector geometry is static, the weather may still have a significant effect. Studies by Lau

(2012) and Wanninger & May (2000) suggest that wet surfaces only slightly reduce the effectiveness of sidereal filtering, but Wanninger & May (2000) reported significant changes in carrier phase multipath on days when there was a covering of snow.

- Sidereal filtering can reduce any error source that repeats every sidereal day. Hence, not only multipath, but also imperfections in antenna phase centre models can also be mitigated.

1.5.1 Position-domain sidereal filtering

Sidereal filtering in the position domain is explained here by means of a simple example. The implementation of position-domain sidereal filtering used in this thesis is described in chapter 2.

In figure 1.5, a time series of easting, northing and height coordinates of PPP GPS-derived positions based on phase measurements is shown for one hour on two consecutive days. The receiver is static, but the plot suggests that the antenna is actually moving by a few centimetres, mostly in the vertical component. For example, note the roughly 5 cm rise in height between about 12:32 and 12:34 on both days). Also, some common shorter-period (tens of seconds) oscillations can be identified on both days. The series of position errors shown in grey (26^{th} March) in figure 1.5 are in fact separated from the black and red series (27^{th} March) by a period of 23 hours, 55 minutes and 55 seconds, which is actually a good approximation of the GPS constellation repeat time. All GPS satellites have a nominal ground-track repeat time close to this period. If the environment surrounding the antenna is identical over the two days, it is reasonable to assume that the multipath error pattern will also repeat over the same period. It is clear that there is a strong correlation between the position time series of the two adjacent days (with correlation coefficients of 0.78, 0.80 and 0.90 for easting, northing and height respectively). Therefore, figure 1.5 would strongly indicate that the positioning errors are largely a result of multipath.

In short, assuming that the true position of the receiving antenna is known, the position-domain sidereal filter works by subtracting the series of position residuals (i.e. position errors) of the first day from the position series of the second day. The position residuals of the first day are usually low-pass filtered before this subtraction takes place in order to minimise the amplification of high-frequency noise. The resulting improved series of positions (shown in red in figure 1.5) is largely free of the lower-frequency time-varying errors induced by the multipath effect. Note how higher-frequency positioning errors largely remain even after application of the sidereal filter.

There are a large number of studies that apply sidereal filtering and they do so in the position (or coordinate) domain, but in the context of using double-differenced measurements rather than PPP. Bilich, Cassidy & Larson (2008), Elósegui et al. (2006) and Wang et al. (2007) are just three examples. Many apply Modified Sidereal Filtering (MSF) proposed by Choi et al. (2004). Prior to this influential paper, the repeat period used for sidereal filtering was one sidereal day, 23 h 56 m 4 s (86,164 s). Choi et al. (2004) pointed out that the average repeat time for each GPS satellite is actually around 23 h 55 m 55 s (86,155 s). This will be discussed further in section 1.5.3. Bilich, Cassidy & Larson (2008) applied the MSF technique and detected low-frequency displacements (10–

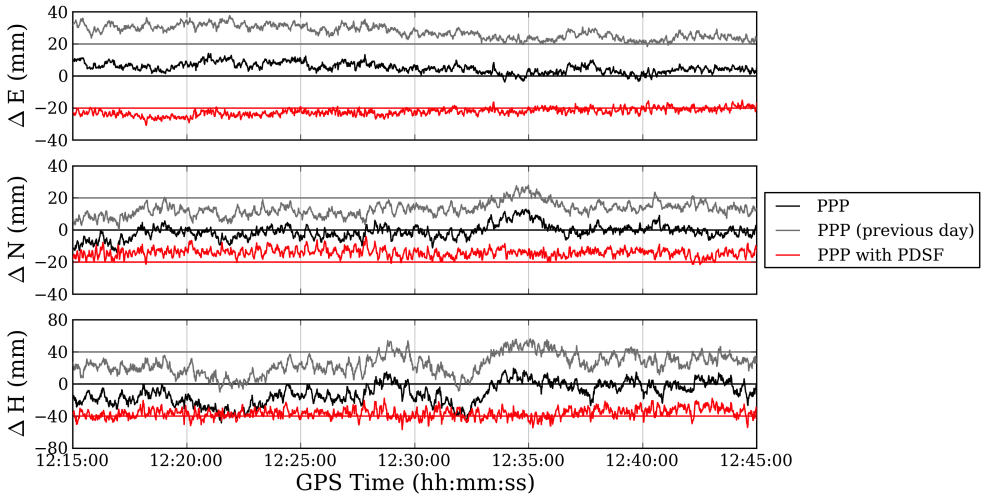

Figure 1.5 – Easting, northing and height errors from 12:19:05 to 12:49:05 on 26$^{\text{th}}$ (grey) and 12:15:00 to 12:45:00 on 27$^{\text{th}}$ (black) March 2012 after processing 1 Hz measurements from the Leica SmartNet reference station located at UCL using PPP software. The data from 26$^{\text{th}}$ March (grey) has been brought forward by 23 hours, 55 minutes and 55 seconds to enable the visualisation of the correlation with the errors from 27$^{\text{th}}$ March on the same axes. Easting, northing and height errors from 27$^{\text{th}}$ March after applying a position-domain sidereal filter are shown in red. (Each data series has been offset by ±20 mm or ±40 mm for clarity).

50 s period) with peak-to-peak amplitudes of 3–4 cm at large epicentral distances (1,000–2,300 km) from the 2002 M_{W} 7.9 Denali Fault earthquake.

1.5.2 Observation-domain sidereal filtering

The method of observation-domain sidereal filtering used in this thesis is detailed in chapter 2 but is broadly described as follows: Consider two consecutive days. The objective is to improve the position solution on the second day using data from the first day. With the position of the receiving antenna assumed to be fixed to a known position, GPS measurements from 'day one' are processed and a series of measurement residuals (i.e. measurement errors) for each satellite are formed. These are low-pass filtered and then subtracted from the series of corresponding measurements made one repeat period later on 'day two'. These 'cleaned' measurements are used by GPS processing software to yield an improved time series of positions with the multipath signature largely removed.

In theory, sidereal filtering in the observation domain, rather than in the position domain, should lead to better performance. This is because the slightly different ground-track repeat periods of each of the GPS satellites, and hence the corresponding multipath signatures, can be considered separately. The observation residuals from adjacent days can be highly correlated. For example, figure 1.6 shows a time series plot of phase residuals for just one particular GPS satellite from two consecutive days: the correlation between the two series is clear to see (with

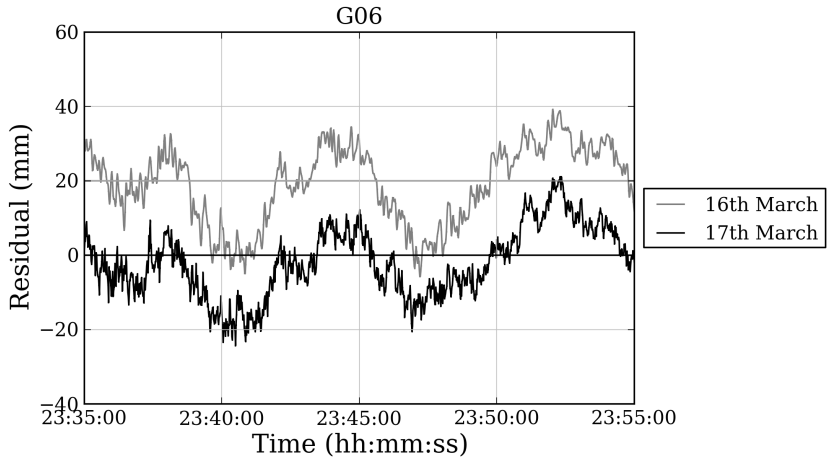

Figure 1.6 – GPS satellite (PRN 6) ionosphere-free phase measurement residuals over 20 minutes on 26$^{\text{th}}$ (grey) and 17$^{\text{th}}$ (black) March 2012 at receiver UCL after PPP processing. The residuals from 26$^{\text{th}}$ March (grey) have been shifted forward by 23 hours, 55 minutes and 55 seconds, the repeat period of G06, to enable the visualisation of the correlation between the two sets of residuals. (The two time series have also been offset from each other by 20 mm for clarity).

correlation coefficient 0.85). Using an accurate repeat time should improve the ability to remove high-frequency phase multipath errors in particular.

Another advantage also arises because of the ability to consider each satellite separately. If the satellite constellation differed from one day to the next, maybe because of a satellite outage, a position-domain sidereal filter would have to be re-calibrated, particularly if the signal from the satellite in question would otherwise have been severely affected by multipath interference. This is because the fundamental premise of the position-domain sidereal filter is that the satellite constellation and the reflectors around the antenna do not change on adjacent days, otherwise the resulting multipath error signatures present in the position time series for both of those days would differ. Larson et al. (2007) addressed this difficulty by pre-editing the input GPS measurement files to ensure that the same satellites were visible each day. Therefore, this approach is not feasible for real-time applications. On the other hand, if an observation-domain sidereal filter were to be used, only the corrections associated with the satellite subject to the outage become invalid. The corrections to the measurements from other satellites should still be valid, therefore making the observation-domain sidereal filter more robust.

However, to take full advantage of observation-domain sidereal filtering, the ground-track repeat times of each satellite have to be calculated accurately.

1.5.3 Calculating GPS satellite ground-track repeat times

When 'sidereal filtering' was first introduced by Genrich & Bock (1992), the time shift used was one sidereal day, 23 h 56 m 4 s (86,164 s). However, an influential study by Choi et al. (2004) pointed out that the repeat time varied for each GPS satellite and could be calculated using values found in the GPS broadcast ephemeris and that the average repeat time for the whole constellation is actually around 23 h 55 m 55 s (86,155 s) (see section 1.5.3.1 below). Since this value is no longer strictly sidereal, the name Modified Sidereal Filtering (MSF) is used. Agnew & Larson (2007) refine this value to (86,154.4 s). The reason for this is that it is an operational requirement for GPS that the ground-track of each satellite is fixed. For this to be achieved, the orbital period is set to be roughly four seconds shorter than a half-sidereal period. This is to compensate for the westward drift of the longitude of the ascending node (the longitude at which a satellite crosses the equatorial plane) caused by the earth's oblateness (Choi et al. 2004). The difference between these two 'sidereal' periods is only about nine seconds, but for high-rate positioning, say 1 Hz, an accurate repeat time is important because, as mentioned in section 1.4.1, multipath error can change by about 75° (over one-fifth of a cycle) over nine seconds.

This figure of 86,154.4 seconds is only a mean of GPS ground-track repeat periods (with outliers excluded). Agnew & Larson (2007) showed that each satellite actually has its own repeat period generally within five seconds of this value. Occasional exceptions do occur with orbital periods differing from this mean value by tens of seconds. The effect of these anomalies on sidereal filtering is examined in chapter 4.

Finding an orbit repeat time accurate to the nearest second is important when considering the application of sidereal filtering to high-rate (≥1 Hz) GPS data. Since each satellite will have a slightly different orbit repeat time, the multipath error signature for each satellite will also have different repeat periods. Hence, considering each satellite separately should yield better multipath corrections (Agnew & Larson 2007), particularly when measurements are affected by high-frequency multipath interference.

1.5.3.1 Derivation of repeat time from broadcast ephemeris

One method is to calculate a repeat period using two values found in the GPS broadcast ephemeris for each satellite, specifically the square-root of the semi-major axis a_s and the correction to mean motion n_c, and Kepler's Third Law (Choi et al. 2004). This repeat period T can be calculated as follows, using the notation of Agnew & Larson (2007):

$$T_0 = \frac{4\pi}{n} \quad \text{where} \quad n = \sqrt{GM}a_s^{-3} + n_c \tag{1.23}$$

where: T_0 is the ground-track repeat time of a satellite.
n is the mean motion.
GM is the standard gravitational parameter for earth: $3.986004 \times 10^{14}\text{km}^3\text{s}^{-2}$.
a_s is the square root of the semi-major axis.
n_c is the correction to mean motion.

Choi et al. (2004), Agnew & Larson (2007), Zhong et al. (2010) and many other studies use this method to calculate a repeat time. It is simple and carries very little in the way of computational burden. It is hereafter referred to as the 'broadcast ephemeris (BE) method'.

1.5.3.2 Derivation of repeat time using line-of-sight unit vectors

Another method of calculating a repeat period appears in Axelrad et al. (2005): Considering one GPS satellite at a particular epoch, an epoch on the preceding day is found that most closely corresponds to the satellite occupying the same position in the sky in terms of azimuth and elevation in the receiver's local topocentric (east-north-up) coordinate system. Such a search is executed by maximising the dot product of the two user-satellite unit vectors. A line-of-sight unit vector, $\hat{\mathbf{u}}$, is calculated by using the following formula:

$$\hat{\mathbf{u}} = \cos(\theta)\sin(\psi)\hat{\mathbf{e}} + \cos(\theta)\cos(\psi)\hat{\mathbf{n}} + \sin(\theta)\hat{\mathbf{h}} \tag{1.24}$$

where: θ is the elevation angle to the satellite from the local horizontal plane.
ψ is the azimuth angle to the satellite from north.
$\hat{\mathbf{e}}$, $\hat{\mathbf{n}}$, $\hat{\mathbf{h}}$ are unit vectors in the directions east, north and 'up' respectively.

This method is hereafter referred to as the 'dot product (DP) method'. An epoch is found on the preceding day that most closely matches the geometry of the satellite, receiving antenna and surrounding reflectors at the current epoch. The effect of multipath interference on the measurement taken at the antenna at those two epochs should, in theory, be the same or at least very similar. This repeat period is not necessarily constant over the duration of a satellite pass, but can vary by a few seconds.

A similar method to determine repeat time is described in Agnew & Larson (2007) and is called 'aspect repeat time (ART)'. However, in that study, the aspect repeat times of all visible satellites are determined but are then averaged to effectively calculate a constellation repeat time at each epoch. That particular implementation is consequently aimed at position-domain sidereal filtering. Nevertheless, it can provide a significant improvement in positioning precision: Larson et al. (2007) showed that the technique could reduce the standard deviation of the north and east components of a 12-hour time series of position error from 8.2 mm to 5.1 mm and from 6.3 mm to 4.0 mm respectively.

Larson et al. (2007) showed that a satellite's aspect repeat period and the repeat period calculated using equation (1.23) agree more closely when that period is closer to the nominal value

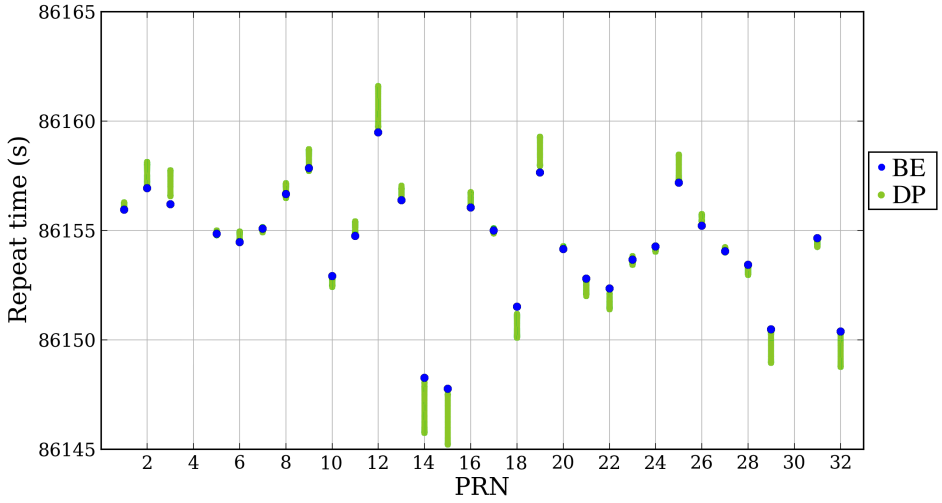

Figure 1.7 – Orbit repeat times, shown in blue, calculated using elements in the broadcast ephemeris (BE) and, shown in green, the *ranges* of repeat times calculated using the dot product (DP) method for each satellite pseudorandom noise code (PRN) visible at UCL on 3rd September 2013.

of around 86,155 seconds. Figure 1.7, which is similar to a figure that appears in Larson et al. (2007), shows the values of these two repeat periods for each visible GPS satellite over a 24-hour period (3rd September 2013) for a receiver antenna at UCL. Notice that as the calculated satellite repeat period deviates from the nominal value, this agreement becomes less valid. The reason for this will be touched upon in chapters 4 and 5. This discrepancy may only be a few seconds, but, as explained in section 1.4, if multipath oscillations occur at high frequencies, then it is thought that an inaccurate repeat time will reduce the effectiveness of the sidereal filter.

1.5.4 Examples of observation-domain sidereal filtering

Relatively few studies have applied sidereal filtering in the observation domain. Of these, most have done so in the context of positioning using double-differenced measurements rather than in precise point positioning (PPP). Measurements are double-differenced (DD) in order to largely eliminate many of the common error sources between satellites and nearby receivers as described in section 1.3.2. However, this complicates the calculation of the sidereal shift period(s) used in sidereal filtering. For example, all DD measurements, and hence DD measurement residuals, would each be associated with two satellites (and two receivers) and therefore two different ground-track repeat periods. Hence, to apply a rigorous sidereal filter to a series of DD measurements, should the average of the two repeat times be used? Should the repeat time of the satellite at the lower elevation be used since that satellite is more likely to be affected by multipath? The answers to these questions are not obvious. Working with position-domain sidereal filters, Choi et al. (2004)

and Agnew & Larson (2007) determine accurate repeat periods for each satellite at each epoch, but then calculate the mean of these repeat periods to find a 'constellation repeat period' for each epoch. However, not all signals at any one time are equally affected by multipath interference. Larson et al. (2007) accounts for this by choosing a repeat time which varies in order to minimise the RMS of a resulting position error time series across a 500 s window after sidereal filtering. However, this method is not applied in this thesis. Nevertheless, in position-domain sidereal filtering, the opportunity to tailor multipath corrections accordingly to suit the repeat period of each individual satellite is lost.

Ragheb et al. (2007) and Lau (2012) both compare sidereal filtering in both the position and DD measurement domains, finding little difference in performance between the two. In both studies, corrections to DD measurements are applied by taking into account the repeat periods of each corresponding satellite pair. Of course, there is the question of how a single repeat period is chosen for DD measurements derived from a pair of satellites that each have their own repeat period. Lau (2012) uses the lower-elevation satellite to determine the shift period since it is the signal from that satellite which is more likely to be affected by multipath interference. In contrast, Ragheb et al. (2007) uses the shift period that is required to produce the maximum correlation of the *position* coordinate residuals from both days over a 10-hour window.

Zhong et al. (2010) has perhaps done the most advanced study of observation-domain sidereal filtering in the context of positioning relative to static receivers. This method operates on receiver-receiver single-differenced measurements (see section 1.3.2), thus allowing consideration of each individual satellite's repeat period. The method is shown to yield an improvement of 82% in the RMS of a five-hour 1 Hz position error time series. However, in this case, the baseline length was very short: the distance from the 'rover' antenna to the reference antenna was only 121 m. With such a short baseline, any error remaining after double-differencing would almost entirely be due to measurement noise, multipath interference and possibly errors due to NLOS. Such a method would not be so effective over longer baselines and certainly could not be applied to PPP processing. Ye et al. (2015) applied this technique to both the GPS and the Chinese BeiDou navigation system, improving precision (RMSE) by 72%, 57% and 67% in easting, northing and height respectively. Note that the satellites of the Beidou system have different repeat periods to those of GPS. The possibility of developing algorithms similar to the sidereal filter algorithms outlined above for BeiDou and other GNSS is discussed below in section 1.6.

Although sidereal filtering has been applied in PPP processing, it has largely taken place in the position-domain. Very few studies have applied sidereal filtering in the observation-domain in the context of PPP. Reuveni et al. (2012) applies observation-domain sidereal filtering in PPP, but does so to GPS data recorded at a rate of only once every thirty seconds in order to measure slow-changing aseismic ground displacements, not short-period effects associated with an earthquake. There appears to be no in-depth study into the potential performance advantages of sidereal filtering in the observation-domain, which is what this thesis seeks to address.

1.6 Other GNSSs

As mentioned at the end of section 1.2.2, this thesis concentrates almost entirely on the GPS. This is because sidereal filtering is not applicable to systems that do not have *sidereal* ground-track repeat times. However, in recent years, new techniques have been developed that use multiple GNSSs in PPP processing (Jokinen et al. 2012, Li et al. 2014, Cai et al. 2015). Using GLONASS, BeiDou and/or Galileo in addition to GPS significantly increases the number of satellites visible to a receiver at any one time. This yields improvements over GPS-only PPP in terms of accuracy and convergence time. For example, Cai et al. (2015) demonstrated that GPS/BeiDou PPP improved the RMS of easting, northing and height error time series by 28%, 6% and 7% and reduced convergence time by 26%, 13% and 14% respectively over GPS-only PPP. With the use of multi-GNSS PPP likely to become more widespread in the future, consideration is given here to an algorithm similar to sidereal filtering that is applicable to GNSSs other than GPS. The relevant aspects of the GLONASS, Galileo and BeiDou systems are briefly described:

- The Russian **Globalnaya Navigatsionnaya Sputnikovaya Sistema (GLONASS)** currently consists of 24 operational satellites with eight orbiting in each of three orbital planes. They are inclined at 64.8° with respect to the equatorial plane thus ensuring greater satellite availability at high latitudes. These medium earth orbit (MEO) satellites orbit at an altitude of 19,000 km and have ground-track repeat periods of eight sidereal days (Fuhrmann et al. 2014).

- The European **Galileo** system is designed to consist of 30 satellites arranged across three orbital planes that are inclined at 56°. The specified altitude of these MEO satellites is 23,222 km with the ground-track repeat period being ten sidereal days (Fuhrmann et al. 2014).

- The Chinese **BeiDou** system is planned to consist of 27 MEO satellites orbiting at an altitude of 21,150 km, three inclined geosynchronous orbit (IGSO) satellites and five geostationary earth orbit (GEO) satellites. The ground-track repeat period of the MEO satellites is seven sidereal days and and the repeat period for the IGSO and GEO satellites is approximately one sidereal day (Ye et al. 2015).

Despite all of these different repeat periods, there is no reason, in principle, why algorithms similar to those outlined in sections 1.5.1 and 1.5.2 above cannot be applied when using these systems. Note that if using the BeiDou system alone, only an observation-domain filter can be applied because of the wide range of satellite repeat periods. This would also be the case if combining the measurements of more than one GNSS in PPP processing. However, the software used in this thesis currently accepts only GPS measurements as input. The use of other GNSSs is discussed further in chapter 10 where it is identified as an area for future research.

1.7 Research questions

As stated in section 1.5.2, observation-domain sidereal filtering enables each satellite to be considered separately. With this in mind, a number of questions arise that this thesis will seek to address:

1. Is an observation-domain sidereal filter more effective than a position-domain sidereal filter at reducing the effect of multipath error, and high-frequency multipath error in particular?

2. How well does observation-domain sidereal filtering perform relative to position-domain sidereal filtering when satellites with particularly anomalous repeat periods are visible?

3. How well does observation-domain sidereal filtering perform relative to position-domain sidereal filtering when a satellite is taken out of service, either expectedly or unexpectedly?

4. Can observation-domain sidereal filtering improve the ability of PPP to accurately measure small centimetre-level displacements of normally static receivers over the course of just a few minutes? In particular, can observation-domain sidereal filtering improve the measurement of permanent coseismic displacement in the immediate aftermath of an earthquake?

5. What impact does observation-domain sidereal filtering have on ones ability to distinguish between seismic waves and multipath error in PPP position time series?

1.8 Thesis Overview

Chapter 2 describes the PPP algorithm and the observation- and position-domain sidereal filtering algorithms that are implemented in this thesis. The research questions listed in section 1.7 are addressed in chapters 3 to 9: Chapter 3 compares the overall performance of the observation- and position-domain sidereal filters by analysing continuous 1 Hz position time series spanning several hours from a number of different antenna types and locations. Chapter 4 addresses the question of the performance of both types of sidereal filter during periods of time when satellites with anomalous repeat periods are visible. Chapter 5 examines the performance of both types of sidereal filter during periods of high-frequency multipath error. Chapter 6 assesses the performance of each of the sidereal filters during satellite outages. The ability of the sidereal filter algorithms to improve the accuracy of measurements of small centimetric displacements is assessed in chapter 7. In chapter 8, the sidereal filter algorithms are applied to GPS measurement data originating from a number of monitoring stations at the time of the 2010 M_{W} 7.2 El Mayor–Cucapah earthquake. The coseismic displacements calculated via PPP processing in this chapter are *not* used to calculate the moment magnitude of this event, but they are compared to displacements inferred from long-term position time series calculated by the University Navstar Consortium (UNAVCO). Chapter 9 examines the ability of the sidereal filter algorithms to remove errors caused by phase multipath interference from a position time series, thus aiding the identification of real transient displacements

caused by seismic waves emanating from the 2011 M_{W} 9.0 Tohoku-Oki earthquake. Chapter 10 summarises the main findings of this thesis and suggests topics for future research.

Chapter 2

Algorithm Implementation

This chapter begins by outlining the PPP algorithm that was used to process GPS measurements in each of the experiments described in the following chapters. The second part of this chapter (section 2.2) describes both the observation-domain and position-domain sidereal filter algorithms in detail.

2.1 PPP algorithm

The software used for all of the precise point positioning (PPP) processing in this thesis was developed by researchers at University College London from 2009. The author has contributed to the development of this software, principally with the addition of algorithms for sidereal filtering. It is largely written using the Python programming language and hence the source code can be edited relatively easily. Third-party software is used for some specific tasks: For example, open source 'GPS Toolkit' software (Tolman et al. 2004) is used to read and extract information from many of the input files.

The PPP software estimates the position of a static (or near-static) receiver antenna at each measurement epoch using un-differenced GPS ionosphere-free phase measurements. This is achieved by the implementation of an extended Kalman filter (EKF). This is an algorithm that estimates recursively the values of a set of parameters using a series of measurements observed over time. Sections 2.1.4 to 2.1.7 describe various aspects of the Kalman filter such as the state vector, system update, measurement innovations, measurement model and the measurement update. Figure 2.1 shows a system diagram outlining the overall structure of the software. The equations and their terms will be defined and detailed in the following discussion.

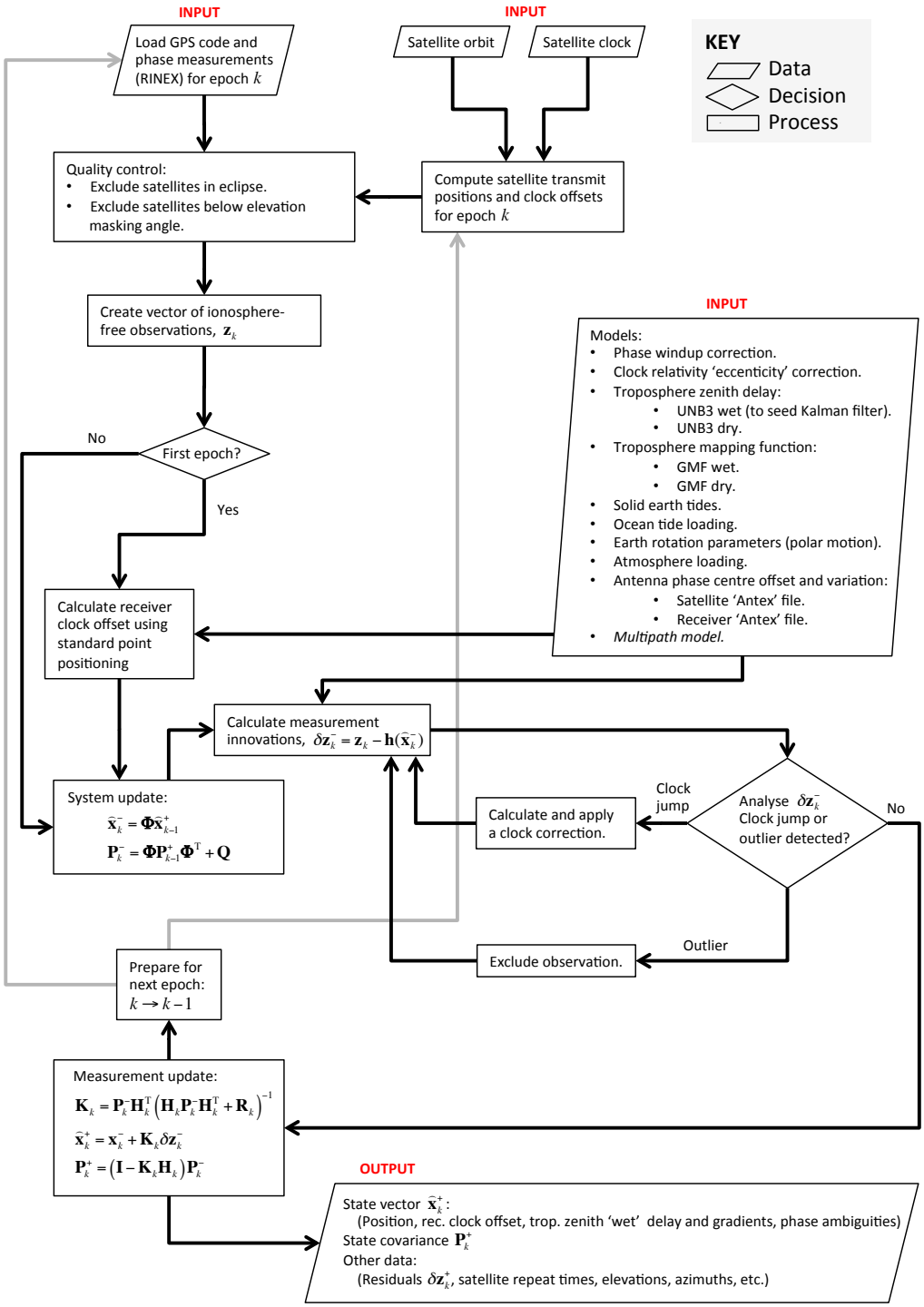

Figure 2.1 – System diagram of the PPP software. Please refer to the main text for descriptions and definitions of the equations and their terms, respectively.

2.1.1 Measurement input

The software accepts as input the GPS phase measurements that have been stored in receiver independent exchange format (RINEX) files.[1] Third-party open-source software, *GPS Toolkit* (Tolman et al. 2004), is used to read the RINEX files.

Satellite orbit and clock models are input via the 'SP3' and RINEX 'CLK' file formats, respectively.[2] In this thesis, these were both sourced from the Centre for Orbit Determination in Europe (CODE). This is because this analysis centre provides high-rate clock corrections at a spacing of only 5 s (Bock et al. 2009) which is suitable for high-rate (≥ 0.2 Hz) PPP processing. Again, GPS Toolkit is used to read the orbit file and interpolate satellite positions at the time of signal transmission. A correction (a rotation) is then applied to that satellite position to account for the rotation of the earth during signal travel time (see equation (1.6)). A relativistic satellite clock correction Δt_{rel} (Leick 2004) is also applied for each satellite to account for the periodic variation in the frequency of the satellite clock relative to an earth-bound clock. This is caused by the varying altitude and velocity of the satellites due to the eccentricity of their orbits. This correction is calculated as follows:

$$\Delta t_{\text{rel}} = -2\frac{\mathbf{r} \cdot \mathbf{v}}{c^2} \tag{2.1}$$

where $\mathbf{r}$ and $\mathbf{v}$ are the position and velocity of the satellite in an inertial frame in units of metres and metres per second, respectively, and c is the speed of light (299,792,458 m/s).

2.1.2 Quality control of input measurements

Any measurements from a satellite that is 'in eclipse', i.e. any satellite that is in the earth's shadow, or had been in the earth's shadow within the previous thirty minutes, is excluded from any processing. This is because of the difficulty in modelling a satellite's attitude when it is in eclipse: While a GPS satellite moves along it's orbital path, it must perform a slow rotation to maintain an attitude such that the transmitting antenna points towards the centre of the earth and the plane formed by the solar panels is perpendicular to the direction of the Sun. However, to maintain this orientation during a period of eclipse would require rapid yaw rotations exceeding the maximum yaw rate of which the satellites are capable. These rotations can potentially cause biases of several centimetres in the receiver-satellite range because of the offset of the transmitting antenna from the centre of mass in some GPS satellites (Weinbach 2013).

Any measurements from satellites that are below a specified elevation masking angle are rejected. This is to avoid excessive tropospheric, ionospheric and multipath interference. A masking angle of 10° is used throughout this thesis.

[1] A description of RINEX (version 2) file format is available at http://geodesy.noaa.gov/CORS/RINEX-2.txt.
[2] Descriptions of SP3 and CLK file formats are available at http://igscb.jpl.nasa.gov/components/formats.html.

2.1.3 Ionosphere-free observations

An ionosphere-free phase measurement Φ_{IF} can be formed by linearly combining phase measurements (in metres) on the GPS L1 and L2 broadcast frequencies, Φ_1 and Φ_2, as described in equation (1.12) (page 39), for any satellite visible at a particular epoch. Assuming that the interpolated position of the satellite is indeed its true position (so that the ephemeris error term O can be omitted), then substituting the phase observation equation (1.10) into equation (1.12) yields the ionosphere-free phase observation equation:

$$\Phi_{\text{IF}} = \rho + c(\delta t_r - \delta t^s) + T + A_{\Phi_{\text{IF}}} + M_{\Phi_{\text{IF}}} + W_{\Phi_{\text{IF}}} + \varepsilon_{\Phi_{\text{IF}}} \tag{2.2}$$

where: $A_{\Phi_{\text{IF}}}$ is the *ionosphere-free phase ambiguity* in metres, i.e.
$M_{\Phi_{\text{IF}}}$ is the *multipath error* affecting the ionosphere-free phase measurement in metres.
$W_{\Phi_{\text{IF}}}$ is the *phase wind-up error* affecting the ionosphere-free phase measurement in metres.
$\varepsilon_{\Phi_{\text{IF}}}$ is the *measurement noise* affecting the ionosphere-free phase measurement in metres.

Strictly speaking, the satellite clock offset δt^s is biased by electronic path delays to the timing signal generated onboard the satellite. Satellite clock offsets implied by the broadcast navigation message or those provided by analysis centres such as CODE are 'ionosphere-free' pseudorange clocks. However, this is not a concern for the method of 'float' PPP that is applied in this thesis because the bias is absorbed into the non-integer ionosphere-free phase ambiguity $A_{\Phi_{\text{IF}}}$.

For this thesis, only ionosphere-free phase measurements are input into the Kalman filter algorithm described in the following section. In practice, it was found that inputting pseudorange measurements into the Kalman filter made almost no difference at all to the resulting position time series after convergence because such measurements were given very little weight compared to the phase observations.

2.1.4 The state vector

The PPP algorithm is used to estimate the 'tide free' three-dimensional Cartesian coordinates (X_r, Y_r, Z_r) of the antenna reference point of a receiver r in an earth-centred earth-fixed (ECEF) reference frame for every epoch of measurement. These coordinates are 'tide free' in the sense that they are free from periodic movements due to the deformation of the body of the earth caused by the gravitational effects of the sun and the moon, polar motion and possible changes in loading on the earth's crust due to ocean tides and the atmosphere. These effects are discussed in section 2.1.6 below. Note that these coordinates contrast with the *instantaneous* coordinates of the antenna reference point which are denoted in this thesis with lower-case letters: (x_r, y_r, z_r).

The PPP software is based upon a *Kalman filter* algorithm. It estimates the value of each

element of a *state vector* $\mathbf{x}$ which consists of several parameters, not just the position of the receiver. The state vector is defined as follows:

$$\mathbf{x} = (X_r \quad Y_r \quad Z_r \quad c\delta t_r \quad T_{\text{zwd}} \quad G_N \quad G_E \quad A_1 \quad \dots \quad A_M)^{\text{T}} \tag{2.3}$$

where:
- X_r, Y_r, Z_r are the tide free coordinates of the reference point of the receiver antenna in metres.
- c is the *speed of light*, 299,792,458 m/s.
- δt_r is the *receiver clock offset* from GPS time in seconds.
- T_{zwd} is the 'wet' *tropospheric delay* at the zenith in metres.
- G_N, G_E are the north and east *troposphere gradient parameters*, respectively (see page 71).
- $A_1 \dots A_M$ are the non-integer ionosphere-free *phase ambiguities*, in meters, of M visible satellites.

The state vector is computed for each epoch using both the state vector that was estimated for the previous epoch and the measurements observed at the current epoch. This computation is carried out in two stages: Firstly, a *system update* (described in section 2.1.5 below) is performed to predict the value of the state vector and its associated covariance matrix for the current epoch. Secondly, a *measurement update* (described in section 2.1.7) is performed which refines the estimate of the state vector using measurements observed at the current epoch. This process is repeated for all subsequent epochs.

2.1.5 System update

The system update equations are defined below using the same notation as used in Groves (2013*b*):

$$\hat{\mathbf{x}}_k^- = \mathbf{\Phi}\hat{\mathbf{x}}_{k-1}^+ \tag{2.4}$$

$$\mathbf{P}_k^- = \mathbf{\Phi}\mathbf{P}_{k-1}^+\mathbf{\Phi}^{\text{T}} + \mathbf{Q} \tag{2.5}$$

where:
- $\hat{\mathbf{x}}_k^-$ is the time-propagated estimate of state vector at epoch k.
- $\hat{\mathbf{x}}_{k-1}^+$ is the estimate of the state vector at epoch $k-1$ following a measurement update (see section 2.1.7).
- $\mathbf{\Phi}$ is the state transition matrix used to propagate the state $\mathbf{x}$ and its co-variance matrix $\mathbf{P}$ from epoch $k-1$ to epoch k.
- $\mathbf{P}_k^-$ is the time-propagated estimate of the state error co-variance matrix at epoch k.
- $\mathbf{P}_{k-1}^+$ is the estimate of the error co-variance matrix at epoch $k-1$ following a measurement update.
- $\mathbf{Q}$ is the system noise co-variance matrix, which is the same for every epoch.

However, the Kalman filter is designed to estimate the position of a static or near-static receiver which has a relatively stable clock offset, so the predicted state vector is always assumed to be identical to the estimated state vector at the previous epoch, i.e. $\hat{\mathbf{x}}_k^- = \hat{\mathbf{x}}_{k-1}^+$. Hence, considering equation (2.4), the state transition matrix is simply the identity matrix, i.e. $\mathbf{\Phi} = \mathbf{I}$. Equation (2.5) also simplifies to $\mathbf{P}_k^- = \mathbf{P}_{k-1}^+ + \mathbf{Q}$.

The system noise co-variance matrix $\mathbf{Q}$ is:

$$\mathbf{Q} = \begin{pmatrix} S_{X_r}\Delta t & 0 & 0 & 0 & 0 & 0 & 0 & 0 & \dots & 0 \\ 0 & S_{Y_r}\Delta t & 0 & 0 & 0 & 0 & 0 & 0 & \dots & 0 \\ 0 & 0 & S_{Z_r}\Delta t & 0 & 0 & 0 & 0 & 0 & \dots & 0 \\ 0 & 0 & 0 & S_{c\delta t_r}\Delta t & 0 & 0 & 0 & 0 & \dots & 0 \\ 0 & 0 & 0 & 0 & S_{T_{\text{zwd}}}\Delta t & 0 & 0 & 0 & \dots & 0 \\ 0 & 0 & 0 & 0 & 0 & S_{G_N}\Delta t & 0 & 0 & \dots & 0 \\ 0 & 0 & 0 & 0 & 0 & 0 & S_{G_E}\Delta t & 0 & \dots & 0 \\ 0 & 0 & 0 & 0 & 0 & 0 & 0 & S_{A_1}\Delta t & \dots & 0 \\ \vdots & \vdots & \vdots & \vdots & \vdots & \vdots & \vdots & \vdots & \ddots & \vdots \\ 0 & 0 & 0 & 0 & 0 & 0 & 0 & 0 & \dots & S_{A_M}\Delta t \end{pmatrix}$$

where S_i is the power spectral density (PSD) of parameter i (in metres-squared per second) and Δt is a small time interval (in seconds). Throughout this thesis, $\Delta t = 1\,\text{s}$ because only 1 Hz measurements are used. For all of the PPP processing necessary for this thesis, the following PSD values were used:

- $S_{X_r} = S_{Y_r} = S_{Z_r} = 0.25\,\text{m}^2\text{s}^{-1}\left(= 30\,\text{m}/\sqrt{\text{hr}}\right)$. However, in some processing runs, the position states themselves were fixed to known (or previously determined) values, and so their PSD values were set to equal zero.
- $S_{c\delta t_r} = 1\,\text{m}^2\text{s}^{-1}\left(= 60\,\text{m}/\sqrt{\text{hr}}\right)$.
- $S_{T_{\text{zwd}}} = 2.5 \times 10^{-9}\,\text{m}^2\text{s}^{-1}\left(= 3\,\text{mm}/\sqrt{\text{hr}}\right)$ as suggested by Bar-Sever et al. (1998).
- $S_{G_N} = S_{G_E} = 2.5 \times 10^{-11}\,\text{m}^2\text{s}^{-1}\left(= 0.3\,\text{mm}/\sqrt{\text{hr}}\right)$ as suggested by Bar-Sever et al. (1998).
- $S_{A_i} = 10^{-10}\,\text{m}^2\text{s}^{-1}\left(= 0.6\,\text{mm}/\sqrt{\text{hr}}\right)$ for satellite i.

2.1.6 Measurement innovations and measurement model

The vector of measurement innovations $\delta\mathbf{z}_k^-$ at epoch k is then calculated. This is formed by subtracting the vector of *computed* measurements predicted using a measurement model, $\mathbf{h}(\hat{\mathbf{x}}_k^-)$ (defined below), from the vector of actual ionosphere-free measurements $\mathbf{z}_k$ at epoch k, i.e.

$$\delta\mathbf{z}_k^- = \mathbf{z}_k - \mathbf{h}(\hat{\mathbf{x}}_k^-) \tag{2.6}$$

The nonlinear measurement model used for an ionosphere-free *phase* measurement of a signal from a satellite at the receiver, h, is defined as follows:

$$\begin{aligned} \mathrm{h}\,(\mathbf{x}) \;=\; & \varphi + c(\delta t_r - \delta t^s) + A_{\Phi_{\mathrm{IF}}} + \mathrm{m}_h(\theta) T_{\mathrm{zhd}} + \mathrm{m}_w(\theta) T_{\mathrm{zwd}} \\ & + \mathrm{m}_w(\theta) \cot\theta \Big[G_N \cos\psi + G_E \sin\psi \Big] + W_{\Phi_{\mathrm{IF}}} - \Delta \end{aligned} \tag{2.7}$$

where: φ is the geometric range between the tide free coordinates of the receiver antenna reference point and the satellite centre of mass, in metres, i.e. $\varphi = \sqrt{(x^s - X_r)^2 + (y^s - Y_r)^2 + (z^s - Z_r)^2}$.

m_h, m_w are hydrostatic and wet mapping functions.

T_{zhd}, T_{zwd} are zenith hydrostatic and wet tropospheric delays, in metres.

θ, ψ are the satellite elevation and azimuth angles, in radians.

G_N, G_E are tropospheric gradient parameters.

Δ is a single term that combines the corrections in metres (in the direction from the receiver to the satellite) from a number of models of natural phenomena described in item 4 in the list below.

This measurement model is similar to equation (2.2) but a number of important remarks need to be made:

1. As described on page 40, the tropospheric delay in equation (2.7) is split into the 'hydrostatic' (or 'dry') and 'wet' components. The **zenith hydrostatic delay** T_{zhd} is calculated using a troposphere model, *UNB3*, from the University of New Brunswick, Canada. It is therefore treated as a known quantity. On the other hand, the **zenith wet delay** T_{zwd}, together with any error in the dry troposphere model, is one of the states estimated in the Kalman filter. Both of these zenith delays have respective hydrostatic and wet **mapping functions**, m_h and m_w respectively, which are functions of the satellite elevation angle θ (see page 40). The software applies the wet and dry Global Mapping Functions (Boehm et al. 2006) by default.

2. Tropospheric delay is generally not azimuthally homogeneous (Bar-Sever et al. 1998), especially if a weather front is approaching where the conditions within the troposphere on one side of the receiver differ to those on the opposite side. This phenomenon is mitigated by estimating two **troposphere gradient parameters**, G_N and G_E, in the Kalman filter. This purposefully introduces a component of the tropospheric delay that depends on the *azimuth* of the satellite—not just the satellite's elevation. This concept was first implemented by Bar-Sever et al. (1998) where it was shown to increase the repeatability of horizontal position estimates by about 15%.

3. Note that the **satellite clock offset** δt^s from GPS system time is considered in the PPP software as a known quantity at every epoch due to the use of precise high-rate clock files (usually 5-second data rate clocks from the CODE) and a simple linear interpolation algorithm.

4. Four models, represented here by the term Δ, are applied in order to account for various natural phenomena such as tidal effects. This is because the coordinates (X_r, Y_r, Z_r) estimated using the Kalman filter are the 'tide free' coordinates, not the true instantaneous coordinates (x_r, y_r, z_r) at any one time. Strictly speaking, the coordinates are 'conventional tide free' coordinates according to conventions described by the International Earth Rotation Service (IERS Conventions 2010). All of these adjustments are estimated using models and are hence not estimated in the Kalman filter:

   - **Solid earth tides.** An adjustment is applied to account for station displacement caused by the deformation of the solid earth caused by the gravitational attraction of the sun and the moon. Such an adjustment is calculated using a third-party Fortran software, *dehanttideinel.f*, from the International Earth Rotation Service (IERS). In terms of position, such an adjustment can be as much as 30 cm in height and 5 cm horizontally (Kouba 2009). The necessary component of the adjustment in the receiver-satellite direction is applied to the predicted phase measurements (and pseudorange measurements, if necessary).
   - **Ocean tide loading.** An adjustment is applied to account for station displacement caused by the weight of moving water in the world's oceans on the underlying crust. These displacements can exceed 10 cm in some coastal areas (Baker et al. 1995). The software calculates this displacement using a Fortran routine, *hardisp.f*, as recommended by IERS Conventions (2010). This routine takes as input the amplitudes and phases of the 11 main ocean tide components (at the station's location) as produced by the Onsala Space Observatory in Sweden (Bos & Scherneck 2011). These amplitudes and phases are produced by convolving the Gutenberg-Bullen continental Earth response model with the Finite Element Solution 2004 (FES2004) numerical ocean tide model (Lyard et al. 2006). Ocean tides also cause movement of the centre of mass of the earth (solid earth, oceans and atmosphere) with respect to the solid body of the earth (IERS Conventions 2010). As stated in Kouba (2009), the given adjustments for ocean tide loading are intentionally not corrected for the motion of the earth's centre of mass relative to the solid body of the earth. This is because the coordinate frame implied by the use of the precise orbit files from the CODE is already fixed to the earth's crust. The appropriate component of these adjustments for ocean tide loading are then applied to the predicted measurements.
   - **Pole tide.** The location of the earth's axis of rotation relative to the earth's crust changes over time. Such movement causes small changes in the earth's centrifugal potential resulting in small deformations in the earth's surface of up to 25 mm vertically and 7 mm horizontally (Kouba 2009). These deformations are calculated using data from the IERS and are applied to the predicted measurements.

- **Atmospheric tide loading.** Displacement of the ground due to variation in atmospheric loading is very small, usually just a few millimetres. Tregoning & van Dam (2005) state that the maximum variation in vertical position within a 24-hour period can be as high as 18 mm. The radial or 'up' displacement dr in millimetres for a given time t (in fractions of a UT1 day) is calculated using equation (2.8) (van Dam & Ray 2010):

$$\mathrm{d}r(t) = \mathrm{A}_{\mathrm{d}r,1}\cos(2\pi t) + \mathrm{B}_{\mathrm{d}r,1}\sin(2\pi t) + \mathrm{A}_{\mathrm{d}r,2}\cos(4\pi t) + \mathrm{B}_{\mathrm{d}r,2}\sin(4\pi t) \tag{2.8}$$

  where $\mathrm{A}_{\mathrm{d}r,1}$, $\mathrm{B}_{\mathrm{d}r,1}$ and $\mathrm{A}_{\mathrm{d}r,2}$, $\mathrm{B}_{\mathrm{d}r,2}$ are the amplitudes (in millimetres) of the cosines and sines of the diurnal (S_1) and semidiurnal (S_2) atmospheric tides, respectively. Similar equations are used for the north and east components. These coefficients are computed for the station's location using the *grdintrp.f* Fortran routine provided by the Global Geophysical Fluid Center at the University of Luxembourg (van Dam & Ray 2010). As with ocean tide loading, these adjustments are not corrected for the motion of the earth's centre of mass relative to the solid body of the earth. The necessary component of the adjustment is applied to each of the predicted measurements at each epoch.

Following the formation of the measurement innovations vector $\delta\mathbf{z}_k^-$, it is analysed for errors such as cycle slips and sudden changes in the receiver clock offset. This is described in section 2.1.8.

2.1.7 Measurement update

The Kalman gain matrix $\mathbf{K}_k$ and the extended Kalman filter measurement update equations (Groves 2013*b*) are defined as:

$$\mathbf{K}_k = \mathbf{P}_k^-\mathbf{H}_k^{\mathrm{T}}\Big(\mathbf{H}_k\mathbf{P}_k^-\mathbf{H}_k^{\mathrm{T}} + \mathbf{R}_k\Big)^{-1} \tag{2.9}$$

$$\hat{\mathbf{x}}_k^+ = \hat{\mathbf{x}}_k^- + \mathbf{K}_k\delta\mathbf{z}_k^- \tag{2.10}$$

$$\mathbf{P}_k^+ = \Big(\mathbf{I} - \mathbf{K}_k\mathbf{H}_k\Big)\mathbf{P}_k^- \tag{2.11}$$

where:
- $\mathbf{P}_k^+$ is the estimate of the error covariance matrix at epoch k following a measurement update.
- $\mathbf{H}_k$ is the measurement matrix at epoch k.
- $\mathbf{R}_k$ is the measurement noise covariance matrix at epoch k.
- $\hat{\mathbf{x}}_k^+$ is the estimate of the state vector at epoch k following a measurement update.

The measurement noise covariance matrix $\mathbf{R}_k$ is, in this case, a diagonal matrix consisting of the modelled variances of the measurement errors. Ionosphere-free phase and code measurements are assigned standard deviations of $1/\sin\theta \times 0.015$ m and $1/\sin\theta \times 2$ m, respectively. The elements of

measurement matrix $\mathbf{H}_k$ are the partial derivatives of the nonlinear measurement model $\mathbf{h}(\mathbf{x})$ with respect to the parameters in the state vector $\mathbf{x}$ evaluated using its estimated values following a system update, i.e.

$$\mathbf{H}_k = \left.\frac{\partial \mathbf{h}(\mathbf{x})}{\partial \mathbf{x}}\right|_{\mathbf{x}=\hat{\mathbf{x}}_k^-} \tag{2.12}$$

If only ionosphere-free phase measurements are input into the Kalman filter, then the matrix $\mathbf{H}_k$ appears as follows:

$$\mathbf{H}_k = \begin{pmatrix} \frac{X_r - x^1}{\varphi_1} & \frac{Y_r - y^1}{\varphi_1} & \frac{Z_r - z^1}{\varphi_1} & 1 & \mathrm{m}_w(\theta_1) & \mathrm{m}_w(\theta_1)\frac{\cos\psi_1}{\tan\theta_1} & \mathrm{m}_w(\theta_1)\frac{\sin\psi_1}{\tan\theta_1} & 1 & 0 & \dots & 0 \\ \frac{X_r - x^2}{\varphi_2} & \frac{Y_r - y^2}{\varphi_2} & \frac{Z_r - z^2}{\varphi_2} & 1 & \mathrm{m}_w(\theta_2) & \mathrm{m}_w(\theta_2)\frac{\cos\psi_2}{\tan\theta_2} & \mathrm{m}_w(\theta_2)\frac{\sin\psi_2}{\tan\theta_2} & 0 & 1 & \dots & 0 \\ \vdots & \vdots & \vdots & \vdots & \vdots & \vdots & \vdots & \vdots & \vdots & \ddots & \vdots \\ \frac{X_r - x^M}{\varphi_M} & \frac{Y_r - y^M}{\varphi_M} & \frac{Z_r - z^M}{\varphi_M} & 1 & \mathrm{m}_w(\theta_M) & \mathrm{m}_w(\theta_M)\frac{\cos\psi_M}{\tan\theta_M} & \mathrm{m}_w(\theta_M)\frac{\sin\psi_M}{\tan\theta_M} & 0 & 0 & \dots & 1 \end{pmatrix}$$

where:
- X_r, Y_r, Z_r are the estimated coordinates of the tide free receiver antenna reference point at epoch k.
- x^s, y^s, z^s are the coordinates of satellite s at epoch k.
- φ_s is the geometric range between the tide free receiver antenna reference point and the centre of mass of satellite s at epoch k.
- θ_s, ψ_s are the elevation and azimuth angles of satellite s at epoch k.

2.1.8 Further quality control

The software implements a layer of quality control before the measurement update step by analysing the vector of measurement innovations $\delta\mathbf{z}_k^-$ at each epoch k using the local overall model (LOM) test described by Teunissen & Kleusberg (1998). This process is called *innovation filtering*. This technique is used to detect measurement outliers caused by cycle slips, sudden changes in the receiver clock offset and non-line-of-sight (NLOS) reception (see page 52). The test statistic T_{LOM} is defined as:

$$T_{\mathrm{LOM}} = \frac{(\delta\mathbf{z}_k^-)^{\mathrm{T}}\mathbf{C}^{-1}\delta\mathbf{z}_k^-}{M} \tag{2.13}$$

where:
- $\mathbf{C}$ is the innovation covariance matrix, which is calculated as $\mathbf{C} = \mathbf{H}_k\mathbf{P}_k^-\mathbf{H}_k^{\mathrm{T}} + \mathbf{R}_k$ which forms part of equation (2.9) above.
- M is the number of measurements used at epoch k.

An error is considered present if T_{LOM} exceeds the F-distribution value corresponding to 5% significance with M (numerator) and infinite (denominator) degrees of freedom, i.e. if $T_{\mathrm{LOM}} \geq F_{0.05}(M, \infty)$ (Teunissen & Kleusberg 1998). If an error is detected, it is then necessary to identify the measurement(s) associated with that error. Firstly, a test statistic w_i is calculated for each

measurement i as follows:

$$w_i = \frac{\mathbf{c}_i^{\mathrm{T}} \mathbf{C}^{-1} \delta \mathbf{z}_k^-}{\sqrt{\mathbf{c}_i^{\mathrm{T}} \mathbf{C}^{-1} \mathbf{c}_i}} \tag{2.14}$$

where $\mathbf{c}_i$ is a column vector of zeros except for element i (where $i \in \{1, \ldots, M\}$) which equals one (El-Mowafy 2015). A test statistic w_0 is also computed for the case where $\mathbf{c}_i$ is replaced with a column vector of ones. This is in order to determine if the error is due to a receiver clock jump, which should affect all measurements equally. If the magnitude of this value w_0 exceeds the absolute value of all values of w_i, a clock jump is assumed. The mean value of all elements of the innovation vector $\delta \mathbf{z}_k^-$ is used to correct the receiver clock state $c\delta t_r$. Otherwise, in this implementation, the fault is assumed to lie with the measurement associated with the largest absolute value of w_i and is excluded. The measurement innovation vector $\delta \mathbf{z}_k^-$ is then recalculated using equation (2.6).

2.1.9 Software output

For every epoch k, the estimated state vector $\hat{\mathbf{x}}_k^+$ and its covariance matrix $\mathbf{P}_k^+$ are time-tagged and stored in a database. Each position (X_r, Y_r, Z_r) in the time series is also transformed into a local topocentric coordinate system. This is a right-handed east-north-height coordinate system with the origin placed at the calculated mean position (or the pre-determined position) of the antenna. The transformation from a Cartesian earth-centred earth-fixed (ECEF) position (X, Y, Z) to a topocentric east-north-height position (E, N, H) is described as follows:

$$\begin{pmatrix} E \\ N \\ H \end{pmatrix} = \begin{pmatrix} -\sin\lambda & \cos\lambda & 0 \\ -\sin\psi\cos\lambda & -\sin\psi\sin\lambda & \cos\psi \\ \cos\psi\cos\lambda & \cos\psi\sin\lambda & \sin\psi \end{pmatrix} \begin{pmatrix} X - \bar{X} \\ Y - \bar{Y} \\ Z - \bar{Z} \end{pmatrix} \tag{2.15}$$

where: ψ, λ are the latitude and longitude (in radians) of the mean position of the antenna with respect to the Geodetic Reference System 1980 (GRS80) ellipsoid (Moritz 2000). These are calculated using the method described in appendix A.

$(\bar{X}, \bar{Y}, \bar{Z})$ are the mean coordinates of the antenna in an ECEF frame (in metres).

The PPP software outputs additional data for each epoch, such as the elevation and azimuth angles for each visible satellite and the vector of measurement residuals $\delta \mathbf{z}_k^+$, defined in the following equation:

$$\delta \mathbf{z}_k^+ = \mathbf{z}_k - \mathbf{h}(\hat{\mathbf{x}}_k^+) \tag{2.16}$$

The storage of these values is important because they are necessary for the observation-domain sidereal filter algorithm—described in the following section—to function: The corrections for multipath error are derived from these measurement residuals.

2.2 Sidereal Filter Algorithms

2.2.1 Observation-domain sidereal filter (ODSF)

In order to best describe the observation-domain sidereal filter (ODSF) algorithm, a simple arbitrary example is used. It is assumed that two sets of GPS data, collected on adjacent days, are available: day 1 and day 2 (which are sometimes referred to as the 'template' and 'current' days, respectively, in this thesis). It is also assumed that the tide free ECEF position of the receiver on day 1 is already known, either after processing day 1 to yield an average position, or by some other method. The objective is to remove the multipath effect from day 2 by applying a sidereal filter. This filter will use information from day 1 to compute the necessary multipath corrections.

The RINEX data from day 1 is processed using the Kalman filter algorithm described in section 2.1, but with the position states X_r, Y_r and Z_r held fixed to the known tide free ECEF position of the receiver antenna r by setting their noise power spectral densities (PSDs) to zero, i.e. $S_{X_r} = S_{Y_r} = S_{Z_r} = 0\,\mathrm{m^2 s^{-1}}$, and setting the initial variances in the error covariance matrix $\mathbf{P}$ corresponding to the position states to zero, i.e. $\sigma^2_{X_r} = \sigma^2_{Y_r} = \sigma^2_{Z_r} = 0\,\mathrm{m^2}$. The resulting time series of measurement residuals (defined in equation (2.16) above) are time-tagged and stored in a database ready to be used to calculate measurement-domain (or observation-domain) multipath corrections for the PPP processing of the measurements on day 2. The following paragraphs describe mathematically how these residuals are used as multipath corrections.

Consider an ionosphere-free phase measurement z. Equation (2.2) is re-stated here for convenience:

$$z = \Phi_{\mathrm{IF}} = \rho + c\delta t_r - c\delta t^s + T + A_{\Phi_{\mathrm{IF}}} + M_{\Phi_{\mathrm{IF}}} + W_{\Phi_{\mathrm{IF}}} + \varepsilon_{\Phi_{\mathrm{IF}}} \tag{2.17}$$

Consider also $\mathrm{h}\left(\hat{\mathbf{x}}_k^+\right)$ which is the computed measurement to a satellite at an epoch k calculated using the state vector *following* a measurement update, $\hat{\mathbf{x}}_k^+$. By omitting the superscript + and subscript k and using equation (2.7), the following equation can be written:

$$\begin{aligned} \mathrm{h}\left(\hat{\mathbf{x}}\right) \;=\; & \widehat{\varphi} + \widehat{c\delta t_r} - c\delta t^{s*} + \widehat{A}_{\Phi_{\mathrm{IF}}} + \mathrm{m}_h(\theta) T^*_{\mathrm{zhd}} + \mathrm{m}_w(\theta)\widehat{T}_{\mathrm{zwd}} \\ & + \mathrm{m}_w(\theta)\cot\theta\Big[\widehat{G}_N\cos\psi + \widehat{G}_E\sin\psi\Big] + W^*_{\Phi_{\mathrm{IF}}} - \Delta^* \end{aligned} \tag{2.18}$$

where a caret symbol $\widehat{\ }$ denotes a parameter to be estimated in the Kalman filter and the terms marked with an asterisk * denote parameters that are estimated using a model and hence treated as known quantities. From equation (2.16), a single measurement residual can be written as $\delta z_k^+ = z_k - \mathrm{h}(\hat{\mathbf{x}}_k^+)$. Using equations (2.17) and (2.18) and omitting the superscript + and subscripts k and Φ_{IF}, this equation can be expanded as follows:

$$\begin{aligned} \delta z \;=\; & \rho + c\delta t_r - c\delta t^s \;+ T \;+ A + W \;+ M + \varepsilon \\ & - \widehat{\varphi} - \widehat{c\delta t_r} + c\delta t^{s*} - \widehat{T}^* - \widehat{A} - W^* + \Delta^* \end{aligned} \tag{2.19}$$

$$\text{where} \quad \widehat{T}^* = \mathrm{m}_h(\theta) T^*_{\mathrm{zhd}} + \mathrm{m}_w(\theta)\widehat{T}_{\mathrm{zwd}} + \mathrm{m}_w(\theta)\cot\theta\Big[\widehat{G}_N\cos\psi + \widehat{G}_E\sin\psi\Big]$$

Once the Kalman filter is initiated, a sufficient number of epochs need to be processed in order for the state vector to converge to a steady state. As discussed in section 1.3.5, this takes around 30 minutes for the position states to reach decimetre-level accuracy. In chapter 3, section 3.4, it is noted that around four hours of 1 Hz GPS measurements have to be processed before the position states converge to within 3 cm of the tide free position. Following convergence, the following *assumptions* are then made:

- $\rho - \widehat{\varphi} + \Delta^* \approx 0$. This assumption is made because the tide free coordinates of the receiver are within a few centimetres of their true value in an ECEF reference frame, the position of the satellite is presumed to be accurate to within 2.5 cm (if IGS 'final' orbits are used), and the tidal corrections are assumed to be accurate at the level of a few centimetres. Note that this assumption is less valid if real-time orbits are used.

- $c\delta t_r - \widehat{c\delta t_r} \approx 0$ because the difference between the true receiver clock offset and its estimated value is assumed to be small.

- $-c\delta t^s + c\delta t^{s*} \approx 0$ because the difference between the true satellite clock offset and the value calculated using a precise clock model is assumed to be small. IGS 'final' satellite clock offsets have a stated RMS accuracy of 75 ps (2 cm). Again, this assumption is less valid if real-time clocks are used.

- $T - \widehat{T}^* \approx 0$ because the difference between the true tropospheric delay and its estimated value is assumed to be small. This is because the difference between the true dry tropospheric delay and the value calculated using the *UNB3* troposphere model is assumed to be small. According to Collins & Langley (1999), the nominal zenith error of the *UNB3* model is -2 ± 5 cm (1σ). Any error in this model is at least partially compensated by the estimation of the zenith wet tropospheric delay $\widehat{T}_{\text{zwd}}$ and the gradient parameters $\widehat{G}_N$ and $\widehat{G}_E$. Also, the difference between the true wet tropospheric delay and its estimated value is assumed to be small.

- $A - \widehat{A} \approx 0$ because the difference between the true ionosphere-free ambiguity—a term that includes satellite and receiver hardware delays—and its estimated value is assumed to be small.

- $W - W^* \approx 0$ because the difference between the true phase wind-up error and the value calculated using GPS Toolkit software (Tolman et al. 2004) is assumed to be small for all visible satellites not in eclipse.

Of course, the true value of each of the above parameters is unknown, but it is assumed that each of the above parameters, either estimated by the Kalman filter or sourced from an external model, are accurate to within a few centimetres. With the exception of the satellite and receiver clock offset parameters, any error in these assumptions should vary slowly with time, i.e. they can be

considered as having a constant value over intervals of a few tens of seconds. With all of the above assumptions, the measurement residual δz can be written as follows:

$$\delta z \approx M + \varepsilon \tag{2.20}$$

However, if the error accumulated by making the above assumptions was combined into a single term E, equation (2.20) can be re-written:

$$\delta z = M + E + \varepsilon \tag{2.21}$$

The phase of a carrier signal can be measured to a precision of around 0.01–0.05 cycles (2 mm–1 cm) (Misra & Enge 2006). Assuming that L1 and L2 phase measurements are made to a precision of 5 mm, then the ionosphere-free phase measurement noise term ε, a stochastic random variable, will have an assumed standard deviation of about 15 mm by equation (1.13). If δz is be used as a multipath correction to a measurement that is also affected by noise, one of the effects of applying that correction would be to further amplify the measurement noise by a factor of about $\sqrt{2}$. To minimise this effect, the time series of residuals is smoothed using a fifth-order Butterworth low-pass filter. The choice of a suitable cut-off frequency for this low-pass filter is discussed in chapter 5. Unless otherwise stated, the cut-off frequency is 0.2 Hz. The choice of cut-off frequency is considered crucial: a balance has to be made between reducing the amplification of measurement noise and yet preserving the effect of high-frequency multipath in the multipath corrections. The residuals can be smoothed by using an appropriately-sized moving average window instead if desired. After this process, equation (2.21) can be re-written as:

$$\langle \delta z \rangle \approx M + E \tag{2.22}$$

where $\langle \delta z \rangle$ denotes δz after smoothing using a low-pass filter. Hence, with all of the above assumptions, the smoothed phase observation residual is approximately equal to the carrier phase multipath error plus a small slowly-varying bias. In practice, the unsmoothed value δz is stored in a database for later use for deriving corrections for multipath by smoothing.

Returning to the example, day 2 is processed via the PPP Kalman filter with the position states no longer fixed and an appropriate residual is retrieved from the database, smoothed, and applied as a correction to the relevant GPS phase measurement at each epoch. The process of pairing measurements with appropriate corrections is implemented using one of the two principles described previously in sections 1.5.3.1 and 1.5.3.2 (page 57), but their implementation is described in the following sections.

2.2.1.1 Using the 'dot product method' to determine repeat time

For each observation at each epoch, an observation residual from the previous day has to be found that corresponds to when the satellite associated with that observation was as close as possible to

the same position in the sky. The search algorithm is outlined by the system diagram in figure 2.2 and is described as follows:

1. Consider a single ionosphere-free phase measurement z_{k_2} at a receiver from one particular satellite at epoch k_2 during day 2. From equation (2.17), z_{k_2} can be written as follows:

$$z_{k_2} = \Phi_{\mathrm{IF}\,k_2} = \rho_{k_2} + c\delta t_{r\,k_2} - c\delta t^s{}_{k_2} + T_{k_2} + A_{k_2} + M_{k_2} + W_{k_2} + \varepsilon_{k_2} \tag{2.23}$$

   Using the most up-to-date estimate of the position of the receiver and the interpolated satellite position, the azimuth θ_{k_2} and elevation ψ_{k_2} of that satellite with respect to the receiver's local topocentric (east-north-up) coordinate system is calculated. A receiver-to-satellite unit-vector, $\hat{\mathbf{u}}_{k_2}$, is then formed using equation (1.24) (page 58), but is re-stated here for convenience as equation (2.24):

$$\hat{\mathbf{u}}_{k_2} = \cos(\theta_{k_2})\sin(\psi_{k_2})\hat{\mathbf{e}} + \cos(\theta_{k_2})\cos(\psi_{k_2})\hat{\mathbf{n}} + \sin(\theta_{k_2})\hat{\mathbf{h}} \tag{2.24}$$

   where: θ_{k_2} is the elevation angle to the satellite from the local horizontal plane.
   ψ_{k_2} is the azimuth angle to the satellite from north.
   $\hat{\mathbf{e}}$, $\hat{\mathbf{n}}$, $\hat{\mathbf{h}}$ are unit vectors in the directions east, north and 'up' respectively.

2. A *preliminary* epoch k_1' is found on day 1 that precedes epoch k_2 by one ground track repeat period of 86,155 seconds.[3] The associated satellite azimuth and elevation angles are retrieved from this epoch and adjacent epochs on either side, forming a 'window' of three epochs. For these epochs, unit-vectors $\hat{\mathbf{u}}_{k_1'-1}$, $\hat{\mathbf{u}}_{k_1'}$ and $\hat{\mathbf{u}}_{k_1'+1}$ are also formed using equation (2.24).

3. The objective is to find the epoch k_1 such that the dot product $\hat{\mathbf{u}}_{k_1} \cdot \hat{\mathbf{u}}_{k_2}$ is maximised. Of the three unit-vectors $\hat{\mathbf{u}}_{k_1'-1}$, $\hat{\mathbf{u}}_{k_1'}$ and $\hat{\mathbf{u}}_{k_1'+1}$, if the maximum dot product does not occur using the 'central' unit-vector, $\hat{\mathbf{u}}_{k_1'}$, the three-epoch window is moved forward or backward by one epoch as appropriate. The process is repeated until the maximum dot product *does* occur with the central unit-vector at which point epoch k_1 is found.

4. The corresponding multipath estimate derived from the smoothed measurement residual at epoch k_1, $\langle \delta z_{k_1} \rangle$, is subtracted from the measurement at epoch k_2, z_{k_2} to form a new corrected measurement $z_{k_2\,\mathrm{corr}}$:

$$\begin{aligned} z_{k_2\,\mathrm{corr}} &= z_{k_2} - \langle \delta z_{k_1} \rangle \\ &= \rho_{k_2} + c\delta t_{r\,k_2} - c\delta t^s{}_{k_2} + T_{k_2} + A_{k_2} + M_{k_2} + W_{k_2} + \varepsilon_{k_2} - \langle \delta z_{k_1} \rangle \end{aligned} \tag{2.25}$$

[3] For subsequent iterations of this algorithm, this value of 86,155 seconds is altered for each visible satellite to match the repeat time found by this algorithm during the processing of the previous epoch, thereby accelerating this search algorithm.

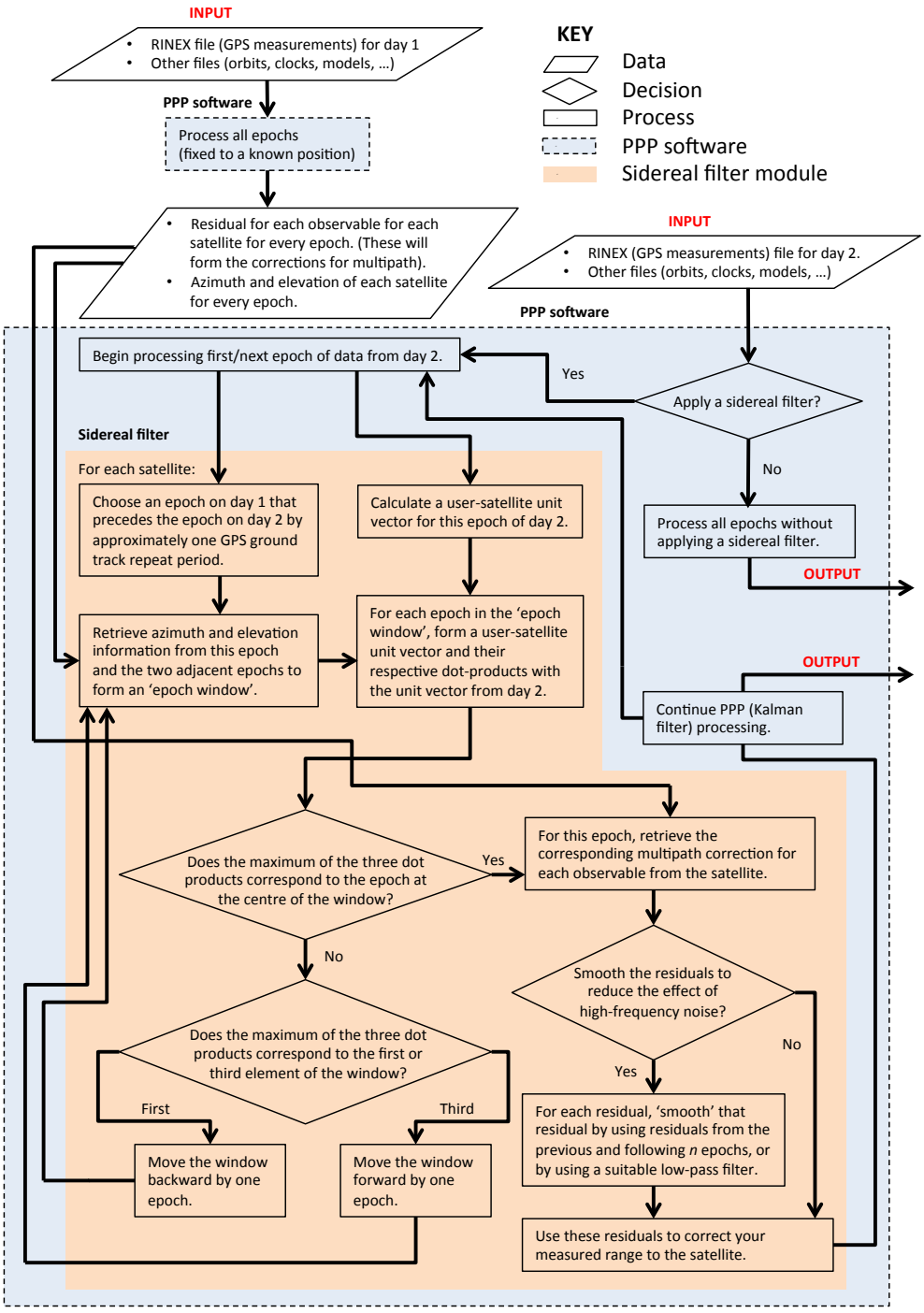

Figure 2.2 – System diagram of the observation-domain sidereal filter software algorithm which uses line-of-sight unit vectors to search for multipath corrections to GPS measurements.

By equation (2.22), $\langle \delta z_{k_1} \rangle \approx M_{k_1} + E_{k_1}$. Also, by making the key assumption that $M_{k_2} \approx M_{k_1}$ (as discussed in section 1.5), equation (2.25) can be re-written as follows:

$$\begin{aligned} z_{k_2\,\mathrm{corr}} &\approx \rho_{k_2} + c\delta t_{r\,k_2} - c\delta t^s{}_{k_2} + T_{k_2} + A_{k_2} + W_{k_2} + M_{k_2} + \varepsilon_{k_2} - M_{k_1} - E_{k_1} \\ &\approx \rho_{k_2} + c\delta t_{r\,k_2} - c\delta t^s{}_{k_2} + T_{k_2} + A_{k_2} + W_{k_2} + \varepsilon_{k_2} - E_{k_1} \end{aligned} \tag{2.26}$$

Notice that the multipath terms have been eliminated by this assumption. In theory, this corrected measurement $z_{k_2\,\mathrm{corr}}$, together with other corrected measurements associated with other satellites at epoch k_2, form a vector of corrected measurements $\mathbf{z}_{k_2}$ that is used to calculate the measurement innovations in equation (2.6). In practice however, the multipath correction $\langle \delta z_{k_1} \rangle$ is *added* to the computed measurement to the satellite $\mathrm{h}(\hat{\mathbf{x}}^-_{k_2})$. i.e.

$$\delta z^-_{k_2} = z_{k_2} - \left[\mathrm{h}(\hat{\mathbf{x}}^-_{k_2}) + \langle \delta z_{k_1} \rangle\right] \tag{2.27}$$

The above process is repeated for each satellite in view at each epoch on day 2. Notice that equation (2.26) still contains the term E_{k_1} which is the error accumulated from errors in the third-party models and the difference between the values of the parameters estimated by the Kalman filter on day 1 and their true values. As mentioned above, this error is assumed to have an absolute magnitude of a few centimetres but varies slowly with time. So if these 'corrected' measurements are used in the Kalman filter algorithm, this error is likely to alias into the estimated parameters, such as the troposphere parameters, phase ambiguities and even the position states. However, this may not be such a problem if the objective is to accurately measure the *changes* in the position of a receiver over a period of a few tens of seconds to a few hundred seconds, not the absolute position. If this accumulated error is relatively stable over such intervals, then its effect on calculating coseismic offsets, for example, should be small.

On some occasions, there may be measurements in day 2 for which no multipath correction can be found. Such cases can arise simply if a series of measurements are missing from the RINEX file, either because of interference or a satellite outage. Unless otherwise stated in this thesis, if no correction is available, then that measurement is excluded from the Kalman filter. This means that if an ODSF is applied in PPP processing, then only the measurements that have been corrected for multipath are used. However, the case for including all available measurements, whether or not they have been corrected for multipath, is examined in chapter 6, section 6.3 (page 185).

2.2.1.2 Using the broadcast ephemeris to calculate repeat time

Alternatively, for each observation at any particular epoch k_2 on day 2, a multipath correction is derived from the epoch k_1 on the previous day that corresponds to the satellite's orbit repeat time as calculated using information within the satellite's broadcast ephemeris: the square root of the semi-major axis a_s and correction to mean motion n_c. A repeat time can then be calculated by using equation (1.23) (page 57). The method by which the correction is applied to the observations

is identical to the one described above for the dot product (DP) method. The repeat time yielded by the broadcast ephemeris (BE) method will differ slightly for the reasons stated in section 1.5.3.2. However, the significance of this small difference in repeat times will be examined in later chapters.

2.2.2 Position-domain sidereal filter (PDSF)

The position-domain sidereal filter (PDSF) algorithm described below is used throughout this thesis. Again, to describe the algorithm, a simple arbitrary example is used. Two sets of GPS measurements are collected on two adjacent days: day 1 and day 2. As before, it is also assumed that the 'true' position of the receiver on day 1 is already known. The objective is to identify the multipath error signature in the position time series of day 1 and use it to remove multipath errors from day 2.

The GPS measurements from day 1 are processed using the PPP Kalman filter as described in section 2.1. In contrast to the formation of the ODSF, the position states are *not* fixed and a time series of position coordinates is produced. The 'true' position of the receiver (X, Y, Z) is then subtracted from each estimated position coordinate in the time series yielding a position residual $(\delta X_k, \delta Y_k, \delta Z_k)$ for each epoch k on day 1. This series is then smoothed using a low-pass Butterworth filter (or a moving average window, if desired). As in the case of the ODSF, the choice of cut-off frequency is crucial and is discussed in section 5.2. These smoothed residuals, $(\langle\delta X_k\rangle, \langle\delta Y_k\rangle, \langle\delta Z_k\rangle)$ for each epoch k, are to be used as multipath corrections.

The GPS measurements from day 2 are then processed in exactly the same way except that the appropriate multipath correction is subtracted from the position coordinates after they are output by the Kalman filter at each epoch. It is assumed that the appropriate multipath correction for any particular epoch k_2 is to be found at epoch k_1 on day 1 such that $t_{k_1} = t_{k_2} - t_{\text{repeat}}$, where t_{k_1} and t_{k_2} are the times at epochs k_1 and k_2, respectively, and t_{repeat} is the 'constellation' repeat period, which is found by averaging the repeat periods of all the satellites that are visible at time t_{k_2}. The repeat periods for each individual satellite can be found either by using the DP method or by calculating it using the Keplerian elements found in the GPS broadcast ephemeris (i.e. the BE method) as described in section 2.2.1.2 above. Alternatively, repeat period can be set to the nominal value, i.e. $t_{\text{repeat}} = 86,155\,\text{s}$. Hence

$$(X_{k_2}, Y_{k_2}, Z_{k_2})_{\text{corr}} = (X_{k_2}, Y_{k_2}, Z_{k_2}) - (\langle\delta X_{k_1}\rangle, \langle\delta Y_{k_1}\rangle, \langle\delta Z_{k_1}\rangle) \tag{2.28}$$

where $(X_{k_2}, Y_{k_2}, Z_{k_2})_{\text{corr}}$ represents the coordinates $(X_{k_2}, Y_{k_2}, Z_{k_2})$ after applying a correction for multipath error.

2.3 Summary

This chapter has described the PPP Kalman filter algorithm and the sidereal filter algorithms that are applied in the remainder of this thesis: the observation-domain sidereal filters based on the dot

product (DP) and broadcast ephemeris (BE) methods (DP ODSF and BE ODSF, respectively) and the position-domain sidereal filter (PDSF). Chapters 3 to 6 examine the ability of the different sidereal filter algorithms to improve the stability of a PPP position time series of a static receiver. Chapters 7 to 9 examine the ability of the sidereal filters to improve the measurement of small displacements.

Chapter 3

Overall Performance

3.1 Introduction

One of the aims of this thesis is to test how well different types of sidereal filter enhance the ability of kinematic PPP to measure small displacements of a normally static receiver. However, it is necessary to assess the performance of both the observation-domain sidereal filter (ODSF) and the position-domain sidereal filter (PDSF) algorithms when the GPS receiver is known to be truly static in relatively benign conditions. In this chapter, the performance of both types of ODSF and the PDSF will be compared with the results of regular PPP processing and with each other using data sourced from a number of static receivers.

For reasons already stated in section 1.5.2, it is anticipated that an ODSF, under particular circumstances such as instances of anomalous satellite repeat periods, high-frequency multipath[1] and satellite outages, will outperform a PDSF. These cases are assessed specifically in chapters 4, 5 and 6 respectively. In this chapter however, the *overall* performance of the filters are assessed over an extended period of time during which the GPS constellation status may be considered 'normal'. Therefore, periods of time were deliberately chosen during which no satellite outages occurred, no visible satellites had highly anomalous repeat periods and no large unexplained anomalies occurred in the given satellite clock offsets. The overall performance of the *two* types of ODSF, described in detail in section 2.2.1, are assessed: the dot product (DP) ODSF and the BE ODSF, which calculates repeat periods using orbital parameters given in the GPS broadcast ephemeris.

3.2 Hypotheses

It is predicted that both types of ODSF will outperform a PDSF in reducing the effect of multipath interference, with the ODSFs yielding lower Allan deviation values (see appendix B) over relatively

[1] Note that, in this thesis, 'high-frequency multipath' refers to oscillatory multipath errors with periods under about 100 s.

small averaging intervals of, say, a few tens of seconds. As discussed in section 1.5.2, this is because an ODSF can calculate different repeat periods for each visible satellite and hence be more effective at removing the oscillating errors caused by high frequency multipath.

When comparing the two types of ODSF, it is anticipated that the BE ODSF will not perform quite as well as a DP ODSF. This is because, as explained in section 1.5.3.2, the repeat time derived by the DP method is slightly different to that derived from the broadcast ephemeris, but is considered to be more accurate from the point of view of an observer. This difference of just a few seconds could have a big impact on the ability of a sidereal filter to remove high-frequency multipath. However, the BE ODSF is expected to have a very similar performance to the DP ODSF over longer averaging intervals. This is because the small difference in repeat times calculated by the two methods is likely not to affect the ability of the sidereal filter to remove lower-frequency multipath.

3.3 Method

In order to assess the performance of the different types of sidereal filter, each was applied within the processing of data from a number of different continuously operating GPS receivers. An initial detailed analysis is made using data from station 'UCL' located at University College London. This single receiver forms part of Leica Geosystems' SmartNet real-time kinematic (RTK) network in the United Kingdom. There then follows a second analysis of another set of GPS measurements made at receiver UCL on a different day, together with simultaneous measurements logged at another Leica SmartNet receiver, 'UEL', located at the University of East London. Further analysis is then carried out using data from a number of continuously operating GPS receivers located in southern California. The sidereal filter algorithms are therefore tested across differing receiver types and surrounding environments. Overall performance of the sidereal filters is assessed by analysing the resulting position time series using Allan deviation as a performance measure. A brief introduction to Allan deviation is given in appendix B (page 263).

3.4 Station UCL, 27$^{\text{th}}$ March 2012

The initial detailed analysis of the performance of the sidereal filter algorithms is made using data from station UCL which is just one receiver in Leica Geosystems' 'SmartNet' real-time kinematic network. The station is equipped with a Leica GRX1200GG PRO receiver and a Leica AT504GG choke-ring antenna, pictured in figure 3.1, sited on a rooftop. Figure 3.2 shows the location of the antenna as it appears in Google Earth when facing west. Note the tall buildings in the background and the sloping glass roof in the centre of the image. Views facing north, east and south are shown in figure E.1 on page 274. RINEX files containing 24 hours of 1 Hz GPS code and phase measurements from the 26$^{\text{th}}$ and 27$^{\text{th}}$ March 2012 were downloaded from the Leica 'SpiderWeb' website[2] with

[2] http://uk.nrtk.eu/spiderweb

Figure 3.1 – Photograph looking east-southeast at the Leica LEIAT504GG choke-ring SmartNet antenna (covered by a radome) at University College London. Image used with permission from Leica Geosystems UK.

each dataset starting at midnight (GPS system time). All 24 hours of phase measurements from 27th March were processed using the standard PPP algorithm as described in section 2.1. The GPS measurements were processed three more times: once with each of the two types of ODSF and once with the PDSF applied using the methods described in section 2.2. Satellite PRN 27 was excluded from all processing because, according to a Notice Advisory to Navstar Users (NANU) issued by the United States Coast Guard Navigation Center[3], it was unusable during the period between 14:18 and 15:56 on 26th March. As described in section 3.1 above, the reason for this exclusion was to recreate ideal conditions where no satellite outages occur. The effect of satellite outages is specifically assessed in chapter 6.

All processing was done using 'final' orbit and high-rate clock data from the Centre for Orbit Determination in Europe (CODE). This was in order to show as fully as possible the ability of the sidereal filter algorithms to remove high-frequency phase multipath errors. Otherwise, if using real-time orbit and clock data, that benefit would likely have been at least partly obscured particularly by mis-modelled satellite clock offsets. The use of real-time orbit and clock products is of course necessary for a tsunami warning system based on the PPP technique. However, because of the loss of accuracy when compared with 'final' products, the fixing of wide-lane and narrow-lane phase ambiguities becomes more pertinent. The fixing of these ambiguities is a capability that the PPP software used in this thesis does not yet have. For this reason, 'final' orbits and clocks are used, not just in this chapter, but throughout this thesis. Nevertheless, it is anticipated that the benefit of sidereal filtering in a real-time scenario will become greater as atomic clocks with better frequency stability are placed onboard future GNSS satellites (Hauschild et al. 2013, Griggs et al. 2015). These allow more accurate predictions of satellite clock behaviour over longer time intervals.

[3]http://www.navcen.uscg.gov/

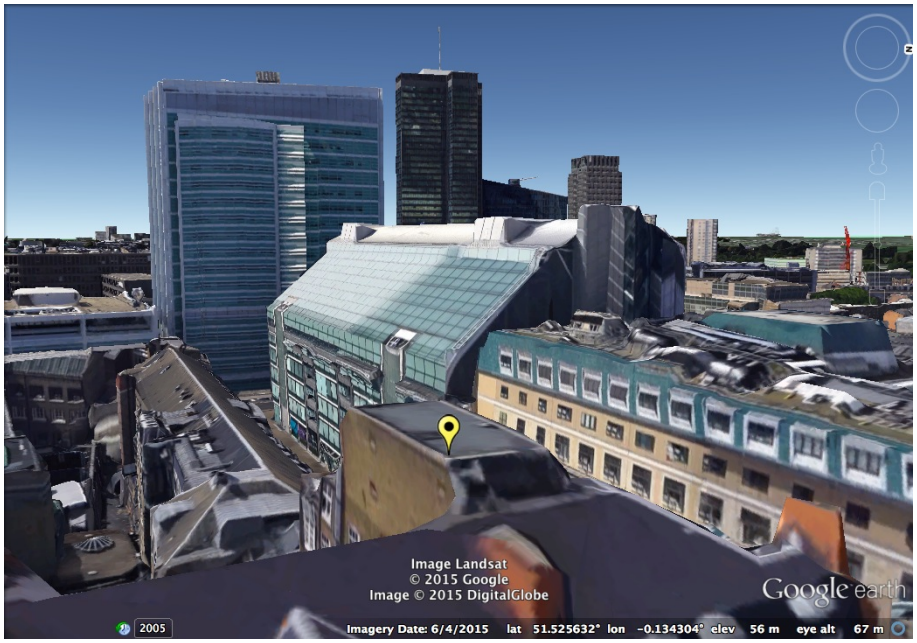

Figure 3.2 – Google Earth image showing the location of the Leica SmartNet antenna UCL (*yellow marker*), facing west. Image: Landsat. Cfig: Rooftop photo, DigitalGlobe.

The easting, northing and height position error time series resulting from the standard PPP processing of all 24 hours of GPS phase observations are shown in figure 3.3. It can be seen that the position solution converges to within 10 cm of the true position within thirty minutes, but takes about three hours to settle to a solution within about 3 cm, particularly in the east component in this case. Of course, the aim of this experiment is to assess the performance of the sidereal filters over a long period of time, but only *after* allowing plenty of time for this convergence to take place. Ideally, a long continuous time series of position error values between the times of 04:00:00 and 23:59:59 would have been chosen for analysis. Unfortunately, there was a significant anomaly that occurred in the horizontal components, particularly in northing, between roughly 09:25 and 09:37. This anomaly so far remains unexplained except to say that the fault seems to lie with a brief period of unusually noisy satellite clock corrections for PRN 13 in the precise clock file provided by the CODE. The period selected for analysis was thus chosen to start at 10:00. Also, the end of this period was curtailed to 23:55 to allow a fair comparison between the results of standard PPP processing and those which had a sidereal filter applied. This is because no multipath corrections can be calculated for GPS measurements after about 23:56 with the sidereal filter algorithms in their current form. This period of almost 14 hours was considered long enough to assess the overall performance of the sidereal filters. Measurements were taken from a total of 26 GPS satellites during this period.

The results of these processing runs for the time period 10:00 to 23:55 are shown in figure 3.4. The result of regular PPP processing is plotted in black while the resulting time series after the

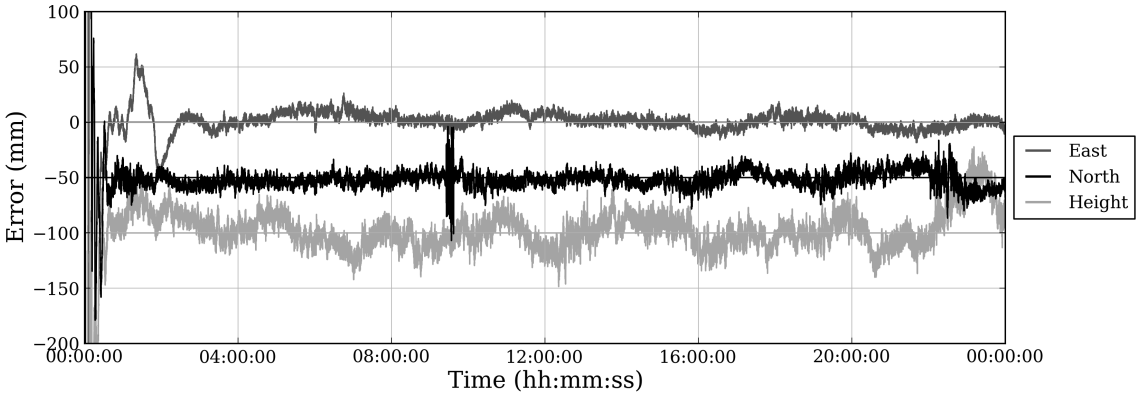

Figure 3.3 – Easting, northing and height position errors at station UCL between 00:00:00 and 23:59:59 (GPS system time) on 27th March 2012 resulting from standard PPP processing. (The northing and height time series have been offset by −50 mm and −100 mm, respectively, for clarity).

application of the PDSF, BE ODSF and DP ODSF are plotted in red, blue and green respectively. Also plotted are the resulting position time series from the regular PPP processing of GPS observations from the previous day, but shifted forward in time by 86,155 s (one sidereal day) for it to appear on the same graph. As explained in the caption, each of the time series have been offset by appropriate multiples of 40 mm or 80 mm for clarity. Upon examination of figure 3.4, the following observations can be made:

- Notice first of all how similar, in all three dimensions, the two PPP time series from the adjacent days (shown in grey and black) are—certainly in terms of the oscillating positioning errors with periods of just a few minutes. Much longer-period errors spanning several hours are also common to both days: the gentle fall in height from about +15 mm to about −10 mm between 11:00 and 12:00 is just one example. However, there are some noticeable differences as well. There is an obvious rise and fall in northing of at least 20 mm between roughly 23:00 and 23:30 on 26th March that does not occur on the following day. Similarly in the height component there is a very low-frequency rise and fall of over 60 mm between 22:00 and midnight on 27th which did not occur on the previous day. There are also inconsistencies between the adjacent days in all three dimensions at around 18:00. All of these inconsistencies affect the performance of each of the sidereal filters.

- It is clear that each type of sidereal filter has been successful at reducing higher-frequency errors, i.e. errors with a period of a few minutes and peak-to-peak amplitude of up to 20 mm. However, many lower-frequency errors remain and all of the inconsistencies described above have degraded the performance of the sidereal filter at those times.

- Both types of ODSF seem to have a very similar performance, but there are some differences between the PDSF and the ODSFs: many of the very-low frequency trends are different.

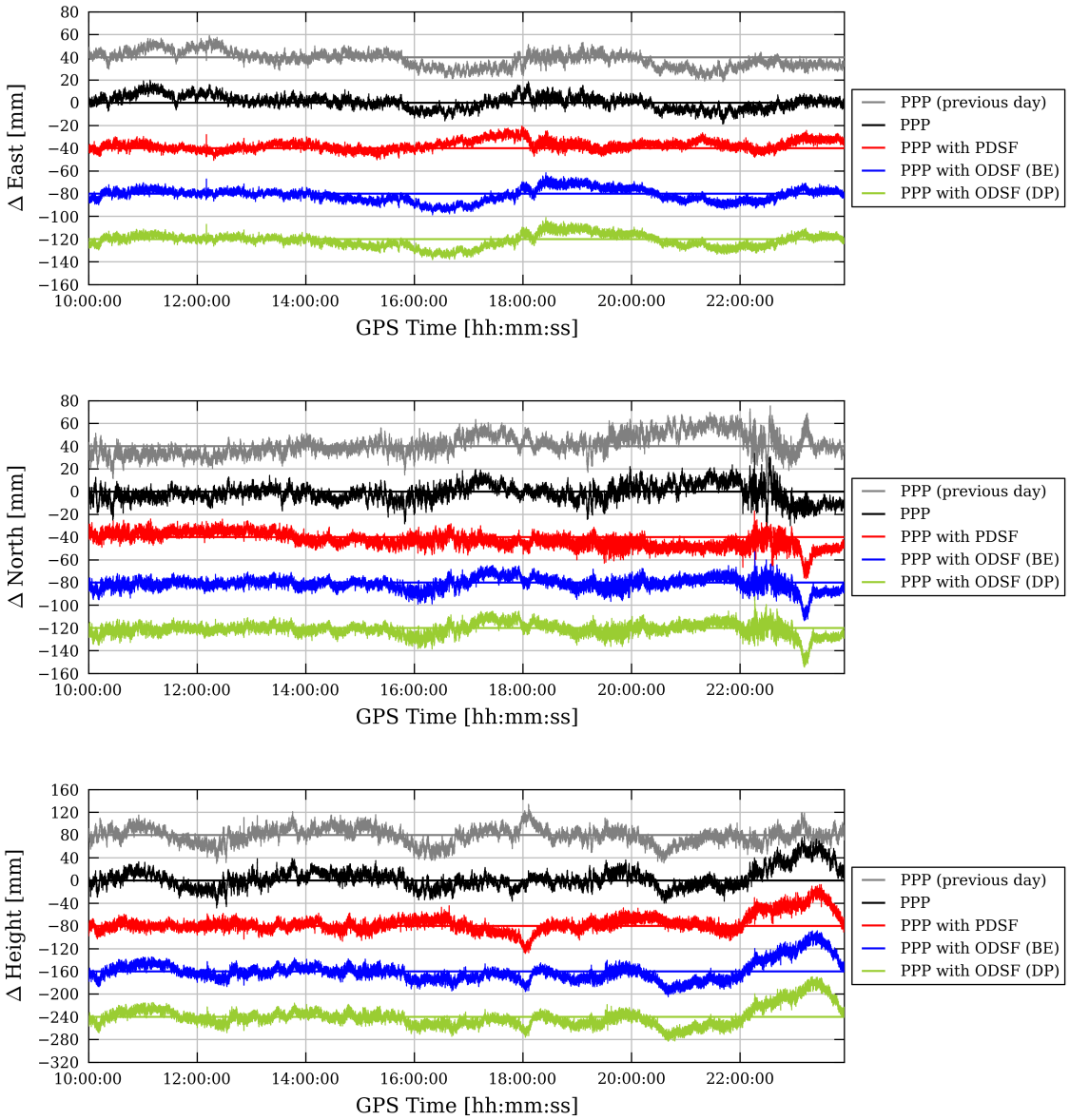

Figure 3.4 – Easting, northing and height errors between 10:00 and 23:55 on 27$^{\text{th}}$ March 2012 for receiver UCL resulting from standard PPP processing and PPP processing with various types of sidereal filter applied. Errors between 10:04:05 and 23:59:05 on 26$^{\text{th}}$ March 2012, plotted in grey, have been shifted forward in time by 23 hours, 55 minutes and 55 seconds to appear on the same plot. The PPP (previous day), PPP + PDSF, PPP + ODSF (BE), PPP + ODSF (DP) errors have been offset by 40 mm, −40 mm, −80 mm, −120 mm), respectively, in the easting and northing components and by 80 mm, −80 mm, −160 mm, −240 mm, respectively, in the height component.

For example, the error in easting from the PDSF steadily rises by 15–20 mm between 15:30 and 18:00 whereas in the ODSFs the easting value falls by around 10 mm between 15:30 and 16:30 before starting to rise again. Another example would be the steady drift upwards and then downwards by around 30 mm in height between about 10:00 and 12:30 in both the time series corresponding to the ODSFs, but does not appear in the PDSF time series. Notice how this example and other examples of long-period errors in both of the ODSF time series closely follow those present in the standard PPP time series.

Table 3.1 shows the standard deviation of each of the time series for each dimension. Notice that the PDSF has reduced the standard deviation of the position residuals in all three dimensions: in this example by 26%, 11% and 11% in easting, northing and height respectively. This is not the case for both of the ODSFs. These actually *increase* the standard deviation in the height component. Table 3.1 also shows the mean value (i.e. mean error) of each time series. The sidereal filters here have produced mixed results: the mean error of the PDSF time series is larger than the mean error calculated for regular PPP in each component. The ODSFs yield an improvement in the accuracy of the height component, although this is insignificant given the relatively high standard deviation of over 17 mm.

Clearly, in this example, sidereal filtering has no clear benefit for improving the accuracy and precision of a position calculation. However, it is clear to see from figure 3.4 that the sidereal filters have all been successful at reducing short-period errors on the order of a few minutes—each of the time series appear to be much 'smoother'. This seems to indicate that sidereal filters of all types should be of more benefit over much smaller time intervals. Indeed, Genrich & Bock (1992) use sidereal filtering to remove multipath errors to measure the length of a short baseline of about 1 km to millimetre-level precision (via double-differencing—see section 1.3.2) using only 200 s of observations at 1 Hz. Otherwise, without multipath modelling, it would have taken around 10 minutes to average out the multipath errors.

Figure 3.5 shows the results of the various types of PPP processing of data from station 'UCL', but only between 12:30 and 12:40. Table 3.2 shows that, in this particular case, each of the sidereal filters improve accuracy in the east component, but not necessarily in the north and height components: The PDSF have reduced accuracy in the north component but improved accuracy in

Processing method	East		North		Height	
	Mean	St.dev.	Mean	St.dev.	Mean	St.dev.
PPP	0.6	5.7	−1.4	7.3	3.7	17.4
PPP + PDSF	2.6	4.2	−3.0	6.5	4.7	15.4
PPP + ODSF (BE)	−1.2	5.7	−1.2	5.5	−0.2	17.5
PPP + ODSF (DP)	−1.2	5.7	−1.2	5.5	−0.1	17.5

Table 3.1 – Mean values and associated standard deviations, in millimetres, of the respective time series of positioning errors shown in figure 3.4 on page 90.

.

the vertical component, whereas the ODSFs have led to a slight improvement in northing but little improvement in height. However, notice how all types of sidereal filter have reduced the *standard deviation* of the mean position by roughly half. One can see from figure 3.5 that the sidereal filters have increased the *stability* of the position time series over this relatively short time interval of ten minutes. Notice that it can also be seen that both of the ODSFs appear to be more effective than the PDSF at improving stability over small time intervals on the order of a few tens of seconds, particularly in the north component between 12:30 and 12:34, indicating that it has been more successful at removing short-period multipath error. Of course, this particular case may or may not be typical, but this example was chosen to illustrate how sidereal filters can improve the stability, but not necessarily the accuracy, of a position time series.

In order to quantify an increase in stability, the *Allan deviation* statistic, denoted by the symbol σ_y, is used (see appendix B). Considering again the analysis of the much longer time period from 10:00 to 23:55, figure 3.6 shows the Allan deviation values across averaging intervals between 1 s and 10,000 s (nearly 2 hours 47 minutes) for each of the easting, northing and height time series corresponding with figure 3.4. It can be seen that both types of ODSF are successful in increasing the stability of the position time series, i.e. they yield a lower Allan deviation, over averaging intervals larger than about 6 s for the horizontal components and 9 s for the vertical component when compared to standard PPP processing. The PDSF yields lower Allan deviation values for averaging intervals larger than about 12 s to 15 s compared to standard PPP. Notice also how the Allan deviation curves corresponding to the sidereal filters have a relatively constant gradient close to -1 across all averaging intervals between around 4 s and 1,000 s, at least for the horizontal components, indicating that the dominant noise process of the position errors across these intervals is either white or flicker noise, whereas the gradient of the curve corresponding to standard PPP is more variable for intervals larger than about 50 s, most likely due to multipath errors causing oscillations in the position time series with periods of roughly 100 s and above. However, for large intervals, roughly above 3,000 s, the performance of both of the ODSFs deteriorate while the PDSF remains relatively stable. Indeed, the performance of the ODSFs over these large intervals is actually worse in the east component than that of regular PPP.

It is not easy to analyse the relative performance of each of the sidereal filters, especially the ODSFs, using figure 3.6. Figure 3.7 was created in order to facilitate closer analysis. These

Processing method	East		North		Height	
	Mean	St.dev.	Mean	St.dev.	Mean	St.dev.
PPP	3.1	2.5	1.2	4.7	−6.6	14.0
PPP + PDSF	−1.6	1.6	5.6	2.2	2.9	6.0
PPP + ODSF (BE)	1.6	1.7	−0.9	2.5	−6.1	8.8
PPP + ODSF (DP)	1.6	1.4	−0.9	2.1	−6.2	8.1

Table 3.2 – Mean values and associated standard deviations, in millimetres, of the respective time series of positioning errors shown in figure 3.5.

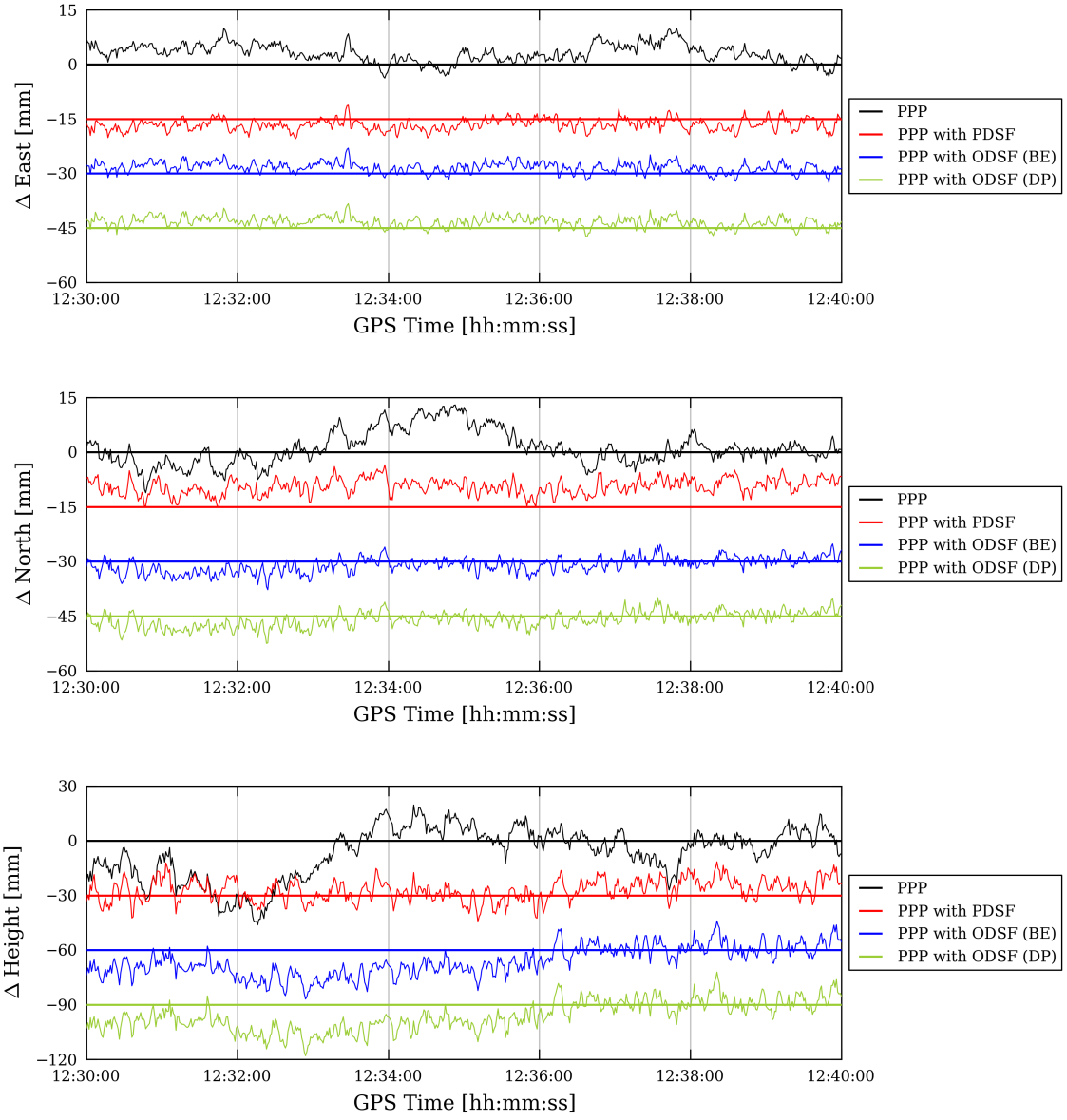

Figure 3.5 – Easting, northing and height errors at station UCL between 12:30 and 12:40 on 27th March 2012 resulting from standard PPP processing and PPP processing with various types of sidereal filter applied. (Each of the time series have been offset from each other by appropriate multiples of 15 mm or 30 mm for clarity)

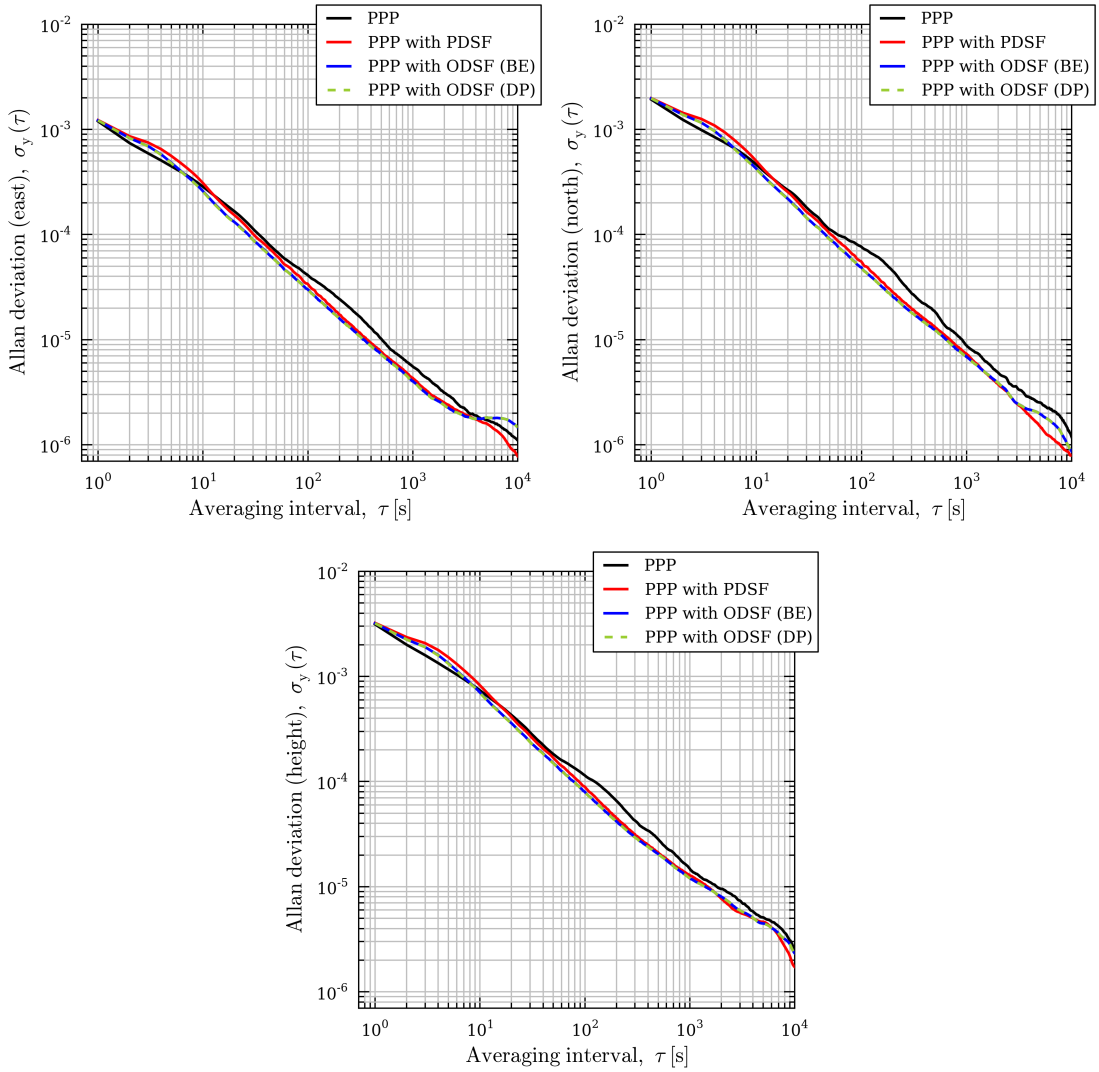

Figure 3.6 – Allan deviation plots of the corresponding position time series (east, north and height) at station UCL between 10:00 and 23:55 on 27$^{\text{th}}$ March 2012 shown in figure 3.4.

graphs show the percentage *improvement* (i.e. percentage reduction) in Allan deviation relative to the Allan deviation curve corresponding to standard PPP processing. For example, for the position-domain sidereal filter (PDSF):

$$\text{Percentage improvement} = \frac{\sigma_{y,\text{PPP}} - \sigma_{y,\text{PPP+PDSF}}}{\sigma_{y,\text{PPP}}} \times 100 \tag{3.1}$$

From figure 3.7, the following observations are made:

- In all three dimensions, the use of ODSF algorithms certainly results in a greater overall reduction in Allan deviation (i.e. increase in stability) than when using a PDSF for averaging intervals under 1,000 s. The maximum improvement of between 35% and 45% occurs for intervals of around 150–200 s. It is thought that the length of these averaging intervals correspond with the typical periods of ranging error oscillations caused by multipath interference between 10:00 and 23:55. The ODSFs often outperform the PDSF by over ten percentage points for most time intervals under about 60 s.

- The two types of ODSF have a very similar overall performance over all averaging intervals. However, it can be seen that the DP ODSF yields a very slightly better improvement in stability (no more than one percentage point) than the BE ODSF over smaller averaging intervals: from just a few seconds up to a few hundred seconds. This could be because the DP ODSF can calculate a more appropriate repeat time for each satellite. For larger averaging intervals, the performances of the two types of ODSF converge.

- For very long averaging intervals, above a few thousand seconds, the application of a PDSF appears to result in a greater improvement (i.e. reduction) in Allan deviation than when either type of ODSF is applied. In the east component, the use of ODSFs actually results in a *higher* Allan deviation for averaging intervals over about 4,500 s than standard PPP processing without a sidereal filter, implying that the former is less stable over very long averaging intervals.

- For very short averaging intervals, in the region of ten to fifteen seconds and under, applying sidereal filters decreases stability. This is because of the amplification of high-frequency noise when the corrections for multipath are applied. A low-pass filter, as described in section 2.2, is applied to the corrections to minimise this effect, but has obviously not removed it completely in this case. This topic is discussed in more detail in chapter 5.

As predicted, both of the observation-domain sidereal filters have been more successful at reducing the impact of sidereally repeating errors (such as multipath errors and possible errors in the antenna phase centre corrections) present in the positions output by standard PPP processing than the position-domain sidereal filter, at least for averaging intervals under 1,000 s. This is likely to be because, unlike a PDSF, an ODSF can calculate a different repeat period for each visible satellite in order to apply a correction to each measurement at each epoch. To test whether this

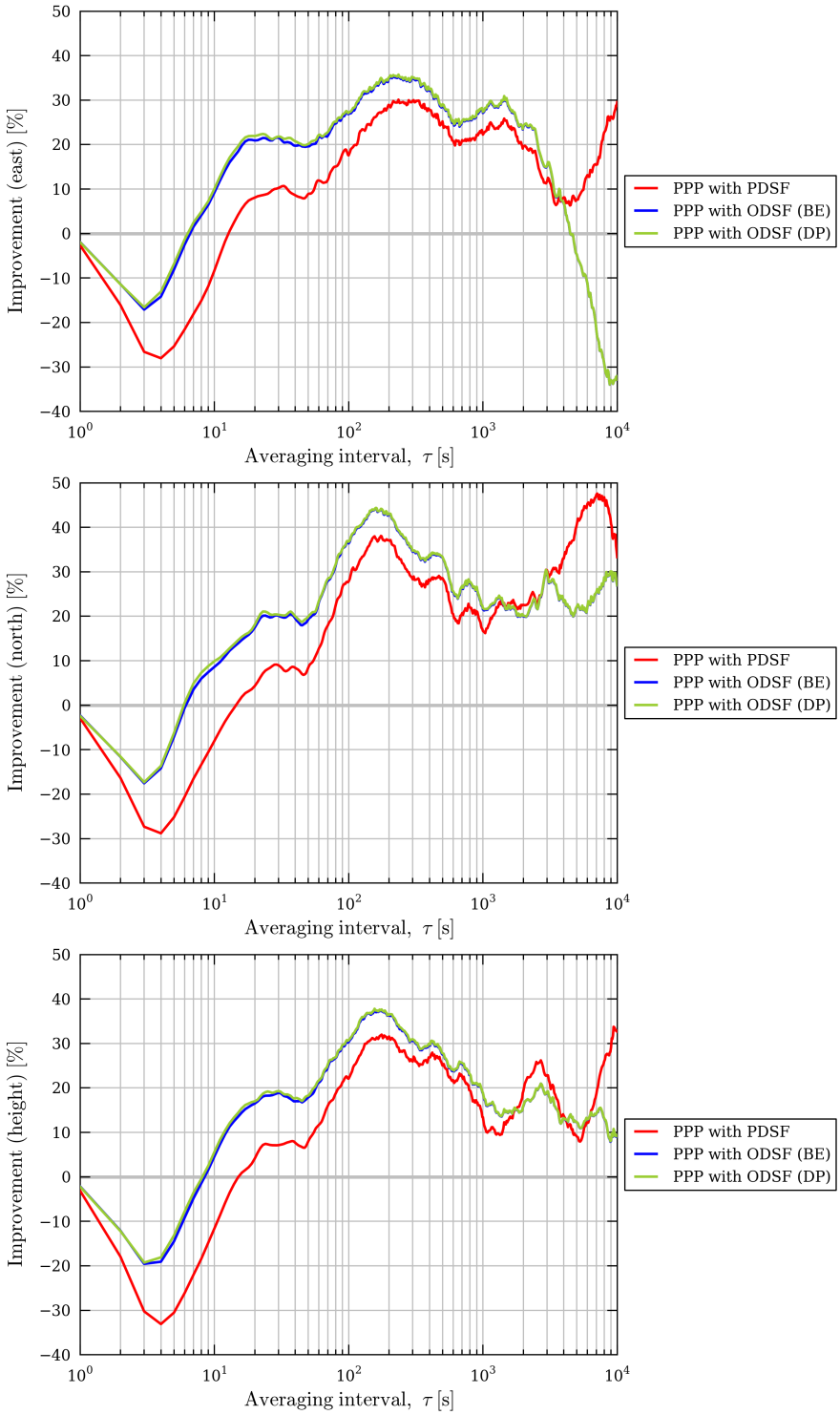

Figure 3.7 – Plots showing the percentage improvement (i.e. reduction) in Allan deviation at station UCL, after applying the various types of sidereal filter, relative to the Allan deviation values corresponding to standard PPP processing that are shown in figure 3.6.

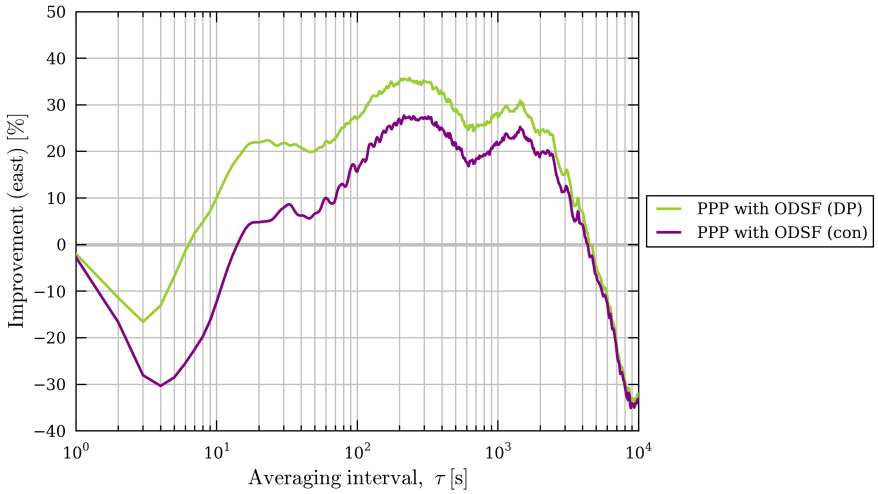

Figure 3.8 – Plots showing the percentage improvement (i.e. reduction) in Allan deviation in the east component at station UCL between 10:00 and 23:55 on 27th March 2012, after applying two types of observation-domain sidereal filter (ODSF): the dot-product (DP) ODSF and the 'constellation repeat time' (con) ODSF.

was so, a third type of ODSF was applied: one in which all measurements are paired with their respective corrections using the mean repeat time of all visible satellites at any one epoch (hereafter referred to as the 'constellation repeat time'). Figure 3.8 shows the percentage improvement in Allan deviation resulting from such a filter relative to the Allan deviation values derived from the easting time series from regular PPP processing. Equivalent plots for the northing and height components are shown in figure E.4 on page 277. Notice that the DP ODSF outperforms the ODSF that uses the constellation repeat time over all averaging intervals. The difference between the two is usually in excess of ten percentage points for averaging intervals below 100 s. The reason for the superior performance of the DP ODSF over such intervals is thus due to its ability to calculate an appropriate repeat time for each individual satellite in view.

However, for very long averaging intervals of thousands of seconds, the performance of the ODSFs seems to deteriorate whereas the PDSF continues to yield an increase in stability in the position time series. This is perhaps because the assumption—that the measurement residuals produced by standard PPP processing closely resemble multipath errors—becomes less valid for lower-frequency multipath errors. These errors are more likely to be absorbed by slowly-varying Kalman filter states such as the wet troposphere zenith delay and the phase ambiguity states and therefore are less likely to appear in the residuals, and yet it is these residuals that are used to form the multipath corrections that are applied within the ODSF algorithms. Also, after the multipath corrections have been applied to the measurements, any low-frequency component of those corrections may again be absorbed by these slowly-varying Kalman filter states, which might explain why the ODSFs are not very effective at increasing stability in the position time series over long time intervals. A PDSF on the other hand applies multipath corrections outside of the

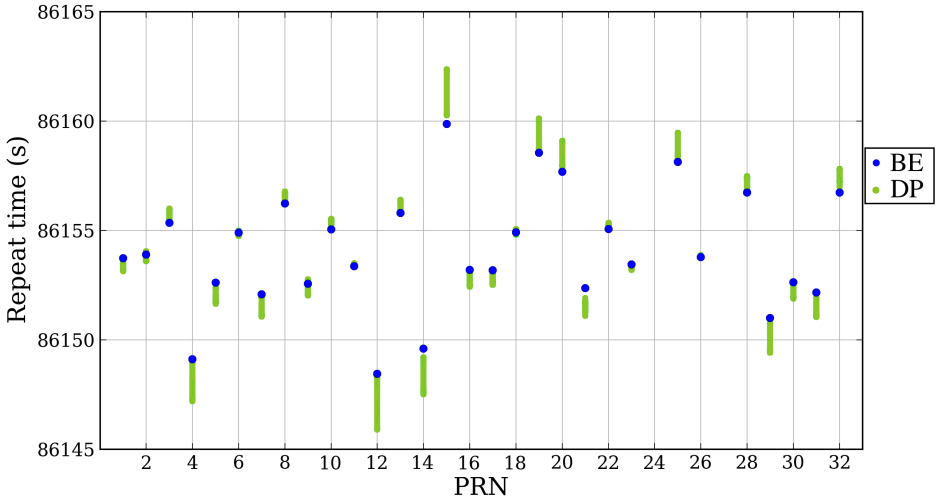

Figure 3.9 – GPS satellite repeat times used by the two types of ODSF during the period from 10:00 to 23:55 on 27$^{\text{th}}$ March 2012. Shown in blue are the ground-track repeat times found using equation (1.23) on page 57 and values given in the GPS broadcast ephemeris. Shown in green are the range of repeat times calculated and used by the DP ODSF algorithm during the period from 10:00 to 23:55.

Kalman filter algorithm and so any low-frequency multipath corrections for position cannot alias into the other Kalman filter states.

As predicted, the performance of the DP ODSF relative to standard PPP is superior to the BE ODSF, but only by a couple of percentage points at most, and generally over shorter averaging intervals of under a few hundred seconds. This is presumably because of the improved ability of the former to cope with high-frequency multipath because the DP ODSF can calculate a more appropriate repeat time for each satellite at each epoch. Figure 3.9 shows that all of the satellites visible during this period have repeat times within ten seconds of the nominal 86,155 s (23 hours, 55 minutes, 55 seconds). None of the repeat times are particularly anomalous, i.e. none have repeat periods that differ by tens of seconds from the nominal period. So the slight difference of just a few seconds in satellite repeat times found by the ODSFs, shown in green and blue dots in figure 3.9, has some effect in determining how effective they are at removing multipath error. Of course, all these results reflect the overall performance over a period of almost 14 hours. There is hence a need to assess how each of the sidereal filter types cope with specific instances of high-frequency multipath, where the difference in performance between the sidereal filters—particularly the two types of ODSF—is likely to be more pronounced. This is explored in chapter 5.

The above analysis and discussion was based on data from one receiver for one particular period of time. In the following sections, similar analyses are made using measurements sourced again from station UCL, from another nearby station, UEL, and from a receiver in Southern California. This is in order to establish whether the observations made in the above analysis hold true at different times and for monitoring stations with different antenna types sited in different environments.

Figure 3.10 – Photograph of the Leica AX1202GG SmartNet antenna at the University of East London.

3.5 Stations UEL and UCL, 3rd September 2013

Using the same method as described in section 3.4, RINEX files containing 24 hours of 1 Hz GPS code and phase observations from the 2nd and 3rd September 2013 for both receivers UEL and UCL were downloaded from the Leica 'SpiderWeb' website. Station UEL is also part of Leica Geosystems' SmartNet real-time kinematic network. It is equipped with a Leica GRX1200GG receiver and AX1202GG antenna which, in contrast to station UCL, does not possess choke-rings. It can be seen from figure 3.10 that it is also sited close to a roof. In contrast, station UCL, pictured in figures 3.1 and 3.2, is sited in a more exposed rooftop location in an urban area and is *not* so close to such a large single planar reflector. Reflected signals reaching the UCL antenna are more likely than at UEL to reach the antenna via 'far-field' reflectors such as surrounding buildings, causing shorter-period multipath errors (see section 1.4.1). The location of the antenna is also shown in figure 3.11. All 24 hours of observations from 3rd September were processed using the regular PPP algorithm as described in section 2.1. The GPS observations were processed three more times: once with both types of ODSF and once with a PDSF applied using the methods described in section 2.2. As with the previous analysis in section 3.4, one satellite, this time PRN 4, was excluded from all processing because it was unavailable on 3rd September. This was necessary to recreate ideal conditions where no satellite outages occur. The effect of satellite outages is assessed in chapter 6.

As in section 3.4, all 24 hours of data were processed using the PPP algorithm both with and without the various types of sidereal filter applied. Again, after allowing plenty of time for the position states to converge, it would have been most ideal to choose as long a period of time as possible for analysis, such as 04:00:00 to 23:59:59. Unfortunately, a number of unexplained anomalies were identified in the position time series for 2nd September output by PPP processing

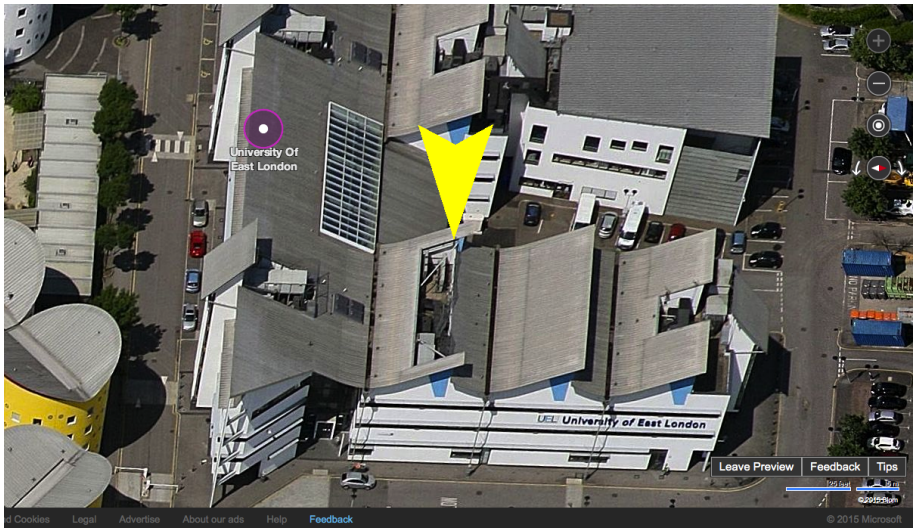

Figure 3.11 – Bing Maps 'bird's eye' image showing the location of the Leica SmartNet antenna UEL (*yellow marker*), facing west. Image: Blom. Copyright: Microsoft.

of both the UEL and UCL data. Many of these anomalies occurred simultaneously in the UCL and UEL time series implying that the errors originated in the satellite clock or orbit data. Rather than try to identify the cause and remedy each of these anomalies, an apparently 'clean' portion of the time series, 14:00 to 22:00, was chosen. This was deemed to be a sufficiently long period of time to test the sidereal filter algorithms under what are considered to be 'normal' conditions.

The resulting easting, northing and height position error time series for station UCL and UEL between 14:00 to 22:00 are shown in figures 3.12 and 3.13 respectively. The result of regular PPP processing is plotted in black while the resulting time series after the application of the PDSF, BE ODSF and DP ODSF are plotted in red, blue and green respectively. The position time series resulting from PPP processing of GPS observations from the previous day, shifted forward in time by 86,155 s, is plotted in grey. When comparing the time series of position error for standard PPP processing (plotted in black) for UEL in figure 3.13 with those for UCL in figure 3.12 (and indeed in figure 3.4), it is immediately apparent that station UEL has been affected by strong multipath interference to a much greater extent than station UCL: The amplitude of the high-frequency multipath errors are noticeably greater at UEL and are highly correlated across the two adjacent days. This is likely to be because of where the UEL antenna is sited: the nearby roof is likely to be the cause of strong reflected signals and hence causing high-amplitude phase measurement errors, as established in section 1.4. Also, the design of the antenna at UEL is not as resistant to reflected signals as the choke-ring antenna at UCL. Hence, while the sidereal filters have generally been successful in removing the higher-frequency errors (i.e. with periods under about 1,000 s) at both stations, the effect is much more obvious at station UEL, where each of the time series associated with the sidereal filters appear to be much 'smoother' than those associated with standard PPP processing. This is understandable: a sidereal filter is likely to be more effective when acting on a

dataset sourced from a receiver placed in a relatively high-multipath environment. Conversely, if GPS measurements have not been affected by strong multipath signals, then a sidereal filter will not yield a dramatic improvement.

Considering lower-frequency errors (i.e. with periods of tens of minutes and above), it appears from figure 3.12 that the application of the sidereal filters seem to have resulted in little improvement in terms of reducing such errors at UCL. However, from figure 3.13, the PDSF appears to have performed better in this respect than either of the two types of ODSF at UEL. Consider the height component, for example: Between 17:00 and 19:00, the error in height in both of the ODSF time series varies from around −60 mm at about 17:30 to 50 mm at 18:50—a peak-to-peak amplitude of about 11 cm. In contrast, the time series resulting from the PDSF clearly shows no such long-period oscillation during this period and height errors only vary between about 10 mm and −30 mm.

Again, as with the previous analysis, Allan deviation is used to quantify any increase (or decrease) in stability. Figures 3.14 and 3.15 show the Allan deviation values across averaging intervals between 1 s and nearly 6,000 s (1 hour and 40 minutes) for each of the easting, northing and height time series corresponding with figures 3.12 (UCL) and 3.13 (UEL), respectively. When comparing these two figures, it is immediately clear that there is a difference between the impact that the sidereal filters have on the position error time series at UCL and the impact at UEL. It has already been noted that the standard PPP position solution from station UEL exhibits higher-amplitude positioning errors. Evidence for this can be seen in all three Allan deviation plots in figure 3.15 where the Allan deviation curves corresponding with standard PPP (plotted in black) deviates further from −1 between averaging intervals of around 10 s to 60 s and even turns positive from about 15 s to 40 s for the horizontal components. This means that on average, in this case, a horizontal position calculated by averaging all the position values across just a 15 s period would actually be more precise or 'stable', though not necessarily accurate, than a horizontal position calculated by averaging across a 40 s period. In contrast, there is no such increase in Allan deviation in figure 3.14 for station UCL: The Allan deviation values for averaging intervals larger than about 10 s for standard PPP processing are all much lower than those at UEL, indicating that the position time series from UCL is generally more stable than at UEL. As figure 3.14 confirms, this means that the sidereal filters give no dramatic reduction in Allan deviation. Indeed, at UCL, all types of sidereal filter have successfully reduced Allan deviation values in all three dimensions between intervals of about 10 s and about 900 s, albeit only slightly, indicating that station UCL was less prone to multipath interference, at least during the period of time used for this analysis.

Notice from both figures 3.14 and 3.15 how the ODSFs are generally a little more successful than the PDSF at reducing the Allan deviation for time intervals of up to a few hundred seconds. However, for larger averaging intervals, the PDSF frequently outperforms both of the ODSFs, particularly at UEL.

As with figure 3.6, it is not easy to analyse the relative performance of each of the sidereal filters using figures 3.14 and 3.15. Figures 3.16 and 3.17 instead show the percentage improvement

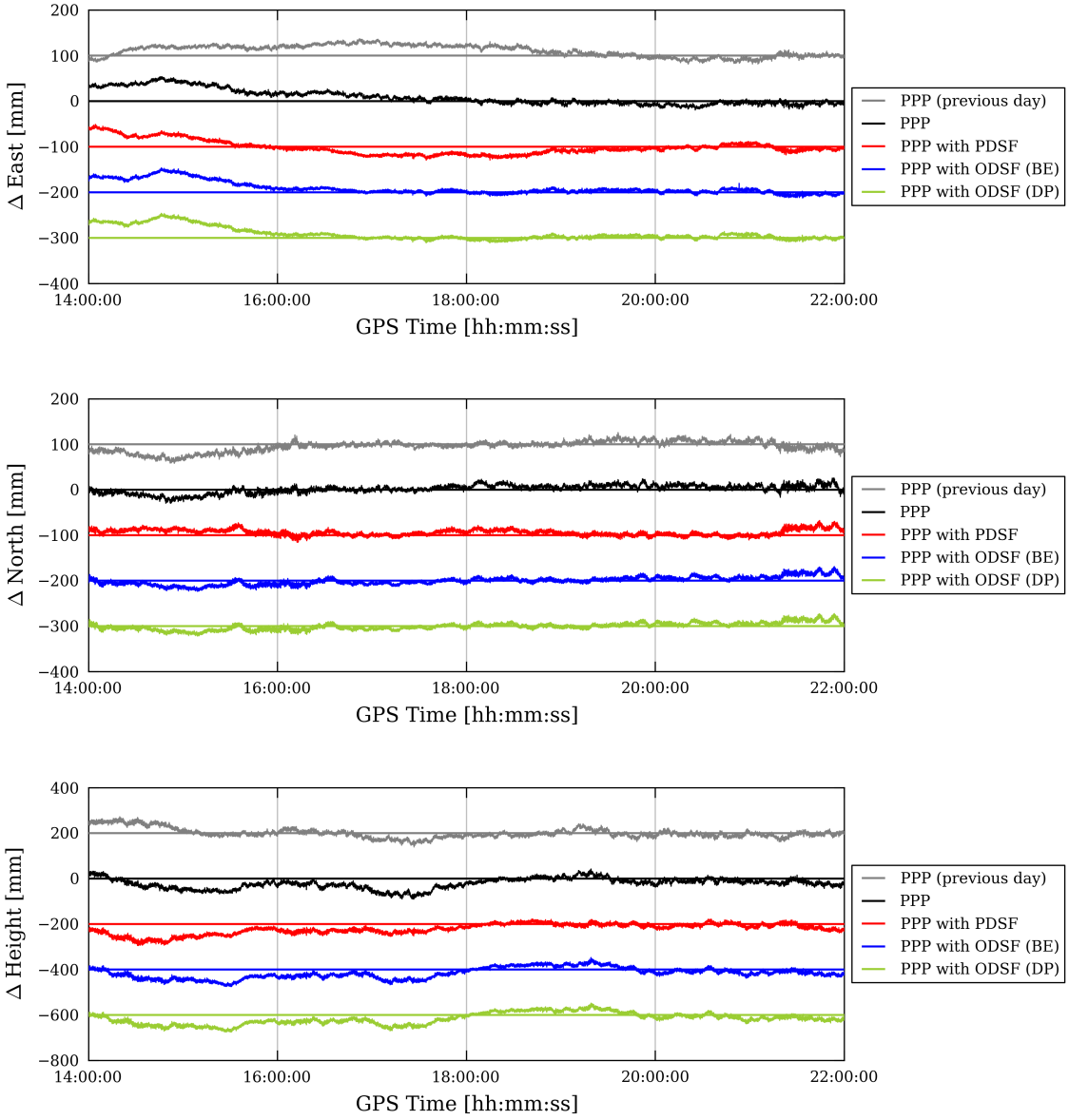

Figure 3.12 – Easting, northing and height errors between 14:00 and 22:00 on 3rd September 2013 for receiver UCL resulting from standard PPP processing and PPP processing with various types of sidereal filter applied. (Each of the time series have been offset from each other by appropriate multiples of 60 mm or 120 mm for clarity).

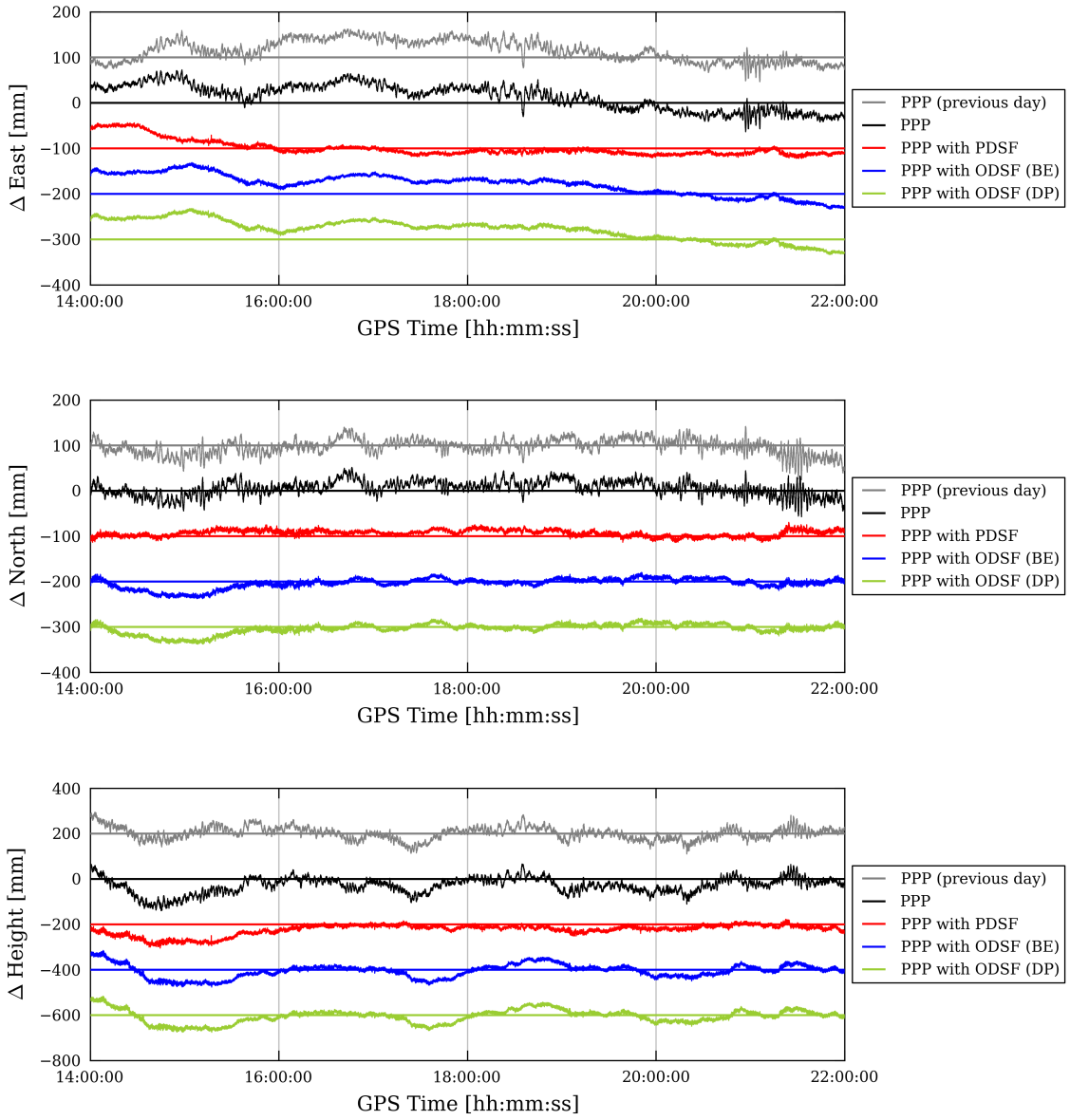

Figure 3.13 – Easting, northing and height errors between 14:00 and 22:00 on 3rd September 2013 for receiver UEL resulting from standard PPP processing and PPP processing with various types of sidereal filter applied. (Each of the time series have been offset from each other by appropriate multiples of 60 mm or 120 mm for clarity).

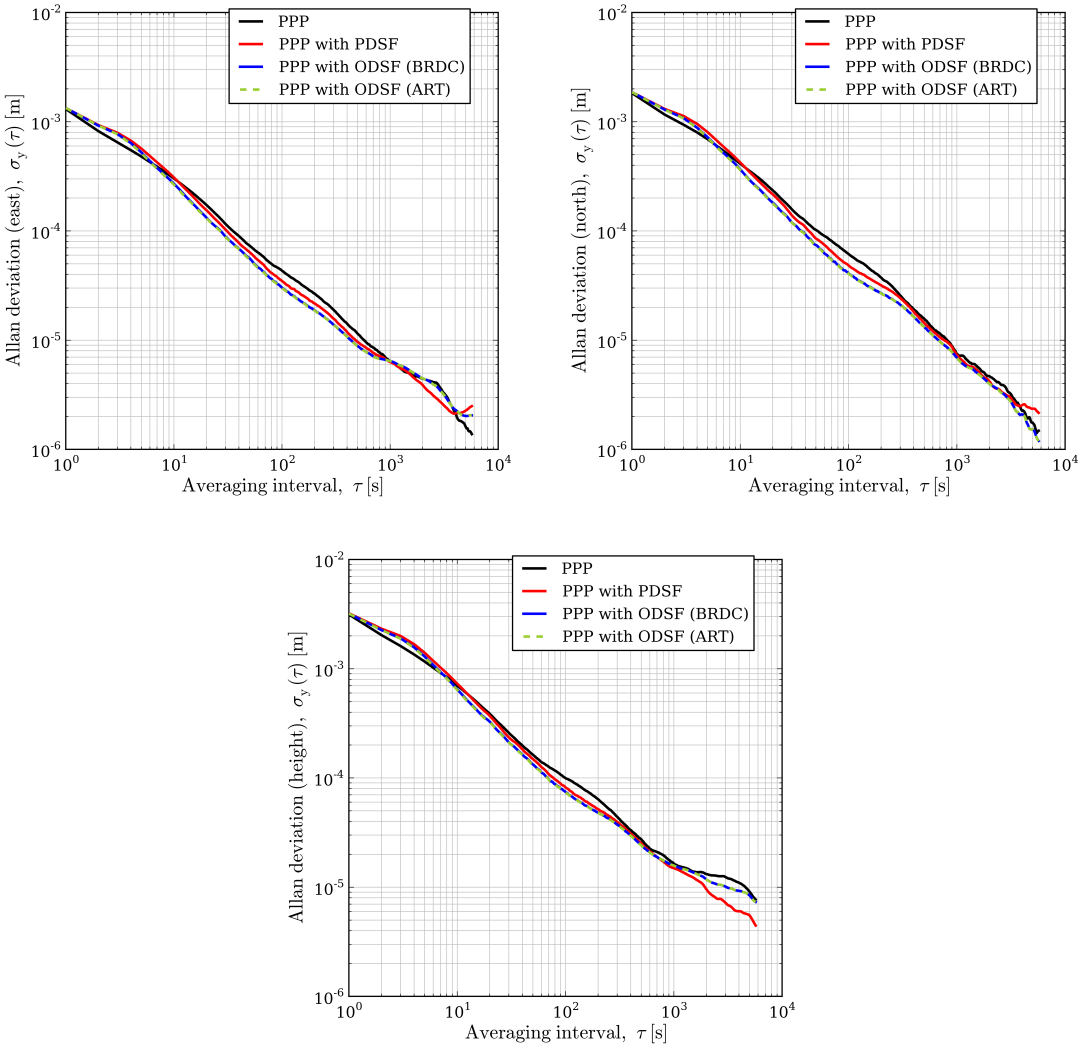

Figure 3.14 – Allan deviation plots of the corresponding position time series at station UCL (east, north and height) between 14:00 and 22:00 on 3rd September 2013 shown in figure 3.12.

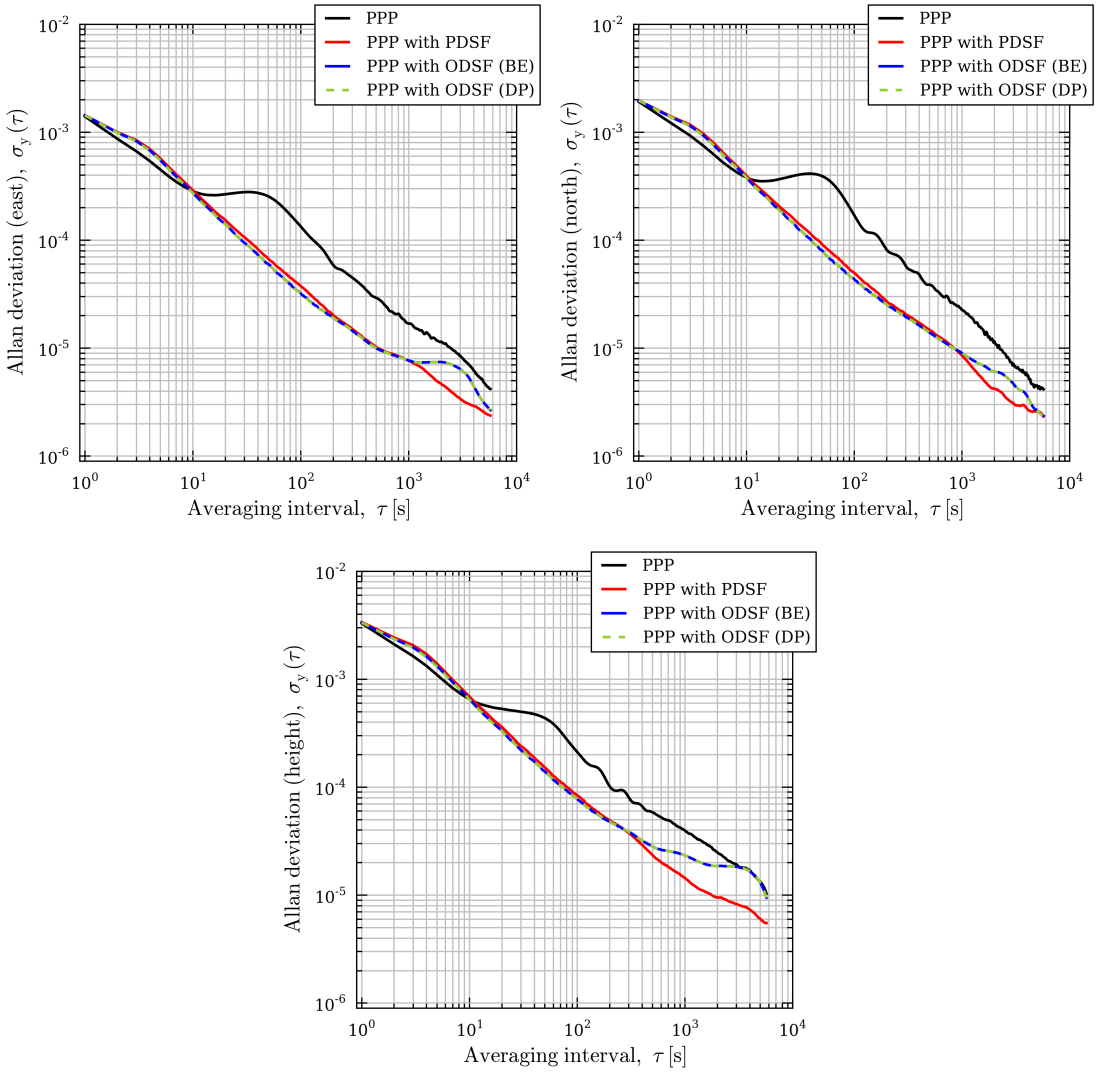

Figure 3.15 – Allan deviation plots of the corresponding position time series at station UEL (east, north and height) between 14:00 and 22:00 on 3rd September 2013 shown in figure 3.13.

in Allan deviation resulting from the application of each of the types of sidereal filter relative to the Allan deviation curve corresponding to standard PPP processing, as calculated using equation 3.1. A number of observations can be made after examining figures 3.16 and 3.17:

- Again, as with figure 3.7, the overall performance of the ODSFs is superior to the PDSF over shorter averaging intervals. At station UCL (figure 3.16), the ODSFs certainly outperform the PDSF at station UCL for all intervals below a few hundred seconds and yield peak improvements of around 25–35% in Allan deviation over intervals of roughly 80–150 s. At UEL (figure 3.17), the ODSFs are most effective over intervals of 60 s with the reduction in Allan deviation approaching 80% in the horizontal and 70% in the vertical. However, at UEL, the difference in performance between the PDSF and ODSFs over shorter time intervals is very slight compared to UCL.

- For larger time intervals, it can be seen that the relative performance of the sidereal filters is much more variable. Generally, the performance of the ODSFs deteriorates over large averaging intervals. Certainly for station UEL (figure 3.17), the PDSF comfortably outperforms the ODSFs for averaging intervals above about 900 s for the horizontal components and above 250 s for the vertical component.

- Notice in both figures 3.16 and 3.17 how similar the performance of the two types of ODSF are. However, as with figure 3.7, it can just about be seen in that the DP ODSF yields slightly better performance over smaller averaging intervals than the BE ODSF at UCL, whereas at UEL the margin of this improvement appears to be negligible.

- Again, over short averaging intervals of just a few seconds (less than 6–10 s), the sidereal filters decrease stability. This is due to the amplification of high-frequency noise as the corrections are applied, despite the application of a low-pass filter. This subject is discussed further in chapter 5.

As with the analysis in section 3.4, both types of ODSF have been more effective than a PDSF at removing short-period multipath errors: the stability of a position time series is improved to a greater extent by an ODSF over periods of time spanning up to a few hundred seconds. This is likely to be because of the ability of an ODSF to calculate a repeat period for each individual satellite in view of the receiving antenna. Figures 3.18 and 3.19 show the percentage improvement in Allan deviation resulting from applying an ODSF that uses the 'constellation repeat time' to pair measurements to their respective corrections. Equivalent plots for the northing and height components are shown in figures E.5 and E.6. Notice again that the DP ODSF outperforms the ODSF that uses the constellation repeat time over all averaging intervals, thus indicating that the ability of a DP ODSF to use a different repeat period for each individual satellite is the reason behind its superior performance. Notice also that the difference between these two types of ODSF, in terms of percentage reduction in Allan deviation, is larger at station UCL than at station UEL, particularly over averaging intervals smaller than about 1000 s. This is likely to be because station

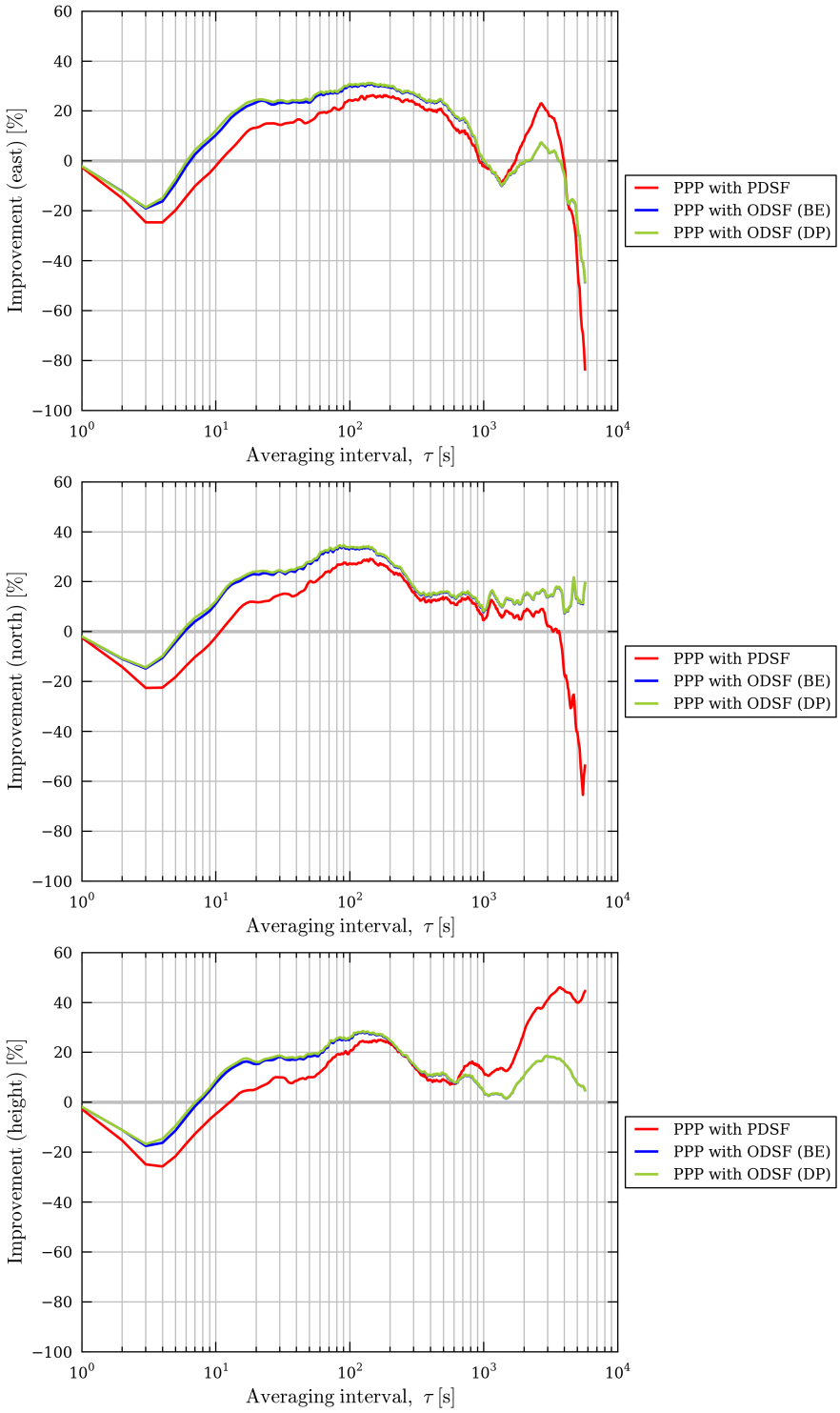

Figure 3.16 – Plots showing the percentage improvement (i.e. reduction) in Allan deviation for station UCL, after applying the various types of sidereal filter, relative to the Allan deviation values corresponding to standard PPP processing that are shown in figure 3.14.

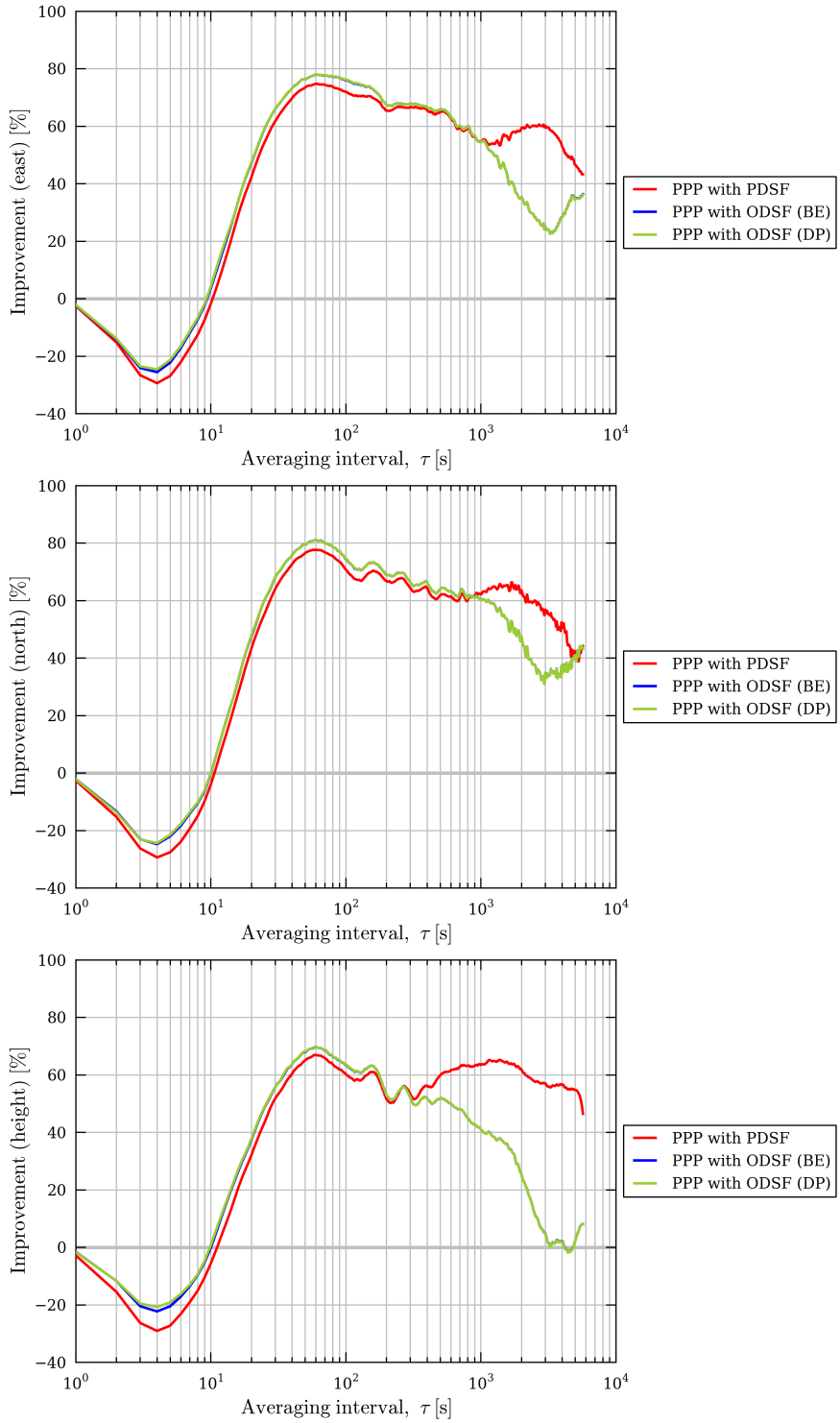

Figure 3.17 – Plots showing the percentage improvement (i.e. reduction) in Allan deviation for station UEL, after applying the various types of sidereal filter, relative to the Allan deviation values corresponding to standard PPP processing that are shown in figure 3.15.

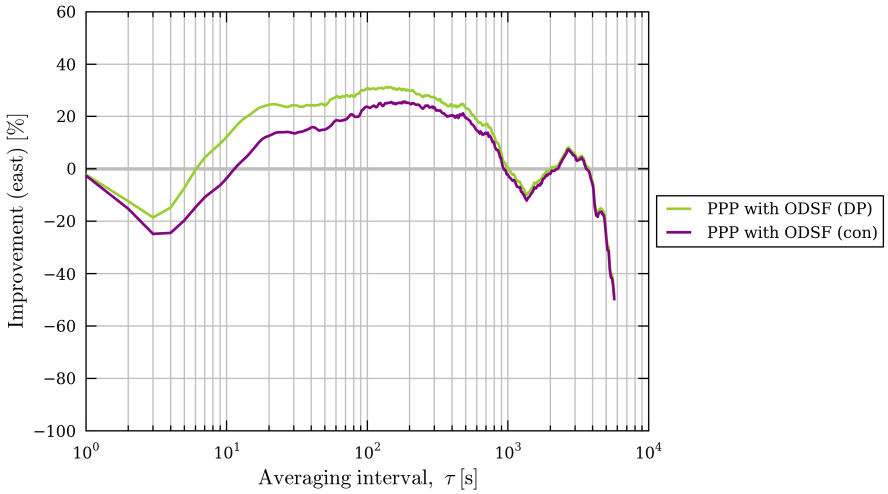

Figure 3.18 – Plots showing the percentage improvement (i.e. reduction) in Allan deviation in the east component at station UCL between 14:00 and 22:00 on 3rd September 2013, after applying two types of observation-domain sidereal filter (ODSF): the dot-product (DP) ODSF and the 'constellation repeat time' (con) ODSF.

UEL is dominated by strong long-period multipath caused by large near-field reflectors and the lack of a choke-ring antenna. The impact of considering the repeat times of individual repeat times is therefore lessened.

For longer averaging intervals the relative performance of the ODSFs and the PDSF becomes more variable with the latter often, but not always, outperforming the former. Again as explained in section 3.4, it is thought that this is due to longer-period multipath errors being absorbed by slowly-varying Kalman filter states such as the wet troposphere zenith delay and phase ambiguities during the stage at which the multipath corrections are formed and during standard PPP processing.

Again, as with the analysis in section 3.4, there does not seem to be much difference in performance at all between the two types of ODSF, particularly at UEL. Nevertheless, there is a slight advantage—by no more than a couple of percentage points—to using a DP ODSF over a BE ODSF at UCL over time intervals of up to roughly 200 s. As stated previously, UCL is more susceptible to short-period 'far-field' multipath interference and is not predominately affected by a single reflector close to the antenna as at UEL. Of course, the repeat times calculated by the two methods are very similar to each other for each satellite. Indeed, figure 3.20 shows that they agree to within just three seconds of each other for all satellites. However, it is evident from figure 3.16 that these small differences in repeat time still have a noticeable effect on the overall performance of an ODSF.

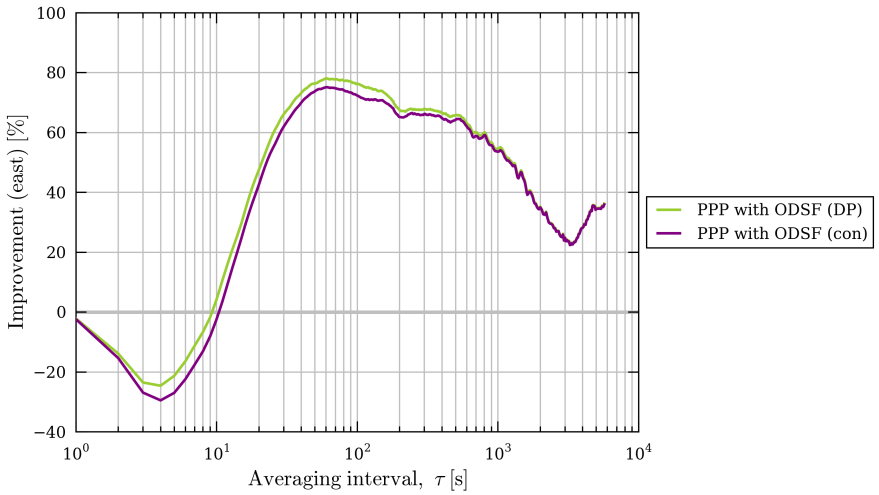

Figure 3.19 – Plots showing the percentage improvement (i.e. reduction) in Allan deviation in the east component at station UEL between 14:00 and 22:00 on 3rd September 2013, after applying two types of observation-domain sidereal filter (ODSF): the dot-product (DP) ODSF and the 'constellation repeat time' (con) ODSF.

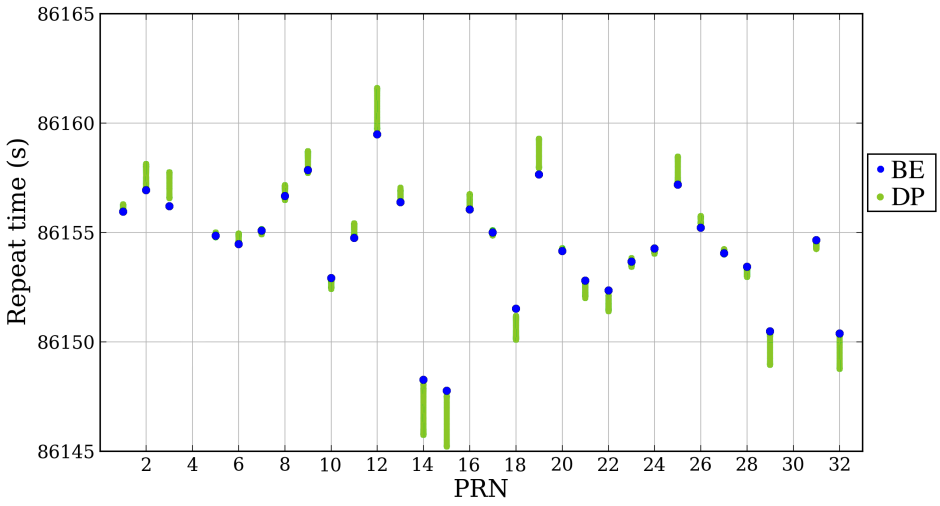

Figure 3.20 – GPS satellite repeat times used by the two types of ODSF during the period from 14:00 to 22:00 on 3rd September 2013 at UCL and UEL. Shown in blue are the ground-track repeat times found using equation (1.23) on page 57 and values given in the GPS broadcast ephemeris. Shown in green are the range of repeat times calculated and used by the DP ODSF algorithm during the period from 14:00 to 22:00.

3.6 Station SLMS, 3rd April 2010

In light of the observations made in sections 3.4 and 3.5, further analysis was undertaken to determine if the observations made above during the analysis using data from UCL and UEL also hold for an antenna sited in what is assumed to be a 'low multipath' environment, i.e. a choke-ring antenna that is not sited in an urban environment and placed well away from potential reflectors. Do the ODSF algorithms remain more effective at removing any short-period multipath than the PDSF algorithm? Does the DP ODSF continue to be at least slightly more effective than the BE ODSF over short time periods?

Here follows a similar analysis to that of section 3.5 above, but applied to data from a continuously operating GPS receiver located in southern California, with station identification code SLMS. This station is operated by the University Navstar Consortium (UNAVCO) Plate Boundary Observatory (PBO) and differs from stations UCL and UEL in terms of equipment and its surrounding environment. It is located well away from nearby buildings and, like station UCL, it is equipped with choke-ring antenna, although manufactured by Ashtech, not Leica. A Google Earth image of station SLMS and its surroundings can be seen in figure E.2a on page 275. Further details of this station, including photographs, can be found on the UNAVCO website[4].

Again, using the same method as described in section 3.4, RINEX files containing 24 hours of 1 Hz GPS code and phase measurements from the 2nd and 3rd April 2010 recorded by the receivers listed above were downloaded from the UNAVCO website.[5] All 24 hours of measurements from 3rd April were processed using the regular PPP algorithm as described in section 2.1. The measurements were processed three more times: once with both types of ODSF and once with a PDSF applied using the methods described in section 2.2.

As stated in section 3.1, the *overall* performance of the filters are assessed over an extended period of time during which the GPS constellation is considered benign or 'normal', so a period of time had to be chosen where there were no satellite outages and no visible satellites had highly anomalous repeat periods. On both 2nd and 3rd April, GPS satellites G24 and G26 were likely undergoing manoeuvres. This is because their respective repeat periods of 86,215 s and 86,088 s were highly anomalous. The effect of these repeat periods on the performance of the sidereal filters is assessed in chapter 4. However, for the purpose of this chapter, the period during which these satellites were visible, approximately 12:39 to 19:30, had to be excluded. A period of almost four and a half hours, 19:30–23:55, was thus chosen for analysis.

The resulting easting, northing and height position error time series for station SLMS between 19:30 and 23:55 is shown in figure 3.21. There are positioning errors with a sidereal repeat period clearly apparent in the northing and height components but less so in the east component. It is speculated that this is due to the nature of the environment surrounding the antenna. These

[4] http://www.unavco.org/instrumentation/networks/status/pbo/overview/SLMS

[5] This material is based on data services provided by the UNAVCO Facility with support from the National Science Foundation (NSF) and National Aeronautics and Space Administration (NASA) under NSF Cooperative Agreement No. EAR-0735156.

time series are similar to those of UCL in the sense that they do not exhibit the kind of strong oscillating position errors with amplitudes of a few tens of millimetres and periods of a few minutes that were found at UEL (figure 3.13). All three types of sidereal filter appear to have a very similar performance, although there are again some differences between the PDSF and the two ODSFs at the lowest frequencies. For example, compare the performance of the sidereal filters between 21:45 and 23:55 in the east component.

As with previous analyses, Allan deviation is used to quantify any overall increase in stability over a wide range of time intervals. Figure 3.22 shows the sigma-tau plots associated with the time series plots of figure 3.21. As expected, it is clear that all types of sidereal filter have not resulted in the dramatic reduction in Allan deviation that was seen at UEL (figure 3.15). In this sense, station SLMS is similar to UCL (figures 3.6 and 3.14) in that if there is no strong multipath error signal with a sidereal repeat period, then sidereal filters will obviously not yield a dramatic improvement. However, notice that figure 3.22 appears to show that all types of sidereal filter have a near identical performance for time intervals under about 600–700 s in the horizontal components and under about 200 s in the vertical component. This contrasts with the previous analyses of UCL and UEL where it was at least possible to discern a slight advantage to using an ODSF over a PDSF over these time intervals in figures 3.6, 3.14 and 3.15.

Also apparent from figure 3.22 is the fact that the sidereal filters have only managed to reduce the Allan deviation values (relative to standard PPP processing) in all three components over only a relatively narrow range of time intervals: from roughly 50 s to around 500 s. This is shown more clearly in figure 3.23 where this range can be seen to exist between 40–60 s and 550–650 s. This range is significantly smaller than for the previous analyses of UCL and UEL—the smallest equivalent range being about 10 s to 900 s at UCL (figure 3.16, easting component). Station SLMS is equipped with a choke-ring antenna and is sited in such a way as to reduce multipath interference, and yet the sidereal filters still manage to improve the stability of the position time series, although only over a relatively narrow range of time intervals. The maximum improvement in stability of nearly 30% occurs over time intervals of between 200 s and 300 s in the horizontal components. Still, there is not so much repeatable high-frequency multipath interference compared to UCL, and so the sidereal filters actually increase noise, or rather decrease stability, over time intervals shorter than about 50 s.

Notice that, even after examining figure 3.23, there is very little difference in performance between the different types of sidereal filter. The ODSFs do provide a greater reduction in Allan deviation, by no more than about three percentage points, than a PDSF over time intervals of under about 200 s in the northing and height components and only 100 s in the east component. However, for longer intervals, the ODSFs no longer necessarily yield the greatest improvement in stability. For time intervals above 600 s, the performance of the sidereal filters becomes much more variable. Indeed, a similar observation was made for the previous analyses of stations UCL and UEL. Notice also that there is negligible difference between the DP and BE ODSFs, which contrasts with the previous analyses of station UCL where there was a small but discernible

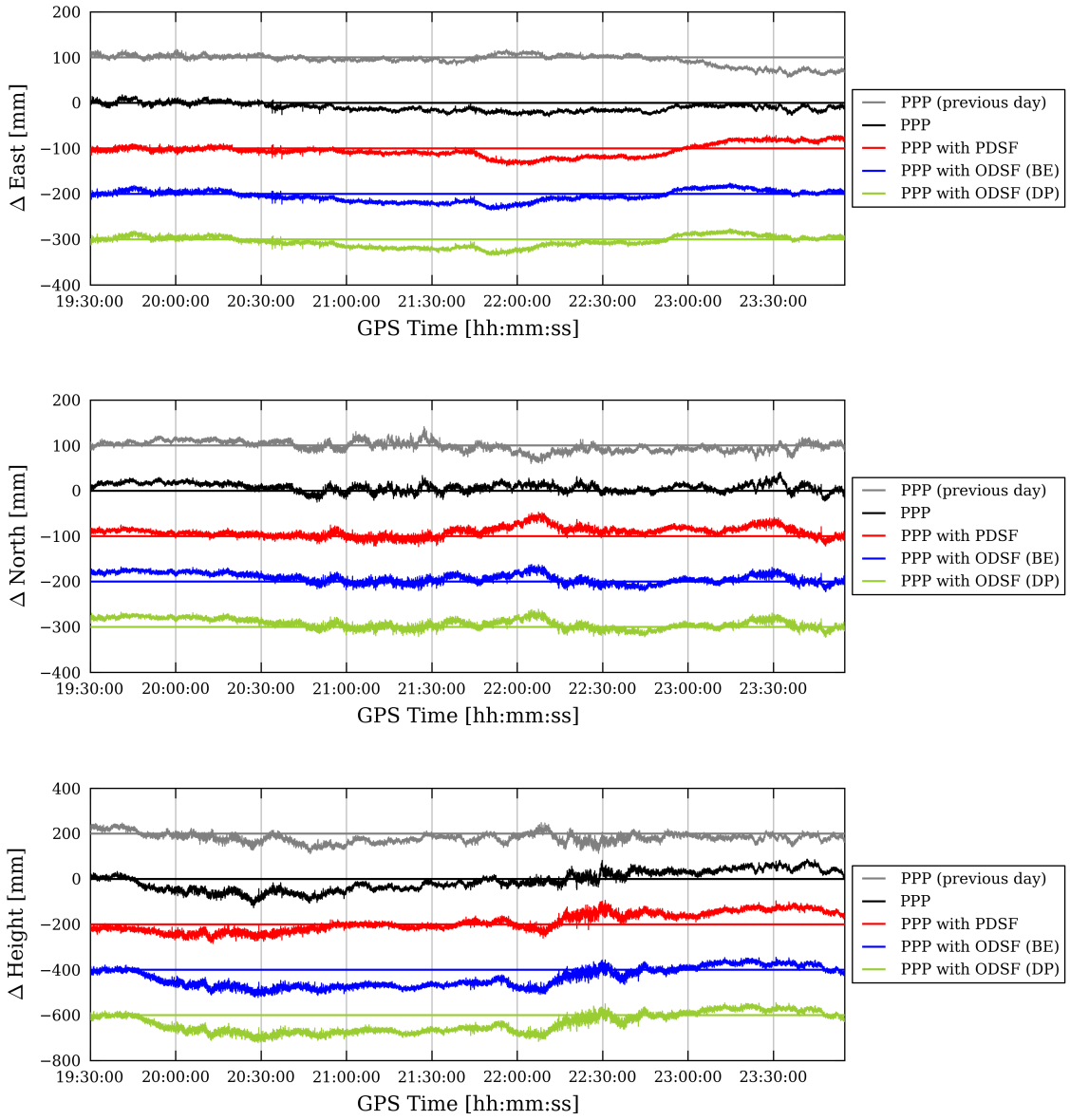

Figure 3.21 – Easting, northing and height errors between 19:30 and 23:55 on 3rd April 2010 for receiver SLMS resulting from standard PPP processing and PPP processing with various types of sidereal filter applied. (Each of the time series have been offset from each other by appropriate multiples of 100 mm or 200 mm for clarity).

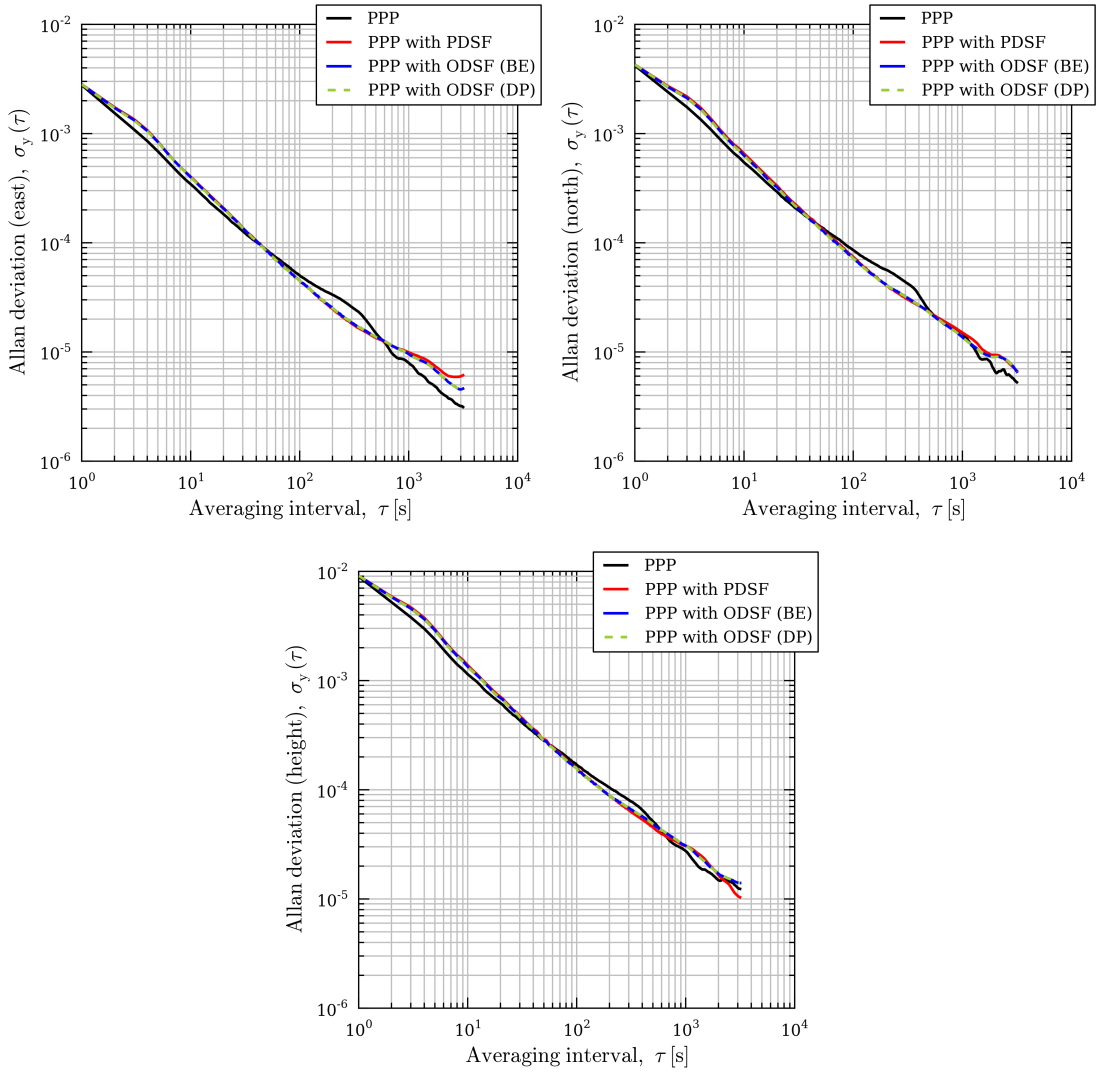

Figure 3.22 – Allan deviation plots of the corresponding position time series (east, north and height) between 19:30 and 23:55 on 3rd April 2010, at station SLMS, shown in figure 3.21.

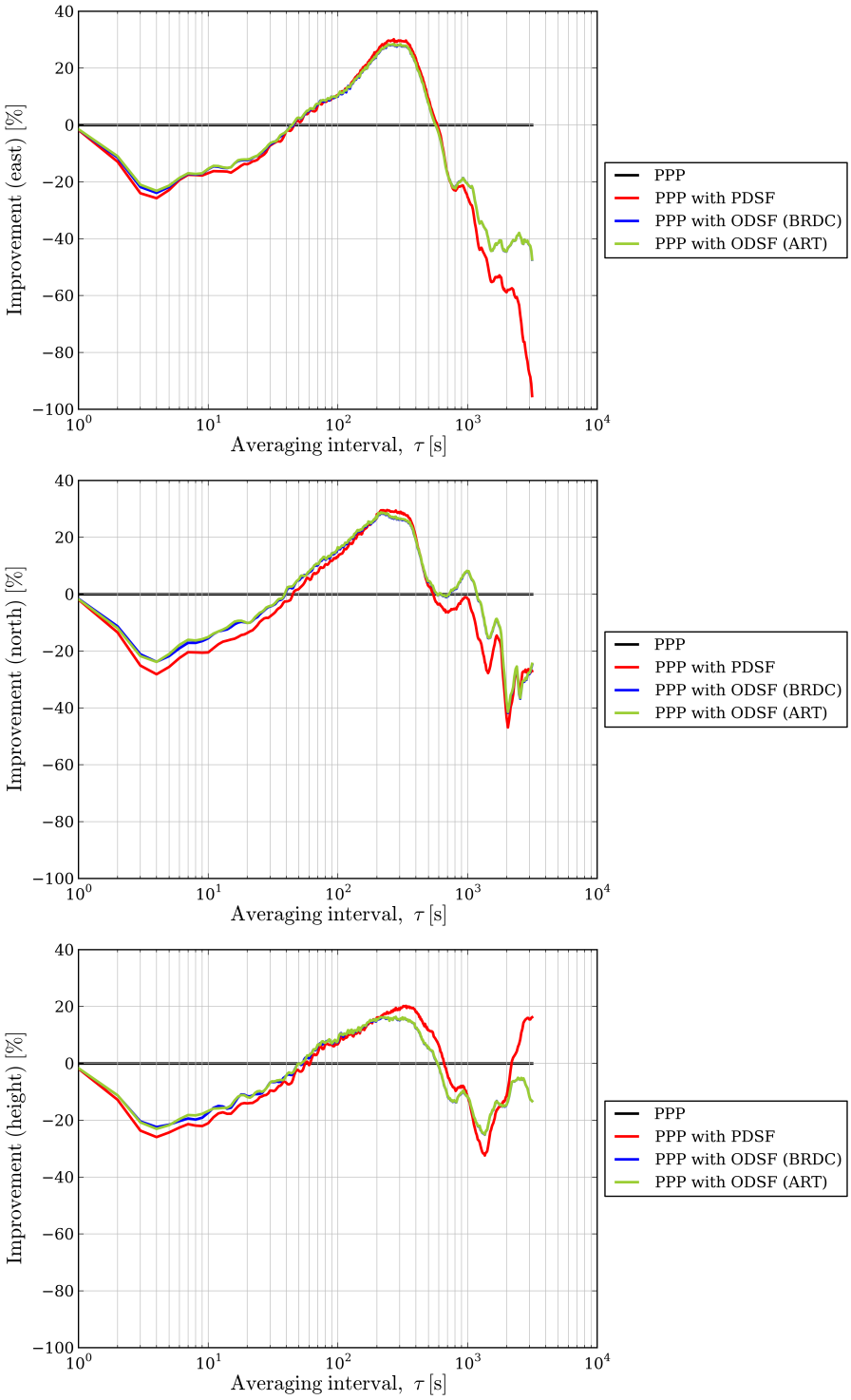

Figure 3.23 – Plots showing the percentage improvement (i.e. reduction) in Allan deviation for station SLMS, after applying the various types of sidereal filter, relative to the Allan deviation values corresponding to standard PPP processing that are shown in figure 3.22.

advantage to using an BE ODSF. Presumably this is because there is little occurrence of the short-period 'far-field' multipath interference at SLMS compared to what was seen at UCL. One can see few potential far-field reflectors at station SLMS relative to UCL when comparing figure E.2a with E.1. The small differences in the repeat times calculated by the two ODSF algorithms can only be influential if a significant amount of short-period multipath is present. Also, with little such multipath interference, there will be little difference between an ODSF and a PDSF in this respect.

3.7 Stations GMPK, P494–6 and P744, 3rd April 2010

GPS measurements from another five continuously operating receivers located in southern California were used to further assess the performance of the sidereal filter algorithms. These stations, like SLMS in the previous section, are operated by the UNAVCO Plate Boundary Observatory (PBO) and have the identification codes GMPK, P494, P495, P496 and P744. Like SLMS, each station is located well away from nearby buildings, has an antenna mounted on a deep-drilled braced monument and is covered by a protective radome. With the exception of station P494, each is equipped with either a Trimble or Ashtech choke-ring antenna. P494, at the time the measurements used in the following analysis were recorded, was equipped with an antenna without choke-rings. Notably, the terrain surrounding station GMPK is rocky. Again, Google Earth images of the surroundings of each of these stations can be seen in figures E.2 and E.3 on pages 275 and 276. Details of each station, including photographs, can be found on the UNAVCO website[6].

For the sake of brevity, a full analysis of each station in the manner of the previous sections of this chapter is not presented here. Instead, only the figures showing the percentage *improvement* (i.e. percentage reduction) in Allan deviation of the position time series caused by sidereal filtering are presented. These are shown in figures E.17 to E.21 in appendix E (pages 290 to 294).

With each antenna intentionally sited in a low multipath environment, it was anticipated that the sidereal filters would perform in a similar manner to those at SLMS, i.e.:

- the sidereal filters would only be successful at increasing the stability of a standard PPP position time series over a relatively narrow range of time intervals, say from roughly 50 s to around 500 s.
- there would be little difference in performance between the PDSF and the ODSFs over time intervals of under a few hundred seconds.
- the two types of ODSF have a near-identical performance.

Figures E.17 to E.21 show that the PDSF and the ODSFs do indeed perform similarly at increasing stability over time intervals under a few hundred seconds, where the difference between the three exceeds no more than six or seven percentage points. As was seen in previous analyses with longer

[6] http://www.unavco.org/instrumentation/networks/status/pbo/

intervals, the performance of the sidereal filters is much more variable with the PDSF frequently, but not always, outperforming the ODSFs.

Station P744 (figure E.21), like SLMS, shows the sidereal filters only improving the stability of the time series over a narrow range of time intervals: 80–100 s to 300–400 s in the easting and height components. For the other stations, this is not necessarily so. As pointed out above, the performance of the sidereal filters becomes much more variable over larger time intervals, but over smaller intervals of less than 100 s, the sidereal filters tend to perform more successfully. The maximum improvement in stability usually occurs for intervals of between 100 s and 400 s, although at P495 (figure E.19), the sidereal filters are notably successful at improving stability for intervals of around 60 s and 80 s for the easting and northing components respectively. The sidereal filters perform particularly well at GMPK (figure E.17), presumably because the rocky terrain surrounding the antenna generates stronger multipath interference. The maximum improvement in stability here approaches 50% for time intervals of around 200 s.

Again, as with SLMS, both types of ODSF have a nearly identical performance. At stations GMPK and P744, a slight advantage to using a DP ODSF can be identified for intervals under a few hundred seconds, but this advantage amounts to no more than two or three percentage points—most noticeable for the northing component of the position time series from P744 (figure E.21).

3.8 Conclusions

The above analyses were designed to test the observation- and position-domain sidereal filter algorithms when applied to PPP processing of GPS phase measurements from monitoring stations with contrasting antenna types and surrounding environments, but under otherwise relatively benign conditions. The following conclusions can be made:

- A sidereal filter is of course likely to be more effective when the observations are strongly affected by multipath. Conversely, if GPS observations have not been affected by strong multipath signals, then a sidereal filter will not yield a dramatic improvement. This is perhaps quite obvious and has unsurprisingly been confirmed by the above analyses. However, all types of sidereal filters were particularly successful at increasing the stability of a PPP position time series over time intervals of about 100–300 s, even for stations with choke-ring antennas sited in low multipath environments such as stations SLMS and P744. This is perhaps indicative of the fact that oscillating errors with periods of a few hundred seconds caused by multipath interference is a common occurrence for many GNSS receivers around the world and that the use of choke-rings and careful antenna siting reduces its effect. This is also encouraging for the application of sidereal filtering to tsunami early warning systems which require the accurate measurement of small ground displacements over the course of just a few minutes. Hence, the improved stability of a position time series over just a few hundred seconds should be beneficial.

- An observation-domain sidereal filter (ODSF) is generally more effective than a position-domain sidereal filter (PDSF) at reducing high-frequency positioning errors caused by multipath interference. At the beginning of this chapter, it was stated that 'high-frequency multipath' referred to "oscillatory multipath errors with periods under about 100 s". It is difficult to generalise the overall performance of the sidereal filter algorithms because the equipment used and the environment surrounding each station is so variable. It is apparent from all of the figures 3.7, 3.16, 3.17, 3.23 and figures E.17 to E.21 that the ODSFs result in a greater improvement in the stability of a PPP position time series than a PDSF, at least for intervals of up to 100 s. But this upper limit can vary enormously: up to almost 4,000 s at UCL (figure 3.7, easting only), for example.

  However, the difference in performance between the ODSFs and the PDSF is generally quite small for intervals under 100 s at all stations with the exception of station UCL. This is because UCL is more susceptible to 'far-field' high-frequency multipath than other stations. It is hence assumed that an ODSF will generally be more effective at removing high-frequency multipath error than a PDSF because of its inherent ability to consider the differing repeat times of each visible GPS satellite separately.

- There is little difference in performance between the two types of ODSF, i.e. it makes little difference as whether the repeat time of a GPS satellite is calculated using the dot product (DP) method or by using the square-root of the semi-major axis and the correction to mean motion given in the broadcast ephemeris (see section 1.5.3). The above analyses did show that there was indeed a small difference between the two, particularly at station UCL where the DP ODSF yielded an improvement of at most two percentage points, in terms of Allan deviation, over the BE ODSF for time intervals under about 200 s. So, a DP ODSF appears to provide slightly better *overall* performance than a BE ODSF. The difference between the two types of ODSF in terms of performance could be more pronounced when satellites with unusually short or long repeat times are visible or under specific instances of high-frequency multipath. This is investigated in chapters 4 and 5, respectively.

- For large averaging intervals, certainly over 3,000 s, the relative performance of the different sidereal filters tends to be more variable with the PDSF frequently outperforming the ODSFs. As discussed in the above analyses, any long-period multipath errors are more likely to be absorbed by slowly-varying Kalman filter states such as the wet troposphere zenith delay and the phase ambiguity states. The performance of the sidereal filters could perhaps be improved if the phase ambiguity states were fixed to integer values as mentioned in section 1.3.5 which should improve the accuracy of the position, receiver clock and troposphere states. However, the PPP software used throughout this thesis does not yet have this capability. For the purposes of tsunami early warning, this ability is not so pertinent because, as mentioned above, it is the stability of a position time series over just a few hundred seconds that is most important.

Chapter 4

Anomalous Repeat Times

4.1 Introduction and hypothesis

In section 2.2.1, it was stated that one of the advantages an observation-domain sidereal filter (ODSF) holds over a position-domain sidereal filter (PDSF) is that it can consider all of the different GPS satellite repeat times separately. From the previous chapter, it was seen that an ODSF consistently outperformed a PDSF at increasing the stability of a position time series over averaging intervals from tens of seconds to a few hundred seconds in relatively benign conditions, i.e. the same set of satellites were visible on adjacent days and all of them had ground track repeat times in the range of $86,155 \pm 8$ s. In this chapter, the performance of each type of sidereal filter is examined during a period of time when satellites with highly abnormal repeat times were visible.

In this thesis, a satellite's repeat period is considered 'anomalous' if it lies outside the range of $86,155 \pm 10$ s. Sometimes, satellite repeat times may lie far outside of this range. One example is shown in figure 4.1. This shows the repeat times for all satellites visible from the antenna at Plate Boundary Observatory (PBO) station P495 on 3$^{\text{rd}}$ April 2010. Two satellites, pseudorandom noise (PRN) codes 24 and 26, were found to have particularly anomalous repeat periods of 86,215 s and 86,088 s, respectively, when calculated using elements in the broadcast ephemeris (BE) (see section 1.5.3.1, page 57). These were hence considered good candidates for analysis. Notice that a repeat time calculated by the dot product (DP) method (section 1.5.3.2) can differ by more than 20 s from that calculated using the broadcast ephemeris for an individual satellite. During this time, it is quite possible for errors caused by multipath interference to change significantly. Indeed, positioning errors oscillating with a period of just 15 s are presented in section 5.5.1 (page 155) in the following chapter. For this reason, it is predicted that the difference in performance between the two types of ODSF (dot product (DP) and broadcast ephemeris (BE)) would be noticeably larger than it appeared during the analysis in chapter 3, with the former outperforming the latter. However, both types of ODSF are predicted to outperform the PDSF, i.e. improve the stability of position time series over intervals of up to a few hundred seconds at least.

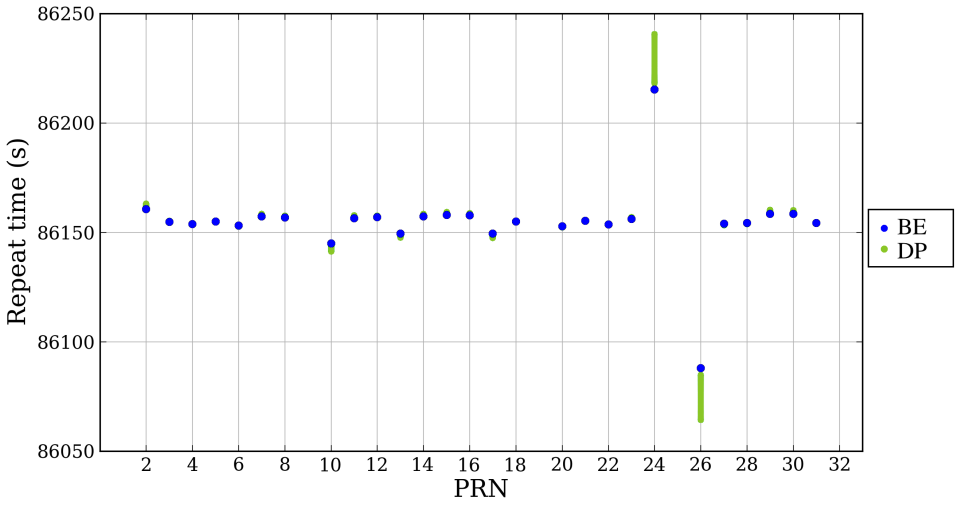

Figure 4.1 – Repeat times for each GPS satellite visible to station P495 in Southern California on 3rd April 2010. Ground-track repeat times calculated using the GPS broadcast ephemeris (BE) are shown in blue; Repeat times calculated using the dot product (DP) method described in section 2.2.1.1 are shown in green.

The method used for the analysis, which is similar to that used in the previous chapter, is described in section 4.2. The chapter includes a detailed analysis of the results of processing GPS measurement data from a single station, P495, in section 4.3. There then follows a less detailed analysis of data from two nearby stations, P494 and P496, in section 4.4. Conclusions are presented in section 4.5.

4.2 Method

To test the impact of measurements from GPS satellites with anomalous repeat times, one would ideally test the results of each of the sidereal filter algorithms against results from a dataset where *all* satellites have repeat times that are not anomalous, i.e. within 10 s of 86,155 s. Unlike satellite outages (which are examined in chapter 6), this is not possible to simulate. One could perhaps move the multipath corrections associated with a satellite with an anomalous repeat period forward or back in time by an appropriate amount to simulate multipath corrections derived from a 'normal' satellite. However, this would ignore the reason that some satellites have anomalous repeat times: they are most likely undergoing a manoeuvre. Hence, the path that such a satellite takes across the sky may deviate from the path taken on the previous day. Deviation from the expected path across the sky (hereafter known as a 'skytrack') is likely to cause the pattern of multipath interference to differ from the previous day. It is the significance of this change which is examined in this chapter. The performance of each type of sidereal filter will be assessed relative to each other for a period during which satellites with anomalous repeat times are visible.

For a few days spanning either side of the M_W 7.2 El Mayor–Cucapah earthquake of 4th April 2010, it was found that GPS satellites G24 and G26 had particularly anomalous periods. For this analysis, one of those days, 3rd April 2010, was chosen to assess the advantage that an ODSF has over a PDSF where multipath corrections are derived from the observation residuals resulting from the processing of data from the previous day, 2nd April. Three receivers were chosen for analysis: UNAVCO PBO stations P494, P495 and P496 in southern California. These stations are within 33 km of each other and so the paths taken across the sky by the GPS satellites from the point of view of the stations should be very similar. The surrounding environment, and hence any multipath interference, will of course be different for each station. As stated in section 3.7, each of these stations are securely anchored to the underlying bedrock and sited well away from any buildings and other potential reflectors. The antennas at stations P495 and P496 possess choke-rings while the antenna at station P494 does not.

The GPS measurements from each of these stations were processed in exactly the same way as for the analysis for the overall performance of the sidereal filters in chapter 3, i.e. measurements were processed four times: once with the PDSF algorithm applied, once with an ODSF algorithm using the dot product (DP) method to calculate repeat time, once with the ODSF algorithm again but using the BE method, and once with no sidereal filter applied at all. The resulting time series of eastings, northings and heights for the period when either satellite was visible, approximately 12:40 to 19:30 (GPS time), were compared with each other using Allan deviation as a performance measure.

4.3 Station P495

4.3.1 Results 12:40–19:30

Figure 4.2 shows the results of each of the processing runs for the time period concerned for easting, northing and height for station P495. At first glance, it is clear that each of the sidereal filters have had at least some beneficial effect in removing the multipath error in the northing and height components at around 13:30 (marked by the letter 'A') and 14:45 (B), and in the east component during the period 15:30–16:00 (C) and after 19:15 (D), for example. None of the sidereal filters did much to remove the longer-term drift westwards, northwards and downwards after about 18:50 (E) or the higher frequency errors between around 17:10 and 17:40 (F) in the height component—the cause of which is unknown. It is possible to see that the effect of the sidereal filters was not always beneficial. For example, the PDSF appears to have introduced further oscillatory errors in the height and north components after about 18:30 (G).

The Allan deviation plots that correspond to the period 12:39–19:30 are shown in figure 4.3. These plots indicate that, on average, there was little difference between the various processing modes in terms of stability. Figure 4.4 instead shows the percentage *improvement* (i.e. reduction) in Allan deviation of each of the filtered time series relative to regular PPP processing where no sidereal filter was applied. From this figure, the following observations are made:

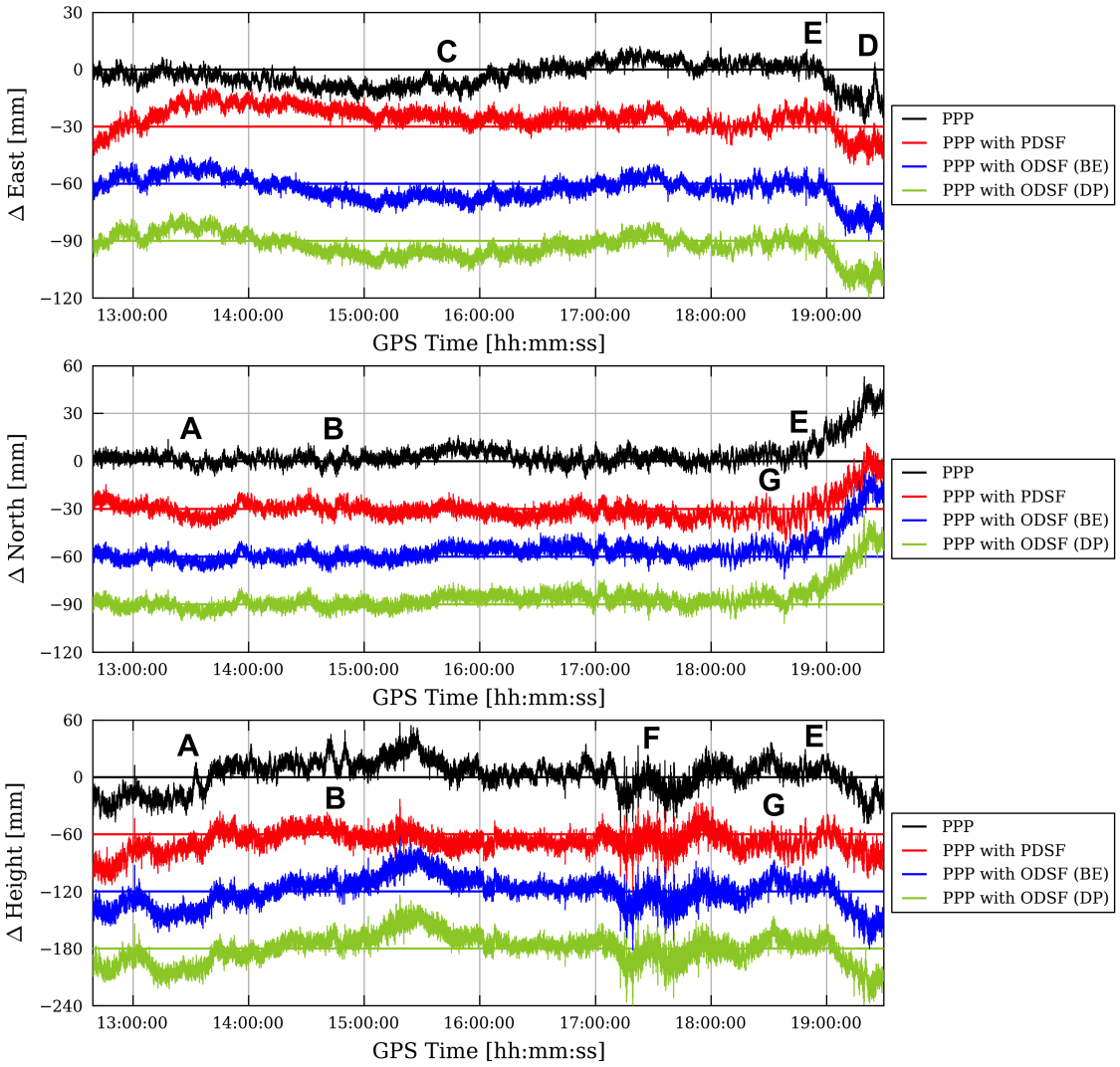

Figure 4.2 – Easting, northing and height errors between 12:40 and 19:30 on 3rd April 2010 for receiver P495 resulting from standard PPP processing and PPP processing with various types of sidereal filter applied. (Each of the time series have been offset from each other by appropriate multiples of 30 mm or 60 mm for clarity). The letters A to G are referred to in the main text.

- For the horizontal components, the sidereal filters were generally of little benefit over intervals of a few hundred seconds: For averaging intervals under 500 s, the maximum improvement in stability over standard PPP is only about 11% for the DP ODSF. For averaging intervals above about 500 s, the ODSFs improved stability by no more than about 5%. This is perhaps because station P495 is located in what can be considered as a low-multipath environment (see section 3.7), so applying a sidereal filter for the purpose of reducing multipath error would have had a limited benefit. Nevertheless, the ODSFs outperformed the PDSF over all but the longest averaging intervals—certainly for all intervals under 600 s. The PDSF resulted in a general worsening of Allan deviation across most averaging intervals. Note how the DP ODSF generally outperformed the BE ODSF for nearly all averaging intervals, although the difference between the two was only slight for the east component.

- For the vertical component, both types of ODSF outperformed the PDSF for all averaging intervals below 600 s and the PDSF performed significantly better than either type of ODSF above averaging intervals of about 1,000 s. Like the east component, the DP ODSF outperformed the BE ODSF over nearly all averaging intervals, but the difference between the two is very slight.

These results refer to the *overall* performance of the different types of sidereal filter across the whole of the period from 12:39 to 19:30. However, within that period, the relative performance of each sidereal filter did vary. To illustrate this, two smaller time periods were identified: 18:33 to 19:10 and 19:10 to 19:30.

4.3.2 Results 18:33–19:10

Figure 4.5 shows the same results of each of the processing runs but just for the time period 18:33 to 19:10. Immediately, it can be seen that the PDSF failed to reduce the multipath effect. It actually increased the oscillatory error, particularly in the north and height components. Both of the ODSFs had more success than the PDSF, but it is clear that there was a noticeable difference between the two types of ODSF in terms of their effectiveness at reducing multipath error. The DP ODSF was more successful than the BE ODSF, particularly in the north and height components between 18:33 and 18:52. Indeed, the BE ODSF did not remove the oscillatory error in this period: An error in northing with a period of about two minutes and a peak-to-peak amplitude of about 2 cm occurred between 18:36 and 18:40 (marked by the letter 'H'), which was actually slightly larger than the error in the equivalent period in the standard PPP time series.

Figure 4.6 shows the respective Allan deviation plots for the position time series in figure 4.5. From these plots, it appears that the sidereal filters had little effect in terms of Allan deviation in the east component. For the north and height components, the PDSF resulted in an *increase* in Allan deviation across all averaging intervals. The DP ODSF appears to be the only type of sidereal filter that has obviously reduced Allan deviation values above about 40 s. Figure 4.7 shows the percentage improvement in Allan deviation for each of the filtered time series relative to regular

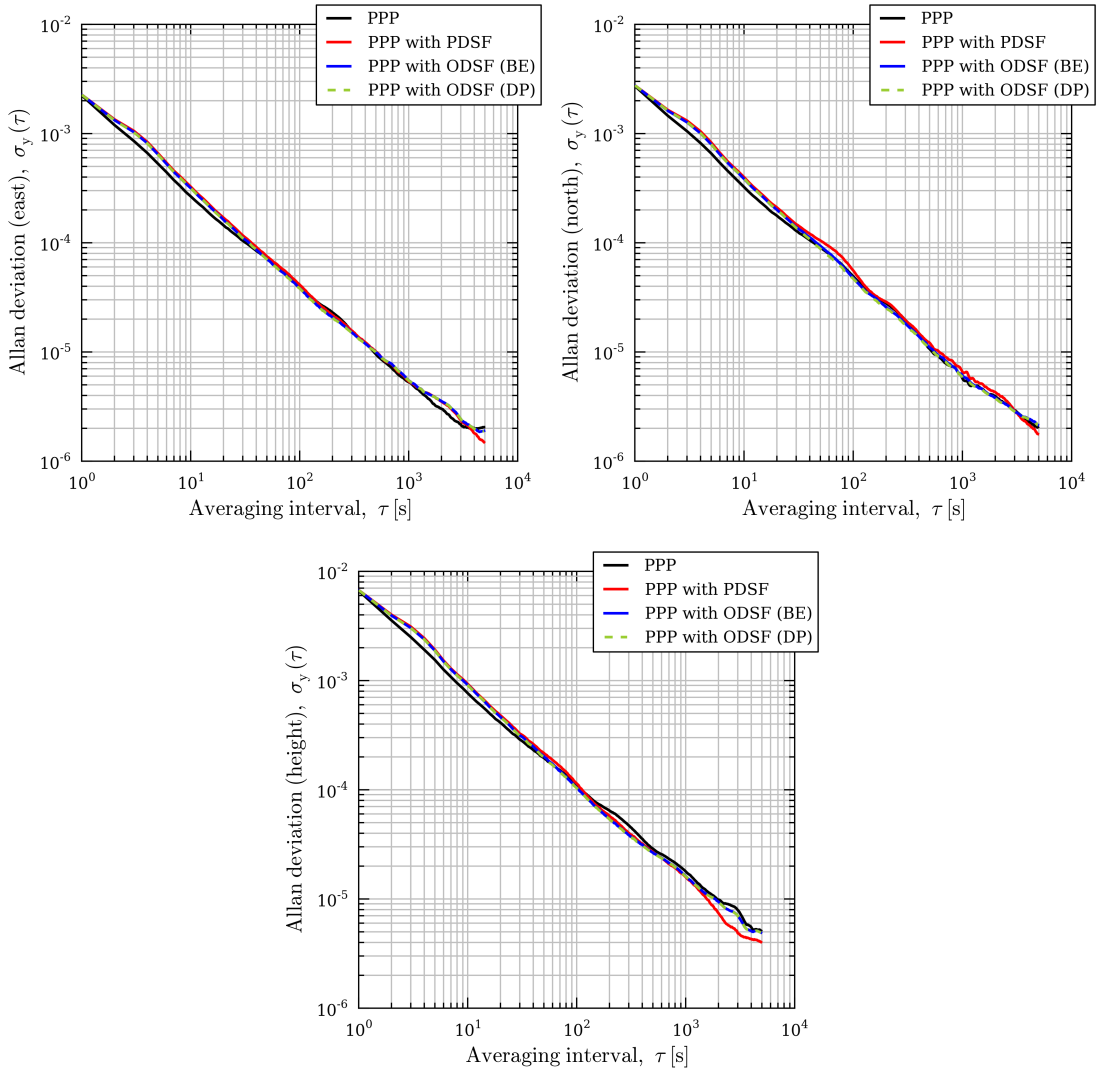

Figure 4.3 – Allan deviation plots of the corresponding position time series (east, north and height) at station P495 between 12:40 and 19:30 on 3rd April 2010 shown in figure 4.2.

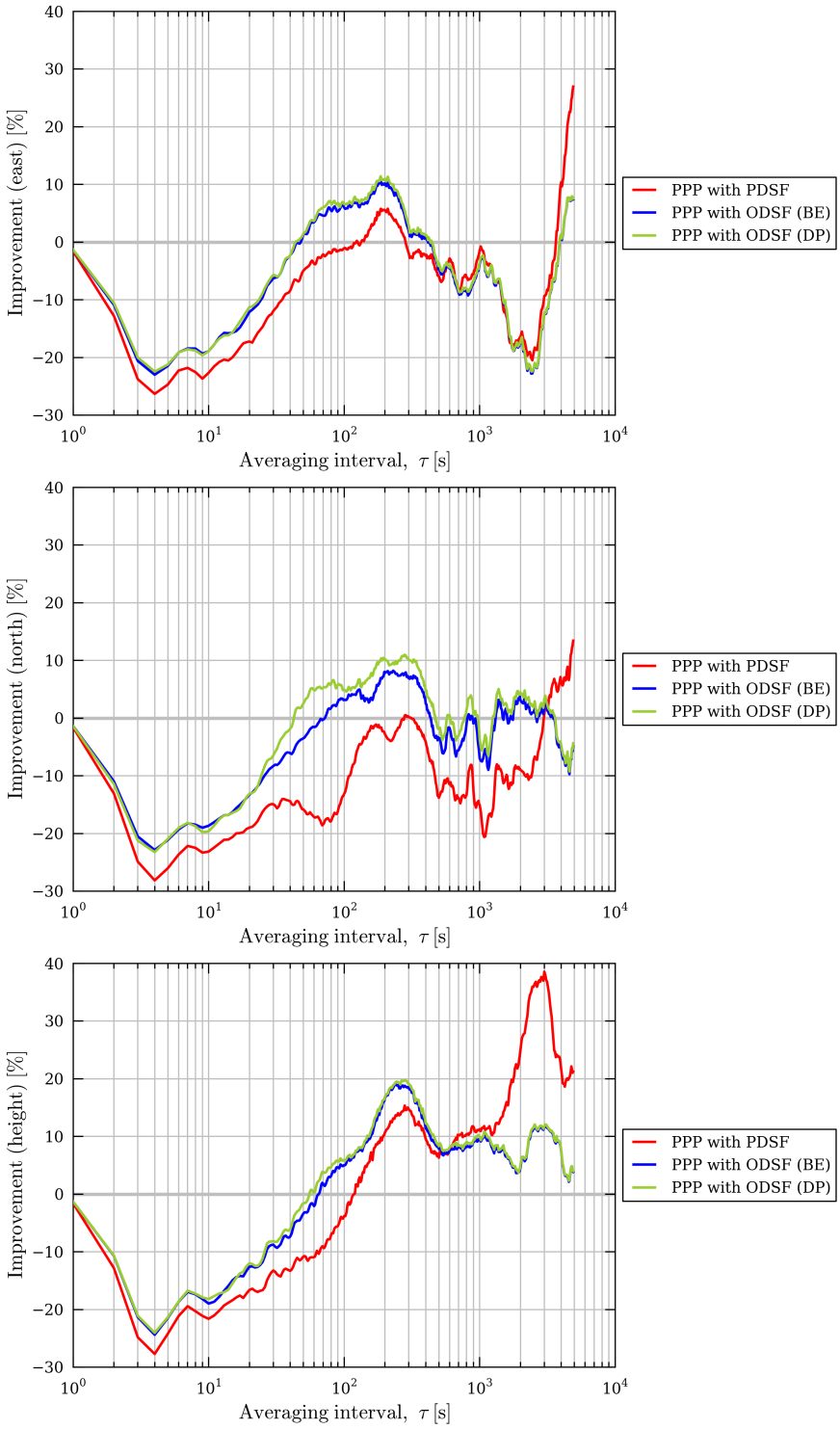

Figure 4.4 – Plots showing the percentage improvement (i.e. reduction) in Allan deviation at station P495, after applying the various types of sidereal filter, relative to the Allan deviation values corresponding to standard PPP processing that are shown in figure 4.3.

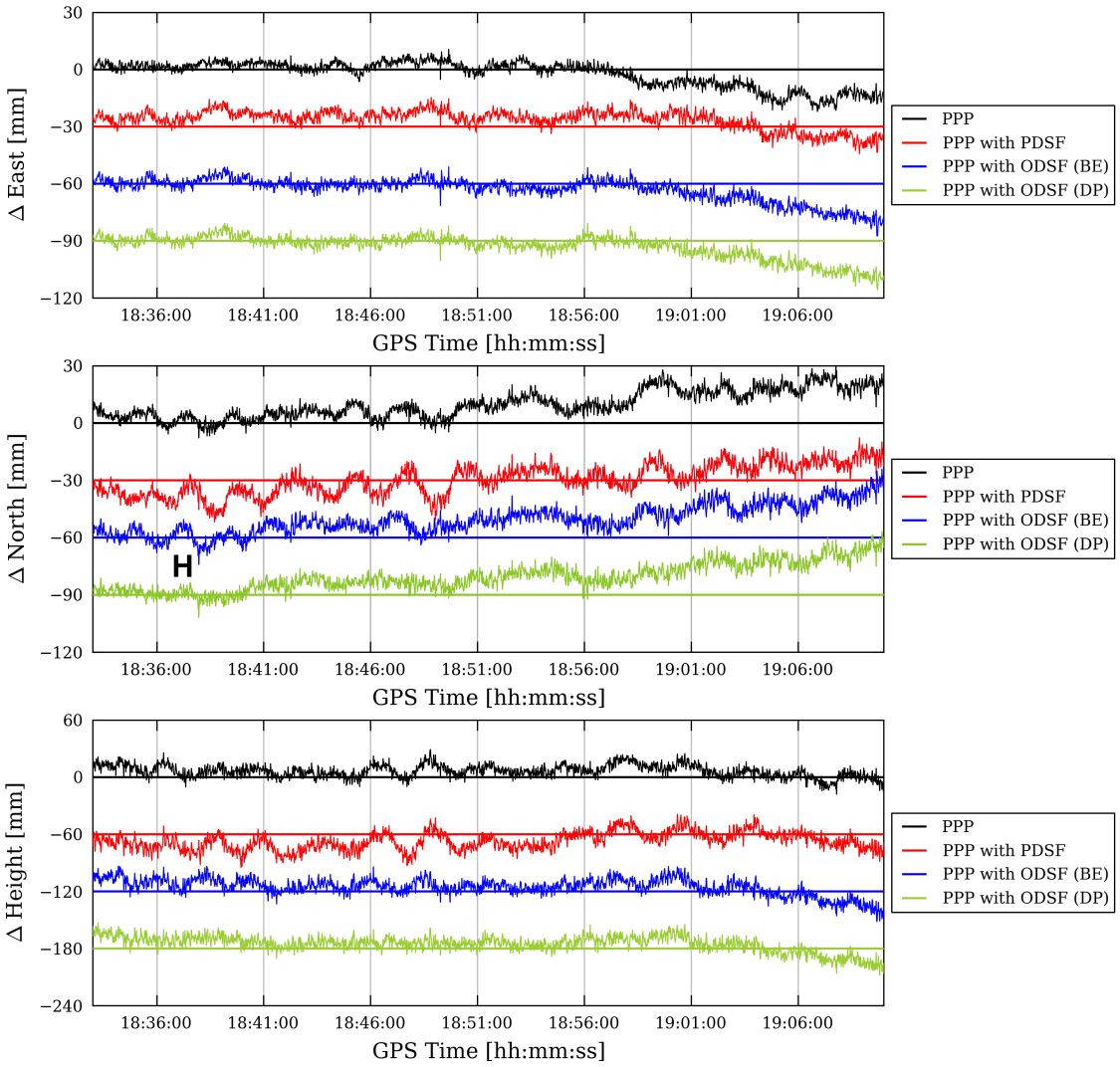

Figure 4.5 – Easting, northing and height errors between 18:33 and 19:10 on 3rd April 2010 for receiver P495 resulting from standard PPP processing and PPP processing with various types of sidereal filter applied. (Each of the time series have been offset from each other by appropriate multiples of 30 mm or 60 mm for clarity). The letter 'H' is referred to in the main text.

PPP processing. Here it is easier to see the relatively poor performance of the BE ODSF when compared to the DP ODSF in the north and height components. For the east component, it is possible to see that the performance of both the BE ODSF and DP ODSF were, in this case, quite similar but only yielding an improvement in Allan deviation of at most 11% for intervals between 40 s and around 250 s.

4.3.3 Results 19:10–19:30

However, the relative performance of the sidereal filters was very different in the period from 19:10 to 19:30. Figure 4.8 shows the resulting easting, northing and height time series after applying the different types of sidereal filter (as well as regular PPP) during this period. This time, all types of sidereal filter were successful at reducing the oscillations caused by multipath interference in the east component. The same cannot be said for northing and height. For example, notice the single small-amplitude oscillation of roughly 20 mm peak-to-peak between 19:19 and 19:21 in the height component of the standard PPP time series (marked by the letter 'J'). This error seems to have been amplified, almost doubled, by both the PDSF and the DP ODSF, but there seems to be less of an increase with the BE ODSF.

Again, it is not easy to see the relative performance of the sidereal filters using the Allan deviation plots in figure 4.9, except to say that all types of sidereal filter were successful in improving Allan deviation in the east component over averaging intervals above about 40 s compared with normal PPP processing. Figure 4.10 shows that both of the ODSFs consistently reduced the Allan deviation in the east component by about five percentage points more than the PDSF above averaging intervals of 40 s, but there was little to choose between the two ODSFs. However, for the north and height components, the results were very different. Both of the ODSFs yielded an improvement over standard PPP by up to 30% in terms of Allan deviation over relatively large averaging intervals of 130 s and above. For smaller averaging intervals, the ODSFs did not perform so well. In contrast to the period between 18:33 and 19:10, the BE ODSF outperformed the DP ODSF—certainly above averaging intervals of about 30 s. Although the performance of both the ODSFs was relatively poor, at least the BE ODSF resulted in a slight improvement in Allan deviation in the north component over standard PPP processing for averaging intervals larger than about 45 s, unlike the DP ODSF.

4.3.4 Analysis

The key observation that can be made from sections 4.3.2 and 4.3.3 is that the DP ODSF was more effective than the BE ODSF from 18:33 to about 19:10, but the BE ODSF was more effective than the DP ODSF between 19:10 and 19:30. Why was this so?

Before this question can be answered, it is necessary to confirm that the difference in performance between the two types of ODSF were a result of just these two satellites and their anomalous repeat times and not for other reasons. It is therefore necessary to check that the multipath cor-

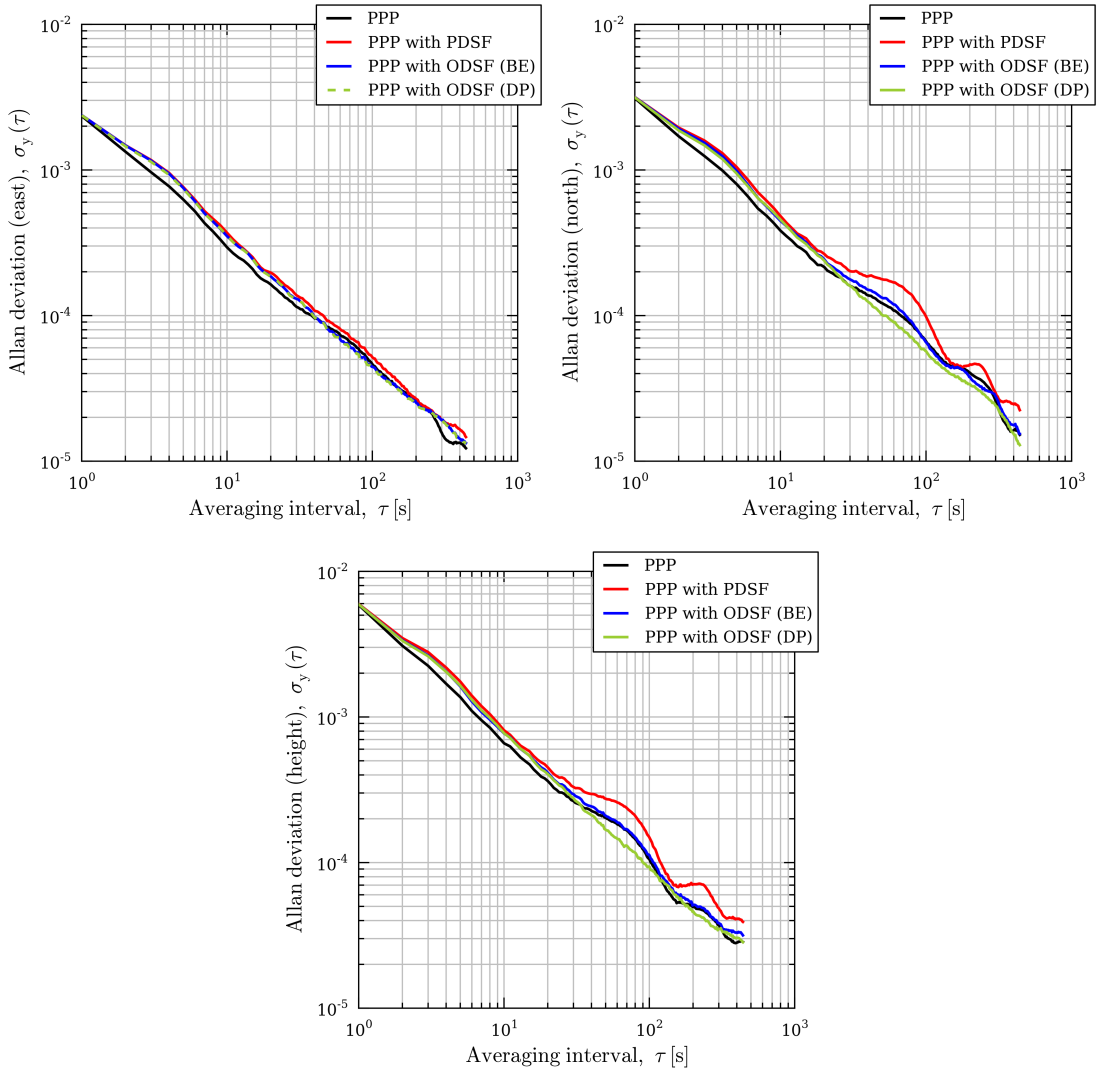

Figure 4.6 – Allan deviation plots of the corresponding position time series (east, north and height) at station P495 between 18:33 and 19:10 on 3rd April 2010 shown in figure 4.5.

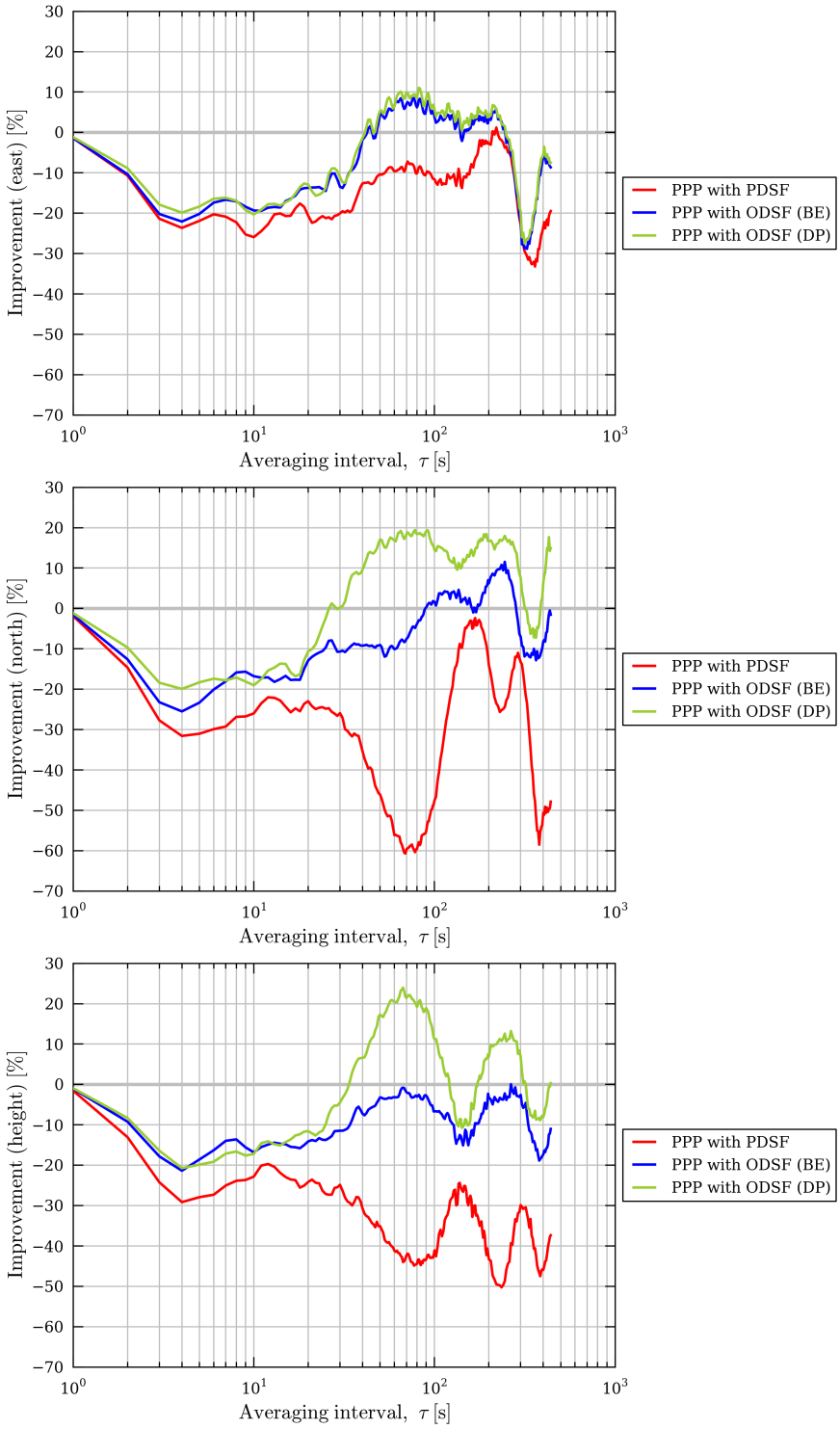

Figure 4.7 – Plots showing the percentage improvement (i.e. reduction) in Allan deviation at station P495, after applying the various types of sidereal filter, relative to the Allan deviation values corresponding to standard PPP processing that are shown in figure 4.6.

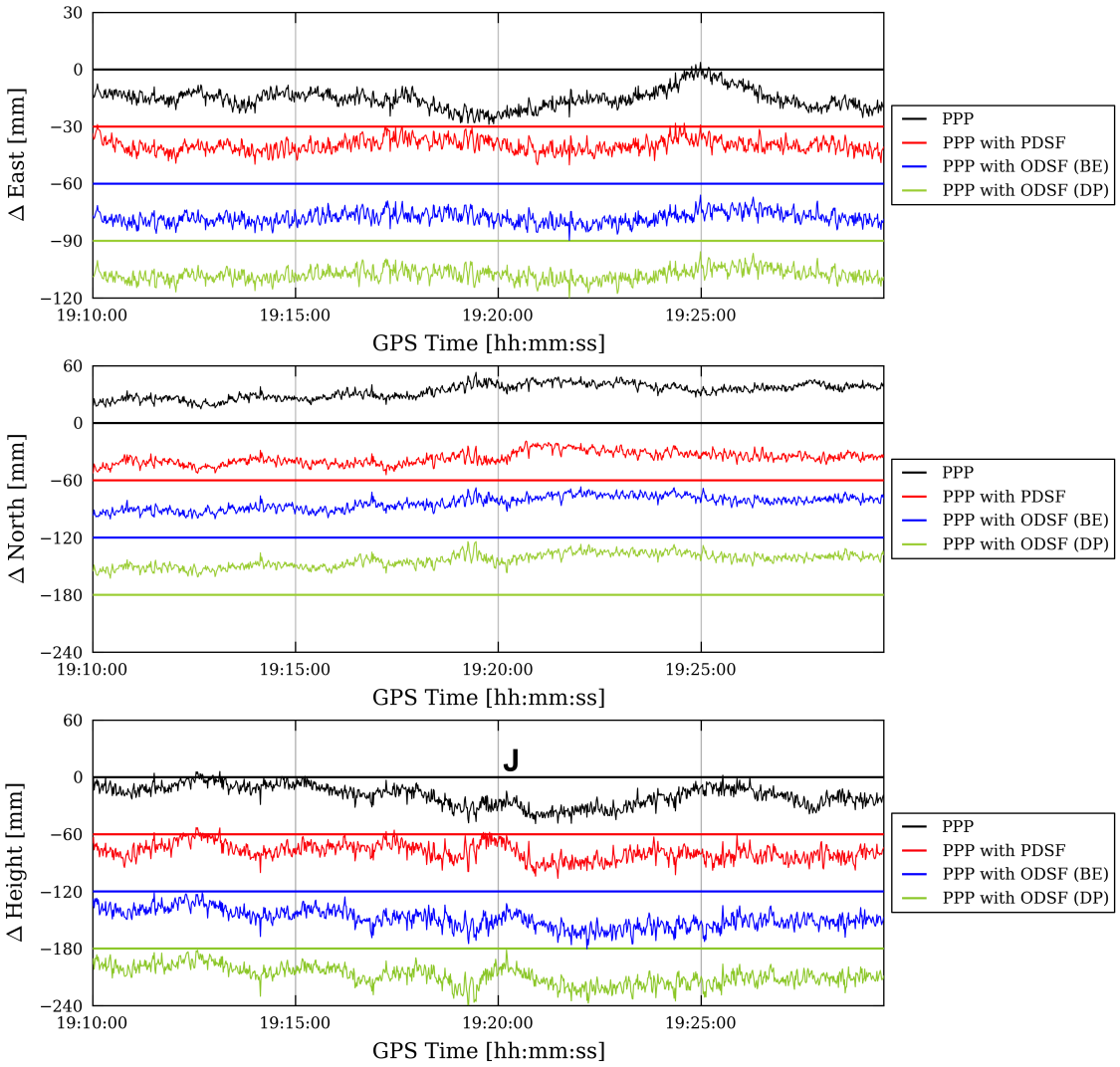

Figure 4.8 – Easting, northing and height errors between 19:10 and 19:30 on 3rd April 2010 for receiver P495 resulting from standard PPP processing and PPP processing with various types of sidereal filter applied. (Each of the time series have been offset from each other by appropriate multiples of 30 mm or 60 mm for clarity). The letter 'J' is referred to in the main text.

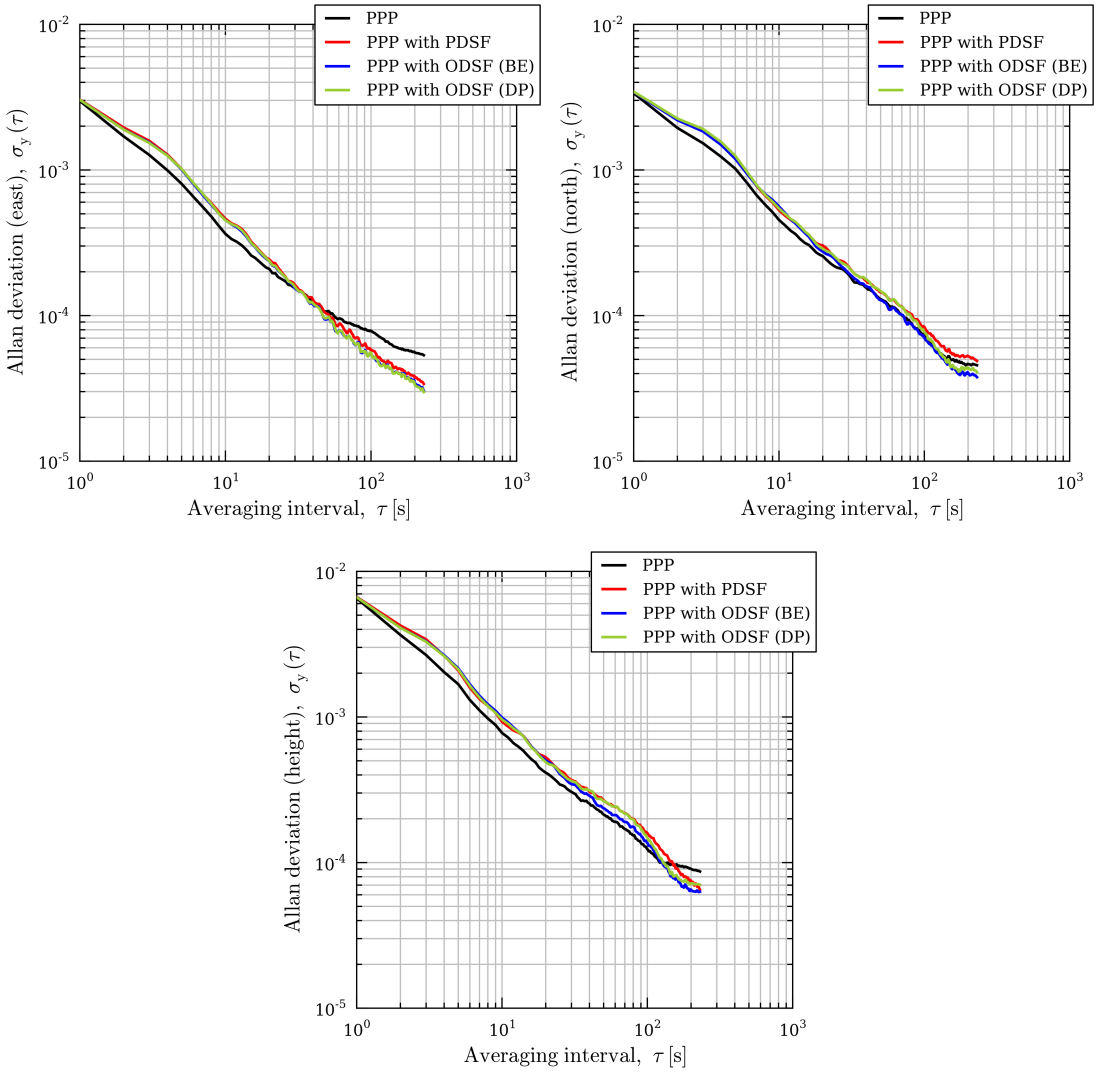

Figure 4.9 – Allan deviation plots of the corresponding position time series (east, north and height) at station P495 between 19:10 and 19:30 on 3rd April 2010 shown in figure 4.8.

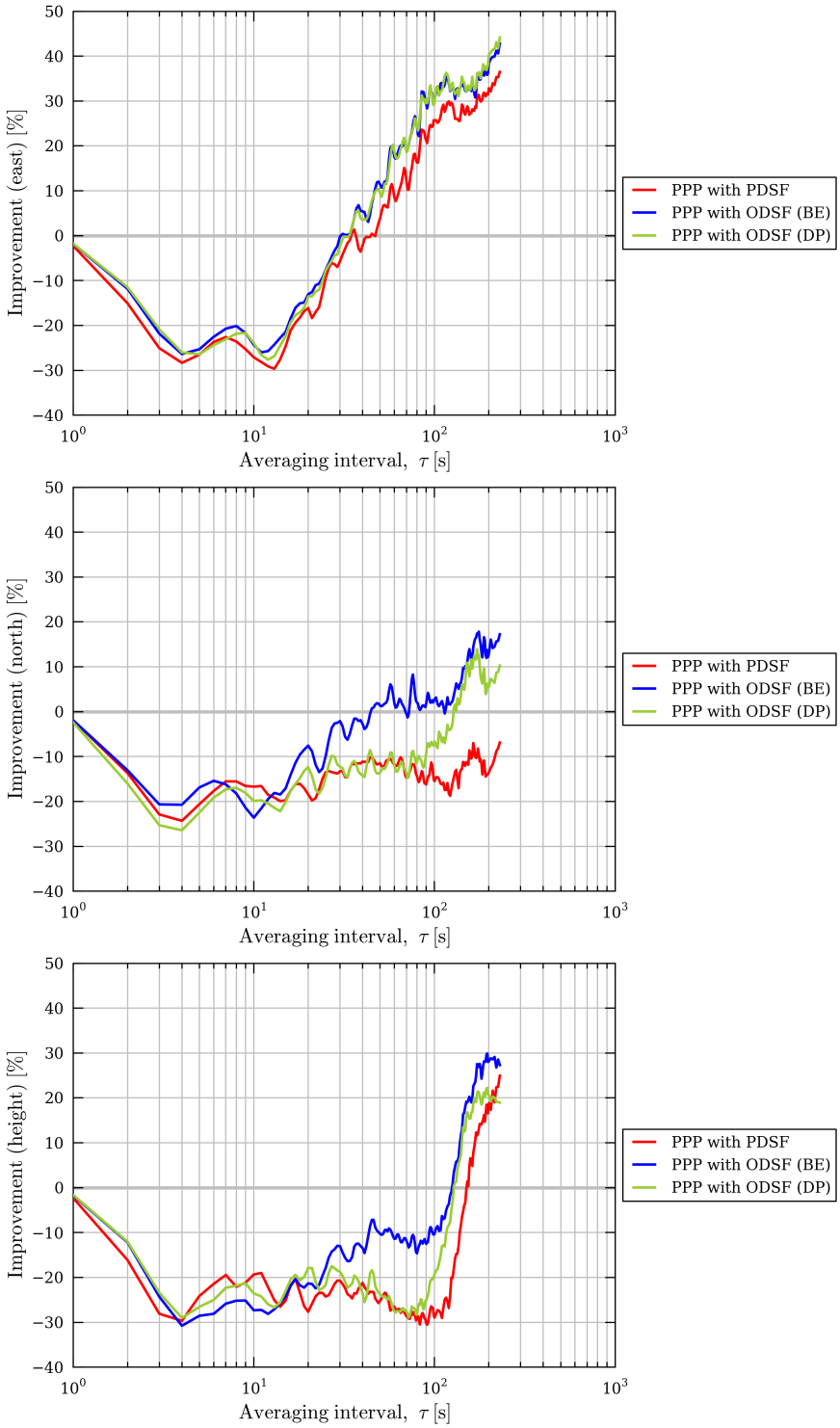

Figure 4.10 – Plots showing the percentage improvement (i.e. reduction) in Allan deviation at station P495, after applying the various types of sidereal filter, relative to the Allan deviation values corresponding to standard PPP processing that are shown in figure 4.9.

rections calculated by the two types of ODSF were largely the same for each satellite except for G24 and G26. All other satellites had repeat periods within $86,155 \pm 10$ s seconds. Figure 4.11 shows the multipath corrections calculated by the DP ODSF and the BE ODSF in green and blue respectively for each visible satellite during the period 18:33–19:29:30. The purple time series show the result of subtracting these two time series from each other. For satellites that had repeat times close to the nominal repeat period of 86,155 s, one would expect the corrections derived by both types of ODSF to be similar or identical and hence the difference between the two, shown in purple, to be zero or have a near-zero mean over averaging intervals of a few seconds. Looking at figure 4.11, this was indeed the case for all visible satellites except for G26. This satellite was the only one where the characteristic multipath signal (oscillations with periods of a few minutes and amplitudes of up to a few tens of millimetres) was present. Satellite G24 also had an anomalous repeat time and yet there was no slowly-oscillating component present in the differenced (purple) time series. It can be seen that whilst the DP and BE corrections for G26 appear to have very similar pattern of oscillations, the two series are offset from each other in time. This means that the oscillations are not eliminated when the two series are subtracted from each other. Indeed, figure 4.12 shows that the offset between the BE repeat time (86,088 s) and the DP repeat times varied between 19 s and 24 s during the period 18:33–19:29:30.

A deeper analysis was conducted by visualising the position in the sky of these satellites at each epoch between 18:33 and 19:29:30 from the point of view of an observer at station P495. Figure 4.13 shows an overview of the skytracks traced by satellite G26 between 18:33 and 19:22 on 3$^{\text{rd}}$ April and the skytrack from the corresponding period on the previous day from which the multipath corrections were derived. The value of the ionosphere-free phase residual for each epoch in the sky is colour-coded. The two separate paths cannot be distinguished in the left and centre panels of figure 4.13 so a schematic diagram of their relative positions is shown to the right. Note that it shows that the angular separation between the two skytracks increases as the elevation angle decreases (from about 28°). To explain why the relative performances of the DP ODSF and the BE ODSF varied over this period of time, two smaller sections of the skytracks were chosen for analysis, marked by areas 'A' and 'B' in figure 4.13. These smaller areas of the sky are shown respectively in figures 4.14 and 4.15.

Figure 4.14 shows an area of sky which was traversed by satellite G26 between 18:46:47 and 18:49:10 on 3$^{\text{rd}}$ April, which is *within* the period 18:30–19:10. This was the period in which it was shown above that the DP ODSF performed better than the BE ODSF. Figure 4.14 explains why this was so: In this figure, a single epoch has been labelled, 18:48:10. Also labelled are the locations of the corresponding multipath corrections associated with the two types of ODSF. It is quite clear that the multipath correction found by the DP ODSF, despite being 0.04° across the sky from the observation on the 'current' day, was more appropriate than the correction found by the BE ODSF. The same applies for most other epochs in this small region of the sky. Despite using the repeat time calculated from the GPS broadcast ephemeris (using equation (1.23) on page 57), the phase multipath correction applied by the BE ODSF was derived from a point in the

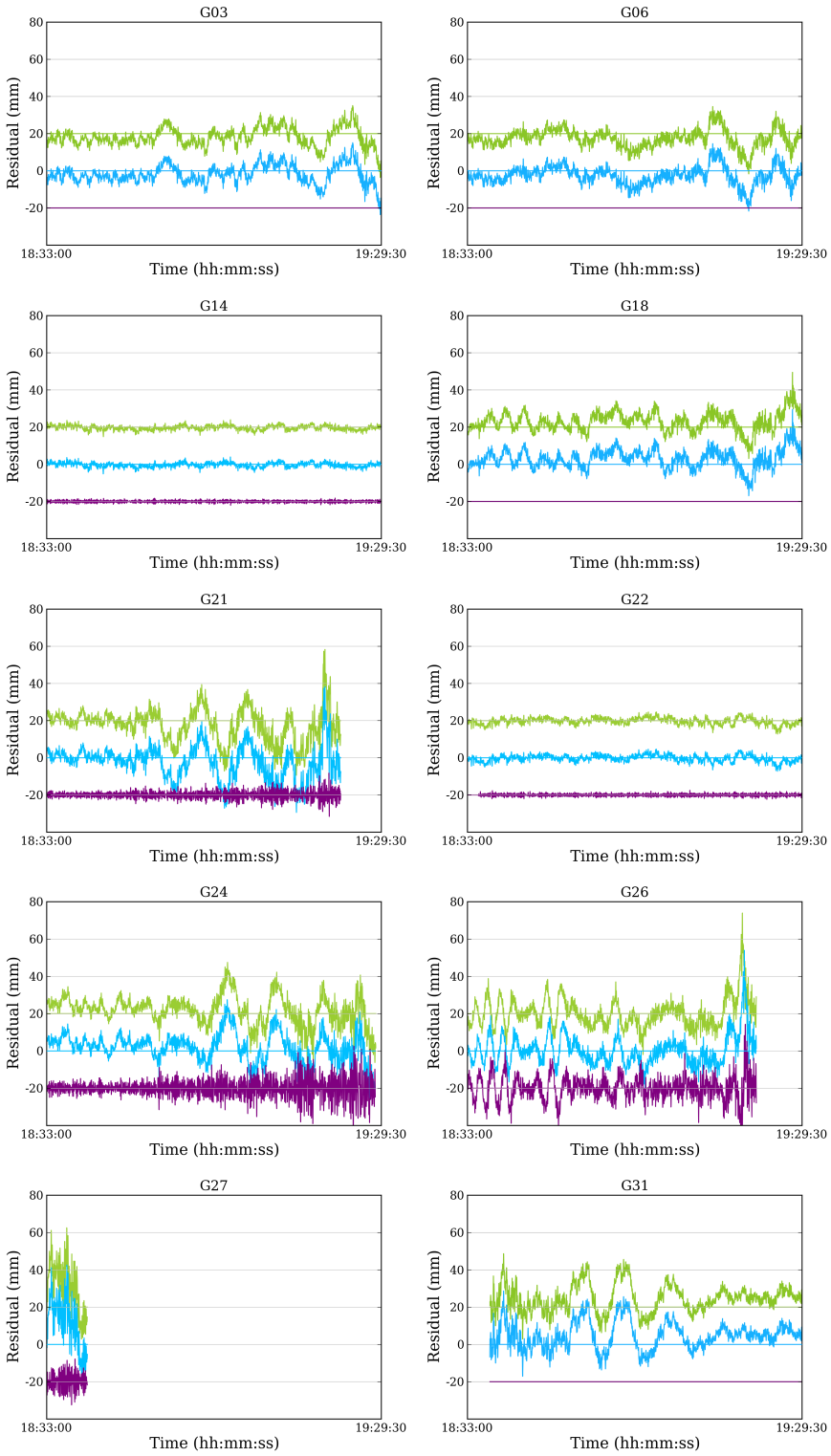

Figure 4.11 – Multipath corrections calculated by the DP and BE ODSFs in *green* and *blue* respectively for each visible satellite during the period 18:33–19:29:30 on 3$^{\text{rd}}$ April. The DP corrections are offset by 20 mm for clarity. The difference between the two series of corrections is shown in *purple* and is offset by −20 mm.

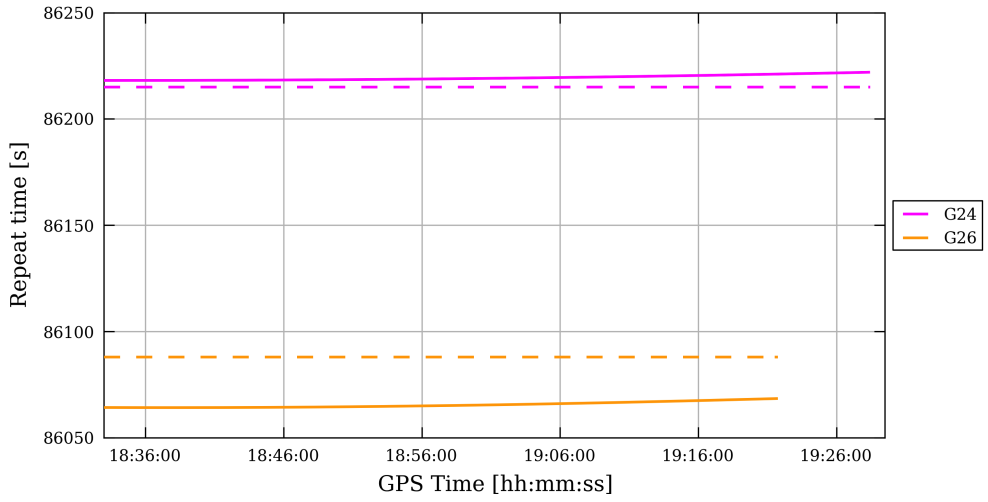

Figure 4.12 – Repeat times calculated by the DP (*solid lines*) and BE (*dashed lines*) observation-domain sidereal filter algorithms during the period 18:33–19:29:30 on 3rd April.

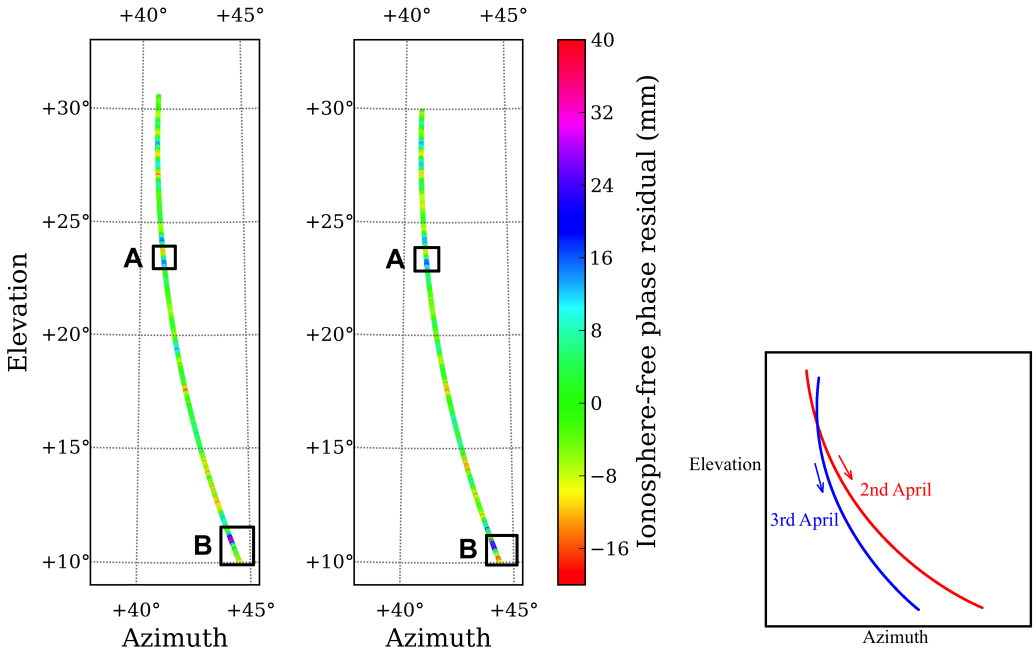

Figure 4.13 – Skyplots of smoothed ionosphere-free phase measurement residuals associated with satellite G26 observed from station P495 during approximately 18:37–19:26 (*left panel*) and 18:33–19:22 (*centre panel*) on 2nd and 3rd April 2010 respectively. *Right panel:* Schematic diagram of the paths taken by satellite G26 in the left and centre panels.

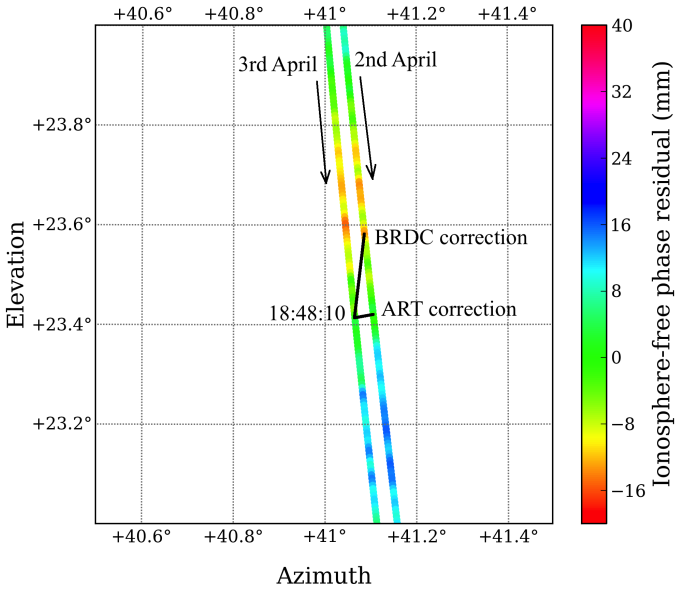

Figure 4.14 – Skyplot of smoothed ionosphere-free phase measurement residuals associated with satellite G26 in area 'A' shown in figure 4.13.

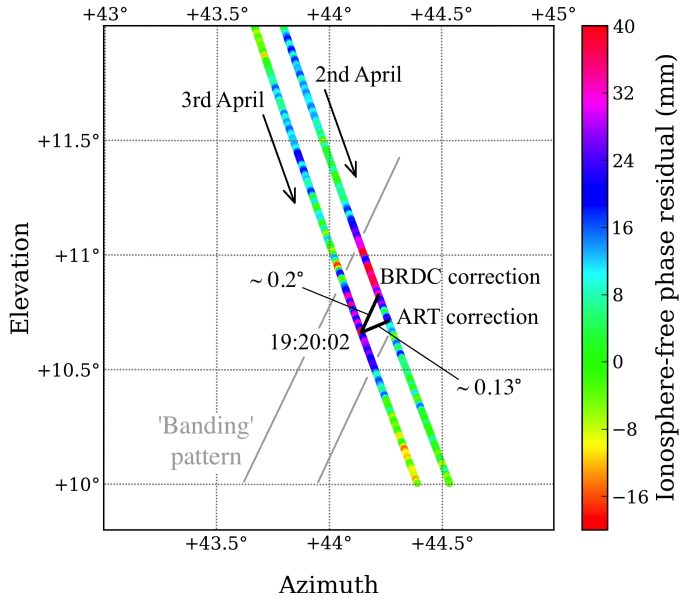

Figure 4.15 – Skyplot of smoothed ionosphere-free phase measurement residuals associated with satellite G26 in area 'B' shown in figure 4.13.

sky nearly 0.2° in elevation from the original observation—about five times further away than the correction found by the DP ODSF. Phase multipath error can change significantly over 0.2°—in this single-epoch example by around 10 mm.

Figure 4.15 can explain why the relative performance of the ODSFs reversed. Here, the correction to the phase observation at epoch 19:20:02 applied by the the BE ODSF, nearly 0.2° across the sky from the original observation, was more appropriate than that applied by the DP ODSF which was only 0.13° away. This was due to the pattern formed by the measurement residuals as marked in grey in the figure. Harris (2002) uses the term 'banding' to describe this pattern. The two diagrams in figure 4.16 illustrate the problem caused by the 'banding' phenomenon: For each measurement on the 'current' day, the DP ODSF algorithm will search for a correction that is associated with the closest measurement residual from the 'previous' day. In theory, if the direction of the banding pattern is near-orthogonal to the path taken by the satellite across the sky, as shown in the top diagram, the optimum correction is chosen. However, if the banding pattern is not orthogonal to the skytrack, as shown in the bottom diagram, the optimum correction is not necessarily chosen.

Note that the angle separating the azimuth/elevation of satellite G26 at 19:20:02 and it's BE and DP corrections in figure 4.15 were quite large: 0.2°and 0.13°, respectively. In the experiments of chapter 3, such angles were usually at most a few hundredths of a degree for satellites with relatively 'normal' repeat periods. With these relatively large angles, the assumption on which sidereal filtering is based, i.e. that a GPS satellite will closely follow the path across the sky as it did the day before, breaks down. In this particular case, the changing relative performance of the two types of ODSF between the periods of 18:33–19:10 and 19:10–19:30 is simply due to the complicated nature of the multipath environment: for one period of time the DP ODSF works well; during another period the BE ODSF happens to be the most appropriate. In this example, for the DP ODSF to work well, the direction of the 'banding' of measurement residuals had to be close to being perpendicular to the direction of travel of the satellite across the sky. If the angles between the observations and the corrections were smaller, as is usually the case for satellites with 'normal' repeat periods, the influence of the direction of banding on the effectiveness on the DP ODSF would be reduced and reliability would increase.

The corrections associated with satellite G24 are similarly analysed. Figure 4.17 shows the skytrack of satellite G24 for the period between approximately 18:33 and 19:30 on 3rd April and the corresponding period from the previous day from which the multipath corrections are derived. During this period, the angular separation between the location of a satellite in the sky at an epoch of observation and the location of the corresponding correction varied between about 0.29° and 0.25°. These are even larger than those for satellite G26. An area labelled 'C' is highlighted for closer inspection. Figure 4.18 shows this area. One particular epoch, 19:05:26, has been labelled together with the corresponding corrections found by the two ODSF algorithms. One can just see that, despite the large angular separation, the corrections derived by those algorithms were very close together in location and hence very similar in value.

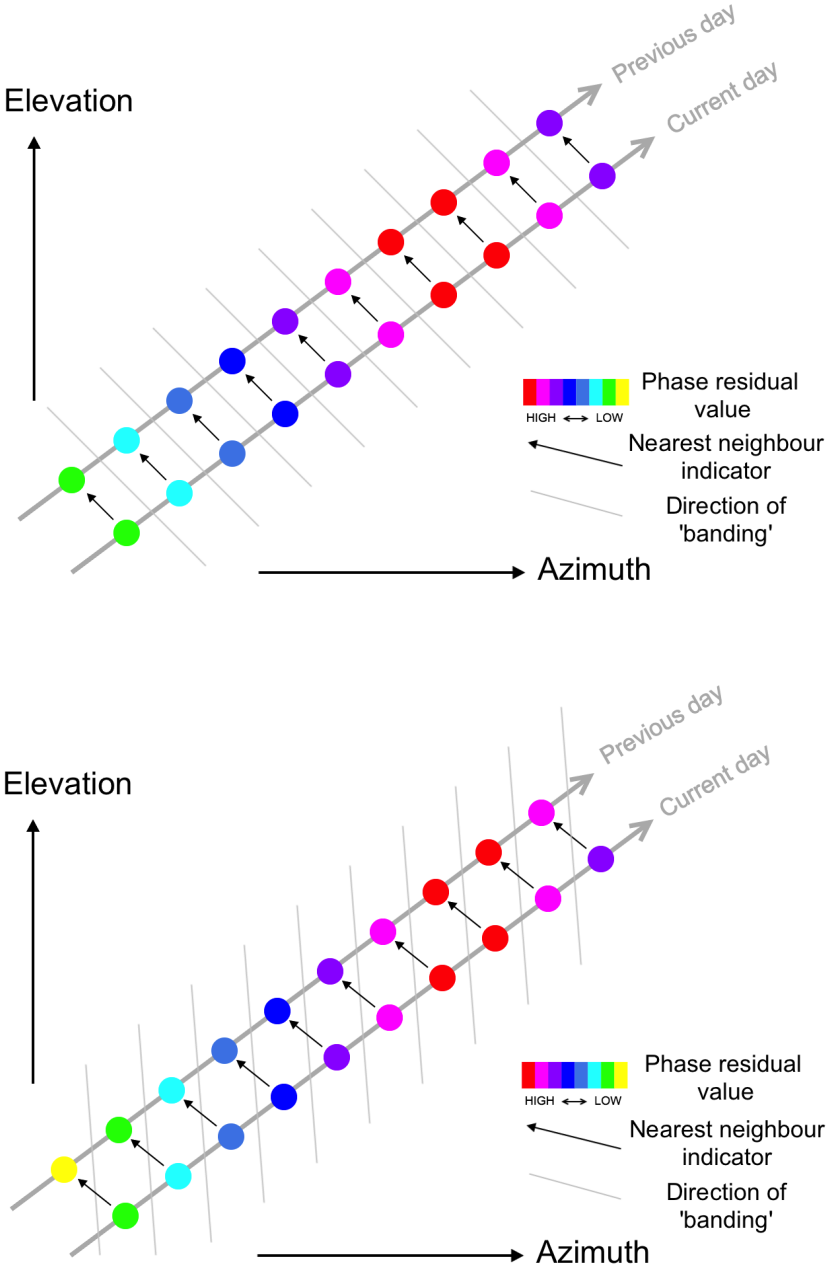

Figure 4.16 – Diagrams illustrating how the direction of 'banding' can affect the performance of the DP ODSF algorithm.

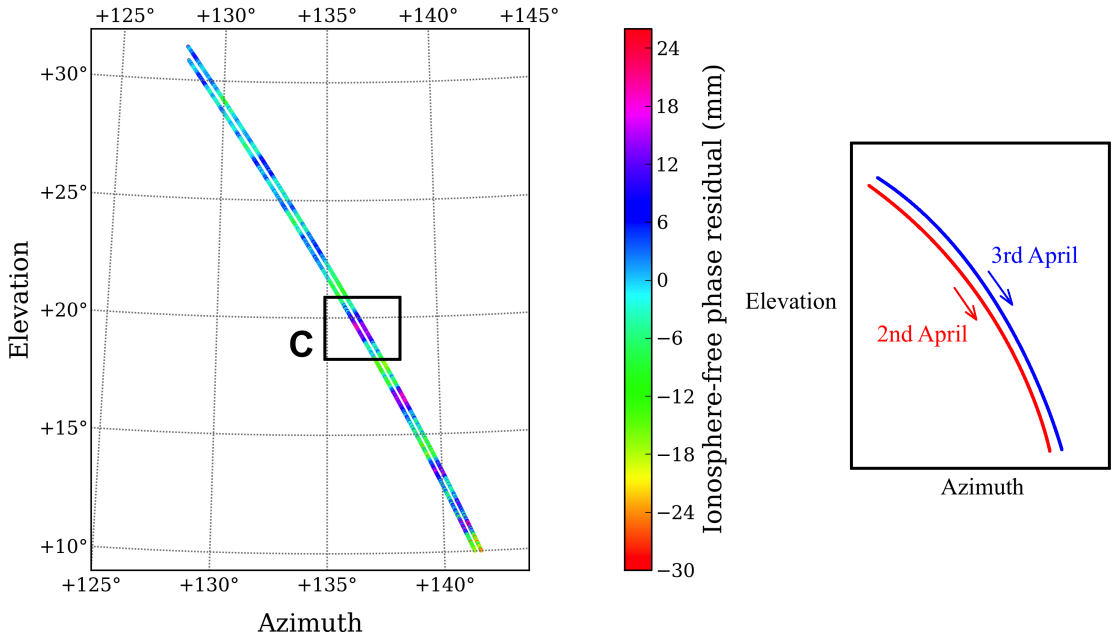

Figure 4.17 – *Left panel:* Skyplot of smoothed ionosphere-free phase measurement residuals associated with satellite G24 observed from station P495 during approximately 18:37–19:34 and 18:33–19:30 on 2nd and 3rd April 2010 respectively. *Right panel:* Schematic diagram of the paths taken by satellite G24 in the left panel.

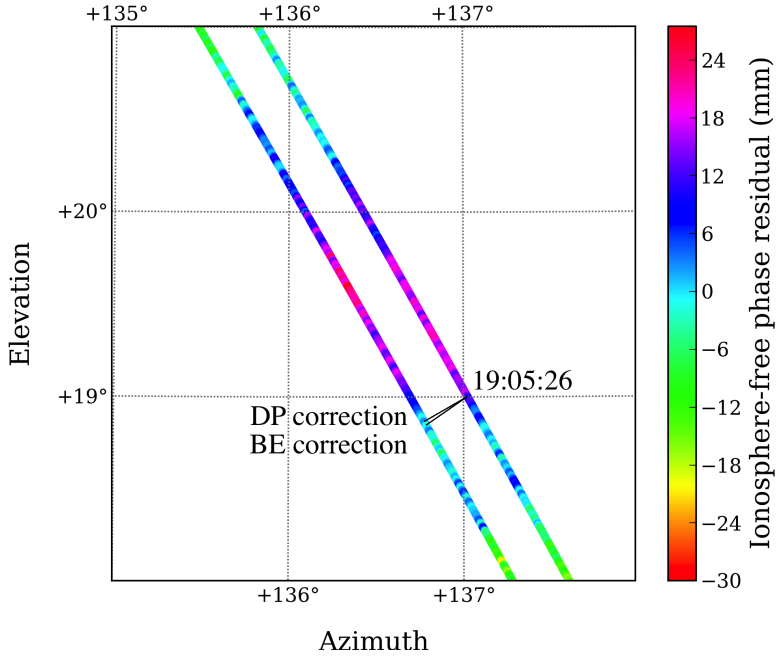

Figure 4.18 – Skyplot of smoothed ionosphere-free phase measurement residuals associated with satellite G24 in area 'C' shown in figure 4.17.

So far, the performance of the two types of ODSF relative to each other appears to be mixed. With large angular separations between skytracks between adjacent days, the effectiveness of the two types of ODSF appears to be haphazard with the DP ODSF being more effective at certain times and the BE ODSF more effective at others. This is not consistent with the prediction that the DP ODSF would outperform the BE ODSF.

4.4 Stations P494 and P496

Despite the detailed analysis in sections 4.3.2 and 4.3.3 of specific periods of time in the position time series at P495, section 4.3.1 showed that over the entire period when satellites G24 and/or G26 were visible, the DP ODSF on average outperformed the BE ODSF. Both types of ODSF outperformed the PDSF, at least over periods of up to 600 s. A similar analysis was applied to the GPS data gathered by stations P494 and P496. This was undertaken to see if these observations also apply to stations P494 and P496. With both being only 33 km away from P495, the paths that the satellites take across the sky will be very similar, but the multipath interference will be different for each station.

4.4.1 Station P494

Figure 4.19 shows the easting, northing and height time series of each of the processing runs for the period in which satellites G24 or G26 were visible from station P494. On first inspection, all sidereal filters have overall been successful at removing much of the higher-frequency components of multipath error that are apparent in the time series resulting from regular PPP processing, although the PDSF is noticeably less successful in this respect after about 18:30 compared with the ODSFs, particularly in the north and east components (marked by the letter 'K'). Figure 4.20 shows that the PDSF yields the largest improvement (i.e. reduction) by up to 40% in Allan deviation for the largest averaging intervals over 1,000 s. The ODSFs yield the biggest improvement (up to about 30%) over smaller averaging intervals, from about 1,000 s down to about 50 s. Notice, however, that there is very little difference between the performance of the DP ODSF and the BE ODSF, especially in the easting and height components.

4.4.2 Station P496

A very similar narrative applies to station P496. The surrounding environment, and hence any multipath interference, will of course be different to that of P494 and P495. Figure 4.21 shows the easting, northing and height time series of each of the processing runs for the period in which satellites G24 and G26 were visible from station P496. All of the sidereal filters have been successful in reducing many of the higher-frequency oscillating positioning errors present in the regular PPP time series, but to varying extents. The PDSF has not reduced much of the higher-frequency positioning errors with periods of just a few minutes. This is true for all three components throughout

much of the nearly seven-hour period in question, but is particularly noticeable during 15:30–16:30 (L) and 18:30–19:00 (M) in the north component and 14:30–16:00 (N) in the height component, for example. This situation is reversed when considering longer-period components, with the PDSF managing to remove much of the slowly-varying bias between 13:00 and 14:00 (O) in the height component. In contrast, the height time series output by the ODSFs exhibit a slowly-varying bias that reaches around −70 mm at 13:25. Figure 4.22 shows that the PDSF yielded greater stability in the vertical component than either of the ODSFs for intervals above around 200 s. It shows that both types of ODSF have a very similar performance in all three components and consistently outperform the PDSF over shorter periods of time, at least up to 200 s, whereas the difference in performance between the ODSFs and the PDSF is much more variable for larger averaging intervals.

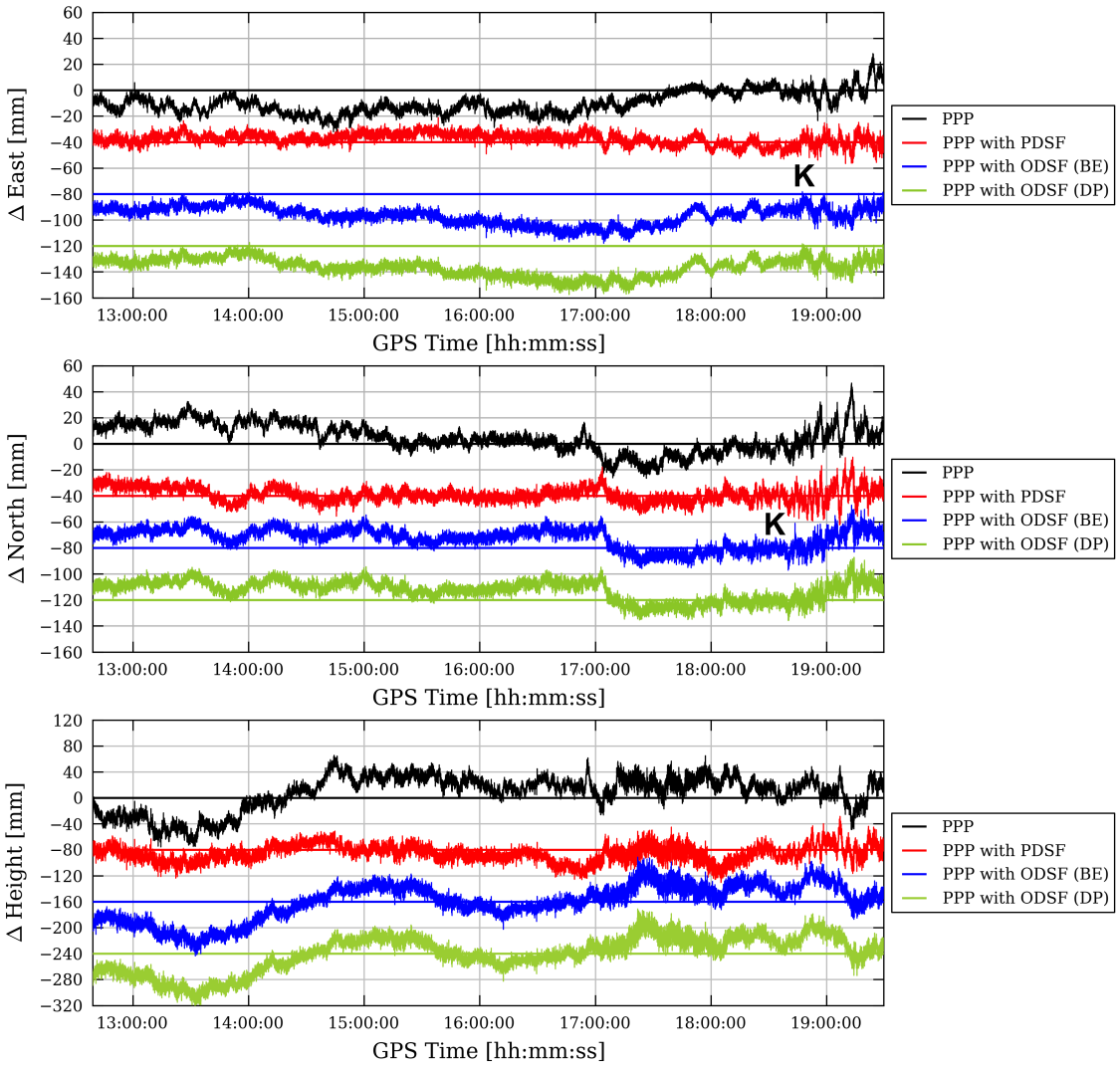

Figure 4.19 – Easting, northing and height errors between 12:40 and 19:30 on 3rd April 2010 for receiver P494 resulting from standard PPP processing and PPP processing with various types of sidereal filter applied. (Each of the time series have been offset from each other by appropriate multiples of 40 mm or 80 mm for clarity). The letter 'K' is referred to in the main text.

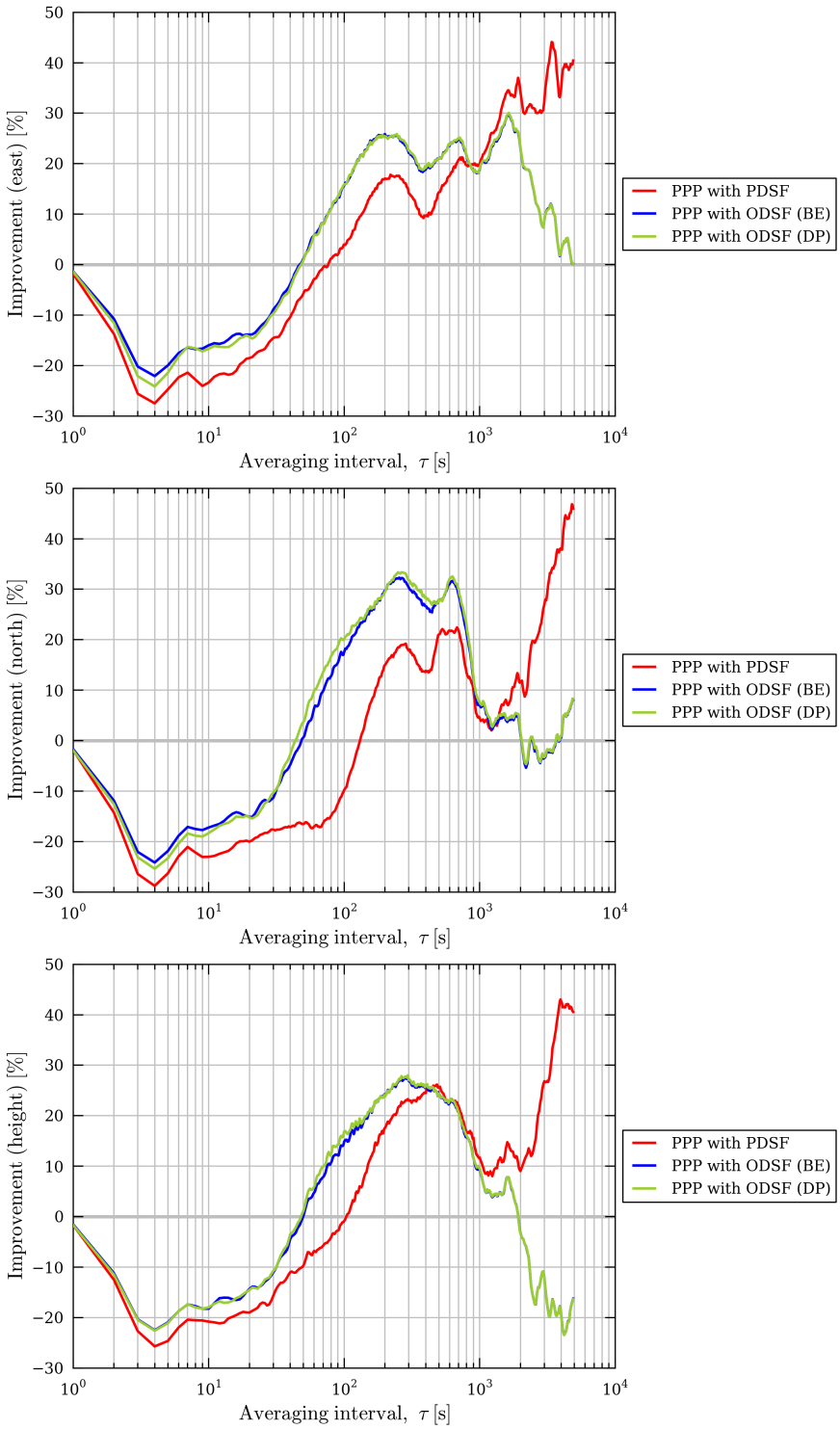

Figure 4.20 – Percentage improvement (i.e. reduction) in Allan deviation at station P494 relative to standard PPP processing corresponding with figure 4.19.

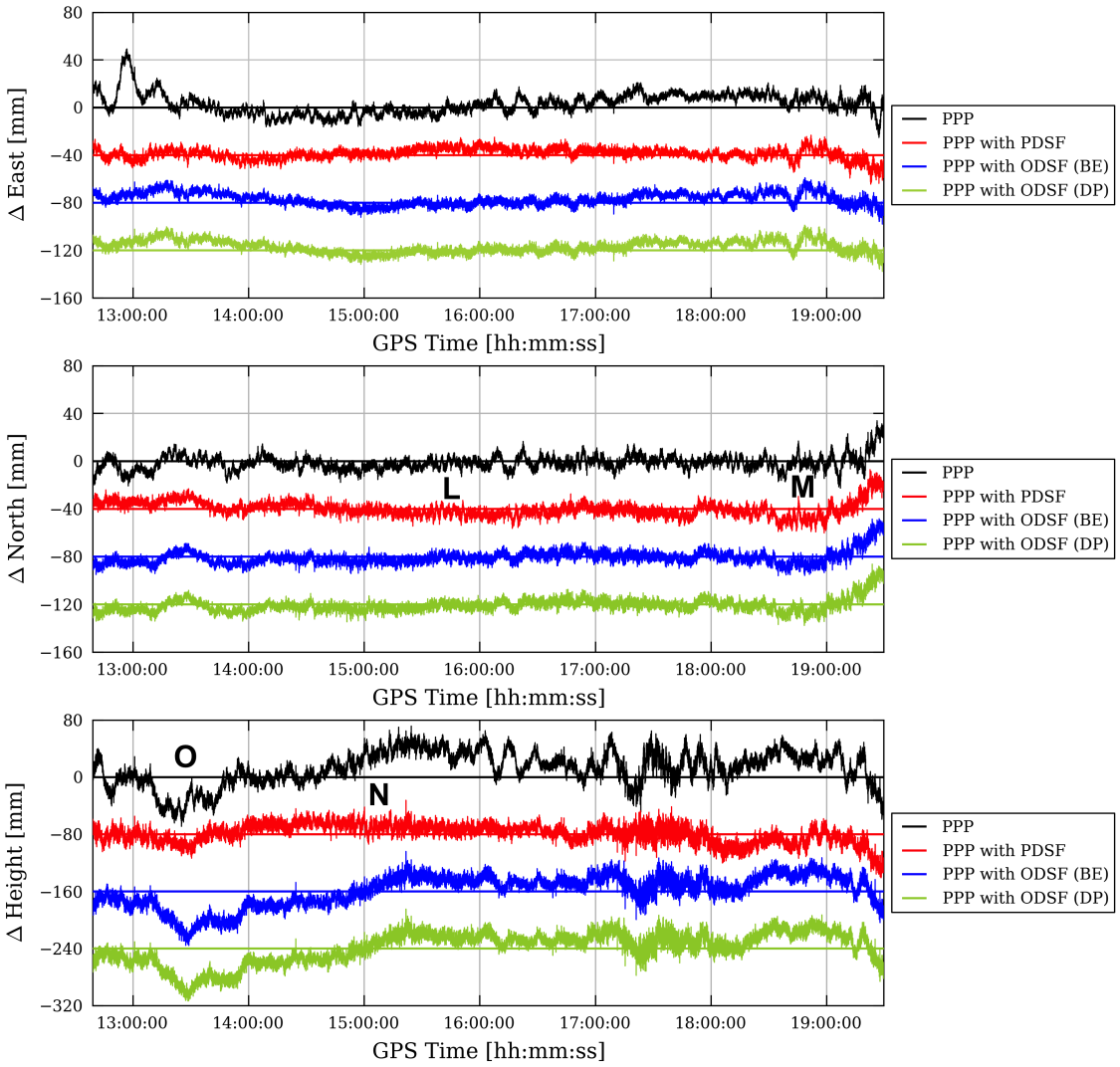

Figure 4.21 – Easting, northing and height errors between 12:40 and 19:30 on 3rd April 2010 for receiver P496 resulting from standard PPP processing and PPP processing with various types of sidereal filter applied. (Each of the time series have been offset from each other by appropriate multiples of 40 mm or 80 mm for clarity). The letters L to O are referred to in the main text.

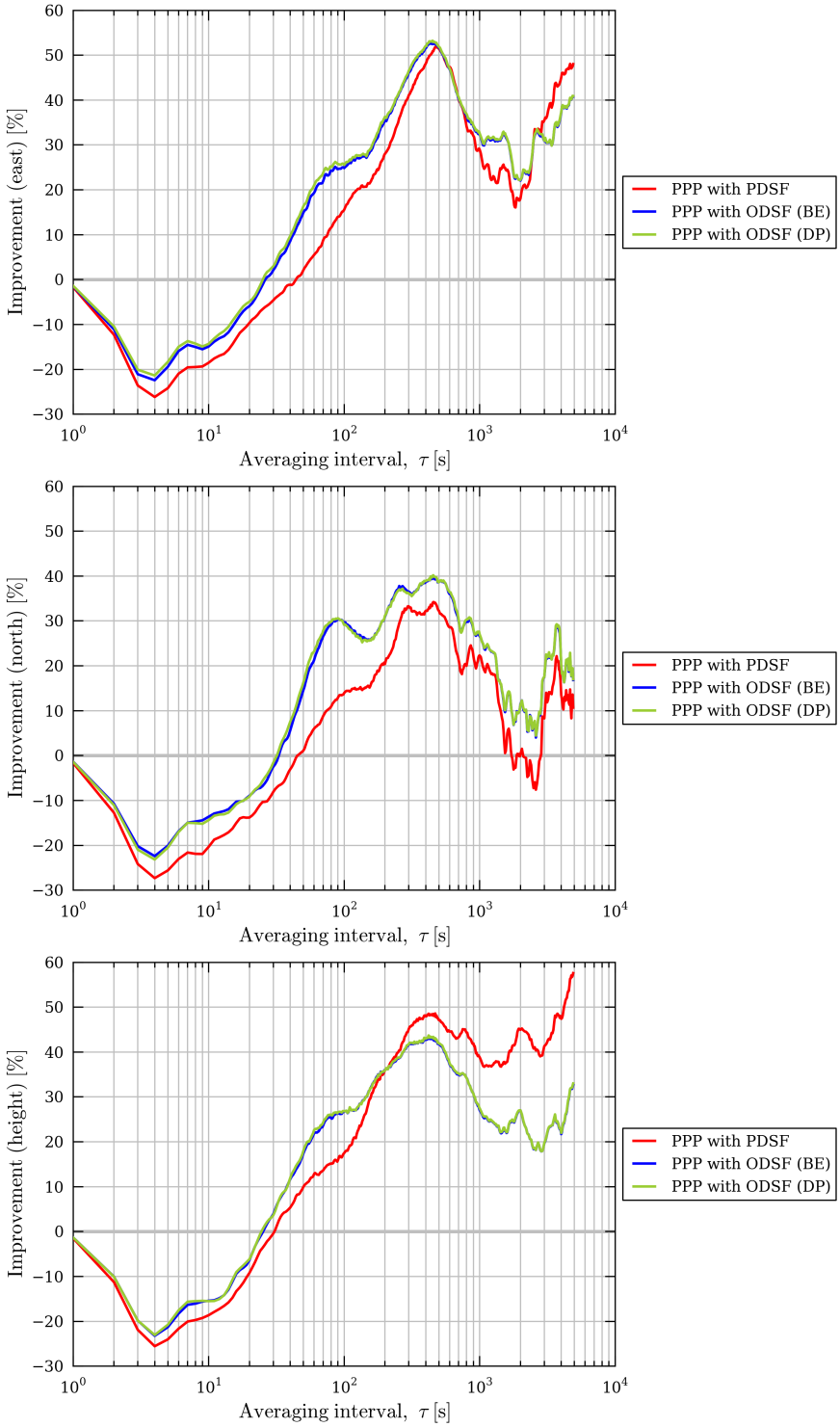

Figure 4.22 – Percentage improvement (i.e. reduction) in Allan deviation at station P496 relative to standard PPP processing corresponding with figure 4.21.

4.5 Conclusions

Results from all these stations, P494, P495 and P496, indicate that an ODSF generally yields a more stable position time series than a PDSF over periods of time of up to a few hundred seconds during periods when satellites with anomalous repeat periods are visible. Over longer periods of time, the performance of the PDSF relative to the ODSFs is more varied. This is no different to the conclusions of chapter 3 when the 'overall' performance of the sidereal filters was assessed.

Regarding the relative performance of the two different types of ODSF, there is little difference between the two. However, there are short periods of time during which one clearly outperforms the other. As discussed in section 4.3.4, much depends on the complicated nature of the multipath effect itself, particularly any 'banding' pattern found when colour-coded phase residual values are plotted by azimuth and elevation angles. The effectiveness of both types of ODSF also depends on the angular separation between the location of a satellite in the sky at an epoch of measurement and its location at the epoch from which the corresponding correction is derived. For satellites with anomalous repeat periods, such angles can be as high as a few tenths of a degree. This compares with angles of a few hundredths of a degree for satellites with repeat times of $86,155 \pm 10\,\mathrm{s}$. With these relatively large angles, the assumption upon which the sidereal filtering algorithms are based, i.e. that a GPS satellite will closely follow the path across the sky as it did the day before, starts to break down. The effectiveness of the ODSFs can then depend more on the 'banding' phenomenon identified in section 4.3.4, making it unreliable: In figure 4.15, it was only by virtue of the banding pattern that the BE ODSF performed better in that period of time than the DP ODSF, despite the large angular separation between skytracks, whereas the reverse was true in figure 4.14.

With a smaller angular separation between skytracks, the influence of the banding pattern on the DP ODSF would not be so strong. This would suggest that a DP ODSF would tend to perform better than a BE ODSF when angular separations are small. Regarding satellites with abnormal repeat times, there are of course occasions when the skytrack of such a satellite from adjacent days cross, as in the case shown by figure 4.13. However, angular separations generally tend to be relatively large. For satellites with 'normal' repeat times, angular separations tend to be small and, as observed in chapter 3, any advantage in performance of a DP ODSF in these circumstances over a BE ODSF is, overall, very slight. This also appears to be the case for when there are satellites in view that have anomalous repeat times. So the prediction made at the beginning of this chapter, that the difference in performance between these two algorithms would be greater, appears not to be true, at least not convincingly so. However, during periods of stronger multipath where there is a noticeable 'banding' pattern present, the relative performances of the two types of ODSF in reducing the multipath signature associated with satellites with anomalous repeat times appears to depend on chance due to the complicated nature of multipath interference.

If the reliability of the ODSF algorithms wanes as angular separation between adjacent skytracks increases, then one idea would be to exclude or reduce the weighting of measurements that have been corrected via residuals beyond a certain threshold in angular separation. This would reduce the problem of the 'wrong' corrections being applied as was the case shown in figures 4.14

and 4.15. However, by excluding observations, measurement redundancy and the strength of the satellite-receiver geometry reduces and may do more harm than good to the stability of a position time series. This idea is not examined in this chapter, but a similar idea is implemented in chapter 6, specifically section 6.3, where measurements for which a correction for multipath cannot be found are excluded from the PPP algorithm.

Chapter 5

High-frequency Multipath

5.1 Introduction

In section 1.5.4, 'high-frequency' multipath referred to the oscillatory positioning errors caused by phase multipath interference with periods of less than about 100 s. Such errors are generally caused by distant 'far-field' reflectors. Section 1.4.1 (page 50) described an example of how a vertical reflector 100 m from a receiving antenna, such as a tall building, could in theory cause ranging errors with a period of 42 s in L1 phase measurements. As mentioned in chapter 1, there is a risk that such high-frequency multipath errors may be misinterpreted as seismic waves or vice versa, and can obscure small coseismic displacements.

In chapter 3, it was indeed found that over a period of several hours, an ODSF would *generally* be more effective than a PDSF at increasing the stability of the position time series over time intervals up to a hundred seconds, and often up to several hundred seconds. This was because an ODSF could apply multipath corrections on a satellite-by-satellite basis, taking into account the slightly different repeat times of each. It was also found that there was little difference between the two types of ODSF, i.e. whether the GPS satellite repeat time is calculated using orbital parameters given in the broadcast ephemeris (BE) or by using the dot product (DP) method. However, that chapter examined the overall performance of the sidereal filter algorithms over a long period of time. In contrast, this chapter assesses in more detail the performance of the sidereal filter algorithms during specific episodes of high-frequency multipath. Here, the sidereal filters are assessed over brief periods of time where oscillatory errors with exceptionally short periods—only a few tens of seconds—were easily identified.

This chapter uses three brief periods of high-frequency multipath to assess the sidereal filters. However, one aspect of the sidereal filter algorithm which relates strongly to the subject of high-frequency multipath must be addressed beforehand: the low-pass filtering of measurement or position residuals to form corrections for multipath error.

5.2 Low-pass filtering of phase multipath corrections

In section 2.2, it was mentioned that a fifth-order Butterworth low-pass filter is applied to the time series of measurement (or position) residuals to form the multipath corrections. The purpose of this is to minimise the amplification of high-frequency measurement noise when applying the corrections to the measurements (or positions) themselves. It is assumed that the standard deviation of an ionosphere-free phase measurement uncontaminated by multipath and other errors is about 15 mm. Applying unsmoothed multipath corrections would in theory increase measurement noise by a factor of $\sqrt{2}$, which in turn further reduces the ability of GPS to accurately measure small displacements.

However, when applying a low-pass filter, care must be taken not to accidentally filter out any high-frequency multipath signatures from the measurement (or position) residuals, otherwise the effectiveness of the sidereal filters to remove high-frequency multipath errors is reduced. The need to minimise the amplification of noise must be balanced with the need to preserve the component of the corrections that does represent multipath error, particularly short-period multipath. Choosing a low cut-off frequency may result in short-period multipath corrections being lost.

Such a cut-off frequency may be difficult to determine accurately. GNSS multipath error is dependent on time: as time passes, the geometry of the satellites relative to the receiving antenna and its surrounding environment changes. Hence, there may be periods of time where the influence of short-period multipath is strong and other times when it is not. Therefore, a cut-off frequency is chosen which is optimal for preserving high-frequency multipath corrections during one particular period of time but may not be optimal during other periods of time when the effect of high-frequency multipath is minimal.

For example, consider figure 5.1. This shows the percentage reduction in Allan deviation brought about by the use of a DP ODSF but with the use of different cut-off frequencies to the low-pass filtering of measurement residuals. This figure is closely related to figure 3.7 (northing component) on page 96 where a 0.2 Hz cut-off frequency was used to form the multipath corrections for each type of sidereal filter. Using this graph, the following observations can be made:

- Both the cut-off frequencies of 0.05 Hz and 0.1 Hz (orange and red lines respectively) provide the greatest reduction in Allan deviation across all averaging intervals. This improvement is as much as 47% at averaging intervals of around 150 seconds in the north component.

- The performance of the 0.01 Hz sidereal filter (represented by the blue line) is poor relative to other cut-off frequencies across all time intervals, but particularly over time intervals of between 10 and 50 seconds in length.

- Using no cut-off frequency at all (shown by the grey line) amplifies high-frequency measurement noise and hence an increase in Allan deviation across all averaging intervals smaller than about 8 seconds. The smaller the averaging interval, the larger the increase in Allan deviation. Indeed for the smallest interval of 1 second, this increase is around 38%.

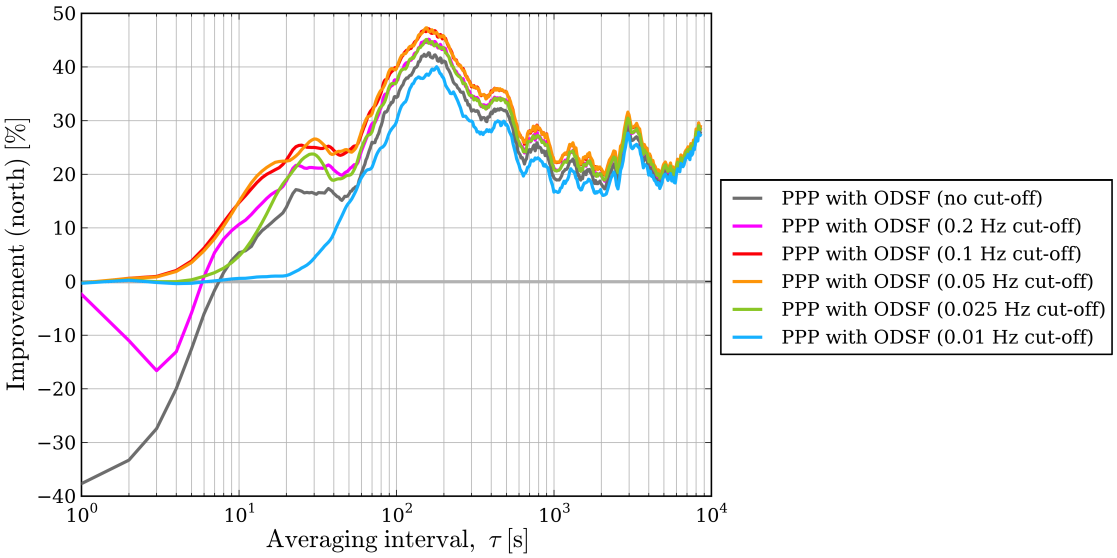

Figure 5.1 – Percentage reduction in Allan deviation of the northing time series, between 10:00 and 23:55 on 27th March 2012 at station UCL, relative to the Allan deviation values corresponding to standard PPP processing as a result of using DP ODSFs with different cut-off frequencies. This figure is closely related to figure 3.7 on page 96. The original PPP position time series is shown in figure 3.4 on page 90.

- Unlike other cut-off frequencies, the use of a 0.2 Hz cut-off frequency (magenta line) results in an *increase* in Allan deviation across very small averaging intervals, particularly over intervals of 3 seconds. This indicates that the cut-off frequency is still rather high and has a net effect of increasing high-frequency noise. Stability is nevertheless improved over averaging intervals larger than 6 s.

With such observations, then perhaps a 0.05 Hz or a 0.1 Hz cut-off frequency should have been used in the low-pass filter for the analysis in section 3.4, not 0.2 Hz.

However, within this period of time two brief episodes of high-frequency multipath were identified: 18:21–18:32 and 23:10–23:18. Figure 5.2 below shows the northing component of the PPP position time series for a fifteen-minute period spanning the latter of these two events. Between 23:10 and 23:18 there is sinusoidal error with a frequency of about 0.065 Hz (15 s period) and a peak-to-peak amplitude of nearly 20 mm in the standard PPP time series. Figure 5.2 also shows the time series resulting from the use of different cut-off frequencies to form the multipath corrections within the DP ODSF. Obviously, using cut-off frequencies that are lower than 0.065 Hz will remove these short-period sinusoidal features from the multipath corrections and hence the sidereal filter will not remove the short-period error. Hence, a sidereal filter that uses a 0.05 Hz cut-off frequency—a frequency that yielded the best overall performance for the 12-hour time period discussed above—is clearly unsuccessful in removing this instance of high-frequency multipath error. It can also be seen that using cut-off frequencies of 0.2 Hz and 0.1 Hz have indeed removed much

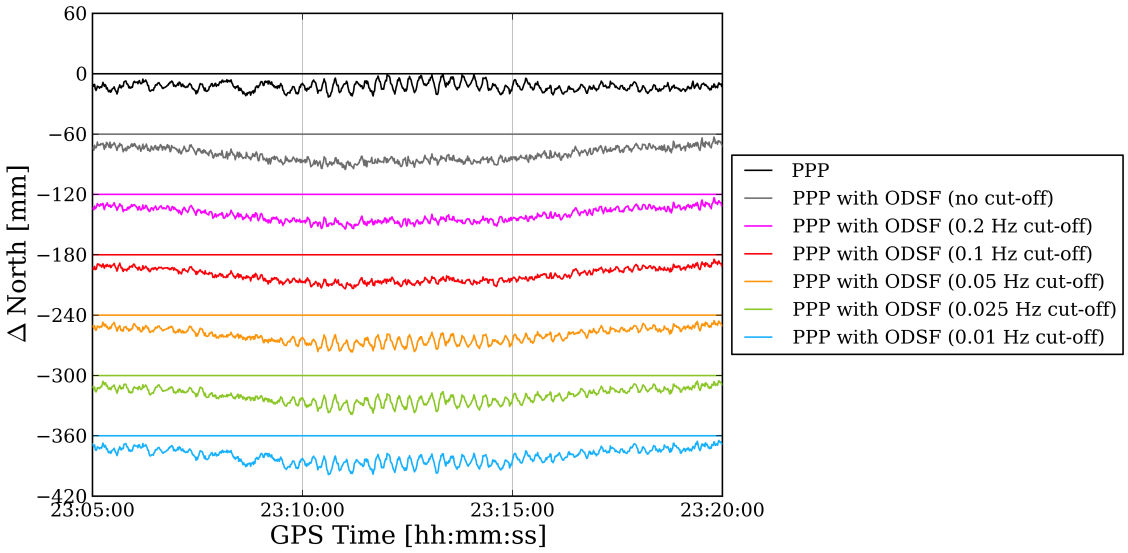

Figure 5.2 – Northing component of the PPP position error time series between 23:05 and 23:20 on 27th March 2012 at station UCL resulting from the use of different cut-off frequencies to form the multipath corrections within the DP ODSF. (Each of the time series have been offset from each other by appropriate multiples of 60 mm for clarity).

of this high-frequency multipath effect from the position time series.

This strong oscillatory effect is because the signal from satellite PRN 31 (hereafter denoted G31) is affected for a brief period by strong far-field multipath interference. This error can clearly be seen in the observation domain: The black time series of figure 5.3 shows the resulting phase observation residuals of satellite G31 resulting from regular PPP processing but with the position states fixed (as described in section 2.2.1). The oscillating multipath error is clearly visible between 23:09 and 23:17. Also shown are the corresponding multipath corrections derived from the ionosphere-free phase observation residuals from the preceding day, with different colours representing the various cut-off frequencies used to smooth those residuals. It is clear that the cut-off frequencies of 0.05 Hz and below are too low: They have filtered out the 0.065 Hz sinusoidal effect of the short-period multipath from the corrections.

The impact of the choice of cut-off frequency on the stability of the position time series shown in figure 5.2 can be further assessed by using the Allan deviation plots shown in figure 5.4. The following observations are made:

- The cut-off frequency of 0.1 Hz yielded best performance with the lowest Allan deviation value for nearly all averaging intervals from 1 s to 180 s (three minutes).
- A 0.2 Hz cut-off frequency does not perform quite as well as a 0.1 Hz cut-off, particularly over averaging intervals smaller than about eight seconds, but still results in a lower Allan deviation across most averaging intervals when compared to a sidereal filter that has no cut-off frequency.

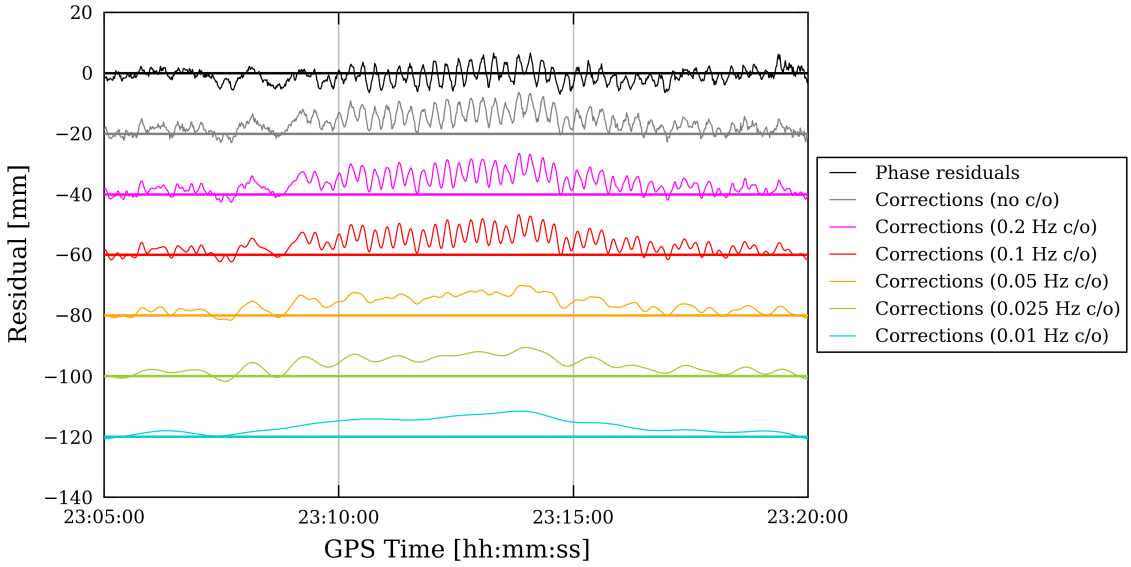

Figure 5.3 – Satellite G31 ionosphere-free phase observation residuals (shown in black) between 23:05 and 23:20 on 27th March 2012 at station UCL. Also shown (in different colours) are the corresponding corrections derived from the previous day by a DP ODSF using various cut-off (c/o) frequencies. (Each of the time series have been offset from each other by appropriate multiples of 20 mm for clarity)

- Figure 5.4 clearly shows that the oscillations remain after using an ODSF with a cut-off frequency of 0.05 Hz and below. The peaks and troughs of some of the Allan deviation curves shown in figure 5.4 are a consequence of the sinusoidal error that occurred between 23:10 and 23:18: Each trough corresponds to an integer multiple of the roughly 15 s period of oscillation (see also figure B.1c, page 265). The figure clearly shows that the oscillations remain after using an ODSF with a cut-off frequency of 0.05 Hz and below.

So in this particular case, a low-pass filter with a cut-off frequency of 0.1 Hz would be the most appropriate of those tested to form multipath corrections.

For this thesis, a suitable cut-off frequency was chosen for all future PPP processing of data from any receiver where sidereal filtering was to be applied. The above example of high-frequency multipath was found by visually checking the 12-hour position time series. No occurrences of oscillating multipath error with a frequency higher than 0.065 Hz were found. Indeed, it seemed apparent that such episodes of high-frequency multipath were rare. However, it was still conceivable that other short episodes of sinusoidal multipath error could occur in other datasets at even higher frequencies, perhaps even higher than 0.1 Hz, and still have amplitudes large enough not to be obscured by the high-frequency noise of the ionosphere-free phase measurements. Although no such examples were found in this dataset, and bearing in mind that it is difficult to spot such errors within the position time series by human eye, the possibility of such instances arising could not be excluded.

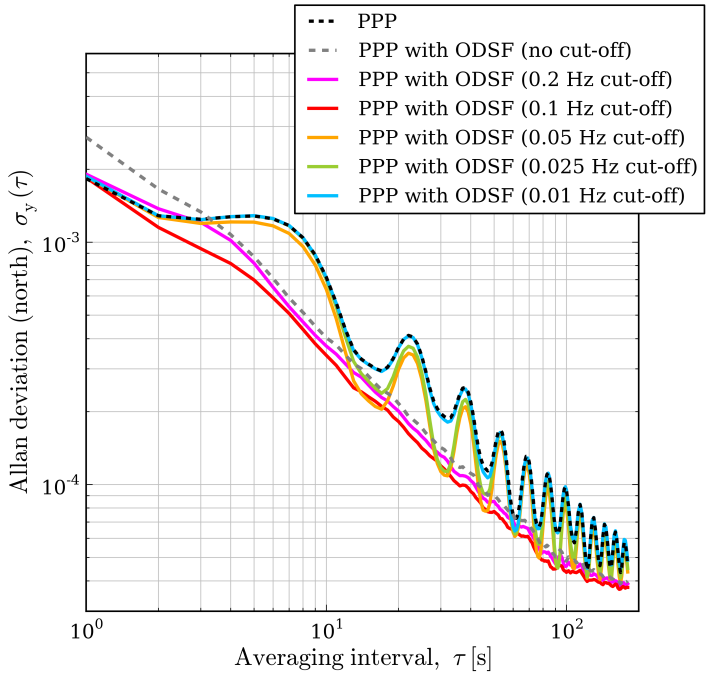

Figure 5.4 – Allan deviation plots of the corresponding position time series (east, north and height) at station UCL between 23:05 and 23:20 on 27$^{\text{th}}$ March 2012 shown in figure 5.2.

For this reason, whilst 0.05 Hz and 0.1 Hz were respectively the most appropriate cut-off frequencies for the 12-hour dataset and the brief period of high-frequency multipath error between 23:10–23:18 respectively, a cut-off frequency of 0.2 Hz was chosen for all future low-pass filtering of multipath corrections in both observation-domain and position-domain sidereal filtering (to allow a fair comparison between the two). Using this cut-off frequency should largely prevent the inadvertent removal of corrections for very short-period multipath error at the expense of a slight increase in the noise of the ionosphere-free phase observations compared to those uncorrected for multipath. This would be very important if sidereal filtering were to be applied to earthquake and tsunami early warning systems. In such an application, the probability of misinterpreting errors caused by phase multipath interference as seismic waves and vice versa of course needs to be minimised, perhaps even at the expense of a slight decrease in noise compared to an ODSF that uses a cut-off of, say, 0.1 Hz.

5.3 Hypothesis

As stated in section 1.5.2, an ODSF is anticipated to be more effective than a PDSF at removing the effect of high-frequency multipath on PPP position time series. This is because an ODSF does not assume that all satellites have the same repeat period. Like in chapter 3, the DP ODSF is

expected to outperform a BE ODSF because the repeat times calculated by the algorithm of the former should be more accurate from the point of view of an observer. However, unlike chapter 3 where there was little *overall* difference between the two types of ODSF over a long period of several hours, the difference between the two in the following analyses should be more pronounced because only periods of time that are dominated by high-frequency multipath error will be analysed. It is during these periods that the small differences in the repeat times calculated by the two types of ODSF (as shown in figure 3.9 on page 98, for example) should become influential in determining how effective they are at removing these errors.

5.4 Method

For this analysis, clear instances of high-frequency multipath had to be found. This was done by careful examination of the position time series output by the PPP software for the analysis in chapter 3. Each 24-hour position time series output by the standard PPP processing (i.e. PPP processing without sidereal filtering) of GPS phase measurements at stations UCL, UEL and the same six UNAVCO stations in Southern California were examined closely by eye for instances of high-frequency multipath interference. Three 15-minute periods were selected for analysis: 23:05–23:20 and 18:20–18:35 on 27$^{\text{th}}$ March 2012 at station UCL and 11:45–12:00 on 3$^{\text{rd}}$ April 2010 at station SLMS. The first of these three periods has already been discussed in section 5.2. The second and third of these periods also exhibited a similar sinusoidal error signature in the position time series with a corresponding sinusoidal error on the preceding day. As with previous analyses, Allan deviation is used to quantify the improvement in stability in the time series as a result of using the various sidereal filters in PPP processing.

5.5 Analysis

5.5.1 Station UCL, 27$^{\text{th}}$ March 2012

Figure 5.5 shows the positioning errors in northing resulting from different processing modes over the period 23:05–23:20 on 27$^{\text{th}}$ March 2012 at station UCL. This plot is very similar to figure 5.2. It can be seen that the actual period of high-frequency oscillations (approximately 0.065 Hz) with a peak-to-peak amplitude of nearly 20 mm occurs between approximately 23:09 and 23:18 and is most likely to be caused by a far-field reflector such as a tall building. It was shown in section 5.2 above that it is the signal from satellite G31 that is associated with this error. Both the observation-domain and position-domain sidereal filters have noticeably reduced the amplitude of most of these oscillations. However, it also appears that both of the ODSFs have been very successful at reducing the oscillating error, more so than the PDSF. Note that the repeat time of satellite G31 calculated by the BE ODSF algorithm during this period, 86,157 s, differs by only three seconds from the 'constellation repeat time' used by the PDSF algorithm, 86,154 s. Also note that there is

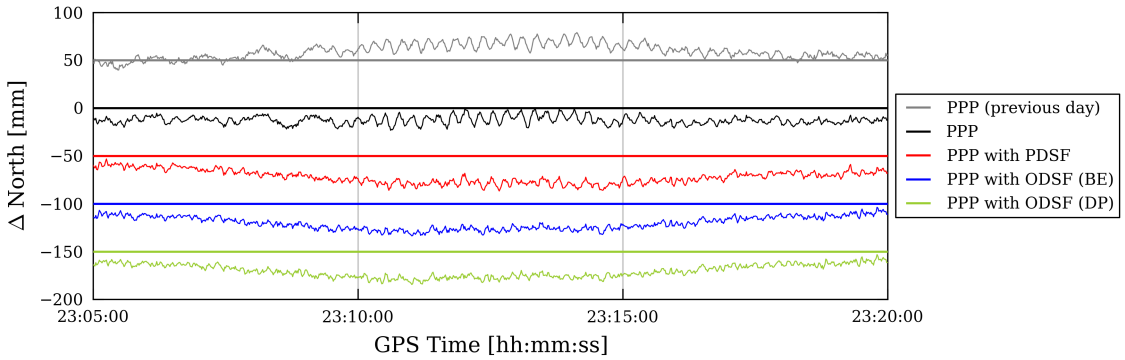

Figure 5.5 – Northing errors between 23:05 and 23:20 on 27$^{\text{th}}$ March 2012 for receiver UCL resulting from standard PPP processing and PPP processing with various types of sidereal filter applied. Errors between 23:09:05 and 23:24:05 on 26$^{\text{th}}$ March 2012, plotted in grey, have been shifted forward in time by 23 hours, 55 minutes and 55 seconds to appear on the same plot. (Each of the time series have been offset from each other by appropriate multiples of 50 mm for clarity).

little difference in the time series between the BE ODSF and the DP ODSF. The corresponding plots for the easting and height components are not shown here because the high-frequency errors occurred almost exclusively in the north-south direction. However, they are shown in figure E.22 on page 295.

From figure 5.6, it appears that all types of sidereal filter have been successful at reducing Allan deviation, i.e. increasing stability, over nearly all averaging intervals. However, the oscillatory pattern visible in the PDSF Allan deviation curve indicates that a 15-second periodic multipath error, indicated by the first 'dip' in the curve, still remains. In contrast, the curves for the two ODSFs have gradients close to -1 over all averaging intervals between 4 s and 80 s, indicating that the position time series is dominated by white or flicker noise over these time intervals. Notice again that there is little difference in performance between the two types of ODSF. Equivalent plots for easting and height are shown on page 296.

The above example showed the ODSF algorithms performing very well during a period of high-frequency multipath. However, this was found not always to be the case. Figure 5.7 shows errors in easting resulting from different processing modes over another 15-minute period earlier on the same day. This time the sidereal filters do not seem to have made much of an improvement on the roughly 22-second period (0.045 Hz) oscillating error and peak-to-peak amplitude of at most 10 mm that is apparent in the standard PPP time series shown in black. In fact the PDSF has appeared to increase that error, not reduce it.

This is confirmed by figure 5.8 where the PDSF has in fact increased Allan deviation values over most time intervals under about 100 s. In contrast, the ODSFs have led to reduced Allan deviation values but clearly some of the periodic (approximately 22 s) multipath error remains. Note also that the BE ODSF outperforms the DP ODSF. Similar results apply to the northing and height components (see figures E.24 and E.25.)

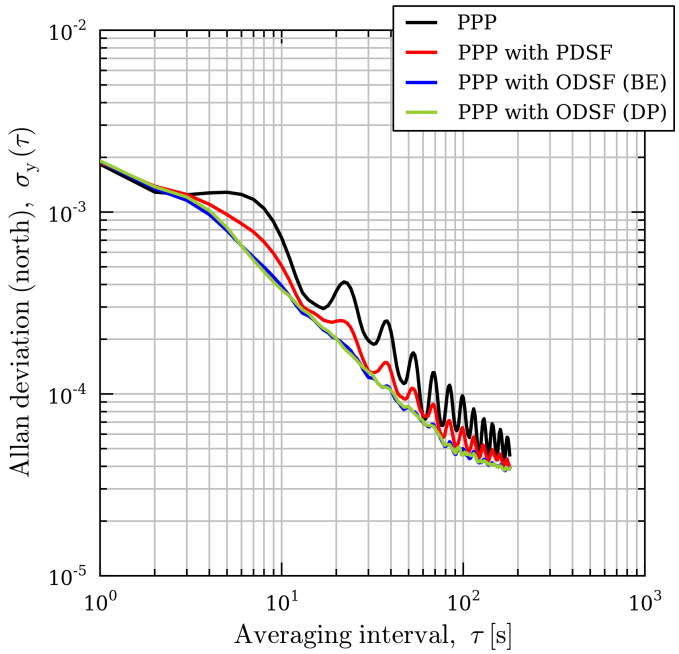

Figure 5.6 – Allan deviation plots of the corresponding northing position time series at station UCL between 23:05 and 23:20 on 27$^{\text{th}}$ March 2012 shown in figure 5.5.

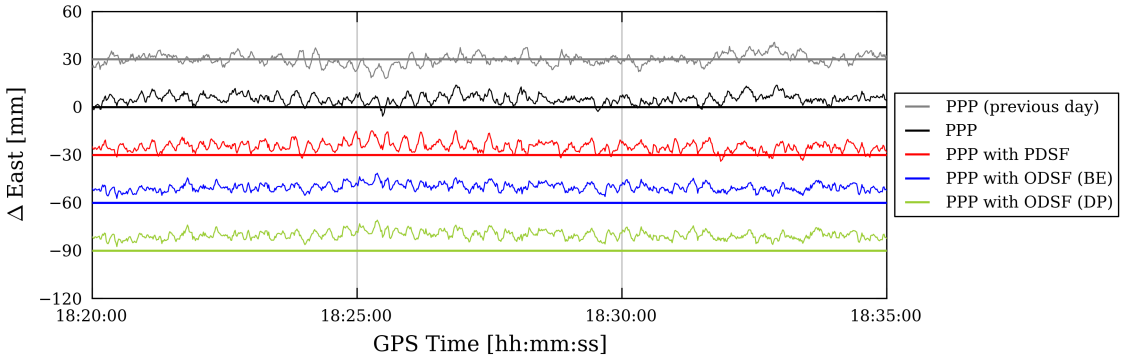

Figure 5.7 – Easting errors between 18:20 and 18:35 on 27$^{\text{th}}$ March 2012 for receiver UCL resulting from standard PPP processing and PPP processing with various types of sidereal filter applied. Errors between 18:24:05 and 18:39:05 on 26$^{\text{th}}$ March 2012, plotted in grey, have been shifted forward in time by 23 hours, 55 minutes and 55 seconds to appear on the same plot. (Each of the time series have been offset from each other by appropriate multiples of 30 mm for clarity).

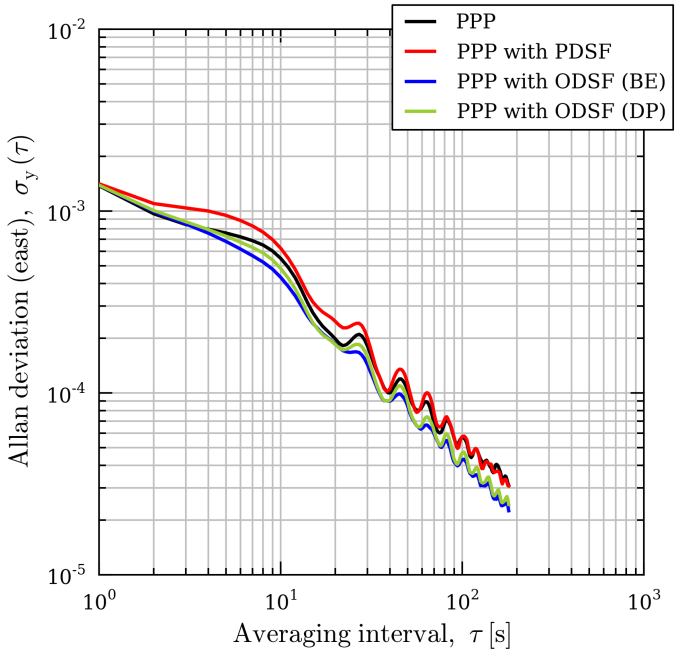

Figure 5.8 – Allan deviation plots of the corresponding easting position time series at station UCL between 18:20 and 18:35 on 27$^{\text{th}}$ March 2012 shown in figure 5.7.

The origin of the high-frequency oscillating errors seen between 18:20 and 18:35 and between 23:05 and 23:20 were caused by phase multipath interference affecting measurements associated with GPS satellites G12 and G31 respectively. Given that the azimuth and elevation of both of these satellites during these periods ranged from roughly 220°–224° and 56°–58° respectively, it is speculated that the reflector is likely to be the sloping glass roof shown in the centre of figure 3.2 on page 88, but no further investigation is carried out here. The poor performance of the PDSF between 18:20 and 18:35 is explained by the fact that the actual repeat time of satellite G12 calculated by the ODSF algorithms, around 86,147 s, is significantly different from the 'constellation repeat time' of 86,154 s calculated by the PDSF algorithm. Considering the period of the error is approximately 22 s, then a difference of around 7 s in the two repeat times means that the position-domain corrections will be out of phase with the oscillating error.

However, why do the ODSFs themselves perform so well between 23:05 and 23:20 but not so well between 18:20 and 18:35? An explanation perhaps lies in figure 5.9. Here we see the smoothed ionosphere-free residuals for satellites G31 and G12 output from the PPP processing runs from five consecutive days (26$^{\text{th}}$–30$^{\text{th}}$ March 2012) where the position states in the Kalman filter state vector have been fixed to their true values. It is the multipath interference affecting the phase measurements of the signals from these two satellites that cause the high-frequency multipath errors seen in figures 5.5 and 5.7. Unlike similar figures that appear in Atkins & Ziebart (2016), the smoothed phase residuals shown in figure 5.9 have also been filtered for a second time using a

third-order Butterworth high-pass filter (0.01 Hz cut-off) in order to largely remove the mean value of the smoothed residuals in each line. This allows one to observe the higher frequency behaviour of the multipath interference more easily. These residuals have been colour-coded by value and mapped onto a skyplot by azimuth and elevation. Notice that only very small 'patches' of sky are shown.

Notice the pattern formed by the colour-coded residuals in figure 5.9a. Harris (2002) uses the term 'banding' to describe this pattern. In this case, it forms what appear to be parallel lines that are roughly orthogonal to the path or 'skytrack' taken by satellite G31 across the sky. Notice also that each skytrack is separated from the skytrack of an adjacent day by a very small angle of about 0.011°. Marked on figure 5.9a is the smoothed phase residual value for one particular epoch chosen as an example: 23:13:19 on 27$^{\text{th}}$ March 2012. Also marked is the location of the phase residual value found by both the DP ODSF and BE ODSF algorithms that is used as a correction. In this particular instance, both algorithms have chosen the same correction value, which means the repeat time determined by the DP algorithm and the period calculated using elements from the broadcast ephemeris are identical.

Another example epoch is shown in figure 5.9b together with the respective corrections found by the two ODSF algorithms. Notice here that neither of the two corrections are optimal, although the value of the correction provided by the BE ODSF algorithm is a little more appropriate which would account for its slightly better performance exhibited in figures 5.7 and 5.8. The reason for this is because the 'banding' pattern is not orthogonal to the path taken by satellite G12 across the sky. Therefore, the corrections found by the DP ODSF algorithm in particular are out of phase with the error pattern of the 'current' day, and this is accentuated by the slightly larger angular separation between adjacent skytracks of 0.016°.

5.5.2 Station SLMS, 3$^{\text{rd}}$ April 2010

Another brief period of high-frequency positioning errors was identified as occurring between 11:47 and 11:58 at station SLMS in Southern California on 3$^{\text{rd}}$ April 2010. As discussed in section 3.6, station SLMS is, like station UCL, equipped with a choke-ring antenna, but is sited in a rural environment, intentionally well away from nearby buildings.

Figure 5.10 shows the positioning errors in the height component resulting from different processing modes over the period 11:45–12:00 on 3$^{\text{rd}}$ April 2010. For the sake of brevity, only the height component is examined here since it is this component that is predominantly affected by multipath interference. Notice first of all that the sinusoidal positioning error in the standard PPP time series has a period of about 40 s (0.025 Hz) and a peak-to-peak amplitude of up to 60 mm, indicating the presence of a stronger reflected signal relative to the direct signal compared to the previous two examples at station UCL. All three types of sidereal filter appear to have similar performance. This is confirmed by the corresponding Allan deviation plot shown in figure 5.11, which shows that all three types of sidereal filter have increased the stability of the vertical position time series for all time intervals over 8 s.

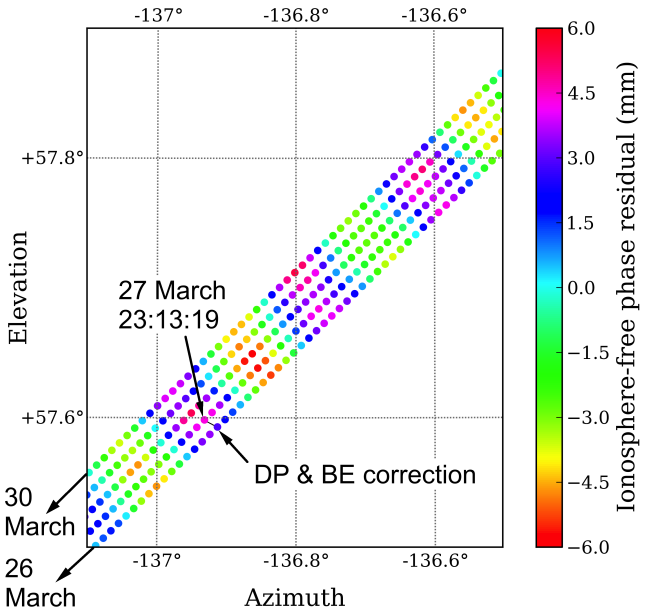

(a) G31

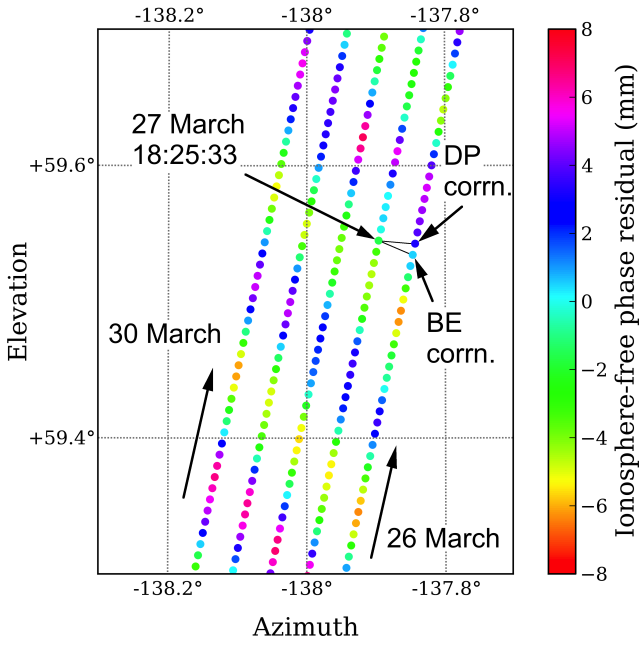

(b) G12

Figure 5.9 – Two skyplots of smoothed ionosphere-free phase measurement residuals associated with satellites G31 and G12 on 26$^{\text{th}}$–30$^{\text{th}}$ March 2012. ('corrn.'—'correction').

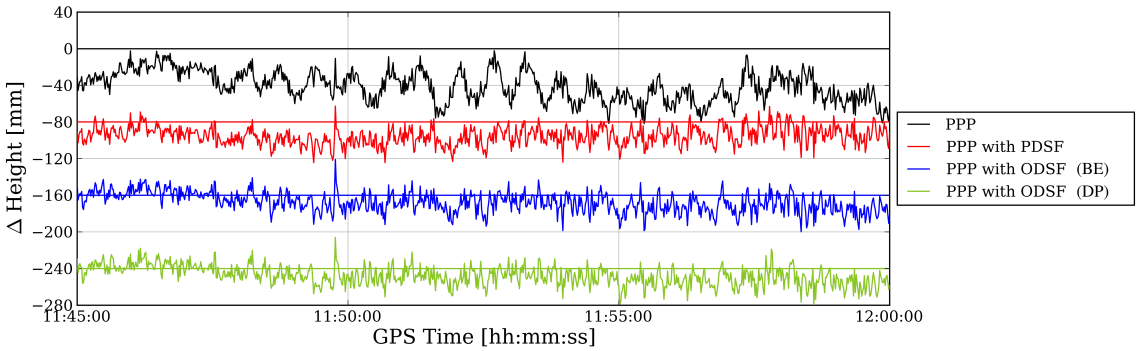

Figure 5.10 – Easting errors between 11:45 and 12:00 on 3rd April 2010 for receiver SLMS resulting from standard PPP processing and PPP processing with various types of sidereal filter applied. (Each of the time series have been offset from each other by appropriate multiples of 80 mm for clarity).

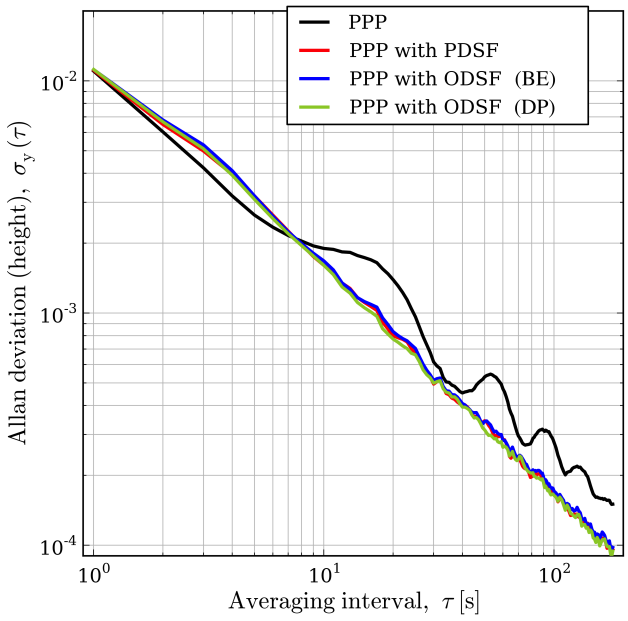

Figure 5.11 – Allan deviation plots of the corresponding height position time series at station SLMS between 11:45 and 12:00 on 3rd April 2010 shown in figure 5.10.

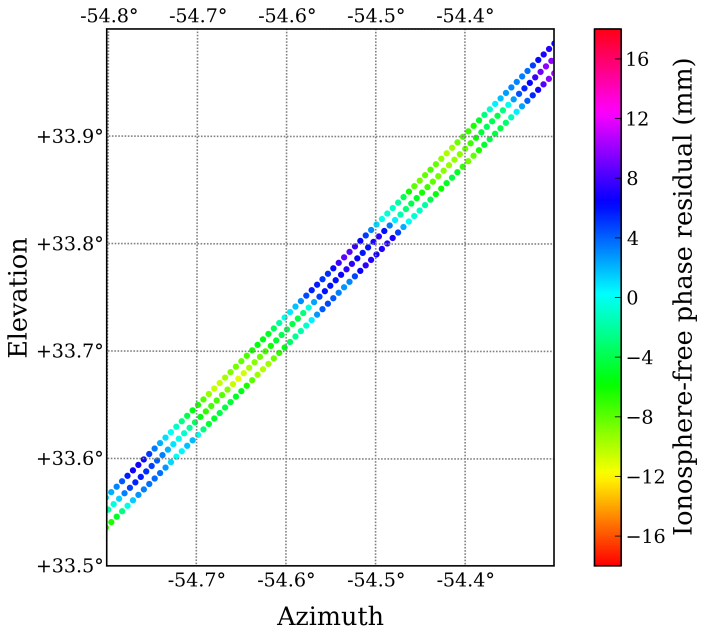

Figure 5.12 – Skyplot of smoothed ionosphere-free phase measurement residuals associated with satellite G29 on 2nd–4th April 2010.

The reasons why all of the sidereal filters perform so well at station SLMS are similar to those for station UCL between 23:05 and 23:20 on 27th March 2012: Firstly, the 'constellation repeat time' of 86,156 s used by the PDSF algorithm is close to the repeat period of satellite G29 associated with the error, 86,158 s. The second reason follows from analysing figure 5.12. This shows, in the same fashion as figure 5.9, the smoothed ionosphere-free residuals for satellite G29 output from the PPP processing runs from three consecutive days (2nd–4th April 2010) where the position states in the Kalman filter state vector have been fixed to their true values. Due to the non-availability of high-rate measurements at station SLMS from UNAVCO, it was not possible to plot more colour-coded residuals from 1st April and before. It is therefore not possible to determine whether or not the 'banding' pattern is close to being orthogonal to the path which G29 follows across the sky. Notice that, like UCL, the skytracks from the adjacent days are separated from each other by a very small angle of about 0.01°. The influence of the angle between the direction of these skytracks and the 'banding' pattern on the effectiveness of the ODSFs was identified in the two previous examples at UCL. However, in this example, such an angle would not matter so much since the skytracks are so close together and the frequency of the oscillations, 0.025 Hz, is lower than either of the two previous examples.

5.6 Conclusions

The above analysis has shown that during periods of high-frequency multipath, a PDSF may struggle to remove the effect if the repeat time used by the algorithm—either the 'constellation repeat time' or the nominal repeat time of 86,155 s—differs significantly from the repeat period of the satellite associated with the error. This is because a PDSF assumes that all visible satellites have the same repeat period at any one time. For example, figure 5.6 shows the inferior performance of the PDSF compared with the ODSFs over a 20-minute period. However, this difference in performance between the two types of sidereal filter was largely due to a difference of just three seconds in the repeat times calculated for satellite G31.

However, the results presented in this chapter show that even the ODSF algorithms struggle to remove the effect of multipath. It was hypothesised that the DP ODSF would outperform a BE ODSF because the former would calculate a more appropriate repeat time. However, it was found that if there was any difference in performance between the two, it was because of the complicated nature of the multipath error itself and the fact that the path that a satellite takes across the sky is not exactly the same from one day to the next. It was not because one method was necessarily better than the other. Indeed, the intricate patterns that observation residuals form when mapped by azimuth and elevation, such as those in figure 5.9, can be highly influential in determining how effective the ODSFs are. Only in one of the three examples above, station SLMS, did the DP ODSF clearly outperform the BE ODSF. Therefore, the results do not strongly support the hypothesis. However, the above analyses have shown that if the ODSF algorithms are to be improved, then it is necessary to take into account the patterns formed by observation residuals. This problem is addressed in the following section.

5.7 An alternative observation-domain method for multipath mitigation

Figure 5.9b has implications for methods that use multiple days to form the sidereal multipath corrections, such as those described in Langbein (2004) and Ragheb et al. (2007) which use five and three days respectively. These studies use multiple days to form a mean correction for multipath error to increase their robustness. However, the effectiveness of this method to remove high-frequency multipath depends on the distribution of the error due to multipath by satellite elevation and azimuth such as the 'banding' patterns seen above. If the angle that the satellite skytrack makes with the lines formed by a banding pattern, as in figure 5.9b, is clearly not orthogonal, then any method that uses multiple days must take this into account. Otherwise, the ability of such a sidereal filter to remove high-frequency multipath error will be reduced further. Even using just the previous day alone, the performance of the DP ODSF was compromised by the fact that the banding pattern was not orthogonal to the skytrack.

One solution to this problem posed by periods of high-frequency multipath interference is to use multiple days to empirically determine the optimum repeat time for applying corrections for multipath error associated with a particular satellite. For example, the time shift that yields the greatest correlation between the observation residuals of day 1 and day 2 could be used as the repeat time for applying corrections on day 3. Such a repeat time would not necessarily match the repeat time determined by the DP or BE ODSF algorithms. Previous studies have determined an optimum repeat time empirically, but not via the observation domain. As mentioned in section 1.5.4, Larson et al. (2007) chose a repeat time which varied in order to minimise the RMS of a resulting *position* error time series across a 500 s window after sidereal filtering. This allowed the shift period to change according to the repeat period of the dominant multipath signal at any one time. A 250 s window was also tested, but this yielded implausible and unstable repeat times. Similarly, Ragheb et al. (2007) calculated repeat times empirically by correlating 1 Hz *position* coordinate residuals over a wide range of window sizes, ranging from 30 s to 10 hours. When using a 10-hour window, the calculated repeat time was found to be very stable, varying by no more than ± 3 s over a period of several hours. Arising from these two studies, it is clear that there is a need to find a balance between the stability of an empirically calculated repeat time and the ability of a sidereal filter to reduce the impact of periods of particularly strong high-frequency multipath interference. Such a concern is also applicable if the same technique were to be applied in the observation domain. For example, a repeat time deemed appropriate for a brief period of strong high-frequency multipath associated with one satellite may not be appropriate a few minutes later, especially if the direction of any 'banding' relative to the skytrack changes. Hence, choosing an appropriate window size is particularly important if the technique is to be applied in a monitoring scenario such as in an earthquake and tsunami monitoring system. In contrast, a large averaging window yielding a stable repeat time is perhaps more appropriate if the priority is to reduce the RMS of a time series of coordinate residuals spanning several hours. Other considerations include how or whether the technique should be applied when there is no strong multipath signal or banding pattern. Indeed, the banding patterns identified in figure 5.9 have been assumed to consist of straight parallel lines. This of course may not always be the case. Consideration also needs to given as to whether it is feasible to empirically derive repeat times by correlating undifferenced measurement residuals associated with PPP processing. These residuals contrast with double-difference measurement residuals which are almost entirely associated with multipath error and measurement noise. Nevertheless, applying a similar method in the observation domain in the context of PPP is worth further investigation.

Another possible solution to this problem is to do away with the need to calculate a repeat time altogether and adopt a method that maps observation residuals onto a hemisphere by azimuth and elevation to form a hemispherical template of multipath corrections and then use that map to derive corrections for other measurements. Mapping observation residuals by azimuth and elevation is not a new idea. Studies such as Wanninger & May (2000) and Harris (2002) right through to Fuhrmann et al. (2014) and Moore et al. (2014) have done so. However, most of

these have stacked the residuals into cells of varying sizes, for example $1^\circ \times 1^\circ$ in azimuth and elevation (Bilich & Larson 2008), in order to increase the robustness of the mean values in each cell. These techniques capture the slowly oscillating multipath effect that often affects observations from satellites at low elevation angles. However, even a cell size of $0.5^\circ \times 0.5^\circ$ will clearly not capture high-frequency multipath effects such as those illustrated in figure 5.9. Importantly, even lower-frequency multipath effects with a period of a few hundred seconds will be lost if such cell sizes are used.

To map high-frequency multipath error, one could create a hemispherical scatter plot of individual observation residuals after processing a sufficient amount of historical high-rate measurement data. If the motivation is to map high-frequency multipath error across as much of the visible sky as possible, then only a very large amount of historical measurements would be 'sufficient', i.e. measurements spanning a period on the order of a few hundred days. Such a map could then be used to interpolate corrections for other measurements as necessary. However, if the motivation is to use the map to derive corrections for multipath for the 'current' day, then, considering the examples above (figures 5.9 and 5.12), only a few of the preceding days—maybe as few as two or three days—may be 'sufficient' to gain an understanding of any banding patterns in order to make accurate predictions of multipath corrections. In this way, the need to process a large amount of historical data is no longer necessary.

The method used to interpolate or extrapolate such corrections at particular azimuths and elevations would need to be sophisticated enough to identify any patterns in the mapped residuals (for example, the banding pattern in figure 5.9b) and use them to intelligently predict the likely multipath corrections, rather than simply use the closest observation residual as the DP ODSF currently does. The development of such an algorithm would be a subject of future research. Research would also be needed to determine the impact of a change of weather on this technique of multipath mitigation, particularly with respect to instances of high-frequency multipath. For example, if it were the case that wet surfaces cause a significant change to the values of the mapped observation residuals, then those residuals could potentially be ignored when corrections for the 'current' day are derived, assuming of course that environment surrounding antenna on the 'current' day is dry. Development of such an algorithm has not been undertaken by the author but is suggested as an avenue for future research in chapter 10.

Chapter 6

Satellite Outages

6.1 Introduction

Sidereal filtering is based upon the assumption that the error due to multipath interference in GPS positioning repeats every sidereal day. However, if a satellite is taken out of service, either expectedly or unexpectedly, this assumption is no longer valid. Satellites occasionally require maintenance of their onboard equipment or are made to perform manoeuvres to keep them in their correct orbits and are made unavailable to users during such times (Dach et al. 2007). Users can get an advance warning of a planned satellite outage via a Notice Advisory to Navstar Users (NANU) message issued by the United States Coast Guard. Geomagnetic storms can cause rapid fluctuations in electron density in the ionosphere. This can cause fluctuations in the carrier phase and amplitude of navigation signals and possibly prevent signal reception (Misra & Enge 2006). Temporary signal blockages can also prevent a signal reaching the receiver antenna and a measurement being made. Also, as mentioned in section 2.1.2, measurements from satellites that are eclipsed by the earth are excluded from entering the PPP processing algorithm. The period of time during which a satellite is eclipsed will not necessarily be the same from one day to the next. This is a problem for a position-domain sidereal filter (PDSF) because it assumes that the same combination of satellites is used on adjacent days. It was mentioned in section 1.5.2 that an observation-domain sidereal filter (ODSF) should perform better than a PDSF in such scenarios, and this is what this chapter seeks to analyse and confirm. Such a concern is important in the context of seismic monitoring applications where continuity of service is desirable.

Unless otherwise stated, all future references in this thesis to the ODSF algorithm refer to the version that uses the dot product (DP) method to determine a satellite's repeat time, i.e. the DP ODSF. This is because, in chapter 3, a DP ODSF was shown to be more effective overall than a broadcast ephemeris (BE) ODSF at removing the effect of phase multipath interference, although that difference was only slight.

Consider the scenario where GPS measurements were made at the same static receiver on two

adjacent days: day 1 and day 2. Suppose one particular satellite that was available during day 1 was not available on day 2. If each dataset was processed separately using the PPP algorithm, then any multipath errors present in the two resulting position time series may not necessarily be as well correlated during the period of the satellite pass as would otherwise be expected. This is of course based on the assumption that the signal from that particular satellite is actually affected by significant multipath interference. Hence, if a conventional PDSF were to be applied to the PPP processing of day 2, the multipath error in the resulting position time series during the period in question may not be reduced and could in fact increase. For a PDSF to achieve the goal of reducing multipath error, it would have to be recalibrated in order to take the missing satellite observations into account, i.e. the measurements from day 1 would have to be processed again, without the relevant satellite, in order to estimate the multpath error signature on day 2. Such an approach was adopted by Larson et al. (2007). If applying a PDSF in real-time, a NANU message can be used to anticipate a scheduled outage: The measurements on the day prior to the outage could be processed without the relevant satellite in order to produce appropriate position-domain corrections for the period of the outage itself. However, this adds complexity to the processing of the GPS measurements and offers no defence in the event of an unplanned outage.

An ODSF does not have this disadvantage and should be more robust. This is because the multipath corrections are applied at the observation level on a per-satellite basis (see section 1.5.2). Whether or not a sidereal filter is applied during PPP processing, any outage of an otherwise healthy satellite is likely to increase positioning error because of the reduced measurement redundancy and the worsening of satellite geometry. However, the multipath corrections applied by the ODSF for other satellites are assumed to remain valid despite any outage.

The example described above is just one scenario. Another scenario exists where a satellite is observable over a period of time on day 2 but not observable for the equivalent period during day 1. Again, unless the satellite in question is excluded from day 2, the PDSF is likely to suffer the same problem: the position time series from the two adjacent days may not be so well correlated which hence reduces the effectiveness of a PDSF. The ODSF algorithm however, by applying multipath corrections on a per-satellite basis, can still apply corrections to measurements of all other satellite signals that *are* available during the equivalent period on day 1. The benefits of using an ODSF over a PDSF in the event of an outage are examined in section 6.2.

For a satellite that is visible on day 2, but not on day 1, three choices arise as to how measurements from that satellite should be treated within the PPP algorithm when an ODSF is applied:

1. Exclude (or down-weight) any measurements from the PPP Kalman filter algorithm on day 2 for which a multipath correction cannot be derived from day 1.

2. Include all measurements in the PPP Kalman filter algorithm on day 2 even if a multipath correction cannot be derived from day 1.

3. If a multipath correction cannot be derived from day 1, attempt to derive a correction from *two* days (or more) prior to day 2.

Unless otherwise stated, option 1 is applied throughout this thesis (with measurements excluded, not down-weighted). However, the advantages and disadvantages of using options 1 and 2 are assessed later in this chapter in section 6.3. Option 3 is not examined via an experiment in this thesis. However, there are potential problems with this approach, especially regarding the removal of high-frequency multipath errors, that have already been discussed in section 5.7.

6.2 Position- and observation-domain sidereal filtering during a satellite outage

6.2.1 Hypothesis

For the reasons given in the previous section, it is predicted that the application of an ODSF will be more effective at removing error caused by multipath interference than a PDSF in the event of a satellite outage, whether that occurs on the 'current' day (day 2) or the 'previous' day (day 1). It is anticipated that the position time series output from PPP processing after applying a PDSF during the period of a satellite outage will exhibit lower stability (i.e. higher Allan deviation values) than the equivalent time series output after applying an ODSF.

6.2.2 Method

To test this prediction, satellite outages are simulated by artificially excluding GPS measurements during periods in which no real outages occurred. This means that the impact of a satellite outage on the performance of the different types of sidereal filter, and regular PPP processing, can be examined by comparing the results with those from the scenario where there is no outage. This would be impossible if this experiment was based on a real satellite outage. For this experiment, data from three receivers was used: Leica SmartNet stations UCL and UEL in London and PBO station P494 in southern California. These three stations were chosen so that the impact of a satellite outage on the different types of sidereal filter could be assessed across differing receiver types and surrounding environments as in chapter 3. Stations UCL and UEL are located only 14 km from each other and the measurements from these receivers were sourced from the same period of time, meaning that the changing geometry of the GPS satellites will be nearly identical at both stations.

The measurements from stations UCL and UEL were recorded on 30$^{\text{th}}$ and 31$^{\text{st}}$ August 2013. Satellite PRN 11 (hereafter referred to as satellite G11) was chosen to simulate a satellite being taken out of service. On 31$^{\text{st}}$ August at station UCL, this satellite rose above an angle of 10° in elevation (i.e. rose above the imposed 10° masking angle) at about 15:17 GPS system time, reached it's highest point in the sky of 87° at 18:10 and fell below 10° just before 21:04. The data from station P494 was recorded on 2$^{\text{nd}}$ and 3$^{\text{rd}}$ April 2010—the two days preceding the day of the M_{W} 7.2 El Mayor–Cucapah earthquake. In this case, satellite PRN 29 (hereafter referred to as satellite G29) was chosen to simulate an outage. On 3$^{\text{rd}}$ April, this satellite rose above 10° in

elevation at about 10:28, reached it's highest point in the sky of 81° at about 14:15 and fell below 10° just before 17:04. Only these periods of time when the satellite used to simulate the outage would have otherwise been visible are considered for analysis. For example: for station UCL on 31st August 2013, only the time period 15:16:59–21:03:38 is considered. As in previous chapters, the performance of each type of sidereal filter is again assessed by calculating Allan deviation values for different averaging intervals for the resulting PPP position time series (east, north and height) during this period.

6.2.3 Results – UCL

Exclusion of satellite G11 from day 2

Figure 6.1 shows time series for the east component for all of the different processing strategies with and without the exclusion of satellite G11 from day 2 (31st August). Immediately, it is clear that the sidereal filters, even when including observations from satellite G11, have not performed very well at all. The sidereal filters appear to have actually increased positioning errors with periods of tens of minutes and above, particularly between 17:00 and 20:00. The reason for this poor performance appears to be that the multipath errors simply do not correlate very well between 31st August and the previous day. This can be seen clearly by comparing the black and grey time series in figure 6.1. The reason for this is unknown: The visible satellite constellation was nearly identical on both days and there is no apparent fault with the satellite orbit or clock files because, as will be shown in section 6.2.4 below, the positioning errors over the same two days at the nearby station UEL *do* correlate well. Therefore, the reason for this poor correlation must lie with the receiver itself or be due to some change in the surrounding environment of the receiving antenna. However, if the nature of the surrounding multipath environment changed significantly between the two days, it could not have been due to any change caused by rainfall changing the reflectivity of the surrounding reflectors: there was no precipitation on either of the two days. It seems that it was not worth applying the sidereal filters in this situation.

Nevertheless, figure 6.1 shows that the exclusion of satellite G11 caused an increase in the bias in the east direction between roughly 16:00 and 19:00 of up to 10–20 mm for all processing strategies. This is despite the fact that, according to figure 6.2, dilution of precision (DOP) values remained low (below 2.0) during the period in question even after excluding satellite G11. This means that the geometry of the visible satellite constellation remained strong (i.e. the visible satellites are well-distributed across the sky) despite the simulated outage.[1] Notice though that it is not easy to see if the outage has brought about an increase in higher-frequency positioning errors. The same can be said for the equivalent plots for the northing and height components shown in figure E.26 (page 299).

Further insight is provided by using Allan deviation. Figure 6.3 shows the Allan deviation curves corresponding with the different time series shown in figure 6.1 (except for day 1). Again,

[1] A brief introduction to dilution of precision (DOP) values can be found in appendix C on page 267.

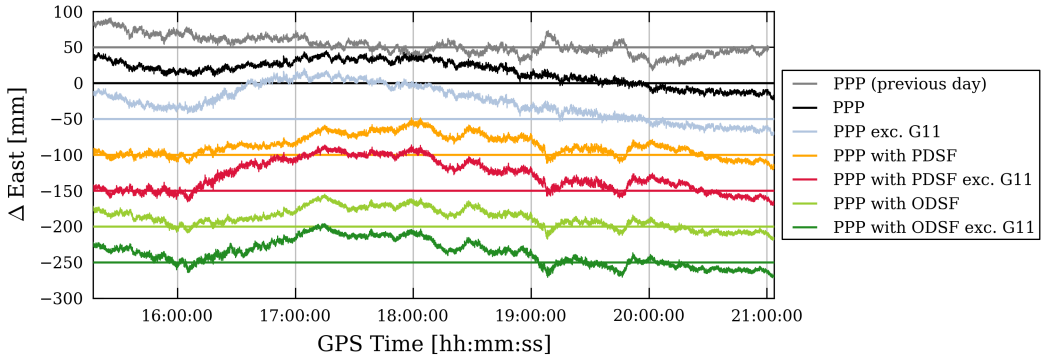

Figure 6.1 – Easting errors between 15:16:59 and 21:03:38 on 31st August 2013 for receiver UCL resulting from standard PPP processing both with (black) and without (blue-grey) measurements from satellite G11 on day 2. Similarly shown in other colours are the errors resulting from PPP processing with position- or observation-domain sidereal filters applied. (Each of the time series have been offset from each other by appropriate multiples of 50 mm for clarity).

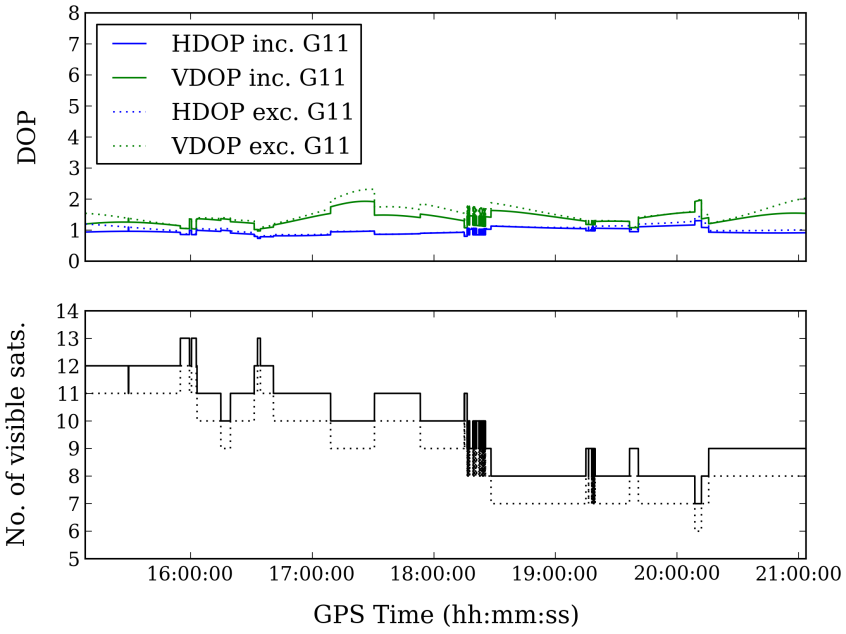

Figure 6.2 – Horizontal and vertical dilution of precision (HDOP and VDOP) and number of visible satellites during the period 15:16:59–21:03:38 (GPS time) on 31st August 2013 at station UCL. *Solid lines* indicate the scenario of no satellite outage; *dotted lines* for the simulated outage of G11.

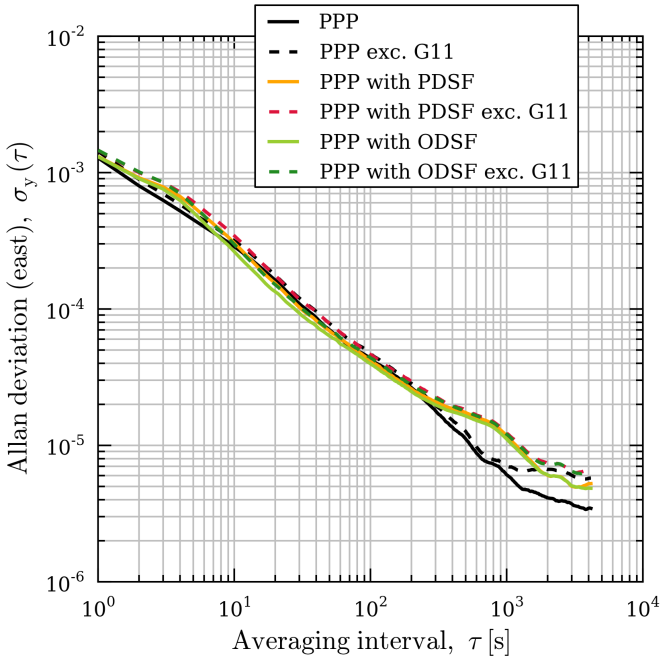

Figure 6.3 – Allan deviation plots of the position time series (east) at station UCL between 15:16:59 and 21:03:38 on 31st August 2013 corresponding with figure 6.1.

it is not easy to compare different processing strategies using this plot, although it is apparent that all types of sidereal filter result in an *increase* in Allan deviation for averaging intervals above roughly 200 s in length. The performance of each of the processing strategies relative to regular PPP processing is shown in figure 6.4. Under normal circumstances, without any satellite outages, the application of an ODSF results in a considerable worsening (i.e. increase) in Allan deviation for averaging intervals larger than about 240 s. This is disappointing considering the performance of the ODSF a few days later on 3rd September which at least managed to reduce Allan deviation for most time intervals up to about 1,000 s in length (figure 3.16, page 107). This poor performance was to be expected in light of the analysis of figure 6.1. Conversely, there is in fact a slight improvement in Allan deviation, albeit no more than 20%, for smaller averaging intervals: between about 8 s and 240 s. Also, the ODSF again outperforms the PDSF, at least for smaller averaging intervals.

As can also be expected, the simulated outage of satellite G11 results in a general degradation in the performance of all processing strategies, whether sidereal filtering is applied or not. In figure 6.4, this increase in Allan deviation seems to be roughly ten percentage points for averaging intervals up to a few hundred seconds for each processing strategy. For example, notice that for standard PPP processing, the exclusion of satellite G11 results in a general decrease in stability of roughly 10% for time intervals up to about 900 s. A similar phenomenon can be seen in the north and height components, shown in figure E.27 (page 300), where for intervals smaller than about 200 s, the impact of the simulated satellite outage is roughly the same no matter which type of sidereal filter is applied.

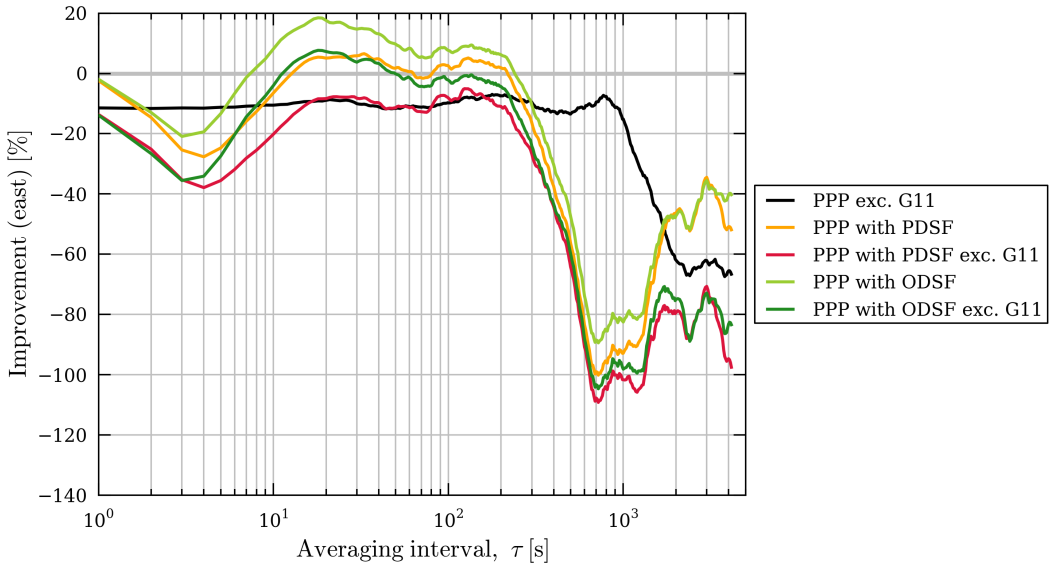

Figure 6.4 – Plots showing the percentage improvement (i.e. reduction) in Allan deviation for station UCL, after applying the various types of sidereal filter, relative to the Allan deviation values corresponding to standard PPP processing that are shown in figure 6.3.

Exclusion of satellite G11 from day 1

Figure 6.5 (and figure E.28 on page 301) show that the ODSF yields very similar results for the case when satellite G11 is excluded from the 'template' day (day 1) compared to when G11 was excluded from the current day (day 2), at least for all but the very largest time intervals. Note that in this particular analysis, the ODSF algorithm is configured to exclude any satellite measurement for which a multipath correction cannot be found. This explains the similarity: No matter if the simulated outage of satellite G11 occurs on day 1 or day 2, measurements from satellite G11 do not enter the Kalman filter process in either case. The slight difference is due to the inclusion of measurements from satellite G11 in the formation of the multipath corrections for the other satellites in the case where the outage occurs on day 2. As mentioned above, the alternative configuration of the ODSF algorithm, where satellite measurements are *included* in the Kalman filter process even if a multipath correction cannot be applied, is examined in section 6.3.

However, the results yielded by the PDSF are noticeably different when comparing figure 6.5 with 6.1. This is to be expected: In the case where measurements associated with G11 are excluded from day 2, the position-domain multipath corrections—which measurements of G11 signals contributed to—are *subtracted* from the time series of day 2. In the case where G11 is excluded from day 1, the ranging errors caused by the multipath interference of G11 signals affect the position time series of day 2 and are not removed by the subtraction of the multipath template. Notice for example the difference in the bias in the east component at 17:00 between figures 6.1 and 6.5 when satellite G11 is excluded: nearly 50 mm and −30 mm respectively.

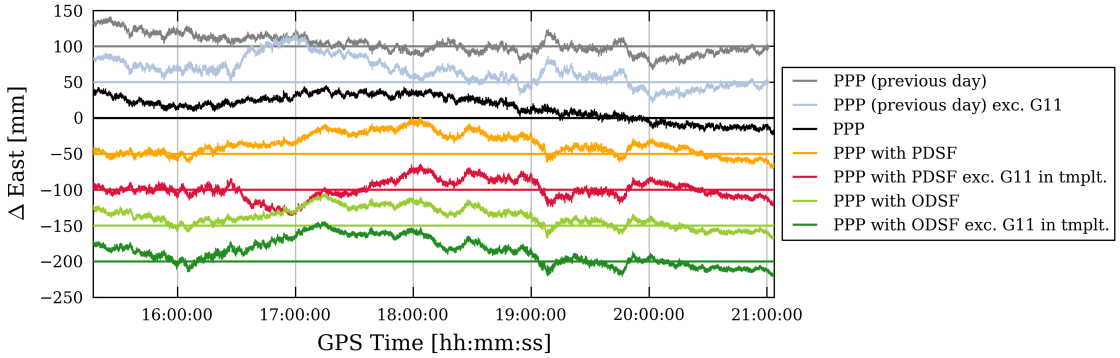

Figure 6.5 – Easting errors between 15:16:59 and 21:03:38 on 31st August 2013 for receiver UCL resulting from standard PPP processing with measurements associated with satellite G11 either included or excluded from day 1 (the 'template' (tmplt.) day). Similarly shown in other colours are the errors resulting from PPP processing with position- or observation-domain sidereal filters applied. (Each of the time series have been offset from each other by appropriate multiples of 50 mm for clarity).

The performance of each of the processing strategies in this scenario relative to regular PPP processing is shown in figure 6.6. Considering the improvement in the *stability* of the position time series, there is still little difference between figures 6.4 and 6.6, at least for intervals smaller than about 200 s. For larger averaging intervals, the PDSF performs even more poorly when G11 was excluded from day 1 than it did when G11 was excluded from day 2.

6.2.4 Results – UEL

Exclusion of satellite G11 from day 2

Figure 6.7 shows time series of errors in easting for station UEL for all of the different processing strategies with and without the exclusion of satellite G11 on day 2. The contrast between this figure and figure 6.1 is striking. This time, the sidereal filters have had much more of a beneficial effect: Multipath errors with periods of the order of a few minutes have clearly been reduced in amplitude. However, it is also clear when comparing the time series resulting from regular PPP processing that the measurements at UEL have been contaminated by multipath interference to a much greater extent than at UCL. The oscillating errors present in the two adjacent days at UEL generally have peak-to-peak amplitudes of over 15–20 mm or more, whereas the amplitude of such oscillations are much smaller at UCL. As discussed in chapter 3, the reason for this is likely to be because the antenna at UEL, which is not a choke-ring antenna, is sited close to a sloping roof that acts as a large single planar reflector.

It is also clear from figure 6.7 that the ability of the PDSF to reduce relatively short-period multipath error (i.e. oscillating errors with a period of just a few minutes) deteriorates markedly when measurements of the signal from satellite G11 are excluded, particularly for the first two hours. It appears that there is not nearly so much deterioration in the case of the ODSF although,

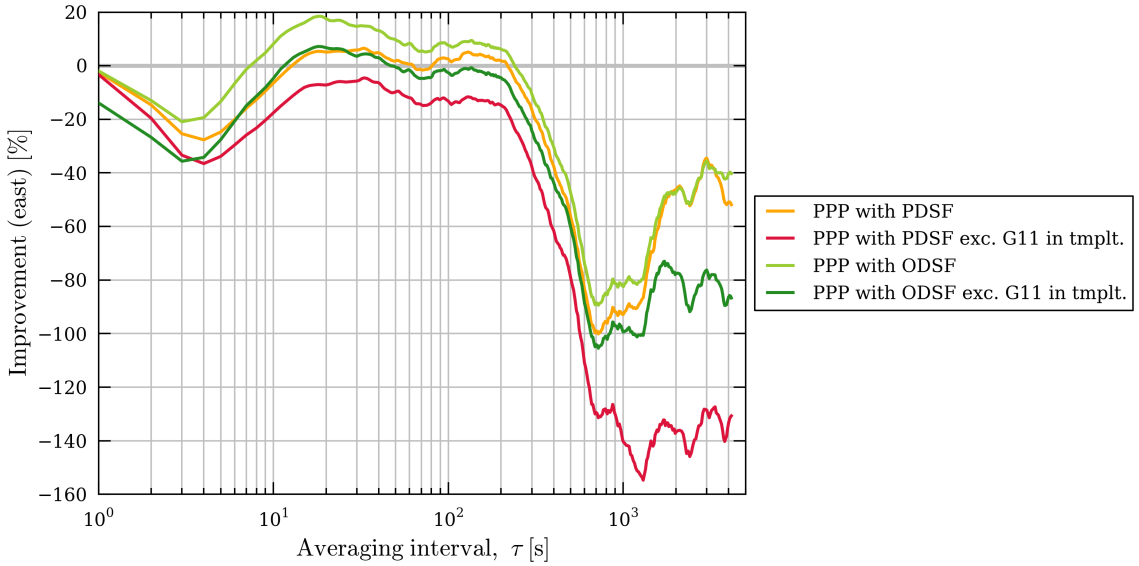

Figure 6.6 – The percentage improvement (i.e. reduction) in Allan deviation values for the easting position time series at UCL shown in figure 6.5 relative to standard PPP processing.

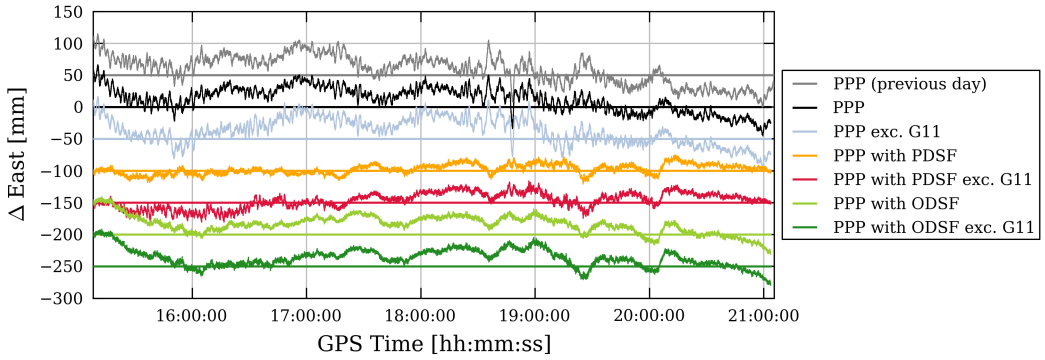

Figure 6.7 – Easting errors between 15:16:59 and 21:03:38 on 31st August 2013 for receiver UEL resulting from standard PPP processing both with (black) and without (blue-grey) measurements from satellite G11 on day 2. Similarly shown in other colours are the errors resulting from PPP processing with position- or observation-domain sidereal filters applied. (Each of the time series have been offset from each other by appropriate multiples of 50 mm for clarity).

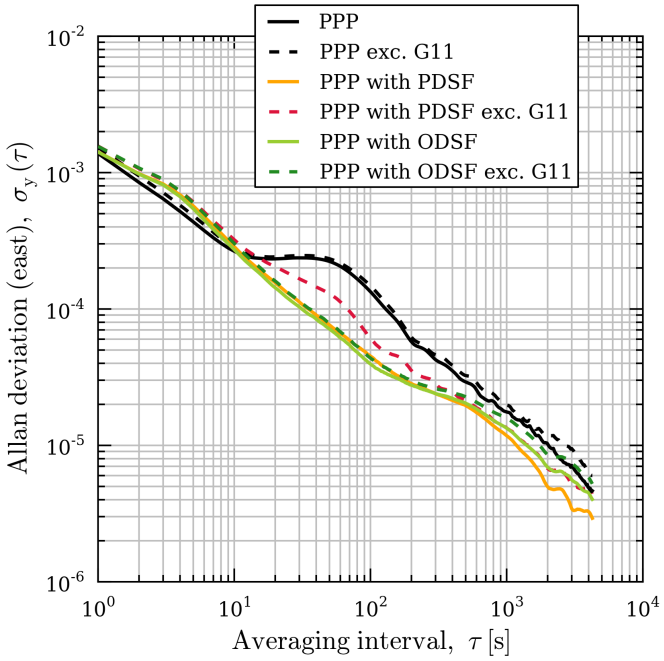

Figure 6.8 – Allan deviation plots of the corresponding easting position time series at station UEL between 15:16:59 and 21:03:38 on 31st August 2013 shown in figure 6.7.

as with previous analyses, the ODSF appears to do little to improve positioning *accuracy*. Similar plots for the north and height components are shown in figure E.30 (page 303). Both of these show a similar deterioration in the performance of the PDSF during the simulated outage.

As with previous analyses, the relative performance of the different processing strategies is further assessed by using Allan deviation. Figure 6.8 shows the Allan deviation curves corresponding with the different time series shown in figure 6.7. Unlike figure 6.3, it is clear to see that both types of sidereal filter, whether measurements from satellite G11 were excluded or not, were successful in reducing Allan deviation at least for all averaging intervals above about 15 s in length. The Allan deviation curves corresponding to the ODSFs have a gradient close to -1 for averaging intervals between 10 s and 100 s, whereas the curves corresponding to regular PPP processing clearly do not—a result of the oscillating short-period multipath errors. Notice also that the simulated outage has resulted in a significant increase in Allan deviation over averaging intervals between roughly 10 s and 300 s when a PDSF has been applied, whereas there is much less of such an increase in the case of the ODSF. In this case, this shows that the ODSF was more robust over these time intervals than the PDSF in the event of the outage. Very similar observations can be made for the north and height components which are shown in figure E.31 (page 304).

As before, the performance of each of the processing strategies relative to regular PPP processing is shown in figure 6.9. This shows that the use of *either* the ODSF or the PDSF result in very similar large (up to around 70%) improvements in Allan deviation between averaging intervals be-

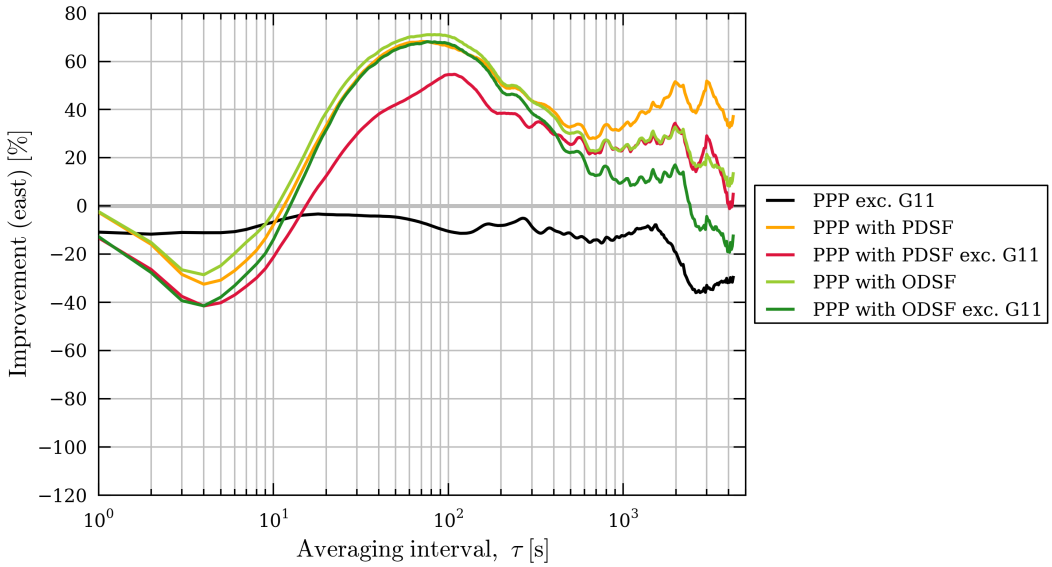

Figure 6.9 – Plots showing the percentage improvement (i.e. reduction) in Allan deviation for station UEL, after applying the various types of sidereal filter, relative to the Allan deviation values corresponding to standard PPP processing that are shown in figure 6.8.

tween about 10 s and 400 s when there is no satellite outage. This is similar to what one would have expected following the analysis in chapter 3, specifically figure 3.17 on page 108. However, when observations from satellite G11 are excluded, the use of a PDSF results in a noticeable reduction in the percentage improvement in Allan deviation for all averaging intervals, but particularly those between 10 s and 300 s where the improvement drops by between ten and twenty-five percentage points. In stark contrast, the performance of the ODSF for these averaging intervals was much closer to what it was without the simulated outage, losing no more than five percentage points. Again, very similar observations can be made when examining figure E.32 (page 305) which shows the equivalent plots for the north and height components.

Exclusion of satellite G11 from day 1

Figure 6.10 shows the positioning errors in the east component for the period of the simulated outage. Again, as was the case for station UCL, the performance of each of the sidereal filters is similar no matter if the outage occurs on day 1 or day 2. The performance of each of the processing strategies relative to regular PPP processing is shown in figure 6.11. When comparing figure 6.11 with figure 6.9, it can be seen that there is a similar pattern in the performance of both types of sidereal filter in terms of stability, at least over time intervals of less than about 300 s. As can be expected following the analysis in chapter 3, the performance of the sidereal filters is more variable over longer time intervals. Equivalent plots for the northing and height components can be seen in figures E.33 and E.34.

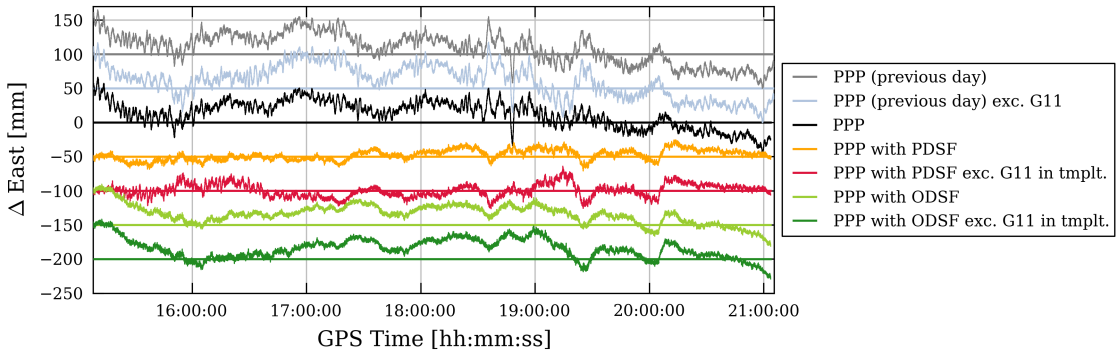

Figure 6.10 – Easting errors between 15:16:59 and 21:03:38 on 31st August 2013 for receiver UEL resulting from standard PPP processing with measurements associated with satellite G11 either included or excluded from day 1 (the 'template' (tmplt.) day). Similarly shown in other colours are the errors resulting from PPP processing with position- or observation-domain sidereal filters applied. (Each of the time series have been offset from each other by appropriate multiples of 50 mm for clarity).

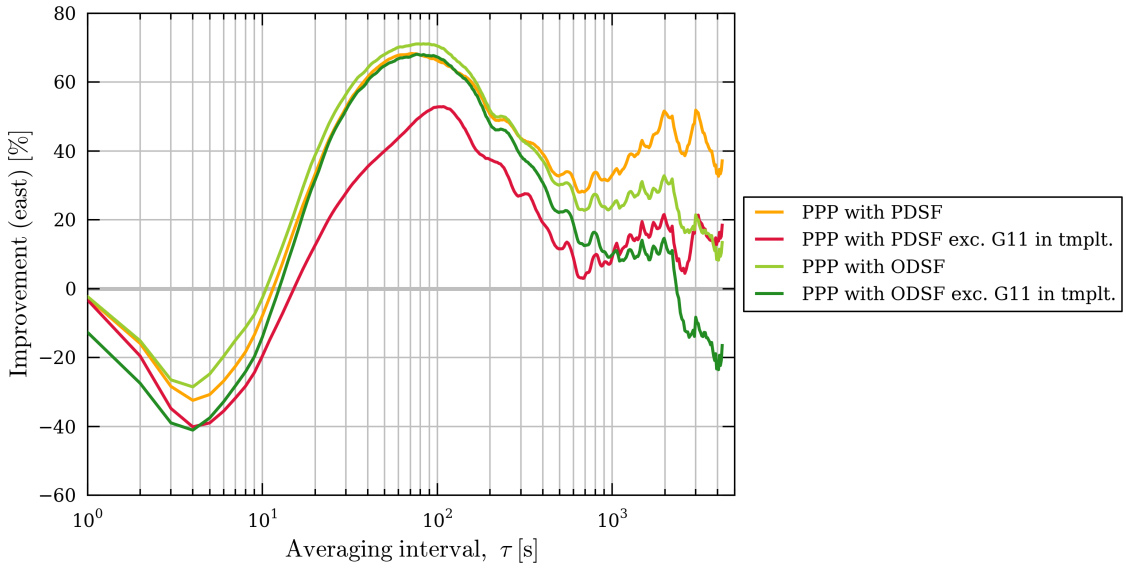

Figure 6.11 – The percentage improvement (i.e. reduction) in Allan deviation values for the easting position time series at UEL shown in figure 6.10 relative to standard PPP processing.

6.2.5 Results – P494

A third receiver, Plate Boundary Observatory (PBO) station P494, was chosen for analysis. This station differs from UCL and UEL in that it is not sited at a rooftop location but in a relatively open area, a field, largely free from strong multipath reflectors such as nearby buildings. A Google Earth image of the location of station P494 is shown in figure E.3 on page 276. At the time during which the data for this experiment was recorded, 2nd and 3rd April 2010, the station was equipped with a Trimble NETRS receiver, a TRM41249.00 antenna (without choke-rings) with a protective radome and mounted on a monument that is attached to the underlying bedrock.

From the analysis in section 3.7, and in particular figure E.18 on page 291, it was found that under 'normal' conditions, both the ODSF and PDSF performed very similarly in terms of their ability to improve stability over time intervals under about 300 s for north and height components and under about 1,000 s for the east component. For longer intervals, the performance of the ODSF deteriorated relative to the PDSF.

The satellite chosen to simulate the outage was PRN 29. On 3rd April 2010 at station P494, this satellite rose above 10° in elevation at 10:28:20 (GPS time), reached its peak elevation of around 80° at about 14:20 and set below 10° at 17:03:35. Figure 6.12 shows the time series for each component for all of the different processing strategies with and without the exclusion of satellite G29 on 3rd April (day 2). Clearly, the outage of satellite G29 had a significant impact on all processing strategies particularly in the height component between about 11:30 and 12:30 and between 13:50 and 14:20. The former of these two events can be explained by figure 6.13. This shows that for much of the time between 11:30 and 12:30 there were only six visible satellites including G29: Decimetre-level high-frequency oscillations occur in the height component during this time in standard PPP processing even without the simulated outage. When G29 *is* excluded, the height component becomes highly unstable between 11:30 and 12:30. The vertical dilution of precision (VDOP) in particular rises dramatically, reaching a maximum approaching 44. This indicates that the geometry of the visible satellites is very poor: This is because only high-elevation satellites remain visible after G29 is excluded. The reason for the decimetre-level errors in the height component between 13:50 and 14:20 is as yet unknown: It can be seen from figure 6.13 that horizontal dilution of precision (HDOP) and VDOP values are quite low during this period indicating that satellite geometry was good even with the simulated outage. It also seems apparent that when there is no satellite outage, the PDSF outperforms the ODSF in terms of stability with respect to the horizontal components. However, as before, it is not easy to see the whole story using just these figures without considering Allan deviation.

Figure 6.14 shows the Allan deviation curves associated with each of the position time series in figure 6.12. It indicates that, when there is no satellite outage, *both* types of sidereal filter yield an improvement in stability for averaging intervals from around 50 s to at least a few thousand seconds. Figure 6.15 shows this more clearly. Indeed, figure 6.15 shows that this reduction in Allan deviation by using either type of sidereal filter can reach beyond 40% for averaging intervals of around 400 s in the height component and about 30% in the horizontal components. For averaging

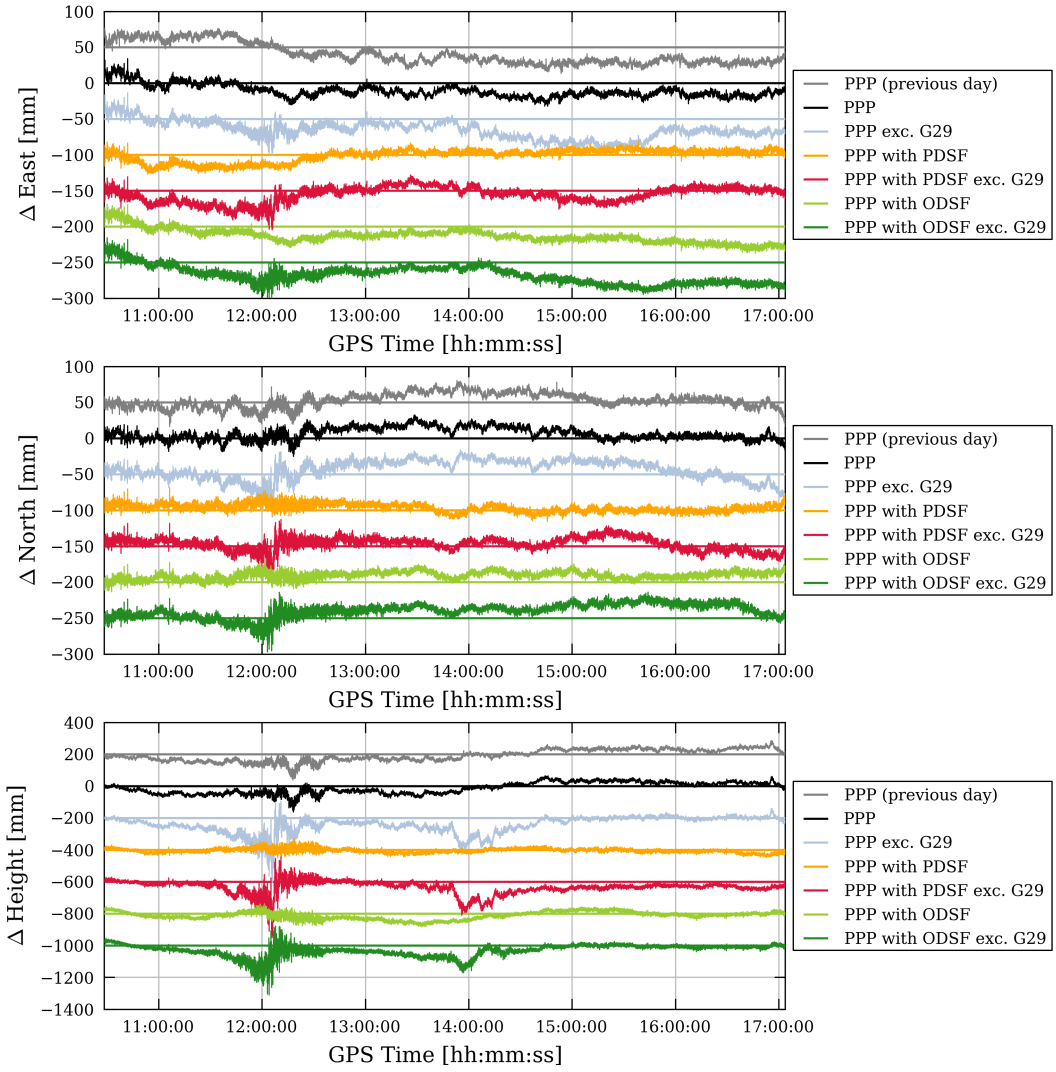

Figure 6.12 – Easting errors between 10:28:20 and 17:03:35 on 3rd April 2010 for receiver P494 resulting from standard PPP processing with measurements associated with satellite G29 either included or excluded from day 2. Similarly shown in other colours are the errors resulting from PPP processing with position- or observation-domain sidereal filters applied. (Each of the time series have been offset from each other by appropriate multiples of 50 mm or 200 mm for clarity).

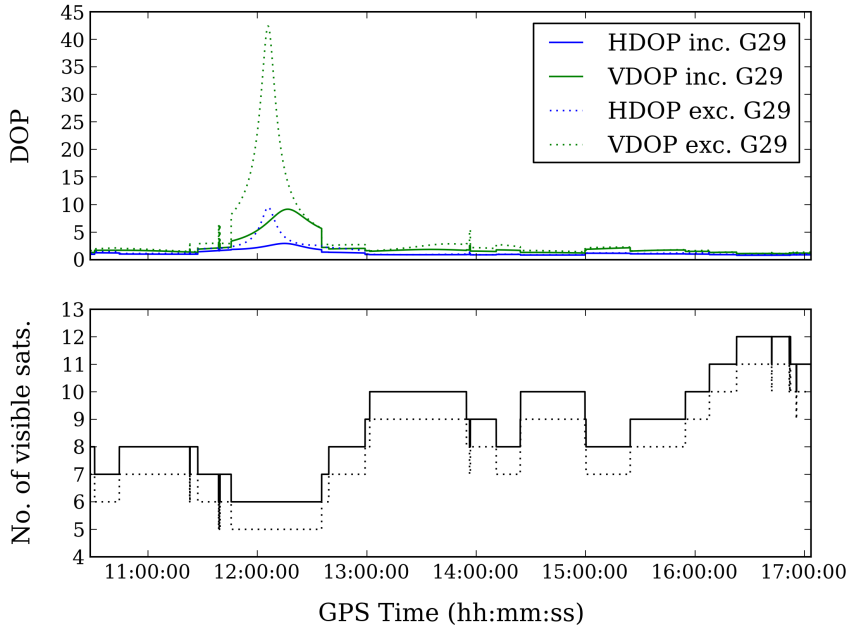

Figure 6.13 – Horizontal and vertical dilution of precision (HDOP and VDOP) and number of visible satellites during the period 10:28:20–17:03:35 (GPS time) on 3rd April 2010 at station P494. *Solid lines* indicate the scenario of no satellite outage; *dotted lines* for the simulated outage of G29. A brief introduction to dilution of precision (DOP) values can be found in appendix C.

intervals below 50 s, the sidereal filters do not have a beneficial effect. Notice that both of the sidereal filters are similar in performance for averaging intervals below around 900 s, with the ODSF marginally outperforming the PDSF for averaging intervals below 1,000 s, 400 s and 300 s for easting, northing and height respectively. For larger time intervals, the relative performance of the two types of sidereal filter is more varied with the PDSF often outperforming the ODSF.

However, when satellite G29 is excluded, the effect on standard PPP processing (without applying a sidereal filter) across time intervals between 50 s and 1,000 s is a *decrease* in stability of up to about 30% in the horizontal components, and up to about 130% for the height component—the latter largely being due to the large decimetre-level high-frequency errors visible in the height component in the period of 11:30 to 12:30 seen in figure 6.12. However, an important observation to draw from figure 6.15 is that for time intervals longer than around 30–40 s, the ODSF outperforms the PDSF by a larger margin during the simulated outage than for the case when there was no outage. A similar phenomenon was identified for station UEL in section 6.2.4. The ODSF even outperforms the PDSF over long time intervals of several thousand seconds. This is most apparent in the height component: When there is no satellite outage, both types of sidereal filter have a very similar performance over time intervals under about 700 s, with divergence between the two occurring for larger time intervals. Under the simulated outage however, the ODSF yields better overall stability than the PDSF for all time intervals longer than about 50 s.

As with the analyses above, there is a similar deterioration in performance in terms of stability if the simulated satellite outage occurs on day 1 rather than day 2, i.e. figures E.35 to E.37 (from page 308) appear to be similar to figures 6.12, 6.14 and 6.15.

6.2.6 Analysis and conclusions

As stated previously in section 3.5, there are differences between stations UCL and UEL with respect to the environment surrounding each of the antennas and the type of antennas used and these explain why the measurements at UEL are generally more prone to strong multipath interference than those at UCL. In each case, whether there was a satellite outage or not, the ODSF generally outperformed the PDSF for all averaging intervals up to a few hundred seconds (and certainly for intervals up to 150 s).

It is also obvious that sidereal filtering is more effective at receivers that are strongly affected by multipath, such as station UEL. However, this would also explain why the simulated satellite outage resulted in a much larger deterioration in the performance of the PDSF than the ODSF at station UEL. The exclusion on one day of a signal that is strongly affected by multipath interference is likely to have a strong impact on the shape of the multipath error signature in the resulting PPP position time series. The correlation between the position time series resulting from regular PPP processing of the two adjacent days, which is clearly high at station UEL (see figure 6.7), would be reduced more significantly. It is of course the strength of this correlation between the position time series of adjacent days on which the effectiveness of a PDSF depends. The weaker this correlation is, the weaker the ability of a PDSF is to reduce positioning errors caused by

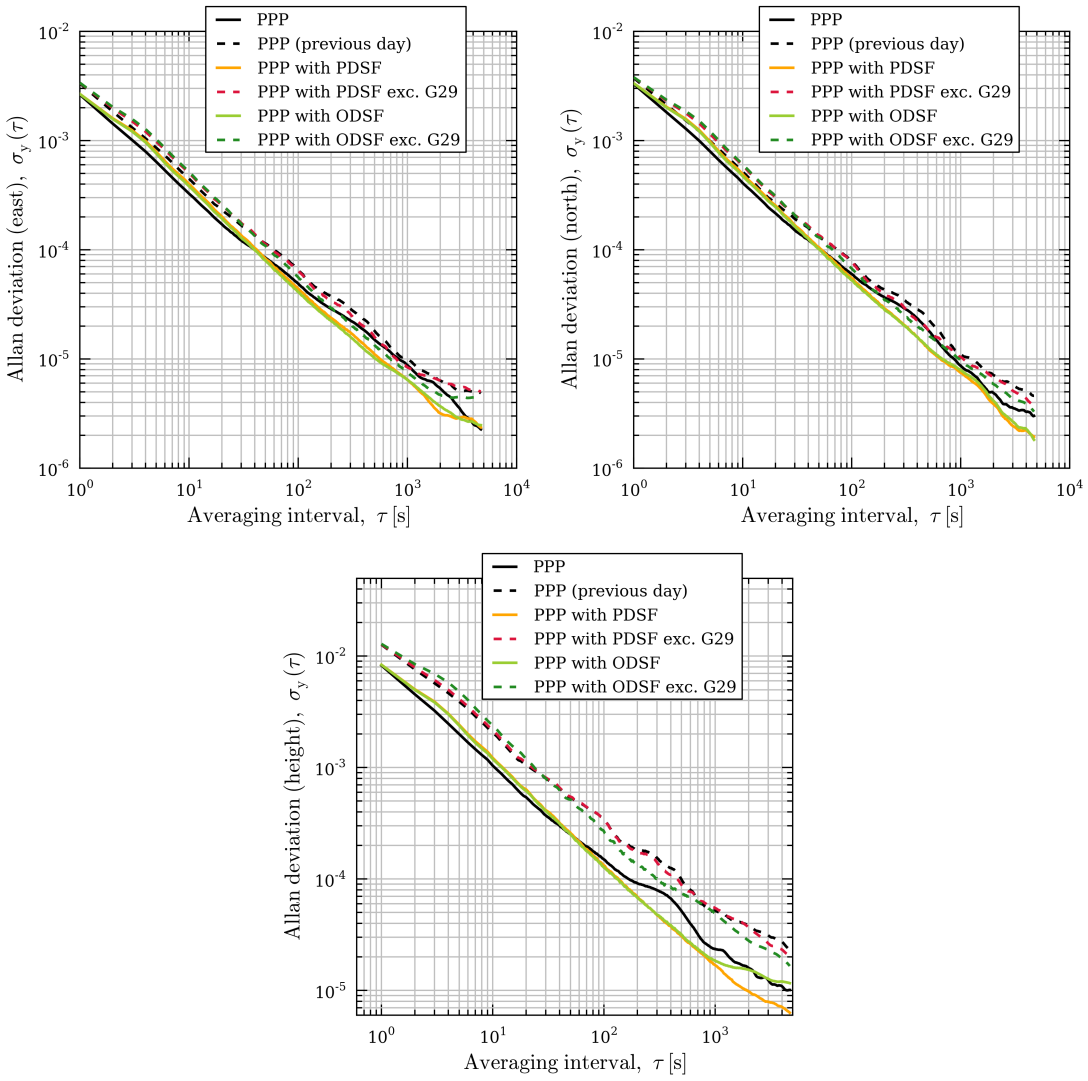

Figure 6.14 – Allan deviation plots of the corresponding easting position time series at station UEL between 10:28:20 and 17:03:35 on 3rd April 2010 shown in figure 6.12.

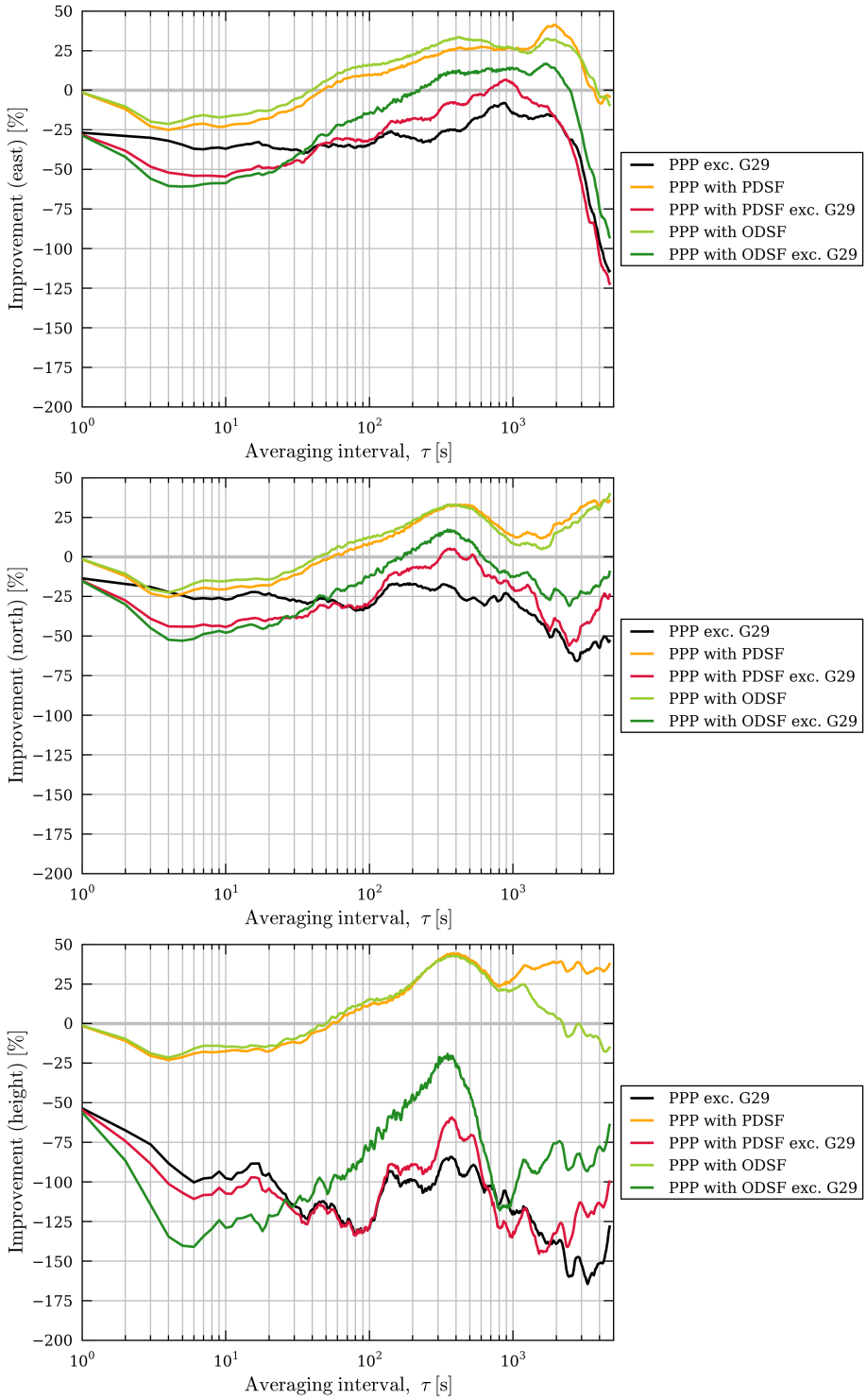

Figure 6.15 – Plots showing the percentage improvement (i.e. reduction) in Allan deviation for station P494, after applying the various types of sidereal filter, relative to the Allan deviation values corresponding to standard PPP processing that are shown in figure 6.14.

multipath interference.

In the case of an ODSF, it is the correlation of *measurement* residuals between adjacent days that determines its effectiveness. In the case of a satellite outage on day 2, the corrections derived from day 1 for that satellite are rendered entirely redundant. If the outage occurs on day 1, then there are no corrections for that satellite for the corresponding period on day 2. The ODSF algorithm in its default configuration (used for all analyses in this thesis unless otherwise stated) excludes any measurements that have not had a multipath correction applied. Therefore, no additional multipath errors can enter the PPP algorithm as a result of an outage. Hence, any deterioration in stability is entirely a result of reduced satellite availability and weaker satellite geometry.

The analysis of the data from P494 illustrates a danger posed by satellite outages: a significant increase in positioning errors due to poor satellite availability and geometry. Despite this, the principal observation made during the analysis of the PPP position time series at stations UCL and UEL still holds: i.e. that there is less of a deterioration in positioning stability in the event of an outage when using an ODSF than when using a PDSF, at least for time intervals longer than 50 s.

6.3 Measurements without a correction for multipath: to exclude or to include?

In the above analyses of simulated satellite outages at stations UCL and UEL, and indeed throughout much of this thesis, the type of ODSF that was used was one that *excluded* any satellite measurements for which a sidereal multipath correction could not be found. This is of course relevant for the case where an ODSF is being applied in the situation where an outage occurs on the day from which the corrections are derived, or 'day 1'. The thinking behind this configuration of the ODSF algorithm was to aim for an entirely 'multipath free' solution: It was thought that by allowing measurements from just one satellite that was significantly affected by multipath interference into the Kalman filter could be detrimental to the stability of the resulting position time series. However, the disadvantage with this approach is that when excluding measurements, redundancy is reduced. Another disadvantage is that satellite geometry may well become less than ideal and adversely affect positioning accuracy. This reduction in redundancy and the degradation of satellite geometry may actually do more harm than good.

The following acronyms are used throughout the rest of this chapter:

- **ODSF1** An ODSF that *excludes* measurements from the PPP algorithm that have not been corrected for multipath.

- **ODSF2** An ODSF that *includes* measurements in the PPP algorithm whether or not they have been corrected for multipath.

Measurement data from stations P494, UCL and UEL are used to examine the performance of the two versions of the ODSF algorithm: the ODSF1 algorithm, which risks an increase in error due to poorer satellite geometry, and the ODSF2 algorithm, which risks further contamination from multipath interference.

6.3.1 Hypothesis

The analysis of data from station P494 in section 6.2.5 above illustrated the problem very clearly: A simulated satellite outage on day 1 caused decimetre-level positioning errors oscillating at both high and low frequencies in the height component during a period of time (approximately 11:30 to 12:30) in which the distribution of satellites across the sky was poor, even without the simulated outage. Nevertheless, figure 6.12 showed that these errors would not have been so large had the outage not occurred. Because the satellite outage resulted in such a large increase in DOP and positioning error, it is predicted that an ODSF that includes measurements from all visible satellites (ODSF2), whether or not they have been corrected for multipath, will result in a more accurate and stable position time series than an ODSF that excludes such measurements (ODSF1) in that particular example. This is because by excluding such measurements, DOP values would increase (i.e. worsen) significantly. The positioning errors that occur in the height component between 13:50 and 14:20 are predicted to reduce despite their cause remaining as yet unknown.

However, as mentioned in sections 6.2.3 and 6.2.4, the decrease in stability at stations UCL and UEL as a result of the simulated outage over time intervals of less than about 200 s was no more than about ten percentage points when using an ODSF (ODSF1). With the impact of the satellite outage being relatively weak compared to P494 (particularly in the vertical component), it is predicted that the inclusion of measurements irrespective of whether they have been corrected for multipath will be a hinderance rather than a benefit, i.e. in contrast to the case of P494, the ODSF1 algorithm is predicted to be more effective than the ODSF2 algorithm, at least over time intervals smaller than a few hundred seconds.

6.3.2 Method

The method of analysis follows the same method used in previous analyses: i.e. any increase or decrease in stability caused by either of the two ODSF algorithms is quantified using Allan deviation values over a wide range of time intervals. Exactly the same datasets and the same simulated outages are used for this analysis as was used in sections 6.2.3, 6.2.4 and 6.2.5 above.

6.3.3 Results – P494

Figure 6.16 shows the position time series (height only) for the period of time during which satellite G29 was visible on 3rd April 2010 (day 2). This satellite was assumed *not* to be visible during the previous day. As predicted, the large slowly-varying errors at 11:30–12:30 and 13:50–14:20

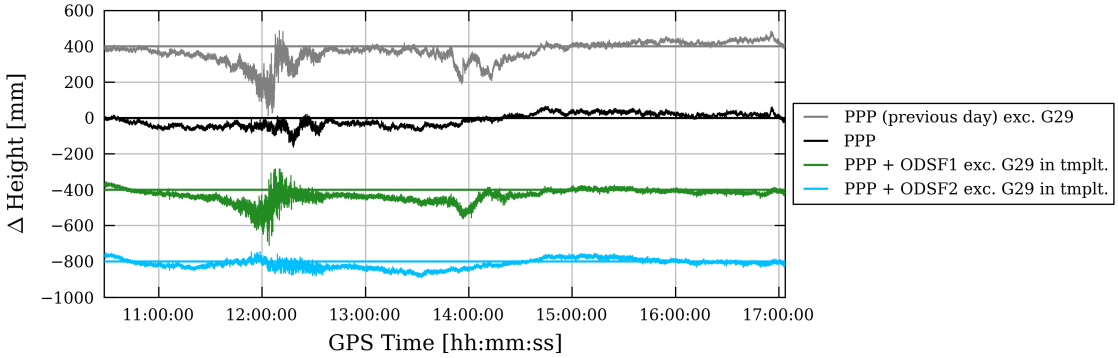

Figure 6.16 – Height errors (shown in black) between 10:28:20 and 17:03:35 on 3rd April 2010 for receiver P494 resulting from standard PPP processing with measurements associated with satellite G29 excluded from day 1 (the 'template' (tmplt.) day). The corresponding errors from the previous day are shown in grey. Similarly shown in green and blue are the errors resulting from PPP processing with ODSF1 or ODSF2 algorithms applied respectively. (Each of the time series have been offset from each other by appropriate multiples of 400 mm for clarity).

resulting from the application of the ODSF1 algorithm are largely removed if the ODSF2 algorithm is applied instead. Figures 6.16 and 6.18 emphasize the superiority of the ODSF2 algorithm, which in this case improved stability by up to 40% over intervals of around 400 s, while the ODSF1 algorithm reduced stability significantly across all time intervals, mostly as a result of the errors at 11:30–12:30 and 13:50–14:20.

Figure 6.19 shows that the ODSF2 also outperformed the ODSF1 in the horizontal components over all time intervals, although the difference in performance between the two algorithms was not so large. The associated time series plots and Allan deviation plots are shown in figure E.38 and E.39, respectively (page 311).

6.3.4 Results – UCL

Figure 6.20 shows the time series for the east component using the two different types of ODSF during the period in which satellite G11 was visible on 31st August (day 2). As has already been discussed in section 6.2.3 via figure 6.7 (and figure E.30, page 303), neither of the ODSF algorithms performed very well at all at reducing multipath error in the position time series relative to regular PPP processing. As discussed in section 6.2.3, the cause of this poor performance remains unknown. Nevertheless, at first glance, it can be seen that the overall trend or 'shape' of the two time series is very similar to each other, but the range of easting errors in the ODSF1 time series is greater than that of ODSF2: 77 mm and 64 mm, respectively.

Considering Allan deviation, figure 6.21 shows that, despite the poor performance of the two ODSF algorithms, particularly for intervals longer than around 200 s, the ODSF2 algorithm results in a lower Allan deviation than the ODSF1 for *all* averaging intervals, i.e. even for time intervals

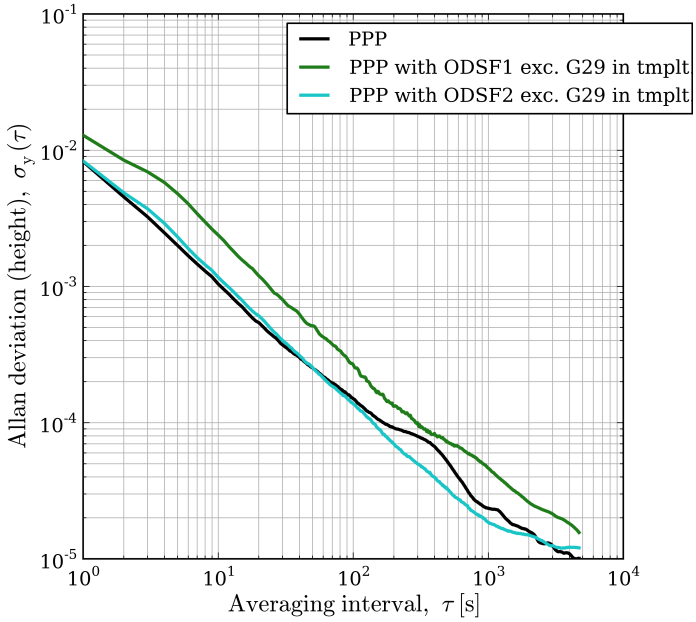

Figure 6.17 – Allan deviation plots of the corresponding vertical position time series at station P494 between 10:28:20 and 17:03:35 on 3rd April 2010 shown in figure 6.16, except for the previous day.

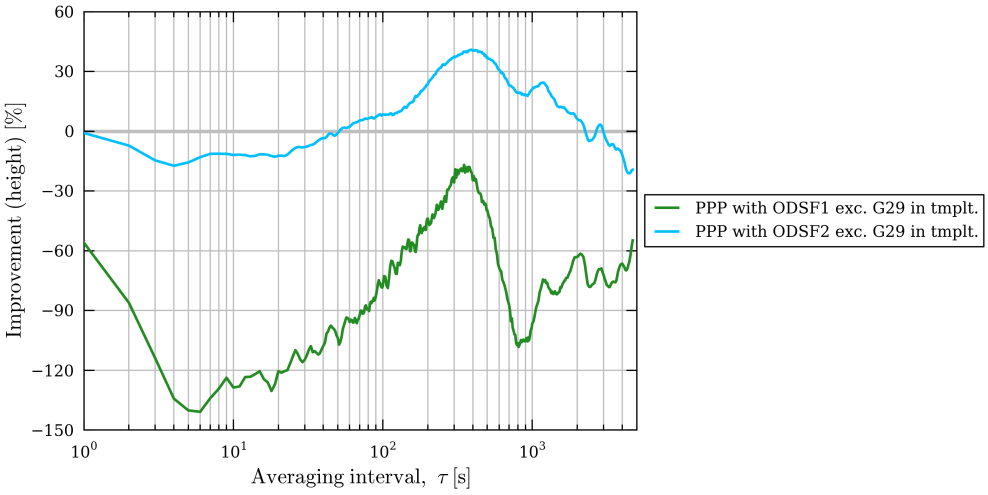

Figure 6.18 – Plots showing the percentage improvement (i.e. reduction) in Allan deviation for station P494, after applying the various types of sidereal filter, relative to the Allan deviation values corresponding to standard PPP processing that are shown in figure 6.17.

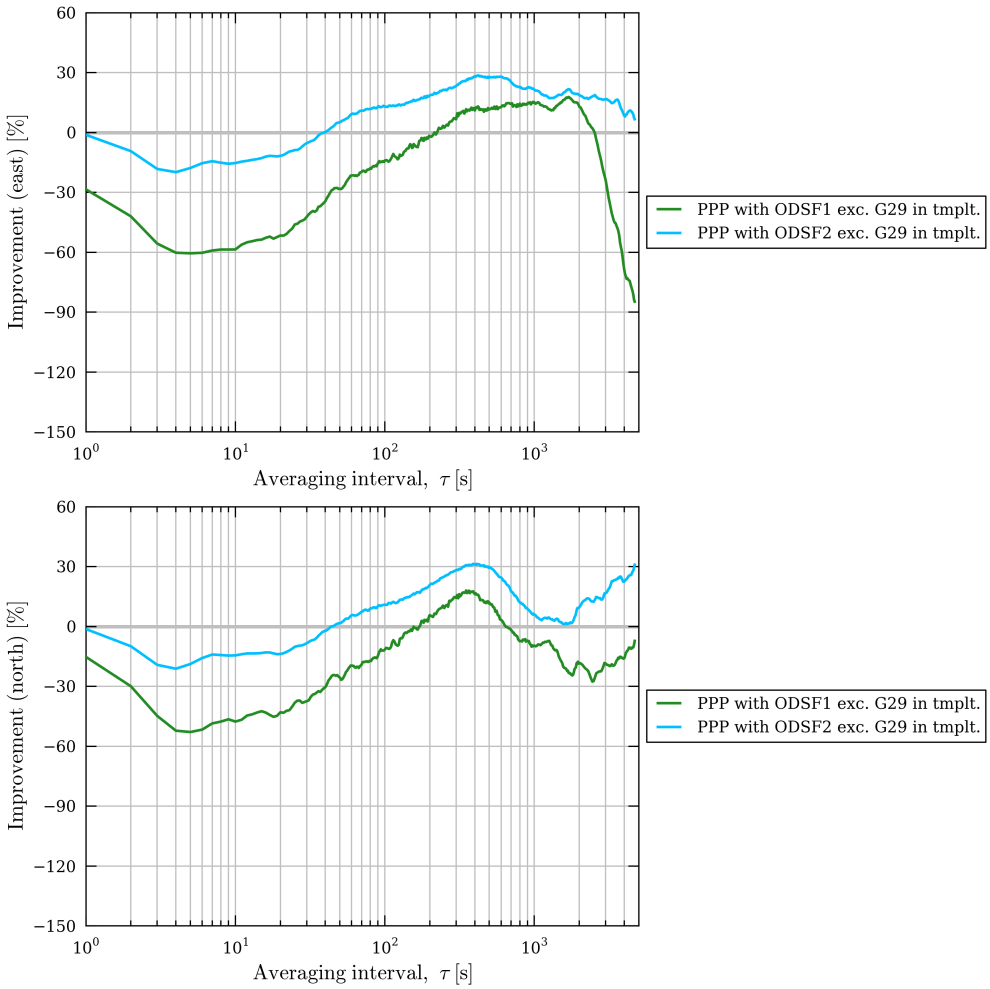

Figure 6.19 – Plots showing the percentage improvement (i.e. reduction) in Allan deviation for station P494, after applying the various types of sidereal filter, relative to the Allan deviation values corresponding to standard PPP processing that are shown in figure E.39.

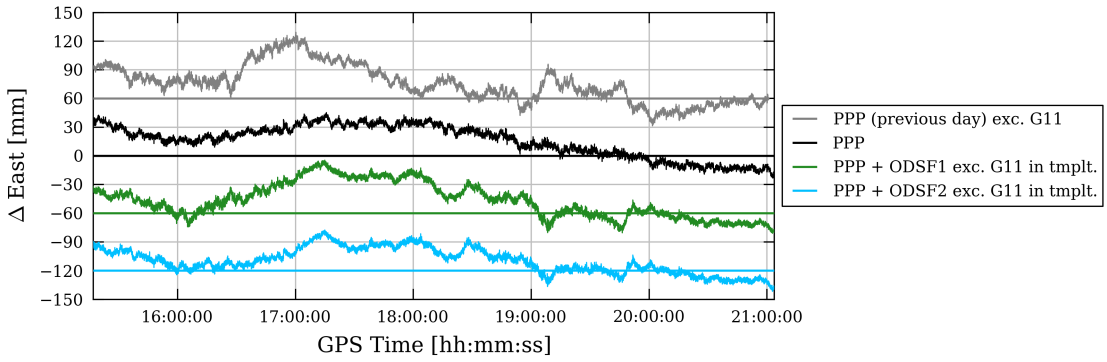

Figure 6.20 – Easting errors (shown in black) between 15:16:59 and 21:03:38 on 31st August 2013 for receiver UCL resulting from standard PPP processing with measurements associated with satellite G11 excluded from day 1 (the 'template' (tmplt.) day). Similarly shown in green and blue are the errors resulting from PPP processing with ODSF1 or ODSF2 algorithms applied respectively. (Each of the time series have been offset from each other by appropriate multiples of 60 mm for clarity).

smaller than a few hundred seconds. This contradicts the prediction that the ODSF1 would outperform the ODSF2 over such time intervals. Despite favourable DOP values throughout the period in question (see figure 6.2), the benefit of using measurements with or without multipath corrections still outweighed the benefit of using only measurements that had been corrected for multipath. The reason for this will be discussed shortly.

Equivalent plots for the northing and height components can be found in figures E.40 and E.41 (from page 313). All show a very similar picture: any improvement yielded by the ODSF2 algorithm over regular PPP occurred for averaging intervals between approximately 8 s and nearly 250 s, but outperformed the ODSF1 algorithm for nearly *all* sizes of averaging interval. However, for the north component, the difference in performance between the two was no more than five percentage points over these intervals.

6.3.5 Results – UEL

Figure 6.22 shows the PPP easting position time series for the two different types of ODSF. Again, both sidereal filters appear to follow a similar long-term trend, but there are some significant higher-frequency errors present in the time series after applying the ODSF2 algorithm that are not so apparent after applying the ODSF1 algorithm, particularly between about 15:20 and 16:20. These errors oscillate with a period of approximately 100 s and have peak-to-peak amplitudes approaching 20 mm. Clearly, the phase measurements of satellite G11 are strongly affected by multipath interference during this time.

The corresponding Allan deviation curves are shown in figure 6.23. Both types of ODSF reduced the Allan deviation value for all averaging intervals from about 10 s up to around 2,000 s (roughly half an hour). The ODSF2 algorithm improved stability across all time intervals above

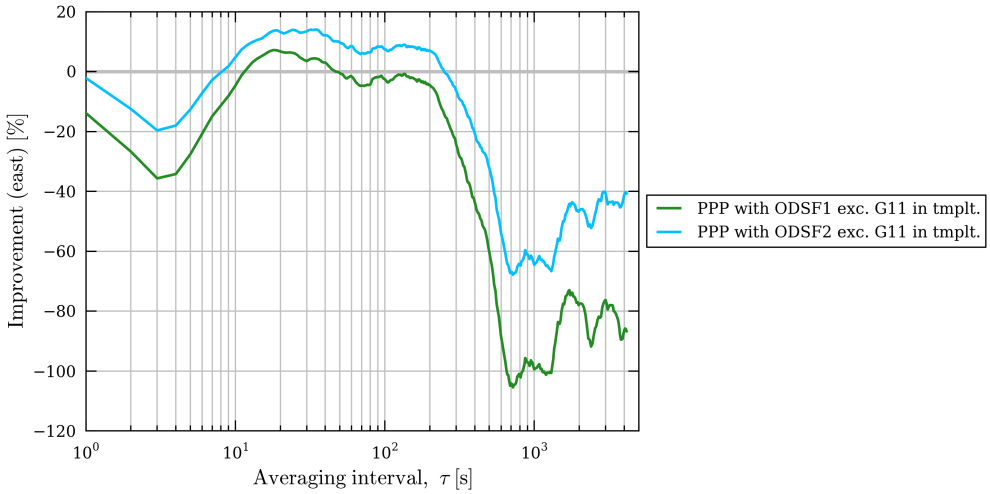

Figure 6.21 – The percentage improvement (i.e. reduction) in Allan deviation values for the ODSF1 and ODSF2 easting position time series at station UCL shown in figure 6.20 relative to standard PPP processing.

10 s. Notice that this time the ODSF1 algorithm outperformed the ODSF2 algorithm between the relatively short averaging intervals of about 15 s and 200 s. The ODSF1 algorithm has thus been more successful at increasing overall stability over these time intervals than ODSF2. For larger averaging intervals the roles were reversed with ODSF2 yielding the lowest Allan deviation values. These results are echoed in figure 6.24 which show that the application of the ODSF1 algorithm resulted in a greater percentage reduction in Allan deviation, up to 68%, than ODSF2 between averaging intervals of about 15 s and 200 s. Above 200 s, the performance of ODSF1 drops below that of OSDF2 and deteriorates faster with increasing averaging interval. Again, very similar results exist for the north and height components: see figures E.42, E.43 and E.44 from page 315.

6.3.6 Discussion

In section 6.3.1, the prediction that the ODSF2 algorithm would outperform the ODSF1 algorithm in terms of increasing the stability of the P494 PPP position time series was correct. This was because the simulated outage of a single satellite on the previous day (day 1) caused the ODSF1 algorithm to reject measurements from that satellite on day 2. This caused a dramatic deterioration of the geometry of satellites available to the PPP algorithm over a period of about an hour which in turn caused a large decrease in overall stability across a wide range of time intervals. In this case, it was shown that the benefit of including measurements with or without multipath corrections clearly outweighed the benefit of using only measurements that had been corrected for multipath.

However, the prediction that the ODSF1 algorithm would outperform the ODSF2 algorithm at both UCL *and* UEL over time intervals smaller than a few hundred seconds was wrong. Only

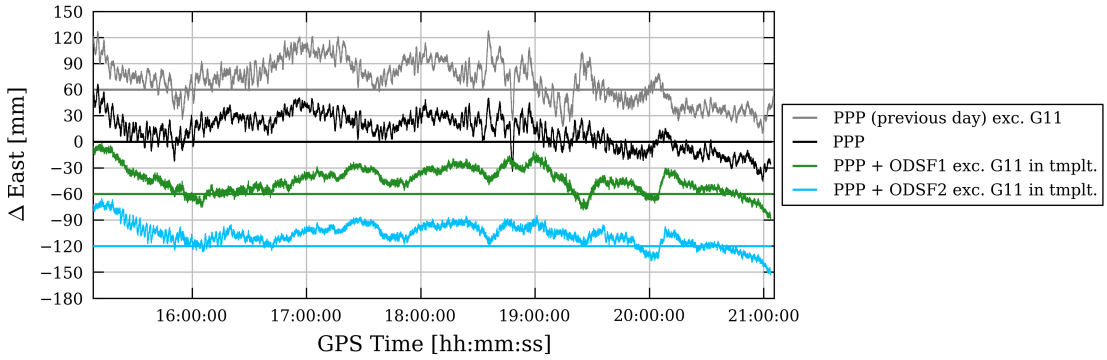

Figure 6.22 – Easting errors (shown in black) between 15:08:00 and 21:03:38 on 31st August 2013 for receiver UEL resulting from standard PPP processing with measurements associated with satellite G11 excluded from day 1 (the 'template' (tmplt.) day). Similarly shown in green and blue are the errors resulting from PPP processing with ODSF1 or ODSF2 algorithms applied respectively. (Each of the time series have been offset from each other by appropriate multiples of 60 mm for clarity).

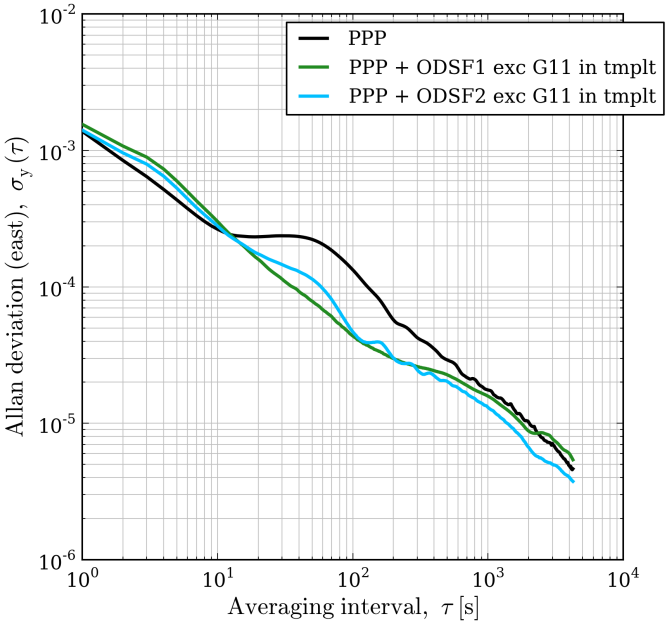

Figure 6.23 – Allan deviation plots of the corresponding easting position time series at station UEL between 15:08:00 and 21:03:38 on 31st August 2013 shown in figure 6.22, except for the previous day.

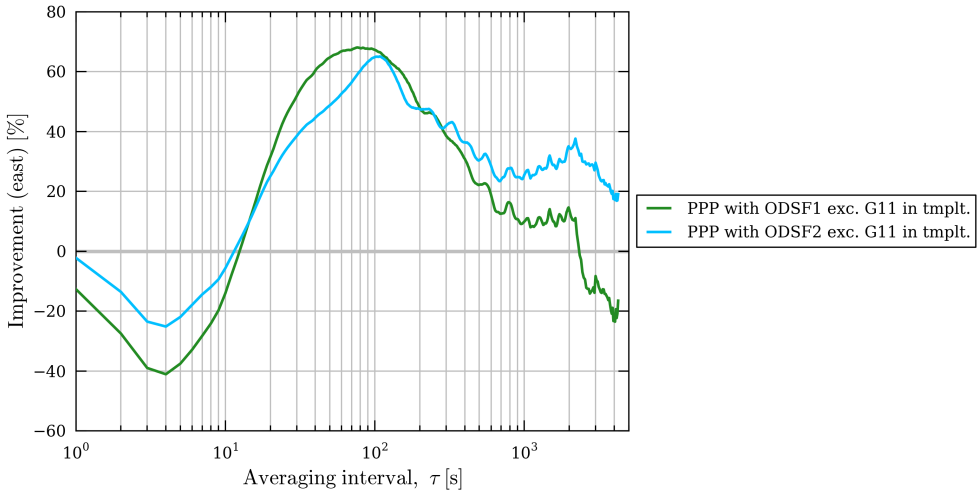

Figure 6.24 – Plots showing the percentage improvement (i.e. reduction) in Allan deviation for station UEL, after applying the various types of sidereal filter, relative to the Allan deviation values corresponding to standard PPP processing that are shown in figure 6.23.

at station UEL did that turn out to be the case. This was despite the fact that DOP values remained low at both stations even when measurements from satellite G11 were excluded. As has already been established in chapter 3, applying any type of sidereal filter to data originating from a station in a low-multipath environment will have a relatively low impact on improving stability over smaller time intervals. Hence, the ODSF2 algorithm at UCL outperformed the ODSF1 algorithm because the benefit of excluding all measurements contaminated by multipath was relatively weak compared to the benefit of including such measurements to improve DOP and increase redundancy. The opposite was true only at UEL, at least for intervals between roughly 10 s and 200 s, because multipath interference was much stronger and hence the multipath corrections had a greater impact.

6.3.7 Conclusions

The above examples have shown again that the performance of the two types of ODSF algorithm relative to each other and to standard PPP processing without sidereal filtering depends on the severity of the prevailing multipath interference. With station UCL not being severely affected by multipath interference during the period in question, applying a sidereal filter arguably did more harm than good: oscillating positioning errors with a relatively short-period (between about 10 s and 200 s) were only marginally reduced, but are significantly worsened for longer-period errors. So if a user is interested in at least reducing short-period positioning errors in low-multipath environments, then applying the ODSF2 algorithm may be the most beneficial of the two types of ODSF, i.e. allowing measurements to be input into the PPP Kalman filter even if they have not been corrected for multipath is more beneficial than excluding them if such measurements are

not affected by strong multipath interference. This contrasts with the situation at station UEL, where the received signals are much more susceptible to the effect of multipath. Here the situation is reversed, with the ODSF1 algorithm outperforming the OSDF2 algorithm, at least at reducing the shorter-period positioning errors.

The most appropriate type of ODSF for a user to apply thus depends on two factors: user requirements and the strength of the multipath interference. If measuring co-seismic offsets quickly, for example, the user is most likely to be interested in increasing the stability of a position solution over just tens of seconds to a few hundred seconds. If the priority is to minimise the occurrence of short-period errors affecting the position solution during satellite outages, such as those apparent between 15:20 and 16:20 in the standard PPP time series in figure 6.22, then the ODSF1 algorithm is most appropriate. However, as seen in section 6.3.3, this runs the risk of decreasing the stability of the position solution during periods when very few satellites are visible. For critical applications, such as earthquake and tsunami early warning, this instability needs to be avoided and this may outweigh the potential advantages of the ODSF1 algorithm. With the ODSF2 algorithm, the risk of increasing stability is reduced, but this may only suit low-multipath conditions and the user must be aware that occasional periods of high-frequency multipath will not be filtered out.

One possible solution to the problem of the potential instability of the ODSF1 algorithm during a satellite outage would be to switch to the ODSF2 algorithm during periods of low satellite availability, i.e. *include* measurements from satellites for which no multipath correction can be found if the number of satellites or a DOP value would otherwise fall below some threshold. Such an algorithm is not implemented in this thesis, but is identified in chapter 10 as a potential area for future research. Other possibilities include giving less weight to measurements that have no correction for multipath rather than exclude them. Indeed, in this thesis, the same elevation-dependent weighting is given to all phase measurements irrespective of whether or not the ODSF algorithm has been applied. Perhaps an improved algorithm would give a higher weighting to measurements that had been corrected for multipath compared to those that had not. This is not a trivial task since the effect of multipath interference is so variable both temporally and spatially. One possibility could be to estimate measurement variances by carefully analysing the RMS values of the measurement innovations or residuals from preceding days for each satellite pass. Whilst one would expect the RMS values to reduce as elevation angle increases, the interest would be to calculate by how much the RMS values are reduced when the ODSF algorithm is applied. Another possibility would be to implement an adaptive Kalman filter where, for example, the measurement error covariance matrix $\mathbf{R}_k$ at an epoch k (see section 2.1.7 on page 73) is calculated using the previous n measurement innovations as follows (Groves 2013*b*).

$$\tilde{\mathbf{R}}_k = \tilde{\mathbf{C}}^-_{\delta\mathbf{z},k} - \mathbf{H}_k\mathbf{P}_k\mathbf{H}_k^{\mathrm{T}} \quad \text{where} \quad \tilde{\mathbf{C}}^-_{\delta\mathbf{z},k} = \frac{1}{n}\sum_{j=k-n}^{k} \delta\mathbf{z}_j^- \delta\mathbf{z}_j^{-\mathrm{T}} \tag{6.1}$$

where: $\tilde{\mathbf{C}}^{-}_{\delta\mathbf{z},k}$ is the calculated covariance matrix of the previous n measurement innovations.
$\tilde{\mathbf{R}}_k$ is the calculated measurement noise covariance matrix.

Determining a suitable value (or values) for n could be a subject for future research. Nevertheless, down-weighting measurements that have not been corrected for multipath error rather than excluding them could reduce the adverse impact of potentially bad satellite geometry.

Another solution would be to use a multipath correction derived from two (or more) days prior to the 'current' day. This idea was discussed in section 5.7 but was not implemented. However, perhaps the best solution would be to significantly increase satellite availability by using additional Global Navigation Satellite Systems (GNSSs). This thesis focuses on the Global Positioning System (GPS). With the addition of other GNSSs, such as GLONASS, BeiDou and Galileo, satellite availability would be boosted significantly. However, the ground track repeat periods of these constellations are much longer than GPS satellites. The possibility of constructing a similar multipath filtering algorithm for other navigation systems is discussed in more detail in chapter 10.

Chapter 7

Measurement of Small Displacements

7.1 Introduction

So far in this thesis, the various sidereal filter algorithms have been tested in scenarios where the receiver antenna is static. In this chapter (and the following two chapters), the algorithms are tested in dynamic situations, such as whether the sidereal filters increase the accuracy and precision of measurements of small displacements of the order of a few centimetres. To do this, the measurements of these small displacements must be compared to a truth model, i.e. displacements that can be considered to be much more accurate and precise. As shall be explained in the following chapter, this is very difficult to achieve in the context of a real seismic event. However, in this chapter, small displacements measured by GPS are compared with those from a truth model that is accurate to within a millimetre. This is achieved by means of a moveable platform.

There are other studies that compare displacements measured by GPS with known displacements but also apply sidereal filtering. One example is Elósegui et al. (2006). In that study, a moving platform was used to simulate the displacements of a real earthquake. A GPS antenna was attached to the platform and its position relative to a nearby static antenna was estimated at a rate of 1 Hz. Although position-domain sidereal filtering was applied, its impact relative to standard processing was not assessed. Nevertheless, all displacement measurements (northing only) were within 10 mm of the true position and 96% were within 5 mm.

Another example can be found in Ragheb et al. (2010). Here, the impact of position-domain sidereal filtering on the measurement of small displacements was assessed in the context of double-difference processing. Sidereal filtering was shown to increase both the accuracy and precision of measured displacements. The overall RMS of all position residuals was 4.5 mm in the horizontal plane with sidereal filtering applied. In contrast to these two studies, in the experiment described in this chapter, GPS measurements are processed using the method of PPP.

There is one notable limitation with such experiments that apply sidereal filtering: As the antenna moves, the position of potential reflectors relative to the antenna will change. Strictly speaking, the multipath corrections become invalid once the antenna moves away from its nominal position. In a real seismic event, it is assumed that the position of an antenna relative to its immediate environment will remain largely unchanged, assuming the surrounding reflectors are rigid and there is no catastrophic damage. Such a situation is difficult to replicate in an experiment, unless the experiment uses measurements gathered during a real earthquake. Indeed, chapter 8 tests the performance of the sidereal filter algorithms during the 2010 El Mayor–Cucapah earthquake.

7.2 Hypothesis

Previous chapters have established that applying an observation-domain sidereal filter (ODSF) is generally beneficial to high-rate PPP processing: It reduces the oscillating errors that are caused by phase multipath interference and hence increases the stability of a position time series over periods of time ranging from just a few seconds to a few hundred seconds. Also, an ODSF is more effective than a position-domain sidereal filter (PDSF) over these time intervals. This has been shown to be the case in circumstances of satellite outages as well as in relatively benign conditions. These characteristics are important for tsunami warning systems which require accurate and prompt displacement measurements as input. It is therefore predicted that an ODSF will yield a bigger improvement than a PDSF in the accuracy and precision of displacement measurements calculated using a PPP position time series spanning a few tens of seconds.

7.3 Method

7.3.1 Experiment design and data processing

This experiment took place on the flat rooftop of a building at the National Physical Laboratory in Teddington, London. A rooftop, shown by the photographs of figure 7.1a and 7.1b, was chosen because it offered a good open view of the sky for a receiver antenna as well as being being secure and easy to access. It offered a relatively simple multipath environment, generally devoid of air conditioning units and other large complex structures often found on flat rooftops. It was surrounded on two sides by parapet walls and a sloping roof on a third side as shown by the sketch plan in figure 7.1c.

As illustrated in figure 7.2, a Leica ‘Viva’ GNSS antenna and a Guralp CMG-5TD strong-motion seismometer (required for a separate experiment not covered in this thesis) were secured to a moveable platform on a stationary table which was placed close to the centre of the rooftop space. The platform could be moved remotely in one dimension (the longitudinal axis of the table) via a simple pulley system. The maximum amount of travel of the platform was adjusted using screws placed at both ends of the table and was measured by eye using a steel rule. The table was

(a) Photograph of the rooftop experiment layout, looking approximately east.

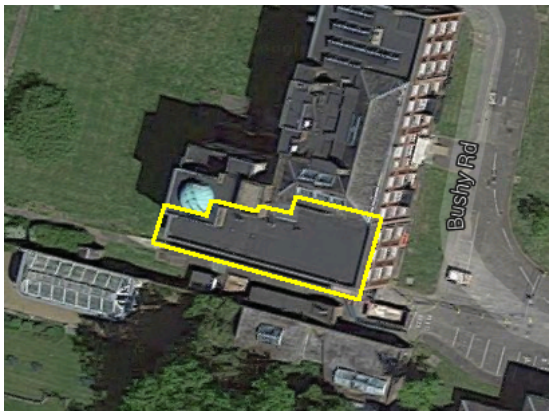

(b) Aerial photograph of the flat roof (outlined in yellow) used for the experiment. Copyright: Google

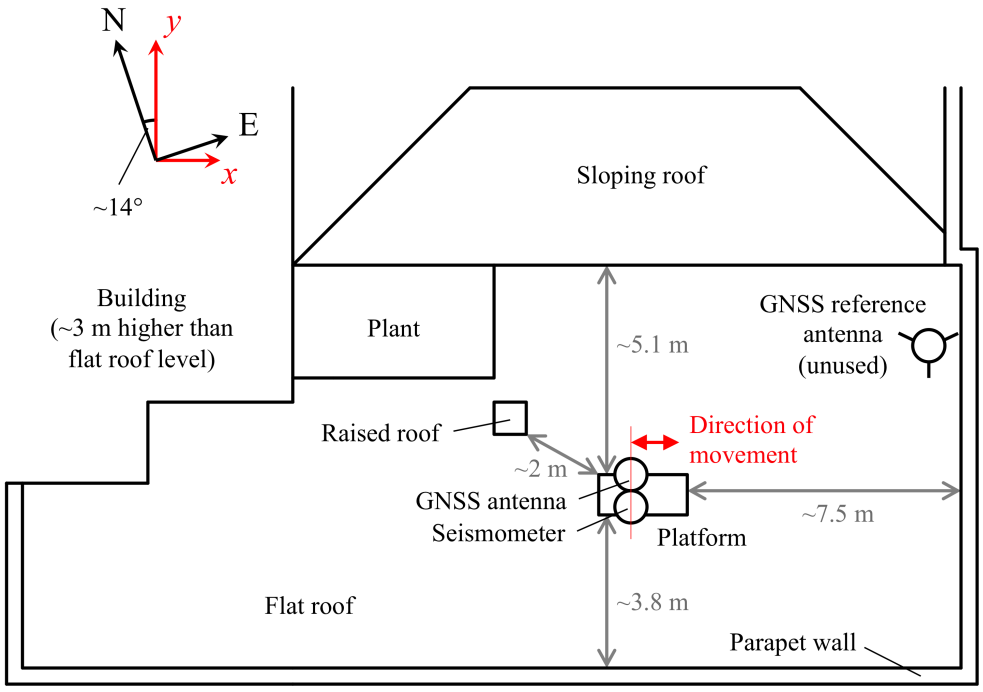

(c) Sketch plan of the rooftop experiment layout (not drawn to scale). The axes at the top-left of the sketch show the orientation of the coordinate system (x,y) chosen for this experiment with respect to east and north (E,N).

Figure 7.1 – Photographs and sketch plan of the rooftop experiment layout.

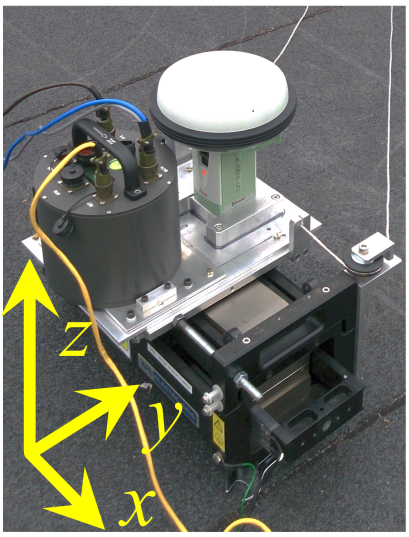

Figure 7.2 – Photographs showing the Leica 'Viva' GNSS antenna and a Guralp CMG-5TD strong-motion seismometer mounted upon the moving platform atop a stationary table. Also shown are the axes of the site coordinate system. The x-axis is aligned with the direction of travel of the moving platform.

placed such that the direction of travel of the platform was parallel to one of the parapet walls at a bearing of approximately 104° from north. This direction of movement defined the x-axis of the coordinate system used for the experiment.

Data collection took place over two consecutive days: 6$^{\text{th}}$ and 7$^{\text{th}}$ March 2014. On 6$^{\text{th}}$ March, the platform was secured to the 'western' side of the table and the receiver was set to log GPS code and phase measurements at a rate of 1 Hz for a five-hour period. The mean position calculated by the PPP processing of the measurements taken during this period was used to define the origin of the coordinate system used in the experiment. The table and the platform on which the receiver and seismometer were mounted were then left in the same position overnight. On 7$^{\text{th}}$ March, the receiver was set to log data for roughly the same five-hour period as the previous day. For approximately the last eighty minutes of that period, the platform was subjected to a series of thirty small displacements ranging from 40 mm down to 5 mm along the x-axis. These displacements are shown in figure 7.3 on page 203. About two minutes separated each displacement event and the time of each of these was recorded to the nearest second.

The GPS measurements were post-processed using a similar procedure as first described in section 3.4, i.e. measurements from 7$^{\text{th}}$ March were processed three times using the PPP algorithm: once without a sidereal filter applied, once with a PDSF and once with a dot product (DP) ODSF. Measurements were processed using 'final' satellite orbit and clock files from the Centre for Orbit Determination in Europe (CODE).

The topocentric coordinates output by the PPP software refer to a right-handed east-north-height coordinate system with respect to the Geodetic Reference System 1980 (GRS80) ellipsoid

(see section 2.1.9). This coordinate frame was rotated clockwise by 14° about the height axis to form an xyz system so that the x-axis was aligned parallel to the direction of travel of the platform, i.e.

$$\begin{pmatrix} x \\ y \\ z \end{pmatrix} = \begin{pmatrix} \cos(-14°) & \sin(-14°) & 0 \\ -\sin(-14°) & \cos(-14°) & 0 \\ 0 & 0 & 1 \end{pmatrix} \begin{pmatrix} E \\ N \\ H \end{pmatrix} \tag{7.1}$$

7.3.2 Data analysis

An estimate of the displacement in three dimensions from the resulting 1 Hz PPP position time series is of course calculated by subtracting the estimated position of the antenna before the displacement event from the estimated position after the event. In this experiment, these two positions are found by calculating the mean position of the antenna over an 'averaging window' of a particular length. A number of different lengths for the averaging window are used and an estimate of the displacement is made for each one.

More formally, consider a single displacement event i that occurred at a particular time. Let Δx_i denote the true value of the displacement along the x-axis at that time. Let $\widehat{\Delta x}_{i,1}$ denote the value of Δx_i *estimated* by subtracting the x-position estimate at the epoch one second before the event, denoted x_{-1}, from the x-position estimate one second after, denoted x_1, i.e. $\widehat{\Delta x}_{i,1} = x_1 - x_{-1}$. Another estimate of the x-displacement using averaging windows of length α, denoted $\widehat{\Delta x}_{i,\alpha}$ is calculated as follows:

$$\widehat{\Delta x}_{i,\alpha} = \bar{x}_{\text{post}} - \bar{x}_{\text{pre}} \tag{7.2}$$

where

$$\bar{x}_{\text{post}} = \frac{x_1 + x_2 + \ldots + x_\alpha}{\alpha}$$

and

$$\bar{x}_{\text{pre}} = \frac{x_{-1} + x_{-2} + \ldots + x_{-\alpha}}{\alpha}$$

For each displacement event, an estimate of its magnitude is made for all (integer) averaging windows of lengths ranging from 1 s to 110 s. The accuracy of each of these displacement estimates is assessed by comparing them to the true offset values. For each displacement event i, the standard deviation of the x-displacement estimate $\sigma_{\widehat{\Delta x}_{i,\alpha}}$ is also calculated:

$$\sigma_{\widehat{\Delta x}_{i,\alpha}} = \sqrt{\frac{1}{\alpha}\sum_{j=1}^{\alpha}(x_j - \bar{x}_{\text{post}})^2 + \frac{1}{\alpha}\sum_{k=-\alpha}^{-1}(x_k - \bar{x}_{\text{pre}})^2} \tag{7.3}$$

Equivalent estimates of displacement in the y and z axes, $\widehat{\Delta y}_{i,\alpha}$ and $\widehat{\Delta z}_{i,\alpha}$, respectively, and their respective standard deviations $\sigma_{\widehat{\Delta y}_{i,\alpha}}$ and $\sigma_{\widehat{\Delta z}_{i,\alpha}}$ are made. It is however assumed that the true magnitude of each displacement event is zero in these directions.

7.4 Results and discussion

Figure 7.3 shows the results of each of the processing runs using 'final' satellite orbits and clock offsets from CODE for the period between 14:35 and 15:55 on 7$^{\text{th}}$ March 2014 for all three dimensions, x, y and z. It is not clear from any of these plots which of the processing strategies are best suited to measuring displacements accurately. The sidereal filters appear to have had little obvious benefit in increasing the stability of the time series in each dimension.

However, previous chapters have shown that the sidereal filters, in particular the ODSF, are most effective at improving stability over relatively short periods ranging from a few tens of seconds up to a few hundred seconds. Figure 7.4 shows a close-up of the results of the processing runs for the period of time covering the six 20 mm displacements in the x-component only. This plot shows some benefit when applying either type of sidereal filter. Notice that both of them have succeeded at increasing the stability of the time series between 15:14:16 to 15:18:17. However, there again appears to be little obvious benefit at other times.

Considering the displacement event at 15:14:16 only as an example: It is clear that the sidereal filters have succeeded in improving the stability of the position time series in the x-component in the two-minute period following that event. The first column of figure 7.5 shows the estimates of the displacement at 15:14:16 for all three components using equation (7.2) with a range of values for α (i.e. length of averaging window in seconds). The top-left plot, displaying displacement estimates in the x-component, shows that for averaging intervals smaller than about 15 s, the accuracy of the estimated displacement calculated using the standard PPP position time series generally exceeds those calculated using sidereal filters. However, for larger averaging intervals, the accuracy when using standard PPP worsens considerably: Using a 110 s averaging window, the 20 mm displacement in the x-component is estimated as only 5 mm, whereas using sidereal filters leads to estimates that are within 2 mm of the true value. Notice also that the first plot in the second column of figure 7.5 shows that the standard deviation of the estimated x-component displacements are reduced to 3–5 mm for averaging windows larger than about 30 s if sidereal filters are used.

However, looking at the results for the y- and z-components in figure 7.5, the sidereal filters have had little obvious overall benefit, especially for the z-component (height). For the y-component, the displacement estimates are within 5 mm of the true value for nearly all averaging windows no matter if a sidereal filter is applied or not. Indeed, results are very varied across all of the displacement events. The PPP position time series for each set of displacement events are shown in figures E.45 to E.49 (pages 318 to 322) and the plots of displacement estimates for every one of those events, equivalent to figure 7.5, are shown in figures E.50 to E.64 (pages 323 to 337). One can quickly look over these and see that the sidereal filters do not necessarily have a positive impact: For example, it can be seen from figure E.51b that both of the sidereal filters generally *increase* the error of the displacement estimates for the 14:44:16 event in all three components, no matter which size of averaging window is used.

To test if the sidereal filters have had *on average* a beneficial effect in estimating the value of

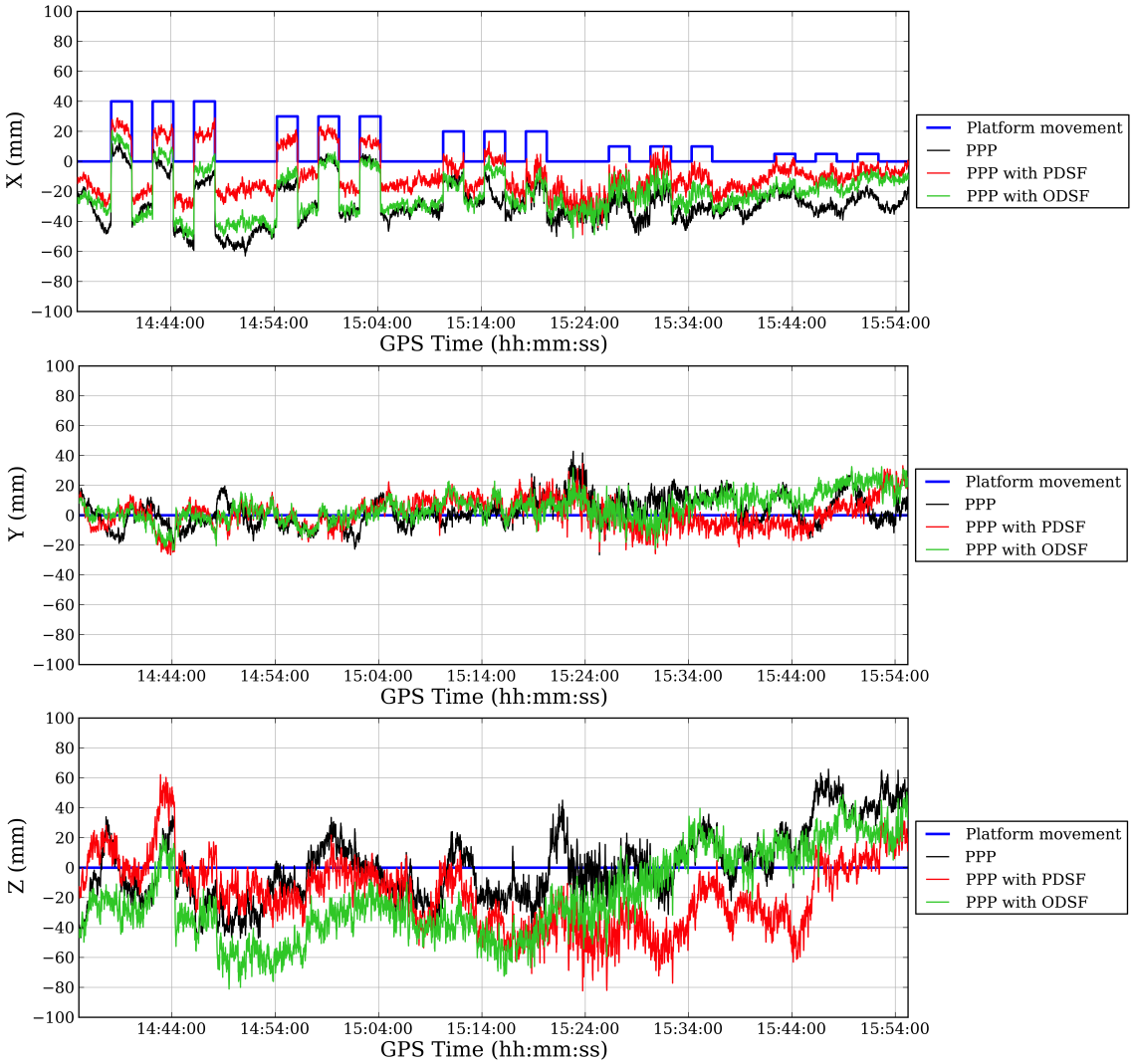

Figure 7.3 – Position time series in the x-, y- and z-directions between 14:35 and 15:55 on 7$^{\text{th}}$ March 2014 resulting from standard PPP processing and PPP processing with various types of sidereal filter applied. Also shown (in blue) is the true motion of the platform.

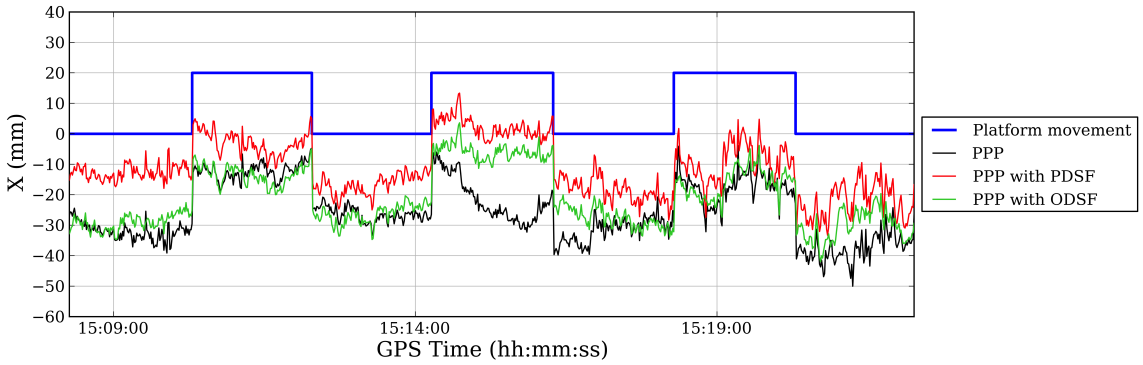

Figure 7.4 – Position time series in the x-direction between 15:08:16 and 15:22:16 on 7$^{\text{th}}$ March 2014 resulting from standard PPP processing and PPP processing with various types of sidereal filter applied. Also shown (in blue) is the true motion of the platform.

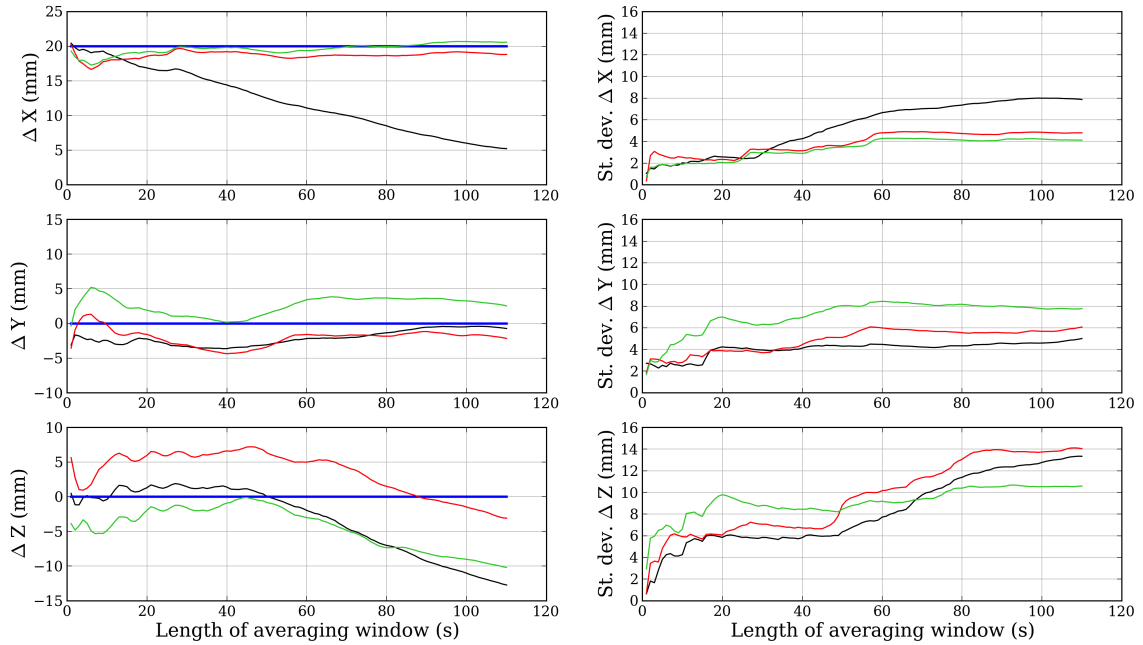

Figure 7.5 – *Left-hand column*: Estimates of the 20 mm displacement event at 15:14:16 using different lengths of averaging window, α. *Right-hand column*: Corresponding standard deviation of the displacement estimates. The black, red and green lines refer to the standard PPP, PPP + PDSF and PPP + ODSF time series, respectively. The blue lines show the true displacement of the platform.

the displacements, the *mean absolute error* of all the displacement estimates calculated using an averaging window of size α is found for each component, i.e. considering m displacement events, the mean absolute error of all displacement estimates calculated using an averaging window of size α, $\bar{e}_{\widehat{\Delta x}_\alpha}$, can be calculated as follows:

$$\bar{e}_{\widehat{\Delta x}_\alpha} = \frac{1}{m} \sum_{i=1}^{m} |\widehat{\Delta x}_{i,\alpha} - \Delta x_i| \tag{7.4}$$

The first column of figure 7.6 shows the mean absolute error in all three components plotted for all lengths of averaging window (values of α) used in the analysis. For averaging intervals larger than about 15–20 s, the sidereal filters have *on average* increased the accuracy of the displacement estimates. For example, estimates of displacement in the x-component using averaging windows above 20 s in length are on average accurate to within 3 mm if an ODSF has been applied, whereas if no sidereal filter had been applied, accuracy would on average be between about 3 mm and 5 mm. For averaging intervals of about 55 s, the improvement in accuracy in the x-component is nearly 45%. For small averaging windows (below about 15 s), the sidereal filters tend to lead to a slight decrease in accuracy. This is probably because of the slight increase in higher-frequency noise caused by applying a sidereal filter (as discussed in section 5.2). Notice also that the accuracy of the displacements is higher if an ODSF has been applied rather than a PDSF, particularly in the x- and z-components.

The second column of figure 7.6 shows the average (mean) standard deviation of all displacement estimates for varying lengths of averaging window. Notice that applying sidereal filters appears to make little difference to the precision of the estimates, particularly in the horizontal components. In the case of the displacements estimated after using the ODSF, there is a slight decrease in precision if using averaging intervals smaller than about 60–80 s. For larger averaging windows, the ODSF yields a slightly better precision. Perhaps if longer averaging intervals were tested (>110 s), the sidereal filters may have yielded more significant increases in precision over standard PPP as longer-period multipath errors are removed.

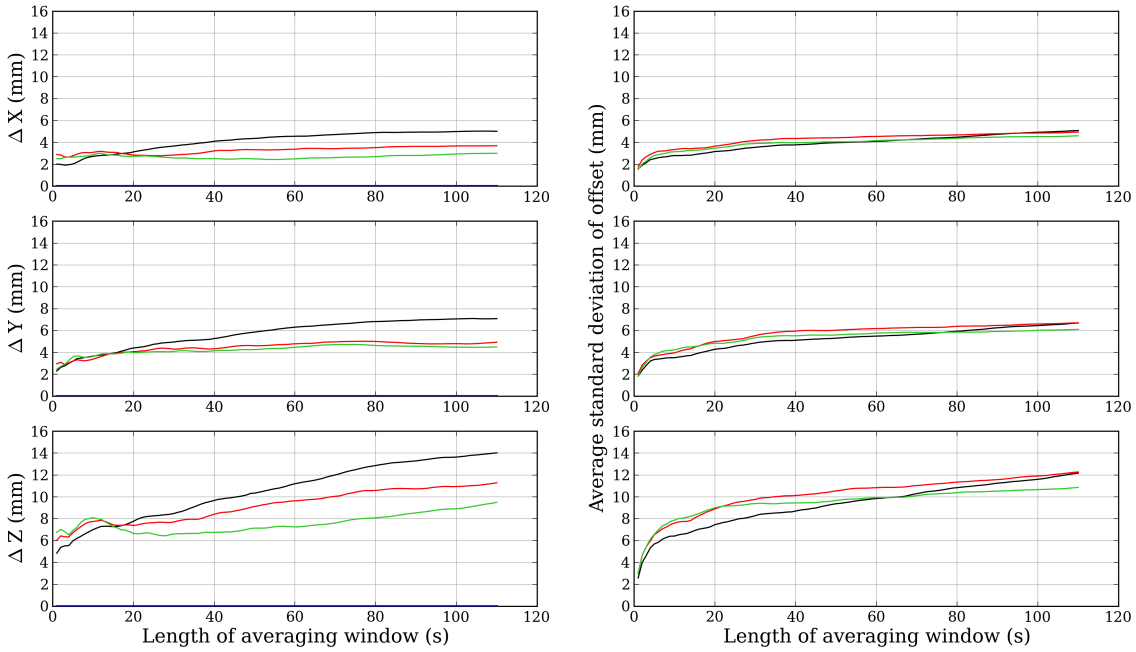

Figure 7.6 – Mean absolute error of all displacement estimates and their corresponding average (mean) standard deviations using different lengths of averaging window, α. The black, red and green lines refer to the standard PPP, PPP + PDSF and PPP + ODSF time series, respectively.

7.5 Conclusions

Considering the prediction made in section 7.2, the above results show that, *on average*, both types of sidereal filter improved the accuracy of the measured displacements if averaging windows from around 15–20 s in length up to 110 s were used. Also, applying the ODSF algorithm, on average, yielded more accurate measurements of the induced displacements than when applying the PDSF algorithm. Regarding the precision of the measurements, as discussed above, the sidereal filters had less of an effect. However, the ODSF marginally outperformed the PDSF in this respect, certainly when using averaging intervals over 20 s. Of course, the ODSF did not outperform the PDSF or standard PPP at every single one of the thirty displacement events, presumably due to the fact that other sources of error are present, particularly those that vary relatively quickly with time, such as satellite clock offset errors and error in the estimated receiver clock offset.

The result that applying the ODSF generally yields more accurate estimates of small displacements is in spite of the fact that the position of any reflector relative to the antenna changes slightly as the antenna moves. In the scenario of a real seismic event, the environment immediately surrounding the antenna will likely experience the same motion as the antenna with respect to an ECEF coordinate system (for example) and hence the multipath template should remain valid before and after the event.

Notice that the most accurate estimates of displacement occurred when using small averaging windows and that for averaging windows smaller than about 15 s, the sidereal filter algorithms do not necessarily have a beneficial effect. However, in a real seismic event, permanent displacements do not occur instantaneously, but over the course of a few tens of seconds, for example, and are often obscured by transient displacements caused by seismic waves that can be larger in amplitude than the permanent offset itself. An example of this will be shown in the next chapter and will be discussed in detail. Still, this means that very short averaging windows cannot be used to estimate permanent displacements reliably. The result of the experiment in this chapter has shown that using a sidereal filter does at least, on average, lead to a more accurate estimate of displacement when using averaging windows larger than about 20 s.

Chapter 8

Measurement of Coseismic Offsets

8.1 Introduction

Determining the co-seismic offsets associated with a seismic event rapidly and accurately is important to earthquake and tsunami monitoring systems. The previous chapter has indicated that applying a sidereal filter, and in particular an observation-domain sidereal filter (ODSF), can increase the accuracy of measurements of small centimetre-level displacements induced by a moving platform by up to 45%. In this chapter, a similar method to that used in the previous chapter is applied to assess the performance of the sidereal filters in increasing the accuracy of measurements of coseismic displacement associated with a real seismic event.

However, in order to do this, those measurements must be compared to other measurements of coseismic displacement that are more accurate and precise. These are much more difficult to obtain for a real seismic event. Section 8.3.1 describes the method used to estimate the 'true' coseismic displacements for the purpose of comparison. Section 8.3.2 describes the method used to calculate the coseismic displacements from the position time series output by the PPP software. The results of the comparison are discussed in section 8.4 and conclusions are made in section 8.5.

The seismic event chosen for analysis was the M_{W} 7.2 El Mayor–Cucapah earthquake. It occurred at 22:40:43 UTC on 4$^{\mathrm{th}}$ April 2010 in Baja California in northern Mexico on a northwest-southeast fault which forms part of the San Andreas fault system (Bock et al. 2011). This is a strike-slip fault, where two parts of the earth's crust slide past one another and any permanent coseismic offset is largely in a horizontal direction. The El Mayor–Cucapah earthquake was not tsunamigenic, but it was chosen for this experiment because of the wealth of data available: Many of the Plate Boundary Observatory (PBO) monitoring stations in southern California were recording high-rate (1 Hz and above) GPS measurements at the time of the rupture.

This earthquake has been the subject of a number of studies. One study in particular by Allen & Ziv (2011) used GPS position time series to calculate coseismic displacements at a number of monitoring stations and used those to estimate the moment magnitude of the earthquake. The

experiment described below uses a method similar to that used by Allen & Ziv (2011) to calculate coseismic offsets. The objective is to determine whether sidereal filters increase the accuracy of the measurement of these offsets.

8.2 Hypothesis

Considering that a sidereal filter, particularly an observation-domain sidereal filter (ODSF), on average yielded an increase in the accuracy of measurements of small displacements in the previous chapter, it is predicted that an ODSF will yield a more accurate calculation of coseismic offset than if a PDSF were applied or if a sidereal filter was not applied.

In the analysis in sections 3.6 and 3.7 (page 111 onwards), it was shown that despite the use of choke-ring antennas and careful siting of the PBO monitoring stations, the sidereal filters were still generally successful at increasing the stability of a PPP position time series over time intervals between 100 s and 300 s. Also, unlike the experiment in the previous chapter, the position of potential reflectors relative to these receiver antennas are thought to remain unchanged after the rupture, meaning that the corrections for multipath error are assumed to remain valid despite the permanent displacement of the antenna.

8.3 Method

8.3.1 Obtaining a truth model

To measure the accuracy of the measured coseismic offsets, one needs to compare them to the *true* coseismic offsets that have been measured to a higher degree of accuracy. A tsunami early warning system must accurately measure coseismic offsets as quickly as possible. Some of these offsets could be as small as just a few centimetres. Therefore, in order to assess the accuracy of the method, the true values of the coseismic offsets need to be known, ideally, with sub-centimetre accuracy.

Fortunately, the University Navstar Consortium (UNAVCO) provide access to daily records of the three-dimensional position calculated by the PBO for each of their monitoring stations with respect to the IGS 2005 international terrestrial reference frame, IGS05 (prior to 17$^{\text{th}}$ April 2011). These records can span several years and are accessible via the Data Archive Interface webpage[1]. Each *daily* estimate of position has an associated standard deviation for each dimension. This is usually under 2 mm for the horizontal components and under 7 mm for the vertical component. These positions are a combination of position solutions calculated by Central Washington University and the New Mexico Institute of Mining and Technology using GIPSY/OASIS-II and GAMIT/GLOBK software, respectively. Further details can be found in Herring (2015).

[1] http://facility.unavco.org/data/dai2/app/dai2.html

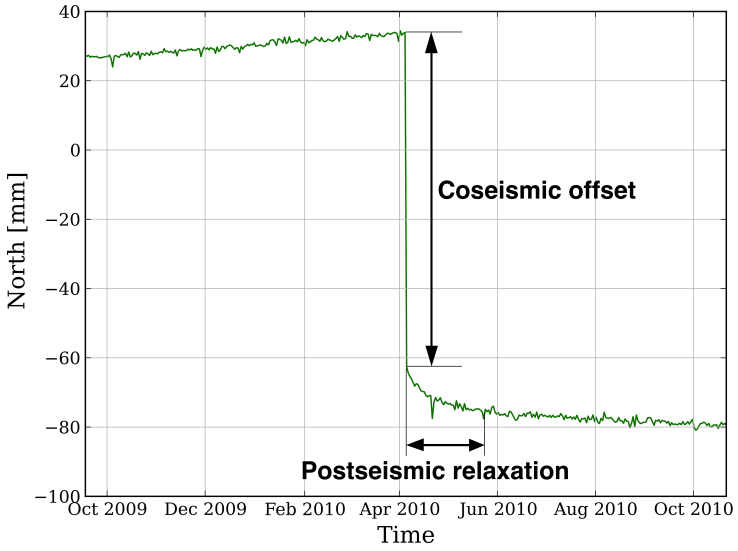

Figure 8.1 – Northing displacements between 15th September 2009 and 22nd October 2010 at station P497 (*green line*). These displacements were supplied by UNAVCO.

To obtain an estimate of the 'true' coseismic offset using such a dataset, one could estimate it simply by subtracting the position given on the day after the earthquake from the position calculated for the day before the earthquake. However, for the best possible estimate of the coseismic offset, a method has been devised that makes use of a time series of daily positions spanning a period of several weeks or months.

For example, figure 8.1 shows the daily position records (northing only) provided by UNAVCO of PBO station P497 over a period of 400 days spanning the date of the El Mayor–Cucapah earthquake. According to the data provided, station P497 moved south by 9.6 cm between 3rd and 5th April 2010 (with an estimated standard deviation of $\sqrt{1.27^2 + 1.86^2} = 2.25$ mm). However, the station then continued to move southwards, but at a decreasing velocity as time passed. Initially this was around 1 mm per day, but after about 50 days, this slowed to what appears to be a constant velocity of about 0.8 mm per month. This is an example of *post-seismic motion*, *deformation* or *relaxation*. This is a transient motion of the ground that can occur and is caused by the change of stresses within the lithosphere following the earthquake event (Ryder 2006). Perhaps if the motion implied by the data during this relaxation period was extrapolated backwards in time to the epoch of the earthquake event itself, 22:41 UTC, the coseismic offset might be slightly less than 9.6 cm.

Consider now figure 8.2. This shows the change in northing over the same period of time but for station P486 instead. In this example, the coseismic offset is much smaller. If one took the northing ordinate from the 5th April 2010 and subtracted it from the northing from 3rd April, one would calculate the coseismic offset to be −7.5 mm. Using the standard deviations provided by

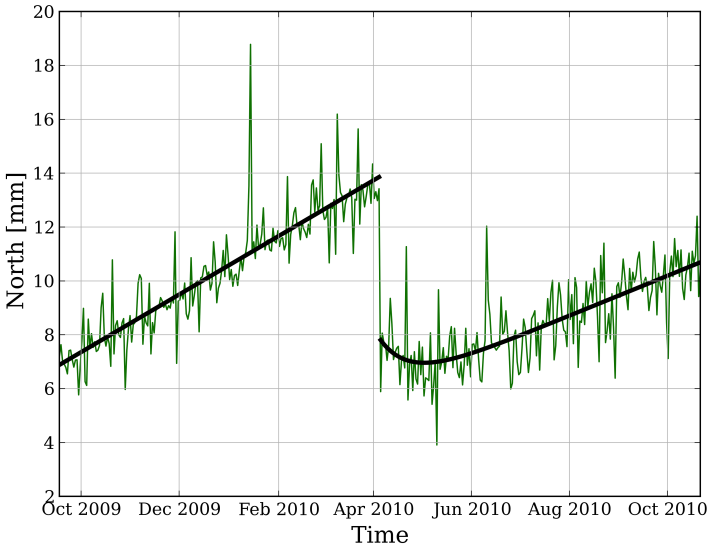

Figure 8.2 – Northing displacements between 15th September 2009 and 22nd October 2010 at station P486 (*green line*). These displacements were supplied by UNAVCO. Also shown are the best-fitting straight line and exponential decay curve used to calculate the easting coseismic displacement on 4th April 2010 (*black lines*).

UNAVCO, this offset would have a standard deviation of 2.6 mm. However, this takes no account of the noise level of the northing values after 5th April and before 3rd April. Also plotted in figure 8.2 are two black lines: one straight line fitted by least squares estimation to the northing values between 3rd April and the preceding 200 days, and a curve of the form $\mathrm{N}(t) = \mathrm{A}e^{\mathrm{B}t} + \mathrm{C}t + \mathrm{D}$ where t is the time in units of days, $\mathrm{N}(t)$ is the northing ordinate in millimetres at time t, and A, B, C, D are real numbers. Such a curve is used by the Institut Géographique National (IGN) to model post-seismic deformation at a number of monitoring stations in their realisation of the International Terrestrial Reference System, ITRF2014 (Altamimi 2016). Indeed, the IGN use logarithmic as well as exponential decay or a combination of the two to model such deformation over periods spanning several years. However, for the experiment described in this chapter, a model based on exponential decay was deemed to be adequate. In the example shown in figure 8.2, a curve is fitted to the northing value on 5th April and the following 200 days. The values, A, B, C, D are found by the iterative process of non-linear least squares estimation. In this case, the curve takes into account the small amount of post-seismic relaxation that occurred in the two months or so following the earthquake. A more precise estimate of the coseismic offset is then found by extrapolating both of these lines to the epoch of the earthquake, yielding a displacement estimate of -5.8 mm rather than -7.5 mm in the north component, and with an estimated standard deviation of less than a millimetre (0.5 mm in this example). The methods used to determine these precise displacements are detailed in appendix D on page 269.

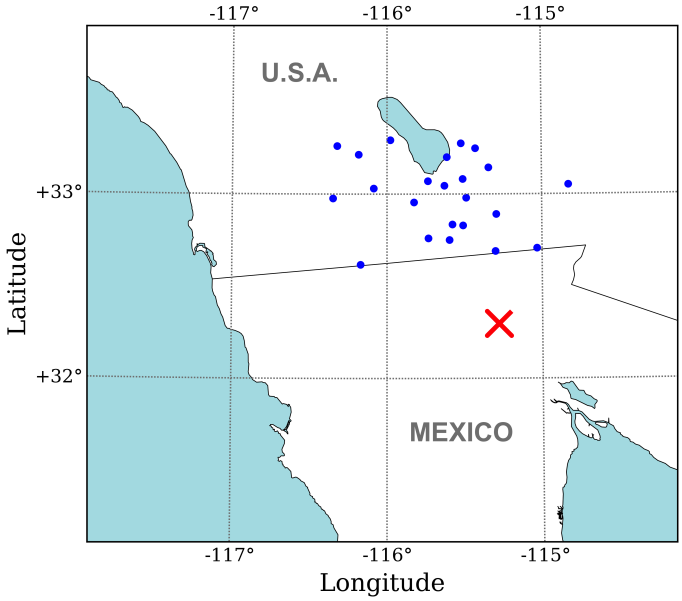

Figure 8.3 – Map showing the locations of the twenty-two PBO monitoring stations (*blue dots*) used in this experiment and the location of the epicentre of the 2010 El Mayor–Cucapah earthquake (*red cross*).

The method described above was used to calculate the 'true' coseismic offset in the easting and northing components for all monitoring stations chosen for this experiment. The height component was ignored because the estimated vertical offsets were often well below 10 mm in magnitude—smaller than their standard deviation and too small to be distinguished from the noise level of the position time series provided by UNAVCO. Twenty-two stations within 150 km of the epicentre were chosen and the location of these are shown in figures 8.3 and 8.4.

Problems were encountered with some of the more distant stations where there was little sign of any post-seismic relaxation. This caused the parameters A, B, C and D, found iteratively by non-linear least squares, to not converge to a solution. Instead, a straight line was fitted to the values for the 200-day period after the earthquake instead of a curve. One such example is shown in figure 8.5. In this example, straight lines were fitted to the easting values at station GLRS over 200-day periods before *and after* the earthquake. There were also problems associated with missing data or other seismic events that prevented the use of all 200 days before or after the earthquake. In such cases, a reduced set of data was selected as appropriate. An example is shown in figure 8.6. In this case, all data after the 14$^{\text{th}}$ June was omitted when calculating the coefficients of the best-fitting exponential decay curve.

The horizontal components of the coseismic offsets calculated by this method are shown in table 8.1 and are also represented by the arrows in figure 8.4. Coseismic offsets calculated using two straight lines, rather than one straight line and one exponential decay curve, are marked in table 8.1 with an asterisk. The values shown in table 8.1 have been rounded to the nearest millimetre. The precise values and estimated standard deviations are shown in table D.1 (page 272).

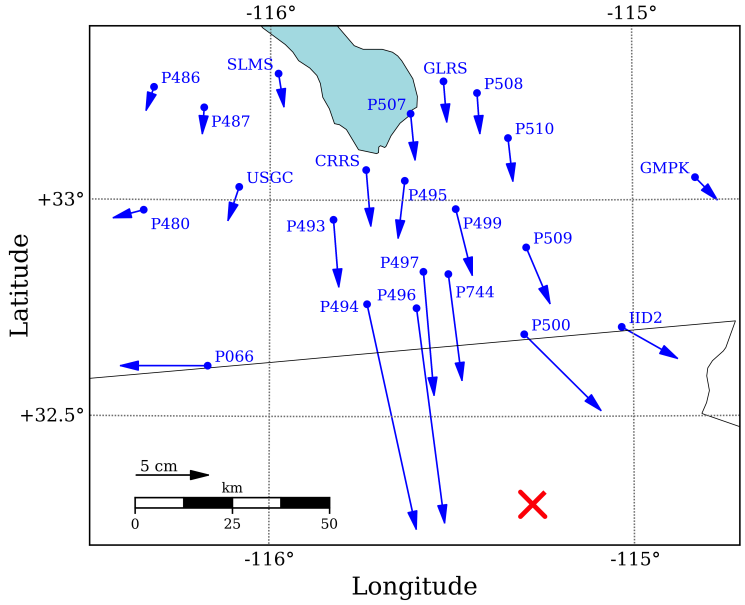

Figure 8.4 – A second map showing the names and locations of the twenty-two PBO monitoring stations (*blue dots*) used in this experiment and the location of the epicentre of the 2010 El Mayor–Cucapah earthquake (*red cross*). The blue arrows illustrate the magnitude and direction of the horizontal coseismic displacements caused by the earthquake calculated using data from UNAVCO.

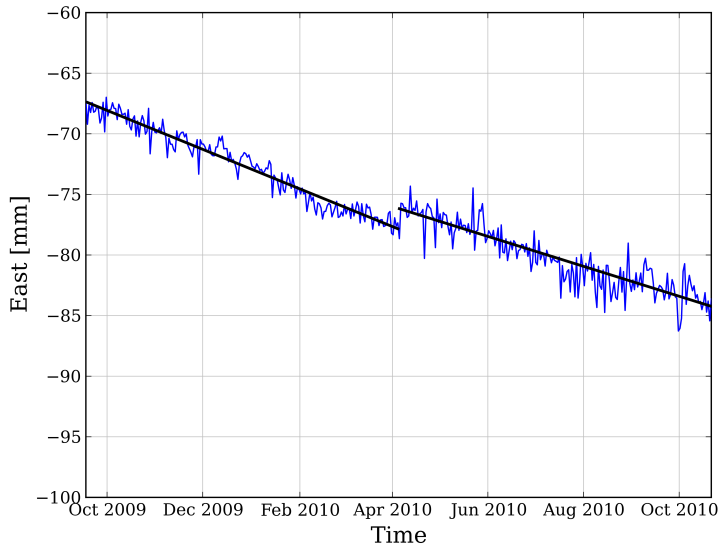

Figure 8.5 – Easting displacements between 15$^{\text{th}}$ September 2009 and 22$^{\text{nd}}$ October 2010 at station GLRS (*blue line*). Also shown are the best-fitting straight lines used to calculate the easting coseismic displacement on 4$^{\text{th}}$ April 2010 (*black lines*).

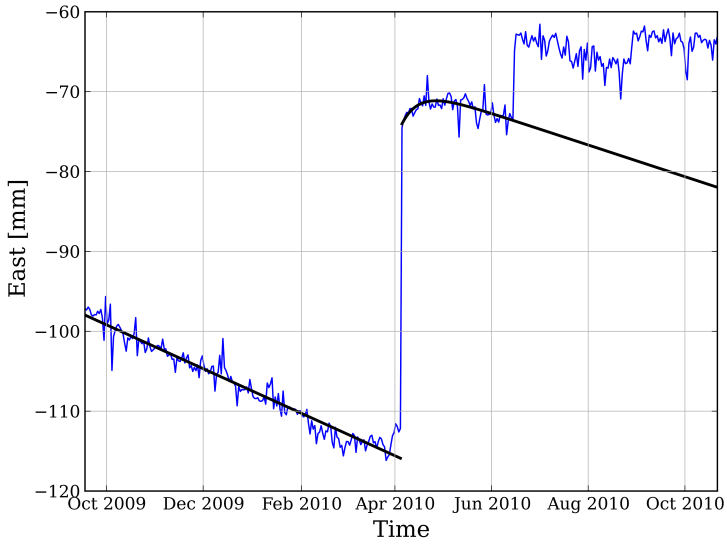

Figure 8.6 – Easting displacements between 15th September 2009 and 22nd October 2010 at station P494 (*blue line*). These displacements were supplied by UNAVCO. Notice the shifts in easting of approximately 10 mm and 4 mm on 15th June and 28th August 2010 respectively. Also shown are the best-fitting straight line and exponential decay curve used to calculate the easting coseismic displacement on 4th April 2010 (*black lines*).

Station ID	Offset (mm)	
	ΔE	ΔN
GMPK	9	−9
P494	42	−191
P495	−4	−37
P496	20	−181
P744	10	−82
SLMS	2⋆	−14
CRRS	3	−35
GLRS	2⋆	−21
IID2	37	−21
P066	−64	0⋆
P480	−12⋆	−3⋆

Station ID	Offset (mm)	
	ΔE	ΔN
P486	−2⋆	−6
P487	−1⋆	−10
P493	4⋆	−45
P497	9	−97
P499	11	−45
P500	59	−59
P507	3⋆	−26
P508	2	−21
P509	15	−36
P510	3	−23
USGC	−5	−15

Table 8.1 – Coseismic displacements in easting (ΔE) and northing (ΔN) associated with the 2010 M_W 7.2 El Mayor–Cucapah earthquake calculated using data from UNAVCO, rounded to the nearest millimetre. Asterisks ⋆ denote displacements calculated by fitting only straight lines to UNAVCO data rather than using an exponential decay curve.

8.3.2 Rapid calculation of coseismic offset

The GPS measurements were post-processed using a similar procedure as first described in section 3.4, i.e. RINEX files containing 24 hours of 1 Hz GPS code and phase measurements were downloaded from the UNAVCO website for each of the monitoring stations listed in table 8.1 for both 3$^{\text{rd}}$ and 4$^{\text{th}}$ April. The measurements contained in each RINEX file were processed using the PPP algorithm as described in section 2.1 using 'final' clocks and orbits from CODE. The GPS measurements from 4$^{\text{th}}$ April were processed two more times: once with the dot product (DP) ODSF applied and once with a PDSF using the algorithms described in section 2.2.

Each of the resulting time series of positions were truncated to the period 22:30–23:00 (GPS system time) on 4$^{\text{th}}$ April spanning the time of the earthquake itself which, according to the United States Geological Survey (USGS), had an origin time of 22:40:43 UTC. Note that at the time of this earthquake, GPS system time was ahead of UTC by 15 seconds.

The method used to estimate a coseismic offset was similar to the technique used in the rooftop experiment of chapter 7: The mean coordinate over a period of time, or 'averaging window', before the earthquake event was subtracted from a mean coordinate over a period of time after the earthquake event. The surface wave arrival time t_0 at each of the monitoring stations was determined by visual inspection of the PPP position time series. This is far from ideal if this algorithm is to be applied in real-time. However, the motivation of this experiment was just to assess the benefit of sidereal filtering in determining an accurate coseismic offset. Besides, an earthquake and tsunami early warning system would use seismometers, not GNSS monitoring stations, to detect the onset of seismic waves, since they are more sensitive to small movements. If GNSS was to be used to detect surface wave arrival in real-time, one possibility would be to apply an algorithm similar to one described in Allen & Ziv (2011). In that study, a long-term averaging window moving forwards in time spanning the previous 100 s is compared to a short-term average spanning the previous 2 s. The arrival time is assumed to be when the short-term average exceeds the long-term average by some chosen amount. A sidereal filter could well reduce the probability of false alarms if applying this method.

As with the previous chapter, many different lengths of averaging window were tested, this time ranging from 10 s to 400 s. However, unlike the rooftop experiment, where the displacement event occurred almost instantaneously, the coseismic offset took some time to manifest itself and was initially obscured by transient surface waves. This was illustrated in figure 1.1 (page 29). For example, consider figure 8.7: This shows the easting component of the 1 Hz displacements at PBO monitoring station P494 spanning a four-minute period during which surface waves arrive from the El Mayor–Cucapah earthquake. The surface waves appear to arrive at approximately 22:41:20. Over the next forty seconds or so, there was some very strong shaking with peak-to-peak amplitudes of tens of centimetres. Between 22:42 and 22:44, the shaking continued, but the amplitude of that shaking subsided significantly. Thereafter, it is clear from the figure that a permanent offset of about 40 mm in easting is present. Indeed, table 8.1 states that this offset is 42 mm. If estimating the value of the offset in real-time, then it would seem wiser to have waited a

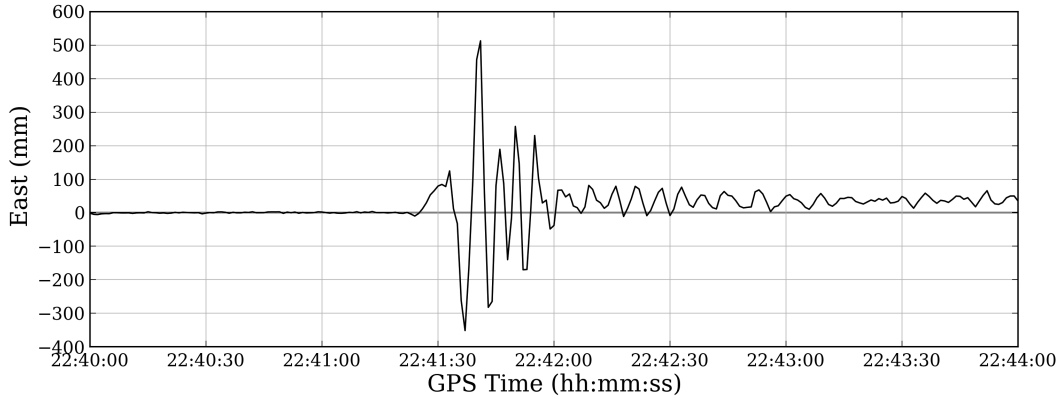

Figure 8.7 – Easting displacements between 22:40 and 22:44 on 4$^{\text{th}}$ April 2010 at station P494 resulting from standard PPP processing.

length of time until the shaking subsided before attempting to estimate any permanent offset via the 'averaging window' method used in chapter 7. Looking back at this example with hindsight, a time of about 40 s would seem to be an appropriate amount of time to wait. This 'waiting time' is shown in red in figure 8.8. The figure also shows how a sidereal filter may help with measuring a more accurate permanent offset by reducing the amplitude of oscillations caused by multipath interference.

So, considering figure 8.8, a 'waiting time' of 70 s after the surface wave arrival time was chosen for all monitoring stations for the sake of simplicity. This waiting time of 70 s was sufficient to allow the amplitude of the surface waves to subside substantially at all of the stations. Also, the smallest averaging window used was 10 s in length. Note that the motivation here is purely to compare the accuracy of the coseismic offsets determined using PPP with and without sidereal filtering, not to determine the optimal wait time, which cannot be determined in real-time. Assuming a 1 Hz position time series and a 'wait' time of w seconds, an estimate of the east component of the coseismic displacement $\widehat{\Delta E}_\alpha$ using an averaging window of length α seconds ($10 \leq \alpha \leq 400$) can be made as follows:

$$\widehat{\Delta E}_\alpha = \bar{E}_{\text{post}} - \bar{E}_{\text{pre}} \tag{8.1}$$

where

$$\bar{E}_{\text{post}} = \frac{E_{w+1} + E_{w+2} + \ldots + E_{w+\alpha}}{\alpha}$$

and

$$\bar{E}_{\text{pre}} = \frac{E_{-1} + E_{-2} + \ldots + E_{-\alpha}}{\alpha}$$

In this case, $w = 70$ and E_n is the easting position n seconds after the surface wave arrival time t_0. The north component is estimated using the same method.

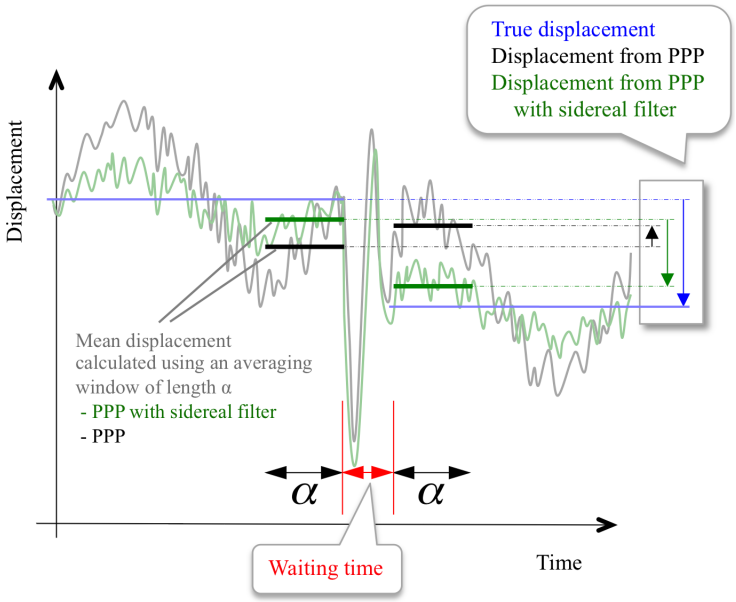

Figure 8.8 – Schematic diagram showing the two averaging windows of length α used to calculate permanent coseismic displacement. These windows are separated in time by a 'waiting time' in order to avoid sampling the highest-amplitude transient displacements in the second averaging window.

8.4 Results and analysis

Figure 8.9 shows the estimates of coseismic offset at station GMPK using averaging windows ranging from 10 s to 400 s in length. The 'true' coseismic offset is shown by the blue horizontal lines. Notice that as the window size increases beyond about 20 s, both of the sidereal filters yield a more accurate estimate of the coseismic offset than regular PPP processing. This is particularly apparent in the northing component where the estimates from sidereal filtering using averaging windows larger than about 50 s are within 2 mm of the true northing displacement while the those from standard PPP can be up to 8 mm from the true value. Note also that the ODSF only yields a more accurate estimate of the northing offset than the PDSF for averaging windows smaller than about 50 s. For the easting component, the PDSF yields a more accurate estimate of the offset than the ODSF for all averaging windows, contrary to the hypothesis.

Similar to the analysis in the previous chapter, the standard deviation of the estimated offsets was calculated for all sizes of averaging window α ($10 \leq \alpha \leq 400$) using equation (8.2). The standard deviation of the estimated offset at station GMPK is shown in figure 8.10. Notice that the sidereal filters improved the precision (as well as the accuracy) of the estimated offsets when using averaging windows larger than about 30 s and 100 s for the east and north components respectively.

$$\sigma_{\widehat{\Delta E}_\alpha} = \sqrt{\frac{1}{\alpha}\sum_{j=1}^{\alpha}(E_{w+j} - \bar{E}_{\text{post}})^2 + \frac{1}{\alpha}\sum_{k=-\alpha}^{-1}(E_k - \bar{E}_{\text{pre}})^2} \tag{8.2}$$

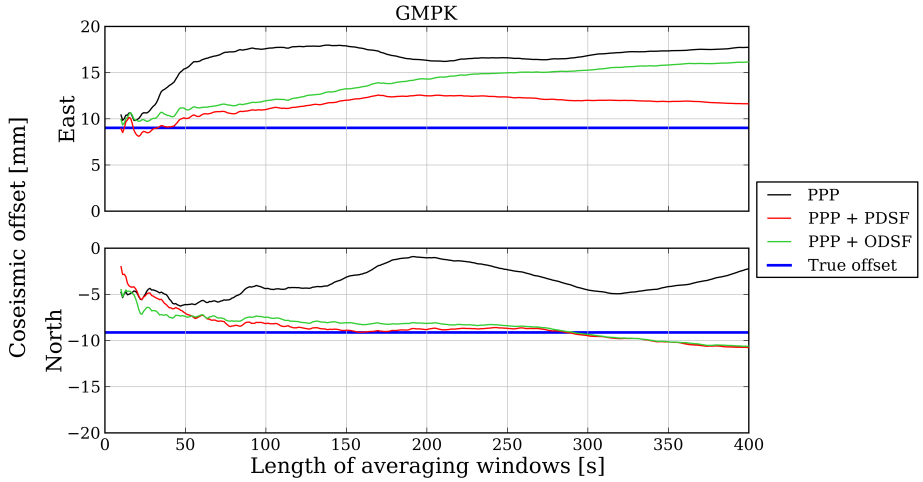

Figure 8.9 – Easting and northing coseismic offsets at PBO station GMPK calculated using different lengths of averaging window. The 'true' value of the offset (calculated using UNAVCO data) is shown by the blue lines.

Figure 8.11 shows the 1 Hz PPP displacements of the GMPK station over a period of sixteen minutes spanning the surface wave arrival time. This figure provides insight into why the accuracy of the estimated offsets generally increased when the sidereal filters were applied. In this case, the surface wave arrival time t_0 was determined to be 22:41:15, and this is shown by the black vertical solid line. The black vertical dashed lines show the extent of the largest averaging windows spanning 400 s, i.e. from left to right, these three lines denote the times $t_0 - 400$ s, $t_0 + 70$ s and $t_0 + 470$ s. It was noted in chapter 3 that the sidereal filters performed particularly well at GMPK, and the same holds true in this sixteen-minute period as well: Both the PDSF and ODSF have clearly reduced the oscillating error visible before and after the earthquake in both dimensions and this explains why better estimates of the coseismic offset follow after applying sidereal filtering, particularly for averaging windows larger than about 50 s. The reason why the PDSF outperforms the ODSF in obtaining a more accurate estimate of the easting offset over longer averaging windows is perhaps because the latter is less effective at removing longer-period multipath error.

The above example was of a case where the sidereal filters generally increased the accuracy of the estimates of coseismic displacement. However, for other monitoring stations, this was certainly not the case. Figure 8.12 shows the estimates of coseismic offset at station P480. Clearly, the sidereal filters have generally *increased* the error of the easting displacement estimates. The time series plots in figure 8.13 show that the sidereal filters have had little, if any, beneficial effect, probably because there is little if any evidence of the characteristic oscillations caused by phase multipath interference anyway.

The two examples above show where the algorithm performs both well (station GMPK) and not so well (station P480). Equivalent plots similar to figures 8.9 and 8.12 for all twenty-two

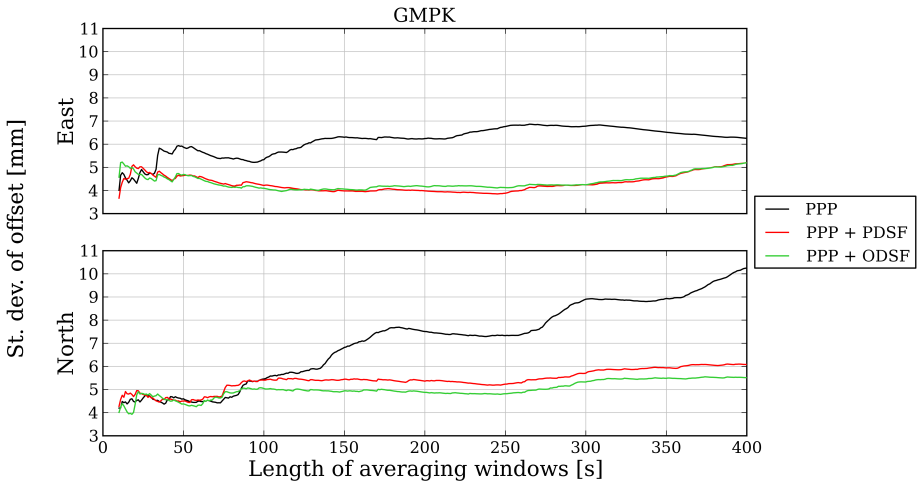

Figure 8.10 – Standard deviation of the easting and northing coseismic offsets at PBO station GMPK calculated using different lengths of averaging window.

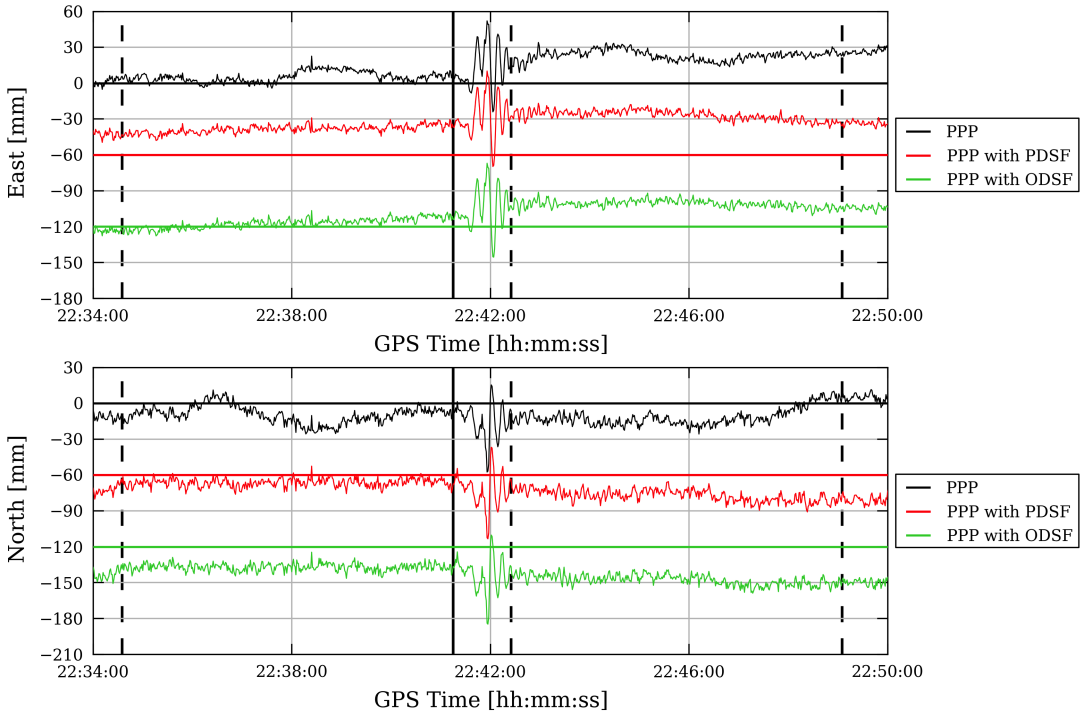

Figure 8.11 – Easting and northing time series between 22:34 and 22:50 GPS time on 4$^{\text{th}}$ April 2010 for receiver GMPK resulting from standard PPP processing and PPP processing with position- and observation-domain sidereal filters applied. The black vertical lines show the surface wave arrival time (solid line) and the extent of the largest averaging windows (dashed lines). The PDSF and ODSF time series have been offset by −60 mm and −120 mm, respectively, for clarity.

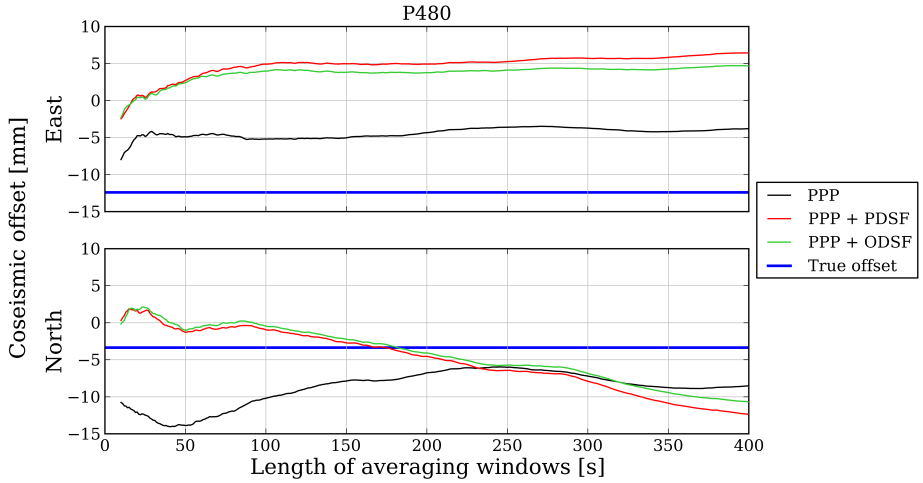

Figure 8.12 – Easting and northing coseismic offsets at PBO station P480 calculated using different lengths of averaging window. The 'true' value of the offset (calculated using UNAVCO data) is shown by the blue lines.

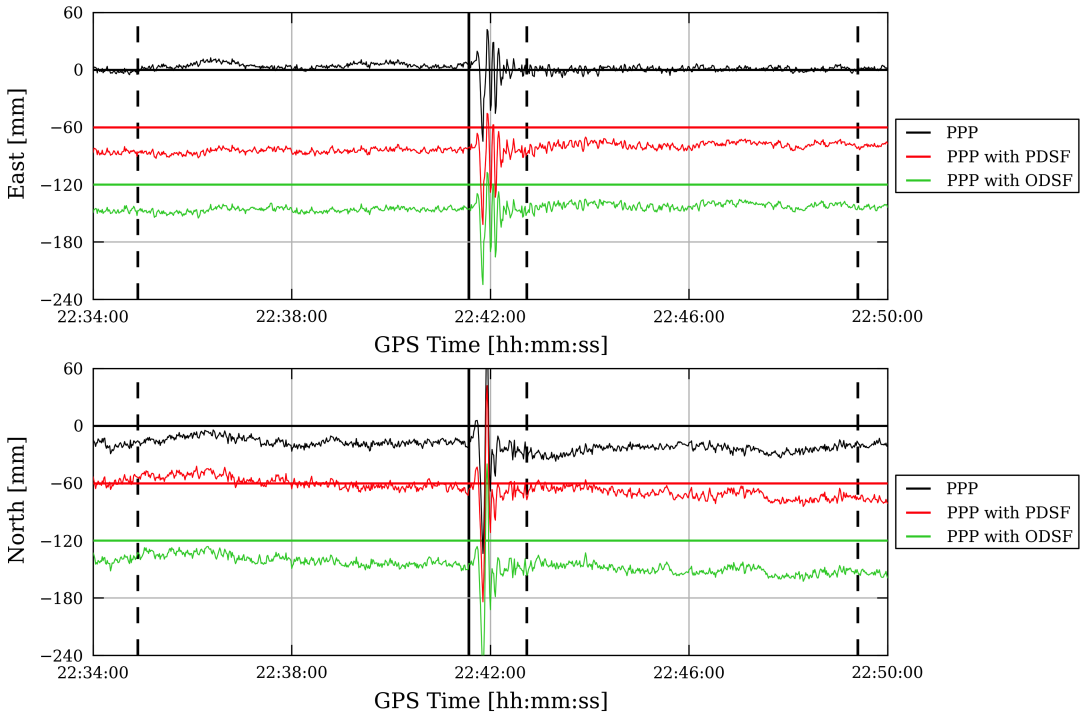

Figure 8.13 – Easting and northing time series between 22:34 and 22:50 GPS time on 4$^{\text{th}}$ April 2010 for receiver P480 resulting from standard PPP processing and PPP processing with position- and observation-domain sidereal filters applied. The black vertical lines show the surface wave arrival time (solid line) and the extent of the largest averaging windows (dashed lines). The PDSF and ODSF time series have been offset by −60 mm and −120 mm, respectively, for clarity.

monitoring stations are shown in figures E.65 to E.72 (pages 338 to 345). From these plots it can be seen that the performance of the technique used to determine coseismic offset across each of the stations was highly variable. One reason for this could be that many of the stations were not affected by strong multipath signals around the time of the earthquake. Another reason could be that the 'true' coseismic offsets derived from daily position calculations by the PBO shown in table 8.1 are not sufficiently accurate. Both of these reasons are discussed further in section 8.5.

The standard deviation of each estimated offset at all 22 stations is shown in figures E.73 to E.80 on pages 346 to 353. Notice that the sidereal filters do not necessarily improve precision. Again, one reason for this could be that many of the stations were not affected by strong multipath signals around the time of the earthquake and so applying a sidereal filter merely increases noise. Also, for many of the stations, the standard deviation of the offsets calculated using shorter averaging windows amounted to several centimetres. This rendered any increase or decrease in accuracy due to sidereal filtering insignificant. This is because, even after waiting 70 s for the amplitude of the seismic waves to subside substantially, ground oscillations tend to continue for several minutes. Such oscillations can clearly be seen at station P494 in figure 8.7.

A similar method to that used in chapter 7 was used to determine if the sidereal filters had *on average* a beneficial effect in estimating the value of each of the displacements: For each size of averaging window (from 10 s to 400 s), the absolute error of the offset estimated using that averaging window is found for each station. A *mean absolute error* can then be calculated, i.e. considering the 22 stations used in this experiment, the *mean absolute error* of all estimates of coseismic offset calculated using an averaging window of size α, $\bar{e}_{\widehat{\Delta E}_\alpha}$, can be calculated as follows:

$$\bar{e}_{\widehat{\Delta E}_\alpha} = \frac{1}{22}\sum_{i=1}^{22} |\widehat{\Delta E}_{i,\alpha} - \Delta E_i| \tag{8.3}$$

where ΔE_i denotes the 'true' value off the coseismic displacement at station i shown in table 8.1 and $\widehat{\Delta E}_{i,\alpha}$ is the value of ΔE_i estimated using averaging windows of length α.

Figure 8.14 shows the mean absolute error of all the estimates of coseismic offset for all averaging windows between 10 s and 400 s in length. For the horizontal components, the sidereal filters have actually decreased the overall accuracy of the calculated offsets, particularly for averaging windows longer than about 50 s in the east component and about 120 s in the north component, albeit by no more than 2 mm. For shorter windows, the sidereal filters make hardly any difference compared to the horizontal offsets calculated using standard PPP data. However, any decrease in accuracy due to the use of sidereal filters is insignificant when considering the standard deviations of the estimated offsets shown in figures E.73 to E.80 which in nearly all cases far exceeds 2 mm.

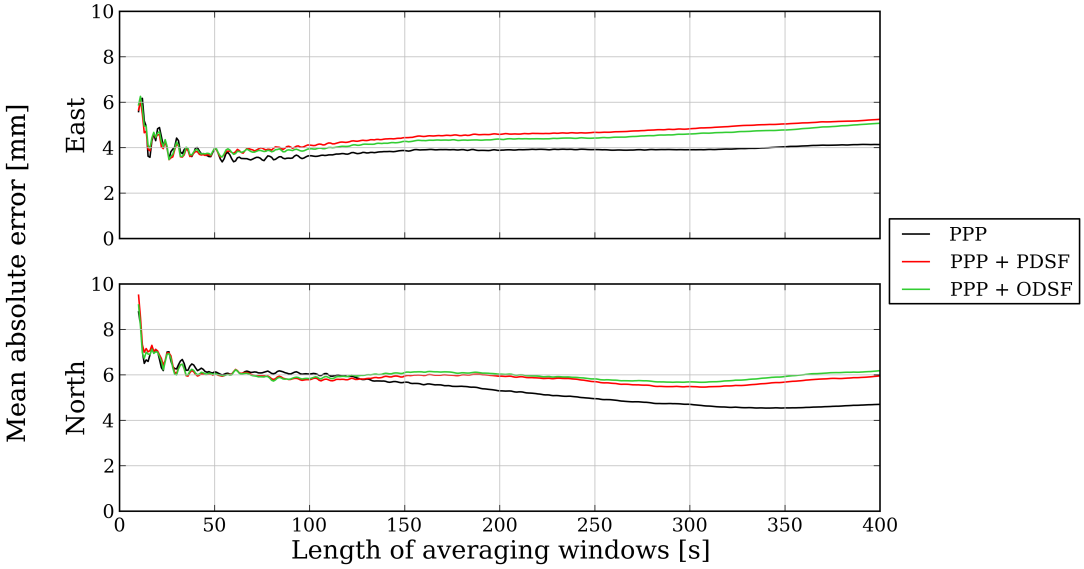

Figure 8.14 – Mean absolute error in easting and northing of all the estimates of coseismic offset for all averaging windows between 10 s and 400 s in length.

8.5 Conclusions

From the above results, it is apparent that sidereal filters do not necessarily improve the accuracy of the calculated coseismic displacements. Indeed, on average, the sidereal filters have been shown to slightly increase errors in the horizontal components (if using averaging windows larger than about 100 s). However, this increase in error is insignificant when considering the estimated precision of the measured displacements. In some cases, the sidereal filters have worked quite well, such as at GMPK and SLMS, but there a number of instances where the effect of the sidereal filters has not been beneficial, such as at P480, P495 and GLRS. Nevertheless, the results of this trial do not support the hypothesis, i.e. it is apparent that applying either type of sidereal filter does *not* generally lead to a more accurate and timely estimate of the coseismic offset. This is contrary to the result in the previous chapter which found that the sidereal filters did *on average* improve the accuracy of the measurement of small displacements.

It has been mentioned that one possible reason for this is that the monitoring stations chosen for this experiment were not generally affected by strong multipath interference at the time of the earthquake itself. The location of the antennas were intentionally chosen to be away from nearby buildings. Other sources of error, such as mis-modelling of the satellite clock, or error in the estimation of the receiver clock offset, may have had more of an impact. As the length of the averaging window increases, any higher-frequency position oscillations caused by phase multipath interference are 'averaged out' by the averaging window anyway, reducing any potential benefit from sidereal filtering in this regard. Therefore, the benefit of sidereal filtering would be more noticeable for short averaging windows if strong high-frequency multipath interference was

present. Presumably, reasonable steps have been taken by UNAVCO to carefully site the stations so as to minimise the occurrence of near-field and mid-field reflectors that might cause longer-period oscillations. Hence, any benefit from using sidereal filters may be minimal if considering longer averaging windows.

Another likely explanation could be that the accuracy of the 'truth' model used in this experiment is not necessarily accurate to the millimetre! The technique described in section 8.3.1 is still considered to be more accurate than simply subtracting the position stated by UNAVCO on the day before the earthquake from the stated position after the earthquake, and so forming a truth model, accurate to just a few millimetres, seemed reasonable if a little ambitious. Perhaps extrapolating the daily position time series from UNAVCO to estimate the coseismic displacement by fitting an exponential decay curve was an over-simplification the displacement process.

However, these results do not necessarily mean that sidereal filtering cannot improve the rapid measurement of coseismic displacements. It would be desirable to conduct the same experiment with similar datasets for other earthquakes, especially larger earthquakes which can cause permanent displacements at the centimetre level at epicentral distances of a few hundred kilometres. Also, it would be useful to analyse GPS data sourced from a number of receivers that form part of existing RTK (Real-Time Kinematic) networks. These receivers may not necessarily be sited or equipped optimally (e.g. some may be equipped with antennas without choke-rings and sited on rooftops in urban areas) and so multipath interference is more likely to occur. In these areas, the sidereal filter algorithms may have more of a beneficial effect. Indeed, measurements from stations UCL and UEL, both part of Leica Geosystem's 'SmartNet' RTK network in the United Kingdom, have been used extensively in this thesis, and the sidereal filters, particularly at station UEL, have been shown to work well. However, a wider analysis across a large number of existing continuously operating receiver stations (CORS) in an area where there is higher seismic activity, such as the TUSAGA-Aktif RTK network in Turkey, would be desirable. Aside from measuring permanent coseismic displacements, sidereal filtering may help with the measurement of *transient* displacements caused by seismic waves, which is the subject of the next chapter.

Chapter 9

The Detection of Surface Waves

9.1 Chapter overview

This chapter aims to show how effective an observation-domain sidereal filter (ODSF) is at separating the centimetre-level oscillations caused by multipath interference from the true surface wave oscillations caused by a real seismic event in GPS PPP position time series. By coincidence, both can occur with amplitudes of a few centimetres and periods of tens of seconds. This chapter begins by describing the phenomenon of surface waves including a brief overview of how they can be used to calculate the magnitude of an earthquake. There then follows a qualitative analysis of PPP position time series spanning a period of an hour following the onset of the 2011 moment magnitude (M_{W}) 9.0 Tohoku-Oki earthquake that occurred off the coast of Japan. This case study demonstrates how the sidereal filters aid the visual identification of two types of surface wave: Love waves and Rayleigh waves.

9.2 Introduction

Much of the energy released by an earthquake is in the form of seismic waves. There are two different types of seismic wave: *body waves* and *surface waves*. Body waves pass through the interior of the earth as an expanding sphere (Yeats 2012) and can be sub-divided into two types: compressional primary waves (P-waves) and secondary waves (S-waves), sometimes known as 'shear waves'. P-waves travel at a velocity dependent on the medium they are travelling through, but this is roughly 5–6 km/s in the upper crust and about 8 km/s in the upper mantle. S-waves travel at about 60% of the P-wave velocity (Doyle 1995). In contrast, surface waves travel along the surface of the earth and are slower. These waves can themselves be sub-divided into two types: Love waves and Rayleigh waves. The nature of their propagation is illustrated in figure 9.1. Love waves travel slightly faster than Rayleigh waves and are the more destructive of the two: the horizontal shaking being particularly harmful to building foundations (Bolt 2006).

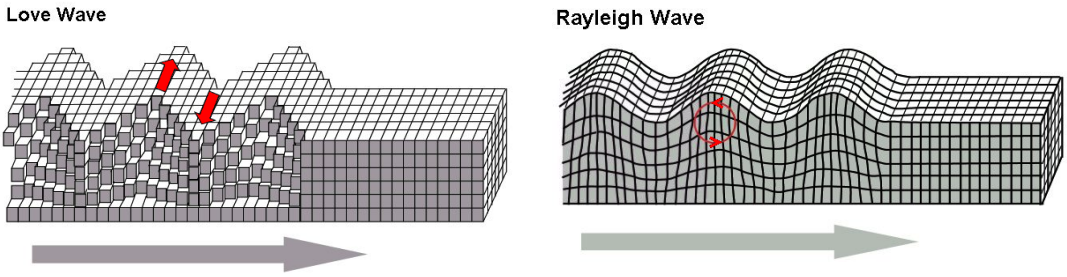

Figure 9.1 – Two diagrams showing the nature of the propagation of two types of surface wave. Note that, for a Love wave, the motion of the ground is perpendicular or *transverse* to the direction of propagation. (Public domain images courtesy of Wikipedia.org).

The amplitude of surface waves that have periods of about 20 s can in fact be used to estimate the size of an earthquake: Surface wave magnitude (M_S) can be estimated using the following formula (Doyle 1995):

$$M_S = \log_{10}\left(\frac{A}{T}\right) + 1.66\log_{10} D + 3.30 \tag{9.1}$$

where: A is maximum vertical amplitude of the ground motion (μm).
T is the period of the motion (18–22 s).
D is the angle between the earthquake epicentre and the location of the measurement of the surface wave subtended at the centre of the earth (degrees).

However, this method under-estimates the size of very large earthquakes (above about M_S 8) because such events radiate much more long-period energy. Hence, using surface wave magnitude is unsuited to tsunami early warning: The moment magnitude (M_W) scale is used to determine the magnitude of such earthquakes. However, surface wave magnitude is still valid for smaller earthquakes (Doyle 1995). Bear in mind that it is possible for phase multipath interference to cause positioning errors that oscillate with a period of about 20 s. Indeed, a 22 s-period oscillation caused by multipath interference was identified at station UCL (see figure 5.7, page 157).

Seismometers can measure both the amplitude and period of the displacements caused by seismic waves, but the double-integration of acceleration data is necessary for the former (or single-integration in the case of velocity output). As discussed in section 1.2.1, such integration can lead to biases in displacement measurements, particularly if the instrument is tilted or rotated, potentially leading to error in the calculation of M_S. By using a GNSS such as GPS, this problem is avoided since displacement is measured directly (and is capable of doing so in near-real-time) and it is immune to the effects of tilting. However, as discussed in section 1.2.2, there are disadvantages associated with the use of GNSS, i.e. that measurements are not as precise as seismometer measurements and that GNSS is affected by a number of other error sources including multipath interference. Phase multipath errors can occur at similar amplitudes and frequencies to surface waves (Larson et al. 2007). Such errors thus have the potential to be misinterpreted as seismic

waves and vice versa thus raising the possibility of false alarms and missed detections. These are unlikely if a GNSS receiver forms part of a network that combines GNSS measurements and seismometry such as the Real-time Earthquake Analysis for Disaster Mitigation Network (READI) in the United States (Sopac.ucsd.edu 2015). Nevertheless, the mitigation of multipath error is desirable if the detection or measurement of surface waves by GNSS is desired.

As has been seen in previous chapters, the effect of multipath interference can be reduced by applying a sidereal filter. In the context of earthquakes, sidereal filtering has an advantage over other filtering techniques, such as band-pass filtering, in that multipath error is reduced while seismic signals are left untouched, assuming that the environment surrounding the antenna remains unchanged. In other words, sidereal filtering can separate the true transient displacements associated with seismic activity from errors caused by phase multipath interference despite their overlapping frequency spectrums. Bilich, Cassidy & Larson (2008) showed that a sidereal filter could reduce the noise floor (i.e. increase the sensitivity) of GPS position time series enabling the identification of small oscillations of ±2–3 cm with periods of around 17–22 s associated with the 2002 M_W 7.9 Denali fault earthquake in Alaska. In that particular study, it was a position-domain sidereal filter (PDSF) that was applied. In contrast, this chapter examines whether this can be achieved using an observation-domain sidereal filter (ODSF) within the context of high-rate PPP processing.

9.3 Hypothesis

Processing GPS measurements using the PPP method allows the application of the ODSF algorithm as described in section 2.2. It was observed in chapters 3 and 5 that in processing GPS measurements, an ODSF *generally* outperforms a PDSF in removing higher-frequency multipath errors. Since these errors have the potential to obscure small-amplitude seismic waves, such as Love and Rayleigh waves, it is predicted that the application of an ODSF, rather than a PDSF, will be more effective at enhancing the ability to visually identify such signals in the resulting PPP time series.

9.4 Method

The M_W 9.0 Tohoku-Oki earthquake occurred on 11th March 2011 at 05:46 UTC approximately 70 km off the east coast of Japan. The size of the slip at the fault itself was estimated to be as high as 80 m (Ito et al. 2011). The Tohoku earthquake was selected for this study for two reasons: Firstly, because it was sufficiently large to produce surface waves that were likely to be detected many thousands of kilometres from the epicentre and, secondly, because of the wealth of archived GNSS and seismometry data available. The aim of this exercise is not to estimate the magnitude of the earthquake using surface waves via equation (9.1). As mentioned in section 9.2, using surface wave amplitude to measure earthquake magnitude will under-estimate the size of

Station ID		Antenna	Receiver	Epicentral distance
AV24	⋆	Trimble TRM59800.00 choke-ring	Trimble NETRS	4,322 km
AV27	⋆⋆	Trimble TRM59800.00 choke-ring	Trimble NETRS	4,324 km
AV16	⋆	Trimble TRM29659.00 choke-ring	Trimble NETRS	5,008 km
AV02	⋆⋆	Trimble TRM29659.00 choke-ring	Trimble NETRS	5,014 km
AB50	⋆ ⋆⋆	Trimble TRM29659.00 choke-ring	Trimble NETRS	6,102 km
NEAH	⋆	Ashtech ASH700936A_M choke-ring	Trimble NETRS	7,157 km
P403	⋆⋆	Trimble TRM29659.00 choke-ring	Trimble NETRS	7,201 km
P213	⋆	Trimble TRM29659.00 choke-ring	Trimble NETRS	7,996 km
P226	⋆⋆	Trimble TRM59800.00 choke-ring	Trimble NETRS	7,999 km
P728	⋆	Trimble TRM29659.00 choke-ring	Trimble NETRS	8,895 km
P029	⋆⋆	Trimble TRM29659.00 choke-ring	Trimble NETRS	8,907 km
P775	⋆	Trimble TRM59800.00 choke-ring	Trimble NETRS	9,945 km
P777	⋆⋆	Trimble TRM29659.00 choke-ring	Trimble NETRS	10,059 km

Table 9.1 – Names, antenna types, receiver types and epicentral distances of all UNAVCO PBO monitoring stations used for the detection of surface waves. In this chapter, the PBO stations are divided into two groups marked with single and double asterisks, ⋆ and ⋆⋆, for convenience.

earthquakes above about M_W 8. Rather, emphasis is placed on a qualitative assessment of the PPP position time series based on the ability to visually identify seismic waves, particularly Love and Rayleigh waves.

A number of UNAVCO PBO monitoring stations with widely varying distances from the epicentre, ranging from around 4,322 km to 10,059 km, were selected for this exercise. These are listed in table 9.1 and their locations shown on the map in figure 9.2. Notice that, with the exception of station AB50, *pairs* of monitoring stations where chosen at roughly every 1,000 km increase in epicentral distance. In table 9.1, the first and second of each pair of stations are marked with single and double asterisks, ⋆ and ⋆⋆, respectively. Notice that station AB50 is a member of both groups because it is not paired with a second station. These stations were chosen to aid the identification of surface waves in the resulting position time series: Firstly, the transient ground displacements caused by a surface wave emanating from a distant earthquake are more likely to be very similar to each other and occur at similar times at two stations if they are within a few kilometres of each other. The second reason will become clear when examining figure 9.9 and other similar figures: By plotting time series of displacements from multiple stations on one pair of axes, with each offset on the vertical axis in proportion to their epicentral distances, one can identify surface waves by virtue of their differing arrival times. It would otherwise be difficult to identify surface waves with much confidence. As shown in table 9.1, all of these monitoring stations were equipped with a choke-ring antenna.

The displacement time series were also compared with seismometer data made available by the Incorporated Research Institutions for Seismology (IRIS). Ideally, data would have been sourced from seismometers co-located with UNAVCO GPS monitoring stations. In fact, finding archived

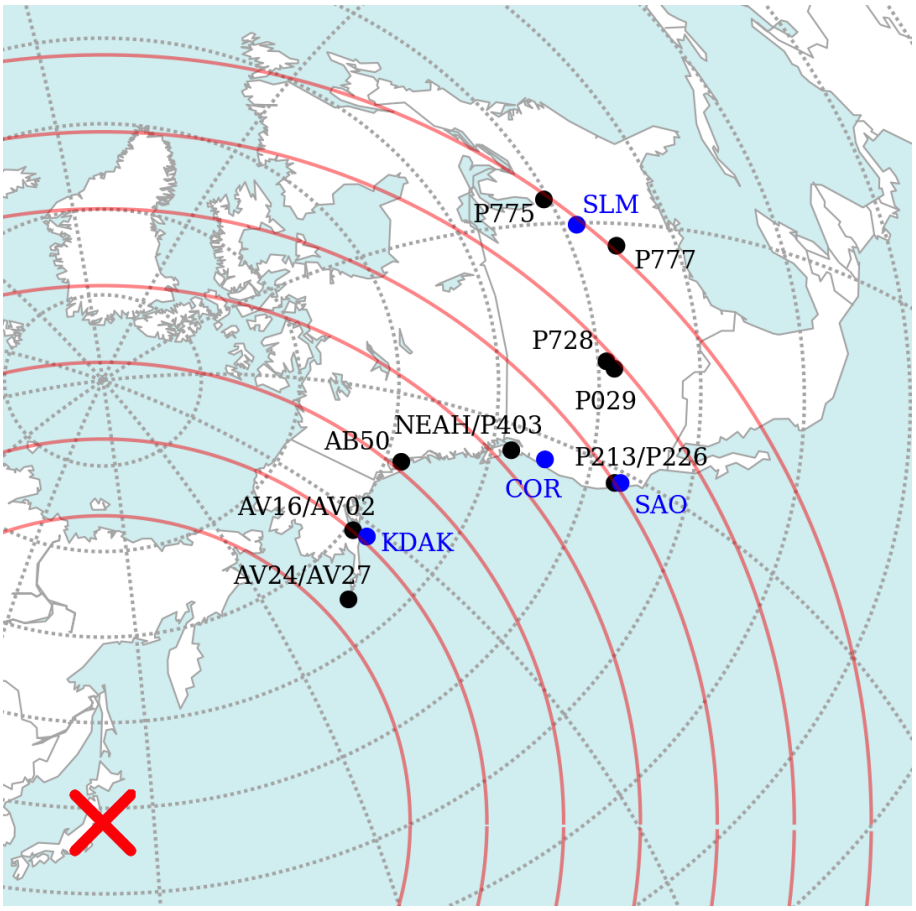

Figure 9.2 – Map showing the location of each of the UNAVCO PBO monitoring stations (*black*) and IRIS broadband seismometer stations (*blue*). The red cross indicates the epicentre of the 2010 M_W 9.0 Tohoku-Oki earthquake. The red circles indicate epicentral distances of 4000, 5000, ... , 10000 km.

Station ID	Seismometer model	Location	Epicentral distance
KDAK	Geotech KS-54000	Kodiak Island, AK, USA	5,072 km
COR	Streckeisen STS-1VBB	Corvallis, OR, USA	7,453 km
SAO	Streckeisen STS-1VBB	San Juan Bautista, CA, USA	8,063 km
SLM	Trillium 120 768	St Louis, MO, USA	9,937 km

Table 9.2 – Names, locations and epicentral distances of all IRIS PBO broadband seismometer stations used for the detection of surface waves.

data from broadband seismometers even within a 100 km radius of the chosen GPS monitoring stations proved to be difficult. Four broadband seismometers were selected, and their locations are shown in figure 9.2 and their epicentral distances in table 9.2. Notice that stations KDAK, SAO and SLM have similar epicentral distances to UNAVCO stations AV02/AV16, P213/P226 and P775/P777, respectively. Three-axis displacement data (velocity data integrated by IRIS) were downloaded via the IRIS Web Services website[1] covering the period 05:45–06:45 UTC. The mean displacement was subtracted from the data and a high-pass filter of 0.001 Hz was applied to filter out most of the non-seismic slowly-varying biases.

GPS measurements were post-processed using the same procedure as first described in section 3.4, i.e. for each station, RINEX data files containing 24 hours of 1 Hz GPS measurements for the day of the earthquake itself, and the preceding day, were downloaded from the UNAVCO archives. All RINEX files were processed using the PPP method with 'final' orbit and clock data from CODE. Measurements from 11$^{\text{th}}$ March were also processed using the PDSF and dot product (DP) ODSF algorithms described in section 2.2.

As mentioned above, analysis of the resulting displacement time series is based on whether the sidereal filter algorithms enhance the ability to visually identify seismic waves. A quantitative analysis is difficult without the two types of instruments being located in exactly the same place and experiencing the same motion. However, possible quantitative tests are discussed in section 9.7.

9.5 Analysis

9.5.1 Stations AV24 and AV27

Figures 9.3, 9.4 and 9.5 show the 40-minute time series of easting, northing and height displacements, respectively, spanning the period during which the surface waves arrive at stations AV24 and AV27. These stations are separated by only 11 km and have very similar epicentral distances. These plots are very good illustrations of how sidereal filtering, especially in the observation domain, can remove multipath error and yet preserve the transient seismic displacements.

For example, consider the northing time series in figure 9.4. Clearly *both* AV24 and AV27 are signficantly affected by phase multipath interference: At station AV24, notice how effective both of the sidereal filters are at largely removing the oscillating error between 05:45 and 06:00, which could be mistakenly interpreted as seismic waves. Indeed, they reveal much more clearly an apparent surface wave arrival time of about 06:00 with the largest displacements occurring between 06:03 and 06:05. Only the ODSF time series of the nearby station AV27 shows very similar displacements to AV24 between 06:00 and 06:07. One can therefore be more confident that these are close to the true seismic displacements. It is also very apparent that the standard PPP time series (plotted in black and grey) at AV27 are severely affected by strong short-period (approximately 11 s) multipath error. The PDSF was unable to remove such a high-frequency error

[1] http://service.iris.edu/

and instead *increased* the amplitude of these oscillations. The ODSF on the other hand was far more effective because it could take into account the differing repeat times of the satellites.

A similar narrative applies to the vertical component (figure 9.5). The surface waves passing AV24 from around 06:05:30 would have been almost indistinguishable from multipath errors had a sidereal filter not been applied. At AV27, the ODSF was again far more effective than the PDSF at removing the very high-frequency multipath errors. In contrast, the easting component was not greatly affected by multipath error and so the sidereal filters had minimal effect.

9.5.2 Stations AV02, AV16 and KDAK

Similarly, figures 9.6, 9.7 and 9.8 show easting, northing and height PPP displacements, respectively, spanning the same 40-minute period but at stations AV02 and AV16. However, also displayed are displacements from broadband seismometer station KDAK. Although located 180 km and 187 km from AV02 and AV16, respectively, KDAK is only 58 km and 64 km further from the epicentre than AV02 and AV16, respectively. Therefore, although the transient displacements are likely to be similar across all three stations, it would be expected that the seismic waves would arrive slightly later at KDAK. This is indeed the case when carefully examining figure 9.6.

Nevertheless, the displacements derived from the seismometer at KDAK help to visualise how well the sidereal filters perform in helping to reveal the true displacements at AV02 and AV16. They have had some benefit at both stations in all three dimensions, but perhaps most obviously

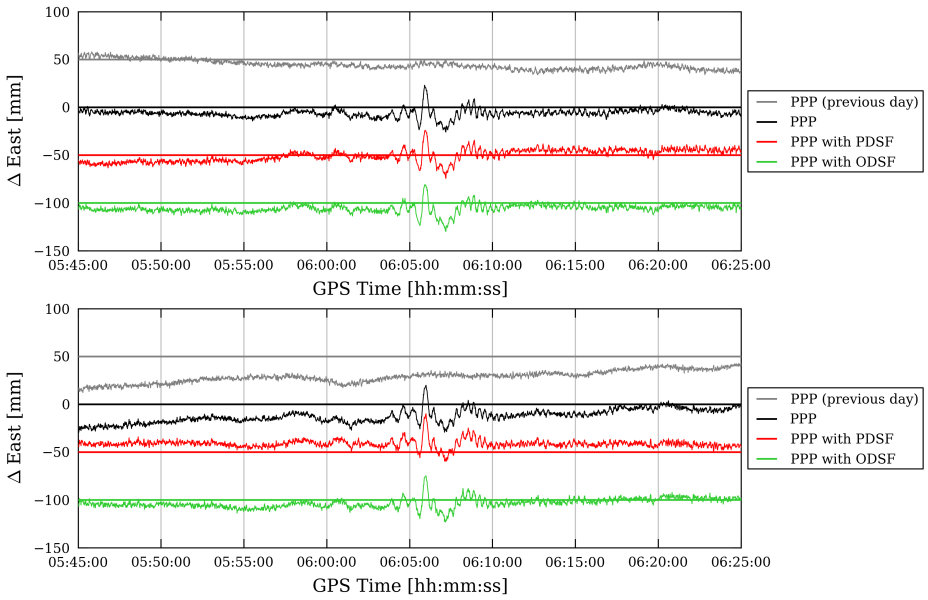

Figure 9.3 – Easting displacements at UNAVCO stations AV24 (*top*) and AV27 (*bottom*) on 11$^{\text{th}}$ March 2011 resulting from standard PPP processing and PPP processing with various types of sidereal filter applied. (Each of the time series have been offset from each other by appropriate multiples of 50 mm for clarity).

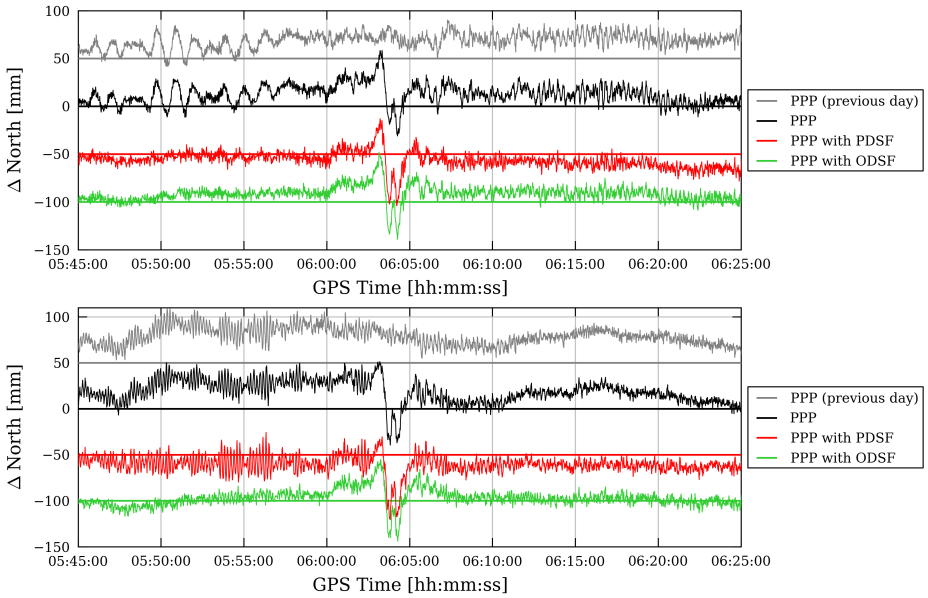

Figure 9.4 – Northing displacements at UNAVCO stations AV24 (*top*) and AV27 (*bottom*) on 11th March 2011 resulting from standard PPP processing and PPP processing with various types of sidereal filter applied. (Each of the time series have been offset from each other by appropriate multiples of 50 mm for clarity).

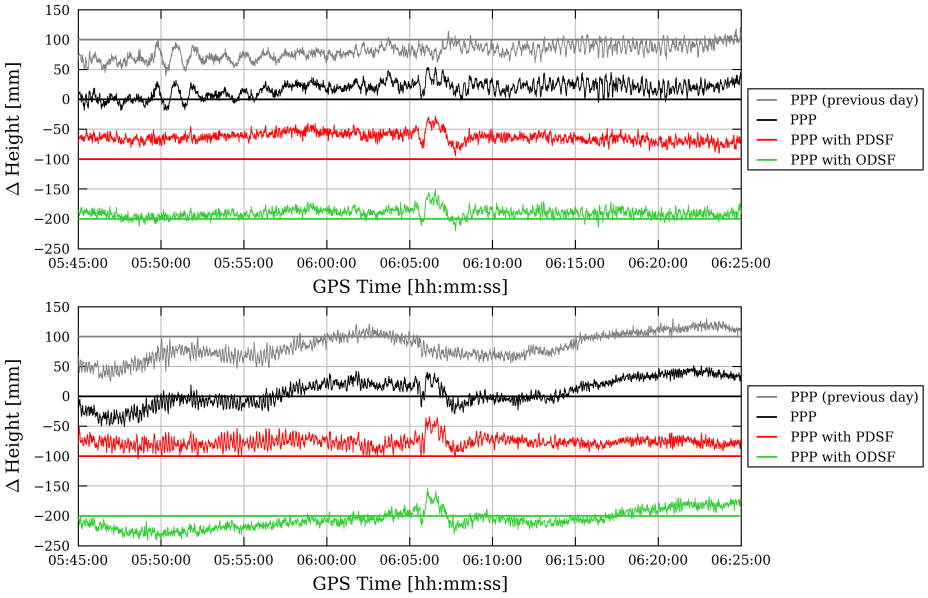

Figure 9.5 – Height displacements at UNAVCO stations AV24 (*top*) and AV27 (*bottom*) on 11th March 2011 resulting from standard PPP processing and PPP processing with various types of sidereal filter applied. (Each of the time series have been offset from each other by appropriate multiples of 100 mm for clarity).

in the northing and height components at AV16: From figure 9.8 (AV16), it can be seen that the sidereal filters have revealed the vertical component of the surface wave between 06:09 and 06:11. This was indistinguishable from the multipath errors present in the standard PPP time series. As a second example, observe the northing time series during the period 05:45–06:07 in figure 9.7 (AV16): Both types of sidereal filter have been very successful at removing the oscillating errors caused by multipath interference. After 06:10, there appear to be oscillations in the north-south direction in the standard PPP time series (black) that could well be interpreted as Love waves (since the north-south direction is perpendicular to the eastward direction of wave propagation at AV16). However, the sidereal filters have largely removed these oscillations, implying that they were caused by multipath interference rather than seismic waves. The frequency of those oscillations, approximately 0.025 Hz, differs from that implied by the seismometer, approximately 0.04 Hz, again implying that they are not caused by the surface waves. The small amplitude of such waves may not be noticeable above the noise of the sidereal filter (red and green) position time series. Indeed, it appears that the amplitude of the largest north-south oscillation measured by the seismometer at KDAK (approximately 170 mm peak-to-peak) is more than double that measured via PPP at AV02 or AV16 (approximately 70 mm peak-to-peak). The cause of this is not known for certain, but it could be due to a scale factor error in the seismometer measurements. Alternatively, it could be because of a difference in the elasticity and rigidity of the underlying bedrock at AV02/AV16 and KDAK.

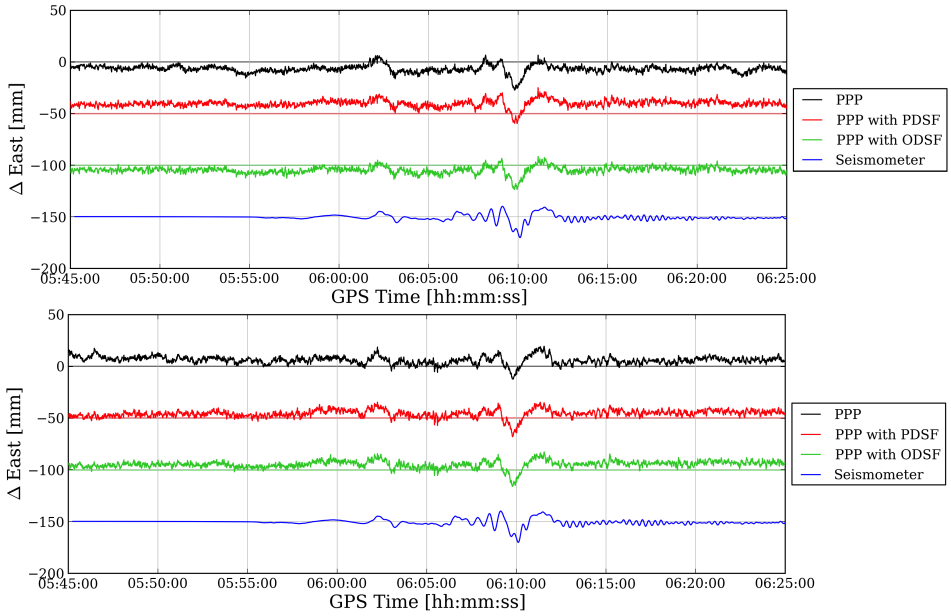

Figure 9.6 – Easting displacements at UNAVCO stations AV02 (*top*) and AV16 (*bottom*) on 11$^{\text{th}}$ March 2011 resulting from standard PPP processing and PPP processing with various types of sidereal filter applied. Also shown are displacements from seismometer station KDAK. (Each of the time series are offset from vertically by appropriate multiples of 50 mm).

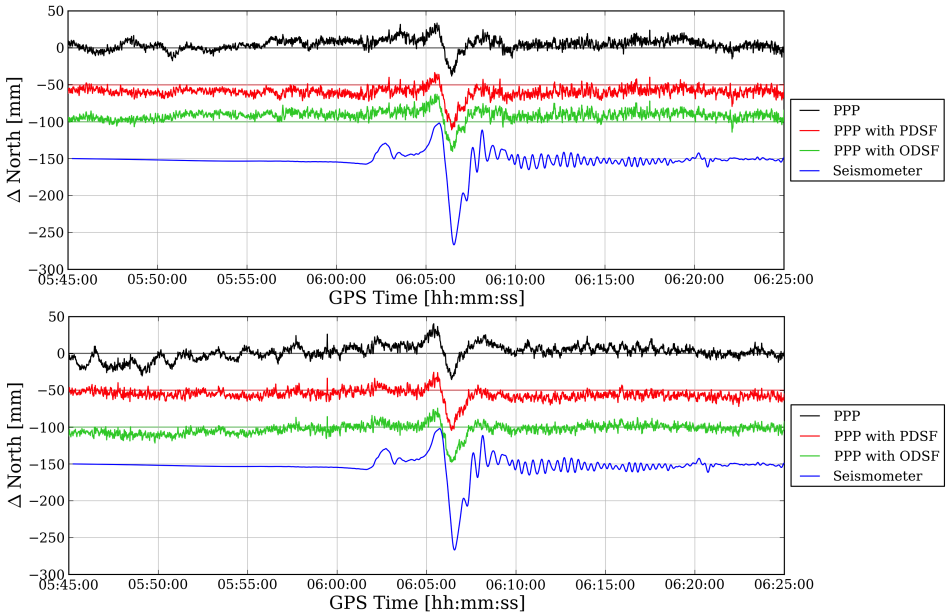

Figure 9.7 – Northing displacements at UNAVCO stations AV02 (*top*) and AV16 (*bottom*) on 11$^{\text{th}}$ March 2011 resulting from standard PPP processing and PPP processing with various types of sidereal filter applied. Also shown are displacements from seismometer station KDAK. (Each of the time series are offset from vertically by appropriate multiples of 50 mm).

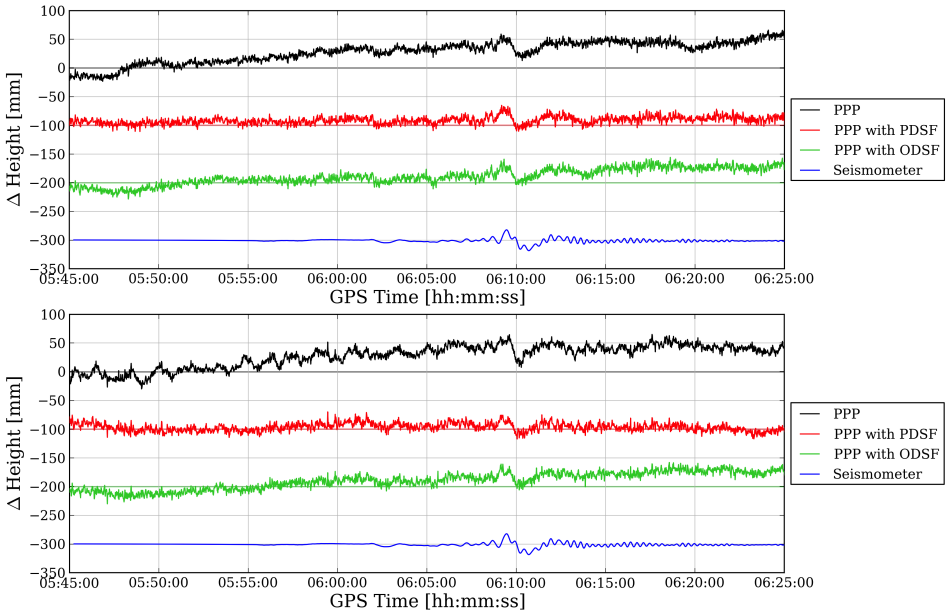

Figure 9.8 – Height displacements at UNAVCO stations AV02 (*top*) and AV16 (*bottom*) on 11$^{\text{th}}$ March 2011 resulting from standard PPP processing and PPP processing with various types of sidereal filter applied. Also shown are displacements from seismometer station KDAK. (Each of the time series are offset from vertically by appropriate multiples of 100 mm).

9.5.3 Detection of Love waves

Further insight is enabled by examining figures 9.9 to 9.27. Figures 9.9 to 9.11 show *transverse* displacements (i.e. horizontal displacements perpendicular to the direction of travel of the seismic waves) at each of the PBO monitoring stations marked in table 9.1 (page 228) with a single asterisk *. The corresponding figures for stations marked with a double asterisk ** are shown in figures 9.12 to 9.14. The division of the PBO monitoring stations into two groups, * and **, is simply to aid the clear presentation of the displacement time series in each of the figures 9.9 to 9.27. Also shown, in blue, are the displacements of the seismometer stations listed in table 9.2. These figures show the horizontal displacements along the axis transverse to the direction of travel of the seismic waves. According to figure 9.1, this is the axis in which Love waves occur. The time series for each station is offset vertically in each figure in proportion to their respective distances from the earthquake epicentre, shown on the right-hand vertical axis. This is in order to aid the visual identification of Love waves from amongst errors caused by, for example, multipath interference. The large-amplitude Love waves should appear roughly along a diagonal line across the plot consistent with the speed of the wave propagation. Identification of Love waves is also aided by the plotting of displacements derived from the seismometer data.

For example: in figure 9.9, the propagation of the large-amplitude Love waves can be identified by eye relatively easily despite the fact that no sidereal filters have been applied. The time at which the largest oscillations occur at each monitoring station imply a Love-wave velocity of *approximately* 4.5 km/s. This is shown as a magenta line. The locations of the magenta lines on these plots have been determined by eye and are for indicative purposes only. The exact surface wave arrival times depend upon the wave velocity which in turn depends upon the elasticity and density of the rock through which the wave is propagating (Bolt 2006). This varies for each station. However, if the PPP time series were each examined in isolation, it would not have been so obvious that these oscillations were indeed Love waves and not a result of some other error such as multipath.

It is apparent, after examining figures 9.9 to 9.11, that both types of sidereal filter perform particularly well at some monitoring stations, but not so well at others. The performance of the sidereal filters at stations AV24 and AV16 have already been discussed in sections 9.5.1 and 9.5.2, respectively. At station NEAH, there appear to be oscillations present in the time series that seem unlikely to be seismic in origin, even after sidereal filtering: For example, there are no corresponding oscillations in the relatively flat time series of seismometer COR in the period 05:45 to 06:06, which is roughly 300 km further from the epicentre. In contrast, at stations P213 and P775, both types of sidereal filter have reduced multipath error to such an extent that even the propagation of another seismic wave can be identified by eye (marked approximately by the yellow line) travelling at around 9 km/s. At these stations, these waves have a peak-to-peak amplitude of only about 1 cm but they are consistent with the displacements from seismometers SAO and SLM, respectively. However, the time of arrival of this possible S-wave at each of those stations is too late to be consistent with an earthquake origin time of 05:46 UTC, assuming simply that the wave velocity was constant. The cause of this wave is not investigated here as it is beyond the scope

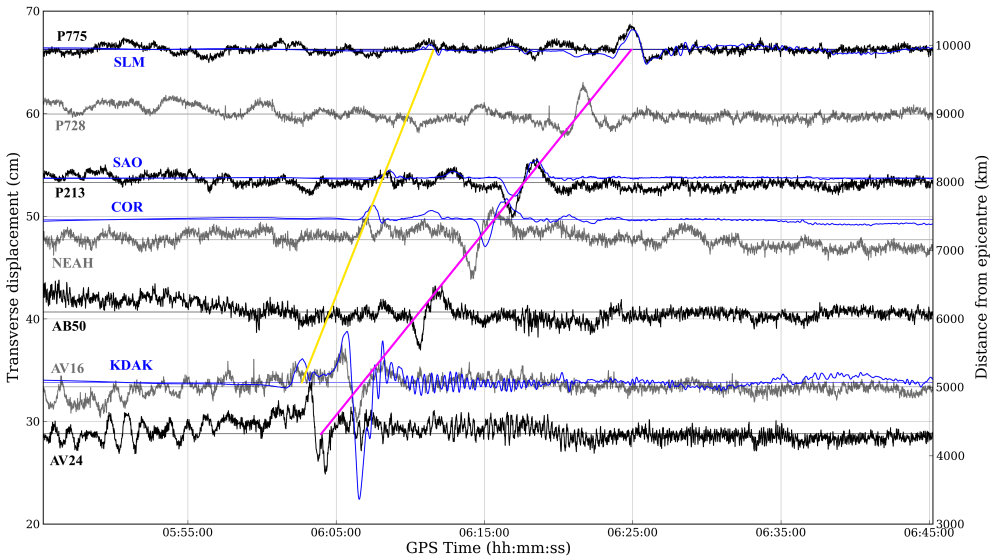

Figure 9.9 – *Black/grey lines*: Transverse displacements resulting from standard PPP processing at all UNAVCO PBO stations marked with a single asterisk ⋆ in table 9.1. *Blue lines*: Transverse displacements derived from integrated velocity data from the IRIS seismometer stations listed in table 9.2. The magenta and yellow lines indicate suspected seismic wave propagation and are referred to in the main text.

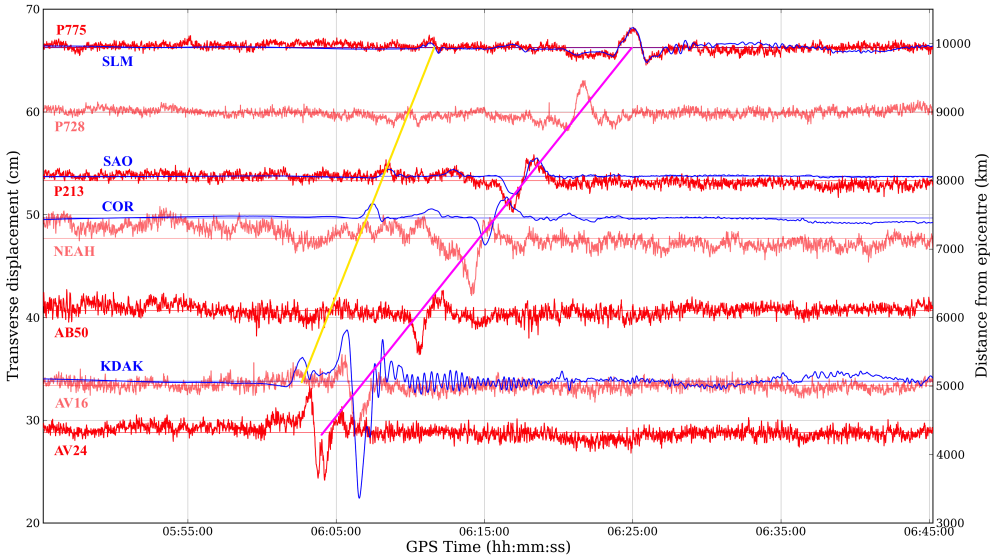

Figure 9.10 – *Red lines*: Transverse displacements resulting from standard PPP processing with a PDSF applied at all UNAVCO PBO stations marked with a single asterisk ⋆ in table 9.1. *Blue lines*: Transverse displacements derived from integrated velocity data from the IRIS seismometer stations listed in table 9.2. The magenta and yellow lines indicate suspected seismic wave propagation and are referred to in the main text.

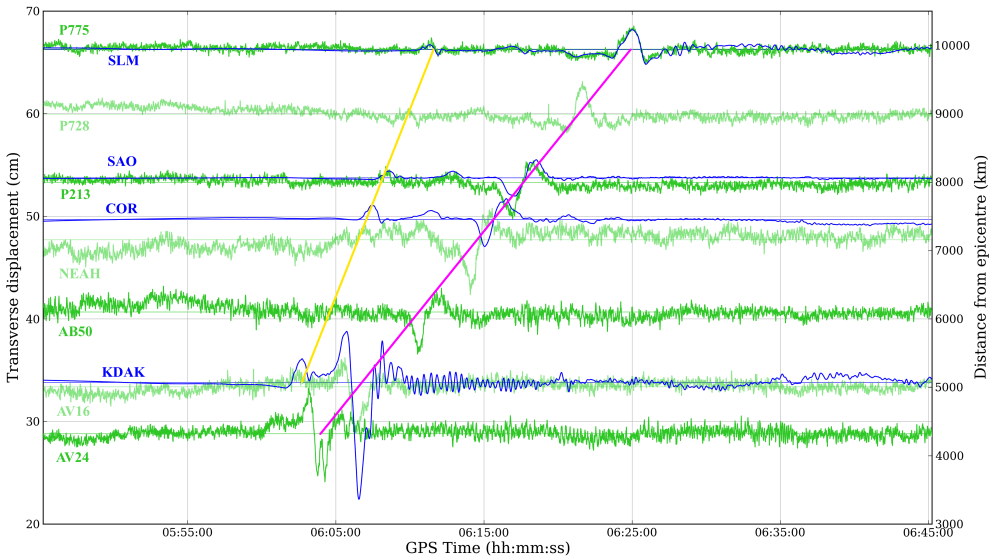

Figure 9.11 – *Green lines*: Transverse displacements resulting from standard PPP processing with an ODSF applied at all UNAVCO PBO stations marked with a single asterisk ⋆ in table 9.1. *Blue lines*: Transverse displacements derived from integrated velocity data from the IRIS seismometer stations listed in table 9.2. The magenta and yellow lines indicate suspected seismic wave propagation and are referred to in the main text.

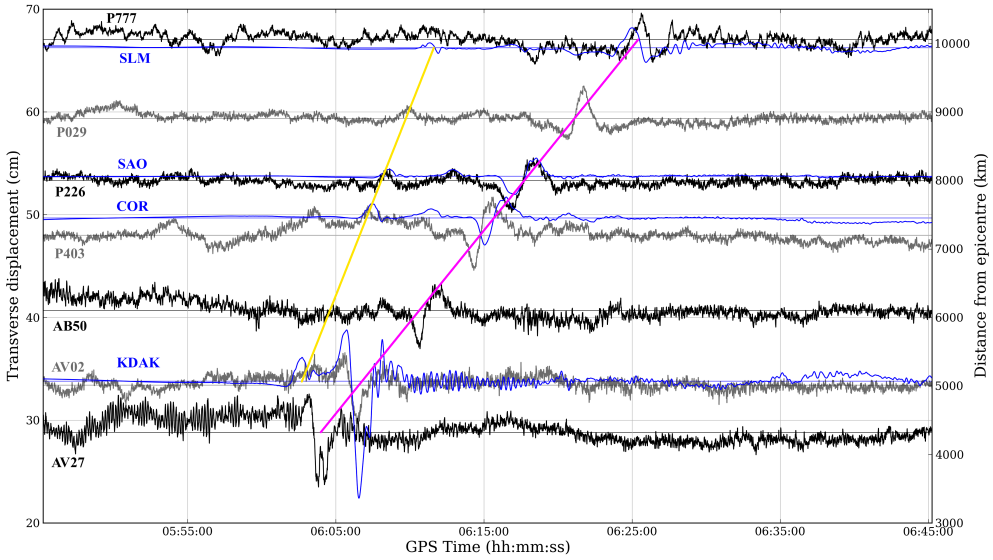

Figure 9.12 – *Black/grey lines*: Transverse displacements resulting from standard PPP processing at all UNAVCO PBO stations marked with two asterisks ⋆⋆ in table 9.1. *Blue lines*: Transverse displacements derived from integrated velocity data from the IRIS seismometer stations listed in table 9.2. The magenta and yellow lines indicate suspected seismic wave propagation and are referred to in the main text.

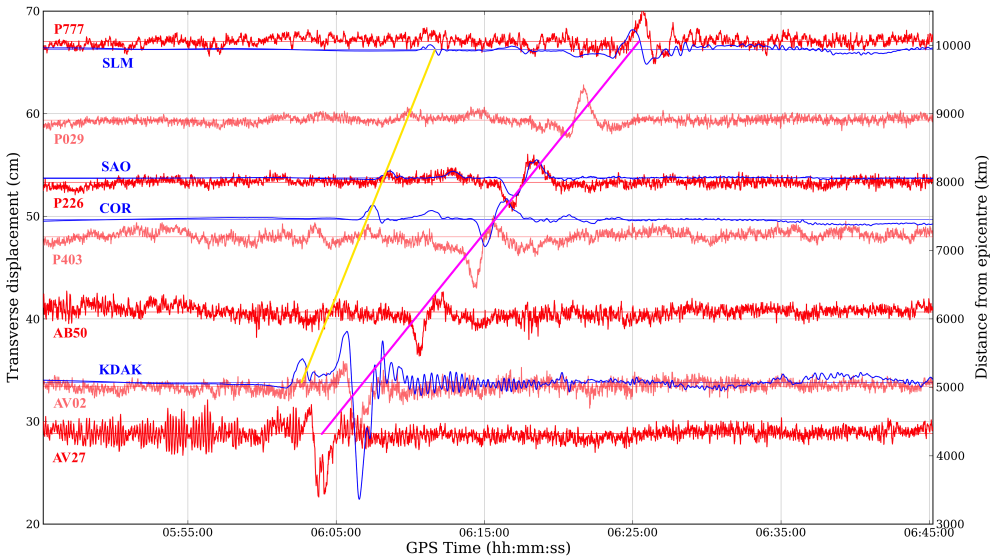

Figure 9.13 – *Red lines*: Transverse displacements resulting from standard PPP processing with a PDSF applied at all UNAVCO PBO stations marked with two asterisks ** in table 9.1. *Blue lines*: Transverse displacements derived from integrated velocity data from the IRIS seismometer stations listed in table 9.2. The magenta and yellow lines indicate suspected seismic wave propagation and are referred to in the main text.

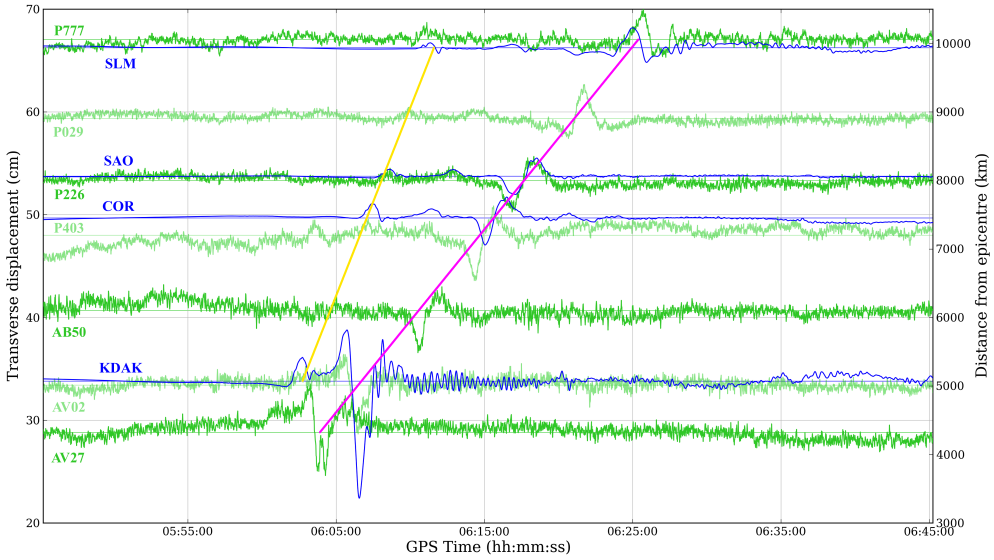

Figure 9.14 – *Green lines*: Transverse displacements resulting from standard PPP processing with an ODSF applied at all UNAVCO PBO stations marked with two asterisks ** in table 9.1. *Blue lines*: Transverse displacements derived from integrated velocity data from the IRIS seismometer stations listed in table 9.2. The magenta and yellow lines indicate suspected seismic wave propagation and are referred to in the main text.

of this thesis. Further evidence for the existence of this wave is just about apparent at stations P226 and P029 in figures 9.12 to 9.14 but is not so obvious at P403 and P777, even after sidereal filtering.

The sidereal filters have had little benefit in reducing positioning errors at station P403. For example, there appears to be an oscillation between 06:03 and 06:05 of roughly 10 cm in peak-to-peak amplitude that remains even after sidereal filtering. It is unlikely to be a seismic wave since there is no corresponding oscillation of roughly the same period at other stations, particularly at seismometer COR or PBO station NEAH. The oscillation could be a result of changes to the reflector environment surrounding the antenna. However, the cause of this oscillation is not investigated further in this analysis.

Regarding the visual identification of Love waves, it is apparent that the performance of two types of sidereal filter at each station are similar to each other, with the exception of station AV27. The poor performance of the PDSF at AV27 between 05:45 and around 06:08 was discussed in section 9.5.1.

9.5.4 Detection of Rayleigh waves

Figures 9.15 to 9.20 show plots for the *radial* axis of the monitoring stations, i.e. the axis in the direction of travel of the seismic waves which radiate out from the epicentre. With each of the position time series arranged as they are in these figures, it is possible to identify a seismic wave with a peak-to-peak amplitude of roughly 3 cm and a period of around three minutes propagating outwards from the epicentre with a speed of about 3.7 km/s. This is marked by a turquoise line. This is a slower speed than the Love waves and they are therefore most likely to be Rayleigh waves (Doyle 1995).

When comparing either figure 9.16 or 9.17 with figure 9.15, it appears that both types of sidereal filter have significantly altered the time series at station NEAH, particularly between 06:19 and 06:28 where they appear to have increased the period of the largest oscillation (from roughly 140 s to 190 s, respectively) and introduced smaller oscillations following it. The oscillations at NEAH during the period 06:22–06:28 in figure 9.17 do not appear at station P403 (in figure 9.20) which is at roughly the same epicentral distance. This suggests that these oscillations are not seismic in origin. If this is the case, then the sidereal filters have introduced errors, possibly because the reflector environment of the antenna had changed since the previous day.

At other monitoring stations, the sidereal filters have had more noticeable effect in reducing multipath in the radial axis, particularly at stations P213, P728 and P775 in figures 9.15 to 9.17 and stations P226 and P777 in figures 9.18 to 9.20. Another seismic wave can be identified travelling at approximately 8.4 km/s (shown by an orange line). These are possibly S-waves: They occur at almost the same time at each station as the possible S-waves in the transverse axis identified at the end of the previous section (section 9.5.3).

Notice also at both stations AV24 and AV27, there are small-amplitude oscillations (up to about 1 cm peak-to-peak) with periods as short as 7.5 s (0.13 Hz) in the time series, most obviously

between about 06:30 and 06:45 in figures 9.15 and 9.18. These oscillations are high-frequency errors caused by multipath interference and are not due to seismic activity. This is because their amplitude is significantly reduced by observation-domain sidereal filtering. When examining figures 9.16 and 9.19, it is apparent that the PDSF has not only failed to remove these oscillations but has actually increased their amplitude. A five-minute sample of the time series at AV24 is shown in figure 9.21 as an example. Notice that the ODSF does not remove all of the oscillations, but nevertheless does a better job than the PDSF because of its ability to account for the differing satellite repeat times. This example also vindicates the decision in section 5.2 to use a cut-off frequency of 0.2 Hz for the low-pass filtering of the measurement corrections. If a cut-off frequency of 0.1 Hz had been chosen, the ODSF would not have had a beneficial effect.

Figures 9.22 to 9.27 show equivalent plots for the *vertical* axis. The displacements from the seismometer data alone indicates the presence of a seismic wave with an amplitude of roughly 2–3 cm propagating with a speed of around 3.7 km/s, the same speed as the Rayleigh waves identified in the radial component, and their approximate arrival times are indicated by a blue diagonal line. Therefore, these are likely to be the vertical component of those Rayleigh waves. These waves are difficult to distinguish by eye from other positioning errors present in the standard PPP time series in figures 9.22 and 9.25. However, it is perhaps a little easier to discern them in figures 9.23, 9.24, 9.26 and 9.27 where sidereal filters have been applied, particularly at stations AV24, AV27 and P226. At other stations, such as AB50, P029, P403 and P777, the Rayleigh wave is barely perceptible above other positioning errors. Again, as with the radial component, the superiority of the ODSF over the PDSF at reducing the amplitude of high-frequency multipath error is most noticeable at AV24 and AV27, especially after 06:25.

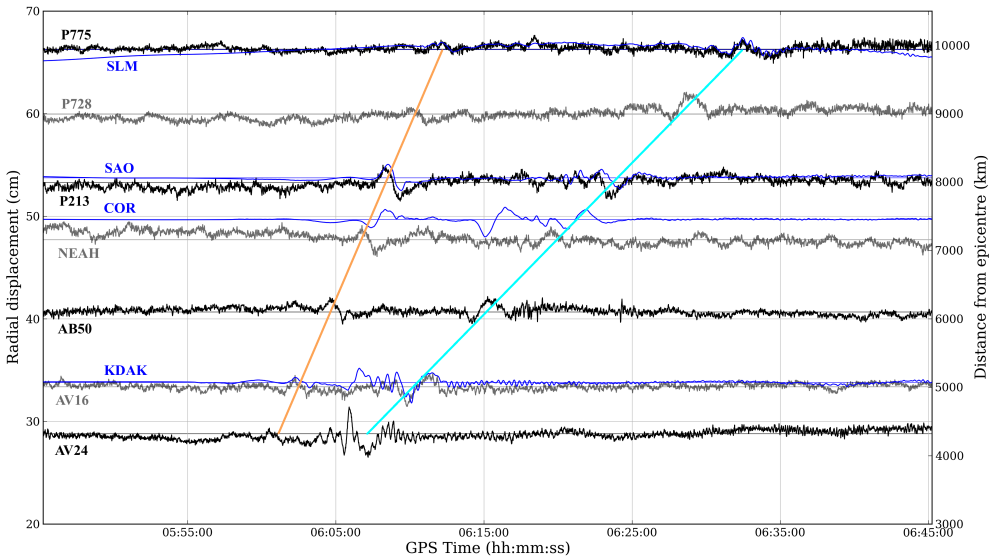

Figure 9.15 – *Black/grey lines*: Radial displacements resulting from standard PPP processing at all UNAVCO PBO stations marked with a single asterisk ⋆ in table 9.1. *Blue lines*: Radial displacements derived from integrated velocity data from the IRIS seismometer stations listed in table 9.2. The turquoise and orange lines indicate suspected seismic wave propagation and are referred to in the main text.

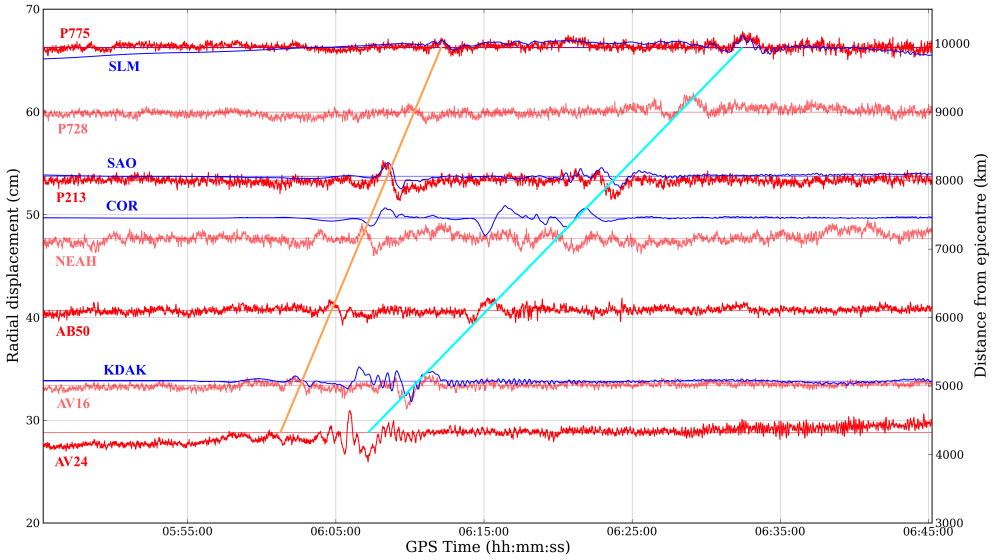

Figure 9.16 – *Red lines*: Radial displacements resulting from standard PPP processing with a PDSF applied at all UNAVCO PBO stations marked with a single asterisk ⋆ in table 9.1. *Blue lines*: Radial displacements derived from integrated velocity data from the IRIS seismometer stations listed in table 9.2. The turquoise and orange lines indicate suspected seismic wave propagation and are referred to in the main text.

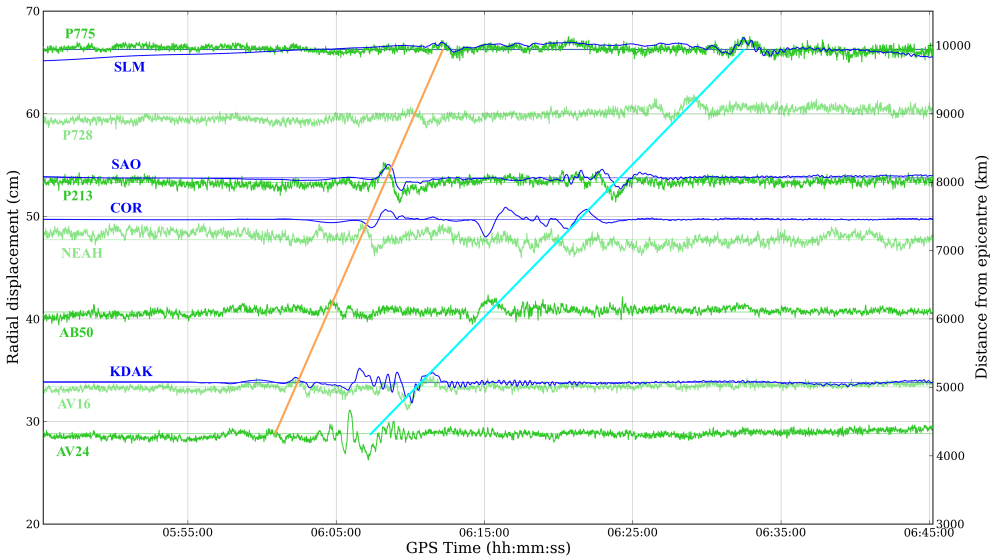

Figure 9.17 – *Green lines*: Radial displacements resulting from standard PPP processing with an ODSF applied at all UNAVCO PBO stations marked with a single asterisk ⋆ in table 9.1. *Blue lines*: Radial displacements derived from integrated velocity data from the IRIS seismometer stations listed in table 9.2. The turquoise and orange lines indicate suspected seismic wave propagation and are referred to in the main text.

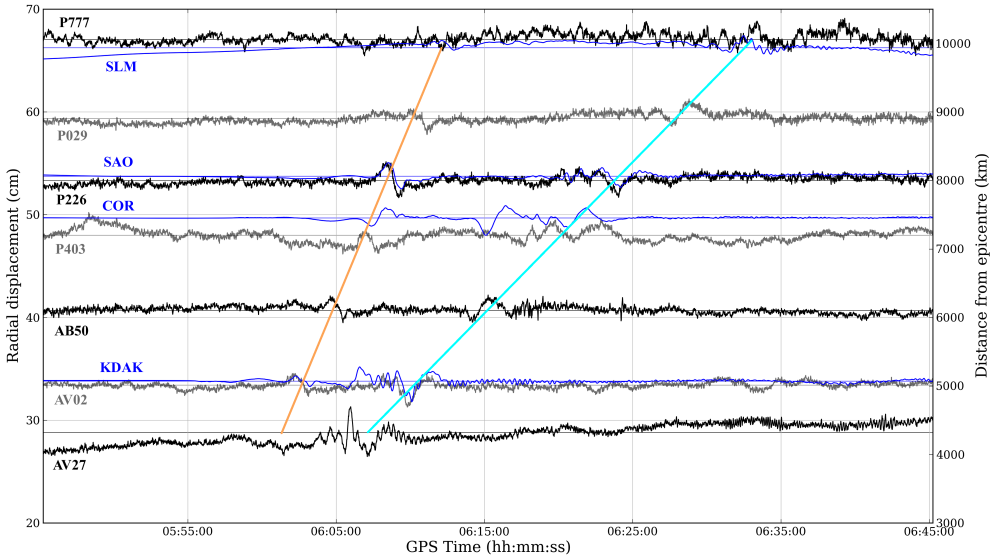

Figure 9.18 – *Black/grey lines*: Radial displacements resulting from standard PPP processing at all UNAVCO PBO stations marked with two asterisks ⋆⋆ in table 9.1. *Blue lines*: Radial displacements derived from integrated velocity data from the IRIS seismometer stations listed in table 9.2. The turquoise and orange lines indicate suspected seismic wave propagation and are referred to in the main text.

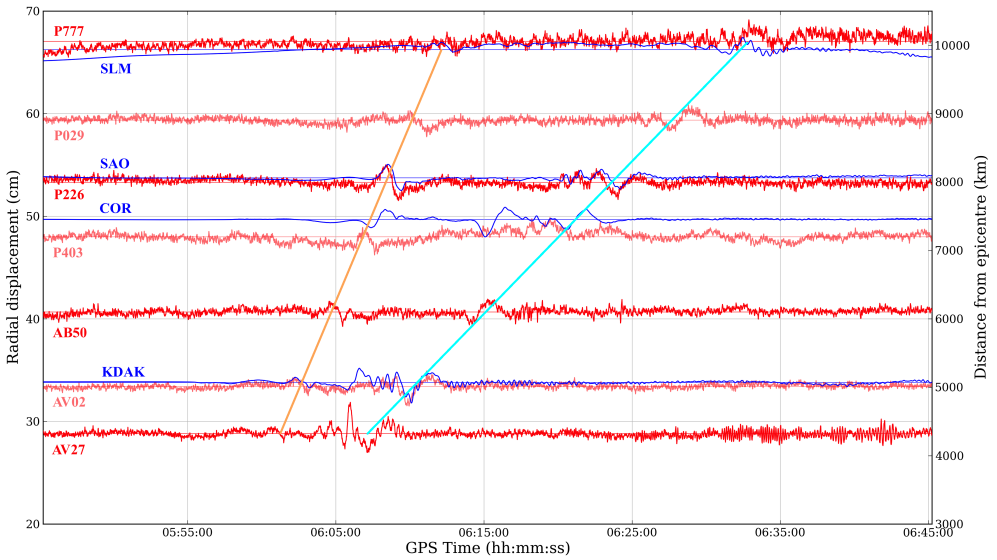

Figure 9.19 – *Red lines*: Radial displacements resulting from standard PPP processing with a PDSF applied at all UNAVCO PBO stations marked with two asterisks ** in table 9.1. *Blue lines*: Radial displacements derived from integrated velocity data from the IRIS seismometer stations listed in table 9.2. The turquoise and orange lines indicate suspected seismic wave propagation and are referred to in the main text.

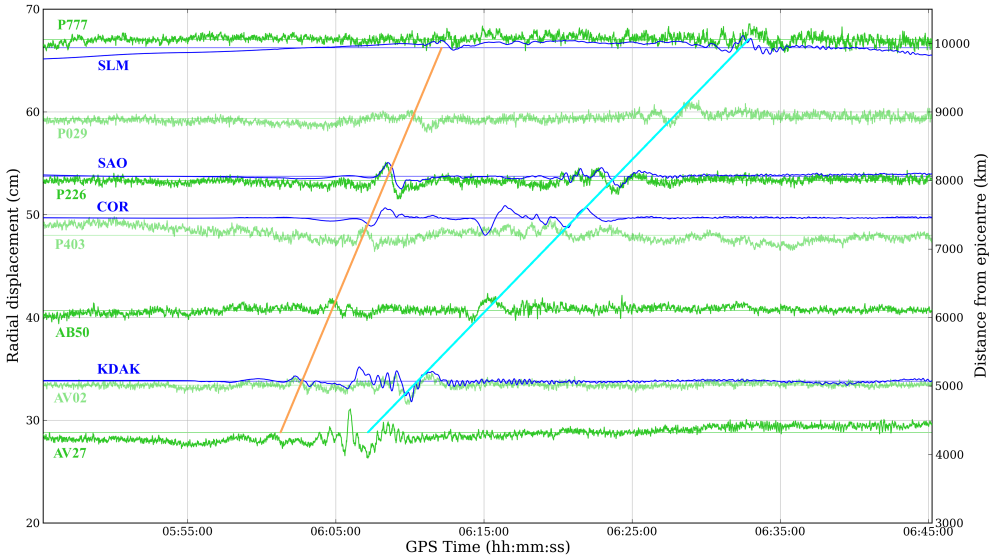

Figure 9.20 – *Green lines*: Radial displacements resulting from standard PPP processing with an ODSF applied at all UNAVCO PBO stations marked with two asterisks ** in table 9.1. *Blue lines*: Radial displacements derived from integrated velocity data from the IRIS seismometer stations listed in table 9.2. The turquoise and orange lines indicate suspected seismic wave propagation and are referred to in the main text.

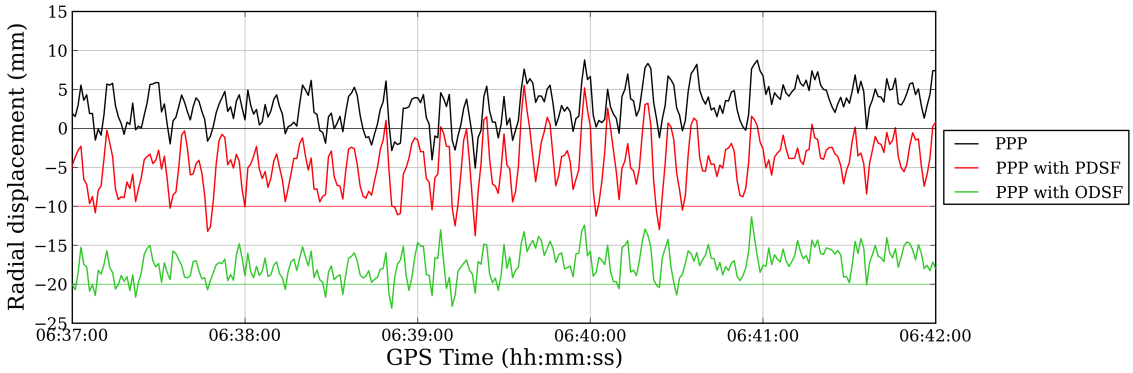

Figure 9.21 – Radial displacements between 06:37 and 06:42 on 11$^{\text{th}}$ March 2011 at station AV24 resulting from standard PPP processing and PPP processing with position- or observation-domain sidereal filters applied. (The PDSF and ODSF time series have been offset by −10 mm and −20 mm, respectively, for clarity).

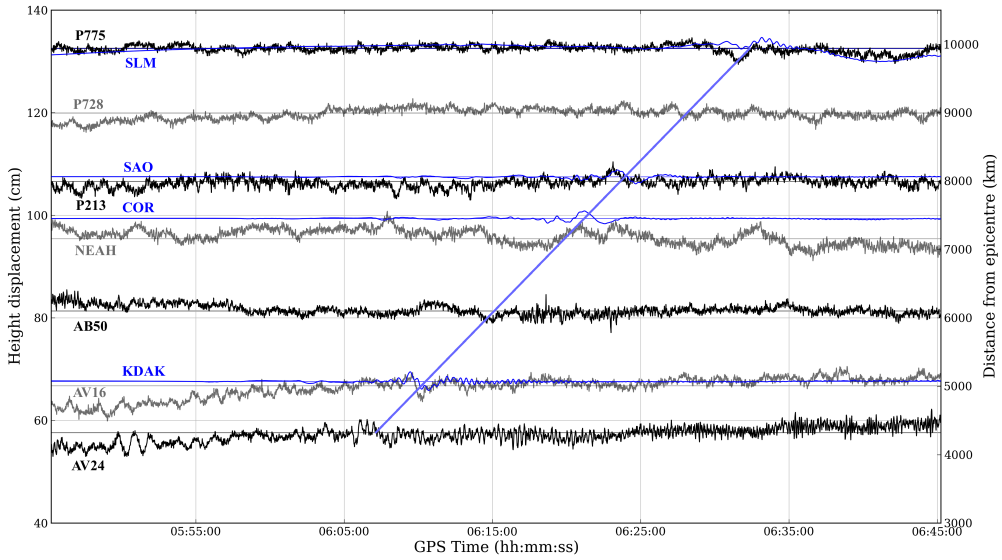

Figure 9.22 – *Black/grey lines*: Vertical displacements resulting from standard PPP processing at all UNAVCO PBO stations marked with a single asterisk ⋆ in table 9.1. *Blue lines*: Vertical displacements derived from integrated velocity data from the IRIS seismometer stations listed in table 9.2. The blue diagonal line indicates suspected seismic wave propagation and is referred to in the main text.

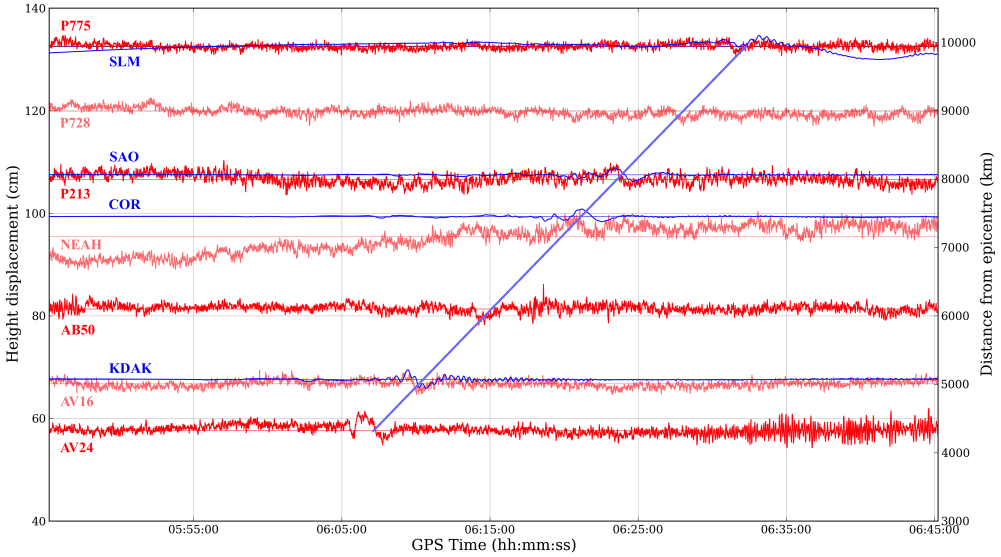

Figure 9.23 – *Red lines*: Vertical displacements resulting from standard PPP processing with a PDSF applied at all UNAVCO PBO stations marked with a single asterisk ⋆ in table 9.1. *Blue lines*: Vertical displacements derived from integrated velocity data from the IRIS seismometer stations listed in table 9.2. The blue diagonal line indicates suspected seismic wave propagation and is referred to in the main text.

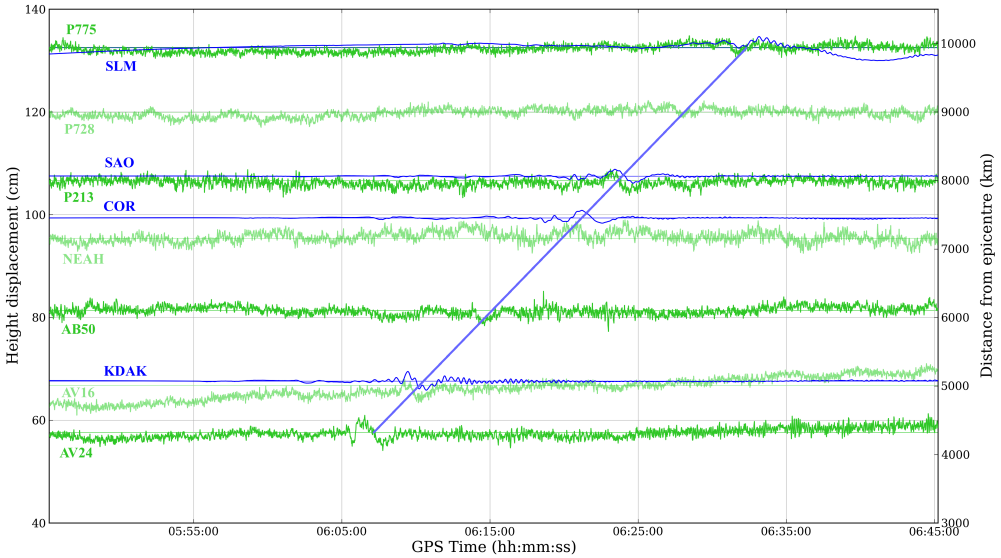

Figure 9.24 – *Green lines*: Vertical displacements resulting from standard PPP processing with an ODSF applied at all UNAVCO PBO stations marked with a single asterisk ⋆ in table 9.1. *Blue lines*: Vertical displacements derived from integrated velocity data from the IRIS seismometer stations listed in table 9.2. The blue diagonal line indicates suspected seismic wave propagation and is referred to in the main text.

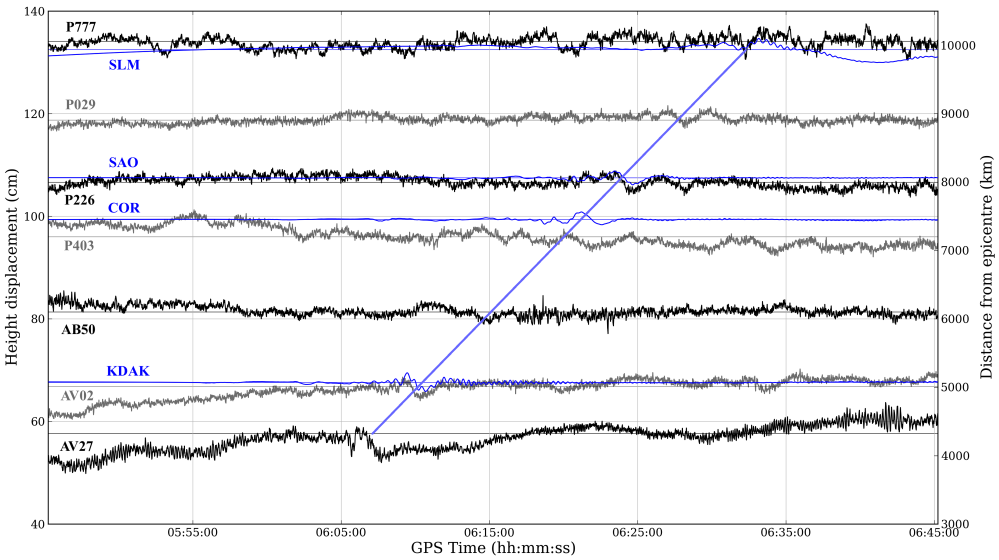

Figure 9.25 – *Black/grey lines*: Vertical displacements resulting from standard PPP processing at all UNAVCO PBO stations marked with two asterisks ** in table 9.1. *Blue lines*: Vertical displacements derived from integrated velocity data from the IRIS seismometer stations listed in table 9.2. The blue diagonal line indicates suspected seismic wave propagation and is referred to in the main text.

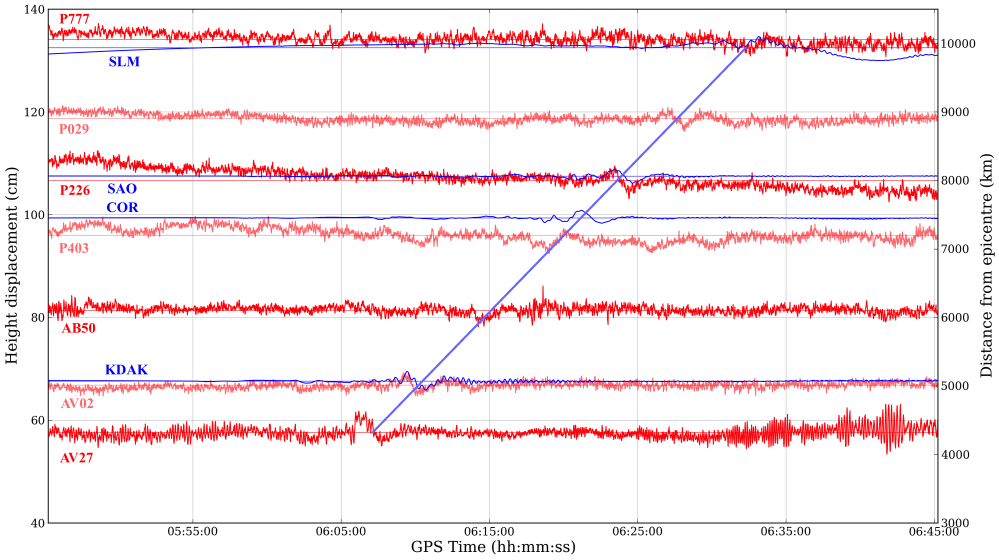

Figure 9.26 – *Red lines*: Vertical displacements resulting from standard PPP processing with a PDSF applied at all UNAVCO PBO stations marked with two asterisks ** in table 9.1. *Blue lines*: Vertical displacements derived from integrated velocity data from the IRIS seismometer stations listed in table 9.2. The blue diagonal line indicates suspected seismic wave propagation and is referred to in the main text.

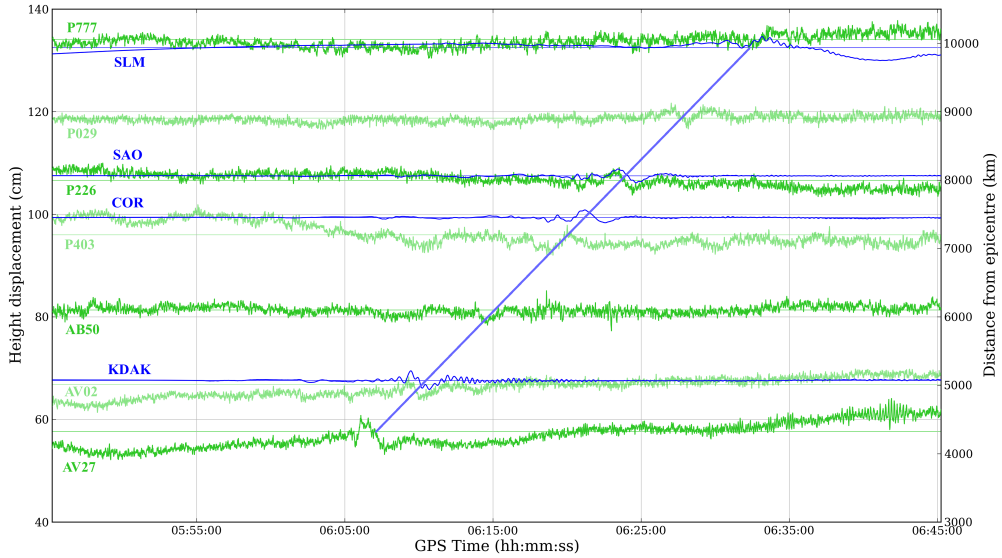

Figure 9.27 – *Green lines*: Vertical displacements resulting from standard PPP processing with an ODSF applied at all UNAVCO PBO stations marked with two asterisks ** in table 9.1. *Blue lines*: Vertical displacements derived from integrated velocity data from the IRIS seismometer stations listed in table 9.2. The blue diagonal line indicates suspected seismic wave propagation and is referred to in the main text.

9.6 Summary and Conclusions

The various analyses in this chapter have demonstrated that sidereal filters do generally aid the indentification, by eye, of surface waves by removing much of the effect of phase multipath interference. However, it is clear that the sidereal filters have been very effective at some stations such as AV24 (figures 9.3 to 9.5) and AV16 (figures 9.7 and 9.8) whilst having minimal obvious benefit at other stations such as NEAH (figures 9.15 to 9.17, for example). This is either because the errors present in the PPP position time series were largely caused by something other than multipath, or that the pattern of multipath interference changed from one day to the next, possibly due to a change in the local environment of the receiver antenna.

The observations made in the analysis broadly reflect the results presented earlier in this thesis. The variable performance of the sidereal filter algorithms has already been observed in previous chapters, particularly in chapter 8 when measuring coseismic offsets, but also across all the monitoring stations analysed in chapter 3. To examine precisely why the benefit provided by the sidereal filters varies so much both spatially and temporally would require an in-depth investigation for each individual case. This would likely involve processing high-rate ($\geq 1\,\text{Hz}$) GPS measurements from each receiver spanning several weeks or months, noting any significant changes in the satellite constellation between adjacent days and plotting colour-coded measurement residuals onto a hemispherical 'skyplot' as suggested in section 5.7. A record of the weather conditions and the

nature of the surrounding reflectors (i.e. if they are wet or covered in snow) would be beneficial. Such an investigation is suggested as an area of future research in chapter 10.

For the purpose of Love and Rayleigh wave identification, both the ODSF and PDSF perform similarly in most cases. However, some very obvious exceptions to this can be seen at stations AV24 and AV27 (figures 9.4 and 9.21 in particular). In these examples, high-frequency errors due to strong multipath interference were actually accentuated (i.e. their amplitude increased) when the PDSF algorithm was applied but were reduced when an ODSF was applied. This agrees with the theory developed in section 1.5.2 (page 55) which stated that the ODSF algorithm should be more effective than a PDSF at removing the effects of multipath interference, particularly with regard to high-frequency multipath errors. This was indeed confirmed by the conclusions of chapter 5.

The displacement time series derived from the seismometer data sourced from IRIS was only used in the above analysis to assist with the visual identification of seismic waves in the PPP position time series. Whilst the seismometer data proved to be useful in this respect, notable differences between the two data types at similar epicentral distances were identified, such as the differences in both amplitude and frequency of the apparent oscillations, most obviously between the seismometer KDAK and the PBO stations AV02 and AV16 (figure 9.7), even after sidereal filtering. These differences were probably because of the fact that no receiver-seismometer pair were actually located in the same place and hence, possibly because of differences in the elasticity of the underlying bedrock, did not experience the same motion as the surface waves passed. This illustrates the importance of analysing the measurements of co-located instruments if a rigorous comparison is to be made. As mentioned in section 1.2.2 (page 30), combining these measurements together to produce a single output has the potential to make up for the deficiencies of each instrument: Firstly, measurements output from seismometers are very precise and are hence much more sensitive to small movements than when using PPP; Secondly, PPP positioning and other GNSS positioning techniques can measure the displacement of the ground directly and are immune to the effects of tilt and rotation. Hence, using GNSS can potentially be used to solve for biases in the seismometer measurements and output precise displacements in real time. This is not a new idea and has already been demonstrated by Bock et al. (2011) and Geng et al. (2013). However, an observation-domain sidereal filter will be useful if such measurements are combined, particularly if a situation arises such as that illustrated by figure 9.7, where the displacements implied by standard PPP processing do not 'agree' with the seismometer measurements because of strong multipath interference.

9.7 Towards a quantitative analysis

This chapter has demonstrated how sidereal filtering, especially in the observation domain, can aid the visual identification of seismic waves from a position time series generated by PPP processing. However, a more rigorous analysis would involve applying quantitative tests to compare the GPS position time series with those derived from seismometers.

One possible test would be to compare the surface wave velocities calculated using seismometer data with those calculated using PPP position time series with and without sidereal filtering. It is possible that severe multipath interference could distort the position time series to such an extent that the apparent time of arrival of a small-amplitude surface wave is altered. However, such an analysis is complicated by a number of factors. Firstly, it is wrong, strictly speaking, to assume that a surface wave has a constant velocity along the path on which it is travelling and that the velocity is the same in all directions from the source. The coloured diagonal lines shown in figures 9.9 to 9.27 (excluding figure 9.21) are for indicative purposes only and the surface wave velocities mentioned in sections 9.5.3 and 9.5.4 are very approximate. The speed of a surface wave actually depends upon the elasticity and density of the rock through which the wave is propagating. Since rock structure varies along the paths travelled by suface waves (Bolt 2006), the speed of those waves will also vary. Seismic waves travel faster through oceanic crust than continental crust. This is because oceanic crust has a higher density (Rogers & Blake 2008). This is important to consider because, by examining figure 9.2, the surface waves arriving at stations P029, P728, P775, P777 and SLM will have travelled a substantial distance through continental crust. Also note that the monitoring stations chosen for this experiment do not lie on the same ray path. One can therefore expect the time of arrival of the different types of surface wave to not lie on a straight line as shown in figures 9.9 to 9.27.

Such an analysis would require the identification of a precise time of arrival at each station for a particular type of wave. This can be difficult to do by eye from amongst a PPP position time series relative to the time series derived from seismometry, even after applying a sidereal filter. One alternative could be to apply an algorithm, such as that developed in Allen & Ziv (2011), to determine the time of arrival. This was summarised in section 8.3.2 but is repeated here for convenience: A long-term moving averaging window moving forwards in time spanning the previous 100 s is compared to a short-term average spanning only 2 s. The onset of the dynamic surface waves is assumed to be when the short-term average exceeds the long-term average by some chosen amount. A similar algorithm could be developed here and a sidereal filter should reduce the probability of false alarms. Another alternative could be to visually identify a feature common to each of the waveforms at the monitoring stations, such as a particular peak or trough, to calculate the phase velocity of a wave. However, this is difficult because, when examining figures 9.9 to 9.27 (excluding figure 9.21), it is apparent that the shape of the waveform at each station changes significantly as epicentral distance increases.

A more rigorous test would be to subtract a displacement time series derived from seismometer data from another displacement time series output by PPP processing. If sidereal filtering has a beneficial effect, then the root-mean-square (RMS) of the differences between the two time series should be smaller than if sidereal filtering were not applied. Of course, this assumes that a seismometer and GPS antenna pair experience the same motion or, rather, that they are co-located. The importance of co-location has already been discussed in the previous section. Unfortunately, there is no such instance in the dataset used in this chapter. Indeed, the closest pairing of a

GPS antenna with a seismometer is about 69 km (stations P213 and SAO) or 67 km in terms of epicentral distance. This contrasts with studies such as Wang et al. (2007) where comparisons are made between stations that are no more than about 5 km apart. Therefore, in order to make such a comparison using the data gathered for this experiment, the position time series derived from the seismometer data would have to be transformed so that the waveform matches that of a selected 'nearby' GPS monitoring station (or vice versa) with respect to the peaks and troughs of the wave. This would not be a simple shift in the time domain but instead would be a 'stretch'. This is because of the spreading of the surface wave train caused by dispersion (Bolt 2006) and the differing speeds of the various types of seismic wave.

When using such a method to compare the displacements derived from seismometry data with data output from PPP processing, it is important to be mindful of the errors present in both data types, not just those associated with GPS positioning. For example, the possibility of a scale factor error in the seismometer measurements at station KDAK was discussed towards the end of section 9.5.2. Another issue is the presence of slowly-varying biases in the displacements derived from seismometry. For example, when examining figures 9.9 to 9.11, 9.15 to 9.17 and 9.22 to 9.24, it would seem reasonable to compare the displacements of PBO station P775 with those derived from seismometer station SLM. This is because the displacement time series at both stations appear to be visually similar, especially after the application of sidereal filtering to the data from station P775. After all, from tables 9.1 and 9.2, these two stations have epicentral distances that differ by only 8 km despite being separated from each other by 346 km. However, upon close inspection of the displacements derived from station SLM, there appear to be very slowly-varying biases present throughout the time series in all three components. These are particularly visible in the radial axis and in the vertical axis, especially between 06:35 and 06:45. It is thought that these are artefacts of the integration process upon retrieval of the seismometer data from IRIS rather than a real displacement signal. Therefore, a high-pass filter with a suitable cut-off frequency should be applied to the data from station SLM, and perhaps to data from other stations, to remove such low-frequency signals before comparison with the displacements output from PPP processing.

Quantifying the benefit of observation-domain sidereal filtering in the context of comparing or combining measurements from GNSS receivers and seismometers is stated in chapter 10 as an area for future research.

Chapter 10

Conclusions

This chapter begins by addressing each of the research questions originally stated in chapter 1 (page 62). This is followed in section 10.2 by a summary of the salient conclusions of this thesis. There then follows a discussion regarding possible future research in section 10.3 and a summary of original contributions to knowledge in section 10.4.

10.1 Responses to the research questions

The first three of the research questions were addressed in chapters 3 to 6. These chapters assessed the impact of the position-domain sidereal filter (PDSF) and observation-domain sidereal filter (ODSF) algorithms on the results of precise point positioning (PPP) using measurements from a *static* receiver antenna. Considering that the focus of this thesis was to use PPP to accurately measure small *displacements* over a relatively short period of time, emphasis was thus placed on how the sidereal filters affected positioning *stability* over such periods rather than assessing their impact on absolute positioning accuracy.

1. Is an observation-domain sidereal filter more effective than a position-domain sidereal filter at reducing the effect of multipath error, and high-frequency multipath error in particular?

In chapter 3, it was found that both types of sidereal filter are generally more effective at increasing positioning stability when measurements are strongly affected by multipath interference, although this is perhaps a statement of the obvious. However, the sidereal filter algorithms were generally successful at increasing positioning stability over periods of time ranging from a few tens of seconds up to a few hundred seconds. Even at receivers where multipath interference was apparently weak, *both* the ODSF and PDSF algorithms were still successful at increasing stability over periods of time ranging from about 100 s to 300 s. The analysis in chapter 3 also showed that a DP or a BE ODSF does indeed outperform the PDSF over shorter time intervals—generally those up to a few hundred seconds in length—indicating that it is more able to remove the effects of high-

frequency multipath. This is due to its ability to use a more appropriate repeat period for each individual satellite in view. This was shown in chapter 3 by comparing the performance of the DP ODSFs with an ODSF that, like the PDSF algorithm, used the same repeat period for each satellite at each epoch. It is difficult to generalise the overall relative performance of the PDSF and ODSF algorithms, but the largest difference in performance between the two was observed in figure 3.7 (page 96) with differences of over ten percentage points in favour of the ODSF, in terms of improvement in Allan deviation.

Indeed, the experiments in chapter 5, together with some of the examples shown in chapter 9, demonstrated the superiority of the ODSF over the PDSF under the circumstances of particularly strong high-frequency multipath interference. However, the performance of the ODSF can be heavily influenced by the pattern formed by the measurement residuals when they are distributed by satellite azimuth and elevation angle. These patterns are described in chapters 4 and 5 as 'banding': If the direction a satellite takes across the sky (i.e. the 'skytrack') is not perpendicular to these banding patterns, then the performance of the ODSF algorithm in its current form may be reduced, no matter if the repeat time was calculated using values given in the GPS broadcast ephemeris (BE) or by using the dot product (DP) method (see sections 1.5.3 and 2.2.1). It was predicted that an ODSF using the DP method would be more effective at removing high-frequency multipath. Results in chapter 3 suggest that this is *generally* true although the difference is very slight: In terms of the improvement in stability (reduction in Allan deviation) relative to standard PPP processing, the difference between the BE and DP methods was at most about two percentage points.

Over longer-intervals of time, say a few thousand seconds or more, the ODSF seems to be unreliable and is frequently out-performed by the PDSF algorithm. As discussed in chapter 3, it is thought that this is because long-period multipath error is more likely to alias into other slowly-varying Kalman filter states, both on the day from which the multipath corrections are derived and on the day on which those corrections are applied.

In short, the ODSF algorithm has been shown to be more effective than the PDSF algorithm with respect to high-frequency multipath, but it is not a panacea. However, there is room to further improve the technique in this respect by developing a more sophisticated algorithm that finds corrections for multipath error through *interpolation* of measurement residual values by their associated azimuth and elevation angles (see section 5.7, page 163). Over longer intervals of time, the ODSF is not reliable.

2. How well does observation-domain sidereal filtering perform relative to position-domain sidereal filtering when satellites with particularly anomalous repeat periods are visible?

Despite the fact that GPS measurements from only three receivers were used for the analysis in chapter 4, the results indicate that an ODSF generally yields a more stable position time series than a PDSF over periods of time of up to a few hundred seconds during periods when satellites with anomalous repeat periods are visible. Over longer periods of time, the performance of the

PDSF relative to the ODSFs is more varied. This is no different to the conclusions of chapter 3 when the 'overall' performance of the sidereal filters was assessed.

However, it was observed that the reliability of the ODSF algorithm also depends on the angular separation between satellite skytracks of adjacent days being small, say around a hundredth of a degree or lower. This is particularly important if the associated measurements are affected by high-frequency multipath caused by a distant reflector. However, chapter 4 showed two examples of satellites with anomalous repeat periods having a large angular separation between skytracks of several tenths of a degree, which reduced the reliability of the ODSF algorithm in removing multipath error. The larger this angular separation, the more important it is for the skytracks to be orthogonal to the direction of any banding patterns for the ODSF to be effective. One solution would be to exclude the measurements associated with satellites with large angular separations between the skytracks of adjacent days, rather than attempt to reduce multipath error in measurements by sidereal filtering. This will be discussed shortly.

3. How well does observation-domain sidereal filtering perform relative to position-domain sidereal filtering when a satellite is taken out of service, either expectedly or unexpectedly?

Chapter 6 showed that the performance of the ODSF was also superior to the PDSF in the circumstances of a satellite outage, although the difference was only slight if the receiver antenna was placed in a low multipath environment. In a higher multipath environment, a satellite outage can cause a dramatic drop in the stability of the position time series after applying the PDSF algorithm—by as much as around twenty-five percentage points (see figure 6.9 on page 177). The loss of stability was significantly reduced when the ODSF algorithm was applied instead.

As well as comparing the ODSF and PDSF algorithms, two different types of ODSF algorithm were also tested under such circumstances: one that *excludes* any measurement for which a multipath correction cannot be derived from the previous day (ODSF1), and one that *includes* measurements whether or not a multipath correction for it exists (ODSF2). Results suggested that in a low-multipath environment, neither type is of much benefit, but the ODSF2 algorithm still outperformed the ODSF1 algorithm over periods of a few hundred seconds. In contrast, if the antenna was placed in a higher-multipath environment and the satellite concerned was strongly affected by multipath errors, the ODSF1 algorithm yielded better stability, at least for periods of time under a few hundred seconds. However, care needs to be taken when there are few satellites and/or there is a poor distribution of satellites across the sky: Excluding the measurements that have not been corrected for multipath in such situations could do more harm than good to the stability of a position time series if there is a significant worsening of satellite geometry and measurement redundancy. Methods to address this problem are discussed shortly.

4. Can observation-domain sidereal filtering improve the ability of PPP to accurately measure small centimetre-level displacements of normally static receivers over the course of just a few minutes? In particular, can observation-domain sidereal filtering improve the measurement of permanent coseismic displacement in the immediate aftermath of an earthquake?

The experiments in chapters 7 and 8 were designed to address this research question. The results from chapters 3 to 6 suggested that, even in relatively benign conditions, the ODSF algorithm is most effective over time intervals of tens of seconds to a few hundred seconds. From the point of view of tsunami early warning, this is encouraging. Measuring coseismic displacement quickly and accurately is of the utmost importance given that the amount of time between the onset of an earthquake and the arrival of any potential tsunami at the nearest coastline may only be a few minutes (20–30 minutes in the case of the 2004 Sumatra-Andaman earthquake).

However, in chapters 7 and 8 where the sidereal filters were tested under dynamic circumstances, results were mixed: In chapter 7, where small displacements were induced by the means of a moveable platform, the ODSF algorithm in particular was shown *on average* to be successful at improving the accuracy of a measured displacement using a relatively short PPP time series of up to 110 s either side of the displacement event (see figure 7.6 on page 206). In contrast, chapter 8 showed that the sidereal filters did *not* on average yield any obvious improvement in the accuracy of the measured horizontal coseismic offsets of a real earthquake. In fact, they slightly reduced the accuracy of the measured offsets (see figure 8.14 on page 223) and hence would not have benefited any calculation of earthquake magnitude. It was postulated that this could be due to the general lack of multipath interference at many of the monitoring stations used in the experiment at the time of the earthquake. Another reason, which is perhaps more likely, could be the difficulty in calculating the true value of the coseismic offsets with sufficient accuracy for the purpose of comparison. Nevertheless, these results appear to be inconsistent with the results from chapters 3 to 6 (i.e. the experiments using measurements from a static receiver) and indeed chapter 7. The results are inconclusive and further research is required.

5. What impact does observation-domain sidereal filtering have on ones ability to distinguish between seismic waves and multipath error in PPP position time series?

In chapter 9, GPS data associated with the 2011 Tohoku-Oki earthquake was used, but not to test the effectiveness of the sidereal filter algorithms in assisting the measurement of coseismic displacements. Instead, this was a 'demonstration of capability', showing how well each of sidereal filter algorithms performed in separating the transient displacements caused by surface waves from the oscillating errors caused by phase multipath interference. At far epicentral distances, the two can be indistinguishable from each other. It was shown, visually at least, that both the PDSF and ODSF algorithms were of benefit in the identification of surface waves. Whilst this demonstration was not directly relevant to the measurement of tsunami early warning, the advantage of using the ODSF over the PDSF was clear to see in at least three of the thirteen monitoring stations used.

Considering the first research question once more, these cases add weight to the conclusion that the ODSF algorithm is more effective at removing high-frequency multipath errors than the PDSF algorithm.

10.2 Summary

- The ODSF algorithm as described in this thesis is generally more effective than a PDSF algorithm at reducing high-frequency positioning errors caused by multipath interference (i.e. oscillating errors with periods of a few tens of seconds).

- Conversely, the ODSF algorithm in its current form is not suited to removing errors that oscillate with periods above a few thousand seconds and repeat every sidereal day (e.g. 'near-field' multipath and errors in antenna phase-centre modelling). This is likely to be because such errors alias into the other slowly-varying Kalman filter states such as the phase ambiguities and tropospheric delay (see chapter 3).

- The results of chapter 3 suggest that, if applying the ODSF algorithm to remove high-frequency multipath errors, there is an advantage in using the DP method rather than calculating a repeat time using values given in the GPS broadcast ephemeris, although that advantage appears to be very small. However, from later chapters, it can be said with certainty that the ability of the ODSF algorithms to remove such errors can be severely limited by the orientation of the path taken across the sky by a satellite relative to the intricate patterns formed by measurement residuals when distributed by azimuth and elevation.

- When attempting to correct for phase multipath errors, the performance of both the PDSF and ODSF algorithms becomes less reliable the more the repeat period of a GPS satellite differs from the nominal repeat period of 86,155 s. This is because the path that such satellites take across the sky differs more significantly from one day to the next.

- The performance of an ODSF is superior to a PDSF in the circumstances of a satellite outage either on the 'previous' day (the day used to calculate the multipath corrections) or the 'current' day (the day on which those corrections are applied). However, the difference in performance between the two algorithms is only slight if the receiver antenna is placed in a low-multipath environment.

- Efforts to determine whether the sidereal filter algorithms (position- or observation-domain) improve the measurement of small centimetre-level displacements have so far been contradictory. The results presented within chapter 7 suggest that sidereal filtering, and the ODSF algorithm in particular, can do so. However, the results from chapter 8, which used data from a real seismic event, suggest not. This could be due to a number of reasons, but more research is required if a conclusion is to be reached. However, chapter 9 demonstrated that the ODSF

algorithm in particular can aid the identification of centimetre-level *transient* displacements associated with surface waves caused by an earthquake.

10.3 Recommendations for future research

10.3.1 Improvement of the ODSF algorithm

As discussed in section 5.7 (page 163), there is a need to develop a more sophisticated ODSF algorithm that finds corrections for multipath error through the *interpolation* of measurement residual values by their associated azimuth and elevation angles. This should be even more effective at reducing instances of high-frequency multipath interference, such as those identified in sections 5.5 and 9.5.4. Such an algorithm would involve creating a hemispherical map or 'skyplot' of measurement residuals created by the PPP processing of months of GNSS data. This map could also be used to identify anomalies in the measurement residuals (such as those identified in figure 3.3 and those mentioned in section 3.5) and help to understand the effect of the weather (i.e. wet surfaces) on the effectiveness of the ODSF algorithm. Indeed, previous studies such as Lau (2012) and Wanninger & May (2000), have found that wet surfaces have little effect on phase multipath error. However, this needs confirmation, particularly with respect to specific instances of high-frequency multipath. An experiment involving the careful examination of measurement residuals over multiple days alongside detailed weather records would be useful.

Also discussed in section 5.7 was the possibility of determining a suitable repeat time empirically by correlating observation residuals from adjacent days. A feasibility study is required to establish whether such a method could be applied in the context of PPP, what size of window is most suitable for correlating the residuals and whether such an algorithm can be realistically applied in a real-time scenario.

A feasibility study could be conducted for the development of an ODSF that was based upon undifferenced phase measurement residuals rather than ionosphere-free residuals (van der Marel 2012). Single-frequency PPP requires the sourcing of ionosphere delays from elsewhere, such as a Gridded Ionosphere Map (GIM) from the IGS (Wienia 2008). If this was found to be feasible, then the ODSF algorithms could be applied to measurements made at reference stations of RTK networks.

10.3.2 Multi-GNSS precise point positioning

It was suggested in chapter 6 that in instances of a satellite outage, the ODSF2 algorithm (which uses all measurements available whether or not a multipath correction for it exists) could be used during periods of low satellite availability or poor geometry and the ODSF1 algorithm (which *excludes* any measurement for which a multipath correction cannot be derived from the previous day) used otherwise. Further research would be needed to identify by what criteria one would switch between the two algorithms. Perhaps a better approach would be to give less weight to

measurements that have not been corrected for multipath rather than simply excluding them. However, it was also suggested that using satellites from other GNSSs such as GLONASS, Galileo and BeiDou could be used to boost satellite availability for PPP (Jokinen et al. 2012, Li et al. 2014, Cai et al. 2015). By using so many additional satellites, one could implement the ODSF1 algorithm and exclude/de-weight observations of satellites with anomalous repeat times with reduced risk of seriously reducing measurement redundancy, dramatically increasing DOP values and impacting negatively on the stability of a PPP position time series. Boosting satellite availability could stimulate research into more sophisticated and innovative observation weighting strategies such as those suggested in section 6.3.7.

The possibility of applying an algorithm similar to the ODSF algorithm to other GNSSs was briefly discussed in section 1.6. In principle, there is no reason why such an algorithm could not be applied to other GNSSs: They each have different ground track repeat periods to GPS satellites. However, some research is required to find out precisely how repeatable these ground tracks are *in terms of the azimuth and elevation* of the satellites from the point of view of a user: As mentioned above and in chapters 4 and 5, the skytrack of a particular satellite needs to repeat itself as closely as possible for this form of multipath filtering to be reliable. As seen in chapter 5, even a small angular separation of just 0.016° between adjacent skytracks can negate the advantages of observation-domain multipath filtering. Also, when viewed from the surface of the earth, the IGSO satellites of the BeiDou constellation—which do have a repeat period of one sidereal day (Ye et al. 2015)—move more slowly across the sky compared to MEO satellites. Measurements from these satellites are hence less likely to be affected by 'high-frequency' multipath errors anyway.

10.3.3 Real-time PPP and ambiguity resolution

Another problem associated with the PPP algorithm implemented in this thesis is the fact that the ionosphere-free phase ambiguity values associated with each satellite are not fixed but are allowed to change over time within the Kalman filter algorithm, albeit slowly. More advanced PPP techniques have been developed (Ge et al. 2008, Laurichesse et al. 2009, Bertiger et al. 2010) that make it possible to fix ambiguity values, allowing better estimation of position and the slowly-varying troposphere states. Since the main aim of this thesis was to measure coseismic offset accurately over the course of just a few minutes, it was reasonable to assume that by tightly constraining the phase ambiguity states by assigning them low power spectral density (PSD) values (see section 2.1.5) would be sufficient. Nevertheless, as discussed in chapter 3, the stability of a PPP position time series over long time intervals of a few thousand seconds (e.g. above 3,000 s) after applying the ODSF algorithm was often worse than if the PDSF was applied. An improvement in accuracy and stability over these longer time intervals is anticipated if ambiguity values were fixed and the ODSF algorithm applied. This is because fixing phase ambiguities effectively reduces the number of Kalman filter states to be estimated and the correlations between them (Leick 2004). For example, error in the troposphere states will no longer alias into the phase ambiguity states.

All of the experiments in this thesis used post-processed 'final' orbit and high-rate clock models

from the Centre for Orbit Determination in Europe (CODE). This was in order to show as fully as possible the ability of those algorithms in removing high-frequency phase multipath errors. Otherwise, that benefit would likely have been at least partly obscured, particularly by mis-modelled satellite clock offsets. Nevertheless, there is no reason why the sidereal filter algorithms described in this thesis cannot be applied in a near-real-time scenario such as a tsunami early-warning system. Near-real-time PPP has been made a reality in recent years through the IGS Real-time Service[1] and via commercial providers such as Veripos. Improvement is anticipated with the atomic clocks placed onboard new GNSS satellites, such as the passive hydrogen maser clocks onboard Galileo satellites, which are more stable over short time intervals (Griggs et al. 2015).

10.3.4 Increasing the breadth and depth of analysis

The results of the experiments in this thesis could be strengthened by sampling data from a much larger number of reference stations. Measurements from only eight monitoring stations were used in chapters 3 to 6 to assess the overall performance of the sidereal filter algorithms under static conditions. As mentioned above, the sidereal filters were found on average to improve the stability of a position time series over periods of time ranging from a few tens of seconds up to a few hundred seconds, but performance varied widely between the different stations. Obtaining high-rate (>1 Hz) GPS measurements from organisations such as UNAVCO is relatively easy at present, so it is not particularly difficult to test the sidereal filter algorithms over a much greater number of receivers. Doing so would greatly increase the strength of the results and yield greater insight into the problem of reducing multipath error across a wide range of antennas and their surrounding environments.

A detailed analysis of the performance of the ODSF algorithms was undertaken in chapters 4 and 5 by plotting colour-coded measurement residuals on a 'skyplot' by azimuth and elevation angle. These plots helped to explain the difference in performance between the two types of ODSF over the periods of time under investigation. No similar analyses were undertaken elsewhere in this thesis, but they may have been useful. For example: A wide variation in the stability of different PPP position time series and the varying success of the sidereal filter algorithms across a number of different continuously operating receiver stations (CORS) was observed in chapter 9 (figures 9.9 to 9.27), but a detailed investigation into why this was so, as suggested in section 9.6, was not undertaken. Was it because of the nature of the environment surrounding each of the antennas, or because of significant changes in those environments between adjacent days? Further analysis could explain the reason why the sidereal filter algorithms performed so poorly at station UCL on 31st August 2013 (see section 6.2.3) and yet perform relatively well at the same location around 17 months earlier on 27th March 2012 (see section 3.4). Was this simply because of the different arrangement of satellites across the sky between these two occasions, or was it due to some significant change in the environment surrounding the antenna? Could these variations in performance both temporally and spatially be due to other reasons, such as anomalies in the

[1] Available at http://beta.igs.org/rts

satellite orbit and clock files or differences in the receiver hardware from one site to another? A detailed and rigorous analysis similar to those in chapters 4 and 5, involving high-rate measurements over periods of several consecutive days, together with weather records and site photographs, would help to answer these questions. Such analyses may be time-consuming but could help identify errors that are not due to multipath interference and hence lead to possible improvements in PPP processing. Isolating and removing such errors would also assist with the development of the more sophisticated multipath correction algorithm discussed in section 5.7 by improving the integrity of the corrections.

Similarly, the rooftop experiment in chapter 7 could be repeated over multiple days with a larger number of displacement events. However, the most pressing issue is to test the effectiveness of the sidereal filter algorithms in accurately determining coseismic displacements associated with a real seismic event. With the results from chapter 8 indicating that the sidereal filters were actually more of a hinderance than a benefit, further testing is therefore needed to establish whether or not this is generally the case. In chapter 8, data from twenty-two stations was used to assess the performance of the sidereal filters in improving the measurement of coseismic displacements. However, these displacements were associated with a *single* earthquake. Similar experiments could be applied to any available high-rate data from other earthquakes with differing magnitudes and type of fault rupture, such as the M_{W} 9.0 2011 Tohoku-Oki earthquake or any earthquake with a magnitude greater than around M_{W} 8.5 that has the potential to generate a tsunami. Following on from the discussion in section 1.2.2, it would be desirable if the coseismic displacements found by PPP processing and sidereal filtering were actually used to estimate moment magnitude and/or tsunami wave height, particularly when using only a few sparsely distributed monitoring stations, e.g. with roughly 100 km between stations.

As mentioned in sections 9.6 and 9.7, it is reasonable to assume that observation domain sidereal filtering would be beneficial when comparing or combining GNSS data with measurements obtained by seismometers, particularly if such instruments were co-located. It is suggested that research be conducted to quantify that benefit, especially in any development of an instrument that combines the measurements of a GNSS receiver and a seismometer.

10.4 Original contributions to knowledge

- Observation-domain sidereal filter (multipath correction) algorithms were developed and applied in the context of high-rate precise point positioning (PPP). The author is not aware of another study of multipath filtering at the measurement level in the context of both PPP and using a measurement rate at or above 1 Hz.

- This thesis contains an in-depth study of observation-domain sidereal filtering and has demonstrated its general superiority over position-domain sidereal filtering in reducing errors caused by phase multipath interference, especially in terms of reducing particularly short-period oscillating errors and in terms of positioning stability during satellite outages.

- Chapter 5 of this thesis has shown that the technique of 'sidereal filtering' is limited by the nature of high-frequency phase multipath errors: The analysis in section 5.5.1 showed that using the most accurate satellite repeat period does not necessarily yield the optimal correction for multipath error. If there is further motivation to remove high-frequency multipath, then future research in this area *must* take into account the potentially intricate patterns formed by measurement residuals when distributed by azimuth and elevation, as mentioned in section 5.7.

Appendix A

Curvilinear position from Cartesian position

This section describes a method used to convert a Cartesian earth-centred earth-fixed (ECEF) position (x, y, z) to geodetic latitude, longitude and geodetic height (ψ, λ, h) with respect to a given ellipsoid—a regular shape used to approximate the shape of the earth. Such an ellipsoid is rotationally symmetric about the north-south axis (Groves 2013*b*) and can be defined by the lengths of its semi-major axis a (the distance from the centre to the equator) and semi-minor axis b (distance from the centre to the north or south pole). Given values for a and b, the eccentricity e of such an ellipsoid can be calculated:

$$e = \sqrt{\frac{a^2 - b^2}{a^2}} \tag{A.1}$$

In the case of the GRS80 ellipsoid (Moritz 2000), $a = 6,378,137.0\,\text{m}$ and $b = 6,356,752.3141\,\text{m}$.

The following method to determine curvilinear position from a given cartesian position is one of four iterative methods described in Groves (2013*b*). It is this method that is implemented in the PPP software.

Given an ECEF position (x, y, z), an initial latitude ψ_k, where k denotes the iteration, is calculated using the following equation:

$$\psi_k = \arctan \frac{z}{\sqrt{x^2 + y^2}\sqrt{1 - e^2}} \tag{A.2}$$

The parameter ν_k (radius of curvature) is then calculated:

$$\nu_k = \frac{a}{\sqrt{1 - e^2 \sin^2 \psi_k}} \tag{A.3}$$

A new value for the latitude ψ_{k+1} can be calculated:

$$\psi_{k+1} = \arctan \frac{z + e^2 \nu \sin \psi_k}{\sqrt{x^2 + y^2}} \tag{A.4}$$

Equations (A.3) and (A.4) are iterated until the desired level of precision is reached.

Given the final values for ψ and ν after the above iteration, geodetic height h can be calculated using the following equation:

$$h = \frac{\sqrt{x^2 + y^2}}{cos(\psi)} - \nu \tag{A.5}$$

The calculation of longitude λ is given by

$$\lambda = \arctan \left(\frac{y}{x} \right) \tag{A.6}$$

Appendix B

An introduction to Allan deviation

Allan deviation is a measure originally developed to analyse the frequency stability of atomic clocks (Allan 1966). However, in this thesis, it is used to analyse the stability of position time series. Other studies such as Dach et al. (2009) and Friederichs (2010) have also used Allan deviation to analyse position time series. This is because Allan deviation can be used to characterise the non-stationary noise processes often present in position time series (such as a random walk, for example). In contrast, while *standard deviation* is perfectly appropriate to describe the 'spread' of a set of data, it alone does not help to characterise any non-stationary noise processes that may be present. Non-stationary processes have a mean and variance that varies with time.

Allan deviation, conventionally denoted by σ_y, is the square-root of Allan variance σ_y^2. For a time series $X = \{x_1, x_2, ..., x_N\}$ regularly-spaced by a time interval τ_0, the Allan variance $\sigma_y^2(\tau)$ for a time interval (or 'averaging interval') $\tau = \tau_0$ is defined by Ferre-Pikal & Walls (2005) as follows:

$$\sigma_y^2(\tau) = \frac{1}{2(N-2)\tau^2} \sum_{i=1}^{N-2} (x_{i+2} - 2x_{i+1} + x_i)^2 \tag{B.1}$$

However, in this thesis and in most other studies, 'overlapping' Allan deviation is used rather than standard Allan deviation due to its superior performance over long averaging intervals. The overlapping Allan variance is defined for a time interval $\tau = n\tau_0$ ($n \in \mathbb{N}$) as follows:

$$\sigma_y^2(\tau) = \frac{1}{2(N-2n)\tau^2} \sum_{i=1}^{N-2n} (x_{i+2n} - 2x_{i+n} + x_i)^2 \tag{B.2}$$

In simple terms, Allan deviation is a measure of a signal's average stability across a given averaging interval τ. A lower Allan deviation value indicates a more stable position time series across that time interval. A higher Allan deviation indicates lower stability. An Allan deviation value can be computed for small averaging intervals, as small as the spacing between the epochs in the original dataset, up to one less than half the length of the dataset itself, if desired. When

examining the summation in equation (B.2), the maximum value of n cannot not equal or exceed half the number of data points. For large values of n, i.e. larger averaging intervals, the number of terms in the summation reduces, leading to a less reliable 'average' for the Allan variance value. For this reason, the largest averaging interval used is limited to at most a fifth of the size of the dataset being examined.

The ability to characterise noise processes arises from plotting the various Allan deviation values for the same set of data against their respective averaging intervals on logarithmic scales (base 10), often referred to as a 'sigma-tau' plot. The gradient of the resulting sigma-tau curve can be used to identify different types of noise process.

For example, figure B.1 shows how three different types of noise process look when plotted both in the time domain and with Allan deviation values $\sigma_y(\tau)$ plotted against averaging interval τ. Notice that two simulated white noise processes are shown in figure B.1a: one with standard deviation $\sigma = 1$ and the other $\sigma = 0.5$. The white noise time series with lower standard deviation has lower Allan deviation values for all averaging intervals. This means that this time series is the more stable of the two over all of those time intervals. The ability of a sidereal filter to simply reduce Allan deviation values is the performance measure that is fundamental to this thesis. The gradient of the sigma-tau curve can be analysed: A gradient of -1 is indicative of either white (or flicker) noise. Indeed in figure B.1a, both Allan deviation curves have a gradient of -1 across all averaging intervals up to 500 s in length, and so the dominant noise process is considered to be white noise or flicker noise across over these time intervals.

In contrast, figure B.1b shows a simulated random walk. The gradient of the corresponding Allan deviation curve for time intervals under about 200 s is close to $-1/2$, which is indeed indicative of a random walk noise process. Notice that the gradient of the line diverges slightly from $-1/2$ for large averaging intervals. As explained above, this is because there are fewer samples to produce a reliable Allan deviation value as averaging intervals get larger.

Figure B.1c shows a sine wave with a period of 100 s, $X(t) = \sin(\pi t/50) + \varepsilon(t)$, where $\varepsilon(t)$ is a random variable with standard deviation $\sigma = 1$. Its corresponding Allan deviation curve has an 'overall' gradient of -1, but possesses peaks and troughs as a consequence of the periodic component of the signal. Each trough corresponds to an integer multiple of the period of the signal with the first trough indicating the fundamental period. Such oscillations are occasionally seen in this thesis when analysing position time series spanning periods of strong phase multipath interference.

An aim of this thesis is to examine to what extent an ODSF can increase the stability of a position time series over time intervals of just a few minutes. Allan deviation is used frequently throughout much of this thesis as a convenient measure of the stability of a time series over various lengths of averaging interval. For a more comprehensive introduction to stability analysis using Allan deviation, the reader is recommended to refer to Riley (2008), Ferre-Pikal & Walls (2005) or Friederichs (2010).

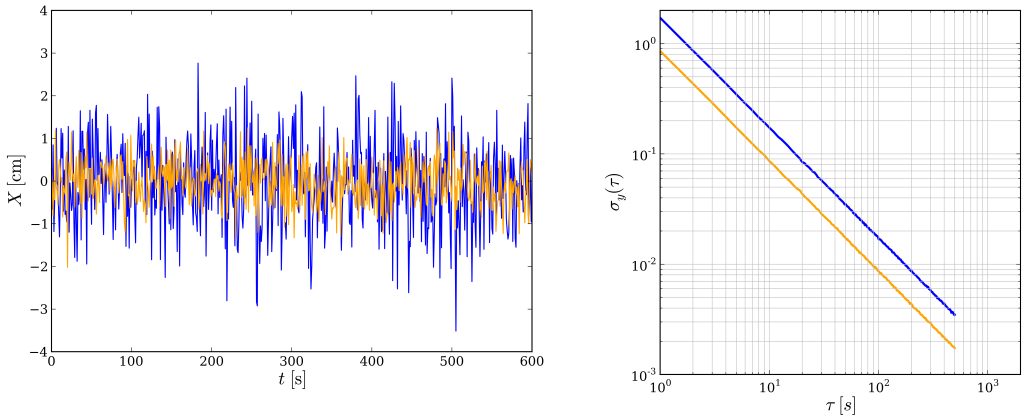

(a) White noise: *blue* – $X(t) \sim \mathcal{N}(\mu = 0,\ \sigma = 1)$; *orange* – $X(t) \sim \mathcal{N}(\mu = 0,\ \sigma = 0.5)$

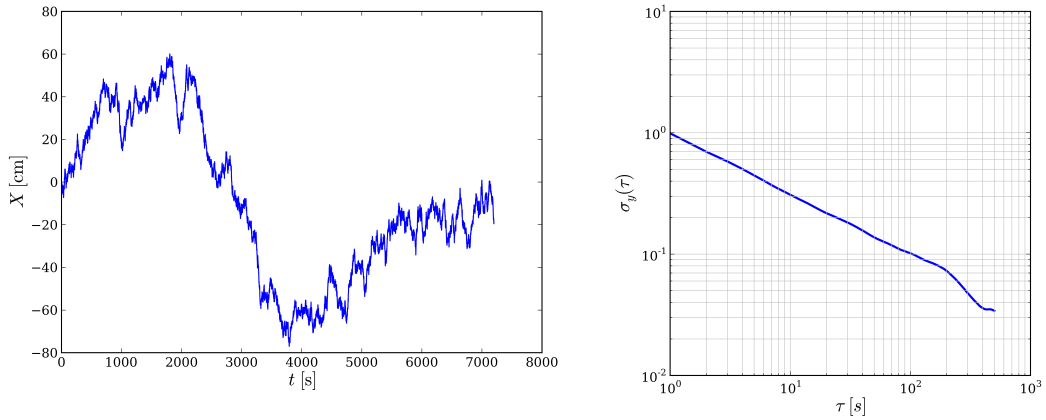

(b) Random walk: $X(t) = X(t-1) + \varepsilon(t)$ where $\varepsilon(t) \sim \mathcal{N}(\mu = 0,\ \sigma = 1)$

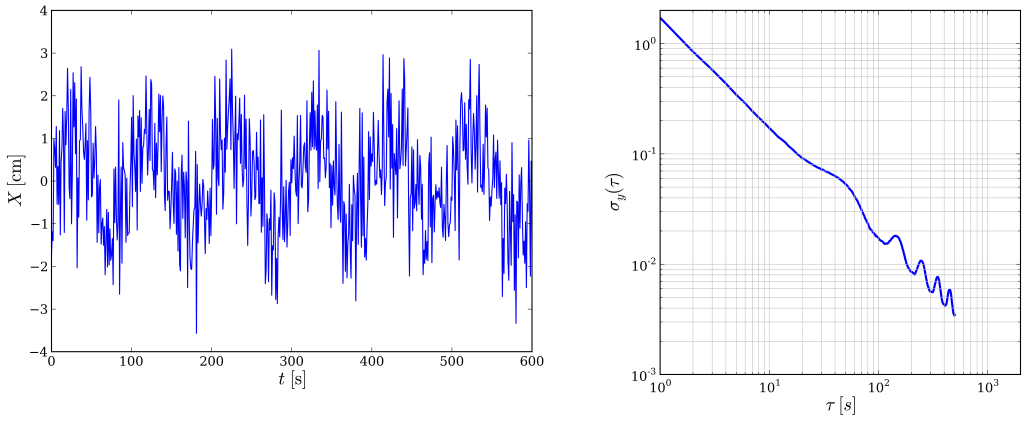

(c) Sine wave plus white noise: $X(t) = \sin(\pi t/50) + \varepsilon(t)$, where $\varepsilon(t) \sim \mathcal{N}(\mu = 0,\ \sigma = 1)$

Figure B.1 – Three examples of noise process types plotted in the time domain together with their corresponding sigma-tau curves. The plots on the left-hand side show simulated data plotted in the time domain. On the right-hand side are their corresponding sigma-tau curves.

Appendix C

Dilution of Precision

Dilution of precision (DOP) values are commonly used to describe the effect of the receiver and satellite geometry on positioning accuracy (Leick 2004). There are different kinds of DOP value: geometric (GDOP), position (PDOP), horizontal (HDOP), vertical (VDOP) and time (TDOP). These values can be used to relate the standard deviation of the measurements (pseudorange or phase) σ_0 to the standard deviation of the three-dimensional position σ_P, horizontal position σ_H, vertical position σ_V, the standard deviation receiver clock offset σ_T, or the standard deviation of the total position and clock solution σ_G by the following simple equations (Groves 2013*b*):

$$\sigma_G = \sigma_0 \text{ GDOP}$$
$$\sigma_P = \sigma_0 \text{ PDOP}$$
$$\sigma_H = \sigma_0 \text{ HDOP}$$
$$\sigma_V = \sigma_0 \text{ VDOP}$$
$$\sigma_T = \sigma_0 \text{ TDOP}$$

However, these equations assume that all measurements have the same standard deviation and that they are uncorrelated (Leick 2004). Of course, the lower the DOP value, the better. A lower DOP value indicates good receiver-satellite geometry.

According to Yarlagadda et al. (2000), DOP values can be calculated using the following procedure: Firstly, a unit-vector from the user receiver u with coordinates $(a_{x_u}, a_{y_u}, a_{z_u})$ to each visible satellite j (of which there are at least four) with coordinates $(a_{x_j}, a_{y_j}, a_{z_j})$ is calculated where

$$a_{\xi_j} = \frac{\xi_j - \xi_u}{\sqrt{(x_j - x_u)^2 + (y_j - y_u)^2 + (z_j - z_u)^2}}, \quad \xi = x, y, z$$

A matrix $\mathbf{A}$ is then formed such that:

$$\mathbf{A} = \begin{pmatrix} a_{x_1} & a_{y_1} & a_{z_1} & 1 \\ a_{x_2} & a_{y_2} & a_{z_2} & 1 \\ \vdots & \vdots & \vdots & \vdots \\ a_{x_j} & a_{y_j} & a_{z_j} & 1 \end{pmatrix}$$

Then the matrix $\mathbf{D}$ is computed:

$$\mathbf{D} = (\mathbf{A}^{\mathrm{T}}\mathbf{A})^{-1} = \begin{pmatrix} d_{11} & d_{21} & d_{31} & d_{41} \\ d_{12} & d_{22} & d_{32} & d_{42} \\ d_{13} & d_{23} & d_{33} & d_{43} \\ d_{14} & d_{24} & d_{34} & d_{44} \end{pmatrix}$$

The DOP values are then calculated as follows:

$$\begin{aligned} \mathrm{GDOP} &= \sqrt{d_{11} + d_{22} + d_{33} + d_{44}} = \sqrt{\mathrm{tr}(\mathbf{D})} \\ \mathrm{PDOP} &= \sqrt{d_{11} + d_{22} + d_{33}} \\ \mathrm{HDOP} &= \sqrt{d_{11} + d_{22}} \\ \mathrm{VDOP} &= \sqrt{d_{33}} \\ \mathrm{TDOP} &= \sqrt{d_{44}} \end{aligned}$$

Note that HDOP and VDOP only make sense in a local east-north-up (or north-east-down) coordinate system. GDOP, PDOP and TDOP are insensitive to the coordinate system used.

For a more comprehensive analysis of GPS dilution of precision (DOP), the reader is recommended to refer to Yarlagadda et al. (2000) or Groves (2013*b*).

Appendix D

Estimation of coseismic offsets and their precision

As stated in section 8.3.1, a more precise estimate of the coseismic offsets at each of the selected PBO monitoring stations were found by fitting lines to time series of daily positions spanning several weeks or months. This section describes the method in more detail.

For example, figure 8.2 on page 212 shows the change in northing over a period of 200 days either side of 4$^{\text{th}}$ April 2010—the day on which the M_{W} 7.2 El Mayor–Cucapah earthquake. A straight line of the form $\text{N}_{\text{pre}}(t) = \text{P}t + \text{Q}$ was fitted to the northing ordinates over the 200 days *preceding* the earthquake, where t is the time in units of days, $\text{N}_{\text{pre}}(t)$ is the northing ordinate in millimetres at time t, and P, Q, are real numbers. This was achieved by the method of least squares estimation which is described below. Similarly, a curve of the form $\text{N}_{\text{post}}(t) = \text{A}e^{\text{B}t} + \text{C}t + \text{D}$ was fitted to the northing values for the 200 days following the event, i.e. *post* earthquake. The values, A, B, C, D were found by the iterative process of non-linear least squares estimation. An estimate of the northing component of the coseismic offset ΔN was then calculated as $\Delta\text{N} = \text{N}_{\text{post}}(t_q) - \text{N}_{\text{pre}}(t_q)$ where t_q is the time of the onset of the earthquake.

D.1 Fitting of a straight line

Consider, for example, 200 measurements of northing $\text{N}_1, \ldots, \text{N}_{200}$ occurring at times $t_1, \ldots, t_{200}$, respectively. Each of these measurements have associated standard deviations $\sigma_{\text{N}_1}, \ldots, \sigma_{\text{N}_{200}}$. In this case, the northing ordinates and their standard deviations are given in units of millimetres and time is given in units of days (each aligned to midday). It is assumed that there is an approximately linear functional relationship between the northing values and time t, i.e. $\text{N}_{\text{pre}}(t) = \text{P}t + \text{Q}$ where the parameters P and Q are real numbers. The values of P and Q can be estimated using the

following equation (Cross 1983):

$$\hat{\mathbf{x}} = (\mathbf{H}^{\mathrm{T}}\mathbf{W}\mathbf{H})^{-1}\mathbf{H}^{\mathrm{T}}\mathbf{W}\tilde{\mathbf{z}} \tag{D.1}$$

$$\text{where} \quad \hat{\mathbf{x}} = \begin{pmatrix} \mathrm{P} \\ \mathrm{Q} \end{pmatrix}, \quad \mathbf{H} = \begin{pmatrix} t_1 & 1 \\ \vdots & \vdots \\ t_{200} & 1 \end{pmatrix}, \quad \tilde{\mathbf{z}} = \begin{pmatrix} \mathrm{N}_1 \\ \vdots \\ \mathrm{N}_{200} \end{pmatrix}, \quad \mathbf{W} = {\mathbf{C}_{\mathbf{z}}}^{-1}$$

$\mathbf{C_z} = \mathrm{diag}(\sigma^2_{\mathrm{N}_1}, \ldots, \sigma^2_{\mathrm{N}_{200}})$ is the covariance matrix of the northing measurements. $\mathbf{W}$ is used to give a higher weighting to the more precise measurements and is equal to the inverse of $\mathbf{C_z}$.

The covariance matrix of the parameters P and Q is

$$\mathbf{C_x} = \begin{pmatrix} \sigma^2_{\mathrm{P}} & C_{\mathrm{PQ}} \\ C_{\mathrm{PQ}} & \sigma^2_{\mathrm{Q}} \end{pmatrix} = (\mathbf{H}^{\mathrm{T}}\mathbf{W}\mathbf{H})^{-1} \tag{D.2}$$

where C_{PQ} denotes the covariance of the parameters P and Q. $C_{\mathrm{PQ}} = \sigma_{\mathrm{P}}\sigma_{\mathrm{Q}}\rho_{\mathrm{PQ}}$ where ρ_{PQ} is the correlation coefficient of P and Q, which varies between -1 and 1, and σ_{P}, σ_{Q} are the standard deviations of P and Q, respectively.

Once the parameters P, Q and their associated covariance matrix $\mathbf{C_x}$ have been estimated, the northing ordinate of the tracking station just before the earthquake occured at time t_q can be estimated as follows:

$$\mathrm{N}_{\mathrm{pre}}(t_q) = \mathrm{P}t_q + \mathrm{Q} \tag{D.3}$$

and its associated standard deviation is estimated as follows:

$$\sigma_{\mathrm{N}_{\mathrm{pre}}(t_q)} = \sqrt{\mathbf{G}\mathbf{C_x}\mathbf{G}^{\mathrm{T}}} \quad \text{where} \quad \mathbf{G} = \begin{pmatrix} t_q & 1 \end{pmatrix} \tag{D.4}$$

The easting component of the coseismic displacement is similarly estimated.

D.2 Fitting of a exponential decay function

Consider, for example, 200 measurements of northing $\mathrm{N}_1, \ldots, \mathrm{N}_{200}$ occurring at times $t_1, \ldots, t_{200}$, with associated standard deviations $\sigma_{\mathrm{N}_1}, \ldots, \sigma_{\mathrm{N}_{200}}$, respectively. In this example, it is assumed that the functional relationship between the northing values and time t is one of exponential decay, i.e. $\mathrm{N}_{\mathrm{post}}(t) = \mathrm{A}e^{\mathrm{B}t} + \mathrm{C}t + \mathrm{D}$ where parameters A, B, C, and D are real numbers. This function is not linear with respect to these parameters. Therefore, they are estimated by the iterative process of non-linear least squares estimation. This involves solving for corrections δA, δB, δC, δD to initial estimates of the parameters $\widehat{\mathrm{A}}^-$, $\widehat{\mathrm{B}}^-$, $\widehat{\mathrm{C}}^-$, $\widehat{\mathrm{D}}^-$, respectively. Updated estimates, $\widehat{\mathrm{A}}^+$, $\widehat{\mathrm{B}}^+$, $\widehat{\mathrm{C}}^+$, $\widehat{\mathrm{D}}^+$ can be obtained using the following equation:

$$\hat{\mathbf{x}}^+ = \hat{\mathbf{x}}^- + (\mathbf{H}^{\mathrm{T}}\mathbf{W}\mathbf{H})^{-1}\mathbf{H}^{\mathrm{T}}\mathbf{W}\mathbf{b} \tag{D.5}$$

$$\text{where} \quad \hat{\mathbf{x}}^{+} = \begin{pmatrix} \widehat{\mathrm{A}}^{+} \\ \widehat{\mathrm{B}}^{+} \\ \widehat{\mathrm{C}}^{+} \\ \widehat{\mathrm{D}}^{+} \end{pmatrix}, \quad \hat{\mathbf{x}}^{-} = \begin{pmatrix} \widehat{\mathrm{A}}^{-} \\ \widehat{\mathrm{B}}^{-} \\ \widehat{\mathrm{C}}^{-} \\ \widehat{\mathrm{D}}^{-} \end{pmatrix}, \quad \mathbf{W} = {\mathbf{C_z}}^{-1} = \left(\mathrm{diag}\left(\sigma^2_{\mathrm{N}_1}, \ldots, \sigma^2_{\mathrm{N}_{200}}\right)\right)^{-1}$$

$$\mathbf{H} = \begin{pmatrix} \frac{\partial N_{\mathrm{post}}}{\partial A}\Big|_{\mathrm{A}=\widehat{\mathrm{A}}^{-},t=t_1} & \frac{\partial N_{\mathrm{post}}}{\partial B}\Big|_{\mathrm{B}=\widehat{\mathrm{B}}^{-},t=t_1} & \frac{\partial N_{\mathrm{post}}}{\partial C}\Big|_{\mathrm{C}=\widehat{\mathrm{C}}^{-},t=t_1} & \frac{\partial N_{\mathrm{post}}}{\partial D}\Big|_{\mathrm{D}=\widehat{\mathrm{D}}^{-},t=t_1} \\ \vdots & \vdots & \vdots & \vdots \\ \frac{\partial N_{\mathrm{post}}}{\partial A}\Big|_{\mathrm{A}=\widehat{\mathrm{A}}^{-},t=t_{200}} & \frac{\partial N_{\mathrm{post}}}{\partial B}\Big|_{\mathrm{B}=\widehat{\mathrm{B}}^{-},t=t_{200}} & \frac{\partial N_{\mathrm{post}}}{\partial C}\Big|_{\mathrm{C}=\widehat{\mathrm{C}}^{-},t=t_{200}} & \frac{\partial N_{\mathrm{post}}}{\partial D}\Big|_{\mathrm{D}=\widehat{\mathrm{D}}^{-},t=t_{200}} \end{pmatrix}$$

$$= \begin{pmatrix} e^{\widehat{\mathrm{B}}^{-}t_1} & \widehat{\mathrm{A}}^{-}t_1 e^{\widehat{\mathrm{B}}^{-}t_1} & t_1 & 1 \\ \vdots & \vdots & \vdots & \vdots \\ e^{\widehat{\mathrm{B}}^{-}t_{200}} & \widehat{\mathrm{A}}^{-}t_{200} e^{\widehat{\mathrm{B}}^{-}t_{200}} & t_{200} & 1 \end{pmatrix}$$

$$\mathbf{b} = \begin{pmatrix} \mathrm{N}_1 - N_{\mathrm{post}}(t_1) \\ \vdots \\ \mathrm{N}_{200} - N_{\mathrm{post}}(t_{200}) \end{pmatrix} = \begin{pmatrix} \mathrm{N}_1 - (\widehat{\mathrm{A}}^{-}e^{\widehat{\mathrm{B}}^{-}t_1} + \widehat{\mathrm{C}}^{-}t_1 + \widehat{\mathrm{D}}^{-}) \\ \vdots \\ \mathrm{N}_{200} - (\widehat{\mathrm{A}}^{-}e^{\widehat{\mathrm{B}}^{-}t_{200}} + \widehat{\mathrm{C}}^{-}t_{200} + \widehat{\mathrm{D}}^{-}) \end{pmatrix}$$

The covariance matrix of the parameters $\widehat{\mathrm{A}}^{-}$, $\widehat{\mathrm{B}}^{-}$, $\widehat{\mathrm{C}}^{-}$, $\widehat{\mathrm{D}}^{-}$ is

$$\mathbf{C_x} = \begin{pmatrix} \sigma^2_{\mathrm{A}} & C_{\mathrm{AB}} & C_{\mathrm{AC}} & C_{\mathrm{AD}} \\ C_{\mathrm{AB}} & \sigma^2_{\mathrm{B}} & C_{\mathrm{BC}} & C_{\mathrm{BD}} \\ C_{\mathrm{AC}} & C_{\mathrm{BC}} & \sigma^2_{\mathrm{C}} & C_{\mathrm{CD}} \\ C_{\mathrm{AD}} & C_{\mathrm{BD}} & C_{\mathrm{CD}} & \sigma^2_{\mathrm{D}} \end{pmatrix} = (\mathbf{H}^{\mathrm{T}}\mathbf{W}\mathbf{H})^{-1} \tag{D.6}$$

where C_{AB} denotes the covariance of the parameters $\widehat{\mathrm{A}}^{-}$ and $\widehat{\mathrm{B}}^{-}$, for example, and σ_{A}, σ_{B}, σ_{C}, σ_{D} are the standard deviations of $\widehat{\mathrm{A}}^{-}$, $\widehat{\mathrm{B}}^{-}$, $\widehat{\mathrm{C}}^{-}$, $\widehat{\mathrm{D}}^{-}$, respectively.

The process can be repeated by substituting the elements in $\hat{\mathbf{x}}^{+}$ with those in $\hat{\mathbf{x}}^{-}$ in equation (D.5) until the desired level of precision in the parameters is reached. For all 22 stations used in the analysis in chapter 8, the parameters A, B, C and D were estimated to three decimal places.

Once the parameters A, B, C, D and the associated covariance matrix $\mathbf{C_x}$ have been estimated, the northing ordinate of the tracking station just *after* the earthquake occured at time t_q can be estimated as follows:

$$\mathrm{N}_{\mathrm{post}}(t_q) = \mathrm{A}e^{\mathrm{B}t_q} + \mathrm{C}t_q + \mathrm{D} \tag{D.7}$$

and its associated standard deviation is estimated as follows:

$$\sigma_{\mathrm{N}_{\mathrm{post}}(t_q)} = \sqrt{\mathbf{G}\mathbf{C_x}\mathbf{G}^{\mathrm{T}}} \quad \text{where} \quad \mathbf{G} = \begin{pmatrix} e^{\mathrm{B}t_q} & \mathrm{A}t_q e^{\mathrm{B}t_q} & t_q & 1 \end{pmatrix} \tag{D.8}$$

Finally, the coseismic displacement (northing component) is estimated:

$$\Delta\mathrm{N} = \mathrm{N}_{\mathrm{post}}(t_q) - \mathrm{N}_{\mathrm{pre}}(t_q) \tag{D.9}$$

and it's estimated precision:

$$\sigma_{\Delta\mathrm{N}} = \sqrt{\sigma^2_{\mathrm{N}_{\mathrm{post}}(t_q)} + \sigma^2_{\mathrm{N}_{\mathrm{pre}}(t_q)}} \tag{D.10}$$

The easting component of the coseismic displacement is similarly estimated.

Using these methods, the coseismic displacements associated with the 2010 M_{W} 7.2 El Mayor–Cucapah earthquake at 22 UNAVCO monitoring stations and their precisions were estimated. These are shown in table D.1.

Station ID	Estimated displacement (mm)			
	ΔE	$\sigma_{\Delta\mathrm{E}}$	ΔN	$\sigma_{\Delta\mathrm{N}}$
GMPK	9.036	0.831	−9.117	0.448
P494	42.106	0.703	−191.207	1.163
P495	−4.268	0.505	−36.691	0.412
P496	20.242	0.959	−181.413	0.512
P744	10.290	0.332	−81.692	0.383
SLMS	2.303⋆	0.302	−14.376	0.371
CRRS	3.045	0.583	−35.143	0.358
GLRS	1.700⋆	0.290	−20.968	0.448
IID2	37.055	0.488	−20.806	0.409
P066	−63.777	1.136	−0.221⋆	0.267
P480	−12.386⋆	0.292	−3.342⋆	0.275
P486	−2.345⋆	0.286	−5.760	0.508
P487	−0.812⋆	0.275	−9.547	0.441
P493	3.579⋆	0.224	−45.198	0.301
P497	8.759	0.328	−97.476	0.393
P499	11.241	0.364	−45.115	0.499
P500	59.414	0.518	−58.598	0.439
P507	2.641⋆	0.291	−26.380	0.442
P508	1.694	0.456	−20.996	0.410
P509	15.210	0.382	−36.466	0.364
P510	2.613	1.136	−23.341	0.478
USGC	−4.984	1.034	−14.978	0.284

Table D.1 – Precise coseismic displacements in easting (ΔE) and northing (ΔN) associated with the 2010 M_{W} 7.2 El Mayor–Cucapah earthquake calculated using data from UNAVCO. Asterisks ⋆ denote displacements calculated by fitting only straight lines to UNAVCO data rather than using an exponential decay curve.

Appendix E

Supplementary figures

(a) View north.

(b) View east.

(c) View south.

Figure E.1 – Google Earth images showing the location of the Leica SmartNet antenna UCL (*yellow markers*). Image: Landsat. Copyright: Google, DigitalGlobe, Getmapping.

(a) PBO station SLMS, looking north.

(b) PBO station GMPK, looking southeast.

(c) PBO station P744, looking southeast.

Figure E.2 – Google Earth images showing the location (*yellow markers*) of PBO antennas SLMS, GMPK and P744. Image: Landsat. Copyright: Google, DigitalGlobe.

(a) PBO station P494, looking northeast.

(b) PBO station P495, looking north.

(c) PBO station P496, looking northwest.

Figure E.3 – Google Earth images showing the location (*yellow markers*) of PBO antennas P494, P495 and P496. Image: Landsat. Copyright: Google, DigitalGlobe.

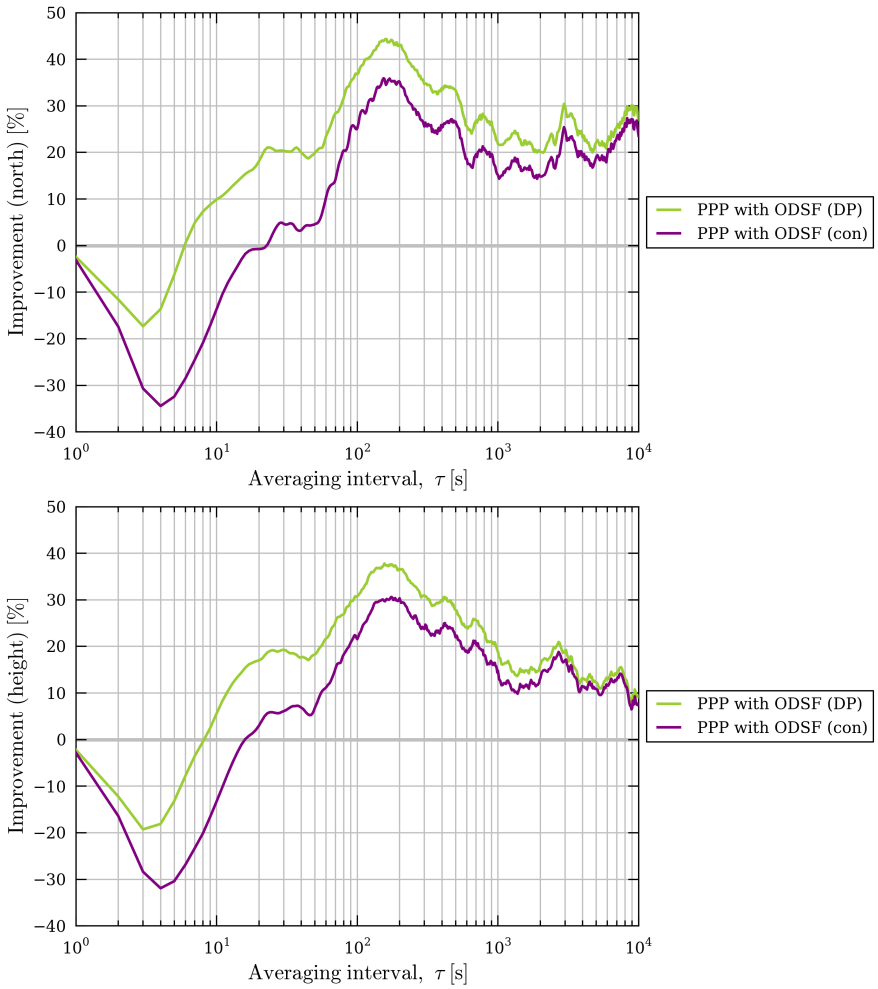

Figure E.4 – Plots showing the percentage improvement (i.e. reduction) in Allan deviation in the north and height components at station UCL between 10:00 and 23:55 on 27$^{\text{th}}$ March 2012, after applying two types of observation-domain sidereal filter (ODSF): the dot-product (DP) ODSF and the 'constellation repeat time' (con) ODSF.

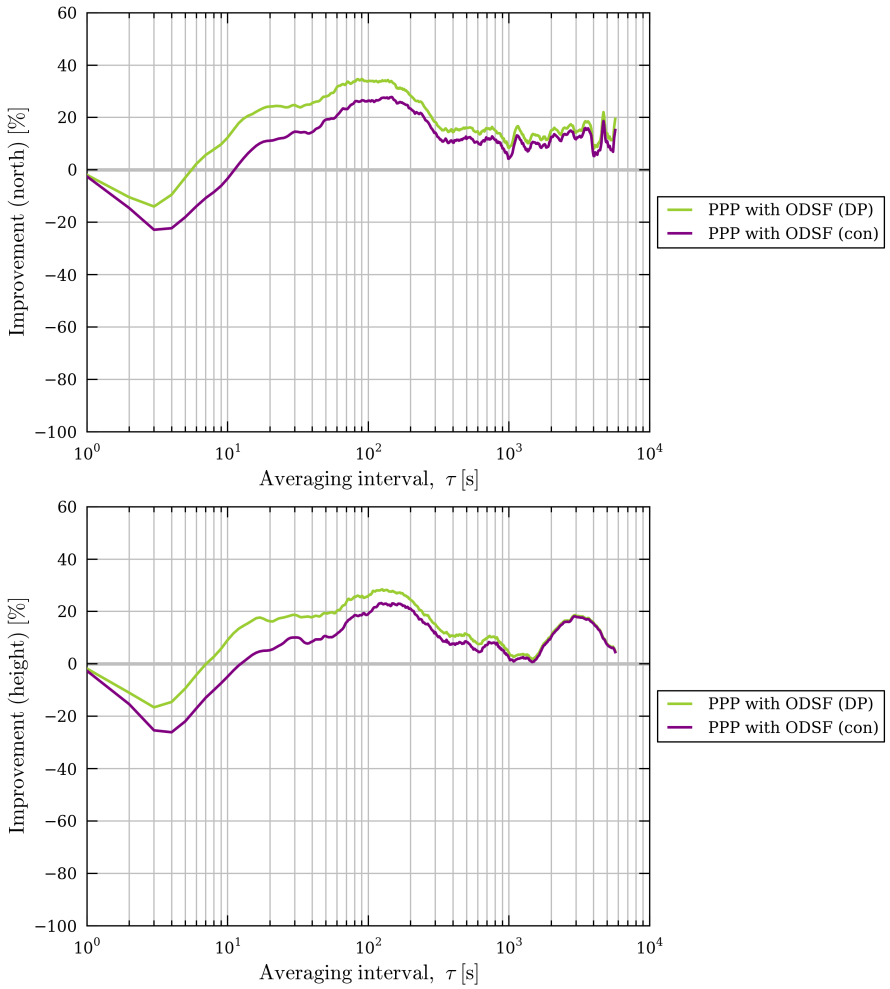

Figure E.5 – Plots showing the percentage improvement (i.e. reduction) in Allan deviation in the north and height components at station UCL between 14:00 and 22:00 on 3$^{\text{rd}}$ September 2013, after applying two types of observation-domain sidereal filter (ODSF): the dot-product (DP) ODSF and the 'constellation repeat time' (con) ODSF.

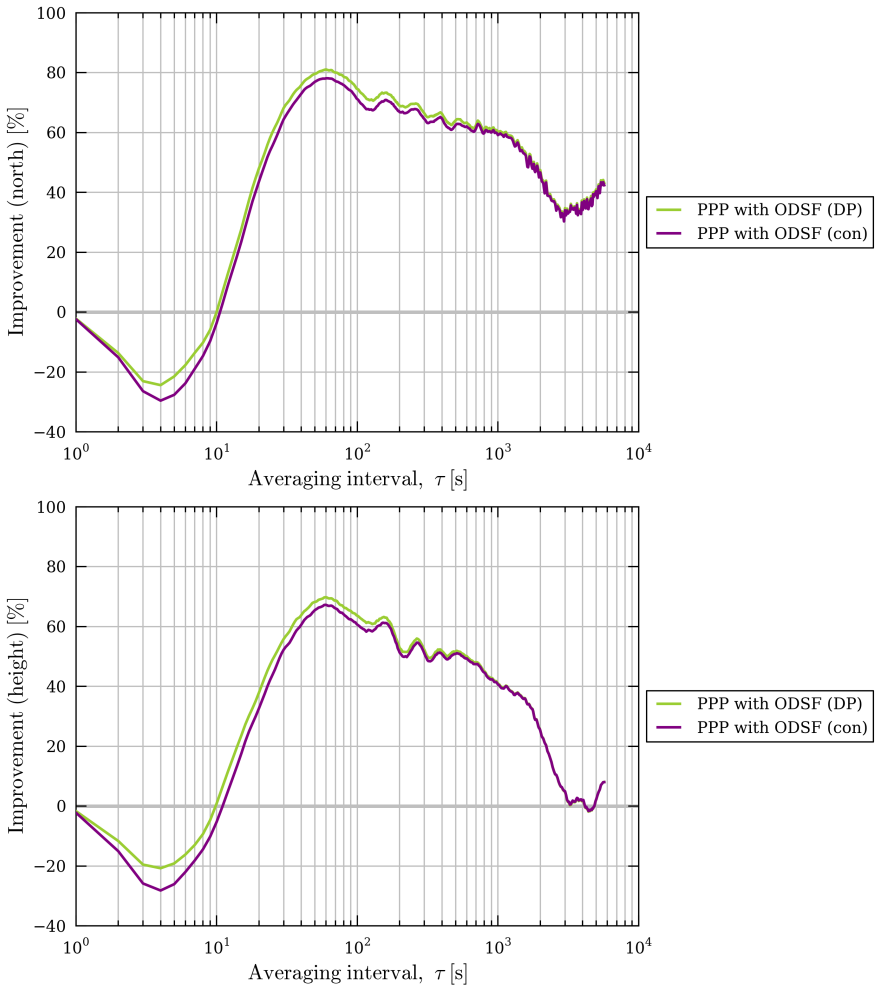

Figure E.6 – Plots showing the percentage improvement (i.e. reduction) in Allan deviation in the north and height components at station UEL between 14:00 and 22:00 on 3rd September 2013, after applying two types of observation-domain sidereal filter (ODSF): the dot-product (DP) ODSF and the 'constellation repeat time' (con) ODSF.

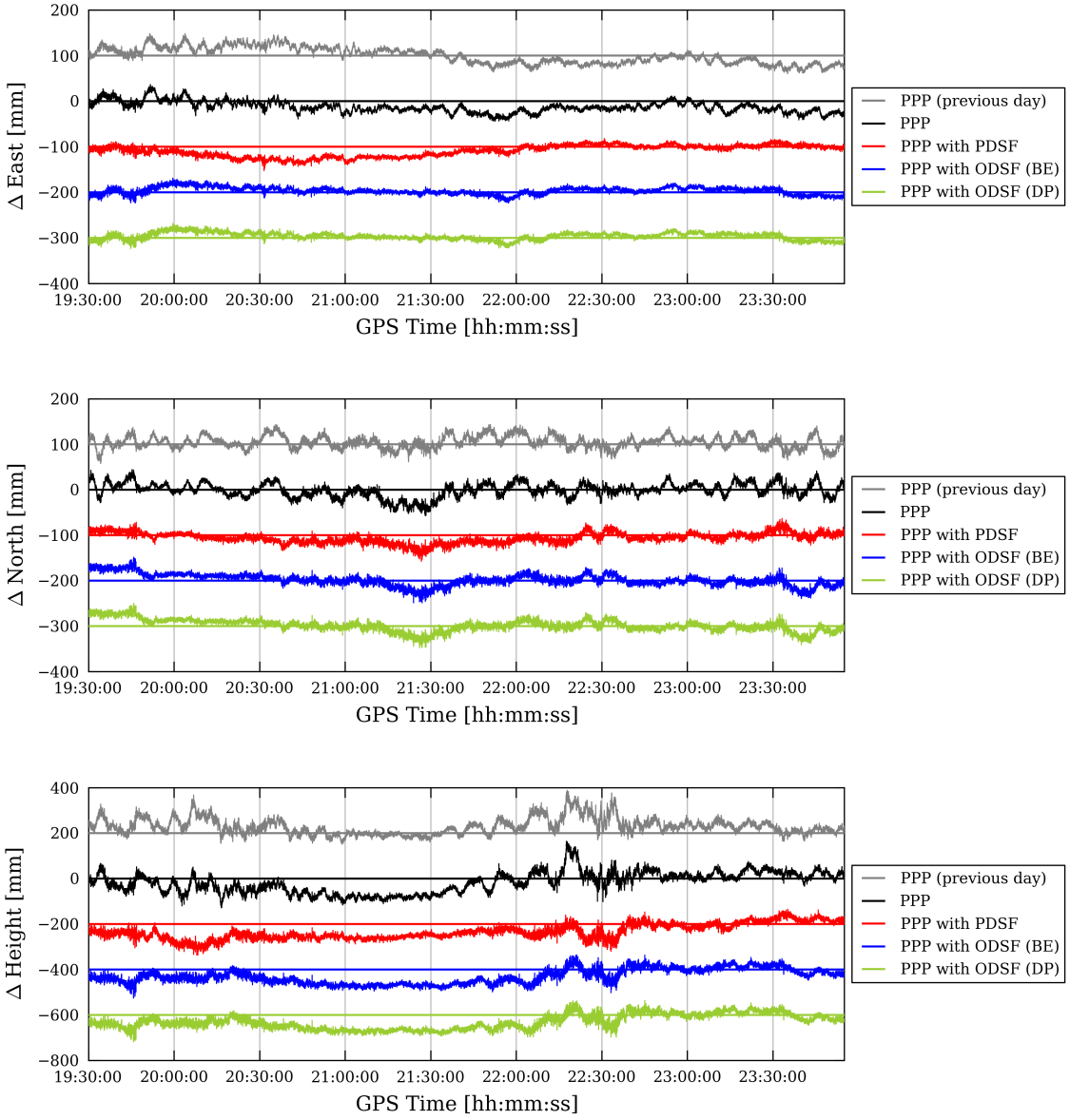

Figure E.7 – Easting, northing and height errors between 19:30 and 23:55 on 3rd April 2010 for receiver GMPK resulting from standard PPP processing and PPP processing with various types of sidereal filter applied. (Each of the time series have been offset from each other by appropriate multiples of 100 mm or 200 mm for clarity).

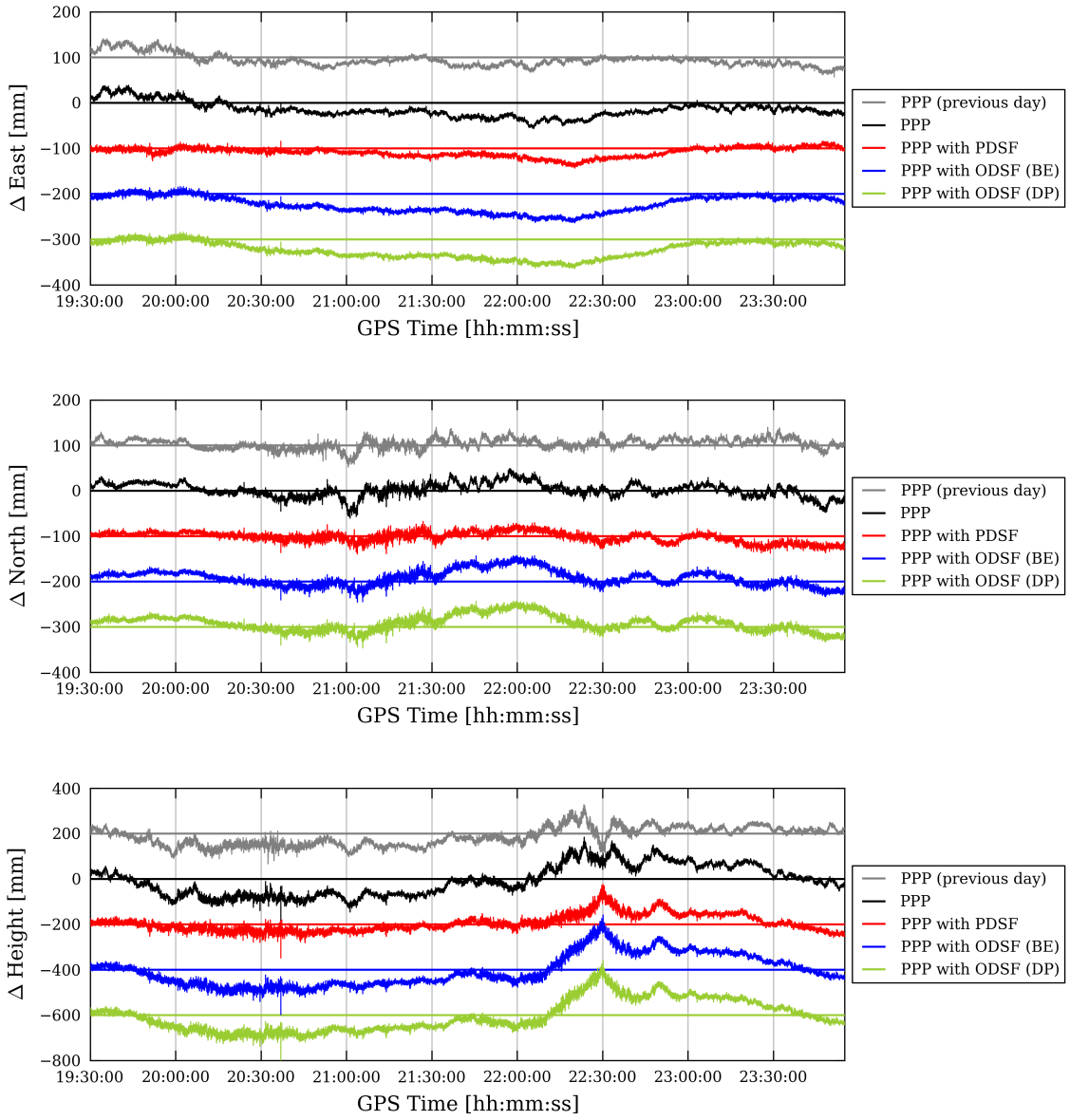

Figure E.8 – Easting, northing and height errors between 19:30 and 23:55 on 3rd April 2010 for receiver P494 resulting from standard PPP processing and PPP processing with various types of sidereal filter applied. (Each of the time series have been offset from each other by appropriate multiples of 100 mm or 200 mm for clarity).

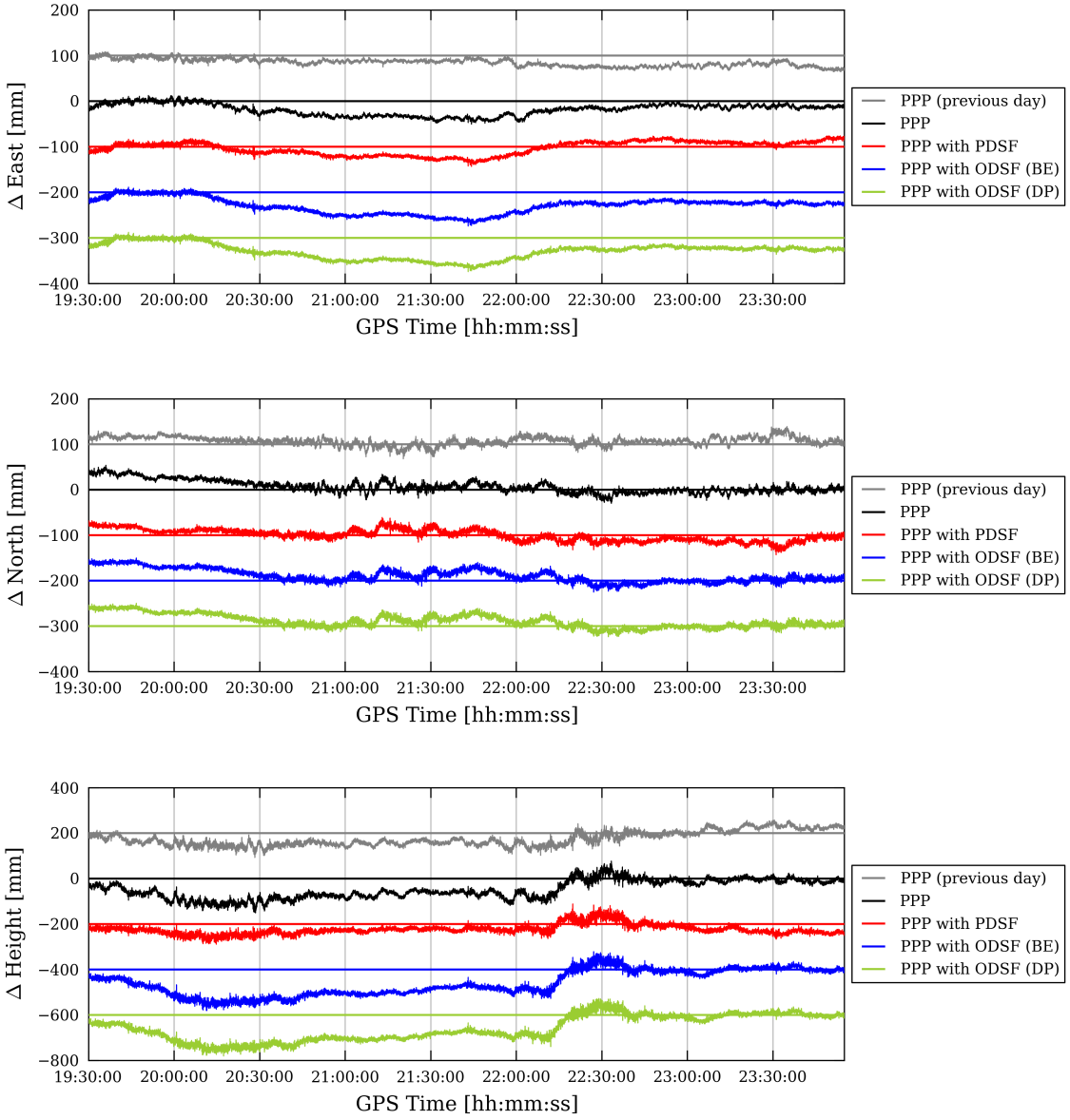

Figure E.9 – Easting, northing and height errors between 19:30 and 23:55 on 3rd April 2010 for receiver P495 resulting from standard PPP processing and PPP processing with various types of sidereal filter applied. (Each of the time series have been offset from each other by appropriate multiples of 100 mm or 200 mm for clarity).

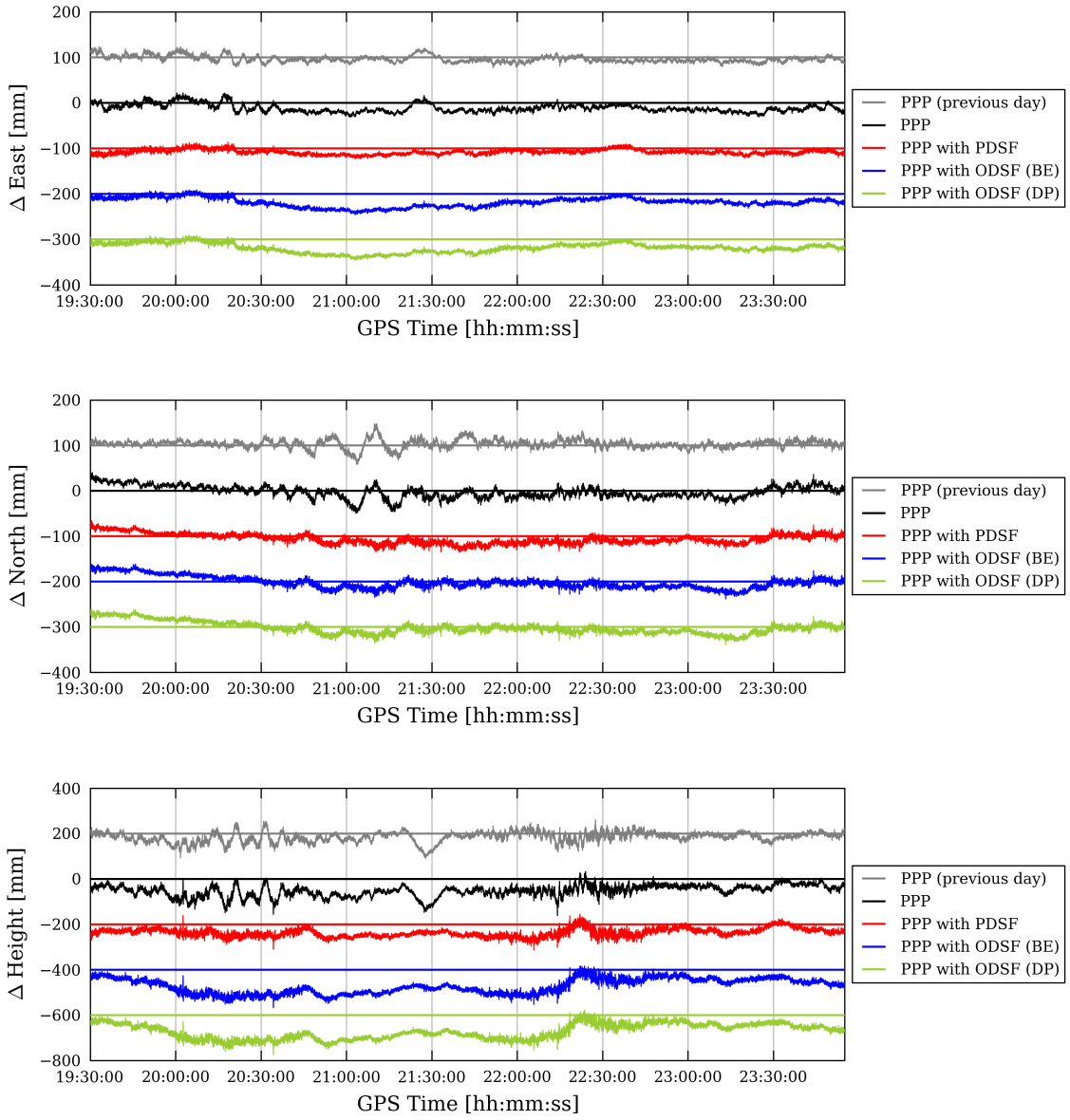

Figure E.10 – Easting, northing and height errors between 19:30 and 23:55 on 3rd April 2010 for receiver P496 resulting from standard PPP processing and PPP processing with various types of sidereal filter applied. (Each of the time series have been offset from each other by appropriate multiples of 100 mm or 200 mm for clarity).

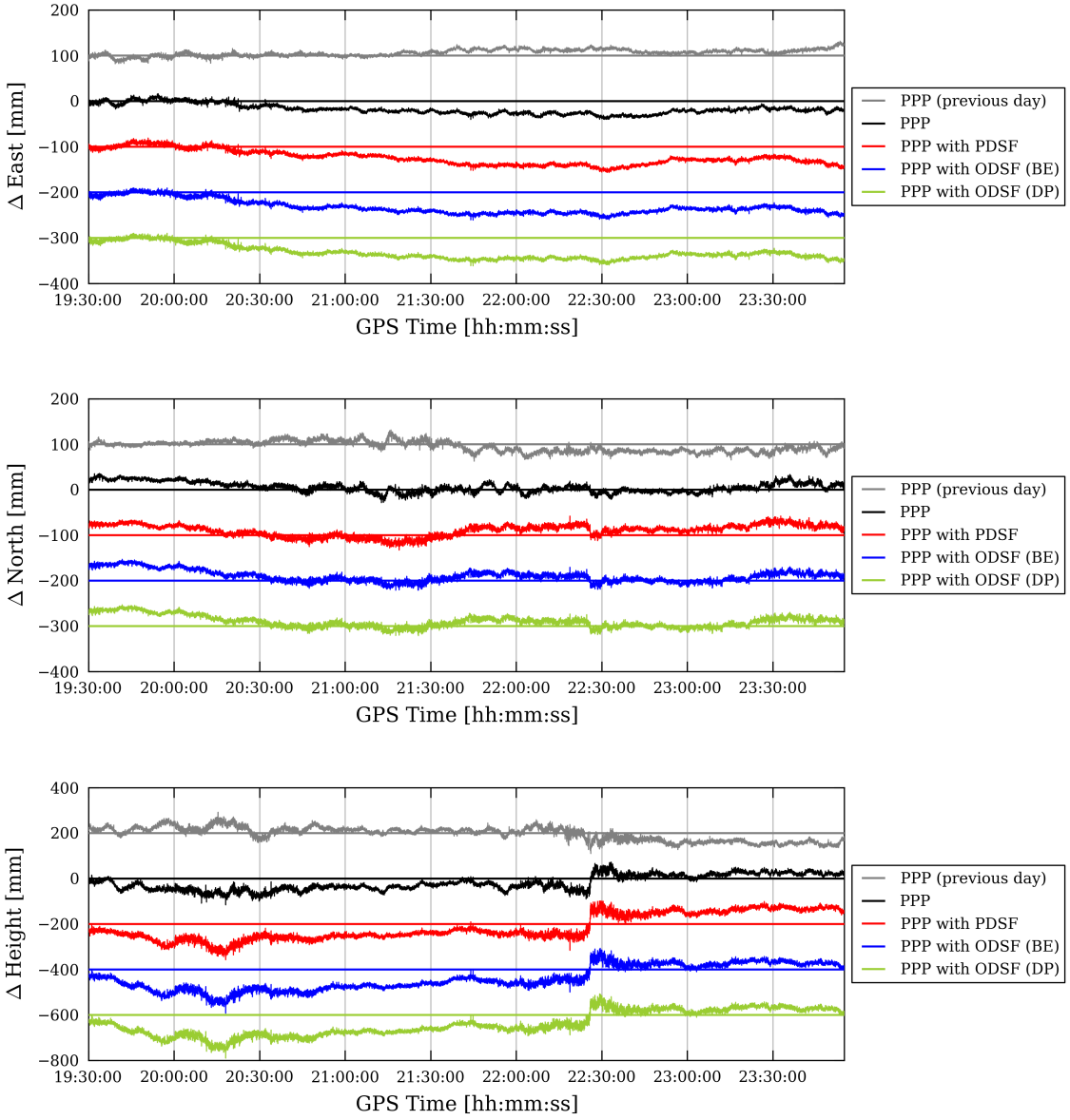

Figure E.11 – Easting, northing and height errors between 19:30 and 23:55 on 3rd April 2010 for receiver P744 resulting from standard PPP processing and PPP processing with various types of sidereal filter applied. (Each of the time series have been offset from each other by appropriate multiples of 100 mm or 200 mm for clarity).

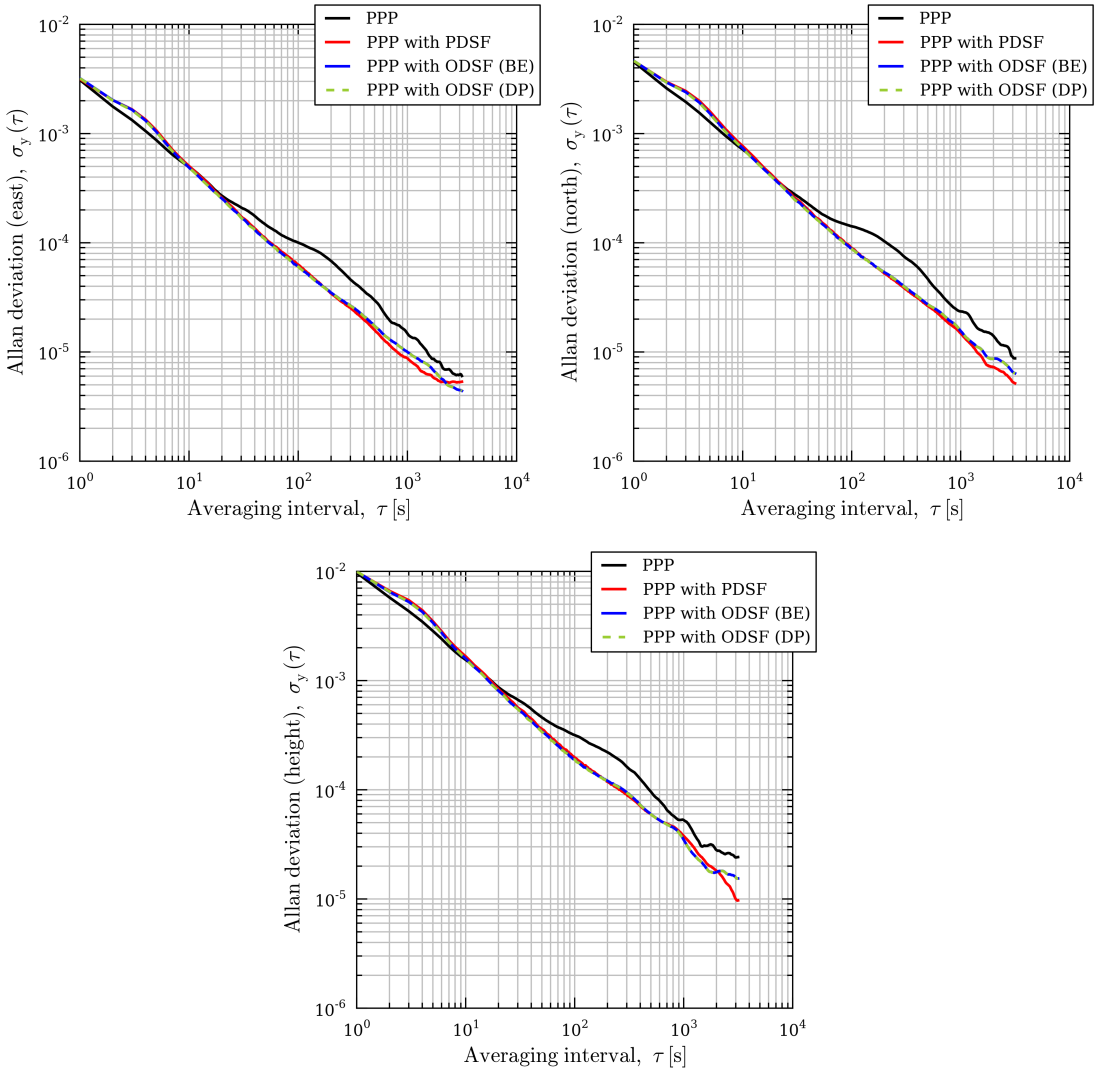

Figure E.12 – Allan deviation plots of the corresponding position time-series (east, north and height) at station GMPK between 19:30 and 23:55 on 3rd April 2010 shown in figure E.7.

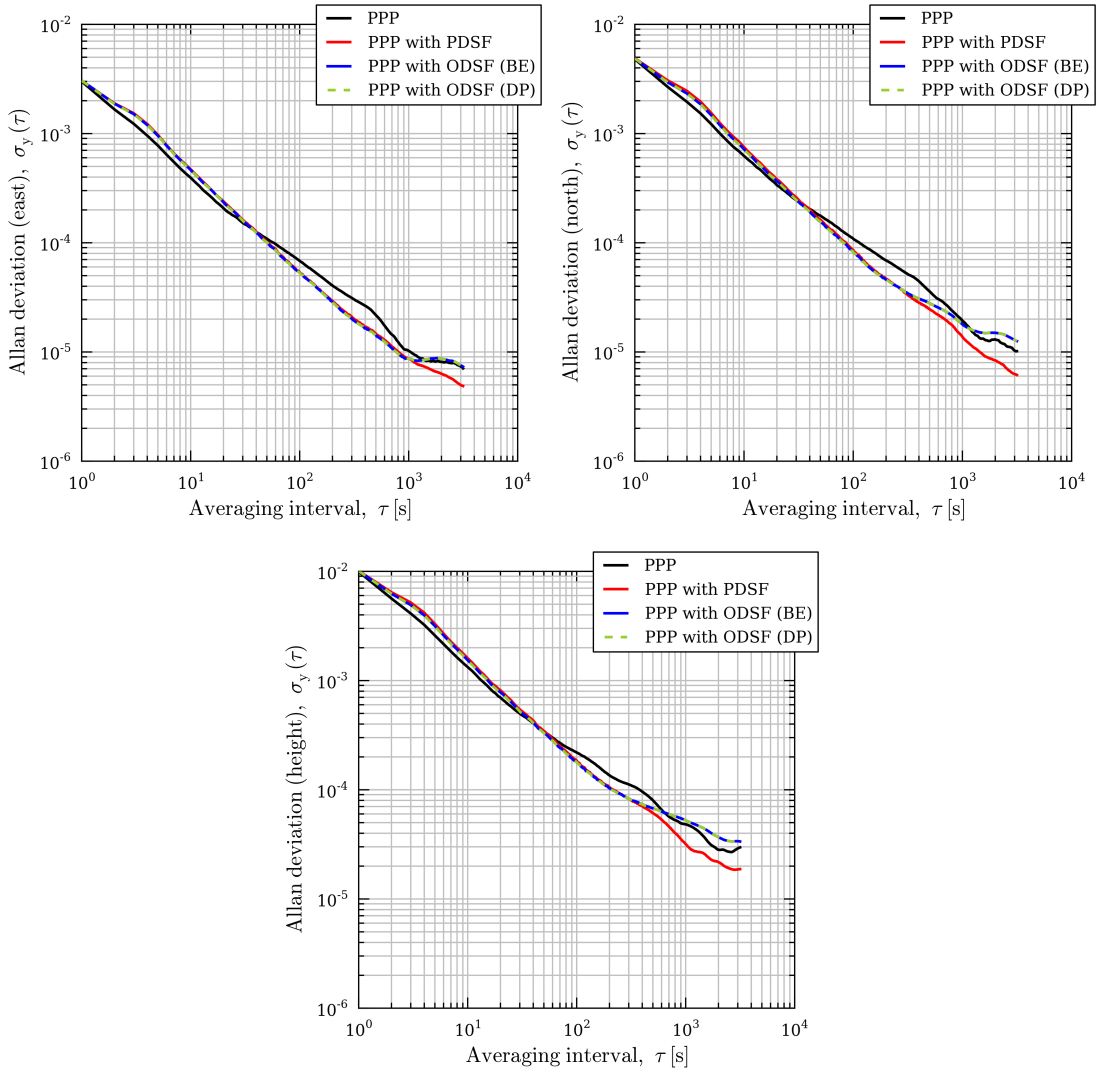

Figure E.13 – Allan deviation plots of the corresponding position time-series (east, north and height) at station P494 between 19:30 and 23:55 on 3rd April 2010 shown in figure E.8.

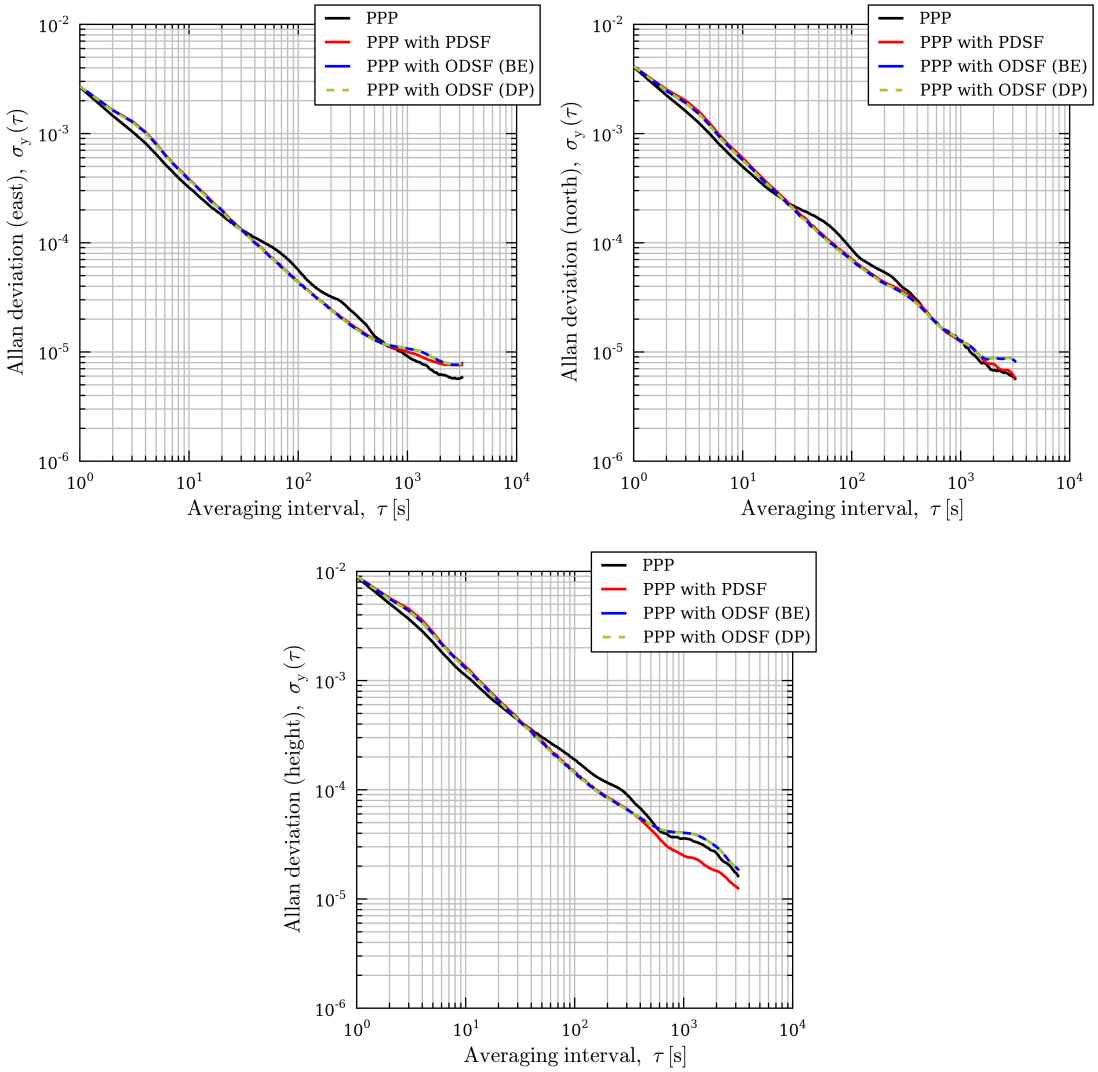

Figure E.14 – Allan deviation plots of the corresponding position time-series (east, north and height) at station P495 between 19:30 and 23:55 on 3rd April 2010 shown in figure E.9.

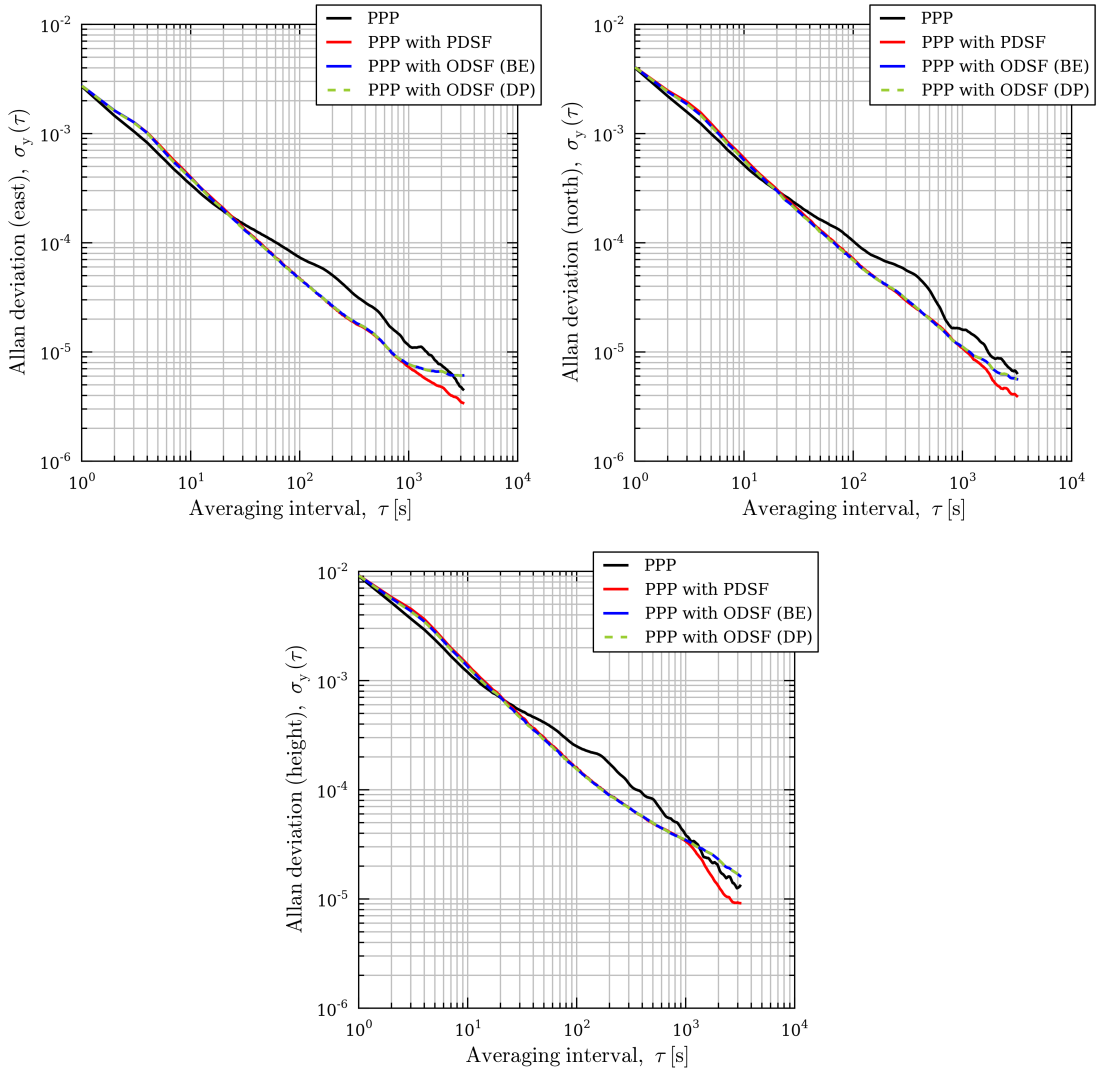

Figure E.15 – Allan deviation plots of the corresponding position time-series (east, north and height) at station P496 between 19:30 and 23:55 on 3rd April 2010 shown in figure E.10.

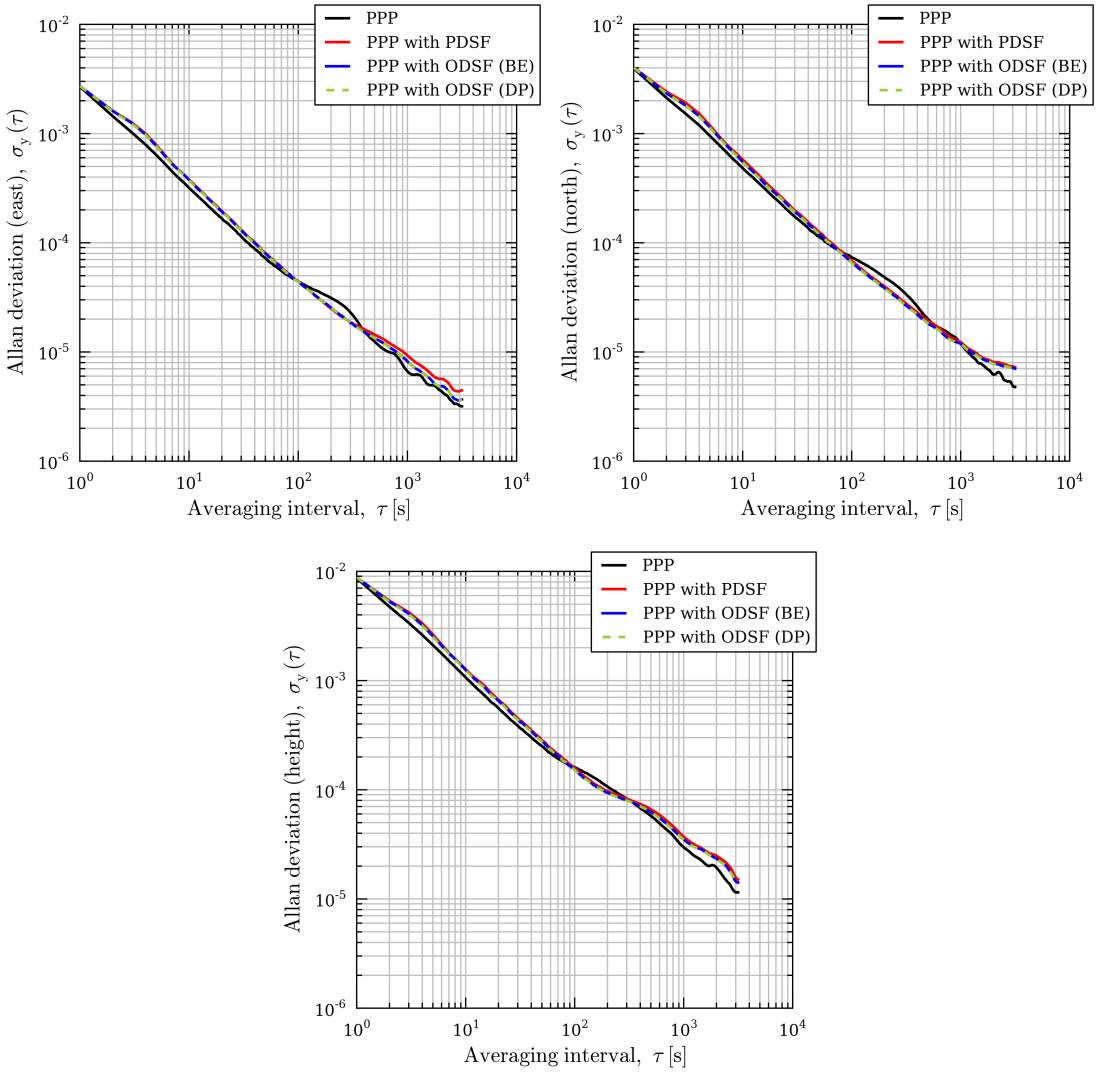

Figure E.16 – Allan deviation plots of the corresponding position time-series (east, north and height) at station P744 between 19:30 and 23:55 on 3rd April 2010 shown in figure E.11.

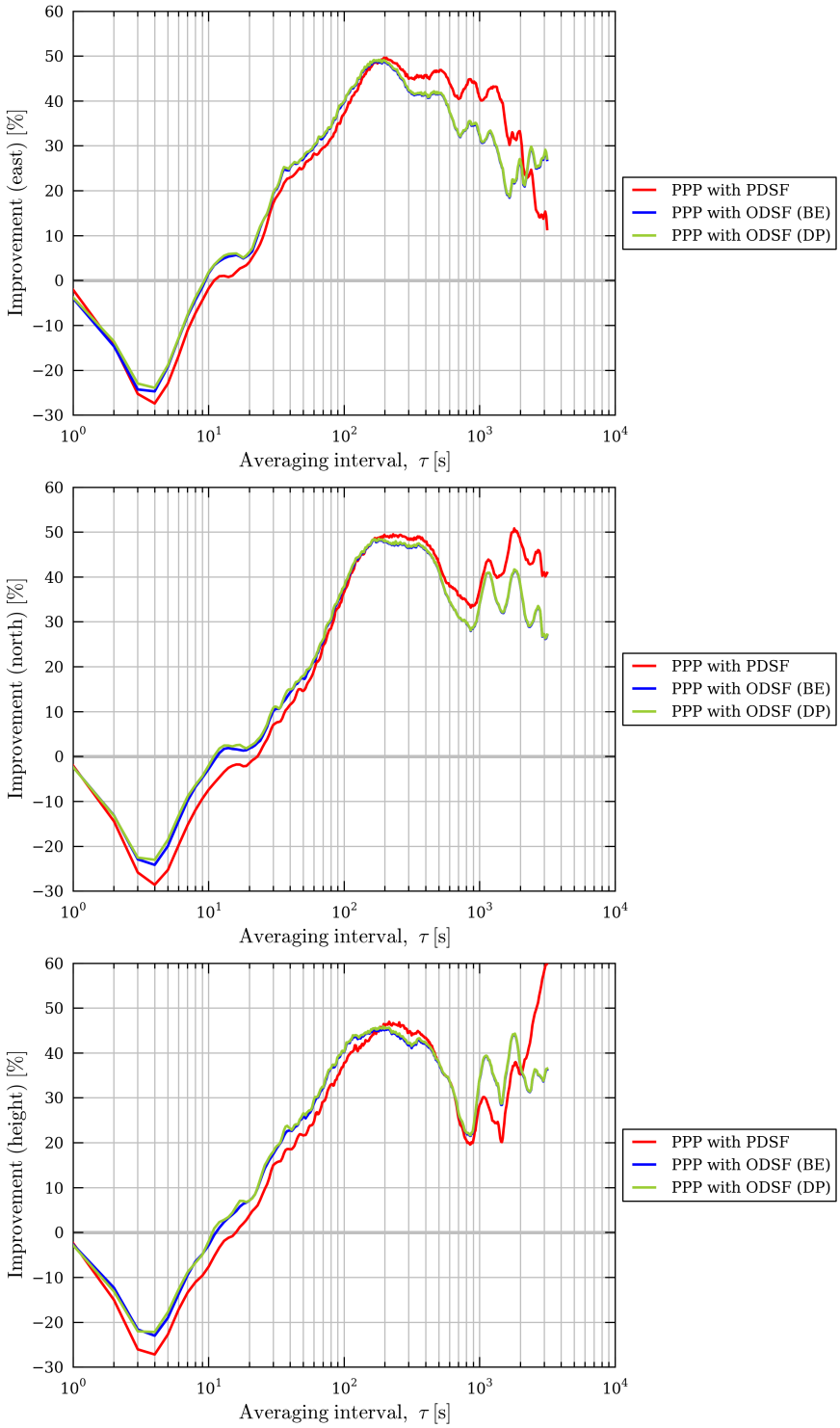

Figure E.17 – Plots showing the percentage improvement (i.e. reduction) in Allan deviation for station GMPK, after applying the various types of sidereal filter, relative to the Allan deviation values corresponding to standard PPP processing that are shown in figure E.12.

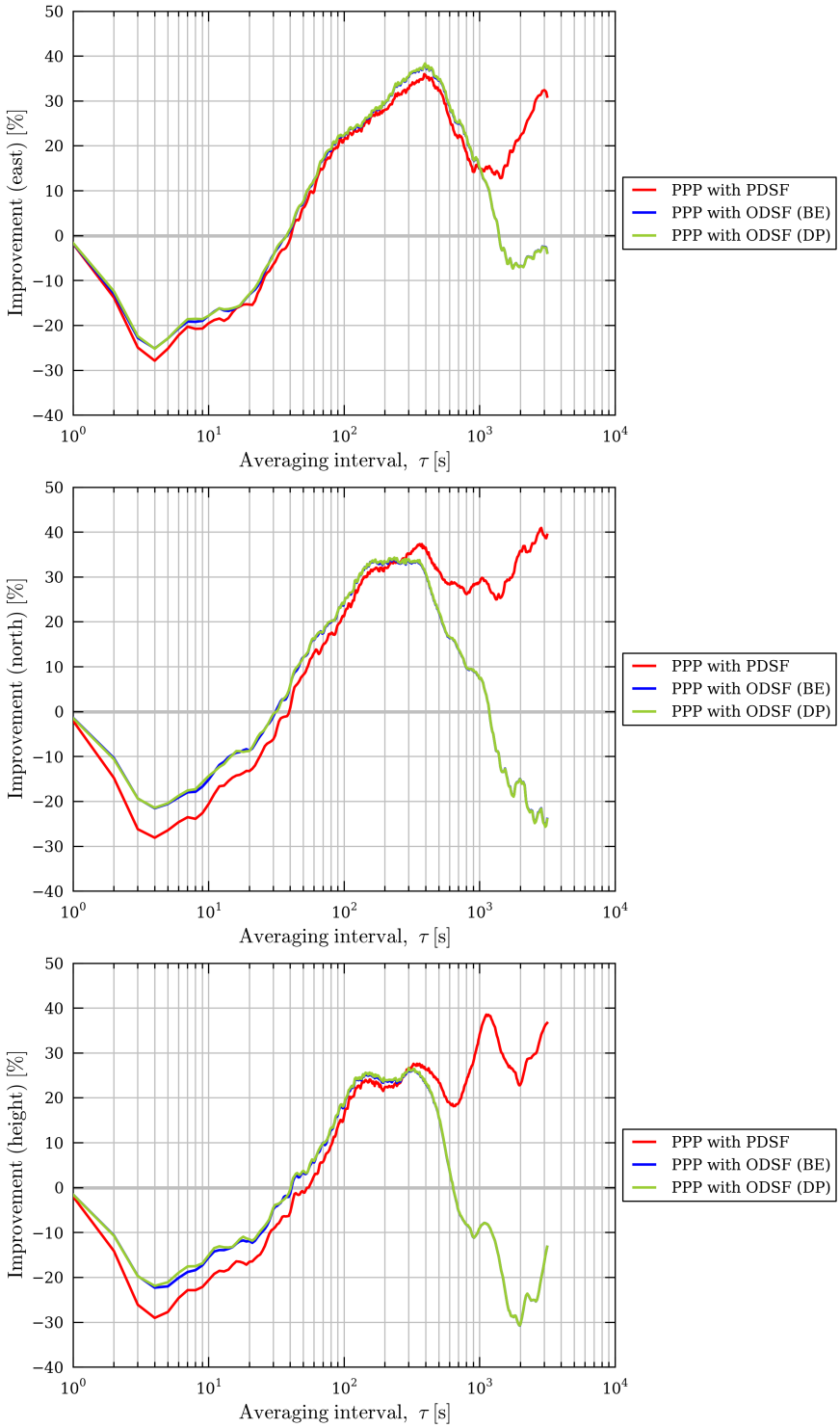

Figure E.18 – Plots showing the percentage improvement (i.e. reduction) in Allan deviation for station P494, after applying the various types of sidereal filter, relative to the Allan deviation values corresponding to standard PPP processing that are shown in figure E.13.

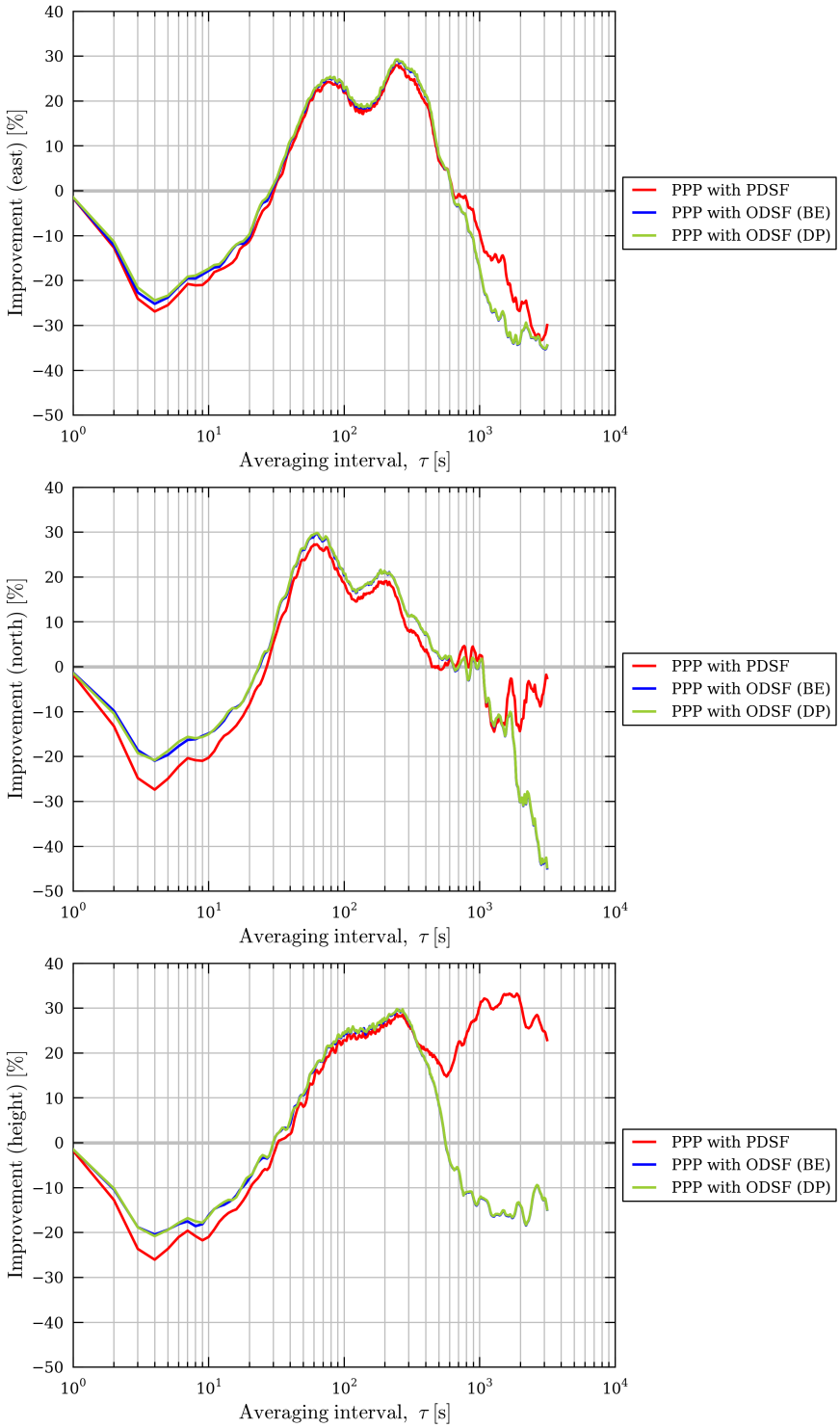

Figure E.19 – Plots showing the percentage improvement (i.e. reduction) in Allan deviation for station P495, after applying the various types of sidereal filter, relative to the Allan deviation values corresponding to standard PPP processing that are shown in figure E.14.

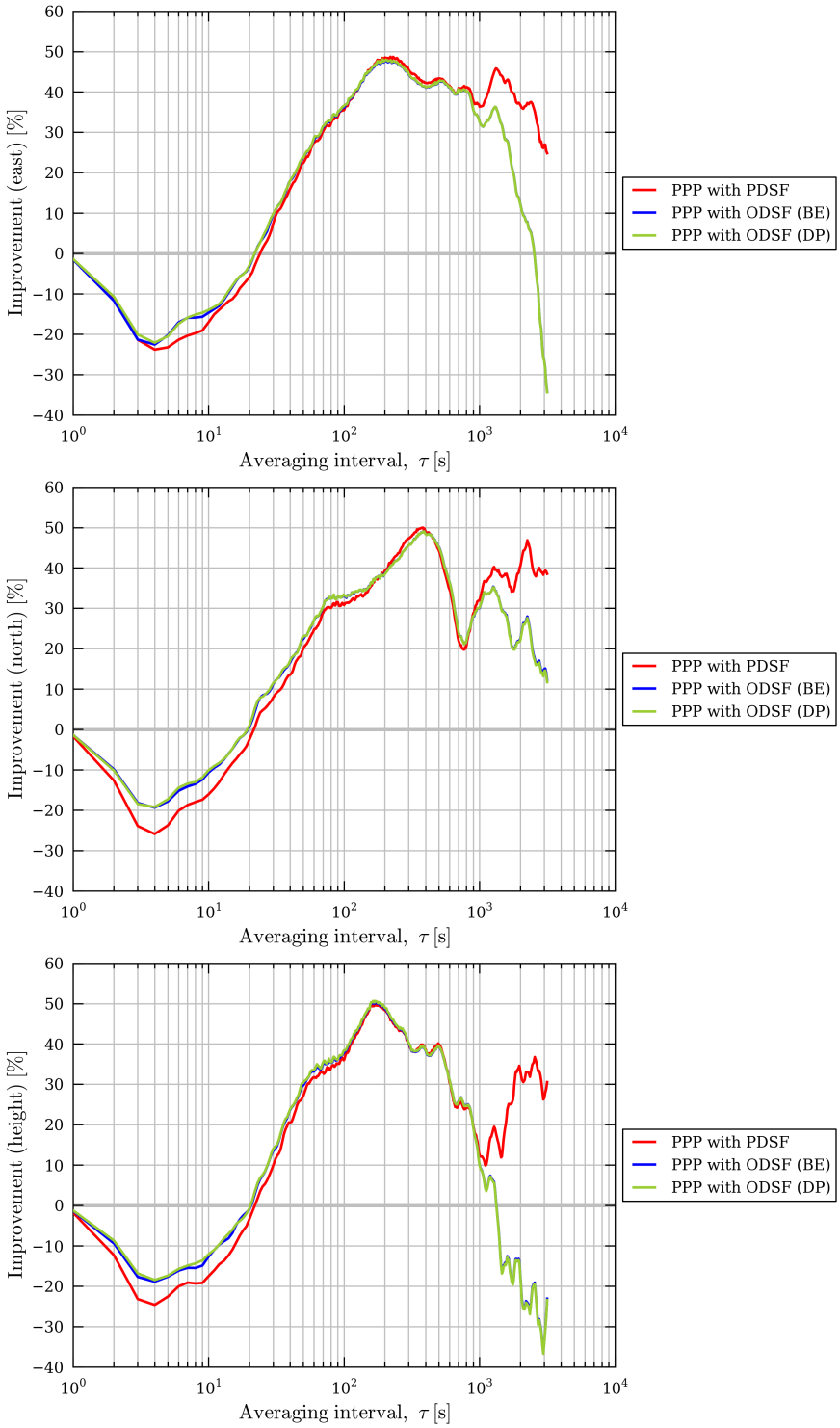

Figure E.20 – Plots showing the percentage improvement (i.e. reduction) in Allan deviation for station P496, after applying the various types of sidereal filter, relative to the Allan deviation values corresponding to standard PPP processing that are shown in figure E.15.

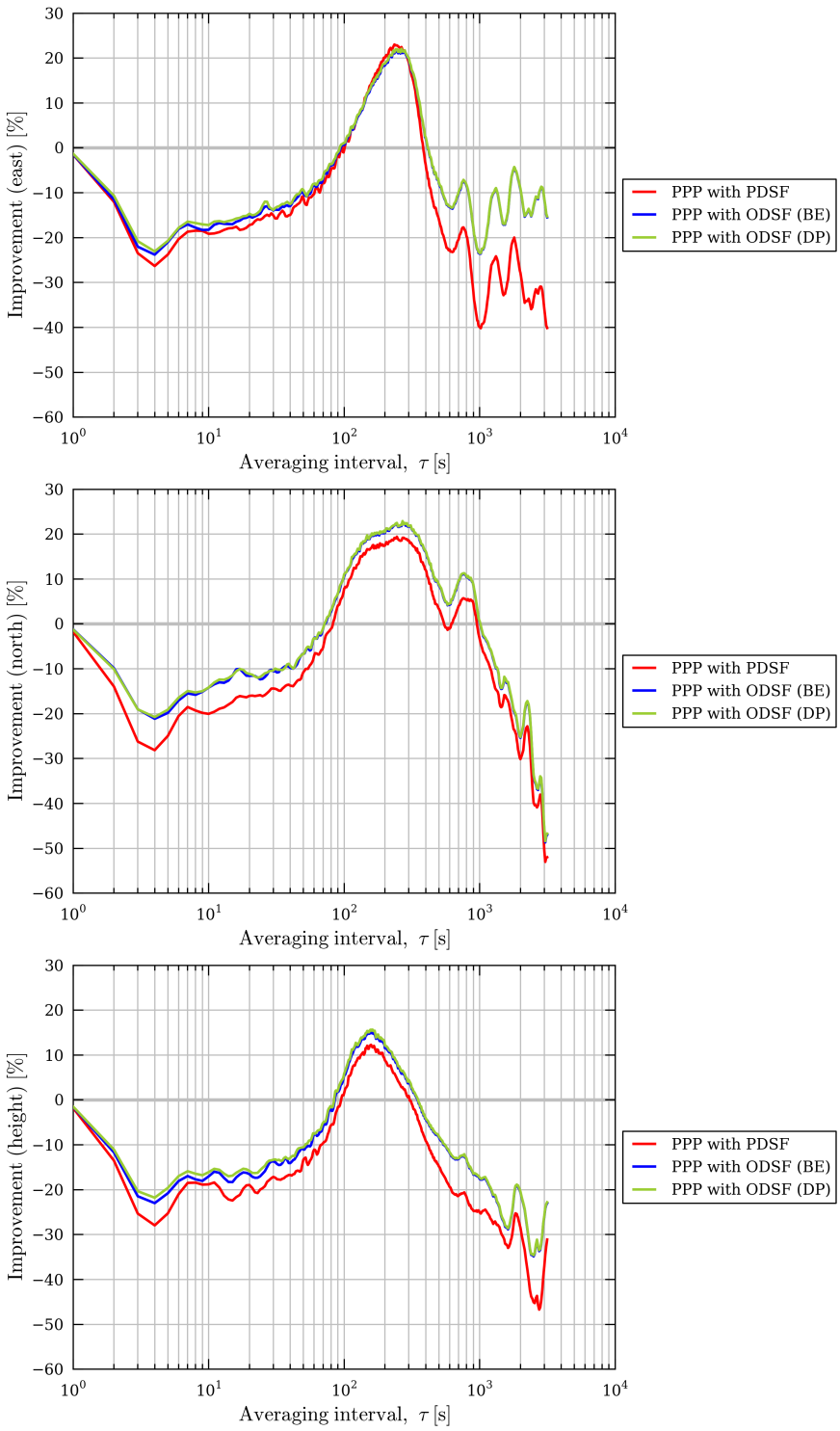

Figure E.21 – Plots showing the percentage improvement (i.e. reduction) in Allan deviation for station P744, after applying the various types of sidereal filter, relative to the Allan deviation values corresponding to standard PPP processing that are shown in figure E.16.

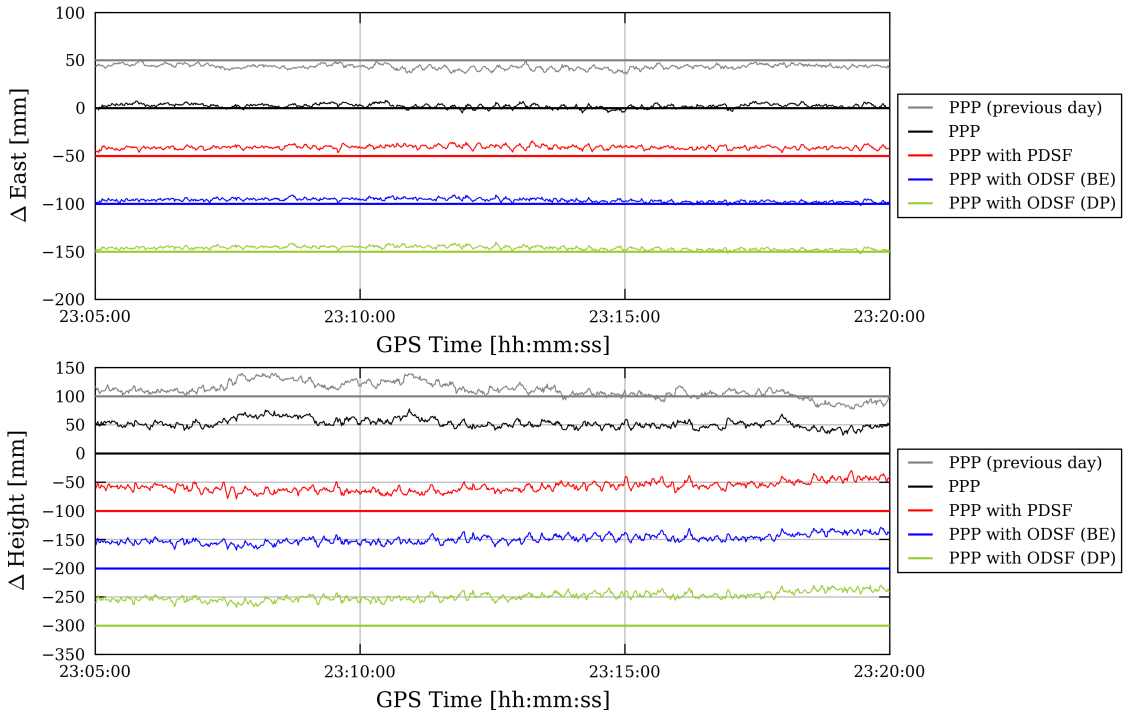

Figure E.22 – Easting and height errors between 23:05 and 23:20 on 27$^{\text{th}}$ March 2012 for receiver UCL resulting from standard PPP processing and PPP processing with various types of sidereal filter applied. Errors between 23:09:05 and 23:24:05 on 26$^{\text{th}}$ March 2012, plotted in grey, have been shifted forward in time by 23 hours, 55 minutes and 5 seconds to appear on the same plot. (Each of the time series have been offset from each other by appropriate multiples of 50 mm or 100 mm for clarity).

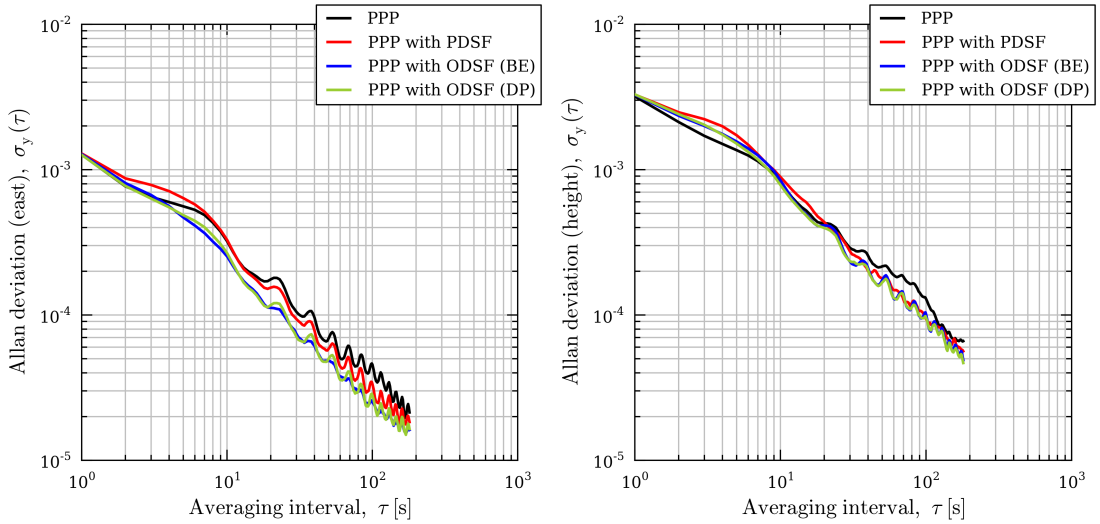

Figure E.23 – Allan deviation plots of the corresponding position time-series (easting and height) at station UCL between 23:05 and 23:20 on 27$^{\text{th}}$ March 2012 shown in figure E.22.

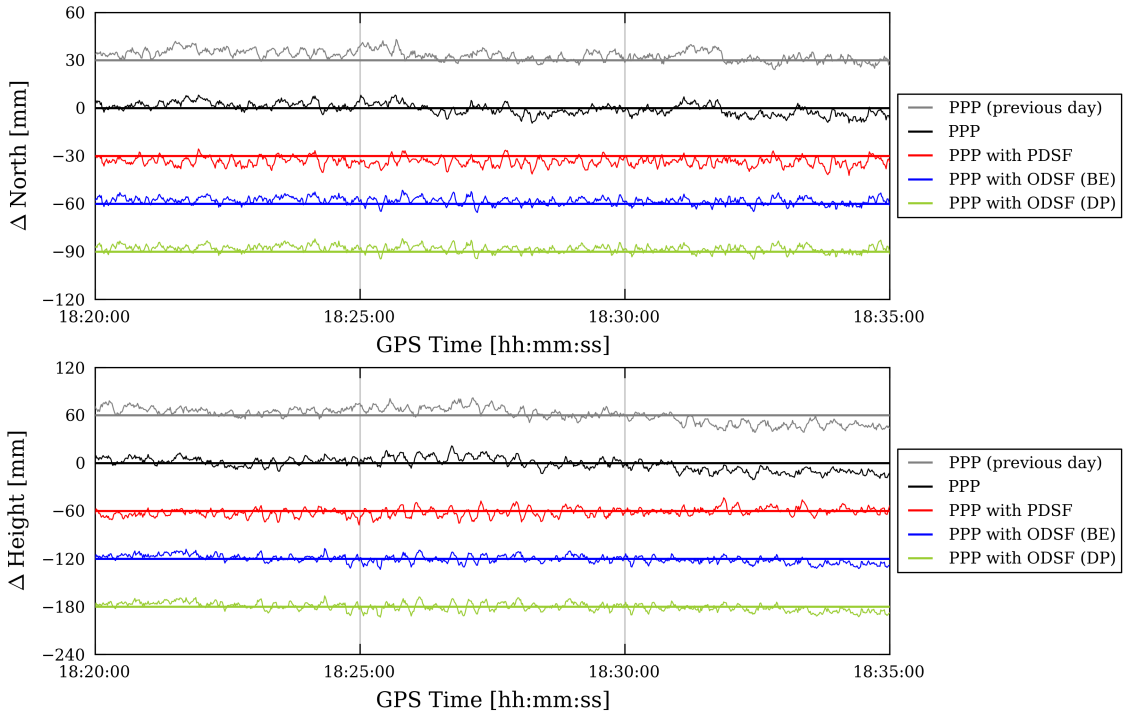

Figure E.24 – Northing and height errors between 18:20 and 18:35 on 27$^{\text{th}}$ March 2012 for receiver UCL resulting from standard PPP processing and PPP processing with various types of sidereal filter applied. Errors between 18:24:05 and 18:39:05 on 26$^{\text{th}}$ March 2012, plotted in grey, have been shifted forward in time by 23 hours, 55 minutes and 55 seconds to appear on the same plot. (Each of the time series have been offset from each other by appropriate multiples of 30 mm or 60 mm for clarity).

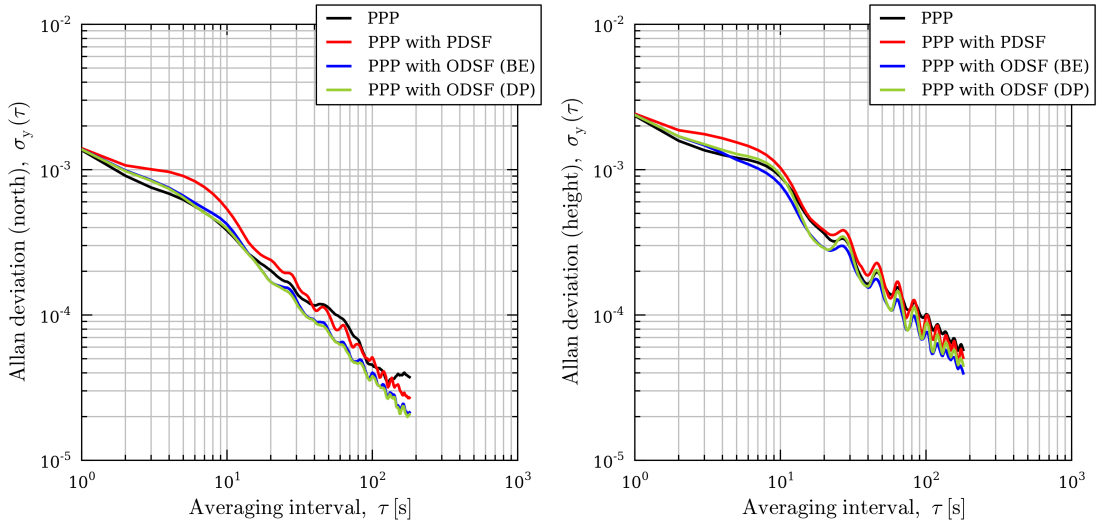

Figure E.25 – Allan deviation plots of the corresponding position time-series (northing and height) at station UCL between 18:20 and 18:35 on 27$^{\text{th}}$ March 2012 shown in figure E.24.

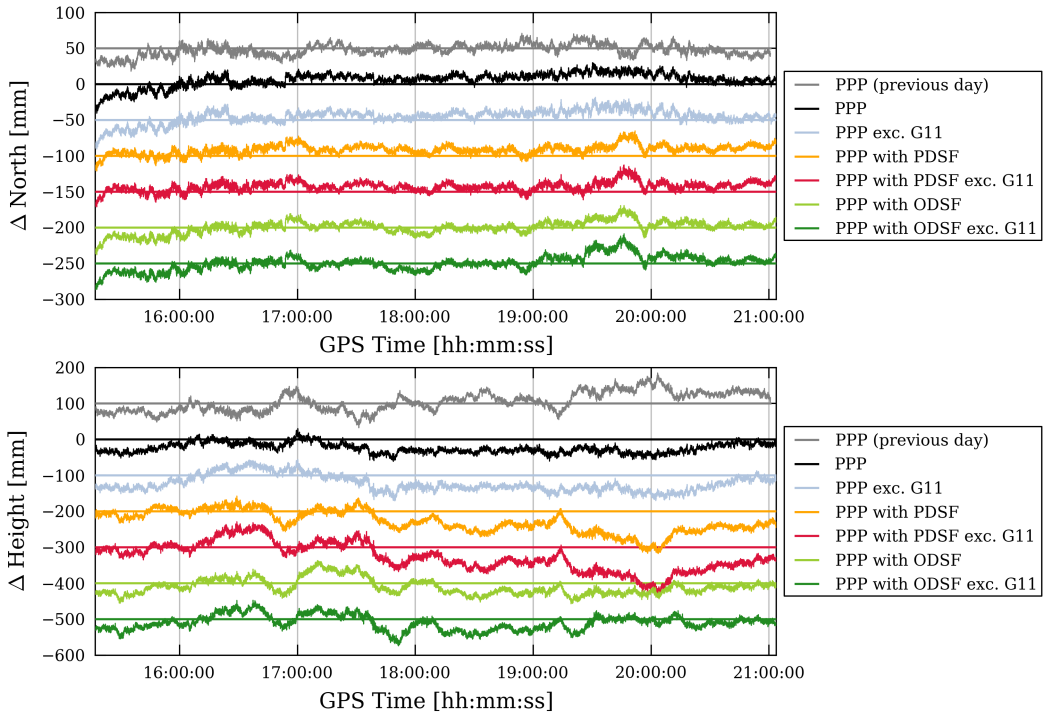

Figure E.26 – Northing and height errors between 15:16:59 and 21:03:38 on 31st August 2013 for receiver UCL resulting from standard PPP processing both with (black) and without (blue-grey) measurements from satellite G11 on day 2. Similarly shown in other colours are the errors resulting from PPP processing with position- or observation-domain sidereal filters applied. (Each of the time series have been offset from each other by appropriate multiples of 50 mm or 100 mm for clarity).

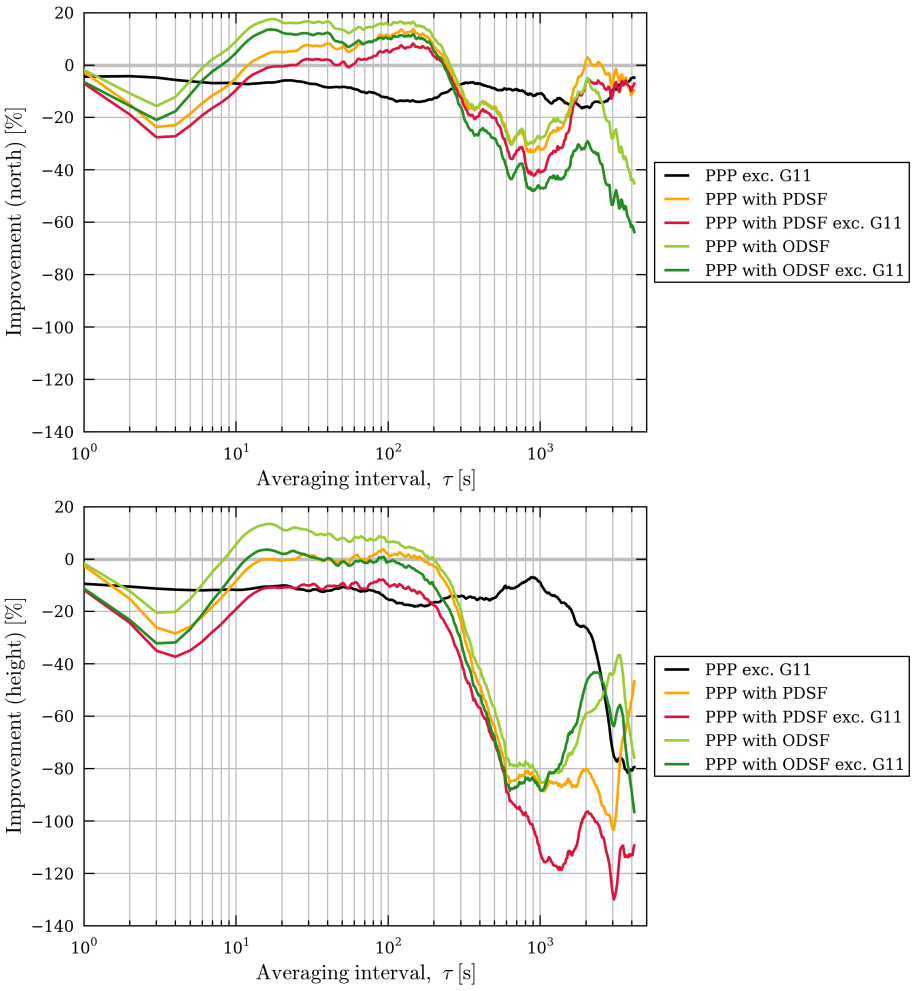

Figure E.27 – The percentage improvement (i.e. reduction) in Allan deviation values for the northing and height position time series at UCL shown in figure E.26 relative to standard PPP processing.

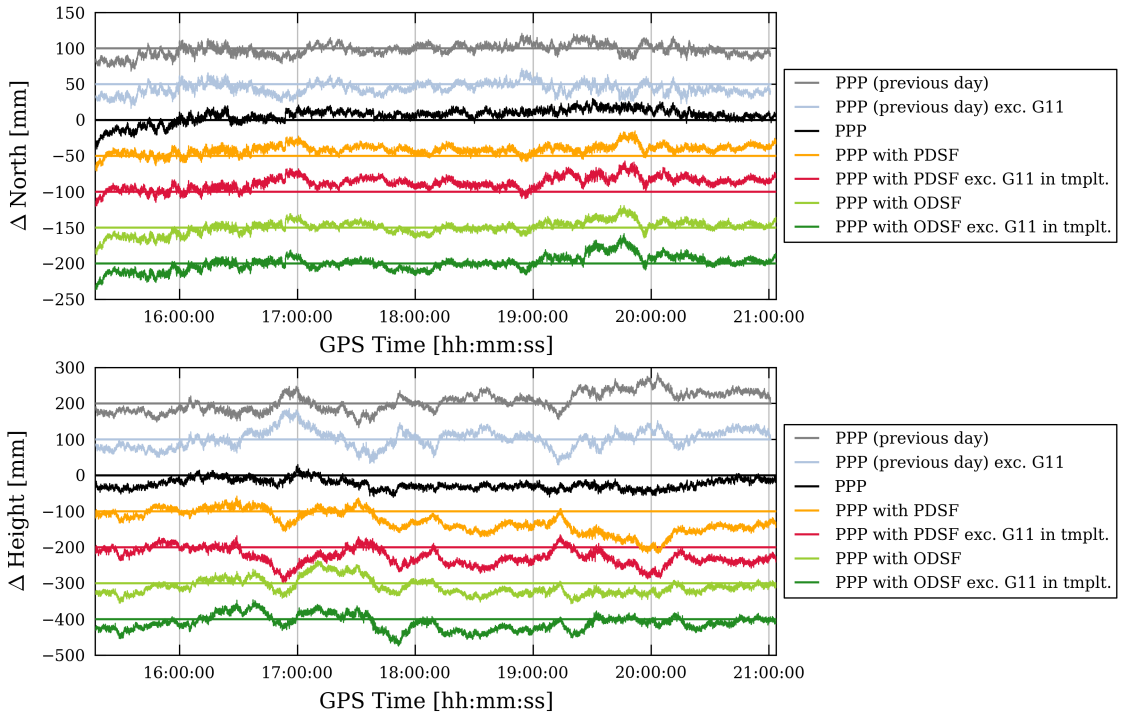

Figure E.28 – Northing and height errors between 15:16:59 and 21:03:38 on 31st August 2013 for receiver UCL resulting from standard PPP processing with measurements associated with satellite G11 either included or excluded from day 1 (the 'template' (tmplt.) day). Similarly shown in other colours are the errors resulting from PPP processing with position- or observation-domain sidereal filters applied. (Each of the time series have been offset from each other by appropriate multiples of 50 mm or 100 mm for clarity).

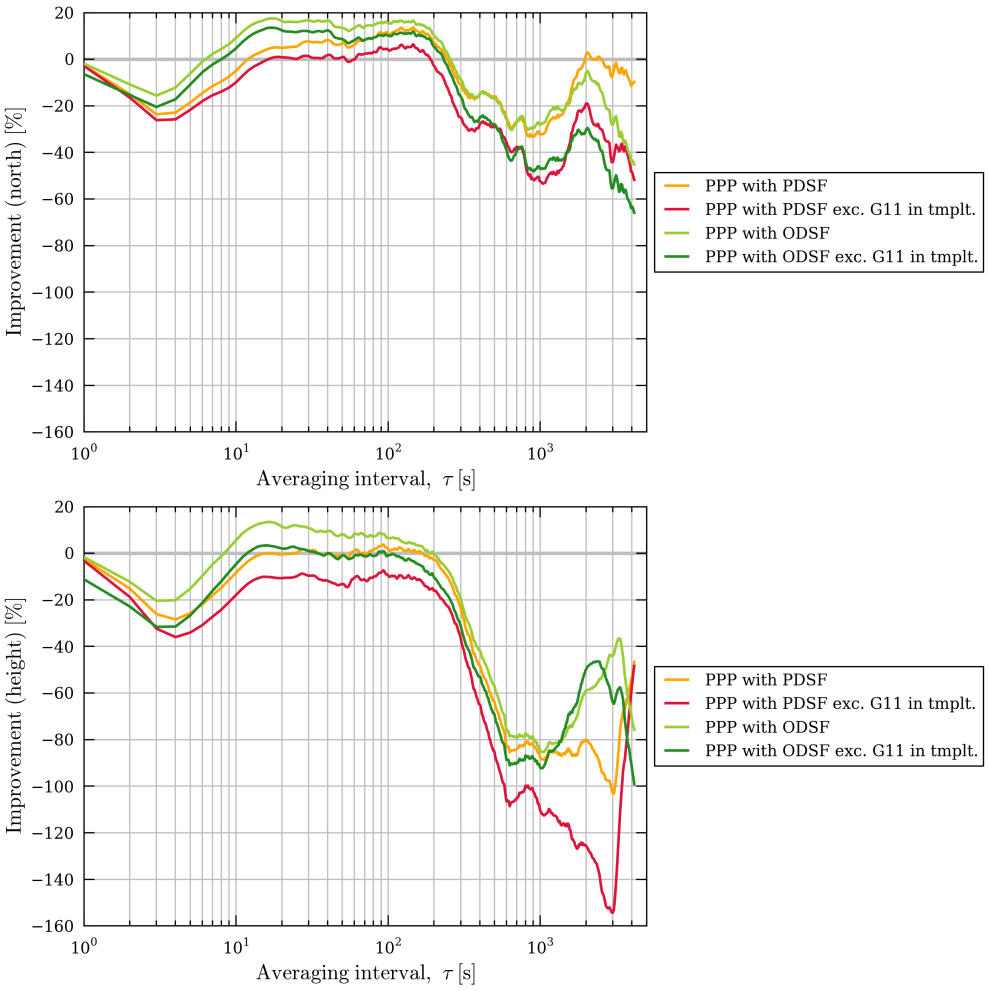

Figure E.29 – The percentage improvement (i.e. reduction) in Allan deviation values for the northing and height position time series at UCL shown in figure E.28 relative to standard PPP processing.

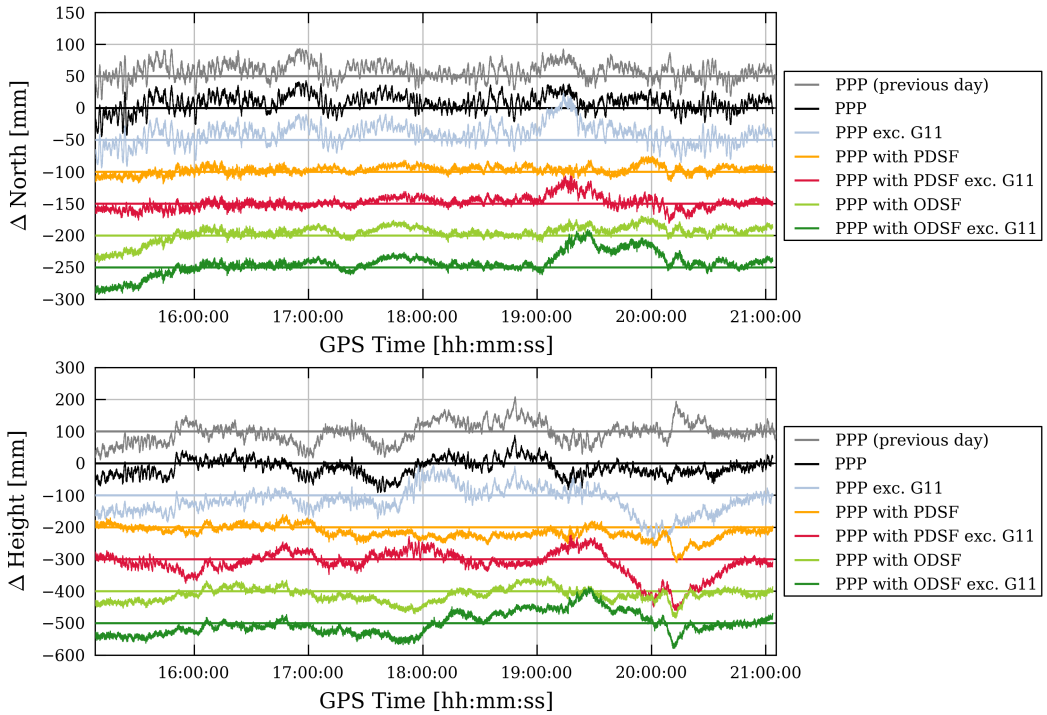

Figure E.30 – Northing and height errors between 15:16:59 and 21:03:38 on 31st August 2013 for receiver UEL resulting from standard PPP processing both with (black) and without (blue-grey) measurements from satellite G11 on day 2. Similarly shown in other colours are the errors resulting from PPP processing with position- or observation-domain sidereal filters applied. (Each of the time series have been offset from each other by appropriate multiples of 50 mm or 100 mm for clarity).

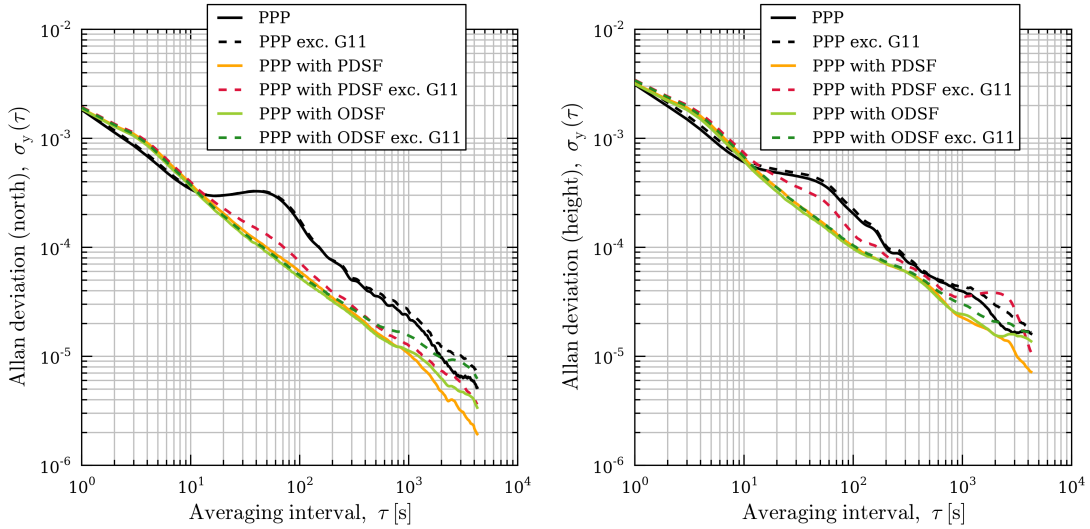

Figure E.31 – Allan deviation plots of the position time-series (northing and height) at station UEL between 15:16:59 and 21:03:38 on 31st August 2013 corresponding with figure E.30.

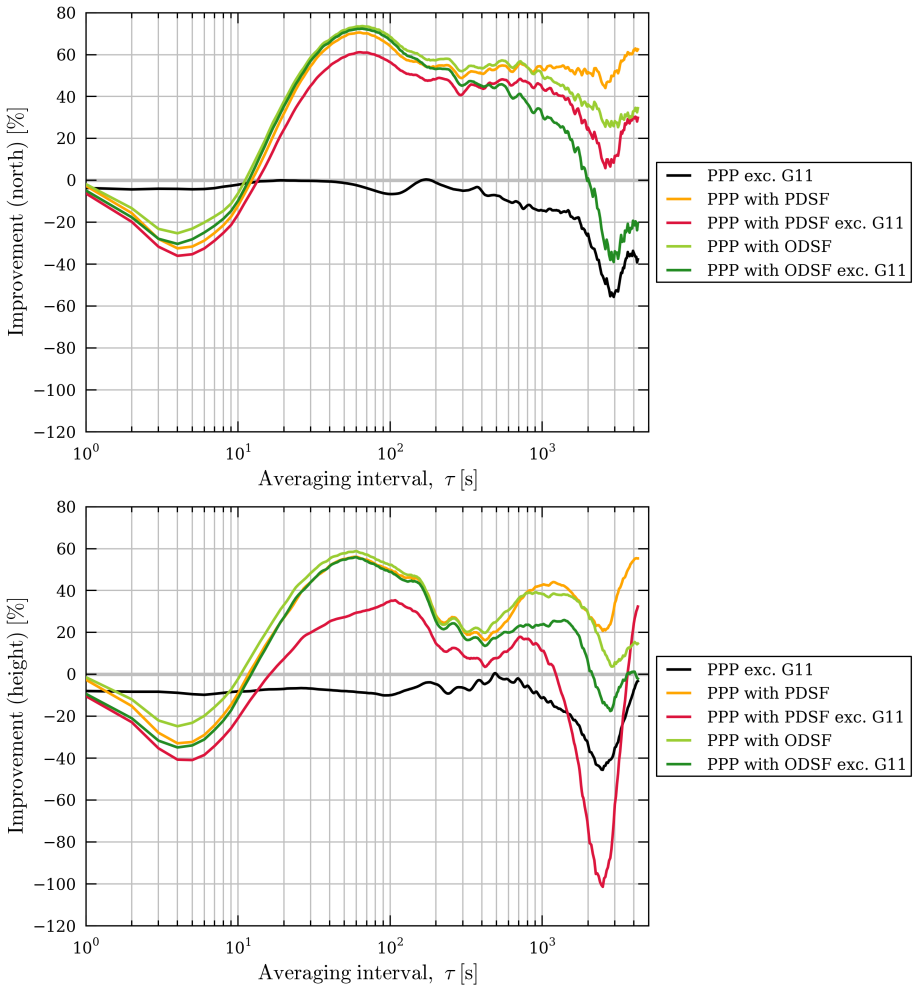

Figure E.32 – Plots showing the percentage improvement (i.e. reduction) in Allan deviation for station UEL, after applying the various types of sidereal filter, relative to the Allan deviation values corresponding to standard PPP processing that are shown in figure E.31.

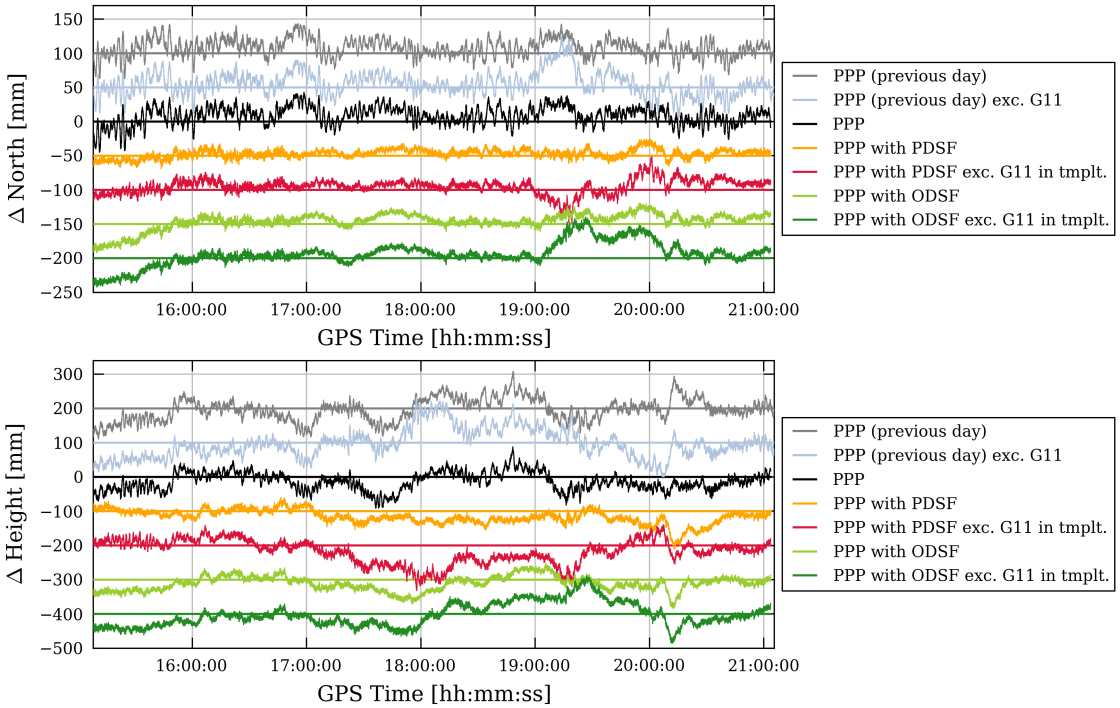

Figure E.33 – Northing and height errors between 15:16:59 and 21:03:38 on 31st August 2013 for receiver UEL resulting from standard PPP processing with measurements associated with satellite G11 either included or excluded from day 1 (the 'template' (tmplt.) day). Similarly shown in other colours are the errors resulting from PPP processing with position- or observation-domain sidereal filters applied. (Each of the time series have been offset from each other by appropriate multiples of 50 mm or 100 mm for clarity).

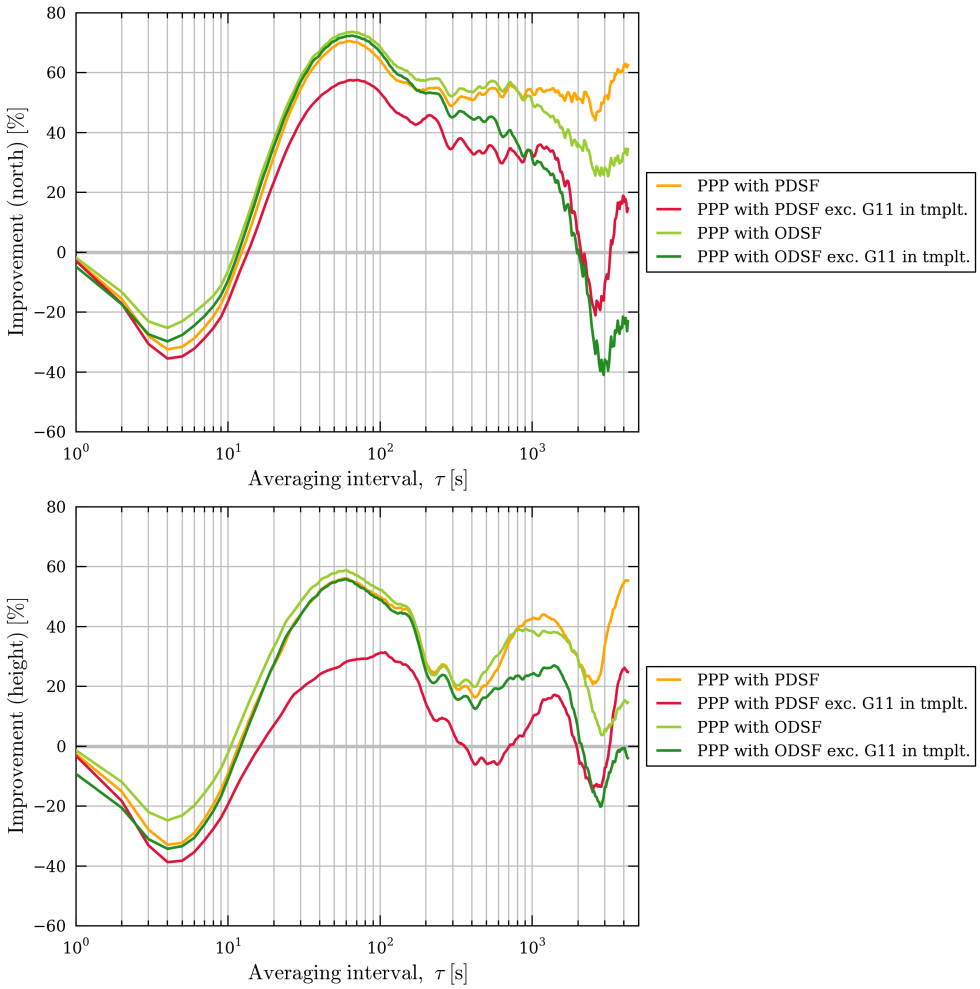

Figure E.34 – The percentage improvement (i.e. reduction) in Allan deviation values for the northing and height position time series at UEL shown in figure E.33 relative to standard PPP processing.

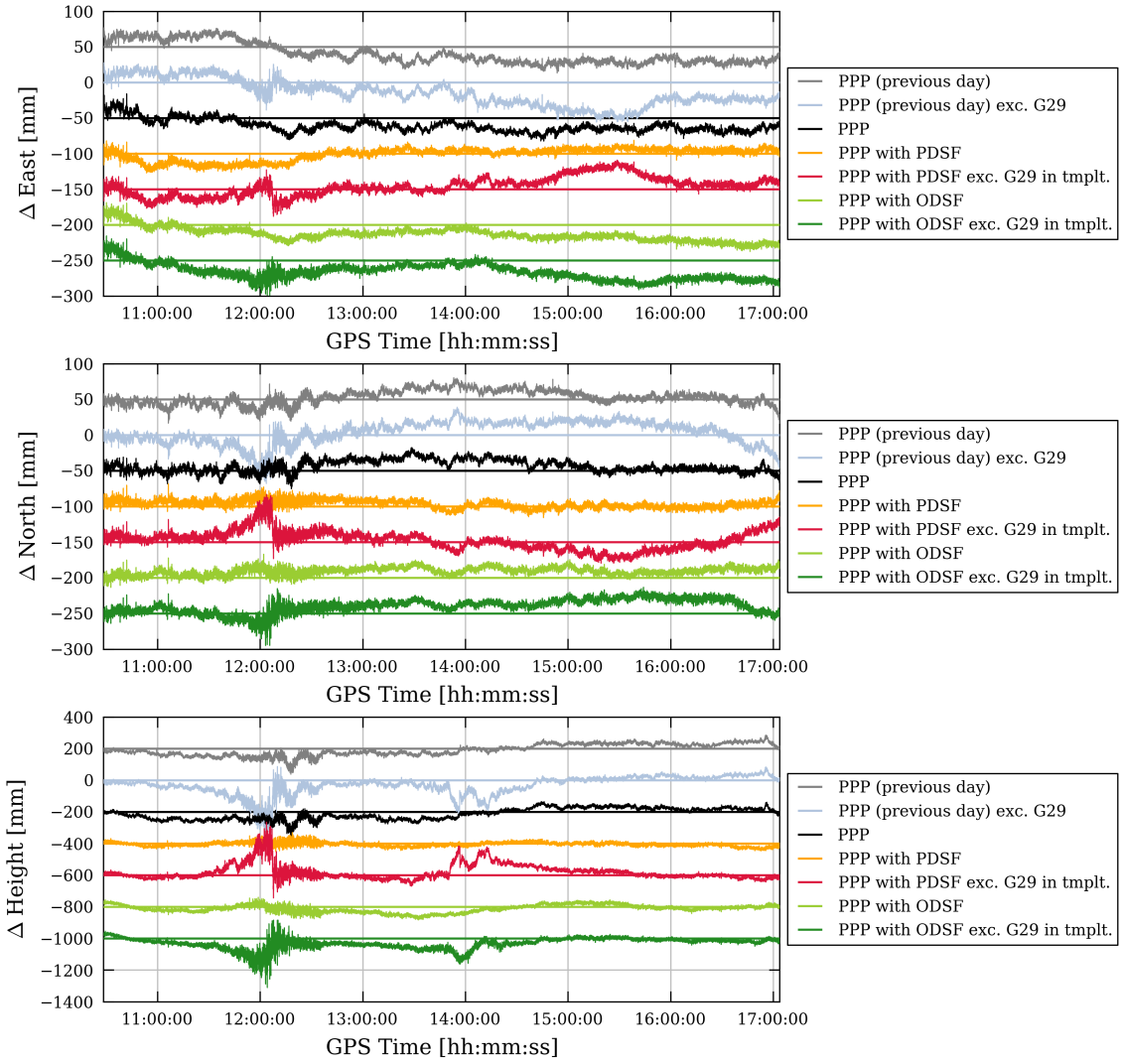

Figure E.35 – Easting, northing and height errors between 10:28:20 and 17:03:35 on 3rd April 2010 for receiver UCL resulting from standard PPP processing with measurements associated with satellite G29 either included or excluded from day 1 (the 'template' (tmplt.) day). Similarly shown in other colours are the errors resulting from PPP processing with position- or observation-domain sidereal filters applied. (Each of the time series have been offset from each other by appropriate multiples of 50 mm or 100 mm for clarity).

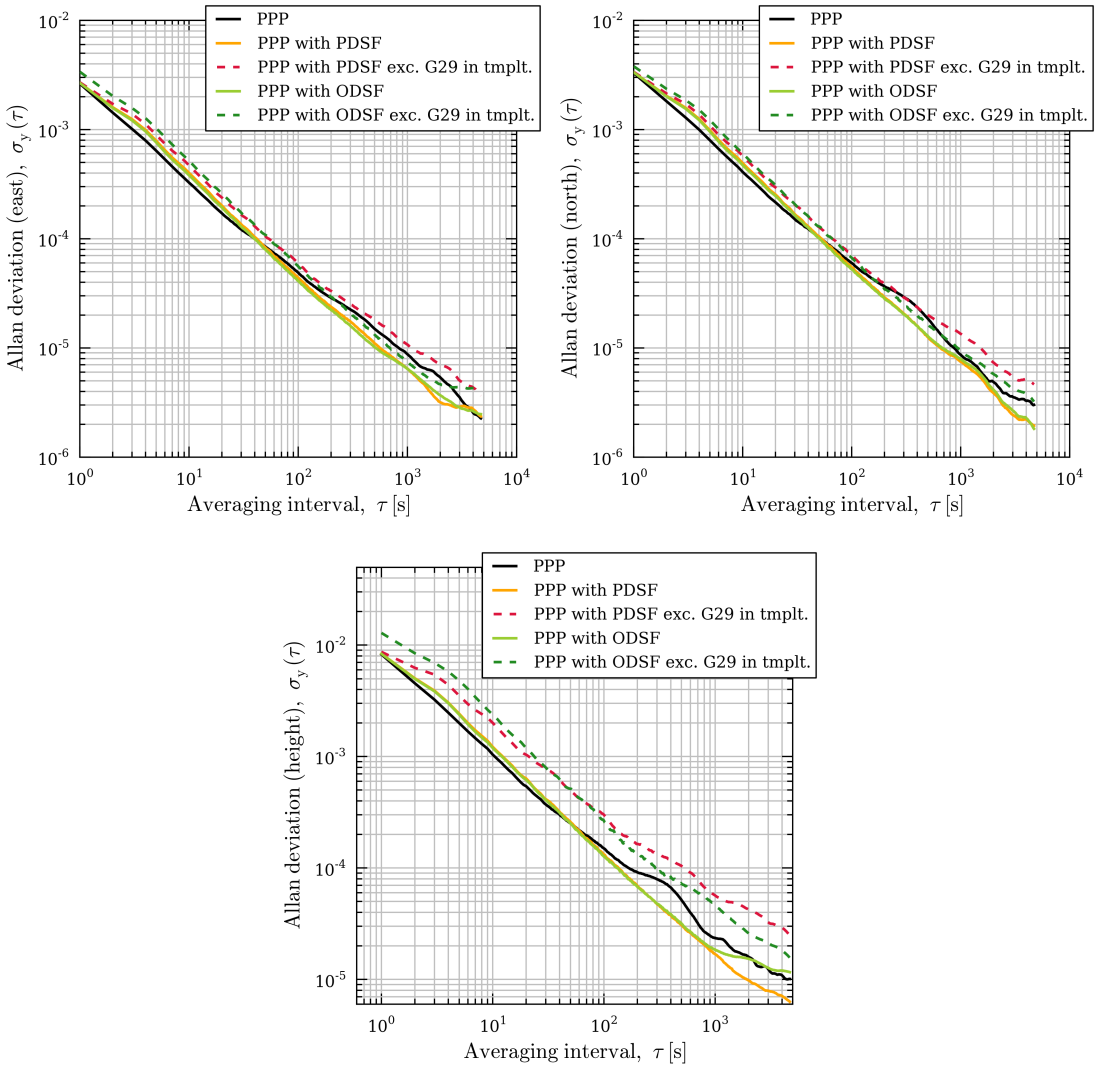

Figure E.36 – Allan deviation plots of the position time-series (easting, northing and height) at station P494 between 10:28:20 and 17:03:35 on 3rd April 2010 corresponding with figure E.35.

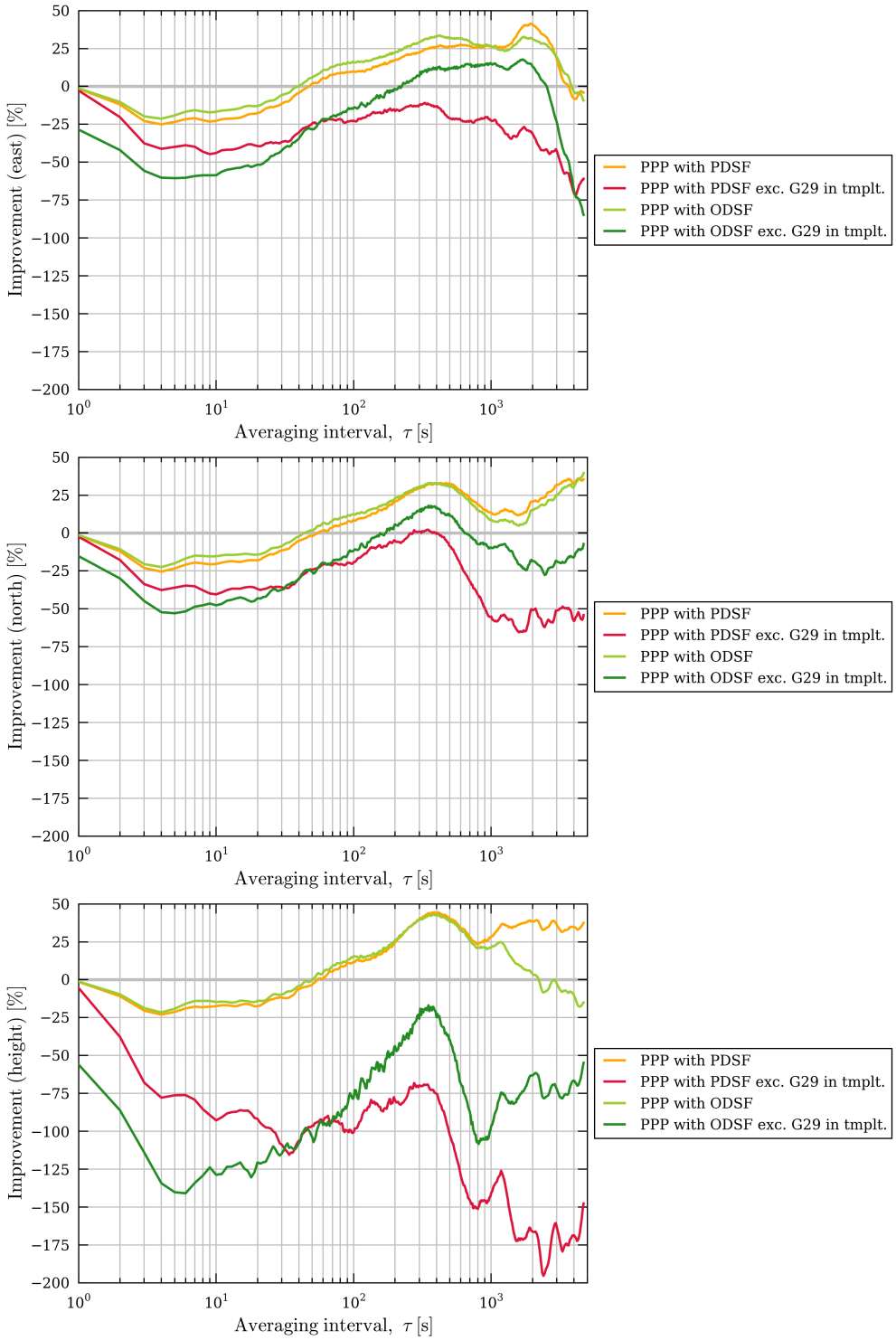

Figure E.37 – Plots showing the percentage improvement (i.e. reduction) in Allan deviation for station P494, after applying the various types of sidereal filter, relative to the Allan deviation values corresponding to standard PPP processing that are shown in figure E.36.

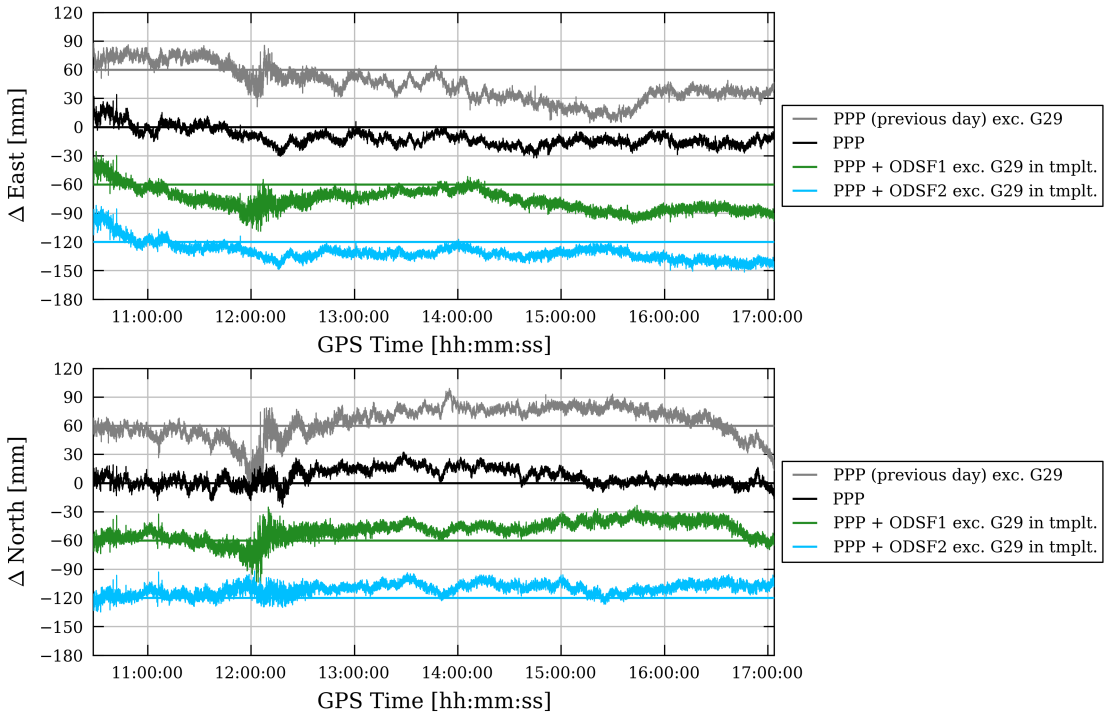

Figure E.38 – Easting and northing errors (shown in black) between 10:28:20 and 17:03:35 on 3rd April 2010 for receiver P494 resulting from standard PPP processing with measurements associated with satellite G29 excluded from day 1 (the 'template' (tmplt.) day). The corresponding errors from the previous day are shown in grey. Similarly shown in green and blue are the errors resulting from PPP processing with ODSF1 or ODSF2 algorithms applied respectively. (Each of the time series have been offset from each other by appropriate multiples of 60 mm for clarity).

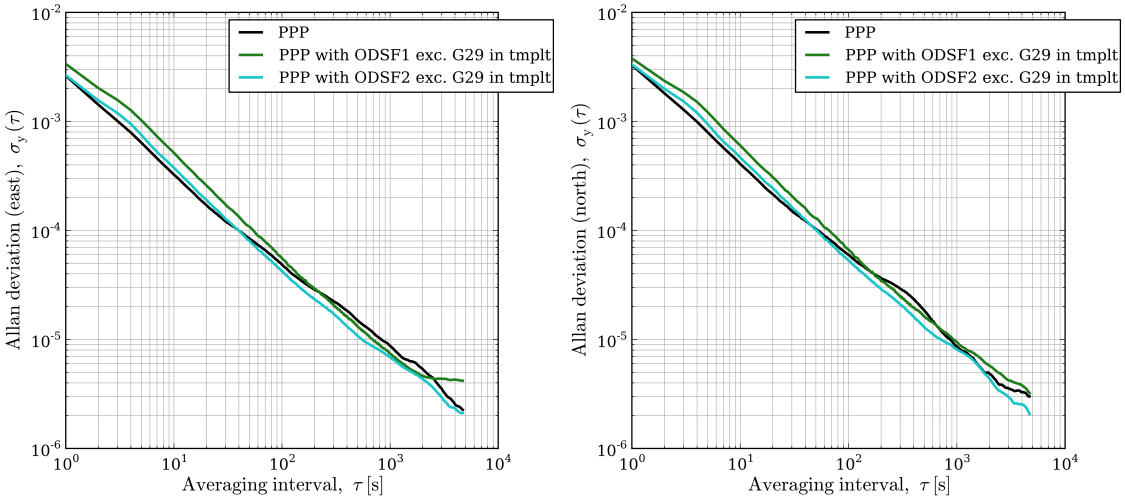

Figure E.39 – Allan deviation plots of the corresponding easting and northing position time-series at station P494 between 10:28:20 and 17:03:35 on 3rd April 2010 shown in figure E.38, except for the previous day.

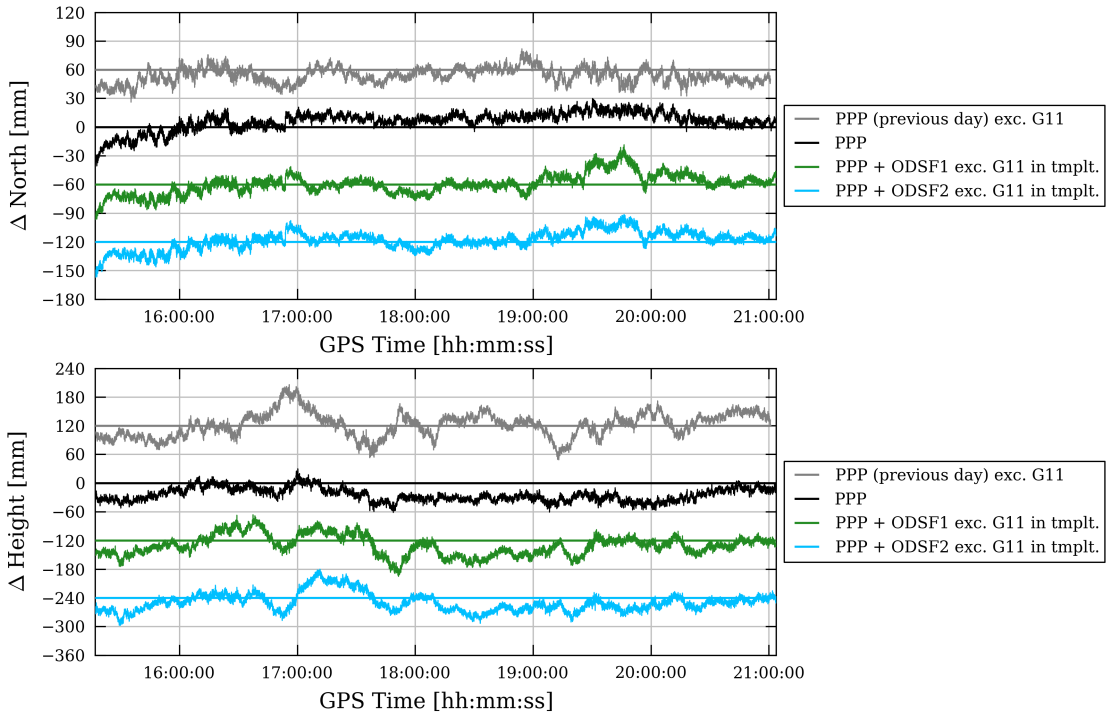

Figure E.40 – Northing and height errors (shown in black) between 15:16:59 and 21:03:38 on 31st August 2013 for receiver UCL resulting from standard PPP processing with measurements associated with satellite G11 excluded from day 1 (the 'template' (tmplt.) day). The corresponding errors from the previous day are shown in grey. Similarly shown in green and blue are the errors resulting from PPP processing with ODSF1 or ODSF2 algorithms applied respectively. (Each of the time series have been offset from each other by appropriate multiples of 60 mm or 120 mm for clarity).

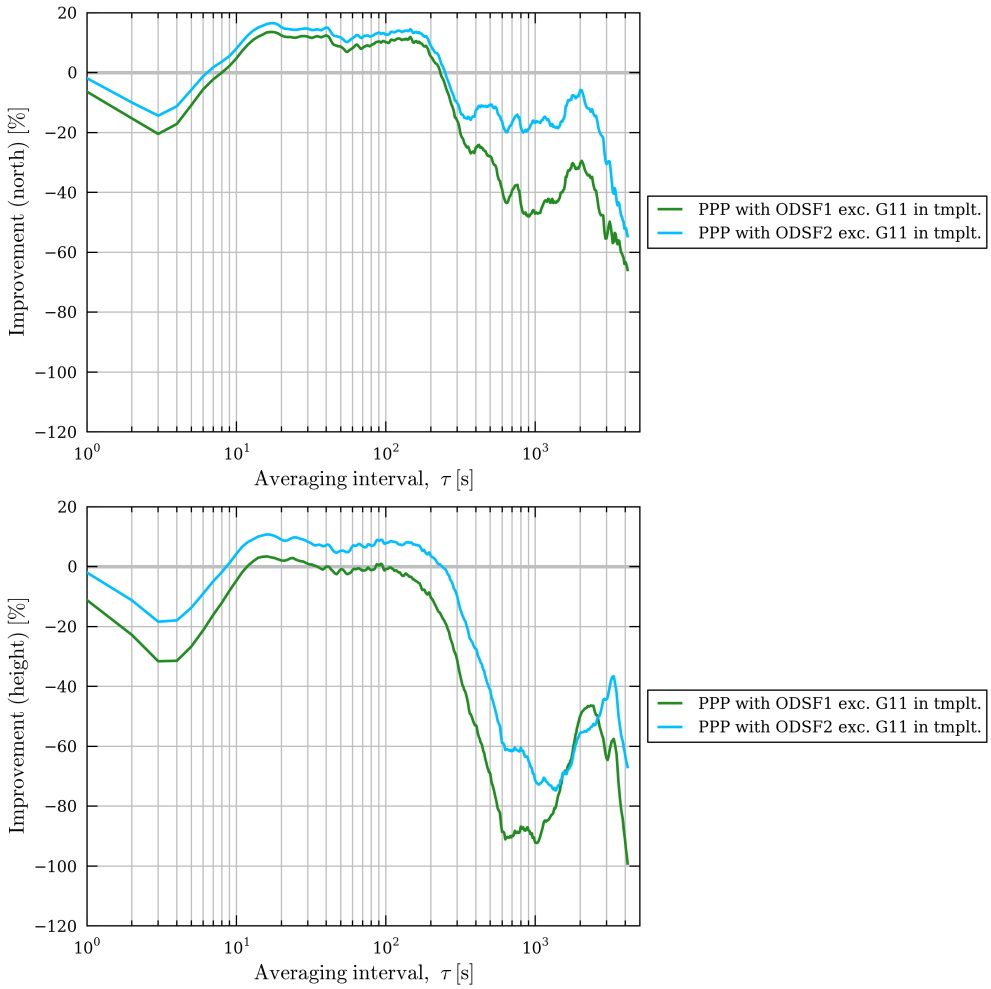

Figure E.41 – The percentage improvement (i.e. reduction) in Allan deviation values for the ODSF1 and ODSF2 northing and easting position time series at station UCL shown in figure E.40 relative to standard PPP processing.

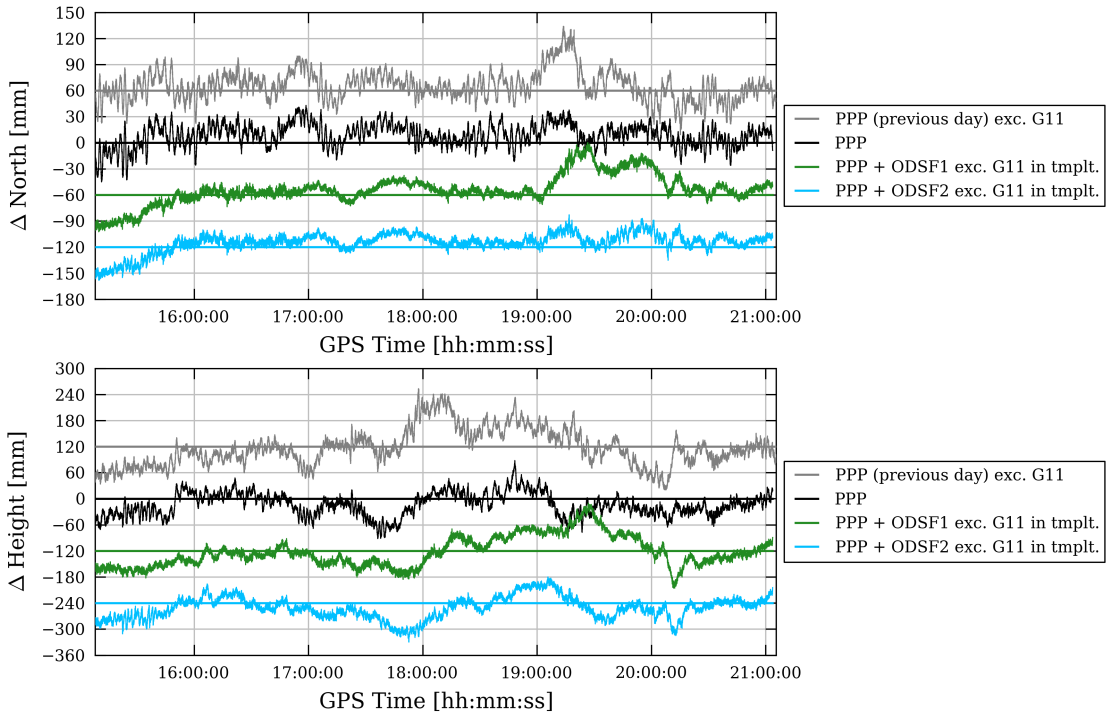

Figure E.42 – Northing and height errors (shown in black) between 15:16:59 and 21:03:38 on 31st August 2013 for receiver UEL resulting from standard PPP processing with measurements associated with satellite G11 excluded from day 1 (the 'template' (tmplt.) day). The corresponding errors from the previous day are shown in grey. Similarly shown in green and blue are the errors resulting from PPP processing with ODSF1 or ODSF2 algorithms applied respectively. (Each of the time series have been offset from each other by appropriate multiples of 60 mm or 120 mm for clarity).

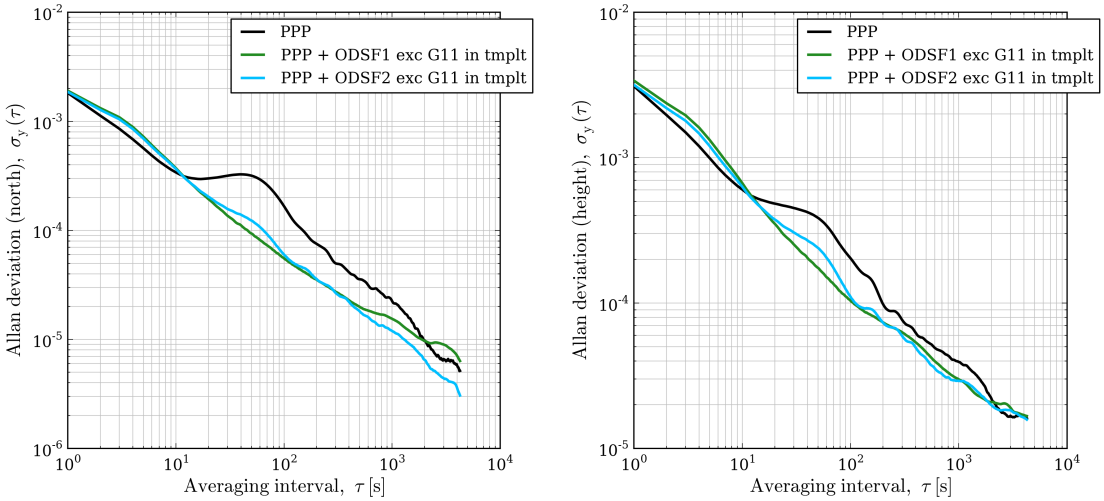

Figure E.43 – Allan deviation plots of the corresponding northing and height position time-series at station UEL between 15:16:59 and 21:03:38 on 31$^{\text{st}}$ August 2013 shown in figure E.42, except for the previous day.

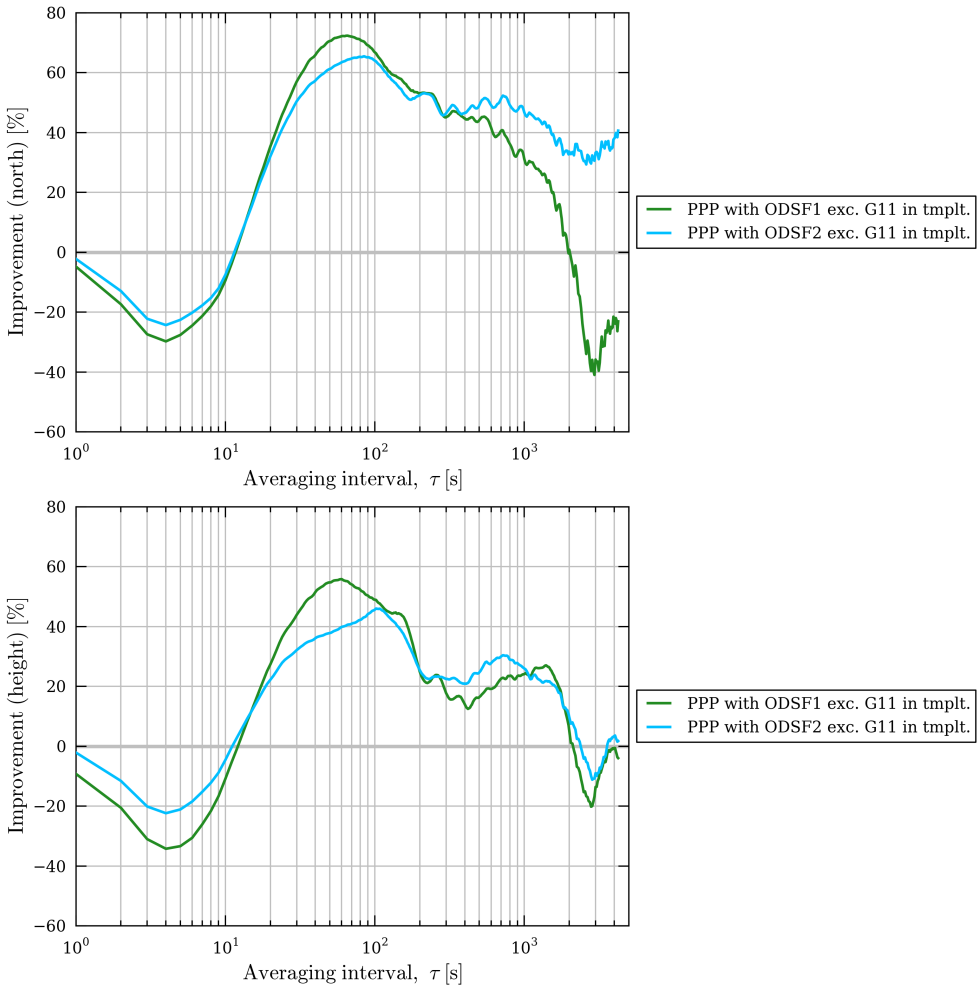

Figure E.44 – Plots showing the percentage improvement (i.e. reduction) in Allan deviation for station UEL, after applying the various types of sidereal filter, relative to the Allan deviation values corresponding to standard PPP processing that are shown in figure E.43.

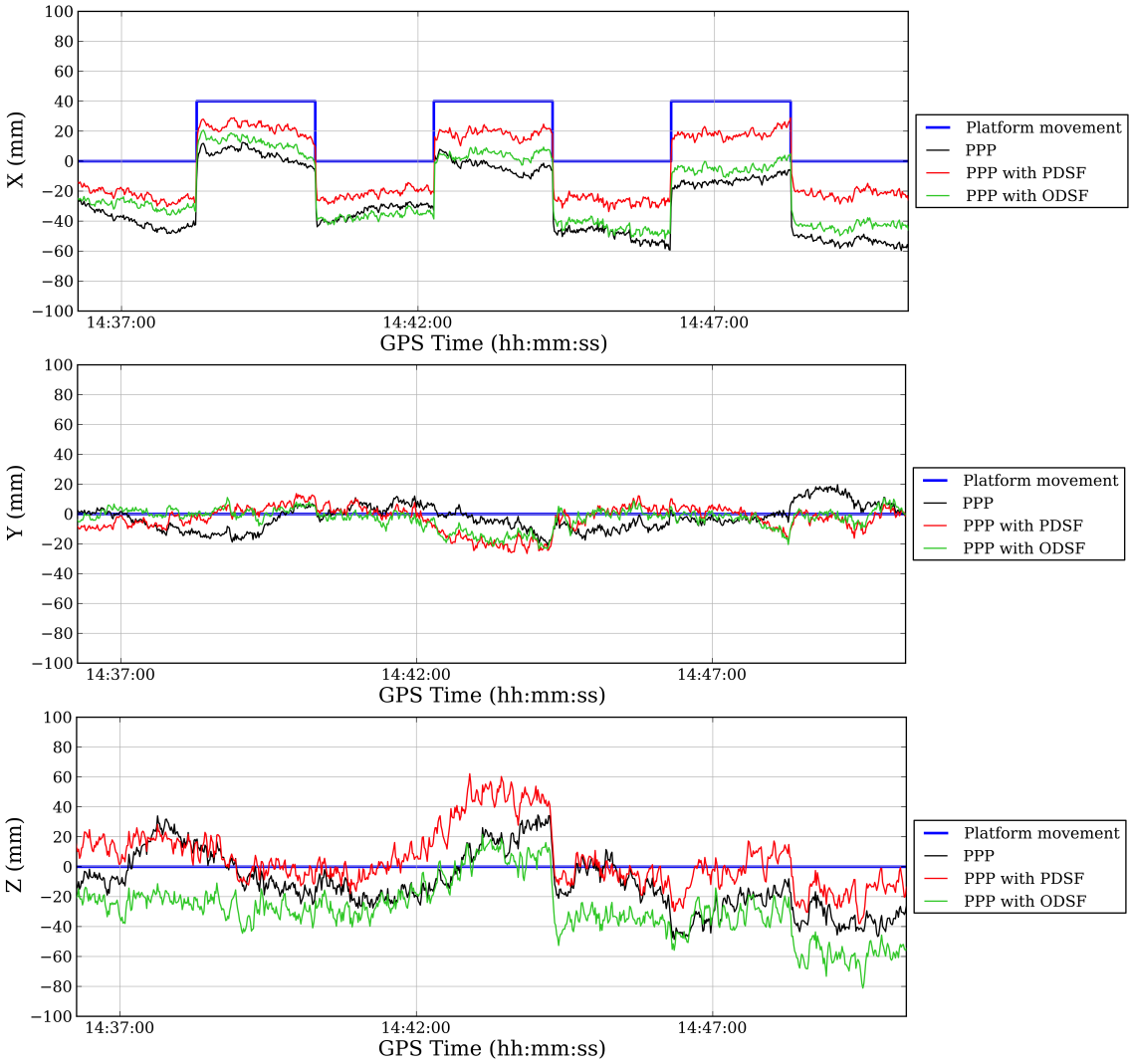

Figure E.45 – Positioning errors between 14:36:16 and 14:50:16 on 7$^{\text{th}}$ March 2014 resulting from standard PPP processing and PPP processing with various types of sidereal filter applied. Also shown (in blue) is the true motion of the platform.

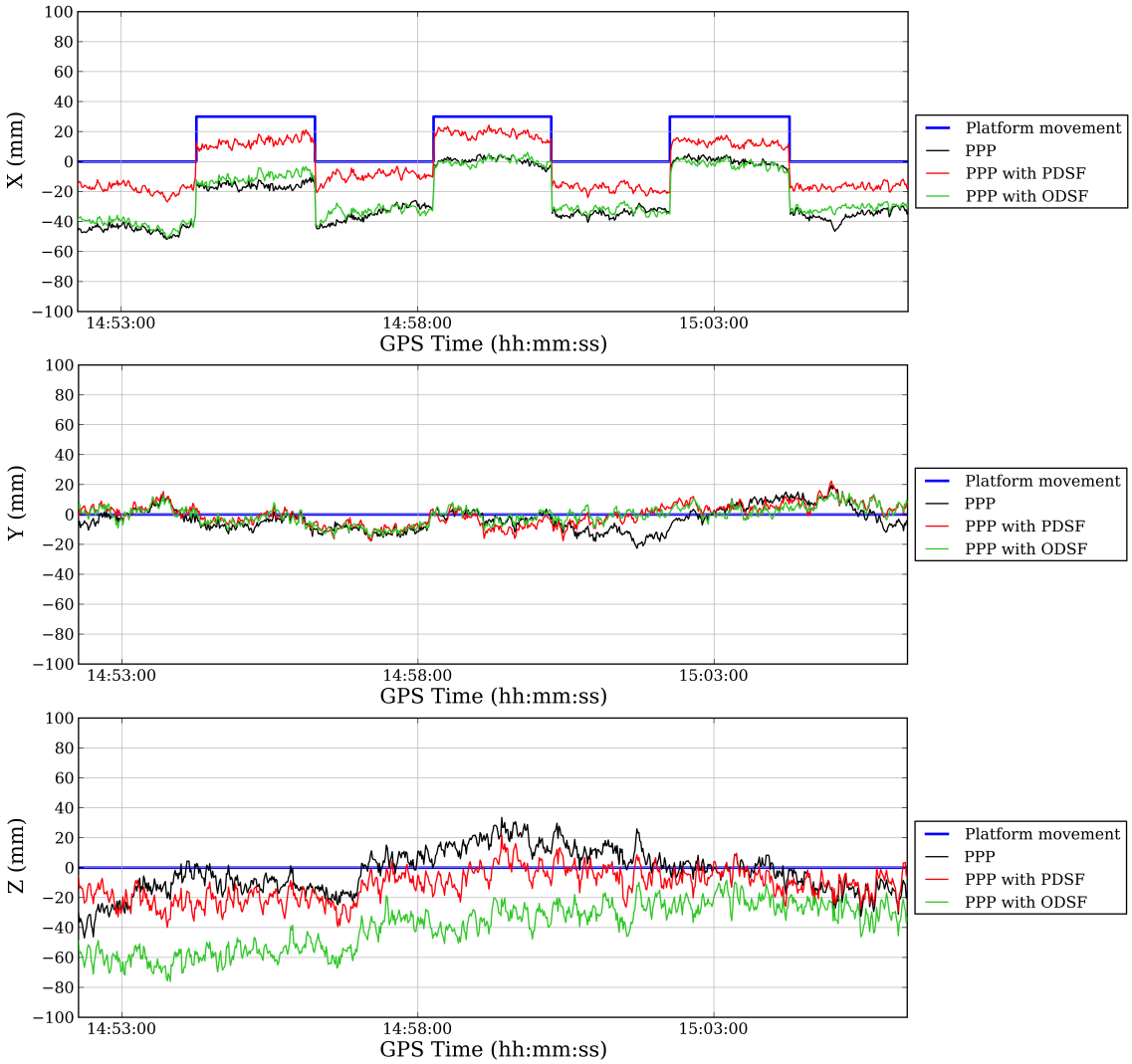

Figure E.46 – Positioning errors between 14:52:16 and 15:06:16 on 7$^{\text{th}}$ March 2014 resulting from standard PPP processing and PPP processing with various types of sidereal filter applied. Also shown (in blue) is the true motion of the platform.

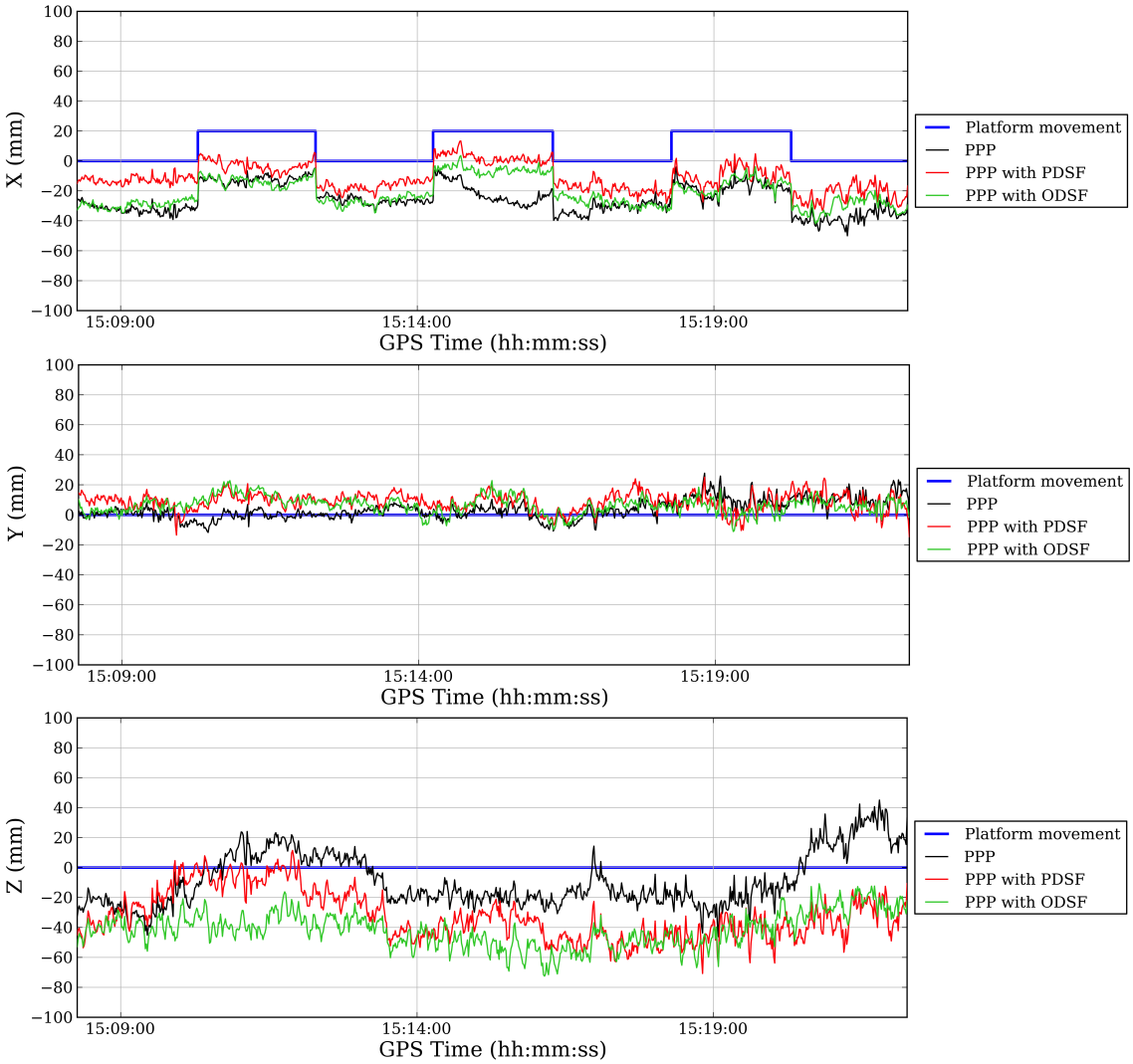

Figure E.47 – Positioning errors between 15:08:16 and 15:22:16 on 7$^{\text{th}}$ March 2014 resulting from standard PPP processing and PPP processing with various types of sidereal filter applied. Also shown (in blue) is the true motion of the platform.

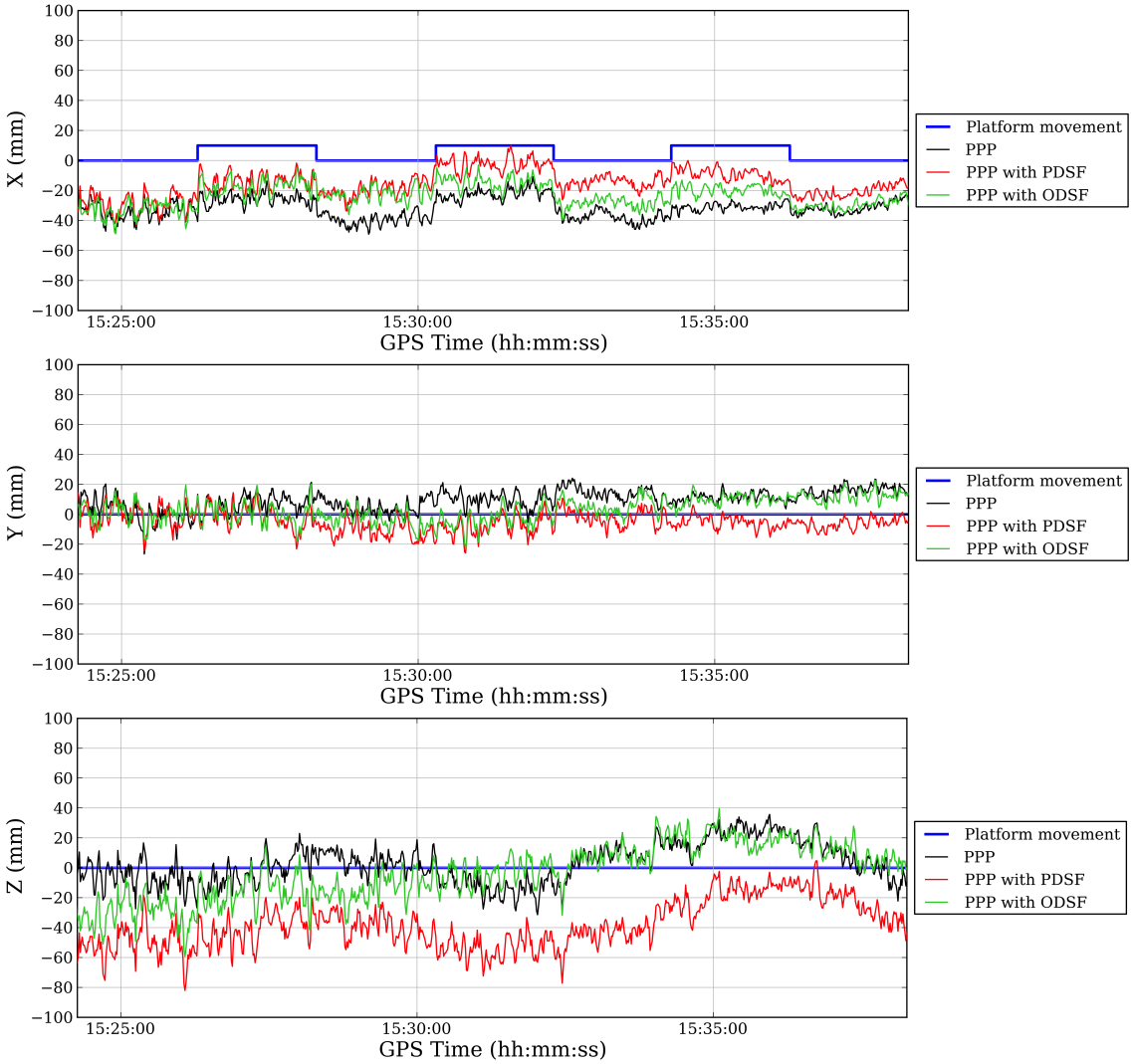

Figure E.48 – Positioning errors between 15:24:16 and 15:38:16 on 7$^{\text{th}}$ March 2014 resulting from standard PPP processing and PPP processing with various types of sidereal filter applied. Also shown (in blue) is the true motion of the platform.

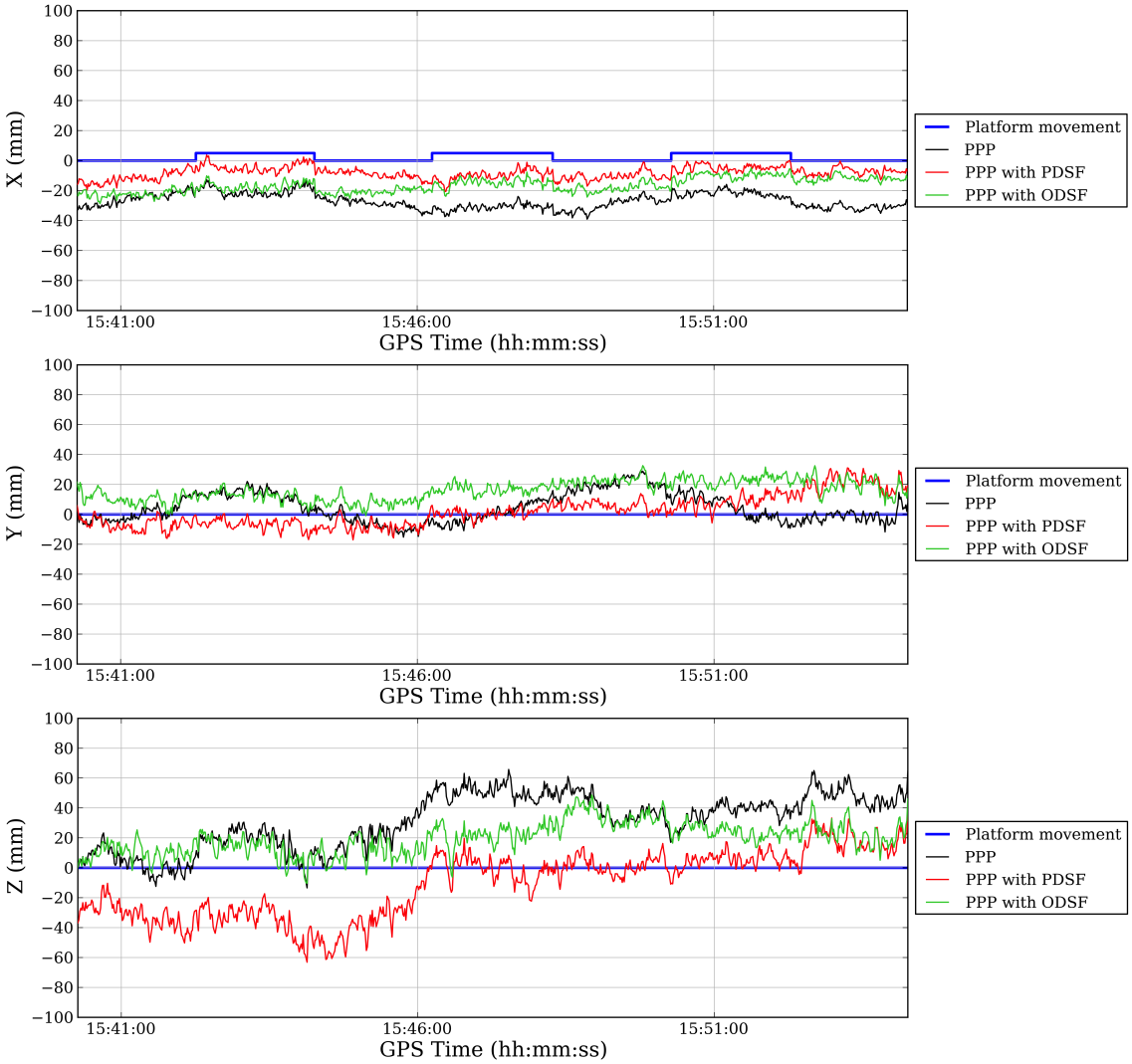

Figure E.49 – Positioning errors between 15:40:16 and 15:54:16 on 7th March 2014 resulting from standard PPP processing and PPP processing with various types of sidereal filter applied. Also shown (in blue) is the true motion of the platform.

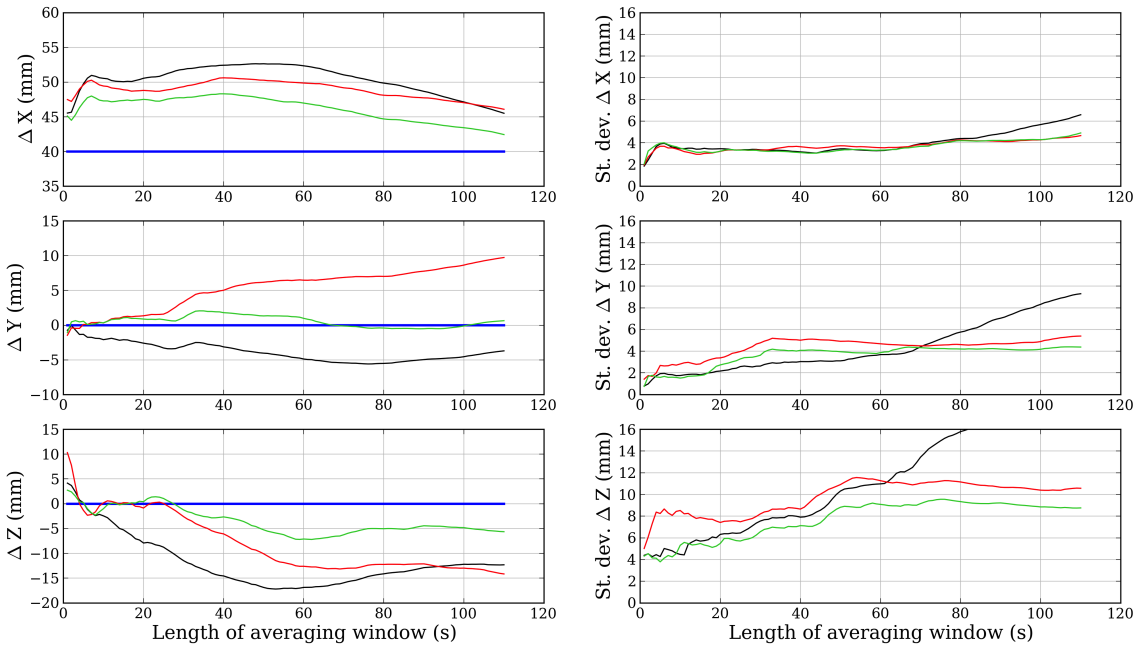

(a) 14:38:16 (40 mm in x-component)

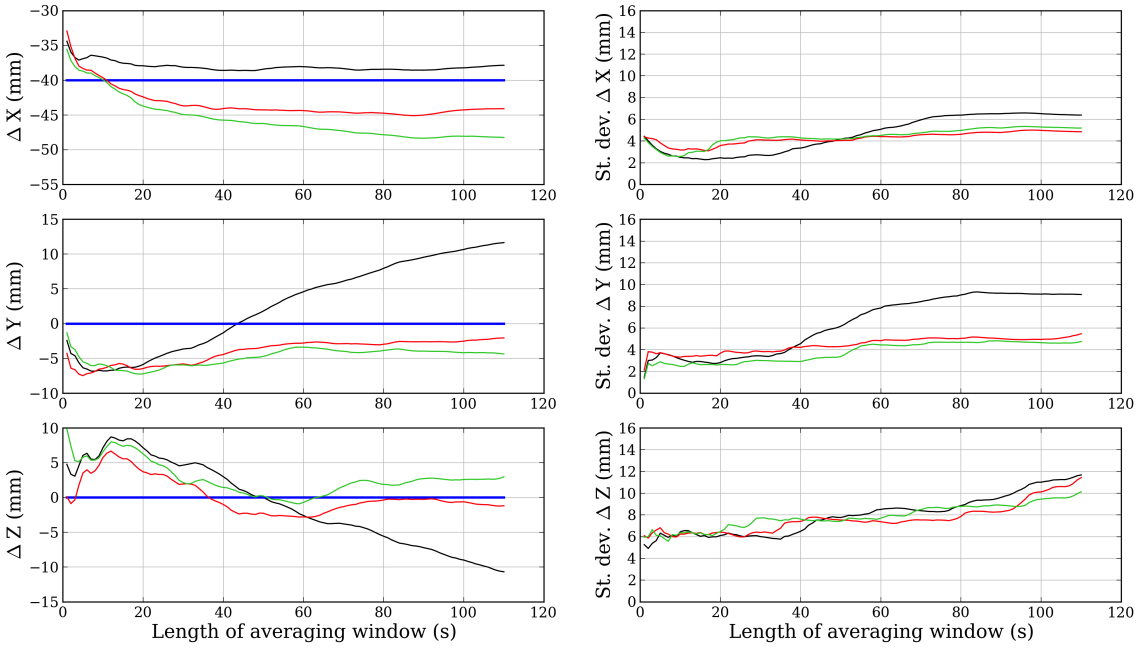

(b) 14:40:16 (-40 mm in x-component)

Figure E.50 – Estimates of the displacement at two separate displacement events and their corresponding standard deviations using different lengths of averaging window, α. The black, red and green lines refer to the standard PPP, PPP + PDSF and PPP + ODSF time series, respectively. The blue lines show the true displacement of the platform.

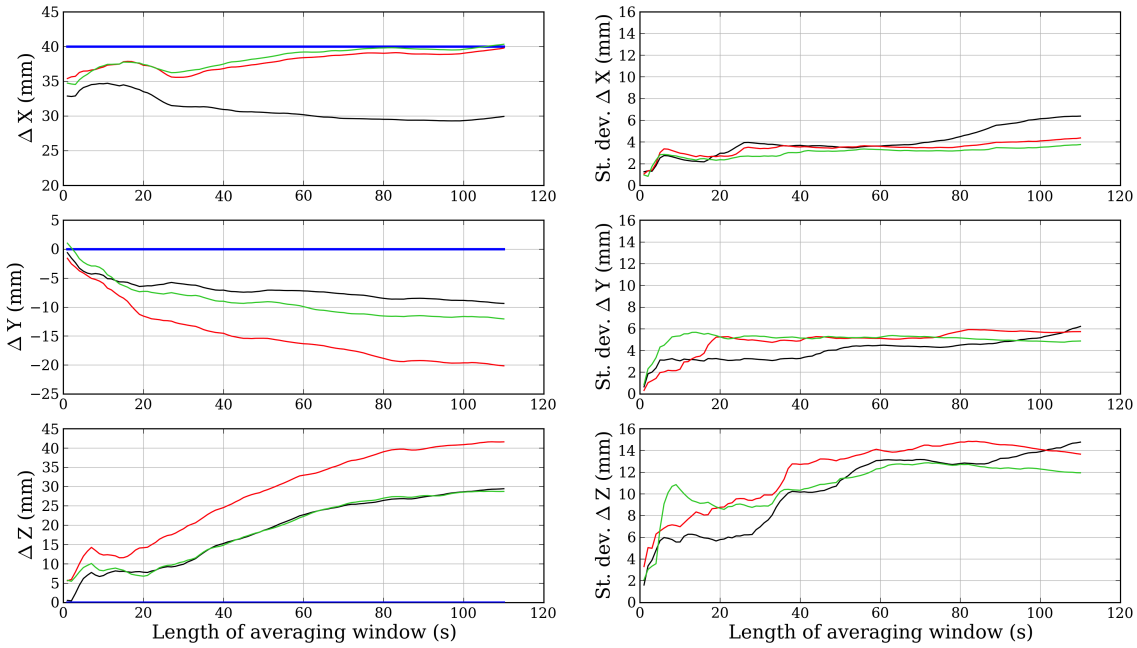

(a) 14:42:16 (40 mm in x-component)

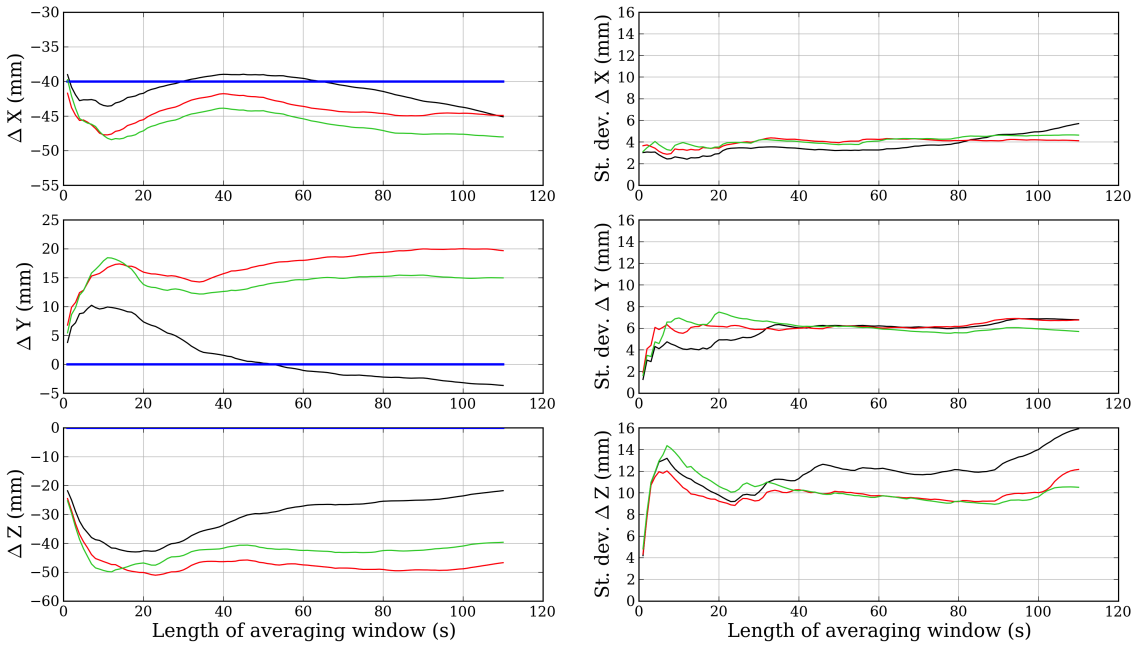

(b) 14:44:16 (-40 mm in x-component)

Figure E.51 – Estimates of the displacement at two separate displacement events and their corresponding standard deviations using different lengths of averaging window, α. The black, red and green lines refer to the standard PPP, PPP + PDSF and PPP + ODSF time series, respectively. The blue lines show the true displacement of the platform.

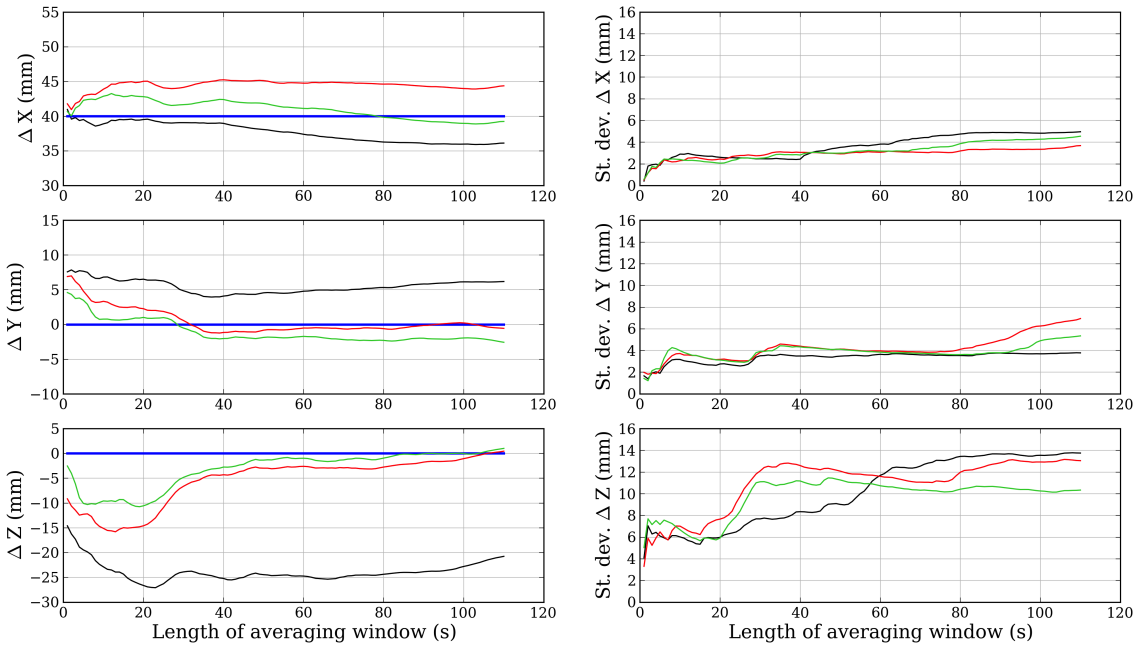

(a) 14:46:16 (40 mm in x-component)

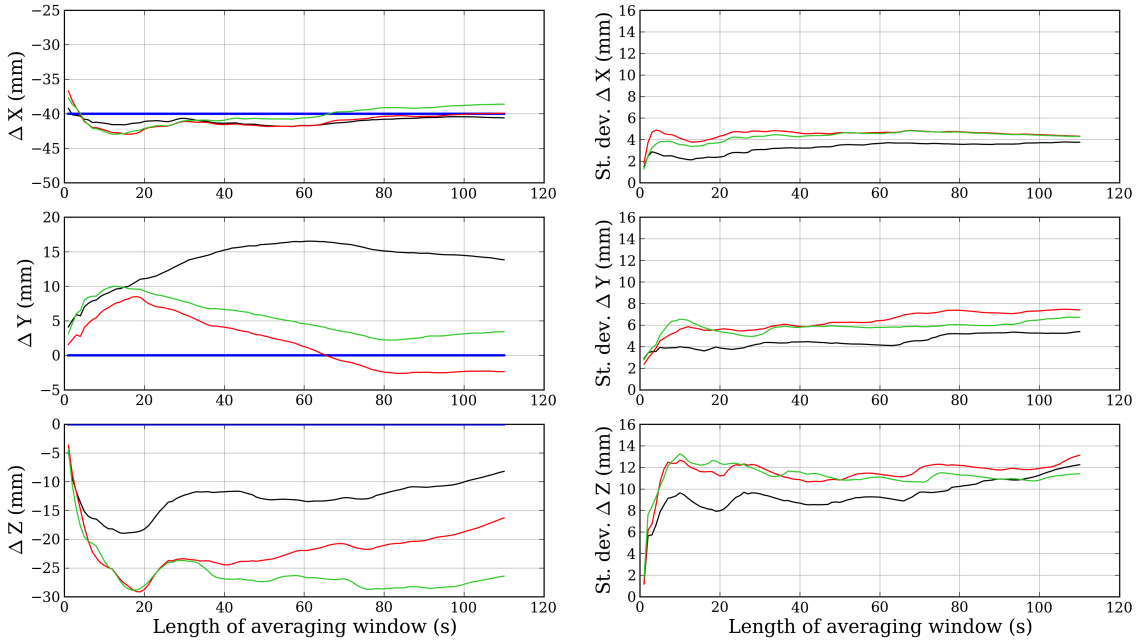

(b) 14:48:17 (-40 mm in x-component)

Figure E.52 – Estimates of the displacement at two separate displacement events and their corresponding standard deviations using different lengths of averaging window, α. The black, red and green lines refer to the standard PPP, PPP + PDSF and PPP + ODSF time series, respectively. The blue lines show the true displacement of the platform.

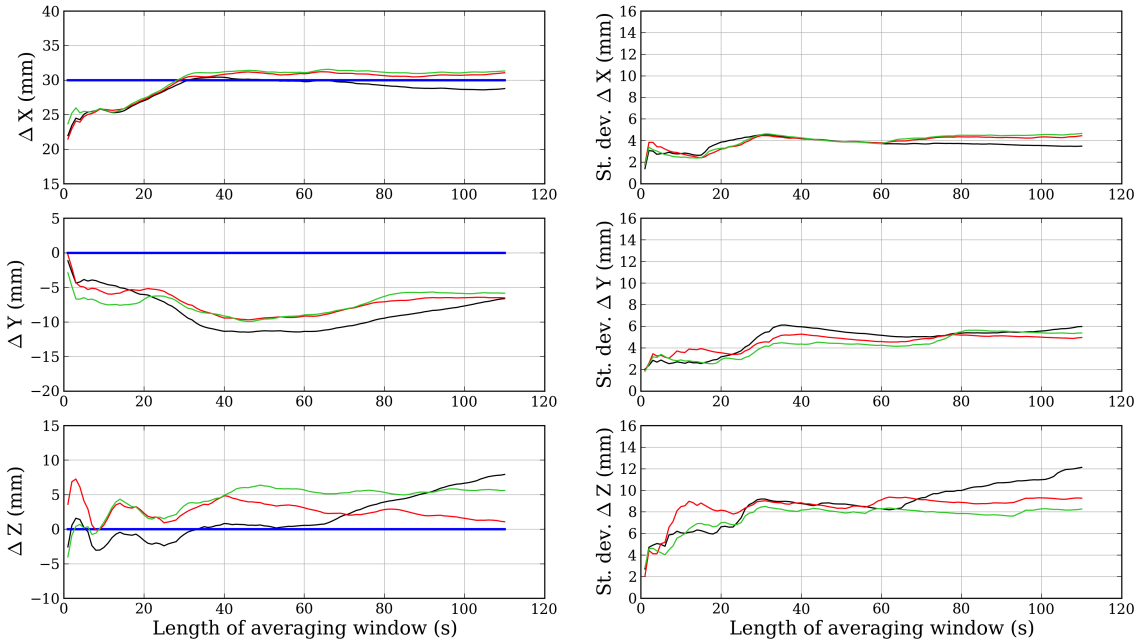

(a) 14:54:16 (30 mm in x-component)

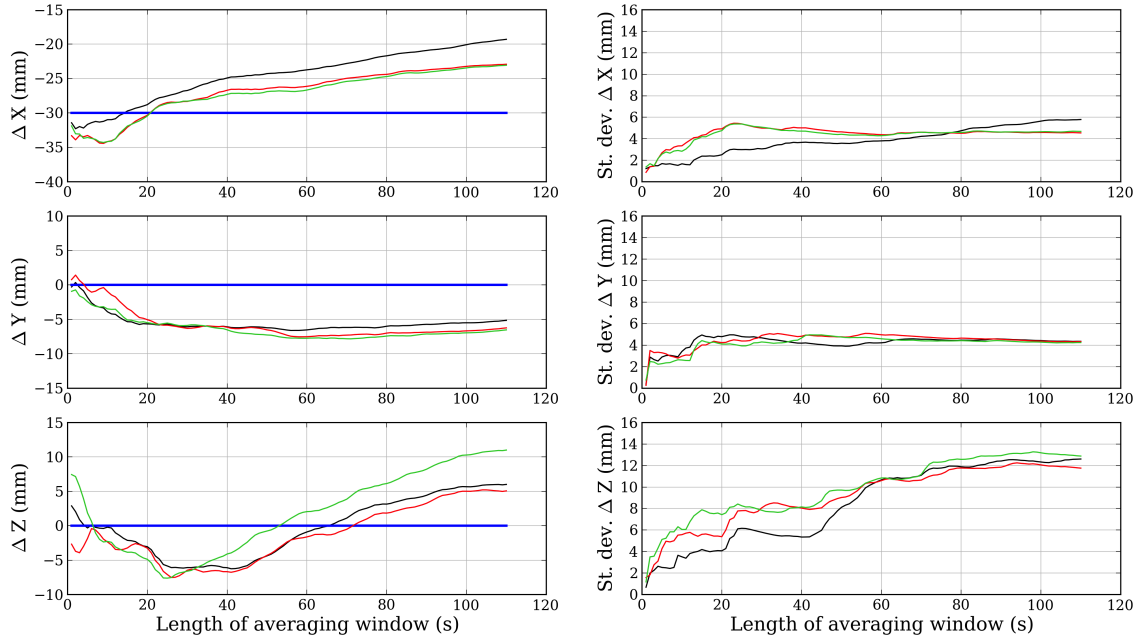

(b) 14:56:16 (-30 mm in x-component)

Figure E.53 – Estimates of the displacement at two separate displacement events and their corresponding standard deviations using different lengths of averaging window, α. The black, red and green lines refer to the standard PPP, PPP + PDSF and PPP + ODSF time series, respectively. The blue lines show the true displacement of the platform.

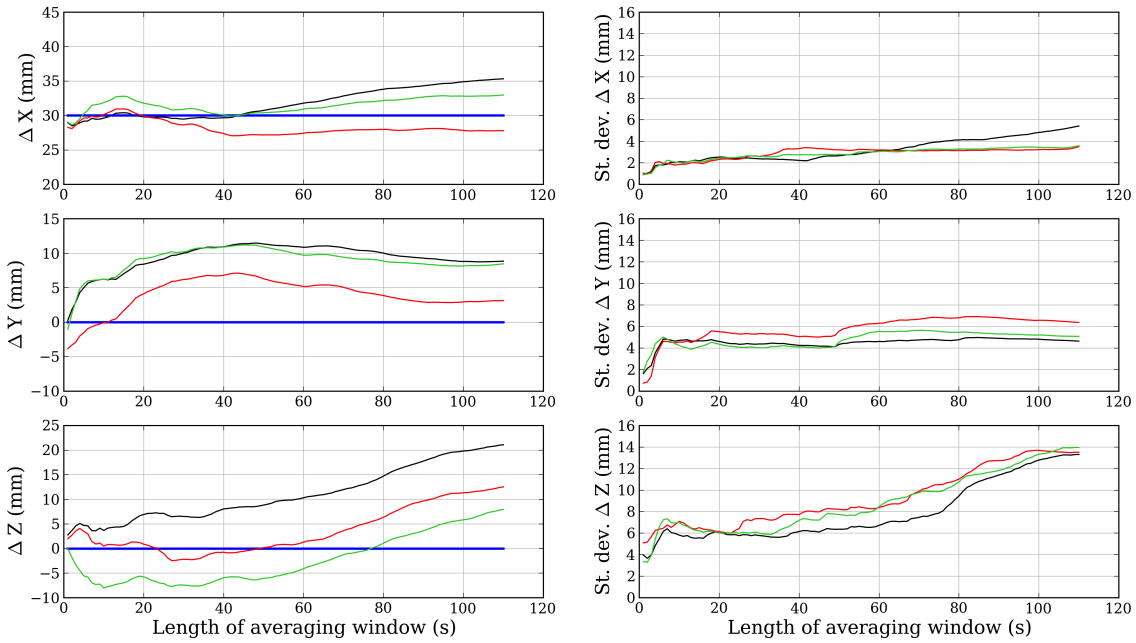

(a) 14:58:16 (30 mm in x-component)

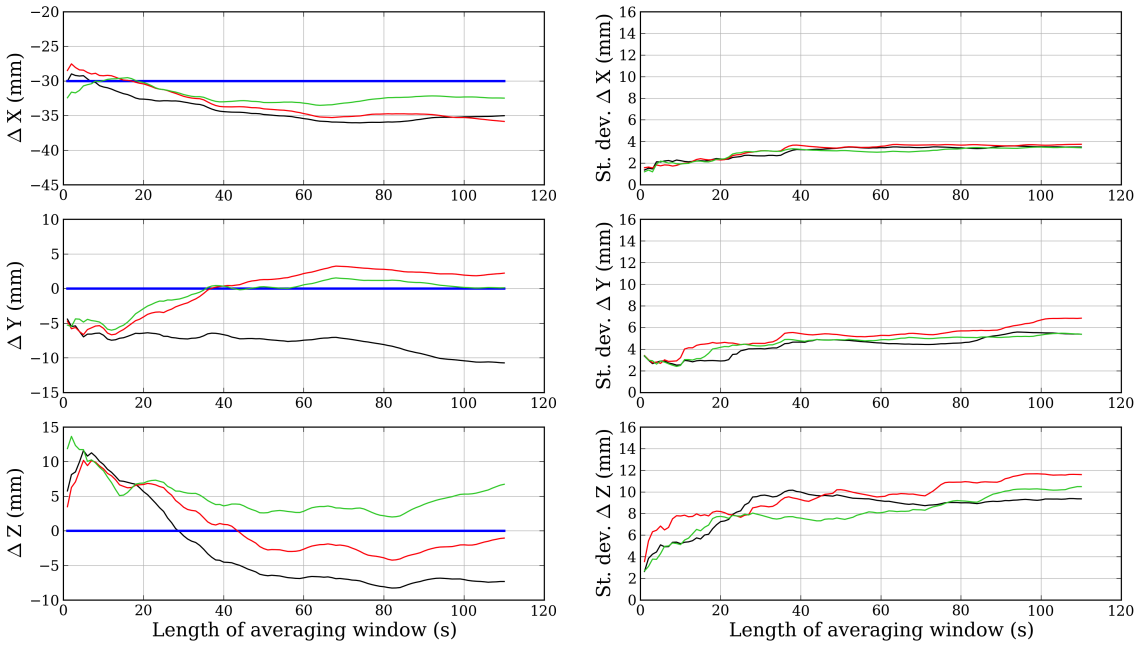

(b) 15:00:15 (-30 mm in x-component)

Figure E.54 – Estimates of the displacement at two separate displacement events and their corresponding standard deviations using different lengths of averaging window, α. The black, red and green lines refer to the standard PPP, PPP + PDSF and PPP + ODSF time series, respectively. The blue lines show the true displacement of the platform.

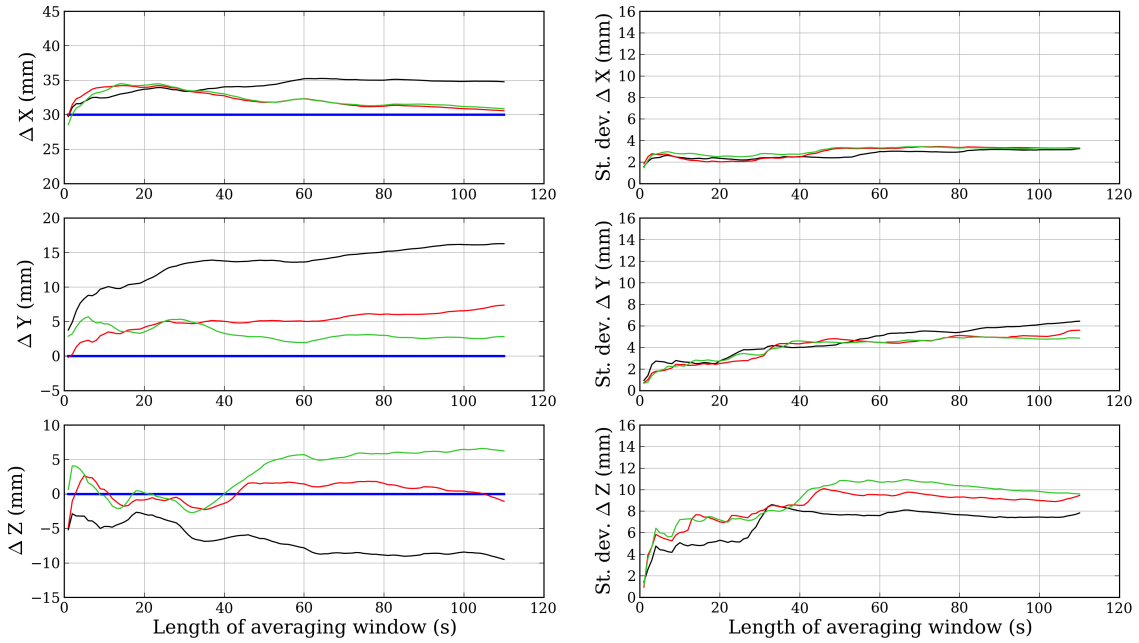

(a) 15:02:15 (30 mm in x-component)

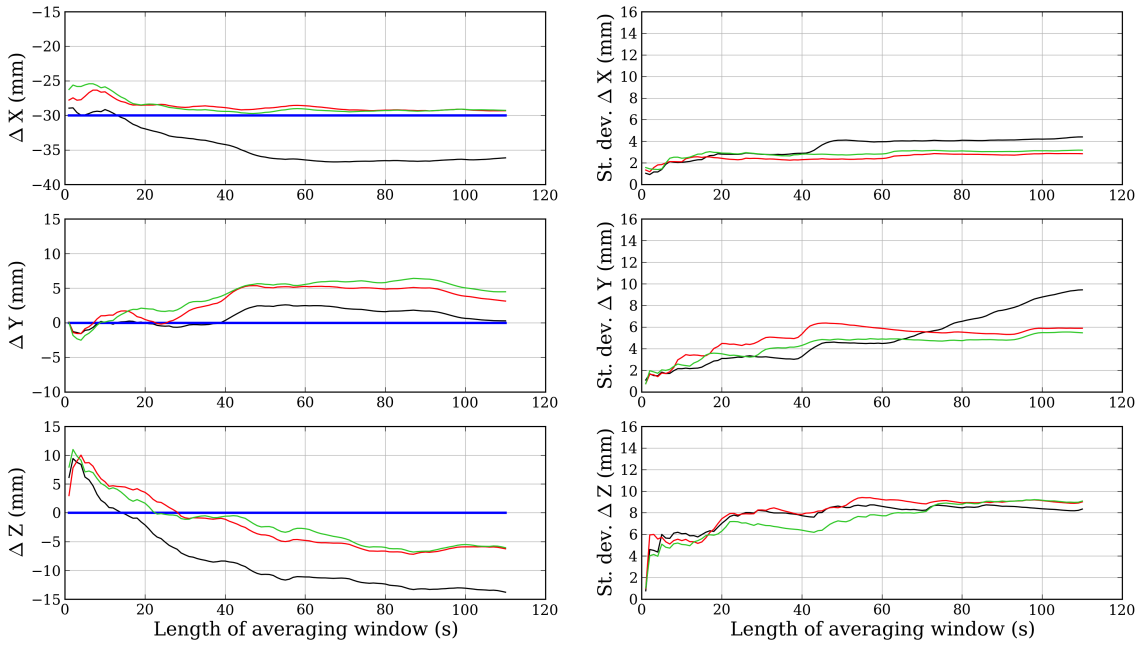

(b) 15:04:16 (-30 mm in x-component)

Figure E.55 – Estimates of the displacement at two separate displacement events and their corresponding standard deviations using different lengths of averaging window, α. The black, red and green lines refer to the standard PPP, PPP + PDSF and PPP + ODSF time series, respectively. The blue lines show the true displacement of the platform.

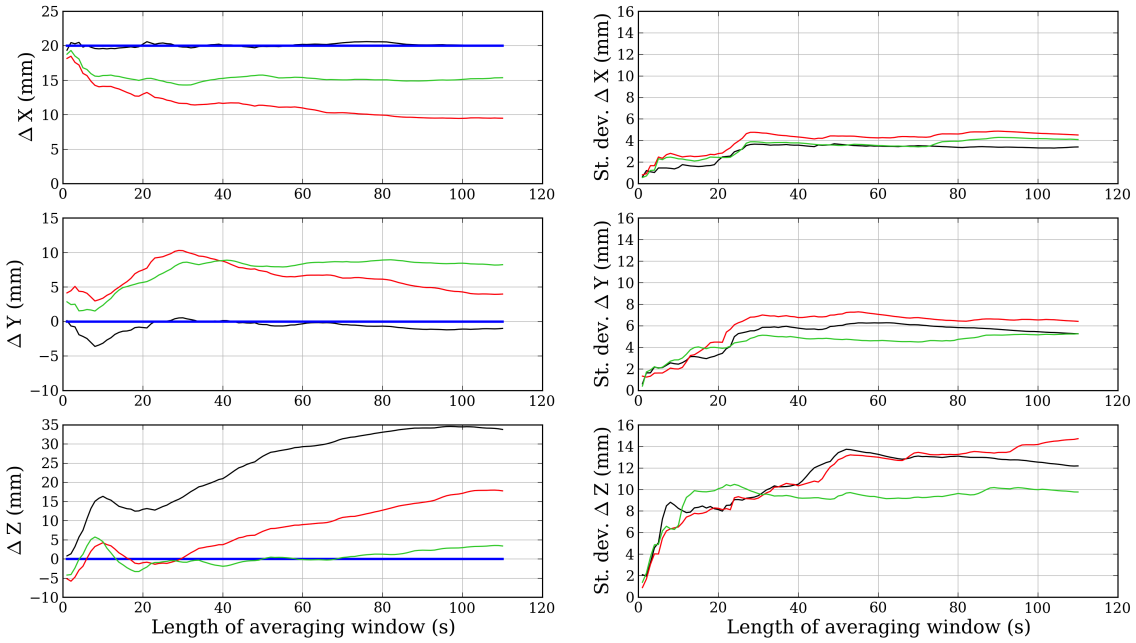

(a) 15:10:18 (20 mm in x-component)

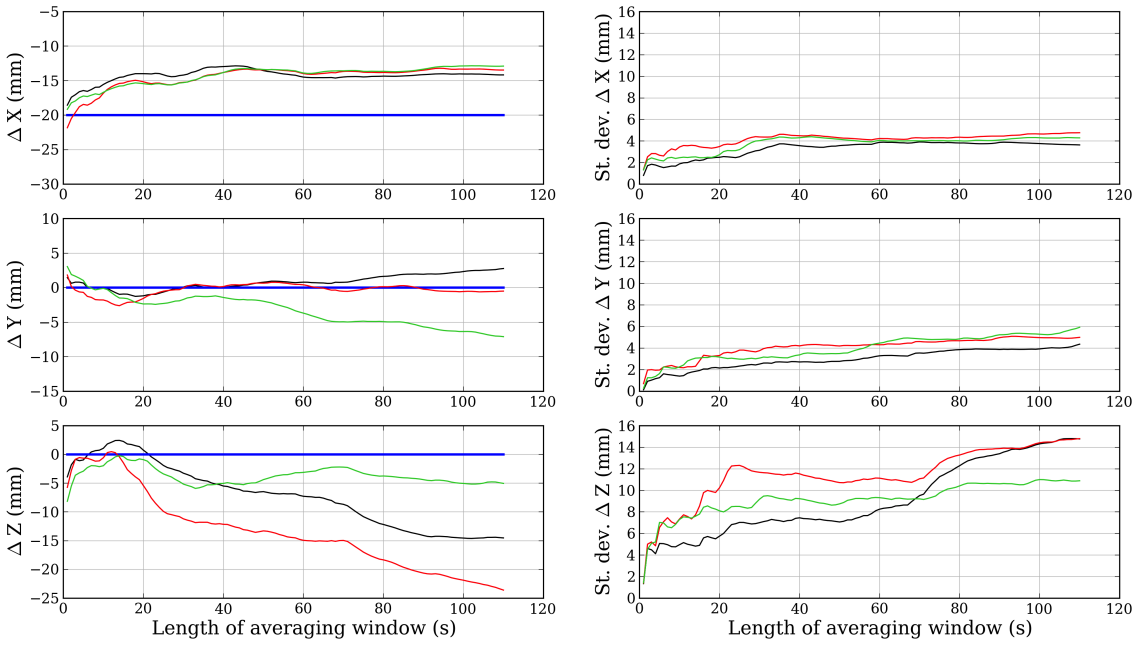

(b) 15:12:17 (-20 mm in x-component)

Figure E.56 – Estimates of the displacement at two separate displacement events and their corresponding standard deviations using different lengths of averaging window, α. The black, red and green lines refer to the standard PPP, PPP + PDSF and PPP + ODSF time series, respectively. The blue lines show the true displacement of the platform.

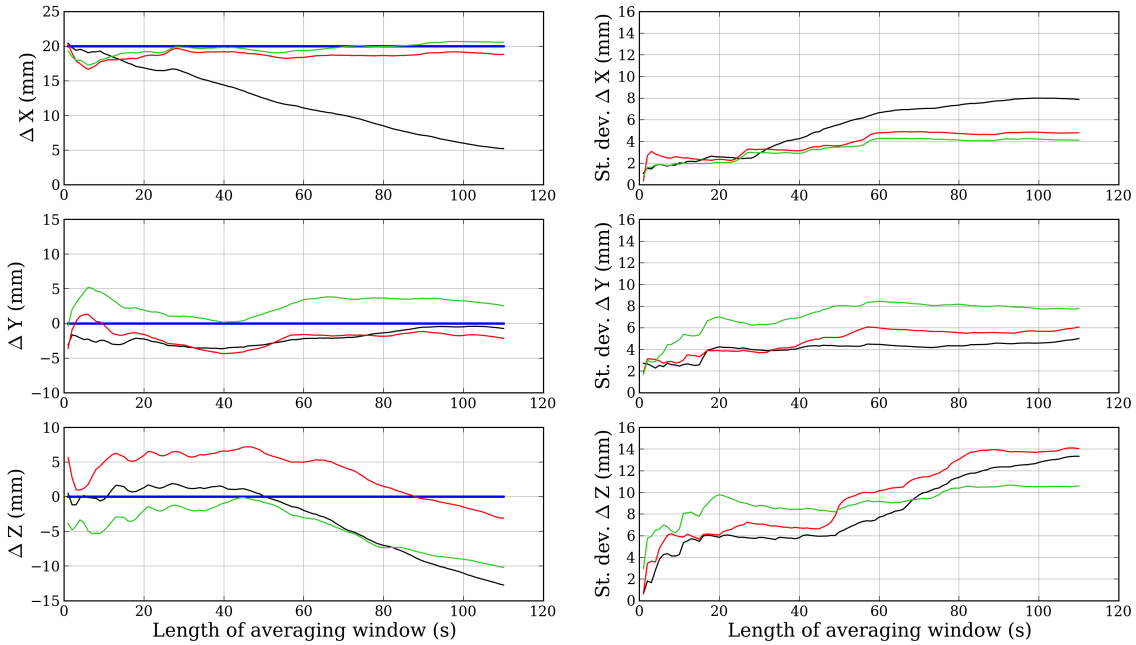

(a) 15:14:16 (20 mm in x-component)

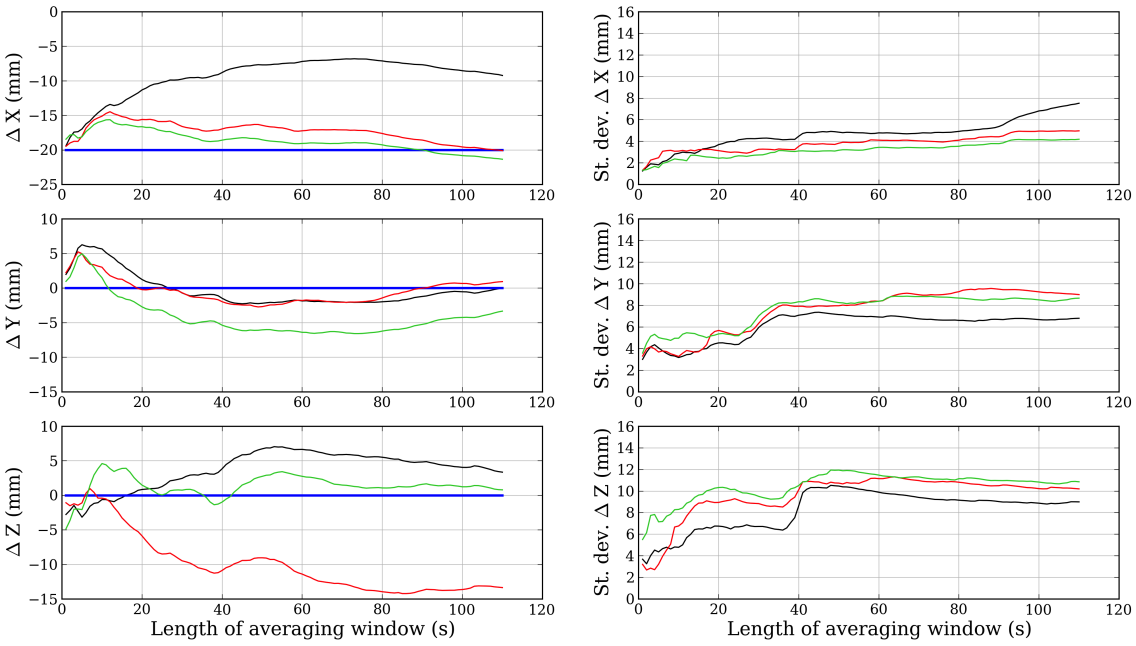

(b) 15:16:17 (-20 mm in x-component)

Figure E.57 – Estimates of the displacement at two separate displacement events and their corresponding standard deviations using different lengths of averaging window, α. The black, red and green lines refer to the standard PPP, PPP + PDSF and PPP + ODSF time series, respectively. The blue lines show the true displacement of the platform.

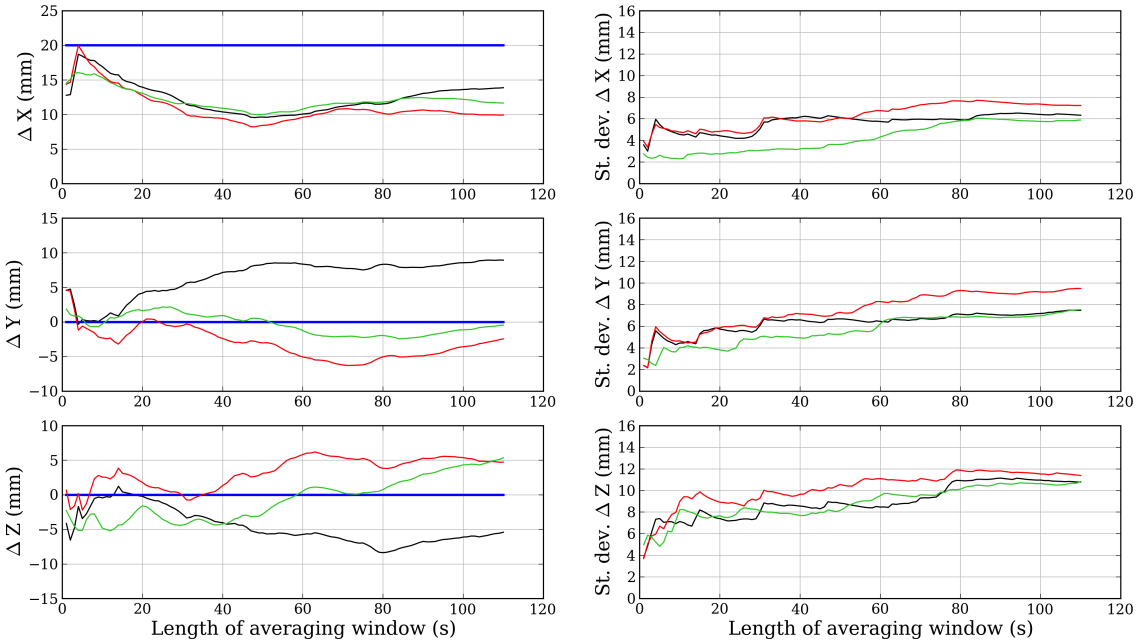

(a) 15:18:17 (20 mm in x-component)

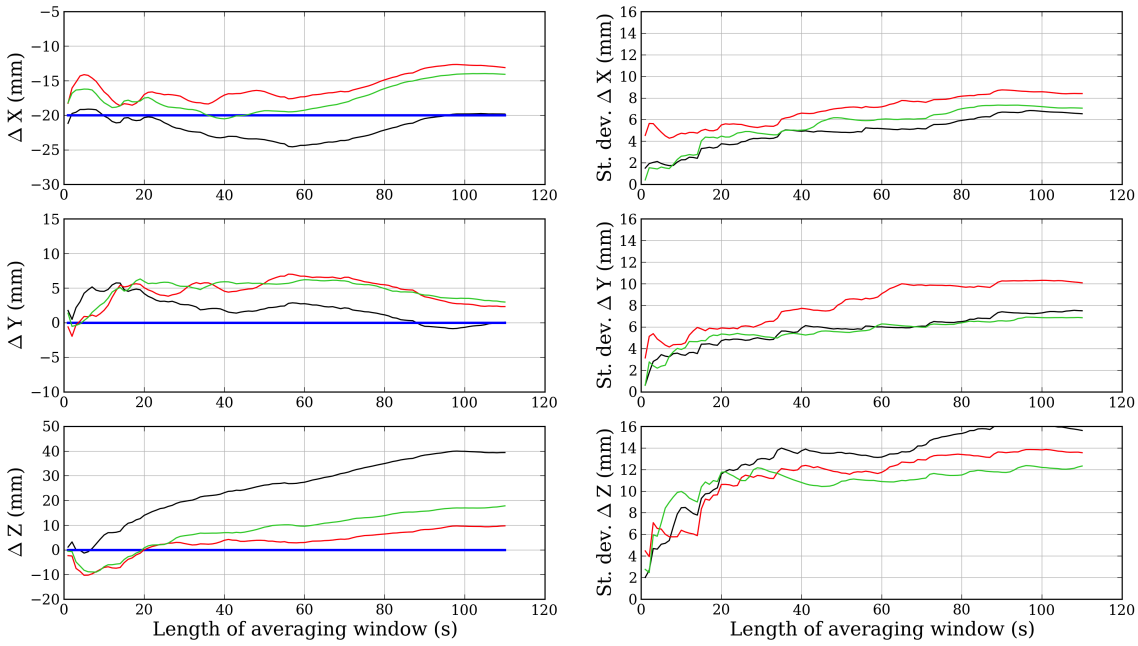

(b) 15:20:18 (-20 mm in x-component)

Figure E.58 – Estimates of the displacement at two separate displacement events and their corresponding standard deviations using different lengths of averaging window, α. The black, red and green lines refer to the standard PPP, PPP + PDSF and PPP + ODSF time series, respectively. The blue lines show the true displacement of the platform.

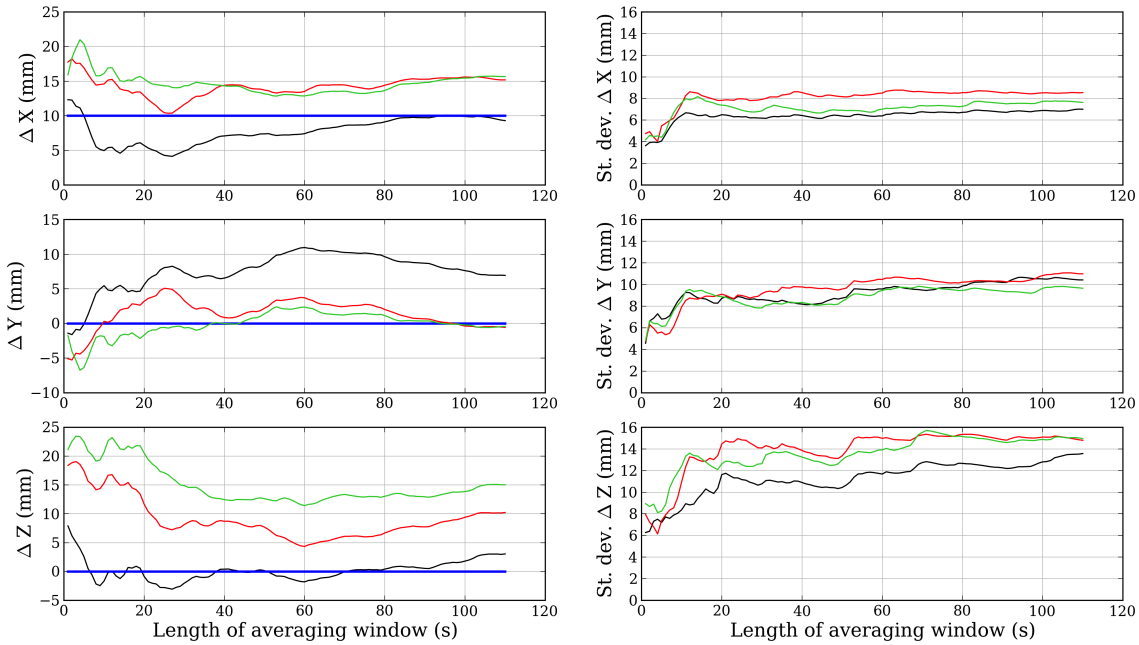

(a) 15:26:17 (10 mm in x-component)

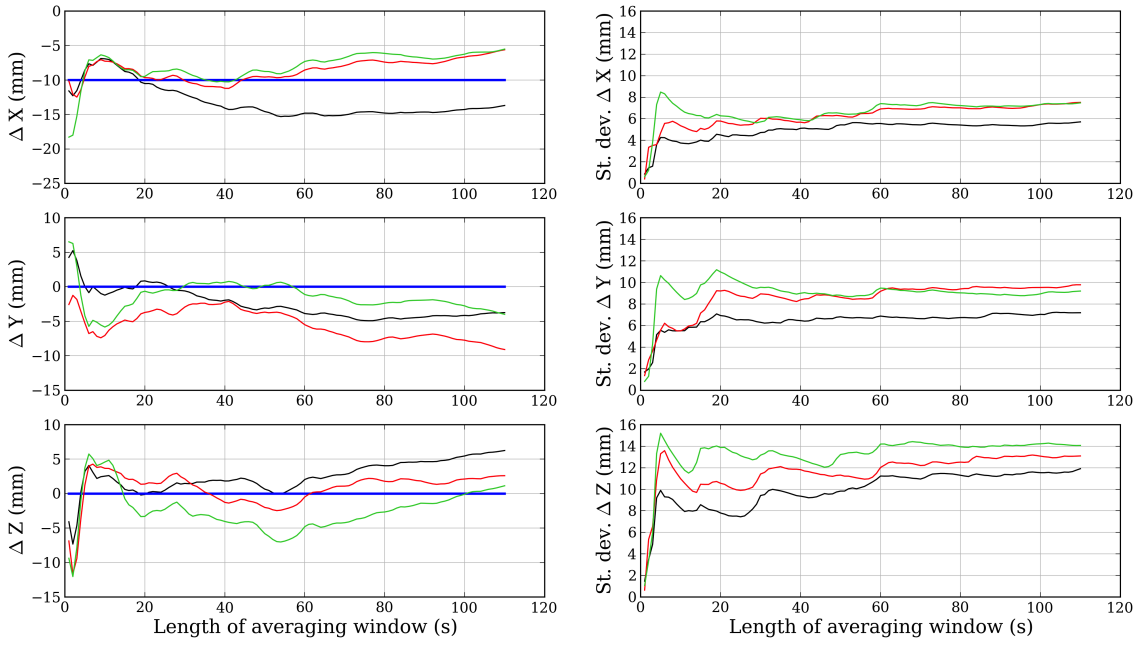

(b) 15:28:17 (-10 mm in x-component)

Figure E.59 – Estimates of the displacement at two separate displacement events and their corresponding standard deviations using different lengths of averaging window, α. The black, red and green lines refer to the standard PPP, PPP + PDSF and PPP + ODSF time series, respectively. The blue lines show the true displacement of the platform.

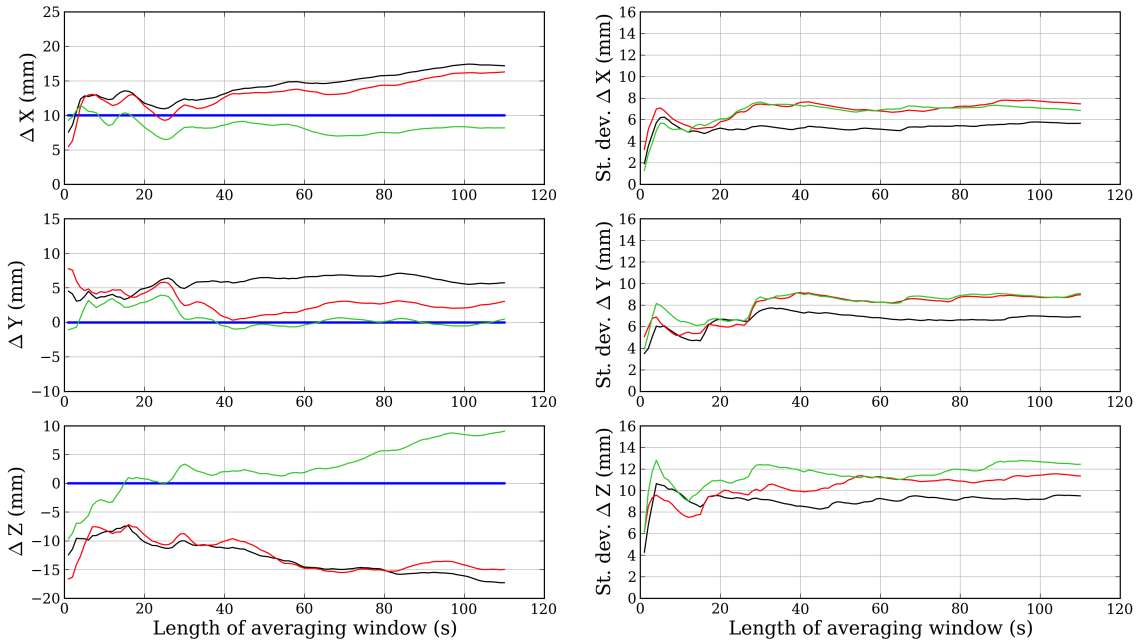

(a) 15:30:18 (10 mm in x-component)

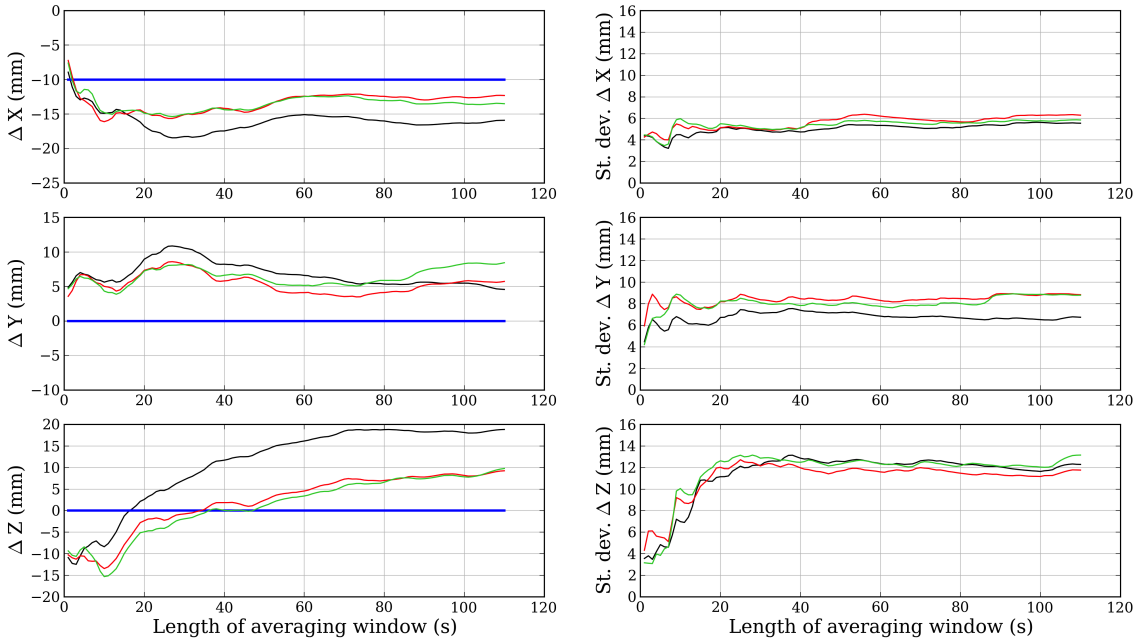

(b) 15:32:17 (-10 mm in x-component)

Figure E.60 – Estimates of the displacement at two separate displacement events and their corresponding standard deviations using different lengths of averaging window, α. The black, red and green lines refer to the standard PPP, PPP + PDSF and PPP + ODSF time series, respectively. The blue lines show the true displacement of the platform.

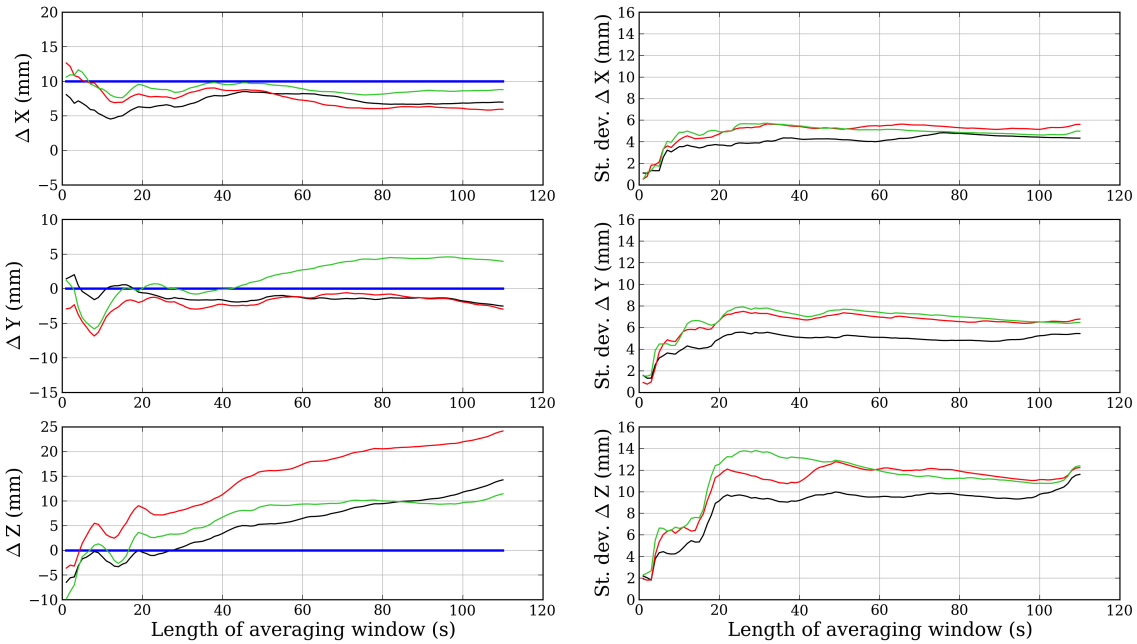

(a) 15:34:16 (10 mm in x-component)

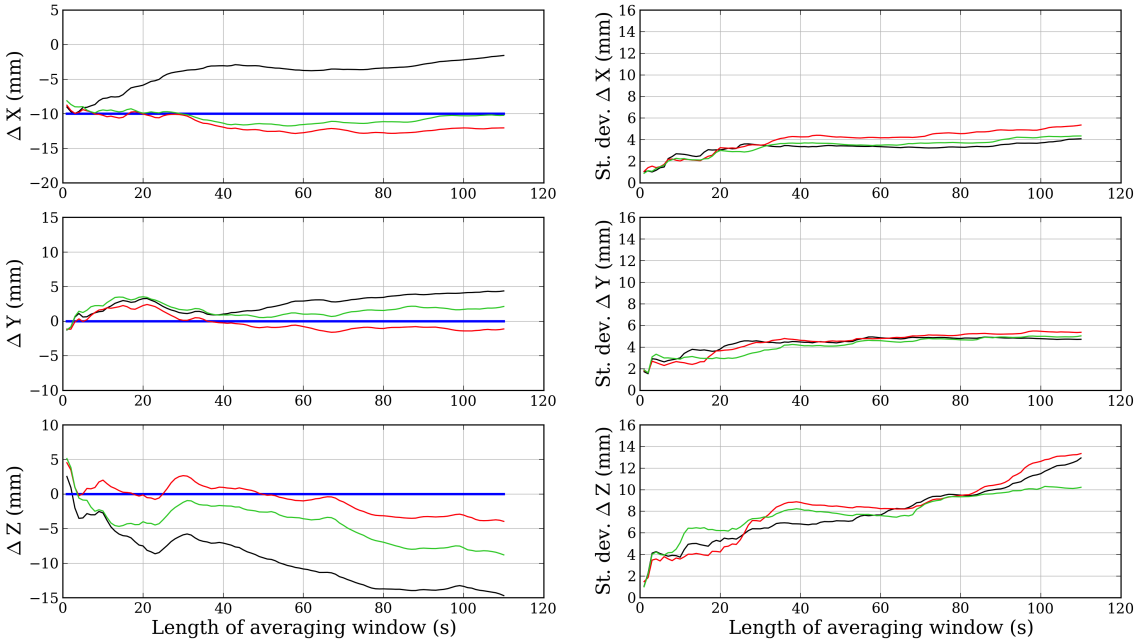

(b) 15:36:16 (-10 mm in x-component)

Figure E.61 – Estimates of the displacement at two separate displacement events and their corresponding standard deviations using different lengths of averaging window, α. The black, red and green lines refer to the standard PPP, PPP + PDSF and PPP + ODSF time series, respectively. The blue lines show the true displacement of the platform.

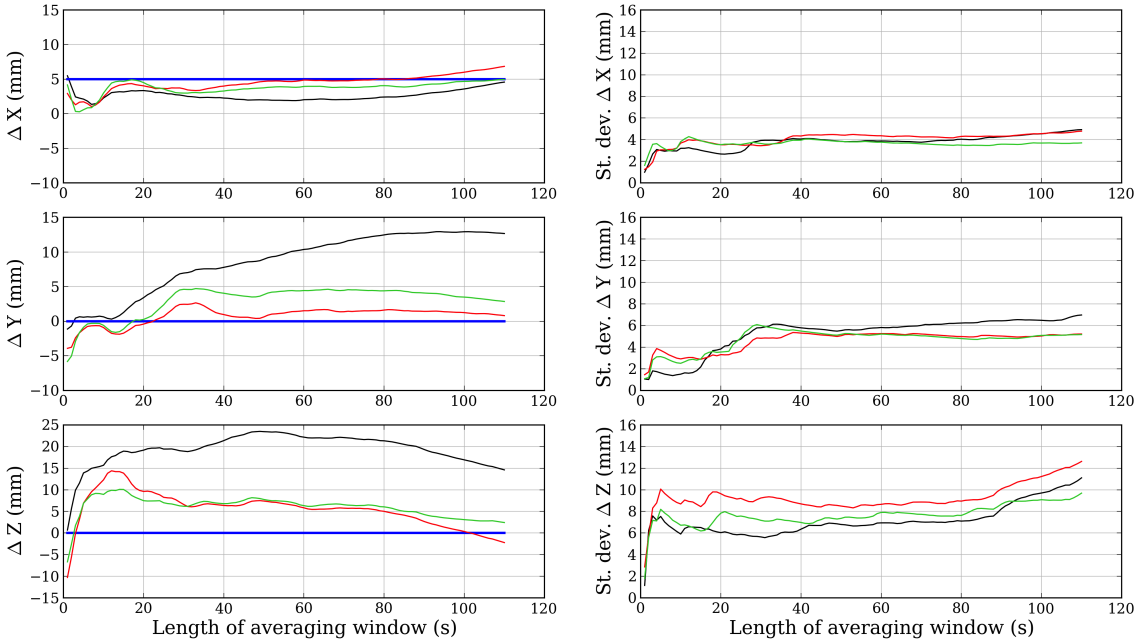

(a) 15:42:16 (5 mm in x-component)

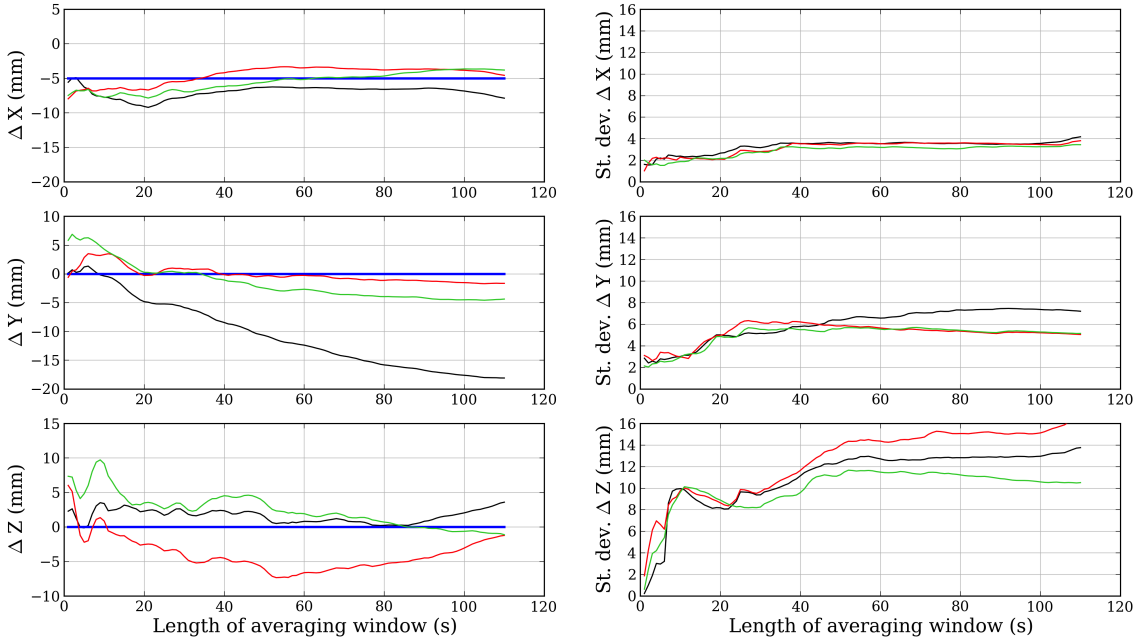

(b) 15:44:16 (-5 mm in x-component)

Figure E.62 – Estimates of the displacement at two separate displacement events and their corresponding standard deviations using different lengths of averaging window, α. The black, red and green lines refer to the standard PPP, PPP + PDSF and PPP + ODSF time series, respectively. The blue lines show the true displacement of the platform.

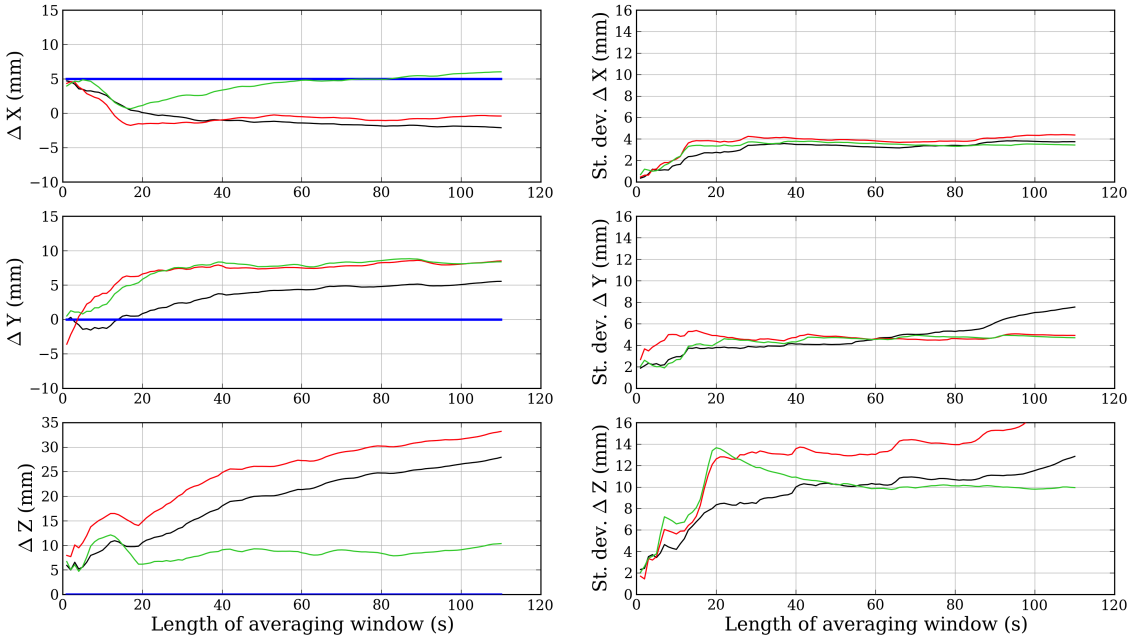

(a) 15:46:15 (5 mm in x-component)

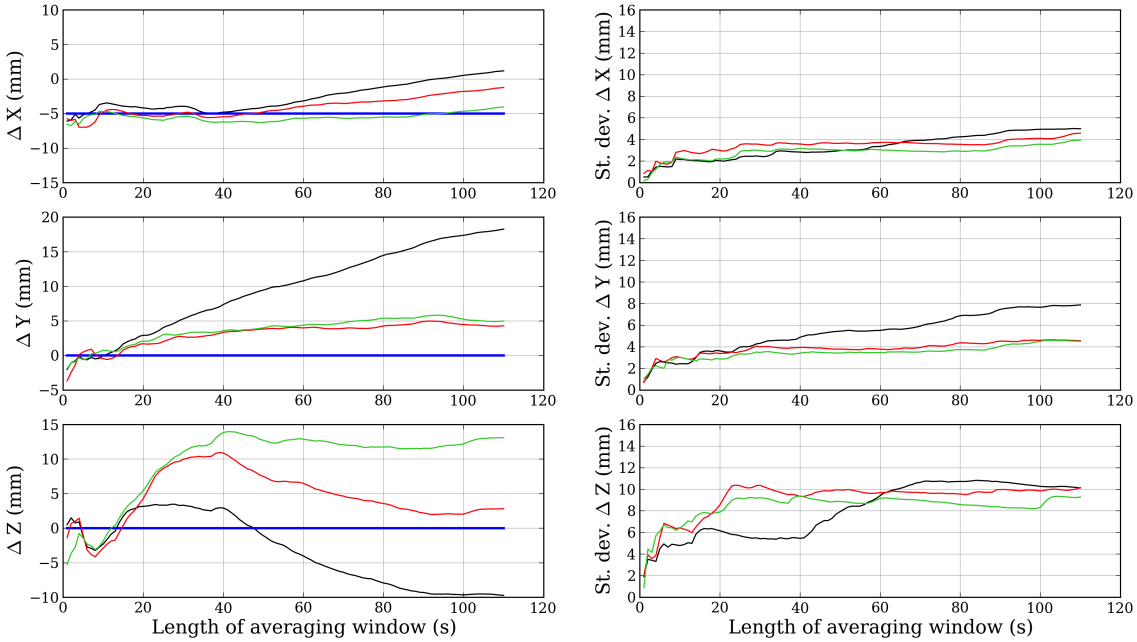

(b) 15:48:17 (-5 mm in x-component)

Figure E.63 – Estimates of the displacement at two separate displacement events and their corresponding standard deviations using different lengths of averaging window, α. The black, red and green lines refer to the standard PPP, PPP + PDSF and PPP + ODSF time series, respectively. The blue lines show the true displacement of the platform.

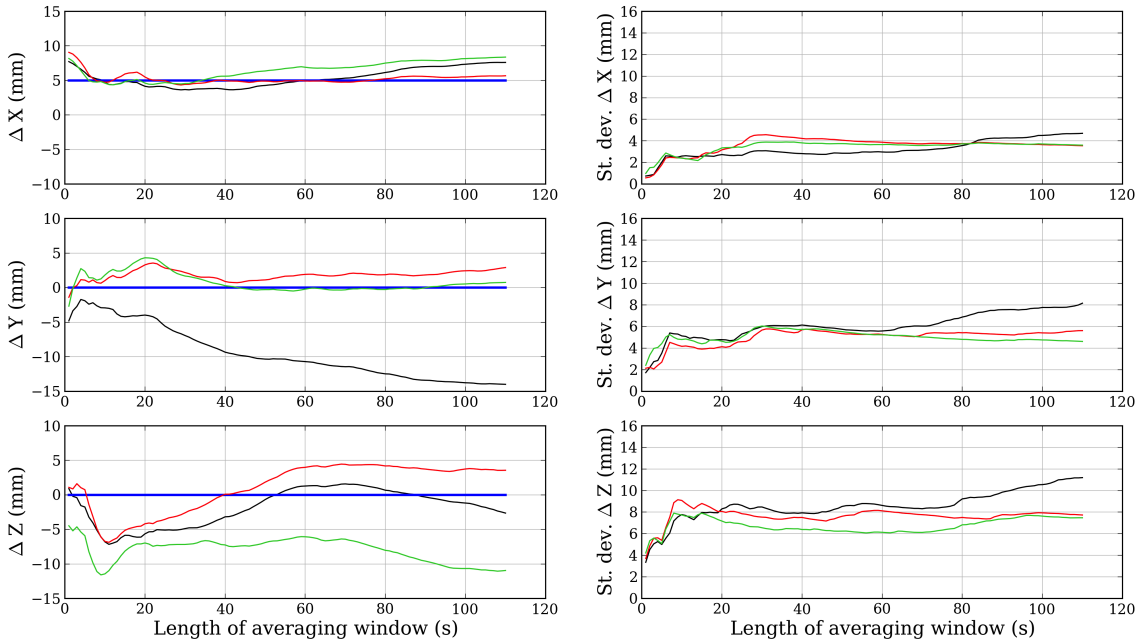

(a) 15:50:17 (5 mm in x-component)

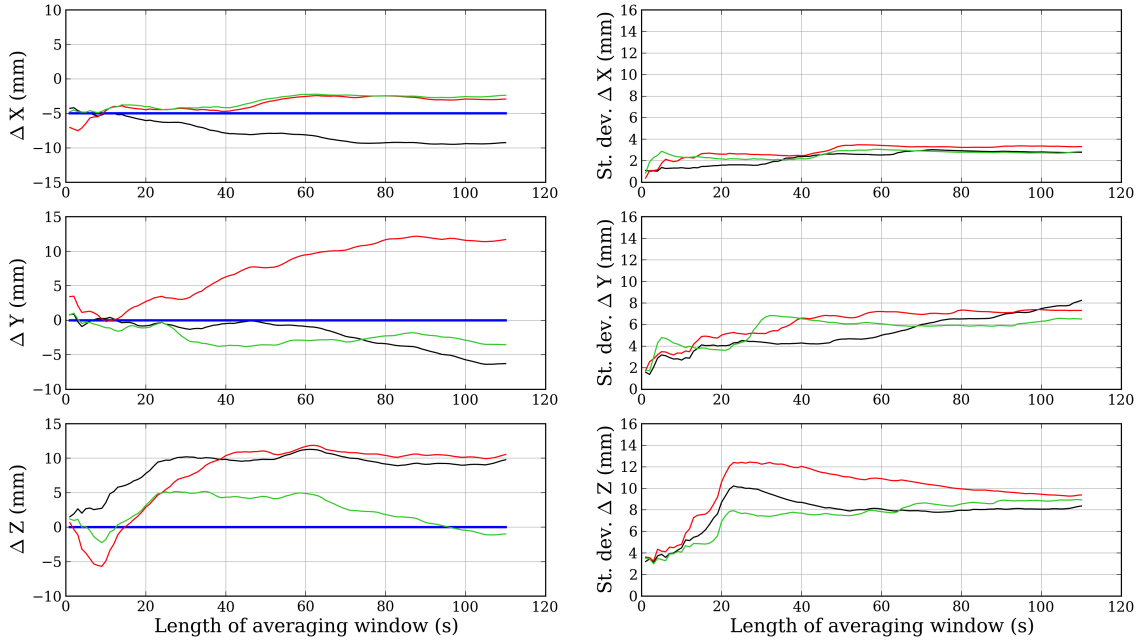

(b) 15:52:18 (-5 mm in x-component)

Figure E.64 – Estimates of the displacement at two separate displacement events and their corresponding standard deviations using different lengths of averaging window, α. The black, red and green lines refer to the standard PPP, PPP + PDSF and PPP + ODSF time series, respectively. The blue lines show the true displacement of the platform.

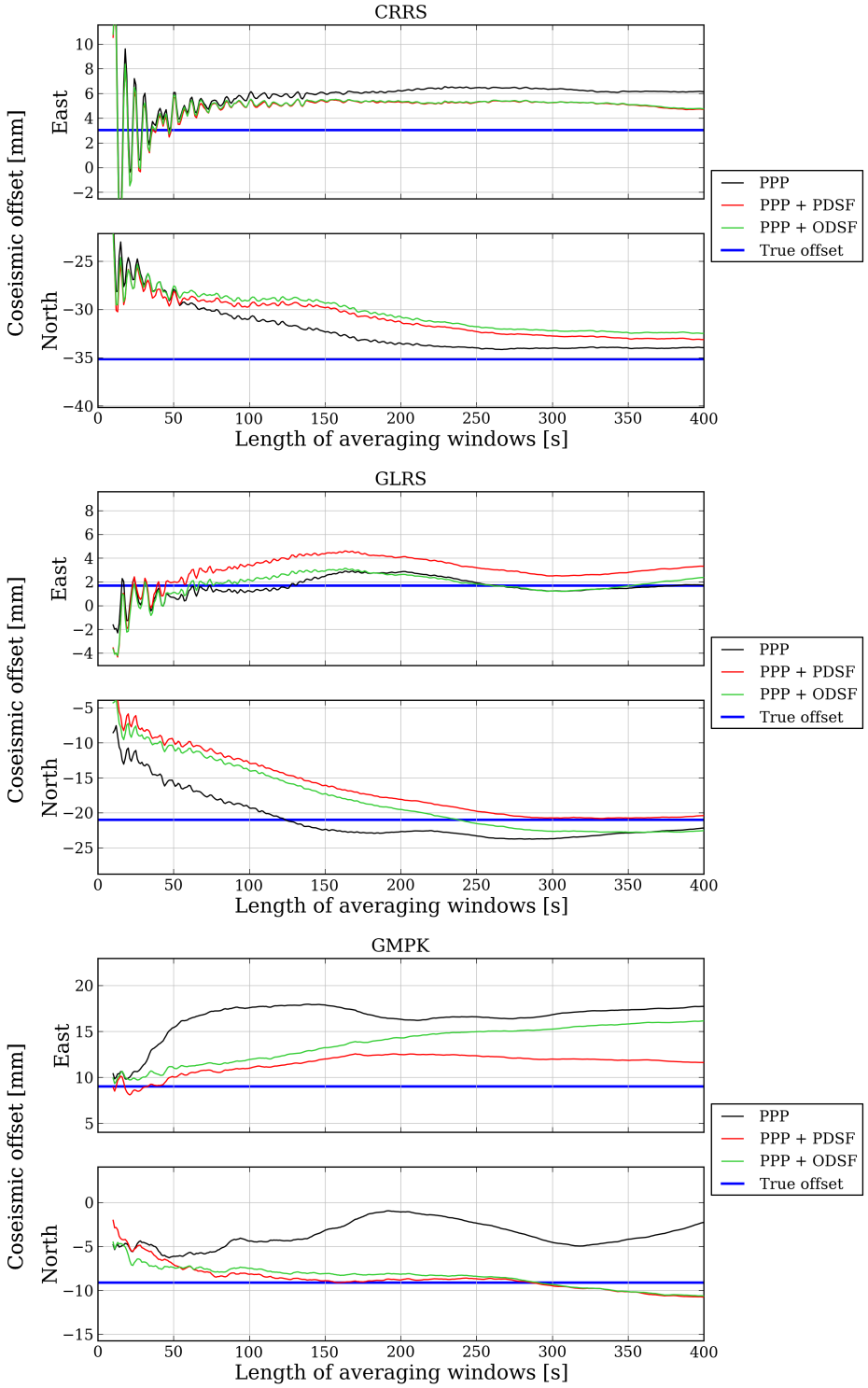

Figure E.65 – Easting and northing coseismic offsets at PBO stations CRRS, GLRS and GMPK calculated using different lengths of averaging window. The 'true' value of the offsets (calculated using UNAVCO data) are shown by the blue lines.

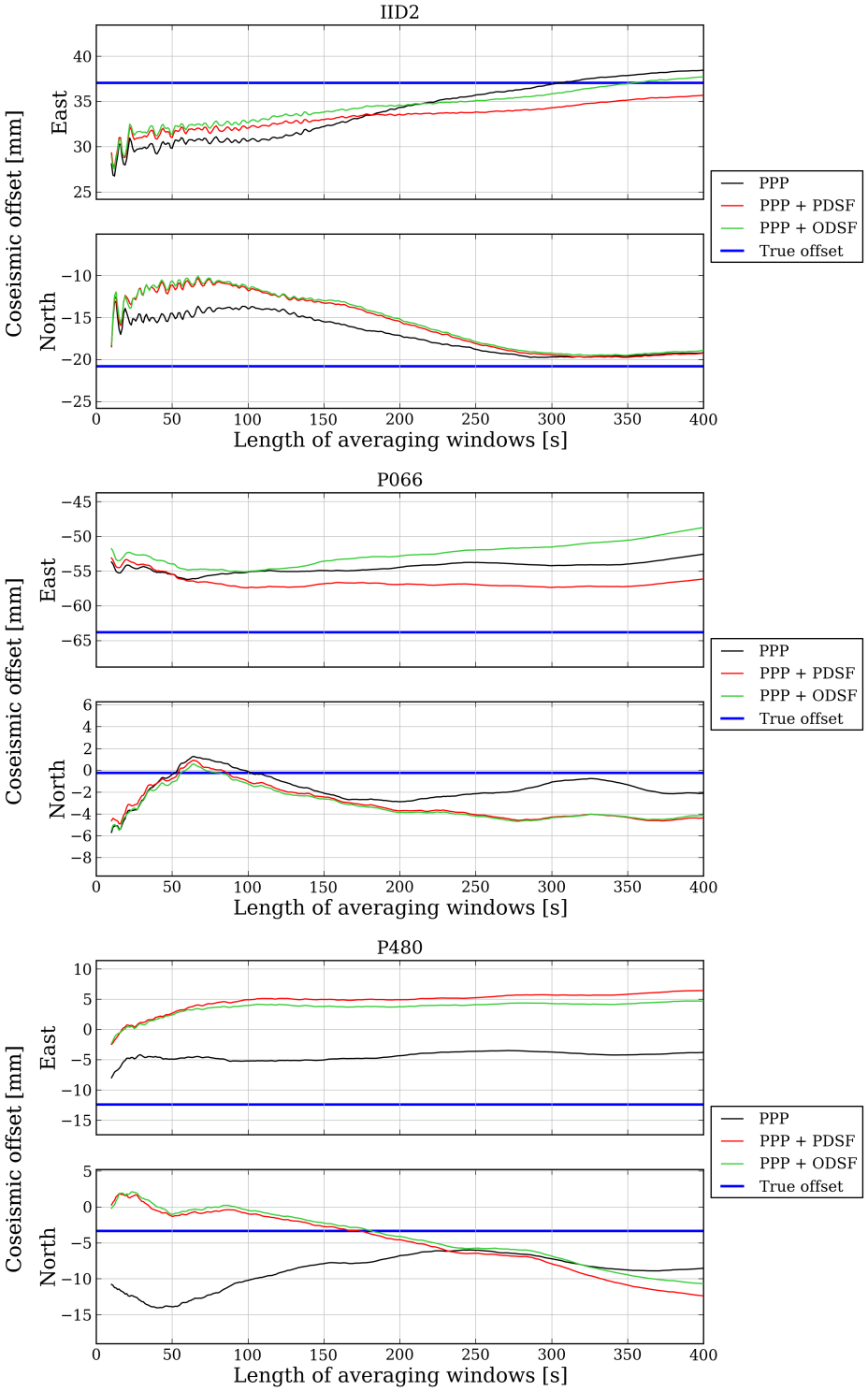

Figure E.66 – Easting and northing coseismic offsets at PBO stations IID2, P066 and P480 calculated using different lengths of averaging window. The 'true' value of the offsets (calculated using UNAVCO data) are shown by the blue lines.

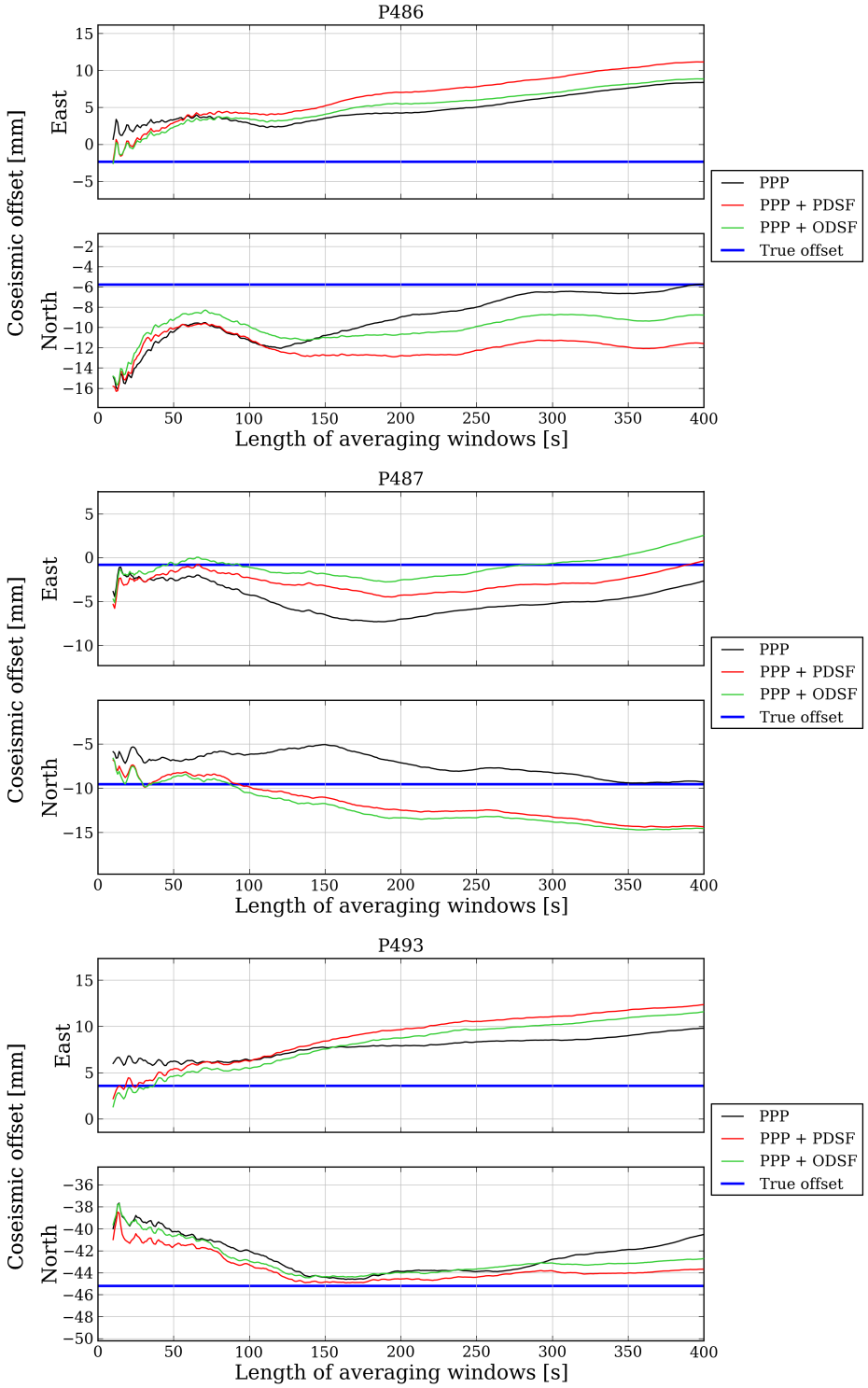

Figure E.67 – Easting and northing coseismic offsets at PBO stations P486, P487 and P493 calculated using different lengths of averaging window. The 'true' value of the offsets (calculated using UNAVCO data) are shown by the blue lines.

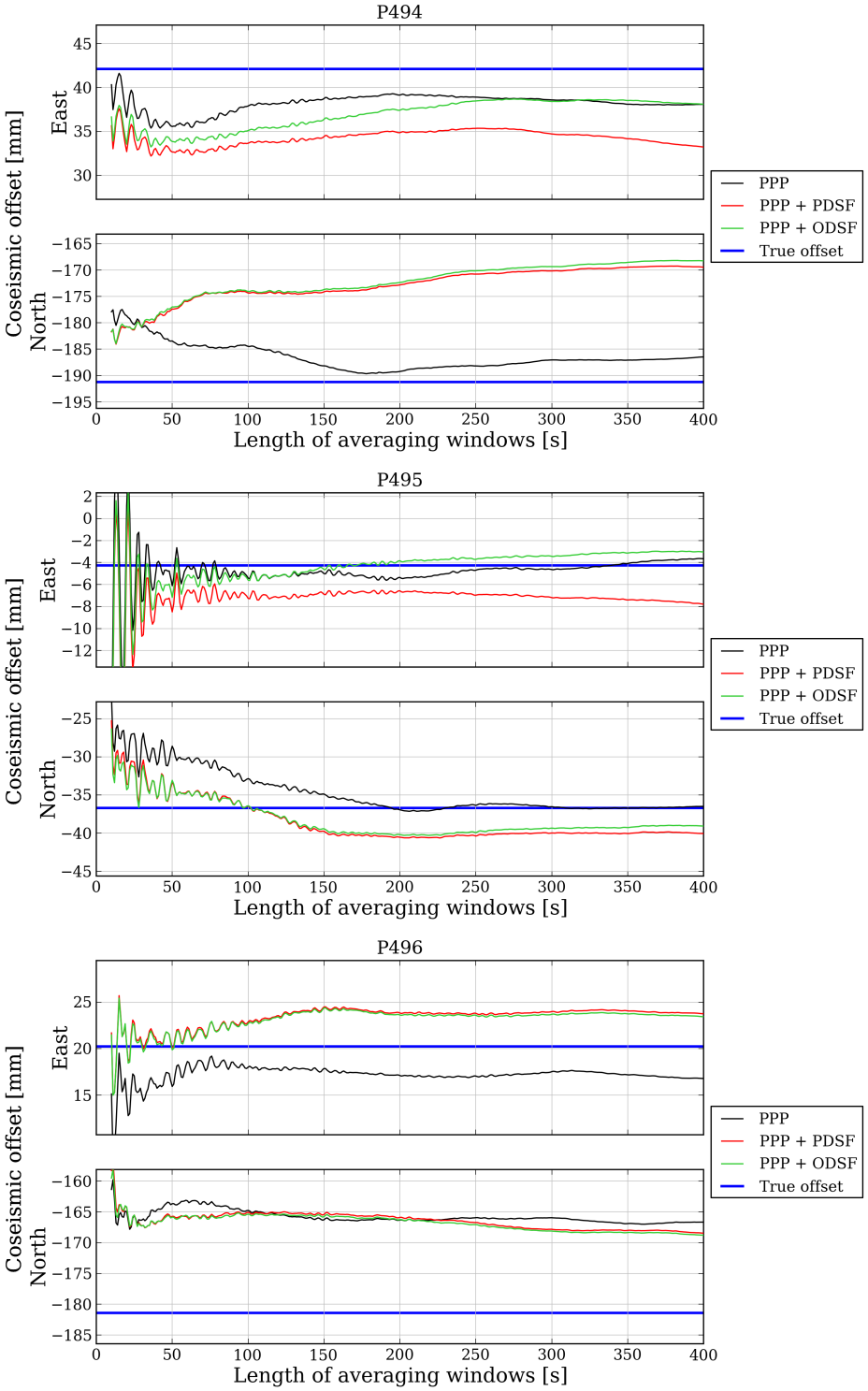

Figure E.68 – Easting and northing coseismic offsets at PBO stations P494, P495 and P496 calculated using different lengths of averaging window. The 'true' value of the offsets (calculated using UNAVCO data) are shown by the blue lines.

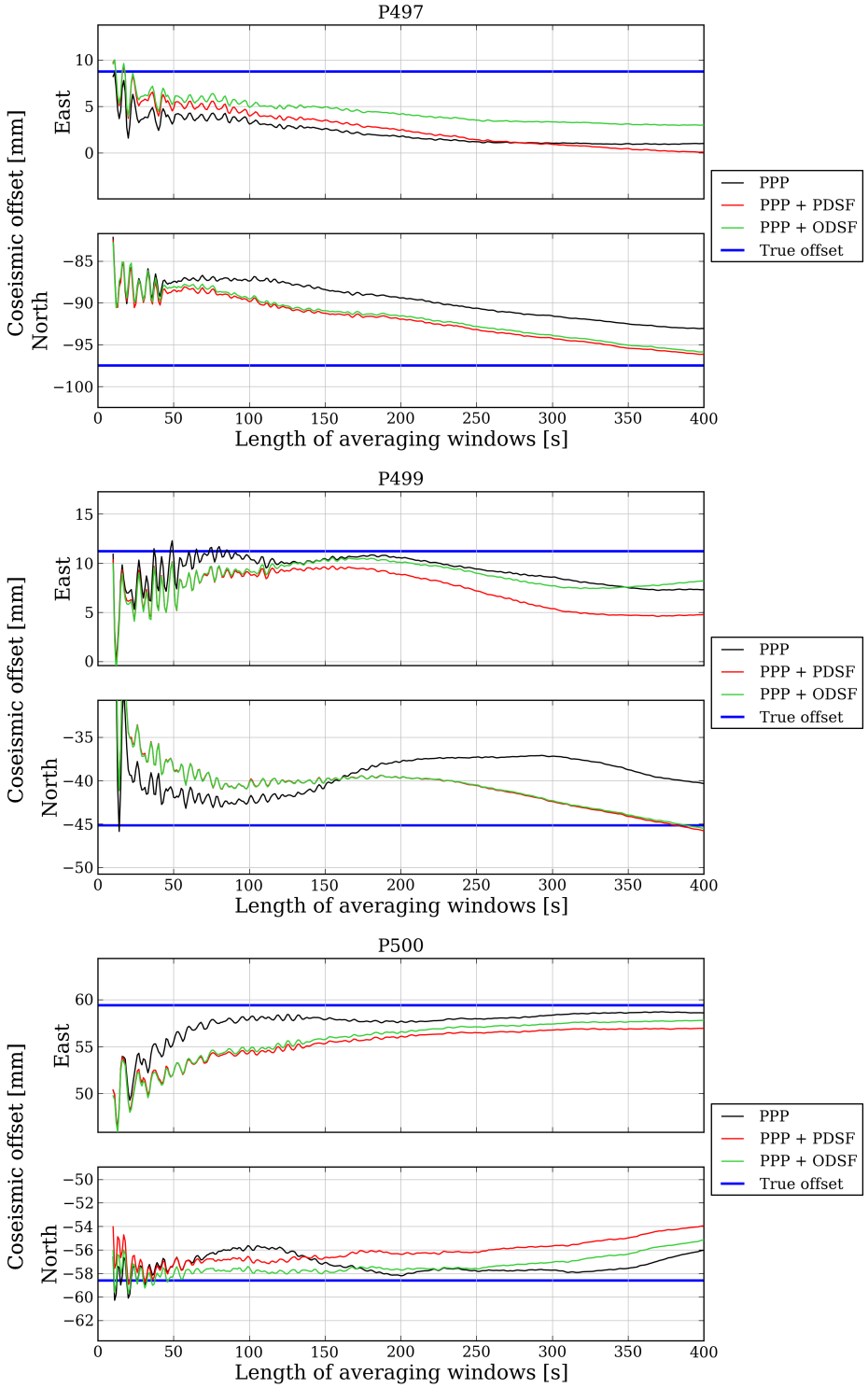

Figure E.69 – Easting and northing coseismic offsets at PBO stations P497, P499 and P500 calculated using different lengths of averaging window. The 'true' value of the offsets (calculated using UNAVCO data) are shown by the blue lines.

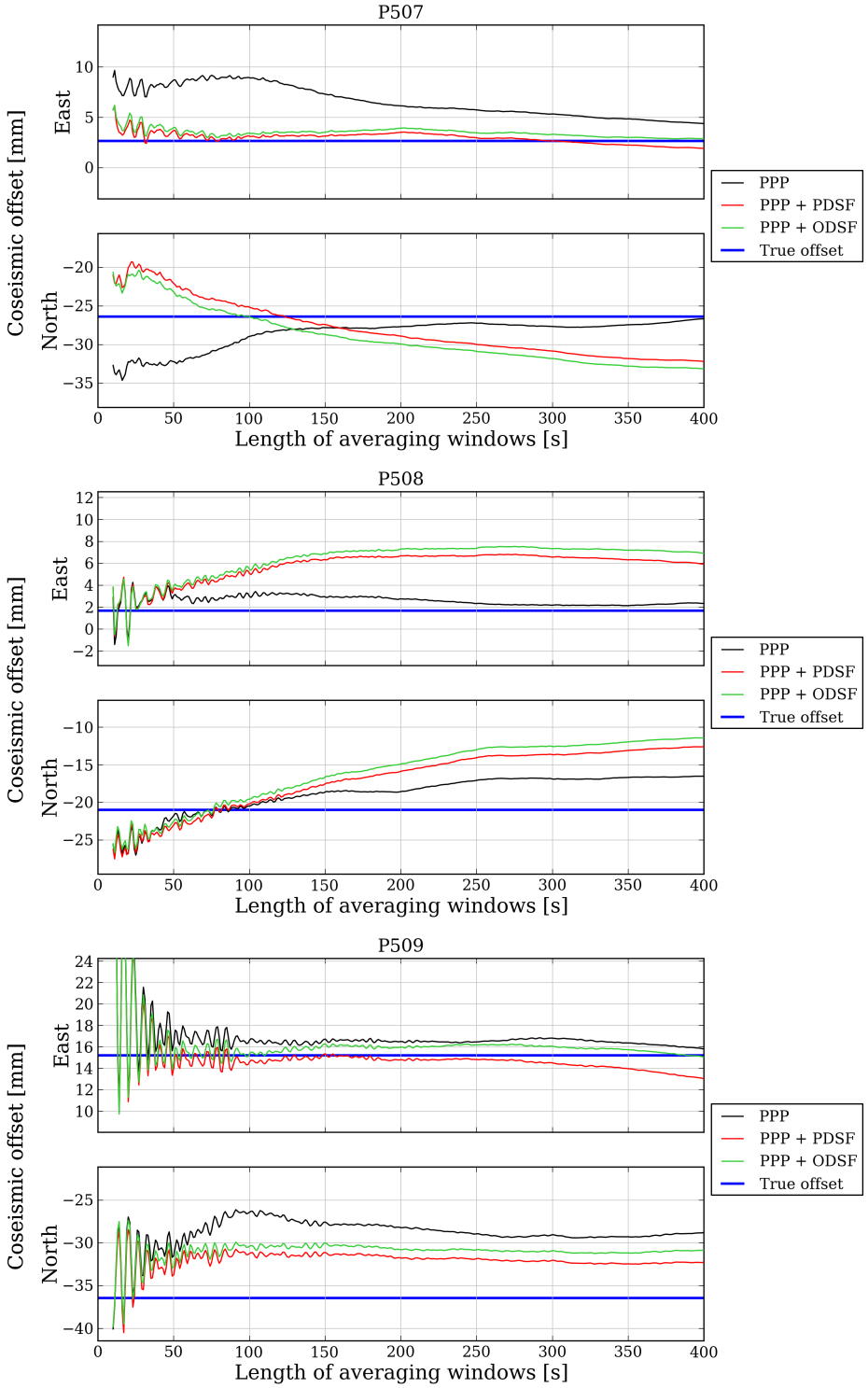

Figure E.70 – Easting and northing coseismic offsets at PBO stations P507, P508 and P509 calculated using different lengths of averaging window. The 'true' value of the offsets (calculated using UNAVCO data) are shown by the blue lines.

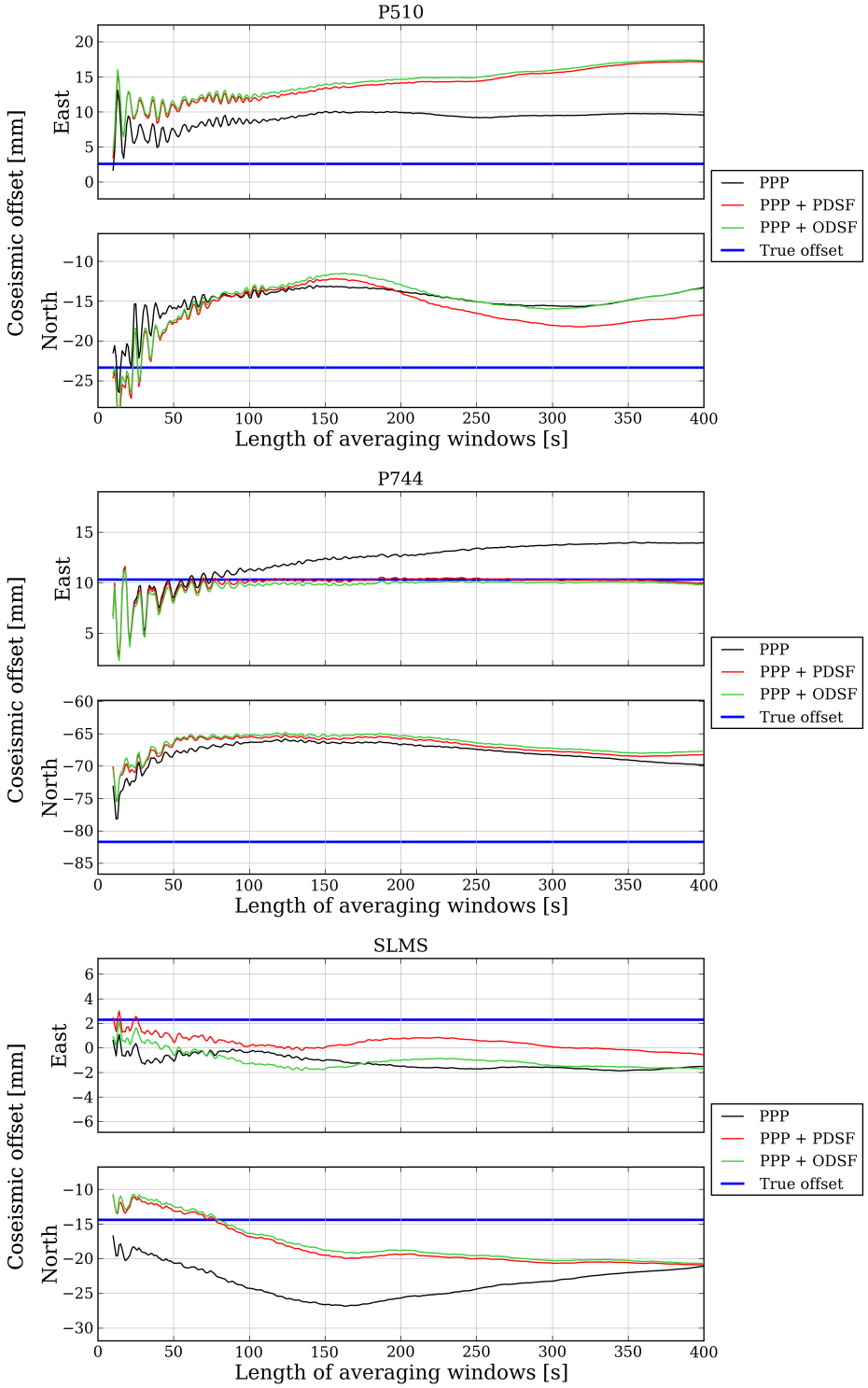

Figure E.71 – Easting and northing coseismic offsets at PBO stations P510, P744 and SLMS calculated using different lengths of averaging window. The 'true' value of the offsets (calculated using UNAVCO data) are shown by the blue lines.

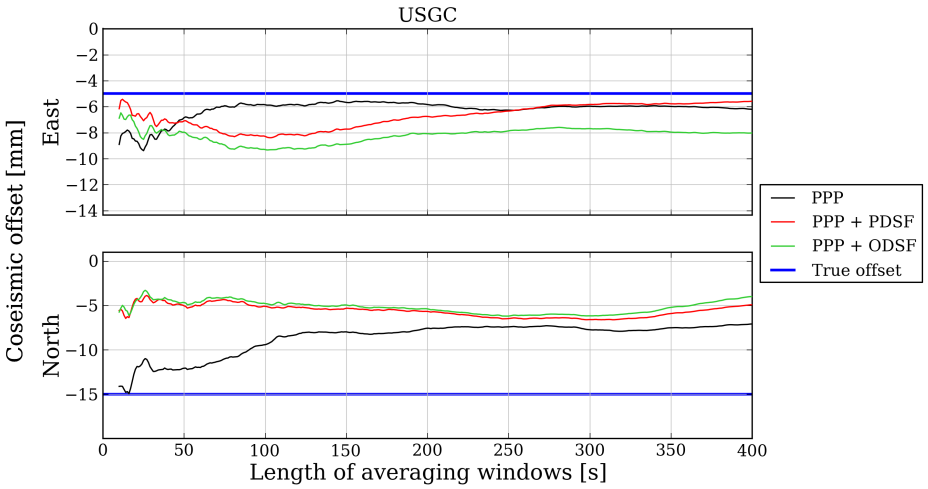

Figure E.72 – Easting and northing coseismic offsets at PBO station USGC calculated using different lengths of averaging window. The 'true' value of the offset (calculated using UNAVCO data) is shown by the blue lines.

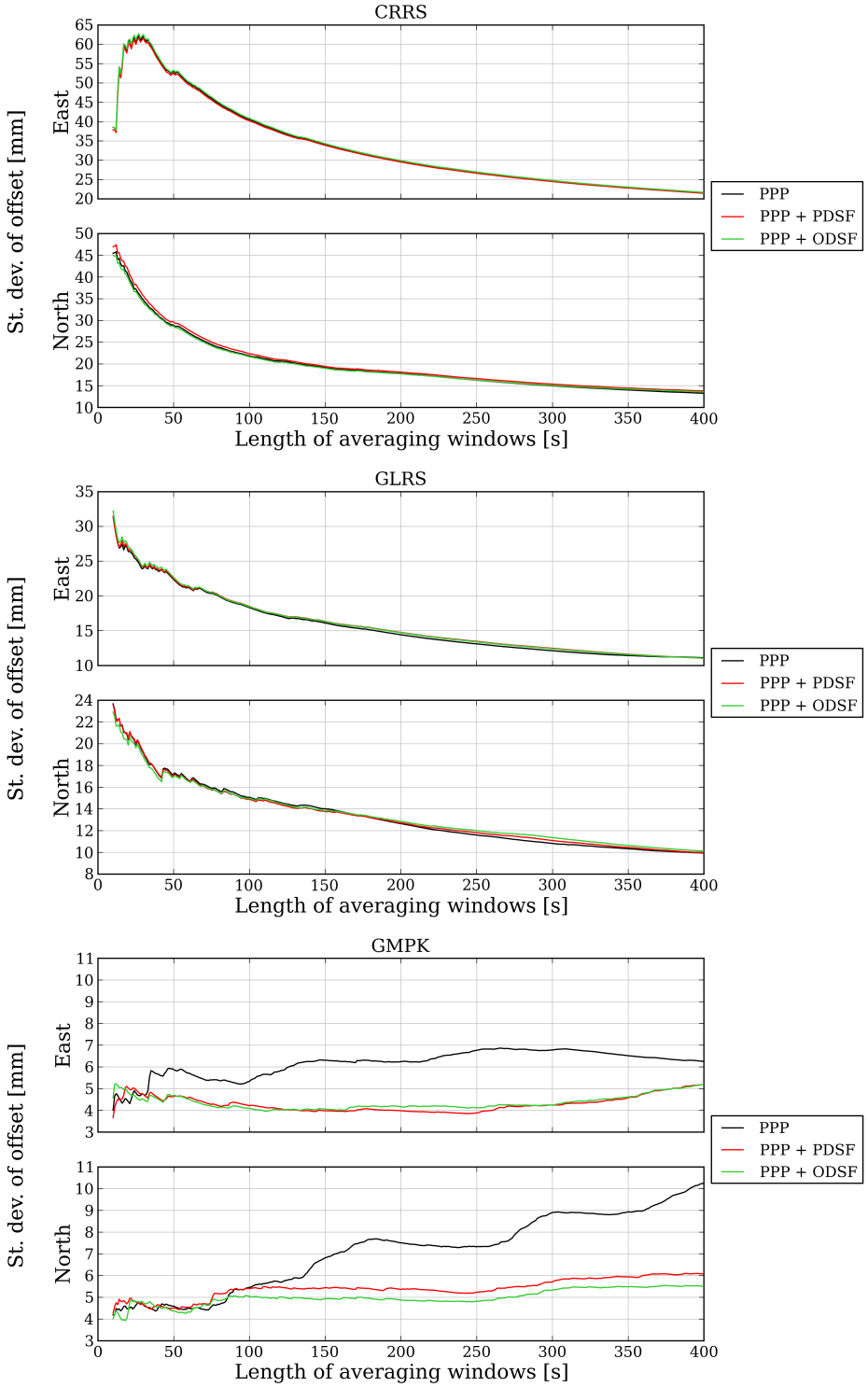

Figure E.73 – Standard deviation of the easting and northing coseismic offsets at PBO stations CRRS, GLRS and GMPK calculated using different lengths of averaging window.

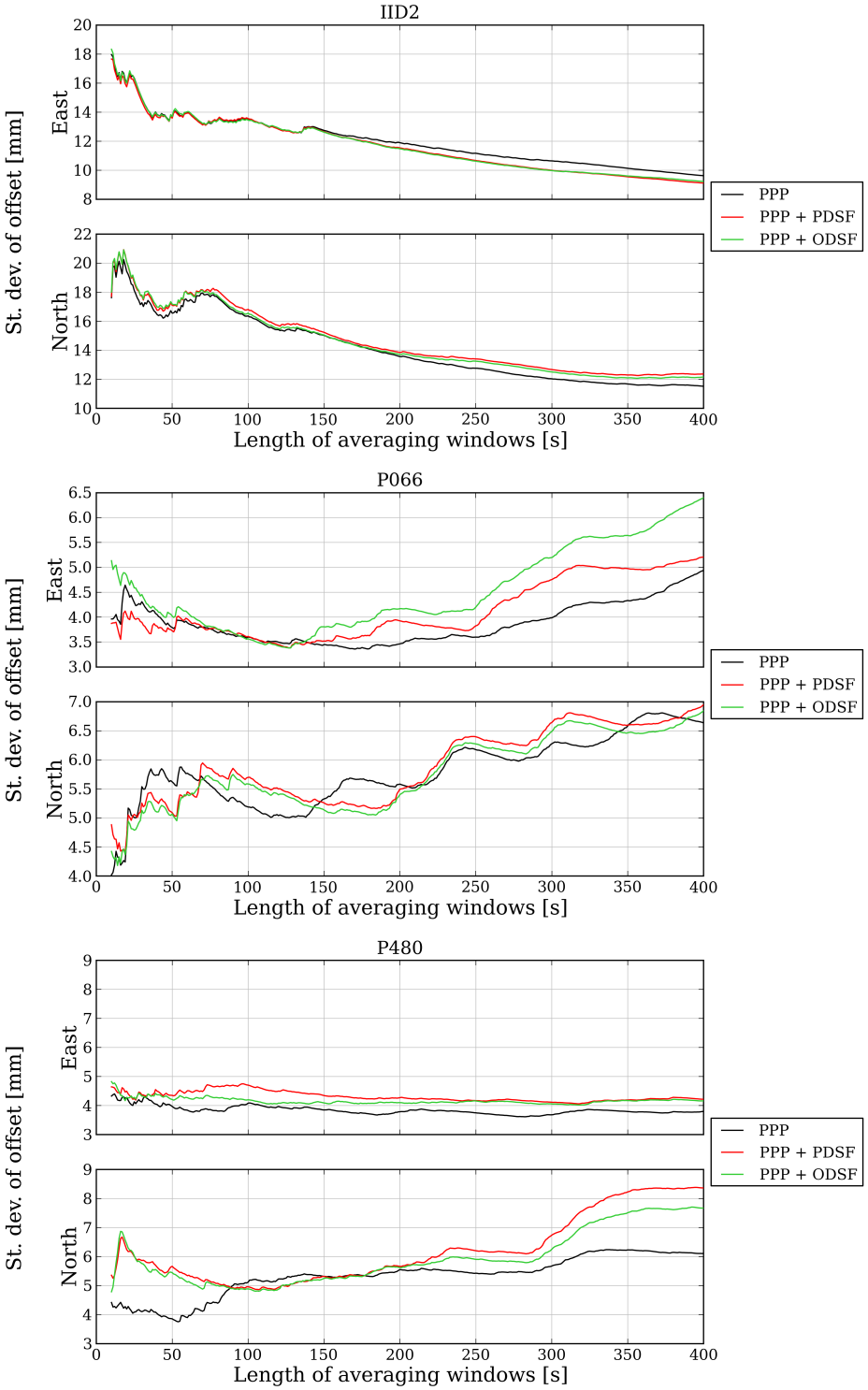

Figure E.74 – Standard deviation of the easting and northing coseismic offsets at PBO stations IID2, P066 and P480 calculated using different lengths of averaging window.

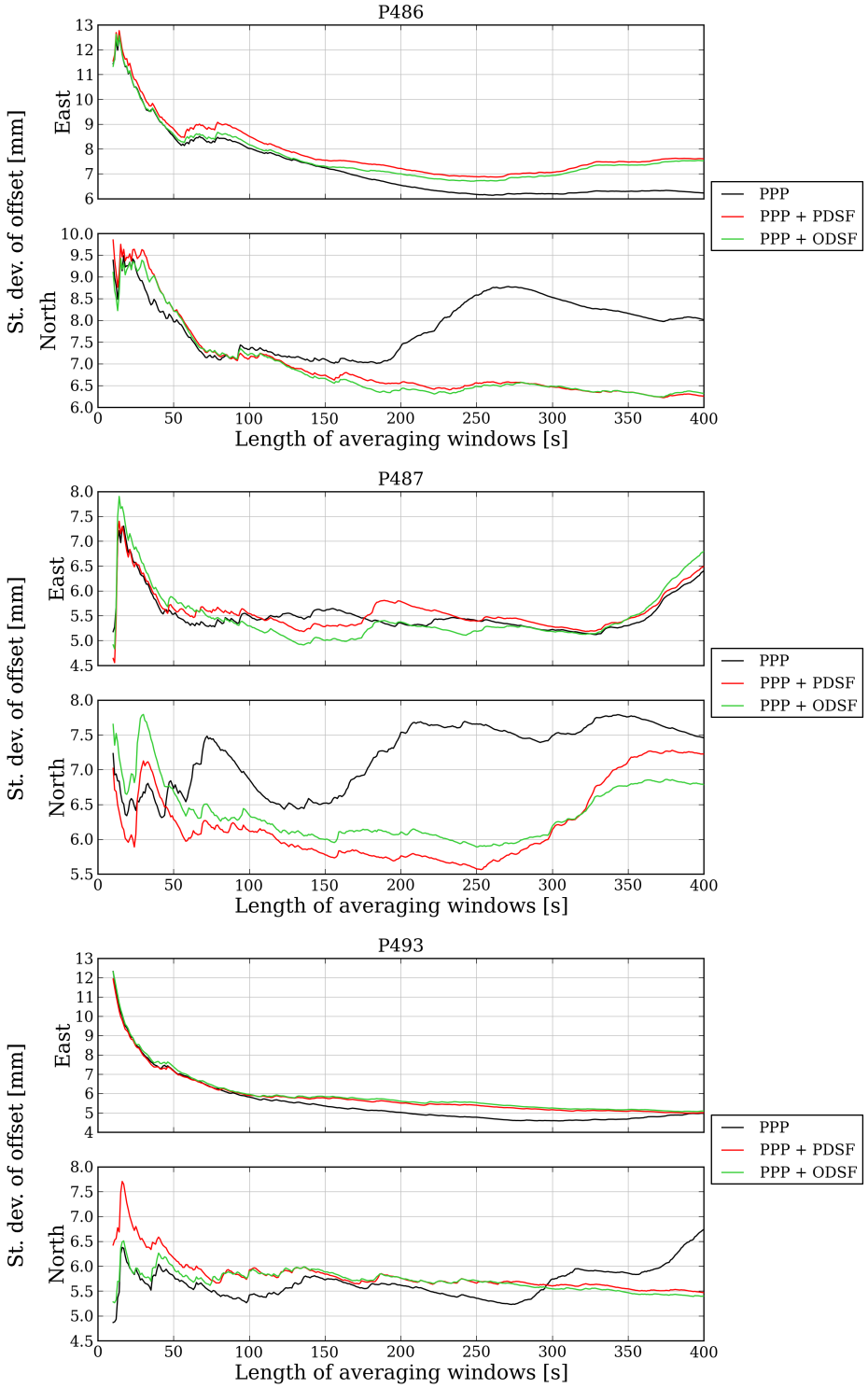

Figure E.75 – Standard deviation of the easting and northing coseismic offsets at PBO stations P486, P487 and P493 calculated using different lengths of averaging window.

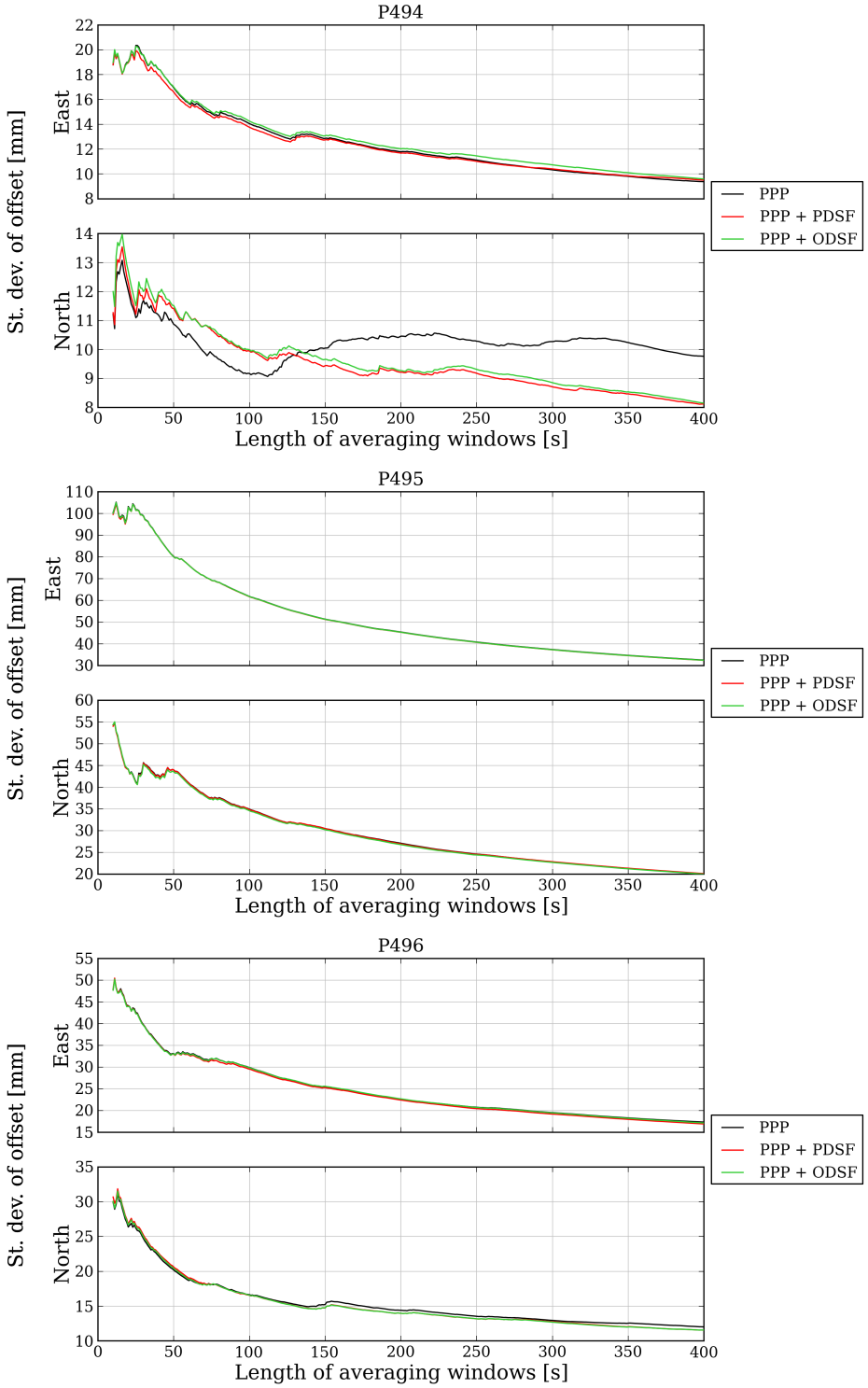

Figure E.76 – Standard deviation of the easting and northing coseismic offsets at PBO stations P494, P495 and P496 calculated using different lengths of averaging window.

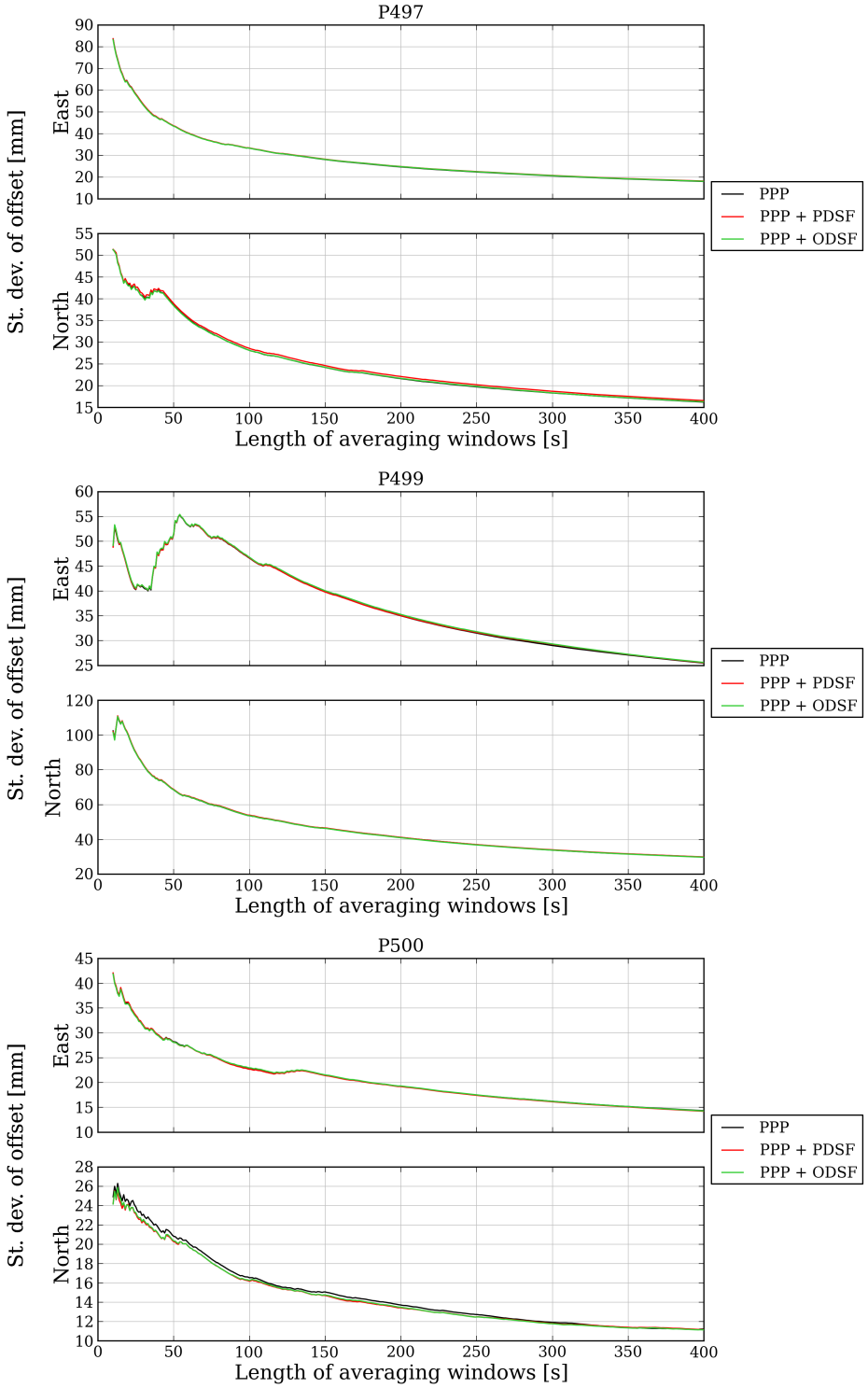

Figure E.77 – Standard deviation of the easting and northing coseismic offsets at PBO stations P497, P499 and P500 calculated using different lengths of averaging window.

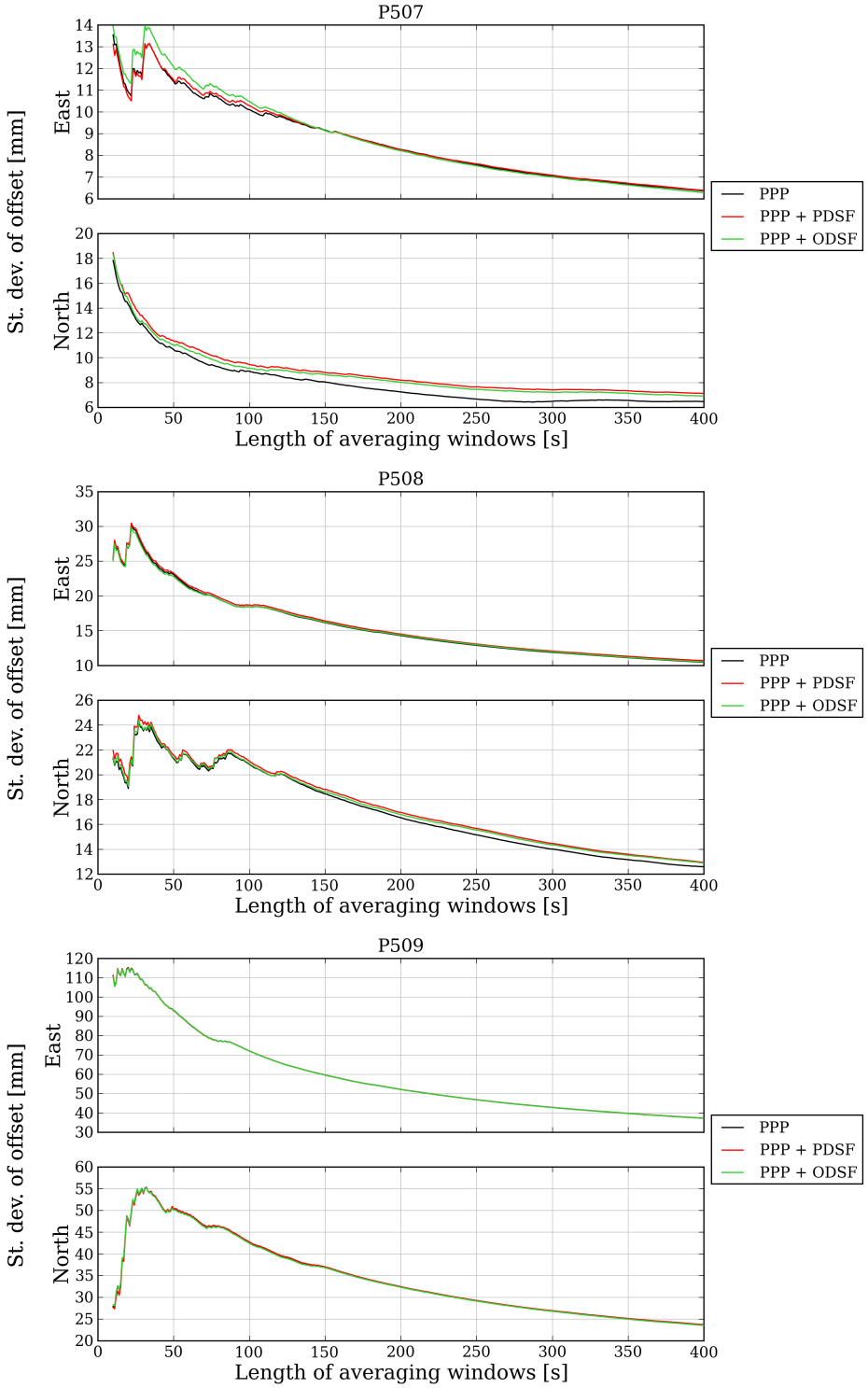

Figure E.78 – Standard deviation of the easting and northing coseismic offsets at PBO stations P507, P508 and P509 calculated using different lengths of averaging window.

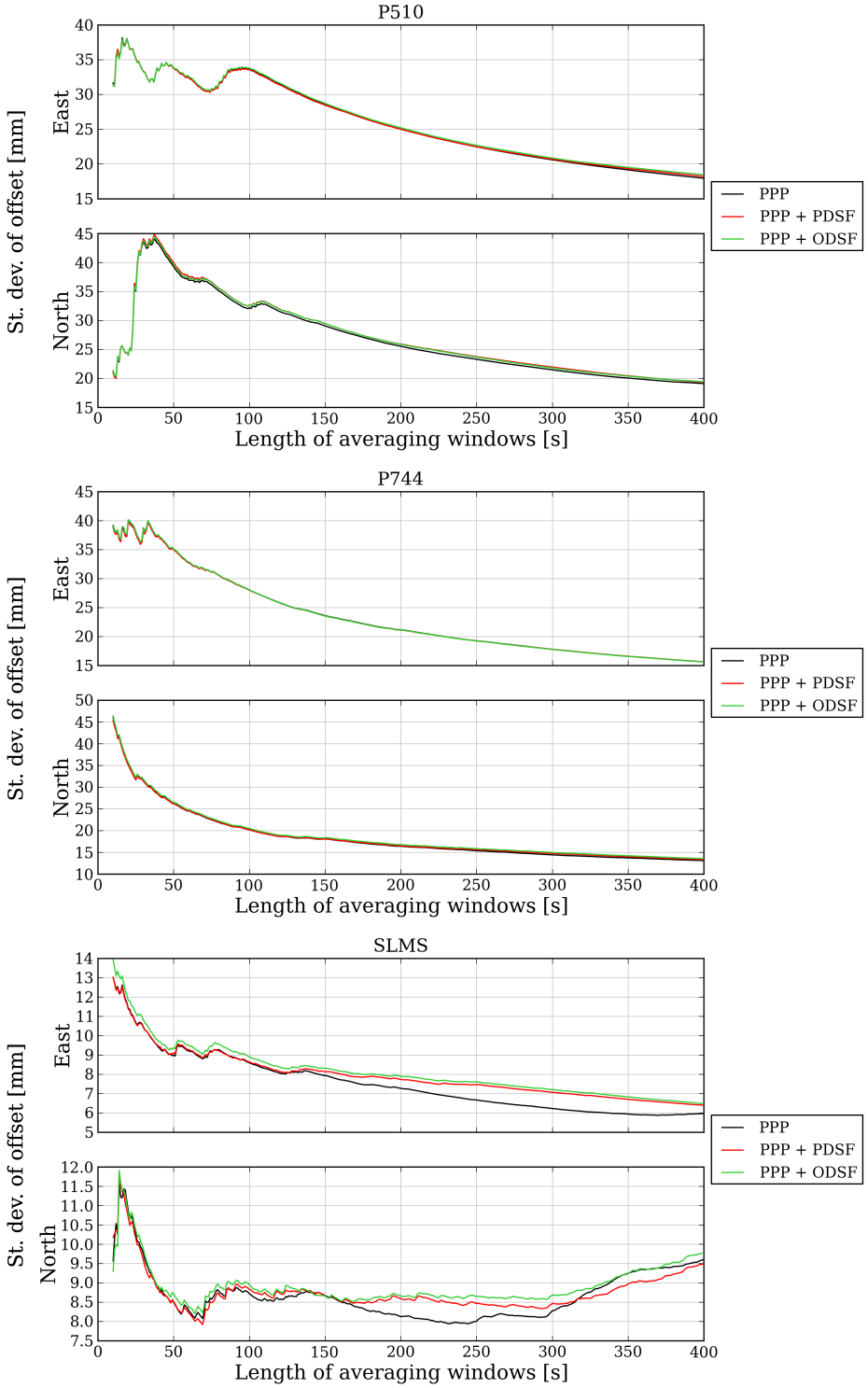

Figure E.79 – Standard deviation of the easting and northing coseismic offsets at PBO stations P510, P744 and SLMS calculated using different lengths of averaging window.

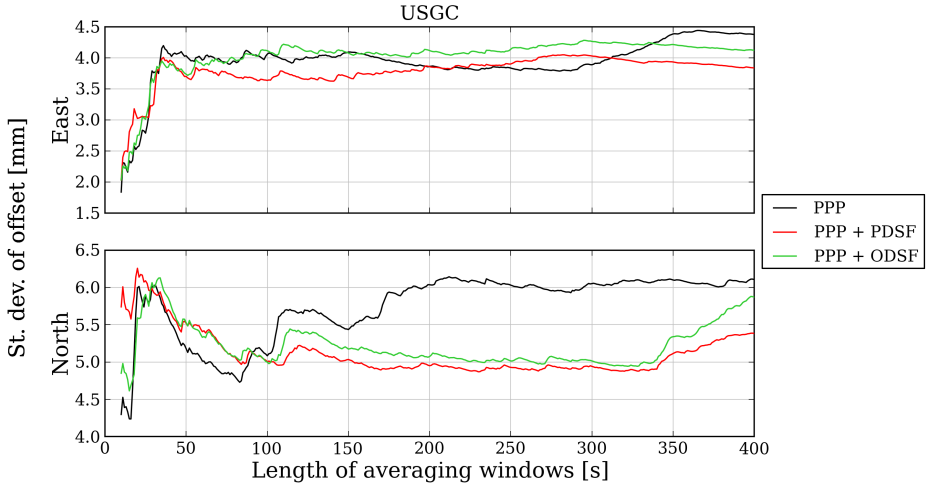

Figure E.80 – Standard deviation of the easting and northing coseismic offsets at PBO station USGC calculated using different lengths of averaging window.

Bibliography

Agnew, D. C. & Larson, K. M. (2007), 'Finding the repeat times of the GPS constellation', *GPS Solutions* **11**(1), 71–76.

Allan, D. W. (1966), 'Statistics of atomic frequency standards', *Proceedings of the IEEE* **54**(2), 221–230.

Allen, R. M. & Ziv, A. (2011), 'Application of real-time GPS to earthquake early warning', *Geophysical Research Letters* **38**(16), L16310.

Altamimi, Z. (2016), 'ITRF2014 and the IGS Contribution', Presentation at IGS Workshop, Sydney, 2016. `http://www.igs.org/assets/pdf/W2016 - PY0606 - Altamimi.pdf`. Accessed: 2016-05-20.

Atkins, C. & Ziebart, M. (2016), 'Effectiveness of observation-domain sidereal filtering for GPS precise point positioning', *GPS Solutions* **20**(1), 111–122.

Axelrad, P., Larson, K. M. & Jones, B. (2005), Use of the correct satellite repeat period to characterize and reduce site-specific multipath errors, *in* 'Proceedings of ION GNSS 2005', Long Beach, CA, pp. 2638–2648.

Baker, T. F., Curtis, D. J. & Dodson, A. H. (1995), 'Ocean tide loading and GPS', *GPS World* **6**(4), 54–59.

Bar-Sever, Y. E., Kroger, P. M. & Borjesson, J. A. (1998), 'Estimating horizontal gradients of tropospheric path delay with a single GPS receiver', *Journal of Geophysical Research* **103**(B3), 5019–5035.

Bertiger, W. I., Desai, S. D., Haines, B., Harvey, N., Moore, A. W., Owen, S. & Weiss, J. P. (2010), 'Single receiver phase ambiguity resolution with GPS data', *Journal of Geodesy* **84**(5), 327–337.

Bilich, A. L., Cassidy, J. F. & Larson, K. M. (2008), 'GPS seismology: application to the 2002 Mw 7.9 Denali Fault earthquake', *Bulletin of the Seismological Society of America* **98**(2), 593–606.

Bilich, A. L. & Larson, K. M. (2008), 'Mapping the GPS multipath environment using the signal-to-noise ratio (SNR)', *Radio Science* **42**(6), RS6003.

Bilich, A. L., Larson, K. M. & Axelrad, P. (2008), 'Modeling GPS phase multipath with SNR: Case study from the Salar de Uyuni, Boliva', *Journal of Geophysical Research* **113**(B4).

Bisnath, S. & Collins, P. (2012), 'Recent developments in precise point positioning', *Geomatica* **66**(2), 103–111.

Bisnath, S. & Gao, Y. (2007), Current state of precise point positioning and future prospects and limitations, *in* 'Observing our Changing Earth', Springer Berlin Heidelberg, Berlin, Heidelberg, pp. 615–623.

Blewitt, G., Hammond, W. C., Kreemer, C., Plag, H.-P., Stein, S. & Okal, E. (2009), 'GPS for real-time earthquake source determination and tsunami warning systems', *Journal of Geodesy* **83**(3-4), 335–343.

Blewitt, G., Kreemer, C., Hammond, W. C., Plag, H. P., Stein, S. & Okal, E. (2006), 'Rapid determination of earthquake magnitude using GPS for tsunami warning systems', *Geophysical Research Letters* **33**(11), L11309.

Bock, H., Dach, R., Jäggi, A. & Beutler, G. (2009), 'High-rate GPS clock corrections from CODE: support of 1 Hz applications', *Journal of Geodesy* **83**(11), 1083–1094.

Bock, Y., Melgar, D. & Crowell, B. W. (2011), 'Real-time strong-motion broadband displacements from collocated GPS and accelerometers', *Bulletin of the Seismological Society of America* **101**(6), 2904–2925.

Boehm, J., Niell, A., Tregoning, P. & Schuh, H. (2006), 'Global Mapping Function (GMF): A new empirical mapping function based on numerical weather model data', *Geophysical Research Letters* **33**(7), L07304.

Bolt, B. A. (2006), *Earthquakes*, 5 edn, W.H. Freeman and Company, New York.

Boore, D. M. (2002), 'Comments on baseline correction of digital strong-motion data: examples from the 1999 Hector Mine, California, earthquake', *Bulletin of the Seismological Society of America* **92**(4), 1543–1560.

Bos, M. S. & Scherneck, H.-G. (2011), 'Free Ocean Tide Loading Website', `http://holt.oso.chalmers.se/loading`. Accessed: 2016-08-02.

Branzanti, M., Colosimo, G., Crespi, M. & Mazzoni, A. (2013), 'GPS near-real-time coseismic displacements for the great Tohoku-Oki earthquake', *IEEE Geoscience and Remote Sensing Letters* **10**(2), 372–376.

Cai, C., Gao, Y., Pan, L. & Zhu, J. (2015), 'Precise point positioning with quad-constellations: GPS, BeiDou, GLONASS and Galileo', *Advances in Space Research* **56**(1), 133–143.

Chen, K. (2004), Real-time precise point positioning and Its potential applications, *in* 'Proceedings of ION GNSS 2004', Long Beach, CA, pp. 1844–1854.

Choi, K., Bilich, A. L., Larson, K. M. & Axelrad, P. (2004), 'Modified sidereal filtering: implications for high-rate GPS positioning', *Geophysical Research Letters* **31**(22), L22608.

Collins, J. P. & Langley, R. B. (1999), Nominal and extreme error performance of the UNB3 tropospheric delay model, PhD thesis, University of New Brunswick.

Collins, P., Henton, J., Mireault, Y. & Héroux, P. (2009), Precise point positioning for real-time determination of co-seismic crustal motion, *in* 'Proceedings of ION GNSS 2009', Savannah, GA, pp. 2479–2488.

Collins, P., Lahaye, F., Heroux, P. & Bisnath, S. (2008), Precise point positioning with ambiguity resolution using the decoupled clock model, *in* 'Proceedings of ION GNSS 2008', Savannah, GA, pp. 1315–1322.

Cross, P. A. (1983), 'Advanced least squares applied to position-fixing', North East London Polytechnic, Dept. of Land Surveying.

Crowell, B. W., Bock, Y. & Melgar, D. (2012), 'Real-time inversion of GPS data for finite fault modeling and rapid hazard assessment', *Geophysical Research Letters* **39**(9), L09305.

Crowell, B. W., Melgar, D., Bock, Y., Haase, J. S. & Geng, J. (2013), 'Earthquake magnitude scaling using seismogeodetic data', *Geophysical Research Letters* **40**(23), 6089–6094.

Dach, R., Brockmann, E., Schaer, S., Beutler, G., Meindl, M., Prange, L., Bock, H., Jäggi, A. & Ostini, L. (2009), 'GNSS processing at CODE: status report', *Journal of Geodesy* **83**(3-4), 353–365.

Dach, R., Hugentobler, U., Fridez, P. & Meindl, M. (2007), *Bernese GPS software version 5.0. User manual*, Astronomical Institute, University of Bern.

Doyle, H. (1995), *Seismology*, John Wiley & Sons, Ltd., Chichester.

El-Mowafy, A. (2015), 'Estimation of multi-constellation GNSS observation stochastic properties using single receiver single satellite data validation method', *Survey Review* **47**(341), 99–108.

Elósegui, P., Davis, J. L., Oberlander, D., Baena, R. & Ekström, G. (2006), 'Accuracy of high-rate GPS for seismology', *Geophysical Research Letters* **33**(11), L11308.

Emore, G. L., Haase, J. S., Choi, K., Larson, K. M. & Yamagiwa, A. (2007), 'Recovering seismic displacements through combined use of 1-Hz GPS and strong-motion accelerometers', *Bulletin of the Seismological Society of America* **97**(2), 357–378.

Ferre-Pikal, E. S. & Walls, F. L. (2005), Frequency standards, characterization, *in* 'Encyclopedia of RF and Microwave Engineering', John Wiley & Sons, Inc., Hoboken, NJ, pp. 767–775.

Fraser, S., Raby, A., Pomonis, A., Goda, K., Chian, S. C., Macabuag, J., Offord, M., Saito, K. & Sammonds, P. (2012), 'Tsunami damage to coastal defences and buildings in the March 11th 2011 Mw 9.0 Great East Japan earthquake and tsunami', *Bulletin of Earthquake Engineering* **11**(1), 205–239.

Friederichs, T. (2010), Analysis of geodetic time series using Allan variances, PhD thesis, University of Stuttgart.

Fuhrmann, T., Luo, X., Knöpfler, A. & Mayer, M. (2014), 'Generating statistically robust multipath stacking maps using congruent cells', *GPS Solutions* **19**(1), 83–92.

Gao, Y. & Chen, K. (2004), 'Performance analysis of precise point positioning using real-time orbit and clock Products', *Journal of Global Positioning Systems* **3**(1-2), 95–100.

Ge, M., Gendt, G., Rothacher, M., Shi, C. & Liu, J. (2008), 'Resolution of GPS carrier-phase ambiguities in precise point positioning (PPP) with daily observations', *Journal of Geodesy* **82**(7), 389–399.

Geng, J. (2011), Rapid integer ambiguity resolution in GPS precise point positioning, PhD thesis, University of Nottingham.

Geng, J. & Bock, Y. (2013), 'Triple-frequency GPS precise point positioning with rapid ambiguity resolution', *Journal of Geodesy* **87**(5), 449–460.

Geng, J., Bock, Y., Melgar, D., Crowell, B. W. & Haase, J. S. (2013), 'A new seismogeodetic approach applied to GPS and accelerometer observations of the 2012 Brawley seismic swarm: Implications for earthquake early warning', *Geochemistry, Geophysics, Geosystems* **14**(7), 2124–2142.

Geng, J., Meng, X., Dodson, A. H., Ge, M. & Teferle, F. N. (2010), 'Rapid re-convergences to ambiguity-fixed solutions in precise point positioning', *Journal of Geodesy* **84**(12), 705–714.

Geng, J., Teferle, F. N., Meng, X. & Dodson, A. H. (2010), 'Towards PPP-RTK: ambiguity resolution in real-time precise point positioning', *Advances in Space Research* **47**(10), 1664–1673.

Genrich, J. F. & Bock, Y. (1992), 'Rapid resolution of crustal motion at short ranges with the global positioning system', *Journal of Geophysical Research* **97**(B3), 3261–3269.

Graizer, V. (2006), 'Tilts in strong ground motion', *Bulletin of the Seismological Society of America* **96**(6), 2090–2102.

Granström, C. (2006), Site-dependent effects in high-accuracy applications of GNSS, PhD thesis, Chalmers University of Technology.

Griggs, E., Kursinski, E. R. & Akos, D. (2015), 'Short-term GNSS satellite clock stability', *Radio Science* **50**(8), 813–826.

Groves, P. D. (2013*a*), 'GNSS Solutions: Multipath vs. NLOS signals. How does non-line-of-sight reception differ from multipath interference.', *Inside GNSS Magazine* **8**(6), 40–42, 63.

Groves, P. D. (2013*b*), *Principles of GNSS, inertial, and multisensor integrated navigation systems*, 2 edn, Artech House, London.

Groves, P. D., Jiang, Z., Rudi, M. & Strode, P. (2013), A portfolio approach to NLOS and multipath mitigation in dense urban areas, *in* 'Proceedings of ION GNSS 2013', The Institute of Navigation, Nashville, TN, pp. 3231 – 3247.

Hanks, T. C. & Kanamori, H. (1979), 'A moment magnitude scale', *Journal of Geophysical Research* **84**(B5), 2348.

Harris, R. B. (2002), Evaluation, refinement and fusion of software-based pseudorange multipath mitigation techniques, *in* 'Proceedings of ION GPS 2002', Portland, OR, pp. 460–471.

Hauschild, A., Montenbruck, O. & Steigenberger, P. (2013), 'Short-term analysis of GNSS clocks', *GPS Solutions* **17**(3), 295–307.

Herring, T. (2015), 'GAGE GPS Data Analysis Plan', `http://www.unavco.org/data/gps-gnss/derived-products/docs/GAGE_GPS_Analysis_ACC_20150908.pdf`. Accessed: 2016-03-15.

Hoechner, A., Ge, M., Babeyko, A. & Sobolev, S. V. (2013), 'Instant tsunami early warning based on real-time GPS: Tohoku 2011 case study', *Natural Hazards and Earth System Science* **13**(5), 1285–1292.

IERS Conventions (2010), Gérard Petit and Brian Luzum (eds.). (IERS Technical Note ; 36) Frankfurt am Main: Verlag des Bundesamts für Kartographie und Geodäsie, 2010. 179 pp., ISBN 3-89888-989-6.

igscb.jpl.nasa.gov (2015), 'IGS Products', `https://igscb.jpl.nasa.gov/components/prods.html`. Accessed: 2016-01-15.

igs.org (2013), 'IGS Real-Time Service', `ftp://igs.org/pub/resource/pubs/IGS_Real_Time_Service-131031.pdf`. Accessed: 2016-01-15.

Ito, Y., Tsuji, T., Osada, Y., Kido, M., Inazu, D., Hayashi, Y., Tsushima, H., Hino, R. & Fujimoto, H. (2011), 'Frontal wedge deformation near the source region of the 2011 Tohoku-Oki earthquake', *Geophysical Research Letters* **38**(7), L00G05.

Jokinen, A., Feng, S., Milner, C. & Schuster, W. (2011), Precise point positioning and integrity monitoring with GPS and GLONASS, *in* 'Proceedings of European Navigation Conference 2011', London.

Jokinen, A., Feng, S., Ochieng, W., Hide, C., Moore, T. & Hill, C. (2012), Fixed ambiguity precise point positioning (PPP) with FDE RAIM, *in* 'Proceedings of IEEE/ION PLANS 2012', IEEE, Myrtle Beach, SC, pp. 643–658.

Juan, J. M., Hernandez-Pajares, M., Sanz, J., Ramos-Bosch, P., Aragon-Angel, A., Orus, R., Ochieng, W., Feng, S., Jofre, M., Coutinho, P., Samson, J. & Tossaint, M. (2012), 'Enhanced precise point positioning for GNSS users', *IEEE Transactions on Geoscience and Remote Sensing* **50**(10), 4213–4222.

Kerkhoff, A., Harris, R. B. & Petersen, C. P. (2010), Modifications to GPS reference station antennas to reduce multipath, *in* 'Proceedings of ION GNSS 2010', Portland, OR, pp. 866–878.

Kouba, J. (2009), 'A guide to using International GNSS Service (IGS) products', `https://igscb.jpl.nasa.gov/igscb/resource/pubs/UsingIGSProductsVer21.pdf`. Accessed: 2015-06-16.

Langbein, J. (2004), 'High-rate real-time GPS network at Parkfield: Utility for detecting fault slip and seismic displacements', *Geophysical Research Letters* **31**(15), L15S20.

Larson, K. M., Bilich, A. L. & Axelrad, P. (2007), 'Improving the precision of high-rate GPS', *Journal of Geophysical Research: Solid Earth* **112**(5), B05422.

Lau, L. (2012), 'Comparison of measurement and position domain multipath filtering techniques with the repeatable GPS orbits for static antennas', *Survey Review* **44**(324), 9–16.

Lau, L. & Cross, P. A. (2006), A new signal-to-noise-ratio based stochastic model for GNSS high-precision carrier phase data processing algorithms in the presence of multipath errors, *in* 'Proceedings of ION GNSS 2006', Fort Worth, TX, pp. 276–285.

Lau, L. & Cross, P. A. (2007), 'Investigations into phase multipath mitigation techniques for high precision positioning in difficult environments', *Journal of Navigation* **60**(03), 457–482.

Laurichesse, D. (2015), 'Handling the biases for improved triple-frequency PPP convergence', *GPS World* **26**(4), 49–54.

Laurichesse, D., Mercier, F., Berthias, J.-P. & Bijac, J. (2008), Real time zero-difference ambiguities fixing and absolute RTK, *in* 'Proceedings of ION NTM 2008', San Diego, CA, pp. 747–755.

Laurichesse, D., Mercier, F., Berthias, J.-P. & Broca, P. (2009), 'Integer ambiguity resolution on undifferenced GPS phase measurements and its application to PPP and satellite precise orbit determination', *Navigation* **56**(2), 135–143.

Leick, A. (2004), *GPS Satellite Surveying*, 3 edn, John Wiley & Sons, Inc., Hoboken, NJ.

Li, T., Wang, J. & Laurichesse, D. (2014), 'Modeling and quality control for reliable precise point positioning integer ambiguity resolution with GNSS modernization', *GPS Solutions* **18**(3), 429–442.

Li, X., Ge, M., Zhang, X., Zhang, Y., Guo, B., Wang, R., Klotz, J. & Wickert, J. (2013), 'Real-time high-rate co-seismic displacement from ambiguity-fixed precise point positioning: Application to earthquake early warning', *Geophysical Research Letters* **40**(2), 295–300.

Liu, Z. (2010), 'A new automated cycle slip detection and repair method for a single dual-frequency GPS receiver', *Journal of Geodesy* **85**(3), 171–183.

Lyard, F., Lefevre, F., Letellier, T. & Francis, O. (2006), 'Modelling the global ocean tides: modern insights from FES2004', *Ocean Dynamics* **56**, 394–415.

Misra, P. & Enge, P. (2006), *Global Positioning System: Signals, Measurement and Performancee*, 2 edn, Ganga-Jamuna Pr, Lincoln, MA.

Moore, M., Watson, C. S., King, M. A., McClusky, S. & Tregoning, P. (2014), 'Empirical modelling of site-specific errors in continuous GPS data', *Journal of Geodesy* **88**(9), 887–900.

Moritz, H. (2000), 'Geodetic Reference System 1980', *Journal of Geodesy* **74**(1), 128–133.

Nabelek, J. L. (1984), Determination of earthquake source parameters from inversion of body waves, PhD thesis, Massachusetts Institute of Technology.

Ogaja, C. & Satirapod, C. (2007), 'Analysis of high-frequency multipath in 1-Hz GPS kinematic solutions', *GPS Solutions* **11**(4), 269–280.

Park, K. D. (2004), 'Development of an antenna and multipath calibration system for Global Positioning System sites', *Radio Science* **39**(5), RS5002.

Petrie, E. J., King, M. A., Moore, P. & Lavallée, D. A. (2010), 'Higher-order ionospheric effects on the GPS reference frame and velocities', *Journal of Geophysical Research* **115**(B3), B03417.

Ragheb, A. E., Clarke, P. J. & Edwards, S. J. (2007), 'GPS sidereal filtering: coordinate- and carrier-phase-level strategies', *Journal of Geodesy* **81**(5), 325–335.

Ragheb, A. E., Edwards, S. J. & Clarke, P. J. (2010), 'Using Filtered and Semicontinuous High Rate GPS for Monitoring Deformations', *Journal of Surveying Engineering* **136**(2), 72.

Reuveni, Y., Kedar, S., Owen, S. E., Moore, A. W. & Webb, F. H. (2012), 'Improving sub-daily strain estimates using GPS measurements', *Geophysical Research Letters* **39**(11), L11311.

Riley, W. J. (2008), Handbook of frequency stability analysis, Technical report, U.S. Dept. of Commerce, National Institute of Standards and Technology, Boulder, CO.

Rogers, N. & Blake, S. (2008), *An introduction to our dynamic planet*, Cambridge University Press, Cambridge.

Ryder, I. (2006), Elastic and viscoelastic modelling of postseismic motion and fault structures, PhD thesis, University of Oxford.

Sobolev, S. V., Babeyko, A. Y., Wang, R., Hoechner, A., Galas, R., Rothacher, M., Sein, D. V., Schröter, J., Lauterjung, J. & Subarya, C. (2007), 'Tsunami early warning using GPS-shield arrays', *Journal of Geophysical Research* **112**(B8), B08415.

Sopac.ucsd.edu (2015), 'READI: Real-time Earthquake Analysis for Disaster Mitigation Network', `http://sopac.ucsd.edu/readiDescription.shtml`. Accessed: 2015-06-04.

Teunissen, P. J. G. & Kleusberg, A. (1998), *GPS for geodesy*, Springer Berlin Heidelberg, Berlin, Heidelberg.

Tolman, B., Harris, R. B., Gaussiran, T., Munton, D., Little, J., Mach, R., Nelsen, S. & Renfro, B. (2004), The GPS toolkit: open source GPS software, *in* 'Proceedings of ION GNSS 2004', Long Beach, CA, pp. 2044–2053.

Tregoning, P. & van Dam, T. (2005), 'Atmospheric pressure loading corrections applied to GPS data at the observation level', *Geophysical Research Letters* **32**(22), L22310.

Urquhart, L., Zhang, Y., Lee, S. & Chan, J. (2012), Nexteqs integer ambiguity-resolved precise point positioning system, *in* 'Proceedings of ION GNSS 2012', Nashville, TN, pp. 3046–3054.

van Dam, T. & Ray, R. (2010), 'Updated October 2010. S1 and S2 Atmospheric Tide Loading Effects for Geodetic Applications', `http://geophy.uni.lu/ggfc-atmosphere/tide-loading-calculator.html`. Accessed: 2016-01-29.

van der Marel, H. (2012), 'Single- versus dual-frequency precise point positioning', *Inside GNSS* **7**(12), 30–35.

Vigny, C., Simons, W. J. F., Abu, S., Bamphenyu, R., Satirapod, C., Choosakul, N., Subarya, C., Socquet, A., Omar, K., Abidin, H. Z. & Ambrosius, B. A. C. (2005), 'Insight into the 2004 Sumatra-Andaman earthquake from GPS measurements in southeast Asia.', *Nature* **436**(7048), 201–6.

Wang, G.-Q., Boore, D. M., Tang, G. & Zhou, X. (2007), 'Comparisons of ground motions from colocated and closely spaced one-sample-per-second Global Positioning System and accelerograph recordings of the 2003 M 6.5 San Simeon, California, Earthquake in the Parkfield region', *Bulletin of the Seismological Society of America* **97**(1B), 76–90.

Wanninger, L. & May, M. (2000), Carrier phase multipath calibration of GPS reference stations, *in* 'Proceedings of ION GPS 2000', Salt Lake City, UT, pp. 113–124.

Weinbach, U. (2013), Feasibility and impact of receiver clock modeling in precise GPS data analysis, PhD thesis, Leibniz University of Hannover.

Wienia, R. J. (2008), Use of Global Ionospheric Maps for Precise Point Positioning, Master's thesis, Delft University of Technology.

Wright, T. J., Houlié, N., Hildyard, M. & Iwabuchi, T. (2012), 'Real-time, reliable magnitudes for large earthquakes from 1 Hz GPS precise point positioning: The 2011 Tohoku-Oki (Japan) earthquake', *Geophysical Research Letters* **39**(12).

Yarlagadda, R., Ali, I., Al-Dhahir, N. & Hershey, J. (2000), 'GPS GDOP metric', *IEE Proceedings - Radar, Sonar and Navigation* **147**(5), 259–264.

Ye, S., Chen, D., Liu, Y., Jiang, P., Tang, W. & Xia, P. (2015), 'Carrier phase multipath mitigation for BeiDou navigation satellite system', *GPS Solutions* **19**(4), 545–557.

Yeats, R. (2012), *Active Faults of the World*, Cambridge University Press, Cambridge.

Zhong, P., Ding, X., Yuan, L., Xu, Y., Kwok, K. & Chen, Y. (2010), 'Sidereal filtering based on single differences for mitigating GPS multipath effects on short baselines', *Journal of Geodesy* **84**(2), 145–158.

Zumberge, J. F., Heflin, M. B., Jefferson, D. C., Watkins, M. M. & Webb, F. H. (1997), 'Precise point positioning for the efficient and robust analysis of GPS data from large networks', *Journal of Geophysical Research* **102**(B3), 5005–5017.